

IntechOpen

Numerical Simulations -  
Examples and Applications  
in Computational Fluid  
Dynamics

*Edited by Lutz Angermann*





---

# **NUMERICAL SIMULATIONS - EXAMPLES AND APPLICATIONS IN COMPUTATIONAL FLUID DYNAMICS**

---

Edited by **Prof. Lutz Angermann**

## Numerical Simulations - Examples and Applications in Computational Fluid Dynamics

<http://dx.doi.org/10.5772/545>

Edited by Lutz Angermann

### Contributors

Pak Wai Chan, Koji Nagata, Hiroki Suzuki, Yasuhiko Sakai, Toshiyuki Hayase, Alexander Lelyakin, Wolfgang Breitung, Mike Kuznetsov, Eva Barreira, João Delgado, Nuno Ramos, Vasco Peixoto de Freitas, Yulin Wu, F.J. Rubio-Hernández, F.J. Galindo-Rosales, Takaaki Uda, Florin Ilinca, Jean-François Héту, Keh-Chia Yeh, Arash Mohammadi, Damian Obidowski, Zhiyong Liang, Genbao Zhang, Weiya Chen, Mohammad Mehdi Salek, Robert J. Martinuzzi, Hernan Tinoco, Michele La Rocca, Allen Bateman Pinzon, Yong-Gang Yu, Shan-Heng Yan, Qi Zhang, Na Zhao, Mohamed Safi, Kais Charfi, Kiminori Takahashi, Giuseppe Pezzella, Edoardo Bucchignani, Alfonso Matrone, Antonio Viviani

### © The Editor(s) and the Author(s) 2010

The moral rights of the and the author(s) have been asserted.

All rights to the book as a whole are reserved by INTECH. The book as a whole (compilation) cannot be reproduced, distributed or used for commercial or non-commercial purposes without INTECH's written permission.

Enquiries concerning the use of the book should be directed to INTECH rights and permissions department ([permissions@intechopen.com](mailto:permissions@intechopen.com)).

Violations are liable to prosecution under the governing Copyright Law.



Individual chapters of this publication are distributed under the terms of the Creative Commons Attribution 3.0 Unported License which permits commercial use, distribution and reproduction of the individual chapters, provided the original author(s) and source publication are appropriately acknowledged. If so indicated, certain images may not be included under the Creative Commons license. In such cases users will need to obtain permission from the license holder to reproduce the material. More details and guidelines concerning content reuse and adaptation can be found at <http://www.intechopen.com/copyright-policy.html>.

### Notice

Statements and opinions expressed in the chapters are those of the individual contributors and not necessarily those of the editors or publisher. No responsibility is accepted for the accuracy of information contained in the published chapters. The publisher assumes no responsibility for any damage or injury to persons or property arising out of the use of any materials, instructions, methods or ideas contained in the book.

First published in Croatia, 2010 by INTECH d.o.o.

eBook (PDF) Published by IN TECH d.o.o.

Place and year of publication of eBook (PDF): Rijeka, 2019.

IntechOpen is the global imprint of IN TECH d.o.o.

Printed in Croatia

Legal deposit, Croatia: National and University Library in Zagreb

Additional hard and PDF copies can be obtained from [orders@intechopen.com](mailto:orders@intechopen.com)

Numerical Simulations - Examples and Applications in Computational Fluid Dynamics

Edited by Lutz Angermann

p. cm.

ISBN 978-953-307-153-4

eBook (PDF) ISBN 978-953-51-5966-7

# We are IntechOpen, the world's leading publisher of Open Access books Built by scientists, for scientists

4,000+

Open access books available

116,000+

International authors and editors

120M+

Downloads

151

Countries delivered to

Our authors are among the  
Top 1%

most cited scientists

12.2%

Contributors from top 500 universities



WEB OF SCIENCE™

Selection of our books indexed in the Book Citation Index  
in Web of Science™ Core Collection (BKCI)

Interested in publishing with us?  
Contact [book.department@intechopen.com](mailto:book.department@intechopen.com)

Numbers displayed above are based on latest data collected.  
For more information visit [www.intechopen.com](http://www.intechopen.com)





# Meet the editor



Lutz Angermann is Professor of Numerical Mathematics in the Mathematical Institute of the University of Technology at Clausthal (Germany) since 2001. His research is concerned with the mathematical analysis of numerical algorithms for partial differential equations with special interests in finite volume and finite element methods. After the study of Mathematics at the University of Kharkov (Ukraine) he earned a Ph.D. from the University of Technology at Dresden in 1987. The University of Erlangen-Nürnberg awarded him a higher doctoral degree (habilitation) in 1995. From 1998 to 2001, he held the post of an Associate Professor of Numerical Mathematics at the University of Magdeburg. He is the author of about 65 scientific papers, among them two co-authored books on numerical methods for partial differential equations.



---

# Contents

---

**Preface** XIII

**Part 1 Flow Models, Complex Geometries and Turbulence** 1

Chapter 1 **Numerical Simulation in Steady flow of Non-Newtonian Fluids in Pipes with Circular Cross-Section** 3

F.J. Galindo-Rosales and F.J. Rubio-Hernández

Chapter 2 **Numerical Simulation on the Steady and Unsteady Internal Flows of a Centrifugal Pump** 23

Wu Yulin, Liu Shuhong and Shao Jie

Chapter 3 **Direct Numerical Simulation of Turbulence with Scalar Transfer Around Complex Geometries Using the Immersed Boundary Method and Fully Conservative Higher-Order Finite-Difference Schemes** 39

Kouji Nagata, Hiroki Suzuki,  
Yasuhiko Sakai and Toshiyuki Hayase

Chapter 4 **Preliminary Plan of Numerical Simulations of Three Dimensional Flow-Field in Street Canyons** 63

Liang Zhiyong, Zhang Genbao and Chen Weiya

Chapter 5 **Advanced Applications of Numerical Weather Prediction Models – Case Studies** 71

P.W. Chan

Chapter 6 **Hygrothermal Numerical Simulation: Application in Moisture Damage Prevention** 97

N.M.M. Ramos, J.M.P.Q. Delgado,  
E. Barreira and V.P. de Freitas

Chapter 7 **Computational Flowfield Analysis of a Planetary Entry Vehicle** 123

Antonio Viviani and Giuseppe Pezzella

- Chapter 8 **Numerical Simulation of Liquid-structure Interaction Problem in a Tank of a Space Re-entry Vehicle** 155  
Edoardo Bucchignani, Giuseppe Pezzella and Alfonso Matrone
- Chapter 9 **Three-Dimensional Numerical Simulation of Injection Moulding** 173  
Florin Ilinca and Jean-François Héту
- Chapter 10 **Numerical Simulation of Fluid Flow and Hydrodynamic Analysis in Commonly Used Biomedical Devices in Biofilm Studies** 193  
Mohammad Mehdi Salek and Robert John Martinuzzi
- Chapter 11 **Comparison of Numerical Simulations and Ultrasonography Measurements of the Blood Flow through Vertebral Arteries** 213  
Damian Obidowski and Krzysztof Jozwik
- Chapter 12 **Numerical Simulation of Industrial Flows** 231  
Hernan Tinoco, Hans Lindqvist and Wiktor Frid
- Part 2 Transport of Sediments and Contaminants** 263
- Chapter 13 **Numerical Simulation of Contaminants Transport in Confined Medium** 265  
Mohamed Jomaa Safi and Kais Charfi
- Chapter 14 **Experimental and Theoretical Modelling of 3D Gravity Currents** 281  
Michele La Rocca and Allen Bateman Pinzon
- Chapter 15 **Numerical Simulation of Sediment Transport and Morphological Change of Upstream and Downstream Reach of Chi-Chi Weir** 311  
Keh-Chia Yeh, Sam S.Y. Wang, Hungkwai Chen, Chung-Ta Liao, Yafei Jia and Yaoxin Zhang
- Chapter 16 **Model for Predicting Topographic Changes on Coast Composed of Sand of Mixed Grain Size and Its Applications** 327  
Takaaki Uda and Masumi Serizawa
- Part 3 Reacting Flows and Combustion** 359
- Chapter 17 **Numerical Simulation of Spark Ignition Engines** 361  
Arash Mohammadi

- Chapter 18 **Advanced Numerical Simulation of Gas Explosion for Assessing the Safety of Oil and Gas Plant 377**  
Kiminori Takahashi and Kazuya Watanabe
- Chapter 19 **Numerical Simulation of Radiolysis Gas Detonations in a BWR Exhaust Pipe and Mechanical Response of the Piping to the Detonation Pressure Loads 389**  
Mike Kuznetsov, Alexander Lelyakin and Wolfgang Breitung
- Chapter 20 **Experimental Investigation and Numerical Simulation on Interaction Process of Plasma Jet and Working Medium 413**  
Yong-gang Yu, Na Zhao, Shan-heng Yan and Qi Zhang



---

## Preface

---

In the recent decades, numerical simulation has become a very important and successful approach for solving complex problems in almost all areas of human life. This book presents a collection of recent contributions of researchers working in the area of numerical simulations. It is aimed to provide new ideas, original results and practical experiences regarding this highly actual field. The subject is mainly driven by the collaboration of scientists working in different disciplines. This interaction can be seen both in the presented topics (for example, problems in fluid dynamics or electromagnetics) as well as in the particular levels of application (for example, numerical calculations, modeling or theoretical investigations).

The papers are organized in thematic sections on computational fluid dynamics (flow models, complex geometries and turbulence, transport of sediments and contaminants, reacting flows and combustion). Since cfd-related topics form a considerable part of the submitted papers, the first volume is devoted to this area. The present second volume is thematically more diverse, it covers the areas of the remaining accepted works ranging from particle physics and optics, electromagnetics, materials science, electrohydraulic systems, and numerical methods up to safety simulation.

In the course of the publishing process it unfortunately came to a difficulty in which consequence the publishing house was forced to win a new editor. Since the undersigned editor entered at a later time into the publishing process, he had only a restricted influence onto the developing process of book. Nevertheless the editor hopes that this book will interest researchers, scientists, engineers and graduate students in many disciplines, who make use of mathematical modeling and computer simulation. Although it represents only a small sample of the research activity on numerical simulations, the book will certainly serve as a valuable tool for researchers interested in getting involved in this multidisciplinary field. It will be useful to encourage further experimental and theoretical researches in the above mentioned areas of numerical simulation.

**Lutz Angermann**

Institut für Mathematik, Technische Universität Clausthal,  
Erzstraße 1, D-38678 Clausthal-Zellerfeld  
Germany



# **Part 1**

## **Flow Models, Complex Geometries and Turbulence**



# Numerical Simulation in Steady flow of Non-Newtonian Fluids in Pipes with Circular Cross-Section

F.J. Galindo-Rosales<sup>1</sup> and F.J. Rubio-Hernández<sup>2</sup>

<sup>1</sup>*Transport Phenomena Research Center  
University of Porto, 4200-465 Porto*

<sup>2</sup>*Department of Applied Physics II  
University of Málaga, 29071 Málaga*

<sup>1</sup>*Portugal*  
<sup>2</sup>*Spain*

## 1. Introduction

In the chemical and process industries, it is often required to pump fluids over long distances from storage to various processing units and/or from one plant site to another. There may be a substantial frictional pressure loss in both the pipe line and in the individual units themselves. It is thus often necessary to consider the problems of calculating the power requirements for pumping through a given pipe network, the selection of optimum pipe diameter, measurement and control of flow rate, etc. A knowledge of these factors also facilitates the optimal design and layout of flow networks which may represent a significant part of the total plant cost (Chhabra & Richardson, 2008).

The treatment in this chapter is restricted to the laminar, steady, incompressible fully developed flow of a non-Newtonian fluid in a circular tube of constant radius. This kind of flow is dominated by shear viscosity. Then, despite the fact that the fluid may have time-dependent behavior, experience has shown that the shear rate dependence of the viscosity is the most significant factor, and the fluid can be treated as a purely viscous or time-independent fluid for which the viscosity model describing the flow curve is given by the Generalized Newtonian model. Time-dependent effects only begin to manifest themselves for flow in non-circular conduits in the form of secondary flows and/or in pipe fittings due to sudden changes in the cross-sectional area available for flow thereby leading to acceleration/deceleration of a fluid element. Even in these circumstances, it is often possible to develop predictive expressions purely in terms of steady-shear viscous properties (Chhabra & Richardson, 1999).

The kind of flow considered in this chapter has been already studied experimentally by Hagen Poiseuille in the first half of the XIX Century for Newtonian fluids and it has analytical solution. However, even though in steady state non-Newtonian fluids can be treated as purely viscous, the shear dependence of viscosity may result in differential equations too complex to permit analytical solutions and, consequently, it is needed to use numerical techniques to obtain numerical solutions. It is in this context when Computational Rheology plays its role

(Crochet et al., 1985). Existing techniques for solving Newtonian fluid mechanics problems have often been adapted with ease to meet the new challenge of a shear-dependent viscosity, the application of numerical techniques being especially helpful and efficacious in this regards (Tanner & Walters, 1998).

Most of the text books dealing with the problem of non-Newtonian fluids through pipes, with a few exceptions, put emphasis on the solution for the power-law fluids, while there are many other industrially important shear-dependent behaviors that are left out of consideration. Here it is intended to cover this gap with the help of numerical techniques.

## 2. Flow problems

In this section we will introduce physical laws governing the deformation of matter, known as *conservation equations* or *field equations*, which are general for any kind of material. After this we will introduce the *constitutive equations*, which provide the viscosity ( $\eta$ ) and the thermal conductivity ( $k$ ) as a function of the state. Moreover, in order to close the entire system of equations, we have to define the thermodynamic relationships between the state variables, which are intrinsic of the material considered in the problem of the fluid. Clearly, these relationships depend on the kind of fluid being considered. Then, the boundary and initial conditions are presented as the equations needed to particularize the flow problem and complete the set of equations in order to be resolved, analytical or numerically. All these equations are defined as a stepping-off point for the study of steady flow of non-Newtonian fluids in pipes with circular cross-section.

### 2.1 Governing equations

The term *fluid dynamics* stands for the investigation of the interactive motion of a large number of individual particles (molecules or atoms). That means, the density of the fluid is considered high enough to be approximated as a continuum. It implies that even an infinitesimally small (in the sense of differential calculus) element of the fluid still contains a sufficient number of particles, for which we can specify mean velocity and mean kinetic energy. In this way, we are able to define velocity, pressure, temperature, density and other important quantities at each point of the fluid.

The derivation of the principal equations of fluid dynamics is based on the fact that the dynamical behaviour of a fluid is determined by the following conservation laws, namely:

1. the conservation of mass<sup>1</sup>,
2. the conservation of momentum, and
3. the conservation of energy.

Hereafter, this set of equations will be known as the *field equations*. We have to supply two additional equations, which have to be thermodynamic relations between the state variables, like for example the pressure as a function of density and temperature, and the internal energy or the enthalpy as a function of pressure and temperature. Beyond this, we have to provide the viscosity ( $\eta$ ) and the thermal conductivity ( $k$ ) as a function of the state of the fluid, in order to

---

<sup>1</sup>In most of the processes occurring in chemical engineering, fluids are generally composed of different components and their concentrations might vary temporarily and spatially due to either potential chemical reactions or molecular diffusion, therefore it would be necessary to consider the conservation of mass for each component being present in the fluid. However, we will consider in this chapter that fluids are sufficiently homogeneous and no chemical reactions occur in it. Then, the conservation of mass can be applied to the fluid as it was composed of only one component.

close the entire system of equations. Clearly, these relationships depend on the kind of fluid being considered (Blazek, 2001), and therefore they will be known hereafter as *constitutive equations*. Then, it can be summarized as **the governing equations consist of field equations and constitutive equations**.

In the isothermal theory, the conservation of energy equation is decoupled from the conservations of mass and momentum. Therefore, the field equations are reduced to the equation of continuity (Equation 1), which is a formal mathematical expression of the principle of conservation of mass, and the stress equations of motion, which arise from the application of Newton's second law of motion to a moving continuum (or the principle of balance of linear momentum) and the local expression of the principle of balance of angular momentum (Equation 2).

$$\frac{\partial \rho}{\partial t} + \nabla \cdot (\rho \vec{v}) \quad (1)$$

$$\frac{\partial \rho \vec{v}}{\partial t} + \nabla \cdot (\rho \vec{v} \vec{v}) = \nabla \cdot \bar{\bar{\tau}} + \rho \vec{f}_m \quad (2)$$

Consequently, the thermal conductivity coefficient and the thermodynamic relations between the state variables are not needed to be known, because they will not participate in the solution of isothermal problems. For this reason, they will not be considered in the rest of the chapter, since we will focus in isothermal problems, without external sources of energy. However, we still require of a relationship between the stress tensor and the suitable kinematic variables expressing the motion of the continuum, i.e. we require of a rheological equation of state.

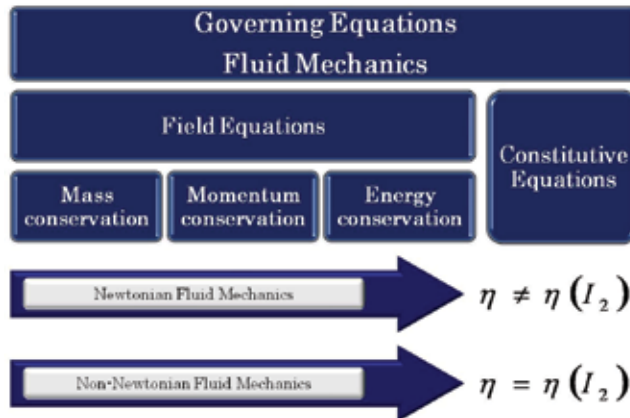


Fig. 1. The governing equations consist of field equations (conservations of mass, momentum and energy) and constitutive equations. The constitutive equations distinguish classical fluid mechanics from non-Newtonian fluid mechanics, due to Newton's viscosity law is valid for all flow situations (the viscosity is constant at any shear rate) and all Newtonian viscous fluids, but not for non-Newtonian fluids, for which their viscosities depend on the flow conditions ( $I_2$  is the second invariant of the tensor of shear rates) among other parameters.

Independently on whether the problem is isothermal or not, the viscosity relates the stress to the motion of the continuum. This equation for non-Newtonian fluids is also known as rheological equation of state. Whereas the field equations are the same for all materials, constitutive equation will in general vary from one non-Newtonian material to another,

and possibly from one type of flow to another. It is this last point which distinguishes non-Newtonian fluid mechanics from classical fluid mechanics, where the use of Newton's viscosity law gives rise to the Navier-Stokes equations, which are valid for all Newtonian viscous fluids (Crochet et al., 1985). Figure 1 shows a sketch of the governing equations. Finally, it will be also needed to define initial and boundary conditions in order to solve the specific problems.

### 2.1.1 Field equations for steady flow in pipes with circular cross-section

Independently on the constitutive equation, the stress tensor ( $\bar{\bar{\tau}}$ ) can be assumed as the sum of hydrostatic pressure, corresponding to a static state of the fluid ( $-p\bar{\bar{I}}$ ), and the viscous stresses ( $\bar{\bar{\tau}}'$ ), which represent the dynamic part of the stress tensor. In 1845, Stokes deduced a constitutive viscosity equation (Equation 3) generalizing Newton's idea, which is valid for many fluids, known as Newtonian fluids:

$$\bar{\bar{\tau}}' = \bar{\bar{A}} : \bar{\bar{\gamma}}, \quad (3)$$

where  $\bar{\bar{A}}$  is a fourth order tensor generally depending on time, position and velocity, and  $\bar{\bar{\gamma}}$  the deformation rate tensor<sup>2</sup>. For Newtonian fluids,  $\bar{\bar{A}}$  does not depend on velocity. Those fluids not accomplishing the Equation 3 are known as Non-Newtonian Fluids.

In the particular case of having an isotropic fluid, the Equation 3 simplifies considerably in Equation 4

$$\bar{\bar{\tau}}' = 2\eta \left[ \frac{1}{2} (\nabla \vec{v} + \nabla \vec{v}^T) - \frac{1}{3} \nabla \cdot \vec{v} \bar{\bar{I}} \right] + \eta_v \nabla \cdot \vec{v} \bar{\bar{I}}, \quad (4)$$

where  $\eta$  is the viscosity associated to the pure shear deformation of the fluid, and  $\eta_v$  is the volumetric viscosity coefficient and it is related to the volumetric deformation of the fluid due to normal forces. Then, for an isotropic fluid, the Navier-Stokes equation is obtained by introducing the Equation 4 in the Equation 2.

$$\rho \frac{\partial \vec{v}}{\partial t} + \nabla \cdot (\rho \vec{v} \vec{v}) = -\nabla p + \nabla \cdot \left[ \eta (\nabla \vec{v} + \nabla \vec{v}^T) \right] + \nabla \cdot \left[ \left( \eta_v - \frac{2}{3} \eta \right) \nabla \cdot \vec{v} \right] + \rho \vec{f}_m. \quad (5)$$

Moreover, if the fluid can be considered incompressible ( $\rho = cte$ ), the equation of continuity reduces to Equation 6

$$\nabla \cdot \vec{v} = 0, \quad (6)$$

and, consequently, the Equation 5 simplifies reaching the form given by Equation 7

$$\rho \left( \frac{\partial \vec{v}}{\partial t} + \vec{v} \cdot \nabla \vec{v} \right) = -\nabla p + \nabla \cdot \left[ \eta (\nabla \vec{v} + \nabla \vec{v}^T) \right] + \rho \vec{f}_m. \quad (7)$$

Reached this point, it is worth to point out that these reduced expressions of field equations (Equations 6 and 7) are only valid for an isotropic and incompressible fluid in isothermal conditions. It is now the moment of considering the simplifications of the field equations due to the facts that the fluid is flowing here in laminar steady state through an horizontal cross-section pipe (Figure 2).

<sup>2</sup>Also known as the rate-of-strain tensor:  $\bar{\bar{\gamma}} = \nabla \vec{v} + \nabla \vec{v}^T$ .

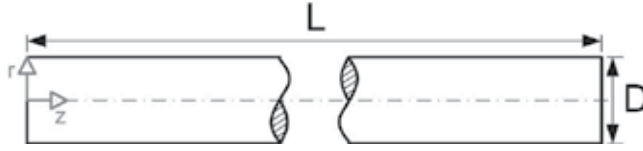


Fig. 2. Sketch of a pipe with length  $L$  and diameter  $D \ll L$ . The coordinates system here considered is cylindrical and its origin is placed and centered at the entrance of the pipe.

This is a canonical problem in Fluid Mechanics. The unidirectional and steady flow of a fluid through this pipe is originated by a constant gradient of reduced pressure  $p_l = -\frac{\partial(p+\rho U)}{\partial z} = cte$ , where  $U$  is a potential from which all massive forces derivate ( $\vec{f}_m = -\nabla U$ ) and  $z$  is the axial coordinate. It can be proved that the laminar and fully developed flow in a pipe is axysymmetric, i.e. there are not dependences with the azimuthal coordinate ( $\vec{e}_\theta$ ). Moreover, the  $r$ -component of vector  $\vec{v}$  is zero. From the continuity equation (Equation 6), it can be derived that  $\frac{dv_z}{dz} = 0$  and, consequently, the velocity vector expressed in cylindrical coordinates is given by Equation 8

$$\vec{v} = (v_r, v_\theta, v_z) = v_z \vec{e}_z, \quad (8)$$

with  $v_z = v_z(r)$ <sup>3</sup> Then, the deformation rate tensor is given by Equation 9

$$\nabla \vec{v} + \nabla \vec{v}^T = \begin{pmatrix} 0 & 0 & \frac{dv_z}{dr} \\ 0 & 0 & 0 \\ \frac{dv_z}{dr} & 0 & 0 \end{pmatrix}, \quad (9)$$

and, subsequently, the term  $\nabla \cdot [\eta (\nabla \vec{v} + \nabla \vec{v}^T)]$  in Equation 7 is reduced to the expression given by Equation 10

$$\nabla \cdot [\eta (\nabla \vec{v} + \nabla \vec{v}^T)] = \begin{pmatrix} 0 \\ 0 \\ \frac{1}{r} \frac{d}{dr} \left( r \eta \frac{dv_z}{dr} \right) \end{pmatrix}. \quad (10)$$

In this way, the field equations are reduced to a second order ordinary differential equation (Equation 11) (Landau & Lifshitz, 1987). It must be noticed that this equation is needed to be completed with two boundary conditions and a constitutive equation, but not initial condition because the flow is steady.

$$p_l + \frac{1}{r} \frac{d}{dr} \left( r \eta \frac{dv_z}{dr} \right) = 0 \quad (11)$$

<sup>3</sup>This dependence can be deduced from the fact that, while  $v_z$  is zero at  $r = D/2$  by the no-slip condition, in other  $r$ -value is that sure  $v_z$  is non-zero.

### 2.1.2 Boundary conditions

For a Newtonian fluid, the constitutive equation for the viscosity does not depend on the flow conditions and it is simply a constant coefficient  $\eta = cte$ . Therefore, the Equation 11 is linear and its general solution is given by Equation 12, where the values of the constants  $C_1$  and  $C_2$  will depend on the boundary conditions.

$$v_z(r) = -\frac{p_l r^2}{4\eta} + C_1 \ln r + C_2 \quad (12)$$

Classically, in Fluid Mechanics, these boundary conditions consists of the following ones:

- The **no-slip condition** holds that the particles of fluid adjacent to the wall of the pipe move with the wall velocity (Equation 13)

$$v_z(r = D/2) = 0. \quad (13)$$

- The **no-singularity condition** consists of assuming that  $v_z$  is a continuous function and its first derivative exists and is also continuous, therefore the Equation 14 must be accomplished

$$\frac{dv_z}{dr}(r = 0) = 0. \quad (14)$$

Then, the Equation 12 reduces to Equation 15, i.e. the velocity profile for a Newtonian, isotropic and incompressible fluid under laminar and steady flow through a circular cross-section pipe is parabolic, as studied experimentally by Hagen in 1839 and Poiseuille in 1840 (Papanastasiou et al., 2000).

$$v_z(r) = \frac{p_l}{4\eta} \left( \frac{D^2}{4} - r^2 \right) \quad (15)$$

However, when it is considered the laminar steady flow of a non-Newtonian fluid through this kind of pipes things change. Even though the no-singularity boundary condition still holds, the assumption of the no-slip condition is not as straightforward as it might seem. Rheologists have, for good reasons, been more concerned about the validity of the concept than workers in Newtonian fluid mechanics. With the benefit of decades of both theoretical and experimental interest, it is possible to assess that at least three factors are of importance concerning slip (Tanner & Walters, 1998):

- No effective slip can occur when molecular size is smaller than the wall roughness scale.
- For large molecules, relative to the wall roughness scale, the temperature and chemical adherence properties may be of great significance in setting the critical shear stress at which slip occurs.
- Normal pressure may assist in reducing slip.

Taking these factors about the slip at the wall into account, we will however assume that the no-slip boundary condition holds in all the cases here considered.

### 2.1.3 Constitutive equations for non-newtonian fluids

Constitutive equations (or rheological equations of state) are equations relating suitably defined stress and deformation variables (Barnes et al., 1993). The simplest example is the constitutive law for the Newtonian viscous liquid (Equation 16), where a constant viscosity coefficient is sufficient to determine the behaviour of incompressible Newtonian liquids under any conditions of motion and stress. The measurement of this viscosity coefficient involves the use of a *viscometer*, defined simply as *an instrument for the measurement of viscosity*.

$$\overline{\tau}^T = \eta \overline{\dot{\gamma}} \quad (16)$$

However, as the viscosity of non-Newtonian liquids may be dependent on the flow conditions, i.e. the rate-of-strain tensor, the viscometer is therefore inadequate to characterize the behaviour of these materials and has to be replaced by a *rheometer*, defined as *an instrument for measuring rheological properties*. One of the objectives of Rheometry is to assist in the construction of rheological equations of state (Walters, 1975).

If non-Newtonian viscosity, a scalar, is dependent on the rate-of-strain tensor, then it must depend only on those particular combination of components of the tensor that are not dependent on the coordinate system, the invariants of the tensor (Bird et al., 1987):

- $I_1 = \sum_{i=1}^3 \dot{\gamma}_{ii}$ .
- $I_2 = \sum_{i=1}^3 \sum_{j=1}^3 \dot{\gamma}_{ij} \dot{\gamma}_{ji}$ .
- $I_3 = \sum_{i=1}^3 \sum_{j=1}^3 \sum_{k=1}^3 \dot{\gamma}_{ij} \dot{\gamma}_{jk} \dot{\gamma}_{ki}$ .

It can be deduced with ease that  $I_1 = 0$  for an incompressible fluid. In addition,  $I_3$  turns out to be zero for shearing flows. Hence, for the flow problems here considered,  $\eta$  is solely dependent on  $I_2$ . Actually, it is preferred to use  $\dot{\gamma}$ , the magnitude of the rate-of-strain tensor ( $\overline{\dot{\gamma}}$ ), instead of  $I_2$ , being both parameters related by the Equation 17 (Macosko, 1994)

$$\dot{\gamma} = \sqrt{\frac{1}{2} \sum_{i=1}^3 \sum_{j=1}^3 \dot{\gamma}_{ij} \dot{\gamma}_{ji}} = \sqrt{\frac{1}{2} I_2}. \quad (17)$$

As this chapter is devoted to the steady flow of non-Newtonian fluids in pipes with circular cross-section, which is a kind of flow dominated by shear viscosity and where the elasticity of the fluid has no considerable repercussions, the most suitable constitutive equation is given by the Generalized Newtonian Model (GNM) given by Equation 18. This is an inelastic model for which the extra stress tensor is proportional to the strain rate tensor, but the “constant” of proportionality (the viscosity) is allowed to depend on the strain rate. The inelastic model possesses neither memory nor elasticity, and therefore it is unsuitable for transient flows, or flows that calls for elastic effects (Phan-Thien, 2002).

$$\overline{\tau}^T = \eta(\dot{\gamma}) \overline{\dot{\gamma}} \quad (18)$$

Consequently, Equation 11 can be rewritten for non-Newtonian liquids as Equation 19

$$p_l + \frac{1}{r} \frac{d}{dr} \left( r \eta(\dot{\gamma}) \frac{dv_z}{dr} \right) = 0. \quad (19)$$

The GNM is quite general because the functional form of  $\eta(\dot{\gamma})$  is not specified. It must be given or fit the data to predict the flow properties. We will introduce different models for

$\eta(\dot{\gamma})$ , but many other functional forms can be used and these can be found in the literature or in flow simulation softwares. Before that, it is important to keep in mind the main limitations of the GNM (Morrison, 2001):

- They rely on the modeling shear viscosity to incorporate non-Newtonian effects, and therefore it is not clear whether these models will be useful in nonshearing conditions.
- They do not predict shear normal stresses  $N_1$  and  $N_2$ , which are elastic effects, and therefore they can not consider memory effects.

Nevertheless, the GNM enjoys success in predicting pressure-drop versus flow curves for steady flow of non-Newtonian fluids in pipes with circular cross-section.

As it has been mentioned above, it is possible to obtain  $\eta(\dot{\gamma})$  by means of experiments carried out in a rheometer. In a shear rheometer, the material is undergone to simple shear conditions, for which the rate-of-strain tensor is given by the Equation 20

$$\bar{\dot{\gamma}} = \left( \nabla \vec{v} + \nabla \vec{v}^T \right) \cong \begin{pmatrix} 0 & 0 & 0 \\ 0 & 0 & \frac{dv_\theta}{dz} \\ 0 & \frac{dv_\theta}{dz} & 0 \end{pmatrix}, \quad (20)$$

whose invariants are the following ones:

- $I_1 = tr(\bar{\dot{\gamma}}) = 0$
- $I_2 = 2 \left( \frac{dv_\theta}{dz} \right)^2$
- $I_3 = det(\bar{\dot{\gamma}}) = 0$

In the case of a steady flow in pipes with circular cross-section, the rate-of-strain tensor is given by the Equation 9 and its invariants are the following ones:

- $I_1 = tr(\bar{\dot{\gamma}}) = 0$
- $I_2 = 2 \left( \frac{dv_z}{dr} \right)^2$
- $I_3 = det(\bar{\dot{\gamma}}) = 0$

It can be observed that in both flow conditions the fluid is undergone to simple shear and it can be stated that  $\dot{\gamma} = \sqrt{\frac{|I_2|}{2}} = \left| \frac{dv_\theta}{dz} \right| = \left| \frac{dv_z}{dr} \right|$ . Then, the shear dependence of the viscosity in steady state observed in the rheological experiments could be used directly in Equation 19. It has been already probed that the experimental data obtained with a rheometer can be used successfully for the prediction of the transport characteristic in pipelines (Masalova et al., 2003).

### 2.1.3.1 GNM for shear thinning fluids

Most of non-Newtonian fluids (foods, biofluids, personal care products and polymers) undergone to steady shear exhibit shear thinning behavior, i.e. their viscosity decreases with increasing shear rates. During flow, these materials may exhibit three distinct regions (see Figure 3): a lower Newtonian region where the apparent viscosity ( $\eta_0$ ), usually called the limiting viscosity at zero shear rate, is constant with changing shear rates; a middle region where the apparent viscosity is decreasing with shear rate and the power law equation is

a suitable model for this region; and an upper Newtonian region where the viscosity ( $\eta_\infty$ ), called the limiting viscosity at infinite shear rate, is constant with changing shear rates (Steffe, 1996). Sometimes the position of the typical behaviour along the shear-rate axis is such that the particular measurement range used is either too low or too high to pick up the higher-shear-rate part of the curve<sup>4</sup>.

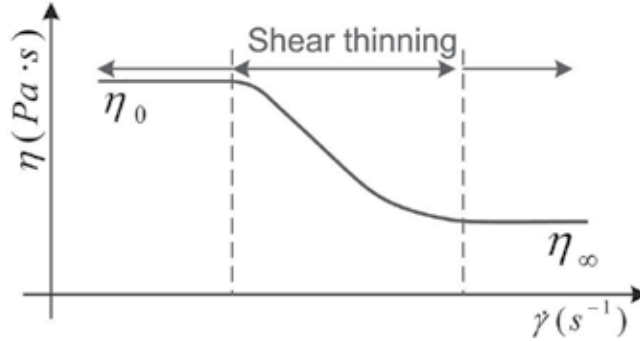


Fig. 3. Typical viscosity curve for a shear thinning behaviour containing the three regions: The two limiting Newtonian viscosities,  $\eta_0$  and  $\eta_\infty$ , separated by a shear thinning region.

One equation for  $\eta(\dot{\gamma})$  that describes the whole shear thinning curve is called the Cross model, named after Malcolm Cross, a rheologist who worked on dye-stuff and pigment dispersions. He found that the viscosity of many suspensions could be described by the equation of the form given by Equation 21

$$\eta(\dot{\gamma}) = \eta_\infty + \frac{\eta_0 - \eta_\infty}{1 + (K\dot{\gamma})^m}, \quad (21)$$

where  $K$  has the dimensions of time, and  $m$  is dimensionless. The degree of shear thinning is dictated by the value of  $m$ , with  $m$  tending to zero describes more Newtonian liquids, while the most shear-thinning liquids have a value of  $m$  tending to unity. If we make various simplifying assumptions, it is not difficult to show that the Cross equation can be reduced to Sisko<sup>5</sup> or power-law models<sup>6</sup>. The Carreau model is very similar to the Cross model (Equation 22)

$$\eta(\dot{\gamma}) = \eta_\infty + \frac{\eta_0 - \eta_\infty}{[1 + (K\dot{\gamma})^2]^{m/2}}, \quad (22)$$

both (Cross and Carreau equations) are the same at very low and very high shear rates, and only differ slightly at  $K\dot{\gamma} \approx 1$  (Barnes, 2000).

The use of Cross or Carreau models in the Equation 19 results in a differential equation that can not be solved analytically and, therefore, numerical techniques are needed.

It is worth to emphasize here that due to the boundary condition of no-singularity imposed at the axis of symmetry, it is highly important choosing a model which contains what happens to the viscosity at low shear rates in order to solve this problem.

<sup>4</sup>Note that the typical shear-rate range of most laboratory viscometers is between  $10^{-2}$  and  $10^3 \text{ s}^{-1}$

<sup>5</sup>When the viscosity is just coming out of the power-law region of the flow curve and flattening off towards  $\eta_\infty$ , the Sisko model is the best fitting equation:  $\eta(\dot{\gamma}) = \eta_\infty + k\dot{\gamma}^{n-1}$ .

<sup>6</sup>In many situations,  $\eta_0 \gg \eta_\infty$ ,  $K\dot{\gamma} \gg 1$ , and  $\eta_\infty$  is small. Then the Cross equation (with a simple change of the variables  $K$  and  $m$ ) reduces to the well-known power-law (or Ostwald-de Waele) model, which is given by  $\eta(\dot{\gamma}) = k\dot{\gamma}^{n-1}$ , where  $k$  is called the consistency and  $n$  the power-law index.

### 2.1.3.2 GNM for shear thickening fluids

Shear thickening is defined in the British Standard Rheological Nomenclature as the increase of viscosity with increase in shear rate (Barnes, 1989). This increase in the effective viscosity occurs when the increasing shear rate exceeds a certain critical value. Although shear thickening fluids (STFs) are much less common than shear thinning materials in industry, an increasing number of applications take advantage of the shear thickening behaviour to improve their performance, i.e. the incorporation of STFs to Kevlar<sup>®</sup> fabrics in order to improve the ballistic protection (Lee et al., 2003; Kirkwood et al., 2004) and enhance stab resistance (Decker et al., 2007). However, shear thickening is an undesirable behaviour in many other cases and it should never be ignored, because this could lead to technical problems and even to the destruction of equipment, i.e. pumps or stirrers (Mezger, 2002).

Figure 4 shows the viscosity curve of a STF containing the three characteristic regions typically exhibited: slight shear thinning at low shear rates, followed by a sharp viscosity increase over a threshold shear rate value (critical shear rate), and a subsequent pronounced shear thinning region at high shear rates. Nowadays, the physics of the phenomenon is deeply understood thanks to the use of modern rheometers, scattering techniques, rheo-optical devices and Stokesian dynamic simulations (Bender & Wagner, 1996; Hoffman, 1974; Boersma et al., 1992; D'Haene et al., 1993; Hoffman, 1998; Maranzano & Wagner, 2002; Larson, 1999). However, there is a lack of experimental or theoretical models able to predict the whole effective viscosity curve of STFs, including the shear thinning behaviours normally present in these materials for low enough and high enough values of the shear rate.

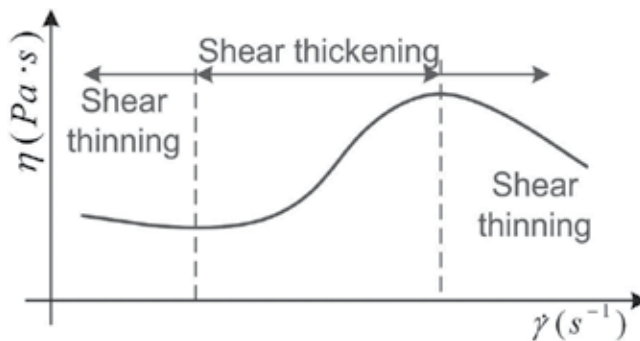


Fig. 4. Typical viscosity curve for a shear thickening behaviour containing the three regions: The two limiting shear thinning behaviours separated by a shear thickening region.

As it has been mentioned above, many functional forms have been proposed in the past for  $\eta(\dot{\gamma})$  in the case of shear thinning fluids. In contrast, for shear thickening fluids only the power-law model, given by (Equation 23), has been commonly used

$$\eta(\dot{\gamma}) = k\dot{\gamma}^{n-1}. \quad (23)$$

Its major drawback is that power-law model can only fit the interval of shear rates where the viscosity increases with the shear rate  $n > 1$ , but it fails to describe the low and the high shear rate regions (Macosko, 1994), where shear-thinning behaviours are normally observed.

Very recently, Galindo-Rosales et al. (2010) have provided a viscosity function for shear thickening behavior able to cover these three characteristic regions of the general viscosity curve exhibited by STF. It consists in using a piecewise definition, taking the three different

regions into account separately. According to this approach, they have defined the viscosity function as follows,

$$\eta(\dot{\gamma}) = \begin{cases} \eta_I(\dot{\gamma}) & \text{for } \dot{\gamma} \leq \dot{\gamma}_c, \\ \eta_{II}(\dot{\gamma}) & \text{for } \dot{\gamma}_c < \dot{\gamma} \leq \dot{\gamma}_{max}, \\ \eta_{III}(\dot{\gamma}) & \text{for } \dot{\gamma}_{max} < \dot{\gamma}, \end{cases} \quad (24)$$

where  $\eta_i(\dot{\gamma})$  is the viscosity function that fits the zone  $i$  of the general viscosity curve (for  $i = I, II, III$ ). As it was pointed out by Souza-Mendes & Dutra (2004), the functions  $\eta_i$  must be chosen such that both, the composite function given by Equation 24, as well as its derivative with respect to  $\dot{\gamma}$ , are continuous. This procedure avoids practical problems in fitting procedures and in numerical simulations. The viscosity function proposed in the work of Galindo-Rosales et al. (2010), given by Equation 25, accomplishes these smoothness requirements.

$$\eta(\dot{\gamma}) = \begin{cases} \eta_I(\dot{\gamma}) = \eta_c + \frac{\eta_0 - \eta_c}{1 + [K_I \left( \frac{\dot{\gamma}^2}{\dot{\gamma} - \dot{\gamma}_c} \right)]^{n_I}} & \text{for } \dot{\gamma} \leq \dot{\gamma}_c, \\ \eta_{II}(\dot{\gamma}) = \eta_{max} + \frac{\eta_c - \eta_{max}}{1 + [K_{II} \left( \frac{\dot{\gamma} - \dot{\gamma}_c}{\dot{\gamma} - \dot{\gamma}_{max}} \right) \dot{\gamma}]^{n_{II}}} & \text{for } \dot{\gamma}_c < \dot{\gamma} \leq \dot{\gamma}_{max}, \\ \eta_{III}(\dot{\gamma}) = \frac{\eta_{max}}{1 + [K_{III}(\dot{\gamma} - \dot{\gamma}_{max})]^{n_{III}}} & \text{for } \dot{\gamma}_{max} < \dot{\gamma}. \end{cases} \quad (25)$$

It must be noticed that the parameters appearing in the branches of Equation 25 have the same dimensions and interpretation than those analogous for the Cross model (Equation 21):  $K_i$  (for  $i = I, II, III$ ) possess dimension of time and are responsible for the transitions between the plateaus and the power-law, while the dimensionless exponents  $n_i$  are related to the slopes of the power-law regimes. Equation 25 is able to capture the three regimes characteristic of STF materials.

Then, substituting any the form of  $\eta(\dot{\gamma})$  given in Equation 25 in the Equation 19 will results in a differential equation that can not be solved analytically and, therefore, numerical techniques will be needed again.

### 3. Numerical simulations

Classical Fluid Mechanics offers a wide variety of possibilities with regards to numerical algorithms based on finite elements, finite volume, finite differences and spectral methods (Wesseling, 2001). Computational rheologists do not have a recipe which lets them know which one is more suitable to work with in each particular problem, although most of the published works related to solve 2-D problems in steady state are based on finite element methods (Keunings, 1999). However, it has been proved that finite volume methods produce better results (O'Callaghan et al., 2003) due mainly to a good conservation of the fluid properties (mass, momentum and energy) and they allow to discretize complex computational domain in a simpler way (Fletcher, 2005).

The problem considered here, because of its geometrical features, can be solved by any of the numerical techniques already mentioned, although we have finally used the finite volume technique (Pinho & Oliveira, 2001; Pinho, 2001). As the flow problem is axysymmetric, the volume domain can be simplified to a 2-D domain with a length<sup>7</sup> ( $L = 2$  m) and a width

<sup>7</sup>Its lenght is long enough to ensure that the regime of fully developed flow is reached.

( $D = 1 \text{ cm} \ll L$ ). This domain is meshed by rectangles in a structured grid: in  $z$ -axis from the inlet (ratio 1.05 and 500 nodes) and  $r$ -axis from the axis (ratio 1.0125 and 50 nodes), which has been validated by correlating the analytical and numerical results given for the case of a Newtonian fluid (Figure 5).

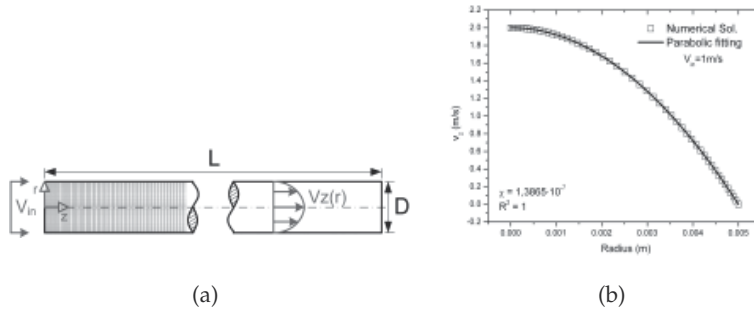


Fig. 5. (a) Horizontal pipeline with  $L \gg R$  in order to ensure that the flow reaches the fully developed region. (b) Validation of the grid by means of the comparison between the numerical result and the analytical solution of the fully developed velocity profile for a Newtonian liquid.

As a consequence of the friction drag, there is a pressure drop. The energy required to compensate the dissipation due to frictional losses against the inside wall and to keep the fluid moving is usually supported by a pump. A large amount of data obtained experimentally for many different Newtonian fluids in pipes having diameters differing by orders of magnitude and roughness have been assembled into the so-called friction-factor chart or Moody chart, relating the friction factor with Reynolds number in laminar and turbulent regime and relative roughness. In laminar flow, the friction factor does not depend on the roughness of the inner surface of the pipe and can be calculated by the Equation 26

$$f = \frac{16}{Re'} \quad (26)$$

where  $f$  is the friction factor and  $Re$  is the Reynolds number. Nevertheless, when the fluid is non Newtonian, the Moody chart and the Equation 26 are useless due to in non-Newtonian fluids there is an extra dissipation of energy spent in modifying the internal structure of the fluid<sup>8</sup>. It then is needed to analyse the particular flow behaviour of the fluid considered, obtain its constitutive equation and solve the momentum conservation equation in order to characterize the steady flow in a pipe of circular cross-section.

As an example of how to proceed, two different non-Newtonian fluids (shear thinning and shear thickening fluids) are considered here. Firstly, their constitutive forms for  $\eta(\dot{\gamma})$  will be obtained from their experimental viscosity curves. Secondly, the momentum conservation equation in the steady state (Equation 19), considering axisymmetry and a cylindrical coordinate system centered in the axis of the pipe, will be solved numerically by volume finite methods. In order to have shear rates values within the limits of the experimental results for each sample, the velocity inlet was always imposed at values below 0.1 m/s. Thus, the

<sup>8</sup>As it is outlined in the following subsection, the variations in the viscosity are due to variation in the internal order of the fluid, which is possible thanks to the mechanical energy supplied by the shearing motion.

velocity profile, shear rate, apparent viscosity, pressure drop and friction factor were obtained for each sample as function of velocity.

### 3.1 Experimental data set

Aerosil<sup>®</sup> fumed silica is a synthetic, amorphous and non-porous silicon dioxide produced by Degussa A.G (Degussa, 1998) following a high temperature process. Aerosil<sup>®</sup> 200 presents a highly hydrophilic surface chemistry with surface silanol groups ( $Si - OH$ ) that can participate in hydrogen bonding. Because of the relatively high surface area ( $200m^2/g$ ) of these particles, the surface functional groups play a major role in the behavior of fumed silica Degussa (2005a). In the unmodified state, the silanol group imparts a hydrophilic character to the material. However, it is possible to modify its surface chemistry by means of a chemical after treatment with silane. In this way, Aerosil<sup>®</sup> R805 is obtained from Aerosil<sup>®</sup> 200 particles by replacing silanol groups with octadecylsilane chains, which results in an hydrophobic behaviour of the particles (Degussa, 2005b).

The degree of network formation by fumed silica in a liquid depends on the concentration of solid and type (hydrophilic versus hydrophobic) of silica, as well as the nature (polarity) of the suspending medium. Therefore, these three main factors allow to the suspensions of Aerosil<sup>®</sup> fumed silica inside a fluid possess a variety of rheological behaviors (Khan & Zoeller, 1993; Raghavan & Khan, 1995). This variety of rheological behaviors makes silica particle a very interesting filler from the point of view of a wide range of applications. For example, gels of fumed silica in mineral or silicone oils are used as filling compounds in fiber-optic cables, while in polyethylene glycols are being considered for application as polymer electrolytes in rechargeable lithium batteries (Jáuregui Belouqui & Martin Martinez, 1999; Dolz et al., 2000; Walls et al., 2000; Li et al., 2002; Fischer et al., 2006; Yziquel et al., 1999; Ouyang et al., 2006).

It has been already reported elsewhere (Galindo-Rosales & Rubio-Hernández, 2007; 2010) that suspensions of Aerosil<sup>®</sup> R805 and Aerosil<sup>®</sup> 200 in Polypropylene Glycol (PPG) with a molecular weight of 400 g/mol exhibit completely different rheological behaviour. PPG molecules interfere in the formation of the fumed silica network by attaching itself to the active  $Si - OH$  sited on the silica surface. Therefore no bridging between silica particles occurs with polar solvents, such as polypropylene glycol, that have a stronger affinity for fumed silica than that existing between two fumed silica. The solvent attaches itself to the surface silanol group of the fumed silica rendering it inactive for further network formation. For that reason, when dispersing Aerosil<sup>®</sup> 200 in polypropylene glycol, it is expected that primary aggregates interconnect, originating flocs with different sizes depending on the weight fraction. On the contrary, a large interconnection between the flocs, which may result in a three dimensional structure, should not take place. Therefore, the suspension would be non-flocculated (Raghavan & Khan, 1997; Raghavan et al., 2000). However the presence of octadecylsilane chemical bonds on the surface of Aerosil<sup>®</sup> R805 avoids that PPG molecules attached to the silica particles and lets them develop a three dimensional network without interacting chemically with polypropylene glycol chains. So a flocculated suspension is formed (Khan & Zoeller, 1993).

The steady viscosity curves, shown in Figure 6, represent the steady viscosity reached by the suspensions at different values of shear rates. Therefore, the shape of these curves is a consequence of the order achieved by silica particles inside the polymer matrix under flow conditions. According to the previous analysis, Aerosil<sup>®</sup> R805 suspension is flocculated after a long time at rest, and the network breaks down when subjected to shear, a behavior known as shear thinning. Figure 6 confirms that the higher the shear rate applied, the lower the apparent

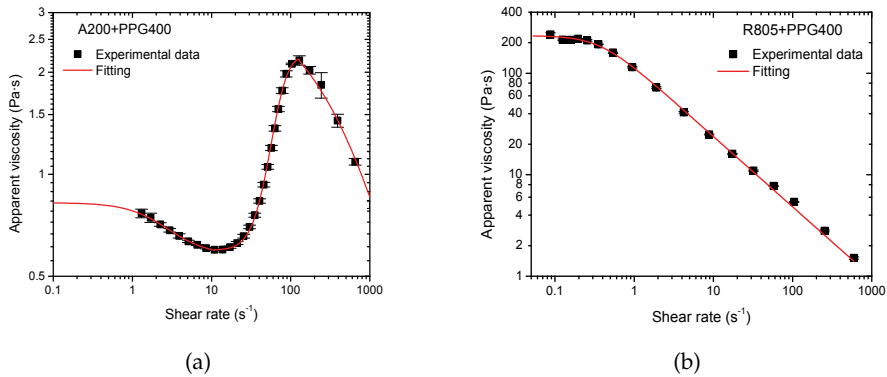


Fig. 6. Steady viscosity curve of A200 (a) and R805 (b) suspension in PPG400 at 5 %v/v and 25 °C fitted by Equation 25 and Carreau model, respectively.

steady viscosity value. As the interconnection between flocs and aggregates disappear under the action of shear stress, the resistance to the flow decreases. On the other hand, the Aerosil® 200 suspension presents a flow curve in which three zones can be distinguished. At low shear rates, there is a reversible and slight shear thinning region ( $\dot{\gamma} \leq 10.91 \pm 0.05 \text{ s}^{-1}$ ). In the interval of shear rates between  $10.91 \pm 0.05 \text{ s}^{-1}$  and  $129 \pm 4 \text{ s}^{-1}$ , the viscosity increases with the shear rate (shear thickening). Finally, at high shear rates ( $\dot{\gamma} \geq 129 \pm 4 \text{ s}^{-1}$ ), the viscosity decreases again in a more pronounced way. This shape of the flow curve is a consequence of the internal microstructure developed by the nanoparticles, and it is characteristic for non-flocculated suspensions, in agreement with the results and analysis presented above. At low shear rates the decrease in the viscosity is a consequence of the effect that the supplied mechanical energy has on the existing flocs. Under shear, agglomerates either break down into smaller sizes or stretch aligning in the flow direction. Both contribute to decrease the resistance to the flow and, subsequently, a viscosity descend. The higher the shear rate applied, the more prominent is this effect. However, when the shear rate is higher than a critical value  $\dot{\gamma}_c$ , the flocs are forced to connect to each other by hydrodynamic forces. This structure formation during flow results in an increase of the flow resistance and, therefore, leads to an increase of viscosity, as well as to the presence of the shear thickening region observed in Figure 6. However, this situation is metastable. When shear rate is higher than a maximum value ( $\dot{\gamma}_m$ ), the stability of the structure developed under flow is lost and the structure breaks down, decreasing the viscosity (Vermant & Solomon, 2005). Shear thickening is not expected at such low volume fraction (Barnes, 1989). Actually, this fact can be explained only by taking into consideration the difference of aggregation between Euclidean and fractal solids. As consequence of their fractal nature, individual silica particles are linked forming open primary aggregates, leading to an effective dispersed phase volume  $\phi_{eff}$  much larger than the nominal one,  $\phi_s$  (Raghavan & Khan, 1997).

The equilibrium viscosity curves of the Aerosil® R805 suspension here considered, shown in Figure 6, can be fitted very accurately by Carreau Model, whose equation is given by Equation 22. This form of  $\eta(\dot{\gamma})$  is able to predict the shape of the general flow curve for shear thinning behavior because of its four parameters (see Figure 6)<sup>9</sup>.

<sup>9</sup>Non-linear least-squares regression method based on the Levenberg-Marquardt algorithm has been

Substituting Equation 22 in Equation 19, the differential equation which predicts the laminar, steady and fully developed velocity profile of our samples when they would flow through a duct is obtained (Equation 27)

$$p_l + \frac{1}{r} \frac{d}{dr} \left[ r \left( \eta_\infty + \frac{\eta_0 - \eta_\infty}{\left[ 1 + \left( K \left| \frac{dv_z}{dr} \right| \right)^2 \right]^{m/2}} \right) \frac{dv_z}{dr} \right] = 0, \quad (27)$$

whose boundary conditions are the same exposed above.

The equilibrium viscosity curves of the Aerosil<sup>®</sup> 200 suspension is also shown in Figure 6 and it can be fitted very accurately by Equation 25. This form of  $\eta(\dot{\gamma})$  is able to predict the shape of the general flow curve for shear thickening behavior because of its eleven parameters (see Figure 6).

Substituting Equation 25 in Equation 19, a set of three differential equations is obtained (Equations 28), which predicts the laminar, steady and fully developed velocity profile of the suspension of A200 in PPG 400 at 5 %v/v and 25 °C, not having any of them analytical solutions. In order to solve them, numerical methods are needed.

$$\begin{aligned} p_l + \frac{1}{r} \frac{d}{dr} \left[ r \left( \eta_c + \frac{\eta_0 - \eta_c}{1 + \left[ K_I \left( \frac{\left| \frac{dv_z}{dr} \right|^2}{\left| \frac{dv_z}{dr} \right| - \dot{\gamma}_c} \right)^{n_I} \right]} \right) \frac{dv_z}{dr} \right] &= 0 & \text{for } \left| \frac{dv_z}{dr} \right| \leq \dot{\gamma}_c, \\ p_l + \frac{1}{r} \frac{d}{dr} \left[ r \left( \eta_{max} + \frac{\eta_c - \eta_{max}}{1 + \left[ K_{II} \left( \frac{\left| \frac{dv_z}{dr} \right| - \dot{\gamma}_c}{\left| \frac{dv_z}{dr} \right| - \dot{\gamma}_{max}} \right)^{n_{II}}} \right) \frac{dv_z}{dr} \right] &= 0 & \text{for } \dot{\gamma}_c < \left| \frac{dv_z}{dr} \right| \leq \dot{\gamma}_{max}, \\ p_l + \frac{1}{r} \frac{d}{dr} \left[ r \left( \frac{\eta_{max}}{1 + \left[ K_{III} \left( \left| \frac{dv_z}{dr} \right| - \dot{\gamma}_{max} \right)^{n_{III}} \right]} \right) \frac{dv_z}{dr} \right] &= 0 & \text{for } \dot{\gamma}_{max} < \left| \frac{dv_z}{dr} \right|. \end{aligned} \quad (28)$$

### 3.2 Results and discussion

Here are exhibited the results obtained from solving numerically the differential equations defined above.

Figure 7 shows the velocity profiles normalized by its maximum value, which is reached at the axis of symmetry (at  $r = 0$ ), for the suspensions of A200 and R805 in PPG400 at 5 %v/v and 25 °C. It can be observed that both do not follow a parabolic profile, as it would be the Newtonian case. In spite of this, their velocity profiles depend on the velocity impose at the inlet of the pipe.

Different velocity profiles imply different shear rates across the section of the pipe, varying from zero at the axis of symmetry to its highest value at the neighborhood of the wall. In addition, the shear rates are higher for higher values of the inlet velocity, as it is shown in Figure 8.

It is noticeable that in the case of the A200, due to its shear thickening behavior, the viscosity increases with the velocity inlet and in the vicinity of the solid wall, where the shear rates are higher, in opposition what happen to R805 suspension. Around the axis, the shear conditions

used to fit the experimental data to the models here considered.

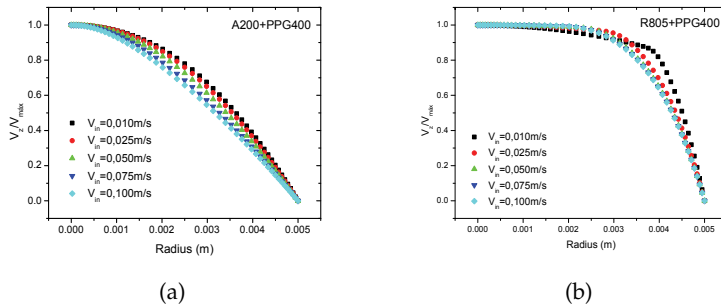


Fig. 7. Velocity profiles normalized by its maximum value, which is reached at the axis of symmetry (at  $r = 0$ ), for the suspensions of A200 (a) and R805 (b) in PPG400 at 5 %v/v and 25 °C.

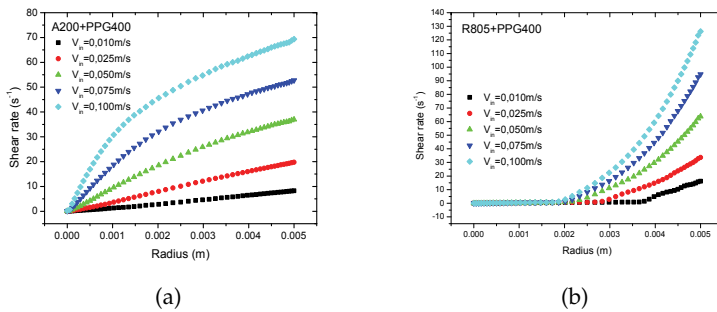


Fig. 8. Shear rate evolution across the section of the pipe in the fully developed region for the suspensions of A200 (a) and R805 (b) in PPG400 at 5 %v/v and 25 °C.

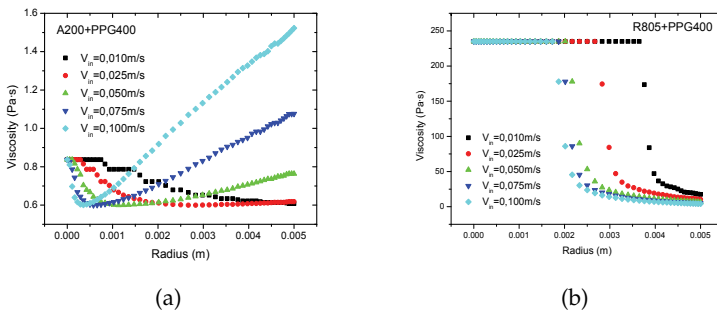


Fig. 9. Variation of the steady viscosity across the section of the pipe in the fully developed region for the suspensions of A200 (a) and R805 (b) in PPG400 at 5 %v/v and 25 °C.

are almost null, what implies that in the A200 suspension the viscosity is relatively low, and relatively high for the R805, according to their viscosity curves (Figure 9). Therefore, that results in different shapes of the velocity profile, which is sharper for the shear thickening suspension and flatter for the one with shear thinning behavior (Figure 7).

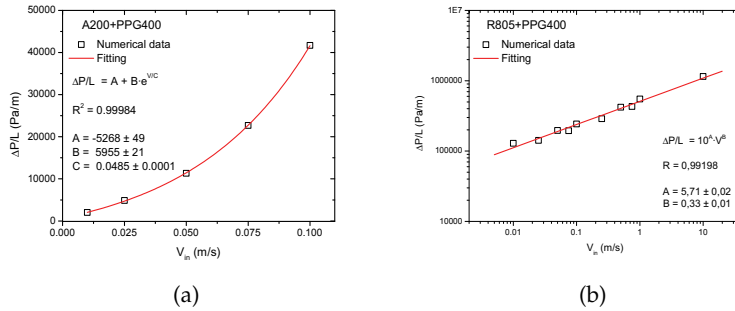


Fig. 10. Pressure-drop per unit of length of the duct as a function of the velocity inlet. Results for the suspensions of A200 (a) and R805 (b) in PPG400 at 5 %v/v and 25 °C.

Non linear differences in the viscosity with the inlet velocity will result in differences in the pressure losses with regards to Hagen-Poiseuille solution. The pressure-drop per meter of pipe is shown in Figure 10 for different values of velocity inlet. It must be notice that the Reynolds number has not been used for those graphs, the reason is that this is a non-dimensional parameter useful when the viscosity is constant and here it is not the case. For a Newtonian flow, it is already known that pressure losses are proportional to the velocity inlet, however, in the case of non-Newtonian fluids, it would depend of their rheological behavior. In the case under study, the pressure-drop for a shear thickening behavior grows exponentially with the velocity inlet, while for the shear thinning one it does potentially. The values of losses are much higher for the case of R805 suspension, due to its higher viscosity values.

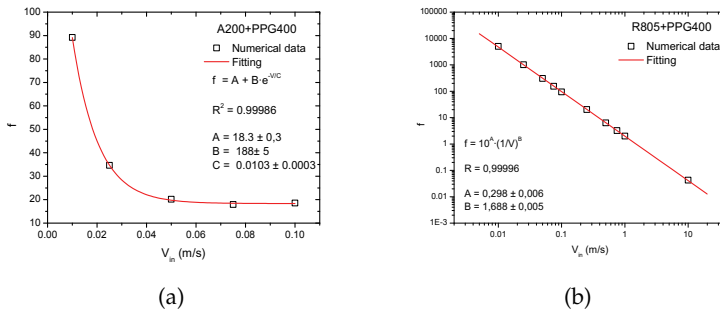


Fig. 11. Friction factor as a function of the velocity inlet. Results for the suspensions of A200 (a) and R805 (b) in PPG400 at 5 %v/v and 25 °C.

This information can also be given expressed by the friction factor (Figure 11). It can be observed that the friction factor in the laminar regime does not depend inversely proportional to the velocity, but it follows a potential or exponential law, depending on the rheological properties of the fluid.

#### 4. Other kind of flows

In this chapter we have been focused in the use of numerical techniques to solve the flow problem of laminar, steady and fully developed flow of non-Newtonian fluids, whose viscosity is described by the GNM. These constitutive equations do not consider elastic behavior and are perfect to describe this kind of flow due to it is dominated by viscous effects. Numerical techniques here are needed because of non-linearities introduced by the constitutive equations of the fluids.

However, there are many other flow geometries in which elastic behaviors are relevant, i.e. contraction/expansion geometries, cross-slot, etc. Then, viscoelastic models must be used as constitutive equations for these fluids instead of the GNM. In this cases, because of complexities in the geometry and the constitutive equation, numerical techniques are also needed to obtain information about the flow properties. Those readers interested in this kind of flows are strongly recommended to have a look at the works of Prof. R. Keunings et al., Prof. K. Walters et al., Prof. M.J. Crochet et al. or Prof. F.T. Pinho et al., among others.

#### 5. References

- Barnes, H. A. (1989). Shear-thickening (dilatancy) in suspensions of nonaggregating solid particles dispersed in newtonian liquids, *Journal of Rheology* 32: 329–366.
- Barnes, H. A. (2000). *Handbook of elementary rheology*, The university of Wales Institute of Non-Newtonian Fluid Mechanics, United Kingdom.
- Barnes, H. A., Hutton, J. F. & Walters, K. (1993). *An introduction to Rheology*, Rheology Series, vol. 3, Ed. Elsevier Science Publishers B.V., Netherlands.
- Bender, J. & Wagner, N. J. (1996). Reversible shear thickening in monodisperse and bidisperse colloidal dispersions, *Journal of Rheology* 40(5): 899–916.
- Bird, R. B., Armstrong, R. C. & Hassager, O. (1987). *Dynamics of polymeric liquids. Volume 1 Fluid Mechanics*, John Wiley and Sons, Inc., USA.
- Blazek, J. (2001). *Computational Fluid Dynamics: Principles and Applications*, Elsevier Science Ltd, Great Britain.
- Boersma, W. H., Laven, J. & Stein, H. N. (1992). Viscoelastic properties of concentrated shear-thickening dispersions, *Journal of Colloid and Interface Science* 419(1): 10–22.
- Chhabra, R. P. & Richardson, J. F. (1999). *Non-Newtonian flow in the process industries. Fundamentals and engineering applications*, Butterworth-Heinemann, USA.
- Chhabra, R. P. & Richardson, J. F. (2008). *Non-Newtonian flow and applied rheology*, Butterworth-Heinemann, USA.
- Crochet, M. J., Davies, A. R. & Walters, K. (1985). *Numerical simulation of non-Newtonian flow*, Rheology Series, vol. 1, Ed. Elsevier Science Publishers B.V., Netherlands.
- Decker, M. J., Halbach, C. J., Nam, C. H., Wagner, N. J. & Wetzel, E. D. (2007). Stab resistance of shear thickening fluid (stf)-treated fabrics, *Composites Science and Technology* 67: 565–578.
- Degussa, A. G. (1998). Basic characteristics of aerosil<sup>®</sup>, *Technical Bulletin - Pigment* 6.
- Degussa, A. G. (2005a). Aerosil<sup>®</sup> 200, hydrophilic fumed silica, *Product Information* .
- Degussa, A. G. (2005b). Aerosil<sup>®</sup> R805, hydrophobic fumed silica, *Product Information* .
- D’Haene, P., Mewis, J. & Fuller, G. G. (1993). Scattering dichroism measurements of flow-induced structure of a shear thickening suspension, *J. Colloid Interface Sci.* 156: 350–358.
- Dolz, M., González, F., Delegido, J., Hernández, M. & Pellicer, J. (2000). A time-dependent

- expression for thixotropic areas. application to aerosil 200 hydrogels, *Journal of Pharmaceutical Sciences* 89(6): 790–797.
- Fischer, C., Braun, S. A., Bourban, P. E., Michaud, V., Plummer, C. J. G. & Manson, J. A. E. (2006). Dynamic properties of sandwich structures with integrated shear-thickening fluids, *Smart Materials and Structures* 15: 1467–1475.
- Fletcher, C. A. J. (2005). *Computational Techniques for Fluid Dynamics. Volume 1-Fundamental and general techniques*, Ed. Springer Verlag, Berlin, Germany.
- Galindo-Rosales, F. J. & Rubio-Hernández, F. J. (2007). Influence of the suspending phase on the rheological behaviour of aerosil R805 suspensions, *Annual Transactions of the Nordic Rheology Society*, Vol. 15, Juvenes Print, Tampere, Finland, pp. 73–79.
- Galindo-Rosales, F. J. & Rubio-Hernández, F. J. (2010). Static and dynamic yield stresses of aerosil® 200 suspension in polypropylene glycol, *Applied Rheology* 20(2): 22787.
- Galindo-Rosales, F.J., Rubio-Hernández, F.J. & Sevilla, A. (2010). An apparent viscosity function for shear thickening fluids (submitted to Journal of Non-Newtonian Fluid Mechanics).
- Hoffman, R. L. (1974). Discontinuous and dilatant viscosity behavior in concentrated suspensions II: Theory and experimental tests, *J. Colloid Interface Sci.* 46(3): 491–506.
- Hoffman, R. L. (1998). Explanations for the cause of shear thickening in concentrated colloidal suspensions, *Journal of Rheology* 42(1): 111–123.
- Jaúregui-Beloqui, B., Fernández-García, J.C., Orgilés-Barceló, C.A., Mahiques-Bujandab, M.M. & Martín-Martínez, J.M (1999). Rheological properties of thermoplastic polyurethane adhesive solutions containing fumed silicas of different surface areas, *International Journal of Adhesion and Adhesives* 19: 321–328.
- Keunings, R. (1999). Advances in the computer modeling of the flow of polymeric liquids, *Keynote Lecture, 8th International Symposium on Computational Fluid Dynamics, Bremen, Germany*.
- Khan, S. A. & Zoeller, N. J. (1993). Dynamic rheological behaviour of flocculated fumed silica suspensions, *Journal of Rheology* 37(6): 1225–1235.
- Kirkwood, K., Kirkwood, J., Wetzal, E. D., Lee, Y. S. & Wagner, N. J. (2004). Yarn pull-out as a mechanism for dissipating ballistic impact energy in kevlar® km-2 fabric - part i: Quasi-static characterization of yarn pull-out, *Textile Research Journal* 74 (10): 920–928.
- Landau, L. D. & Lifshitz, E. M. (1987). *Fluid Mechanics*, Pergamon Press, Oxford, Great Britain.
- Larson, R. G. (1999). *The Structure and Rheology of Complex Fluids*, Oxford University Press, Nueva York, USA.
- Lee, Y. S., Wetzal, E. D. & Wagner, N. J. (2003). The ballistic impact characteristics of kevlar® woven fabrics impregnated with a colloidal shear thickening fluid, *Journal of Materials Science* 38: 2825–2833.
- Li, Y., Fedkiw, P. S. & Khan, S. A. (2002). Tithium/v6o13 cells using silica nanoparticled-based composite electrolyte, *Electrochimica Acta* 47: 3853–3861.
- Macosko, C. W. (1994). *Rheology: Principles, measurements, and applications*, Wiley-VCH, Inc., USA.
- Maranzano, B. J. & Wagner, N. J. (2002). Flow-small angle neutron scattering measurements of colloidal dispersion microstructure evolution through the shear thickening transition, *J. Chem. Phys.* 117(22): 10291–10302.
- Masalova, I., Malkin, A. Y., Slatter, P. & Wilson, K. (2003). The rheological characterization and pipeline flow of high concentration water-in-oil emulsions, *Journal of Non-Newtonian Fluid Mechanics* 112: 101–114.

- Mezger, T. G. (2002). *The Rheology Handbook: for user of rotational and oscillatory rheometers*, Ed. Vincentz Verlag, Germany.
- Morrison, F. A. (2001). *Understanding Rheology*, Oxford University Press, USA.
- O'Callaghan, S., Walsh, M. & McGloughlin, T. (2003). Comparison of finite volume, finite element and theoretical predictions of blood flow through an idealised femoral artery, *Summer Bioengineering Conference*, Florida, USA, pp. 417–418.
- Ouyang, C., Wang, S., Zhang, Y. & Zhang, Y. (2006). Low-density polyethylene/silica compound modified asphalt with high-temperature storage stability, *Journal of Applied Polymer Science* 101: 472–479.
- Papanastasiou, T. C., Georgiou, G. C. & Alexandrou, A. N. (2000). *Viscous fluid flow*, CRC Press LLC, USA.
- Phan-Thien, N. (2002). *Understanding Viscoelasticity*, Springer-Verlag Berlin Heidelberg, Germany.
- Pinho, F. (2001). The methodology of finite volumes applied to computational rheology. ii-fundamentals for stress-explicit fluids, *Journal of the Portuguese Society of Rheology* 1: 63–100.
- Pinho, F. & Oliveira, M. (2001). The methodology of finite volumes applied to computational rheology: I- introduction, *Journal of the Portuguese Society of Rheology* 1: 1–15.
- Raghavan, S. R. & Khan, S. A. (1995). Shear-induced microstructural changes in flocculated suspensions of fumed silica, *Journal of Rheology* 39(6): 1311–1325.
- Raghavan, S. R. & Khan, S. A. (1997). Shear-thickening response of fumed silica suspensions under steady and oscillatory shear, *Journal of Colloid and Interface Science* 185: 57–67.
- Raghavan, S. R., Walls, H. J. & Khan, S. A. (2000). Rheology of silica dispersions in organic liquids: New evidence of solvations forces dictated by hydrogen bonding, *Langmuir* 16(21): 7920–7930.
- Souza-Mendes, P. R. & Dutra, E. S. S. (2004). Viscosity function for yield-stress liquids, *Applied Rheology* 14: 296–302.
- Steffe, J. (1996). *Rheological methods in food process engineering*, Ed. Freeman Press, Michigan, USA.
- Tanner, R. I. & Walters, K. (1998). *Rheology: An Historical Perspective*, Rheology Series, vol. 7, Ed. Elsevier Science Publishers B.V., Netherlands.
- Vermant, J. & Solomon, M. J. (2005). Flow-induced structure in colloidal suspensions, *Journal of Physics: Condensed Matter* 17: 187–216.
- Walls, H. J., Zhou, J., Yerian, J. A., Fedkiw, P. S., Khan, S. A., Stowe, M. K. & Baker, B. L. (2000). Fumed-silica based composite polymer electrolyte: synthesis, rheology and electrochemistry, *Journal of Power Sources* 89: 156–162.
- Walters, K. (1975). *Rheometry*, Chapman and Hall Ltd., London, Great Britain.
- Wesseling, P. (2001). *Principles of computational fluid dynamics*, Ed. Springer Verlag, Berlin, Germany.
- Yziquel, F., Carreau, P. J. & Tanguy, P. A. (1999). Non-linear viscoelastic behavior of fumed silica suspensions, *Rheologica Acta* 34: 14–25.

# Numerical Simulation on the Steady and Unsteady Internal Flows of a Centrifugal Pump

Wu Yulin, Liu Shuhong and Shao Jie  
*Tsinghua University*  
*China*

## 1. Introduction

Nowadays, pumps of different size are needed for a great variety of purposes. In the past, both computational fluid dynamics (CFD) and experimental flow visualization were performed to reveal flow characteristics within centrifugal pumps, to examine a specific design and to guide design improvement (see Burgreen et al. 1996, 2000). Li et al. (2007) studied the interior viscous flow in a mini pump with an asymmetric axis using CFD and PIV (particle image velocimetry) for improvement of the pump design. Matsui et al. (2002) adopted the the  $k-\omega$  model in the CFD simulation for a centrifugal pump, and the computational grid system only consisted of one flow passage for LDV (laser Doppler velocimetry) test impeller.

Byskov et al. (2003a) and Pedersen & Larsen (2003 b) investigated the flow inside the rotating passages of a six-bladed shrouded centrifugal pump impeller using LES simulation and PIV and LDV measurements. The velocities predicted with LES were in good agreement with the experimental data. The two RANS simulations were, however, not able to predict this complex flow field. It was thus found that using LES for analyzing the flow field in centrifugal pumps could shed light on basic fluid dynamic with a satisfactory accuracy compared to experiments.

A transient simulation was used to study the effects of pulsatile blood flow due to the heartbeat through blood pumps by Song et al. (2003). The micro-sized geometry of the pump made the choice of turbulence models significant for the accuracy of calculation. The comparison showed that the  $k-\omega$  model gave better predictions of the shear level within the near wall regions than the  $k-\epsilon$  model. Guleren and Pinarbasi (2004) indicated that the stall cell size extended from one to two diffuser passages. Comparisons of the computational results with experimental data were made and showed good agreement.

The unsteady flow in a low specific speed radial diffuser was simulated by the CFD code CFX-10 by Feng et al. (2009). The PIV and LDV measurements had been conducted to validate the CFD results. Both the phase-averaged velocity fields and the turbulence fields obtained from different methods are presented and compared.

In this study, in order to get more information about the internal flow of a centrifugal pump, both experimental measurement and numerical simulation are engaged. A centrifugal model pump test rig is built for PIV measurement. The test, involving the technology of index match and fluorescent, is for acquiring flow pattern in a fixed rotational speed, the velocity distribution of the flow field are thus obtained. And, the RANS (Reynolds

Averaged Navier-Stokes) turbulent equations with the SST  $k-\omega$  turbulence model are applied to simulate its 3D steady whole passage flow and the DES (Detached Eddy Simulation) method to simulate this unsteady flow. The external characteristics and the internal flow pattern of the centrifugal pump are calculated. According to comparison with experimental data, the unsteady simulation is proved to be relatively accurate in predicting the flow status in the centrifugal model pump.

## 2. Numerical simulation

The three-dimensional geometry model of the mini pump is generated using a 3D modeling software package (Gambit, v2.2.60, Fluent Inc., Lebanon, NH, USA). The computational domains include the inlet, outlet, impeller and the volute. Then the geometry is meshed in 3D Tet/Hybrid elements.

An unstructured-mesh finite-volume-based commercial CFD package, Fluent (v6.2.16, Fluent Inc.), is used to solve the incompressible steady Navier-Stokes equations.

The incompressible continuity equation and Reynolds averaged the N-S equations are employed to simulate the steady turbulent flow through the pump, and the SST  $k-\omega$  double equation turbulence model is adopted to make the equations closed.

### 2.1 Turbulence model

The  $k-\omega$  based Shear-Stress-Transport (SST) model is designed to give highly accurate predictions of the onset and the amount of flow separation under adverse pressure gradients, because it takes transport effects into the formulation of the eddy-viscosity. This resulted in a major improvement in terms of flow separation predictions by Menter (1994).

In the SST  $k-\omega$  turbulence model, the turbulent kinetic energy  $k$  equation is used. But the turbulent dissipation rate equation in  $k-\epsilon$  is replaced by the turbulent dissipation frequency  $\omega$ ,

$$\omega = \frac{\epsilon}{C_k k} \quad (1)$$

And  $k$  and  $\omega$  equations are as follows:

$$\frac{\partial}{\partial t}(\rho k) + \frac{\partial}{\partial x_j}(\rho k \bar{u}_j) = \frac{\partial}{\partial x_j} \left( \Gamma_k \frac{\partial k}{\partial x_j} \right) + P_k - Y_k \quad (2)$$

$$\frac{\partial}{\partial t}(\rho \omega) + \frac{\partial}{\partial x_j}(\rho \omega \bar{u}_j) = \frac{\partial}{\partial x_j} \left( \Gamma_\omega \frac{\partial \omega}{\partial x_j} \right) + P_\omega - Y_\omega + D_\omega \quad (3)$$

where  $P_k$  is the productive term of  $k$ ,  $P_\omega$  the productive term of  $\omega$ ,  $\Gamma_k$  and  $\Gamma_\omega$  are the diffusion coefficients of  $k$  and  $\omega$ ,  $Y_k$  and  $Y_\omega$  the dissipation terms of  $k$  and  $\omega$  respectively, and  $D_\omega$  is the orthogonal diffusion term. The productive terms are as follows:

$$P_k = -\rho \overline{u_i' u_j'} \frac{\partial \bar{u}_i}{\partial x_j}, \quad P_\omega = \frac{\alpha_\infty}{\nu_t} P_k,$$

where  $\alpha_\infty = F_1\alpha_{\infty,1} + (1-F_1)\alpha_{\infty,2}$ ,  $\alpha_{\infty,1} = \frac{\beta_{i,1}}{\beta_\infty^*} - \frac{\kappa^2}{\sigma_{\omega,1}\sqrt{\beta_\infty^*}}$ ,  $\alpha_{\infty,2} = \frac{\beta_{i,2}}{\beta_\infty^*} - \frac{\kappa^2}{\sigma_{\omega,2}\sqrt{\beta_\infty^*}}$ , and

$F_1 = \tanh(\arg_1^4)$  ( $\arg_1 = \max\left(\min\left(\frac{\sqrt{k}}{0.09\omega y}, 0.45\frac{\omega}{\Omega}\right), \frac{400\mu}{\rho l^2\omega}\right)$ ,  $l$  is the distance to next

surface).

The diffusion coefficients are

$$\Gamma_k = \mu + \frac{\mu_t}{\sigma_k}, \quad \Gamma_\omega = \mu + \frac{\mu_t}{\sigma_\omega}$$

where  $\sigma_k$  and  $\sigma_\omega$  are the Prandtl numbers of  $k$  and  $\omega$ , and the eddy viscosity is:

$$\mu_t = \left(\frac{\rho k}{\omega}\right) / \max\left[\frac{1}{\alpha^*}, \frac{\bar{\Omega} F_2}{\alpha_1 \omega}\right] \quad (4)$$

where  $\alpha^* = \alpha_\infty^* \left(\frac{\alpha_0^* + \text{Re}_t / R_k}{1 + \text{Re}_t / R_k}\right)$ ,  $\bar{\Omega} \equiv \sqrt{\bar{\Omega}_{ij} \bar{\Omega}_{ij}}$ ,  $\sigma_k = \frac{1}{F_1 / \sigma_{k,1} + (1-F_1) / \sigma_{k,2}}$ ,

$\sigma_\omega = \frac{1}{F_1 / \sigma_{\omega,1} + (1-F_1) / \sigma_{\omega,2}}$ ,  $F_2 = \tanh(\arg_2^2)$  ( $\arg_2 = \max\left(2\frac{\sqrt{k}}{0.09\omega y}, \frac{400\mu}{\rho y^2\omega}\right)$ ), where  $\bar{\Omega}_{ij}$  is

vorticity.

The dissipation terms  $Y_k$ ,  $Y_\omega$  and  $D_\omega$  are as follows:

$$Y_k = \rho\beta_\infty^* k\omega, \quad Y_\omega = \rho\beta_\infty^* \omega^2, \quad D_\omega = 2(1-F_1)\rho\sigma_{\omega,2} \frac{1}{\omega} \frac{\partial k}{\partial x_j} \frac{\partial \omega}{\partial x_j}$$

The constants in this model are  $\sigma_{k1} = 0.85$ ,  $\sigma_{\omega1} = 0.65$ ,  $\sigma_{k2} = 1.0$ ,  $\sigma_{\omega2} = 0.856$ ,  $\kappa = 0.42$ ,  $\beta_{i,1} = 0.075$ ,  $\beta_{i,2} = 0.0828$ ,  $\alpha_\infty^* = 1$ ,  $\beta_\infty^* = 0.09$ .

## 2.2 DES simulation based on SST k- $\omega$ model

The DES method is adapted to simulate the unsteady turbulent flow through the whole flow passage of the centrifugal pump. In DES method, the RANS turbulent flow simulation with the SST k- $\omega$  turbulence model is applied to simulate the boundary layer flow near solid walls and the LES simulation with the Smagorinski SGS (Subgrid Stress) model is used to simulate the flow in other regions.

The turbulence length  $l_{k-\omega}$  of the SST k- $\omega$  model can be defined as

$$l_{k-\omega} = \sqrt{k} / (\beta_\infty^* \omega) \quad (5)$$

In DES simulation, the length  $l_{k-\omega}$  will be replaced by the following expression:

$$\bar{l} = \min(l_{k-\omega}, C_{DES}\Delta) \quad (6)$$

where  $\Delta = \max(\Delta x, \Delta y, \Delta z)$  is the maximum distance between two adjacent grid nodes. When  $l_{k-\omega} < \Delta$ , the RANS simulation with SST k- $\omega$  model is used, and when  $l_{k-\omega} > \Delta$ , the

LES is adopted for simulation of the turbulent flow. If the grid sizes are fine enough in whole computational region, the LES will be applied in the entire domain. The DES method is used in unstructured grid system in the present work. Near solid walls in the grid system where the value of  $\omega$  is very large,  $k$  still remains the finite value, and  $l_{k-\omega}$  is smaller than  $\Delta = \max(\Delta x, \Delta y, \Delta z)$ . Therefore RANS simulation with SST  $k-\omega$  model is suitable for turbulent flow computation near walls as described by Mitchell et al. (2006) and  $C_{DES} = 0.65$  for unstructured grid system.

### 3. Computational model of the centrifugal pump

#### 3.1 Pump model and geometry

The pump and its impeller under investigation are centrifugal type shown in Fig. 1. The impeller consists of six two-dimensional curvature backward swept blades of constant thickness with arc profile leading edges and blunt trailing edges. Axial height of the impeller blade is tapered linearly from 15.13 mm at the inlet to 8.11 mm at the outlet. The entire impeller is manufactured in acryl for the PIV measurements at impeller passages. Table 1 summarizes the main dimensions of the test impeller. The computational domain includes the inlet, impeller, volute and outlet shown in Fig. 1.

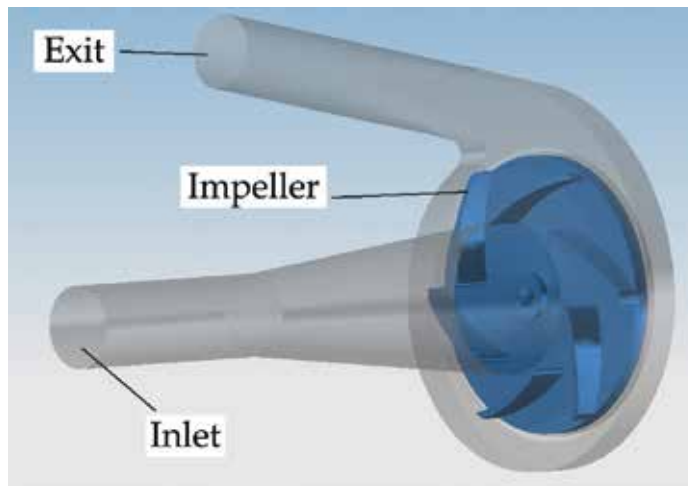


Fig. 1. The centrifugal pump

Geometry	Symbol	Value	Unit
Inlet diameter	$D_1$	55.14	mm
Outlet diameter	$D_2$	100	mm
Inlet height	$b_1$	15.13	mm
Outlet height	$b_2$	8.11	mm
Number of blades	$Z$	6	–
Blade thickness	$t$	2.7	mm
Inlet blade angle	$\beta_1$	15	deg.
Outlet blade angle	$\beta_2$	39	deg.

Table 1. Impeller geometry

### 3.2 Grid system independency verification

It is necessary to carry out independency verification of the grid system before CFD computation. The varified case of the pump is design flow rate case with rotating speed of 1000rpm, flow rate of 46.65L/min and the design head of 1.36m (test result is 1.39m). 6 different grid systems are formed in the computational domain to perform this independy verification as drawn in Fig. 2.

Fig. 2 shows head variation with grid number of pump grid system at design flow rate case for grid number independency verification. According to it, once the total grid number of pump system is larger than 2,150,000, its calculated head will not change apparently. So the grid number for its steady and unsteady flow computation is selected as 2,150,000.

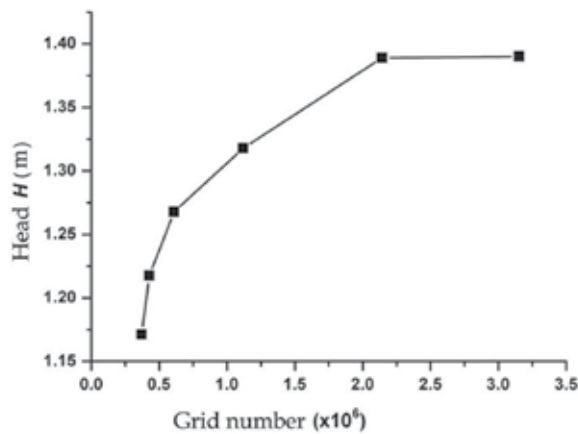


Fig. 2. Head variation with grid number of pump grid system at design flow rate case

### 3.3 Time step independency verification for unsteady flow computation

It is necessary to carry out independency verification of the time step before unsteady CFD computation. Tested case of the pump is also the design flow rate case. 6 different time steps are selected for the unsteady computation to perform this independy verification as listed in Table 2. The calculated pump heads in Table 2 are obtained after the unsteady computation. If the time step in computation is less than 0.0006 second, the pump head from unsteady flow computations will not change. So the time step is selected as 0.0006 for both calculation accuracy and economic time consumption.

Time step (s)	0.03	0.006	0.002	0.001	0.0006	0.0002
Iteration steps	1000	1000	1000	1000	1000	1000
Calculated head (m)	No coverage	1.2907	1.3312	1.3681	1.4007	1.3971

Table 2. Calculated head for different time steps of unsteady flow simulation

### 3.4 Numerical simulation methods

#### Steady numerical simulation method

For the steady turbulent flow simulation in the centrifugal pump, the pump impeller is frozen in a definite position and the multiple reference frame is selected. The whole flow

passage of the pump includes spiral volute, inlet suction and impeller computed sub-domains. The impeller region is in the rotating reference frame, and other regions are in the stationary reference frame. The continuity of velocity vectors should be kept on the interface between two reference frames.

An unstructured-mesh finite-volume-based commercial CFD package, Fluent (v6.2.16, Fluent Inc.), is adopted to discretize governing equations of the flow computation. The variables are saved up at the center of a control volume. The SIMPLEC algorithm is applied for decoupling velocity and pressure solution. The second order central differencing scheme is adopted for the diffusive term, and the second order upwind differencing scheme for the convective terms. Calculated fluid is the refractive index solution for the pump test with density of  $1050\text{kg/m}^3$  and viscosity of  $0.0035\text{kg/m}\cdot\text{s}$ .

The boundary conditions of the steady flow computation in the pump are set as follows:

- a. A mass-flow boundary condition is specified at the inlet. The Dirichlet condition of each variable is given at the inlet of computational domain. For example, the velocity at inlet section is given according to the flow rate of the case and it was perpendicular to the inlet section.
- b. An outflow condition is set at the outlet. The Neumann conditions is given for each variable.
- c. The wall function is adopted near the fixed wall, and non-slip boundary condition is adopted on the stationary wall. If the boundary is rotary, the velocity on the boundary wall is set as  $\Omega r$  (where  $r$  is radius;  $\Omega$  is the rotating speed of impeller).
- d. For the pressure condition, Neumann conditions are specified on all boundaries, except for the pressure at one point. This point pressure would be specified as a reference value and it remains the same at each iteration. Then pressures at all stations are recalculated according to the reference value after each iteration.

#### **Unsteady numerical simulation method**

The DES turbulent computation is adopted for the unsteady flow in the centrifugal pump with SST  $k\text{-}\omega$  turbulence model in this work. In the computation, the sliding meshes are formed between its stationary components and rotating ones in order to model the rotor-stator interactions between inlet and runner, and runner and volute. Based on the sliding mesh modeling, the unsteady characters of the pump could be obtained with the second order implicit time advancing scheme. The time step value had been verified and adopted as above. Then at each time step the same discrete numerical treatment and boundary conditions are utilized as those in steady flow simulation to capture the convergent instantaneous flow situation after the discretizing equations being solved. In the next step, with sliding meshes' moving to new position, the new position simulation would be carried out according to last time results and the second order implicit time advancing scheme.

#### **4. Instantaneous PIV measurement on internal flows of the centrifugal pump**

PIV is a technique which measures the instantaneous velocity field within an illuminated plane of fluid field by using light scattered from particles seeded into the fluid. PIV has recently matured to a reliable technique that is used in a wide variety of applications (Wu et al. 2009). The PIV hardware for this research consists of a  $120\text{mJ/pulse}$  dual-cavity pulsed Nd: YAG laser, laser light sheet optics, a charge coupled device (CCD) camera, a synchronizer and a data's process system.

In order to eliminate the effect of refraction/reflection light from the area close to the walls and enhance the measurement accuracy, fluorescent particles are scattered into the working fluid with the tracing particles. The refractive index of water in pump and of the transparent material of pump impeller and volute with curved walls is different (Budwig, 1994). The beams of rays with different angles of incidence can not focus at a definite point, which will result in imaging defocused and deformed, and that leads to an error in the PIV measurement. The refractive index matched (RIM) fluid with the same refractive index as the transparent material has been prepared and applied in the present test of pump with geometrical complex walls to eliminate this type of error of PIV measurement.

The present PIV measurement with both the laser induced fluorescence (LIF) particles and the refractive index matched (RIM) facilities in the centrifugal pump is carried out and gives a reliable flow patterns in the pump. It is obvious that the application of LIF particle and RIM are the key methods to get good PIV measurement results in pump internal flow (see Wu et al. 2009).

#### 4.1 Absolute velocity distribution and streamlines in impeller at design flow rate

Fig. 3 (a) shows the mean absolute velocity distribution and streamlines of the PIV measurement in impeller under design flow rate condition at the moment of  $t=0$  (see Fig. 4 (a)). The absolute streamlines in the pump are distributed smoothly; the absolute mean velocity magnitude varies from the value less than 1 m/s at the impeller inlet area to more 4 m/s at the outlet of impeller. And near the impeller outlet, the absolute velocity near suction surfaces of blades is larger than that near pressure surfaces.

Fig. 3 (a) shows the distributions of sampling points in the measuring plan of the pump, where point 1 is in the impeller passage and point 2 in the outlet area. Fig. 3 (b) shows measuring uncertainty at design flow rate condition with respective to times of measurement. From this figure, it can be observed that if the time of measurement is larger than 200, the uncertainty of measuring velocity is less than  $\pm 0.03\text{m/s}$  which means the error of this velocity measurement is less than  $\pm 4\%$ .

#### 4.2 Relative velocity distribution and streamlines in impeller at design flow rate

Fig. 4 shows the relative velocity and streamlines distribution in impeller at design flow rate condition ( $Q=Q_d=2.70\text{m}^3/\text{s}$ ) from this PIV measurement. In Fig. 4, there are 5 pictures (a) to (e) to display the velocity for different position of impeller vanes. The time interval between two positions is one fifth of the period  $T$  of impeller rotation. The flow distributions on 5 pictures are almost the same which illustrates the impeller manufactured axisymmetrically and also the measurement with reliability. The flow difference in different blade channels occurs near the tongue, which affects the flow in the channel greatly.

At the design flow rate condition, the relative velocity in the blade channel distributes smoothly and decreases from inlet to exit. And at impeller exit, the relative velocity is lower close to suction side than that near pressure side of blade in most of blade channels. This flow structure is somewhat of jet-wake flow structure in centrifugal impeller. It is because the blade exit angle is  $39^\circ$ , greater than that of conventional centrifugal pump. There are some differences in flow patterns between different blade channels. The relative velocity in the blade channel close to pump exit is higher than that in other channels. The relative streamlines in blade channel distribute along the blade surface smoothly and there is no circulation in the channel under this condition.

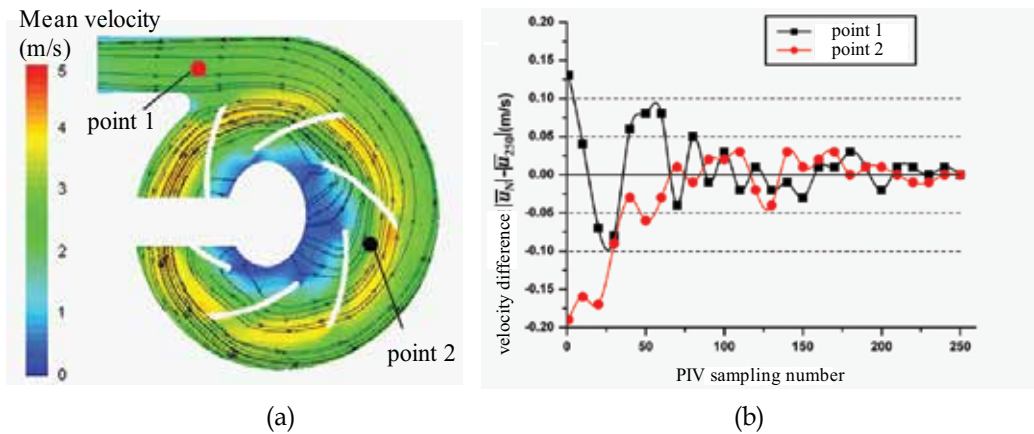


Fig. 3. The distributions of sampling points (a) and measuring uncertainty (b) at design flow rate condition

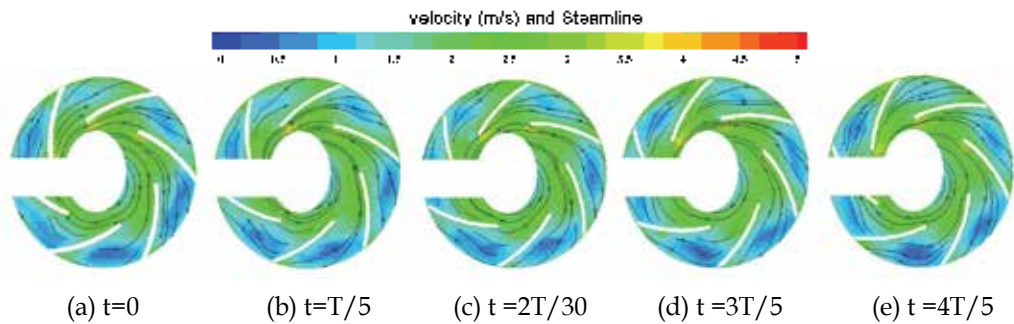


Fig. 4. Relative velocity and streamlines in impeller at design flow rate condition ( $Q=Q_d$ )

#### 4.3 Absolute velocity distribution and streamlines in volute at design flow rate

Fig. 5 shows the absolute velocity and streamlines in volute at design flow rate condition. The flow distributions on 5 pictures of volute at different moments are almost the same that are smooth and almost even. The absolute velocity is higher than that in other position near the tongue. So the flow pattern in the pump volute is stable under the design flow rate condition.

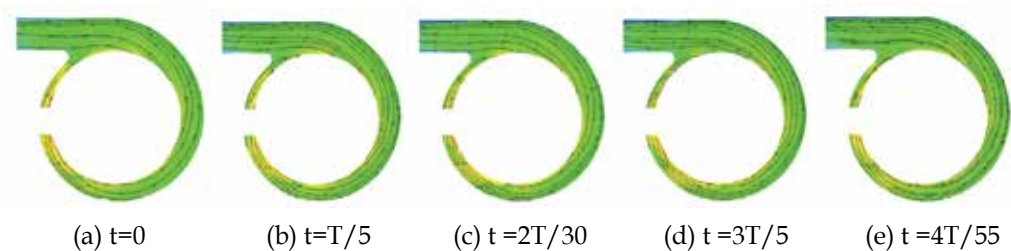


Fig. 5. The absolute velocity and streamlines in volute at design flow rate condition ( $Q=Q_d$ )

## 5. Computational results and discussion

### 5.1 Pump energy performances' prediction

Table 3 and Fig. 6 show the steady and unsteady calculated and tested energy performances of the centrifugal pump in 8 different flow rate cases. The calculated energy performances are predicted with distributions of velocity and pressure obtained through either steady flow simulation or unsteady flow simulation in the computational domain.

flow rate	tested head	tested efficiency	Steady calculated head	steady calculated efficiency	unsteady calculated head	unsteady calculated efficiency
$Q(\text{m}^3/\text{h})$	$H_{\text{exp}}(\text{m})$	$\eta_{\text{exp}}(\%)$	$H_{\text{ss}}(\text{m})$	$\eta_{\text{ss}}(\%)$	$H_{\text{us}}(\text{m})$	$\eta_{\text{us}}(\%)$
0.85	1.4879	31.40	1.5538	30.62	1.5316	30.02
1.00	1.4883	34.10	1.5354	34.85	1.5226	34.11
1.41	1.4859	42.14	1.4934	40.50	1.4760	40.01
2.00	1.4578	47.89	1.4363	45.92	1.4498	46.04
2.41	1.4196	51.02	1.3724	46.59	1.4224	51.12
2.70	1.3912	52.40	1.3889	58.03	1.4007	54.67
2.98	1.3466	52.86	1.3524	57.71	1.3785	55.15
3.36	1.3006	51.16	1.2467	53.62	1.3209	52.27

Table 3. Calculated and tested energy performances of the centrifugal pump

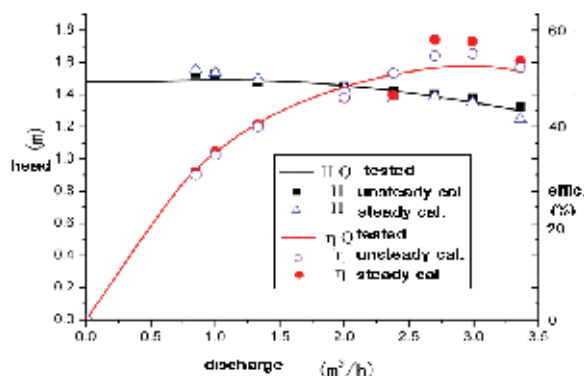


Fig. 6. Calculated and tested energy performances of the centrifugal pump

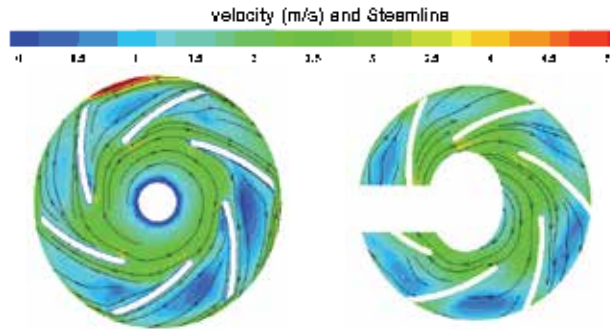
Fig. 6 shows that predicted pump energy performances both in steady and unsteady flow computations agree with test data. The calculated head of the pump is larger than tested one in small flow rate cases and smaller in large flow rate cases. But errors between calculated head and tested one are less than 5%. The predicted efficiency is closed to the test one in design and small flow rate cases, and higher than the tested one in large flow rate cases. As a whole, the predicted performance data in unsteady flow simulation are closer to test data than those in steady flow simulation.

### 5.2 Internal flow patterns verification

In order to verify the reliability of CFD results, it is necessary to compare computational and PIV measured flow velocity distributions both in the pump impeller and in its volute.

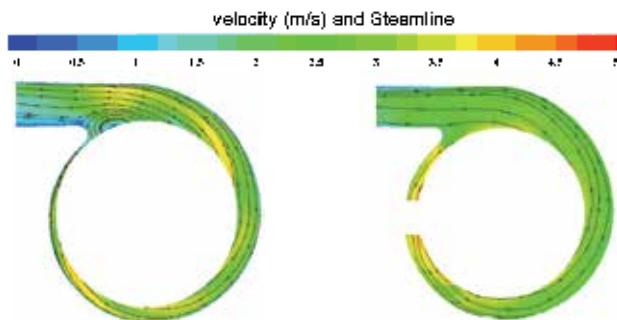
### Steady numerical simulation method

Fig. 7 show relative velocity distributions and streamlines in impeller in design flow case both in CFD steady flow simulation (a) at the frozen position of impeller for  $t = 0$  moment and in PIV measurement at this position. The PIV data are the averaged results of 200 times of measurement. Fig. 8 is absolute velocity and streamlines in volute in design flow case obtained through the same computation and measurement as those in Fig. 5.



(a) Velocity by steady flow simulation (b) PIV measured velocity

Fig. 7. Relative velocity and streamlines in impeller at design flow rate case ( $Q=Q_d$ )



(a) Velocity by steady flow simulation (b) PIV measured velocity

Fig. 8. Absolute velocity and streamlines in volute at design flow rate case ( $Q=Q_d$ )

Comparison of tested results at  $t = 0$  moment of PIV measurement shows that the relative velocity in CFD steady flow simulation in the impeller is larger than that of test data under design flow rate condition (see Fig. 7). In the volute, there is a circulation area at its outlet in steady flow simulation (shown in Fig. 8), but there is no such circulation in Fig. 8 (b) of PIV results. And the simulated absolute velocity values by CFD at the volute outlet section varies greatly.

### Verification of velocity distributions of unsteady flow computation

Fig. 9 show relative velocity distributions and streamlines in impeller in design flow case in CFD unsteady flow simulation at its positions selected for (a)  $t=0$ , (b)  $t=T/5$ , (c)  $t=2T/5$  (d)  $t=3T/5$  and (e)  $t=4T/5$  moments. And Fig. 4 displays the same results by in PIV instantaneous measurement as those in Fig. 9. Fig. 10 and Fig. 5 are absolute velocity distributions and

streamlines in volute in design flow case obtained through the same unsteady flow computation and measurement.

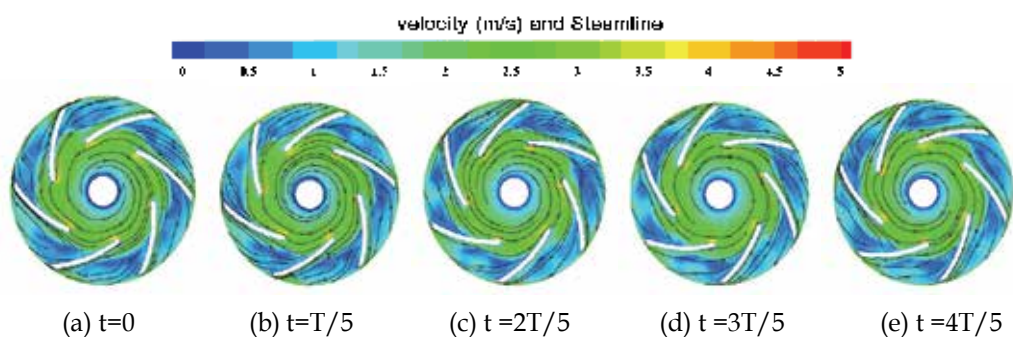


Fig. 9. Computed relative velocity and streamlines in impeller at design flow rate ( $Q=Q_d$ )

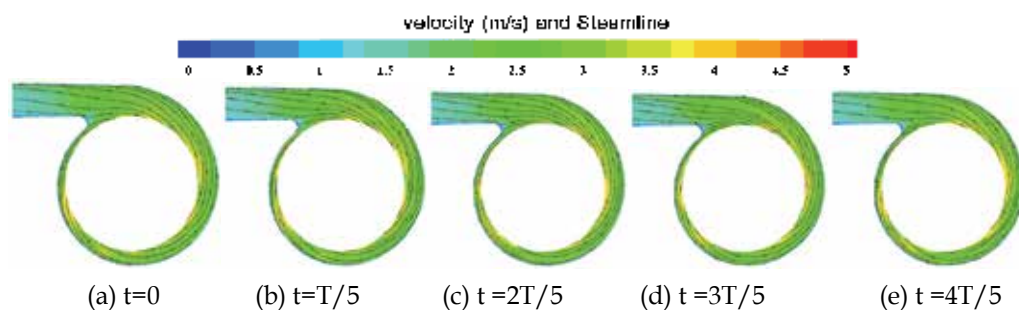


Fig. 10. Computed absolute velocity and streamlines in volute at design flow rate ( $Q=Q_d$ )

Under this design flow rate condition, the numerical results of unsteady flow computation agree with PIV instantaneous measurement data, which indicates the unsteady turbulent flow simulation in the centrifugal pump is successful and reliable.

### 5.3 Steady flow simulation results

Fig. 11 (a) to (c) are the steady flow calculation results of relative velocity and streamlines in the pump impeller at  $t=0$  moment in small flow rate case,  $Q=52\%Q_d$ , in design flow rate case,  $Q=Q_d$ , and in large flow rate case,  $Q=124\%Q_d$ , respectively. Fig. 13 (a) to (c) are the steady flow calculation results of absolute velocity and streamlines in the volute at  $t=0$  moment in the three flow rate cases. The corresponding PIV tested results are shown in Fig. 12 and Fig. 14.

In Fig. 11 and Fig. 12, it is shown that under the small flow rate condition, the vortex positions in pump impeller of calculated results do not agree with the test data, and the distribution of relative velocities are different with each other. Under the design condition and the large flow rate condition, the numerical predicted relative velocity magnitudes are larger than those obtained from PIV measurement (shown in Fig. 12). There are some vortices in the pump volute in the three flow rate cases from the calculated results in Fig. 13, but those vortices do not appear in PIV test results in Fig. 14.

The predicted performances in steady flow simulation agree with the test data very well (shown in Fig. 6). But there are some differences of velocities both in the pump impeller and

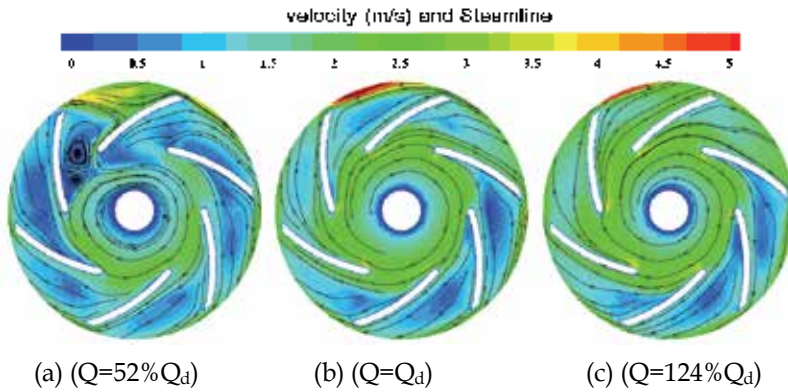


Fig. 11. Steady flow calculation results of relative velocity and streamlines in impeller at  $t=0$   
 (a) At small flow rate case (b) At design flow rate case (c) At large flow rate case

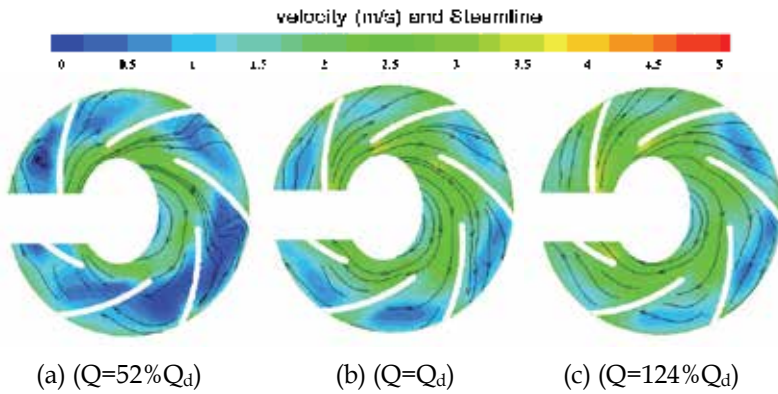


Fig. 12. PIV tested results of relative velocity and streamlines in impeller at  $t=0$   
 (a) At small flow rate case (b) At design flow rate case (c) At large flow rate case

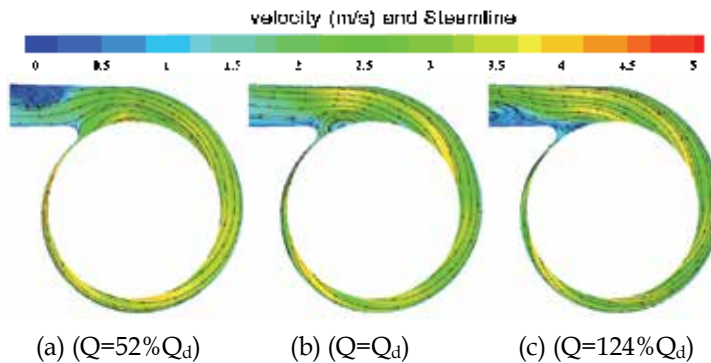


Fig. 13. Steady flow calculation results of absolute velocity and streamlines in volute at  $t=0$   
 (a) At small flow rate case (b) At design flow rate case (c) At large flow rate case

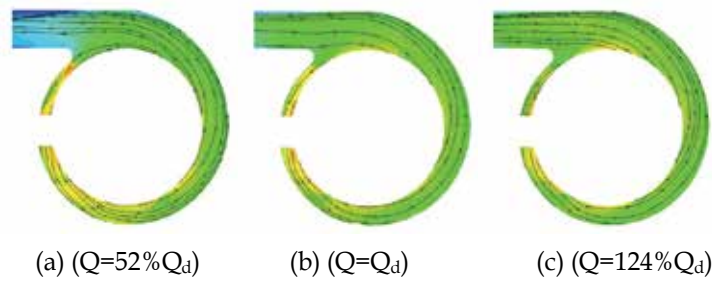


Fig. 14. PIV tested results of absolute velocity and streamlines in volute at  $t=0$   
 (a) At small flow rate case (b) At design flow rate case (c) At large flow rate case

the pump volute between steady flow simulation and PIV measurement. The steady flow simulation is based on the frozen model, that is, the fixed position of impeller blades in this computation. But in reality, the blades are rotating, and that is not simulated in the steady flow calculation.

#### 5.4 Unsteady flow simulation results at off-design flow rate conditions

Fig. 15 and Fig. 16 show the unsteady flow calculation results of relative velocity and streamlines in the pump impeller in small flow rate case,  $Q=52\%Q_d$ , and in large flow rate case,  $Q=124\%Q_d$ , respectively, at different moments. Fig. 17 and Fig. 18 indicate the unsteady flow calculation results of absolute velocity and streamlines in the pump volute in the two off-design flow rate cases, respectively.

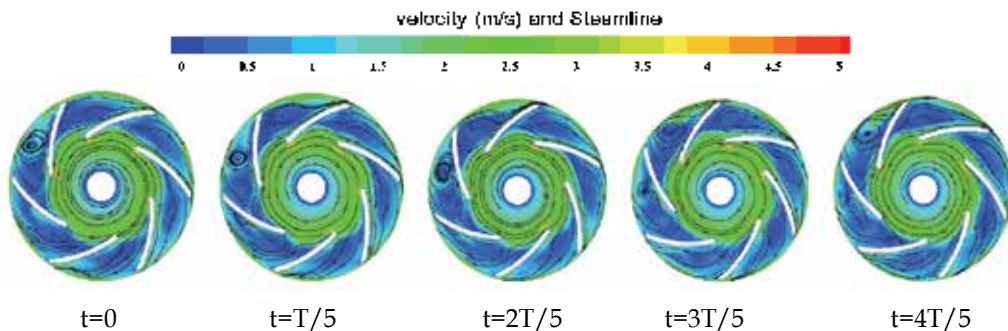


Fig. 15. Unsteady flow calculation results of relative velocity and streamlines in impeller at the small flow rate case ( $Q=52\%Q_d$ )

From Fig. 15, it is obvious that under the small flow rate condition, there are some vortices in the pump impeller according to the unsteady flow simulation, and their magnitudes are basically the same as those in the PIV instantaneous measurement (see Fig. 12 (a)). The absolute velocities and streamlines distributions in the pump volute agree well between the unsteady flow simulation in Fig. 17 and PIV instantaneous measurement in the small flow rate case (see Fig. 14 (a)). But under the large flow rate condition, the agreement between them is worse than that under small flow rate condition (see (see Figs. 12 (c) and 14(c)).

All the comparisons between unsteady flow simulation and the PIV instantaneous measurement indicate that the model and method of the simulation in this work are reliable for prediction of the centrifugal pump internal flow.

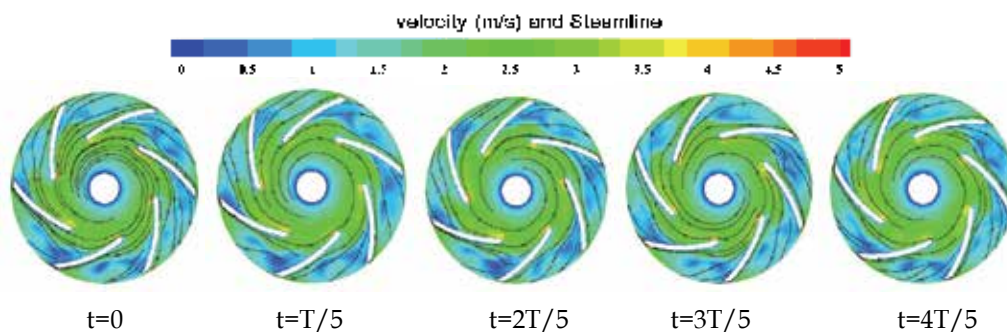


Fig. 16. Unsteady flow calculation results of relative velocity and streamlines in impeller at the large flow rate case ( $Q=124\%Q_d$ )

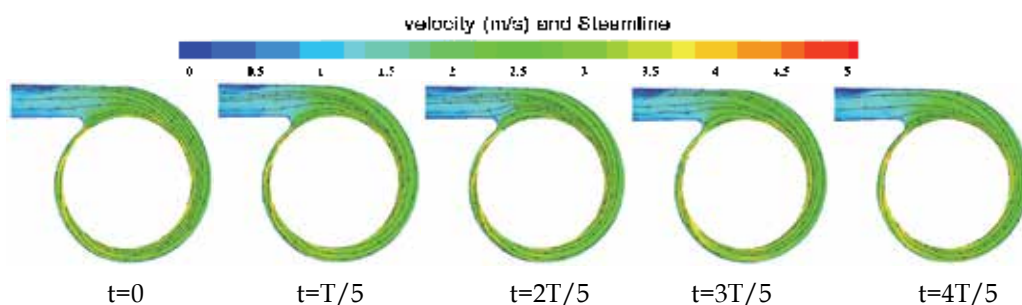


Fig. 17. Unsteady flow calculation results of absolute velocity and streamlines in volute at the small flow rate case ( $Q=52\%Q_d$ )

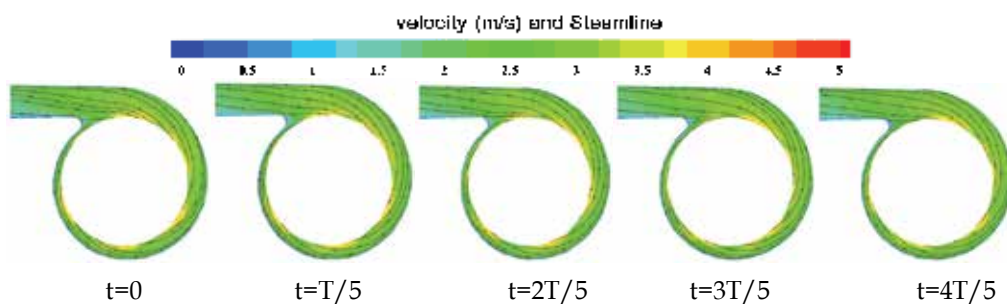


Fig. 18. Unsteady flow calculation results of absolute velocity and streamlines in volute at the large flow rate case ( $Q=124\%Q_d$ )

## 6. Conclusion

The RANS turbulent equations with the SST  $k-\omega$  turbulence model are applied to simulate the 3D steady whole passage flow in a centrifugal pump and the DES method based on the SST  $k-\omega$  turbulence model to simulate this unsteady flow. The external characteristics and the internal flow pattern of the centrifugal pump are calculated. From the computational results compared with the pump performance test and its PIV measurement the following conclusions could be drawn:

1. The calculated energy performances can be predicted through distributions of velocity and pressure obtained in either steady flow simulation or unsteady flow simulation in the pump computational domain. The predicted performance data in unsteady flow simulation are closer to test data than those in steady flow simulation.
2. Comparison between tested results at  $t=0$  moment of PIV measurement and calculated ones, the velocity distribution in CFD steady flow simulation both in pump impeller and volute is larger than those of test data under design flow rate condition.
3. Under design flow rate condition, the numerical results of unsteady flow computation agree with PIV instantaneous measurement data, which indicates the unsteady turbulent flow simulation in the centrifugal pump is reliable.
4. The unsteady flow simulation in the pump are also carried out under off-design conditions. The velocities and streamlines distributions agree well between the unsteady flow simulation and PIV instantaneous measurement in the small flow rate case. But under the large flow rate condition, the agreement between them has more tolerance than that under small flow rate condition.

## 7. References

- Budwig, R. (1994). Refractive index matching methods for liquid flow investigations, *Experiments in Fluids*, Vol.17, (Oct. 1994) 350-355, ISSN 0723-4864
- Burgreen, G.W.; Antaki, J.F. & Griffith, B.P. (1996). A design improvement strategy for axial blood pumps using computational fluid dynamics, *ASAIO J.*, Vol. 24, No. 5, (Sept. 1996) M354-M360, ISSN 10582916
- Burgreen, G.W.; Antaki, J.F.; Wu, J. & Holmes, A. J. (2000). CFD-based design optimization of the UoP streamliner rotary blood pump, *Proc. 2000 Annual Fall Meeting of the Biomedical Engr. Society, Washington*, Oct. 2000, ISBN: 00906964, Am Inst Phys, Woodbury, NY
- Byskov, R.K.; Jacobsen, C.B. & Pedersen, N. (2003a). Flow in a centrifugal pump impeller at design and off-design conditions – Part II: Large Eddy Simulations, *J. Fluids Eng.*, Vol. 125, No. 1, (Jan. 2003) 73-82, ISBN 00982202
- Feng, J.; Benra, F.K. & Dohmen, H.J. (2009). Comparison of periodic flow fields in a radial pump among CFD, PIV, and LDV results, *Inter. J. of Rotating Machinery*, Vol. 2009. Article ID 410838, 10 pages, ISBN 1023621X
- Guleren, K.M. & Pinarbasi, A. (2004). Numerical simulation of the stalled flow within a vaned centrifugal pump, *Proc Instn Mech. Engrs, J. Mechanical Engineering Science*, Vol. 218, Part C, (Apr. 2004) 425-435, ISBN 09544062
- Li, J.W.; Liu, S.H.; Luo, X.W. & Wu, Y.L. (2007). Viscous flow field in a mini pump with an asymmetric axis, *J. Tsinghua Univ. (Sci & Tech)*, Vol 47, No.5, (May 2007) 682-685, ISSN 10000054
- Matsui, J.; Choi, Y.D.; Kurokawa, J.; Imamura, H. & Hara, M. (2002). Internal flow in a centrifugal pump of a low specific speed with semi-open impeller, *Tran. of the JSME, Part B*, Vol. 6, No. 668, (Apr. 2002) 1174-1180, ISSN 03875016
- Menter, F. R. (1994). Two-equation eddy-viscosity turbulence models for engineering applications. *AIAA Journal*, Vol. 32, No. 1, (Jan. 1994) pp: 269-289, ISBN: 00011452
- Mitchell, A.M.; Morton, S.A.; Forsythe, J. R. & Cummings, R.M. (2006). Analysis of delta-wing vortical substructures using detached-eddy simulation. *AIAA Journal*, Vol. 44, No. 5, (May 2006) 964-972, ISSN 0001452

- Pedersen, N. & Larsen, P.S. (2003b). Flow in a centrifugal pump impeller at design and off-design conditions—Part I: Particle image velocimetry (PIV) and laser doppler velocimetry (LDV) measurements, *J. Fluids Eng.*, Vol. 125, No. 1, (Jan. 2003) 61-72, ISBN 00982202
- Song X.; Wood H., G.; Day S. W. & Olsen D. D. (2003). Studies of turbulence models in a CFD model of a blood pump, *Artificial Organs*, Vol. 27, No. 10, (2003 Oct.) 938-941, ISBN: 0160-564X
- Wu, Y.L., Yuan, H.J., Shao, J. & Liu, S.H. (Apr. 2009). Experimental study on internal flow of a mini centrifugal pump by PIV measurement. *Inter. J. of Fluid Machinery*, Vol. 2, No. 2, (Feb. 2009), 121-126, ISSN 1882-9554

# Direct Numerical Simulation of Turbulence with Scalar Transfer Around Complex Geometries Using the Immersed Boundary Method and Fully Conservative Higher-Order Finite-Difference Schemes

Kouji Nagata<sup>1</sup>, Hiroki Suzuki<sup>1</sup>, Yasuhiko Sakai<sup>1</sup> and Toshiyuki Hayase<sup>2</sup>

<sup>1</sup>*Nagoya University*

<sup>2</sup>*Tohoku University*  
*Japan*

## 1. Introduction

Direct numerical simulation (DNS) of turbulence is a powerful tool for the detailed investigation of a three-dimensional turbulent flow field, although the applications of DNS are currently restricted to moderate Reynolds numbers owing to limitations in computer resources. The numerical methods for DNS of turbulent flows are broadly categorized into the spectral method and finite difference method according to their numerical method (The finite element method is also used for coupling problems of fluid-structure interaction, but this method is beyond the scope of this chapter). The spectral method is highly accurate; however, owing to the numerical procedure involved, its application is limited to simple domains such as a cubic domain. On the other hand, the finite difference method can be applied to complex geometries, although its accuracy is generally lower than that of the spectral method. However, with recent developments in fully conservative higher-order finite-difference schemes (Morinishi et al. 1998), in the higher-order compact scheme originally developed for compressible flows (Lele 1992), and in the immersed boundary method for handling complex wall geometries (Fadlun et al. 2000; Ikeno & Kajishima 2007), DNS with spectral-like accuracy can be carried out around complex geometries with scalar transfer.

In this chapter, we demonstrate the method for performing DNS of incompressible turbulent flows with scalar transfer around complex geometries. In the first section, we present the results for the canonical channel flow with scalar transfer obtained using our DNS code and compare them with results obtained using the spectral method (Iwamoto et al. 2002; Kasagi et al. 1992). Then, we describe the numerical methods for the DNS of turbulent fields with scalar transfer around and downstream of regular and fractal grids (Hurst & Vassilicos 2007; Seoud & Vassilicos 2007; Mazellier & Vassilicos 2010) as an example of flow around complex geometries. The turbulence-generating grids are reproduced using the immersed boundary method (Fadlun 2000) with a direct forcing scheme in the Navier-Stokes equations. The fractional step method is employed for solving the governing equations. The use of

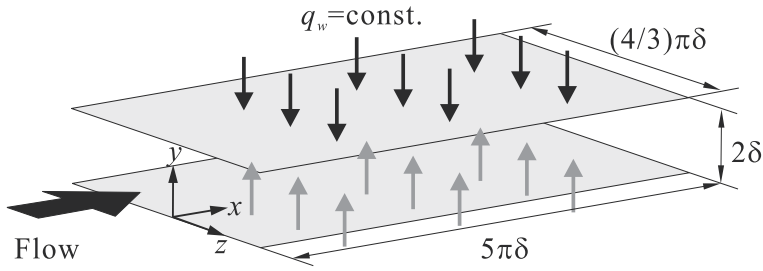


Fig. 1. Computational domain for the channel flow with scalar transfer (constant scalar flux condition)

the present method ensures a divergence-free condition up to machine accuracy ( $\sim 10^{-14}$ ). Instantaneous flow fields and various turbulence quantities are presented and discussed. The method and results shown in this chapter pertain to state-of-the-art DNS of turbulence with scalar transfer around complex geometries based on the finite-difference method.

## 2. DNS of a channel flow with scalar transfer: validation of numerical technique

To validate our numerical simulation, we present the DNS results of a channel flow with scalar (heat) transfer. The results are compared with those obtained by the spectral method (Iwamoto et al. 2002; Kasagi et al. 1992).

### 2.1 Computational domain

Figure 1 shows the computational domain for the channel flow with scalar transfer (with a constant heat flux  $q_w$ ). Table 1 lists the domain size ( $L_x, L_y, L_z$ ), grid mesh points ( $N_x, N_y, N_z$ ), and spatial resolutions ( $\Delta_x^+, \Delta_y^+, \Delta_z^+$ ). The superscript  $+$  denotes the nondimensional quantities normalized by the inner parameters of the flow.

In the wall-normal  $y$  direction, we set the mesh points according to

$$y_j = 1 - \frac{\tanh [(2(1 - 2j/(N_y - 1)))]}{\tanh 2}, \quad (j = 0 \sim N_y - 1) \quad (1)$$

to ensure spatial resolution near the wall.

	Present	Spectral (Iwamoto et al. 2002)	Spectral (Kasagi et al. 1992)
$L_x(L_x^+)$	$5\pi\delta$ (2,356)	$5\pi\delta$ (2,356)	$5\pi\delta$ (2,356)
$L_y(L_y^+)$	$2\delta$ (300)	$2\delta$ (300)	$2\delta$ (300)
$L_z(L_z^+)$	$(4/3)\pi\delta$ (942)	$2\pi\delta$ (628)	$2\pi\delta$ (628)
$N_x$	256	128	128
$N_y$	128	97	97
$N_z$	128	128	128
$\Delta_x^+$	9.2	18.4	18.4
$\Delta_y^+$	0.35 ~ 4.86	0.08 ~ 4.9	0.08 ~ 4.9
$\Delta_z^+$	4.91	7.36	7.36
$Re_\tau$	150	150	150
$Pr$	0.71	-	0.71

Table 1. Computational conditions

## 2.2 Governing equations

The governing equations are the incompressible Navier-Stokes equations (2), the continuity equation (3), and the transport equation for temperature fluctuations (4):

$$\frac{\partial U_i^+}{\partial t} + U_j^+ \frac{\partial U_i^+}{\partial x_j} = -\frac{\partial P^+}{\partial x_i} + \frac{1}{Re_\tau} \frac{\partial^2 U_i^+}{\partial x_j \partial x_j} + \frac{\partial P_w^+}{\partial x_i} \delta_{i1}, \quad (2)$$

$$\frac{\partial U_i^+}{\partial x_i} = 0, \quad (3)$$

$$\frac{\partial \theta^+}{\partial t} + U_j^+ \frac{\partial \theta^+}{\partial x_j} = \frac{1}{Re_\tau Pr} \frac{\partial^2 \theta^+}{\partial x_j \partial x_j} + U_1^+ \frac{\partial \langle T_m^+ \rangle}{\partial x_1}, \quad (4)$$

where  $U_1, U_2, U_3$  is  $U, V, W$ ,  $(x_1, x_2, x_3)$  is  $(x, y, z)$  and the last term in Equation (2) is the streamwise mean pressure gradient to drive the flow. The equations are normalized using the inner parameters.  $Re_\tau = u_\tau \delta / \nu$  is the friction Reynolds number and  $Pr = \nu / \kappa$  is the Prandtl number (same as the Schmidt number  $Sc$  for scalar transfer);  $u_\tau$  is the friction velocity,  $\delta$  the half width of the channel (see Fig. 1),  $\nu$  the kinematic viscosity, and  $\kappa$  the thermal diffusivity. In Equation (4),  $\langle T_m^+ \rangle$  is the mixed mean temperature averaged over the channel section, defined as (Kasagi et al. 1992)

$$\langle T_m^+ \rangle = \int_0^{2\delta} \langle U_1^+ \rangle \langle T^+ \rangle dy / \int_0^{2\delta} \langle U_1^+ \rangle dy, \quad (5)$$

where  $T^+$  is the instantaneous temperature normalized by the friction temperature  $T_\tau (= q_w / (\rho c_p u_\tau))$ ;  $\rho$  is the fluid density,  $c_p$  is the specific heat at constant pressure, and  $\langle \rangle$  denotes the ensemble average.

## 2.3 Numerical methods

The fractional step method is employed for solving the governing equations. The Crank-Nicolson method is used for time-advancement of viscous and diffusion terms along  $y$  (wall-normal) direction, and the third-order Runge-Kutta method is used for the time advancement of other terms. The Poisson equation for pressure is solved using the diagonal matrix algorithm (DMA) along the vertical ( $y$ ) direction and the fast Fourier transform (FFT) along the streamwise ( $x$ ) and spanwise ( $z$ ) directions. The Poisson equation is solved at each step of the Runge-Kutta method. In Equations (2) and (4), the pressure and convection terms along the  $x$  and  $z$  directions are discretized by the fully conservative 4th-order central scheme (CDS4) (Morinishi et al. 1998) and those along  $y$  direction are discretized by the fully conservative 2nd-order central scheme (CDS2) (Morinishi et al. 1998). Further, in these

	CCS4	CCS8
$\alpha$	1/22	75/354
$a$	12/11	(37,950 - 39,275 $\alpha$ )/31,368
$b$	0	(65,115 $\alpha$ - 3,550)/20,912
$c$	0	(25,669 $\alpha$ - 6,114)/62,736
$a_0$	23/22	-

Table 2. Coefficients in the 4th- and 8th-order central compact scheme (CCS4 and CCS8) on a cell-centered mesh (Lele 1992)

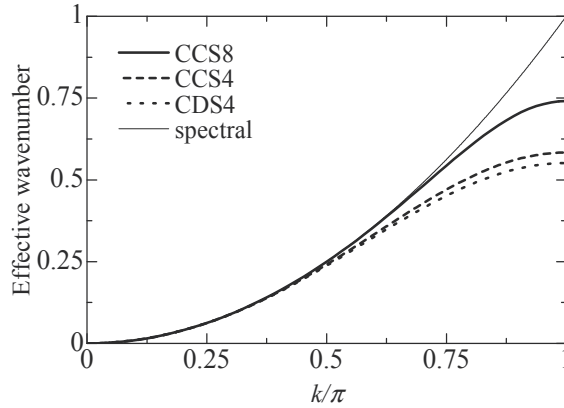


Fig. 2. Effective wavenumber for the cell-centered second derivative approximations (Lele 1992)

equations, the viscous and diffusion terms along the  $x$  and  $z$  directions are discretized by the 8th-order central compact scheme (CCS8) on a cell-centered mesh (Lele 1992) and those along the  $y$  direction are discretized by the 4th-order central compact scheme (CCS4) on a cell-centered mesh (Lele 1992). Here, the 4th- and 8th-order central compact scheme on a cell-centered mesh is expressed as

$$\alpha f'_{i-1} + f'_i + \alpha f'_{i+1} = a \frac{-f_{i-1/2} + f_{i+1/2}}{h} + b \frac{-f_{i-3/2} + f_{i+3/2}}{3h} + c \frac{-f_{i-5/2} + f_{i+5/2}}{5h}, \quad (6)$$

where  $f$  is a variable to be discretized;  $f'$ , the derivative of  $f$ ;  $h(y)$ , the width of the cell and is a function of  $y$  only. The coefficients are listed in Table 2. The truncation errors are  $((9 - 62\alpha) / 1,920) h^4 f^{(5)}$  for CCS4 and  $((96,850 - 288,529\alpha) / 1,686,343,680) h^8 f^{(9)}$  for CCS8 (Lele 1992). At the solid surface, the following discretization is used:

$$f'_i + \alpha f'_{i+1} = a_0 \frac{-f_{i-1/2} + f_{i+1/2}}{h}. \quad (7)$$

The second derivative of  $f$  is also calculated using Equation (6). Figure 2 shows the effective (or modified) wavenumber (Lele 1992) for the cell-centered second derivative approximations. Figure 2 shows that compact schemes (CCS4 and CCS8) provide accurate results up to the high wavenumber region.

In our code, the compact schemes are used only for the diffusion and viscous terms since the energy and mass conservations at the wall have not been comprehensively discussed for the compact scheme applied to nonlinear terms. In addition, the application of the compact scheme to nonlinear terms requires an iterative method for solving the Poisson equation, resulting in a huge computational cost. It should be noted that the viscous effect is considered an important factor in the behavior at the near-wall region and when evaluating spectra in high wavenumber regions.

Using the above schemes, the divergence-free condition is ensured up to the machine accuracy ( $\sim 10^{-14}$ ). Simulations were carried out using the NEC SX-8 supercomputer at the Advanced Fluid Information Research Center, Institute of Fluid Science, Tohoku University. The vectorization ratio is 99.7%. The effective performance is 13 GFLOPS and this value corresponds to approximately 81% of the theoretical performance of 16.0 GFLOPS. These results indicate that our code has been highly optimized.

## 2.4 Flow conditions

The friction Reynolds number  $Re_\tau$  is 150, which is the same value as that used in Iwamoto et al. (2002) and Kasagi et al. (1992). The uniform heat flux condition (same as in Kasagi et al. 1992) is applied to the lower and upper walls. The Prandtl number is set at  $Pr = 0.71$ , considering heat transfer in an air flow.

## 2.5 Results and discussions

### 2.5.1 Flow field

Figure 3 shows the vertical ( $y^+ = yu_\tau/\nu$ ) profiles of mean velocity and rms values of velocity fluctuations normalized by  $u_\tau$ . Figure 4 shows the vertical profiles of the Reynolds shear stress normalized by  $u_\tau^2$ . These profiles indicate that our results are in good agreement with those obtained using the spectral method.

Figure 5 shows the vertical profiles of various terms in the transport equation for the Reynolds stress. Using the notation of the Einstein summation convention for index  $k$ , the transport equation can be expressed as

$$\frac{D\langle u_i^+ u_j^+ \rangle}{Dt} = P_{ij} + T_{ij} + \Pi_{ij} + D_{ij} - \varepsilon_{ij}, \quad (8)$$

$$P_{ij} = -\langle u_j^+ u_k^+ \rangle \frac{\partial U_i^+}{\partial x_k^+} - \langle u_i^+ u_k^+ \rangle \frac{\partial U_j^+}{\partial x_k^+}, \quad (9)$$

$$T_{ij} = -\frac{\partial \langle u_i^+ u_j^+ u_k^+ \rangle}{\partial x_k^+}, \quad (10)$$

$$\Pi_{ij} = -\left\langle u_j^+ \frac{\partial p^+}{\partial x_i^+} \right\rangle - \left\langle u_i^+ \frac{\partial p^+}{\partial x_j^+} \right\rangle, \quad (11)$$

$$D_{ij} = \frac{\partial^2 \langle u_i^+ u_j^+ \rangle}{\partial x_k^+ \partial x_k^+}, \quad (12)$$

$$\varepsilon_{ij} = 2 \left\langle \frac{\partial u_i^+}{\partial x_k^+} \frac{\partial u_i^+}{\partial x_k^+} \right\rangle, \quad (13)$$

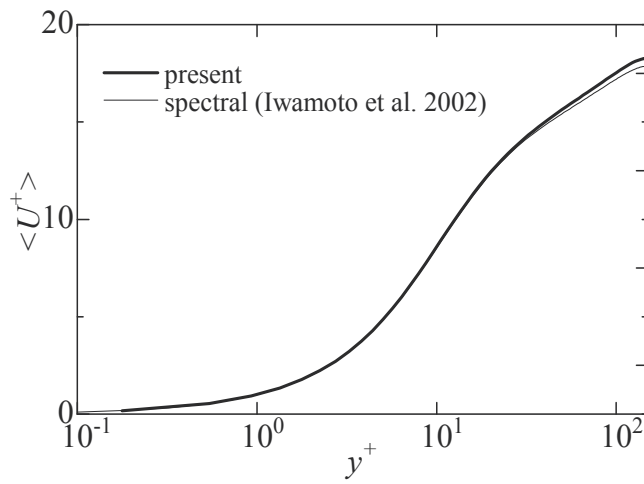
where  $U_i^+ = \langle U_i^+ \rangle + u_i^+$  and  $P^+ = \langle P^+ \rangle + p^+$ .  $\Pi_{ij}$  can be divided into the pressure-diffusion term  $\Psi_{ij}$  and pressure-strain term  $\Phi_{ij}$ :

$$\Pi_{ij} = \Psi_{ij} + \Phi_{ij}, \quad (14)$$

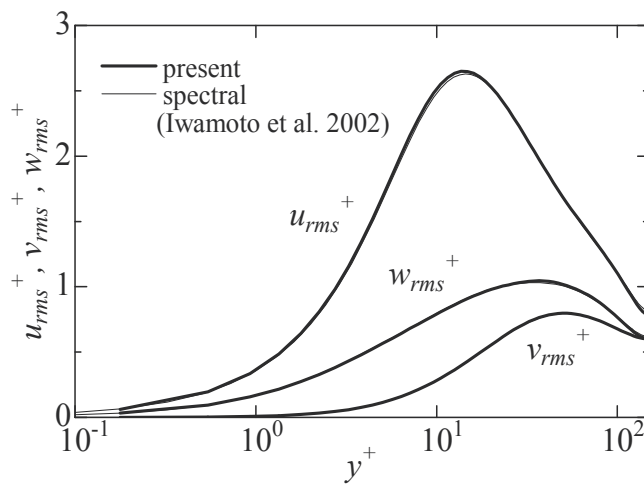
$$\Psi_{ij} = -\left\langle \frac{\partial(u_j^+ p^+)}{\partial x_i^+} \right\rangle - \left\langle \frac{\partial(u_i^+ p^+)}{\partial x_j^+} \right\rangle, \quad (15)$$

$$\Phi_{ij} = \left\langle p^+ \frac{\partial u_j^+}{\partial x_i^+} \right\rangle + \left\langle p^+ \frac{\partial u_i^+}{\partial x_j^+} \right\rangle. \quad (16)$$

Figure 5 shows that our results are in good agreement with those obtained using the spectral method.



(a) Mean velocity



(b) Rms of velocity fluctuations

Fig. 3. Vertical profiles of mean and rms values

Figure 6 shows the dissipation spectra of  $u_i^+$ ,  $(k_z \delta)^2 E_{u_i u_i}$ , and cospectra of  $\langle u^+ v^+ \rangle$ ,  $E_{uv}$ , evaluated at  $y^+ = 15$ . It can be observed that up to the high-frequency range, our results are in good agreement with those obtained using the spectral method.

### 2.5.2 Scalar field

Owing to space restrictions, only four profiles are presented here. Figure 7 shows the vertical profiles of mean temperature  $\langle T^+ \rangle$  and temperature variance  $k_\theta^+ = \frac{1}{2} \langle \theta^{+2} \rangle$ , normalized using  $T_\tau$ . Figure 7 shows that our results are in good agreement with those obtained using the spectral method.

Figure 8 shows the vertical profiles of  $-\phi_{v\theta}$  and  $-\psi_{v\theta}$  in the transport equation for vertical turbulent heat flux  $-\langle v^+ \theta^+ \rangle$ :

$$-\phi_{v\theta} = \left\langle p^+ \frac{\partial \theta^+}{\partial y^+} \right\rangle, \quad (17)$$

$$-\psi_{v\theta} = -\frac{\partial \langle p^+ \theta^+ \rangle}{\partial y^+}. \quad (18)$$

In general, the computational errors of these terms are larger than those of the other terms. Figure 8 shows that our results are in good agreement with those obtained using the spectral method. We have also confirmed that other statistics on scalar quantities (not shown here) are in good agreements with those obtained using the spectral method.

These results on turbulent and scalar fields indicate that the accuracy of our code is comparable to that of the spectral code. In the next section, we will show the computational results for grid turbulence with scalar transfer as an example of flow around complex geometries. The code employed is based on the code presented in this section, along with the immersed boundary method for handling complex wall geometries (Fadlun et al. 2000).

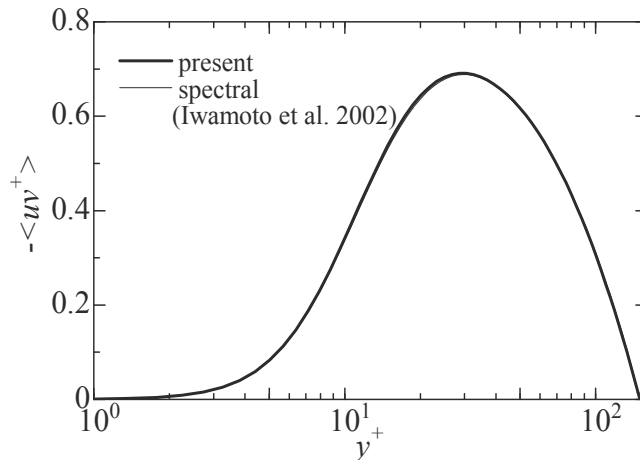


Fig. 4. Vertical profiles of Reynolds shear stress

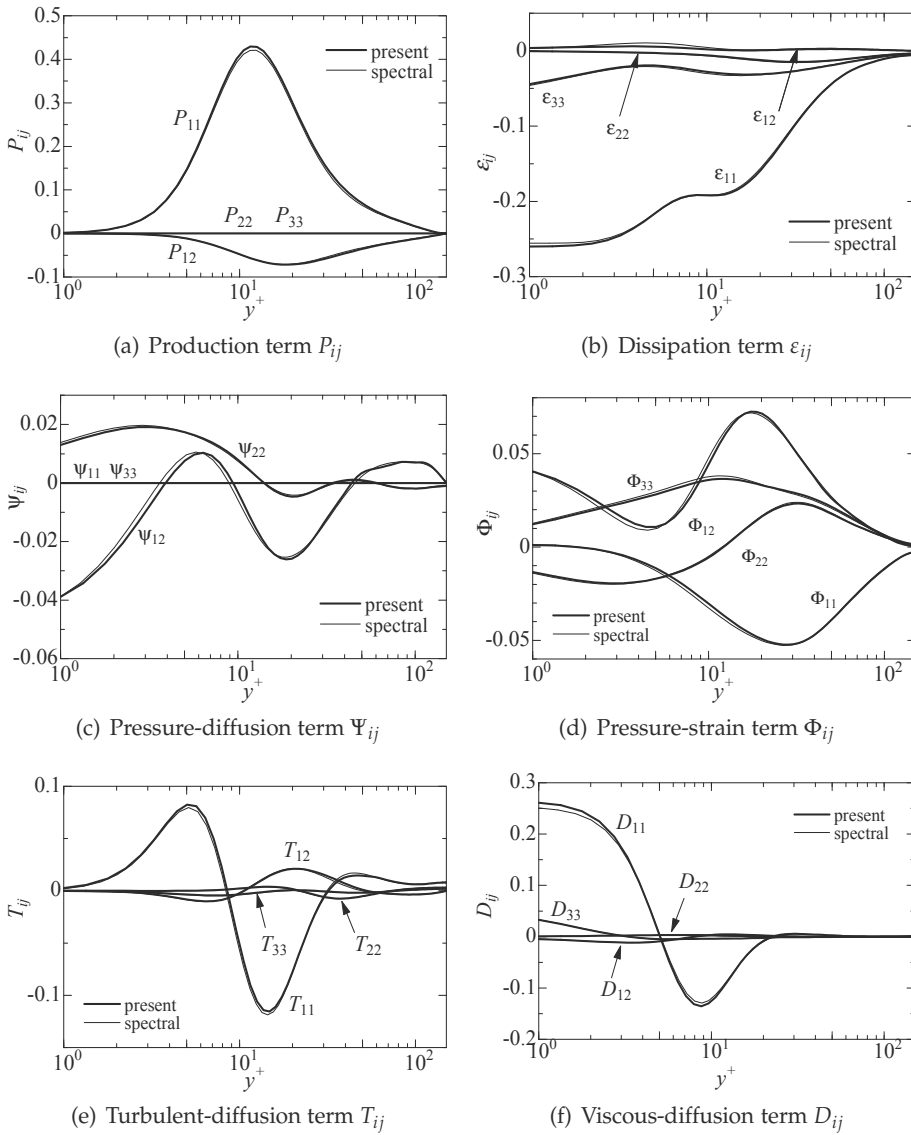


Fig. 5. Vertical profiles of various terms in the transport equation for the Reynolds stress

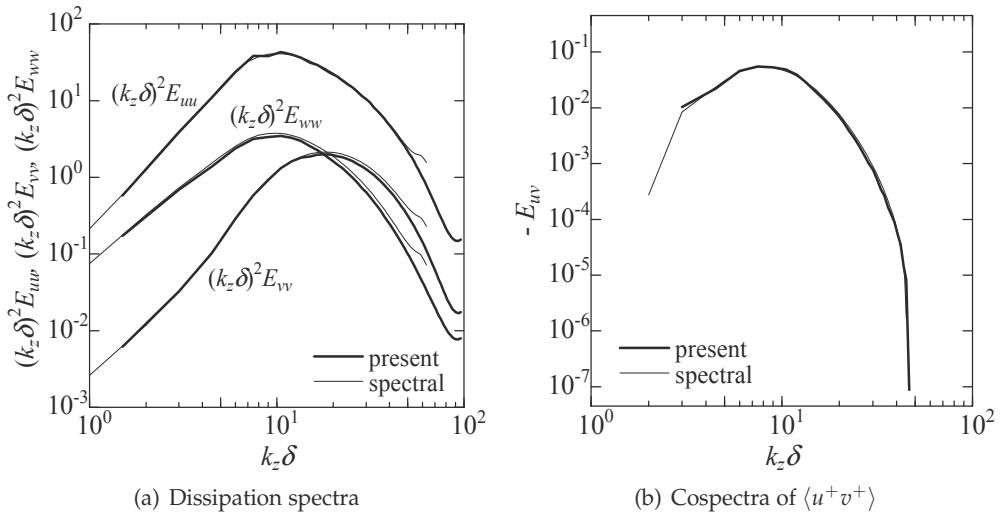


Fig. 6. Dissipation spectra and cospectra at  $y^+ = 15$

### 3. DNS of grid-generated turbulence: an example of flow around complex geometries

#### 3.1 Background

Grid-generated turbulence has been widely used to generate quasi-isotropic turbulence in wind tunnels and water channels and has been applied to investigate the heat transfer in a wind tunnel (Warhaft & Lumley 1978; Sreenivasan et al. 1980; Budwig et al. 1985), mass transfer in a water channel (Huq & Britter 1995), scalar diffusion from line and point sources (Stapountzis et al. 1986; Nakamura et al. 1987), turbulent transport of small particles in a wind tunnel (Gad-el-Hak & Morton 1979), heat and mass transfer in stable density stratification (Stillinger et al. 1983; Lienhard & Van Atta 1990; Jayesh et al. 1991; Komori & Nagata 1996; Nagata & Komori 2001), mass transfer in unstable density stratification (Nagata & Komori 2000), and mass transfer with a chemical reaction (Komori et al. 1993; Nagata & Komori 2000; Ito et al. 2002). Grid-generated turbulence is also considered in turbulence analysis (Nagata et al. 2006, 2010).

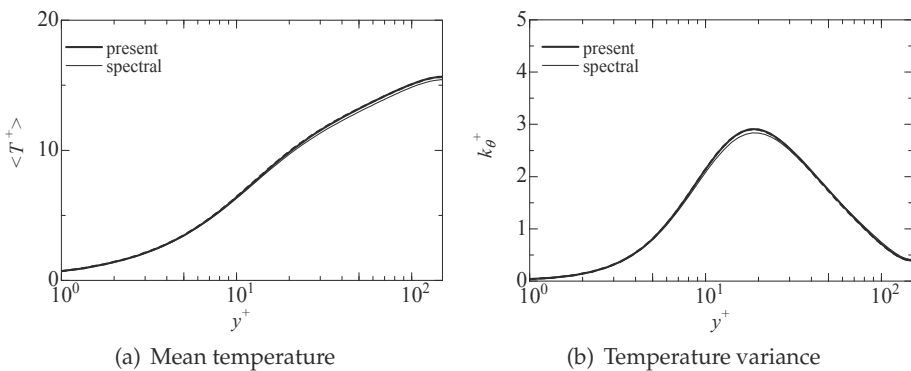


Fig. 7. Vertical profiles of mean temperature and temperature variance

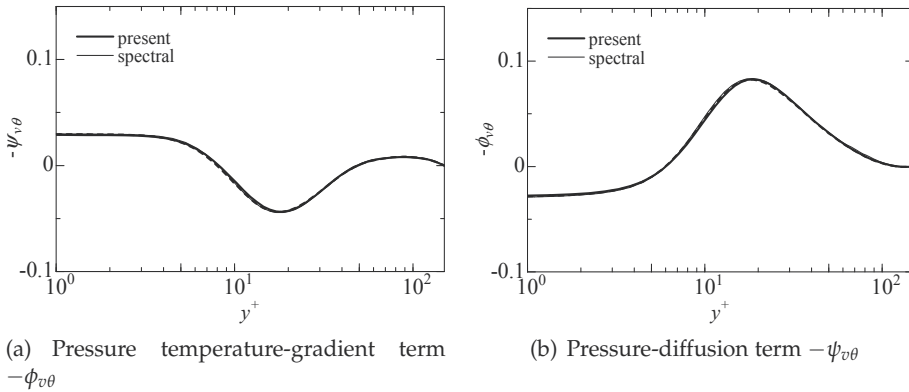


Fig. 8. Vertical profiles of  $-\phi_{v\theta}$  and  $-\psi_{v\theta}$  in the transport equation for vertical turbulent heat flux  $-\langle v^+\theta^+\rangle$

However, it is very difficult to completely understand the turbulence and scalar fields in the aforementioned flows through conventional measurements using hot wire/film probes or laser Doppler velocimetry for velocity field and using a cold-wire or electrode-conductivity probes (e.g., Gibson & Schwarz 1963) or laser induced fluorescence (LIF) technique for scalar field. For instance, the direct measurement of fundamental statistics such as those including pressure fluctuation and/or spatial derivatives is difficult; these statistics are usually estimated from limited measurable quantities using certain hypotheses. Recently, the measurements of grid-generated turbulence have been conducted using particle image velocimetry (PIV) (Proud et al. 2005; Suzuki et al. 2010a), and more detailed information on the flow field has been obtained. However, it is still difficult to elucidate three-dimensional structures in the aforementioned flows.

Recently, turbulence generated by the fractal grid has also been investigated in previous studies (Hurst & Vassilicos 2007; Seoud & Vassilicos 2007; Mazellier & Vassilicos 2010). These studies showed that fractal grids generate unusually high turbulence intensities and that fractal forcing by the fractal grids modifies turbulence so greatly that the dissipation, spectra, and evolution of integral and Taylor microscales exhibit considerably unusual behaviors. To completely understand these new types of turbulence generated by fractal grids, information on the three-dimensional flow field is required.

DNS of the grid-generated turbulence is the most suitable approach for addressing these issues, although the application of DNS to complex geometry is currently limited to low to moderate Reynolds numbers. It should be noted that the Reynolds numbers in some

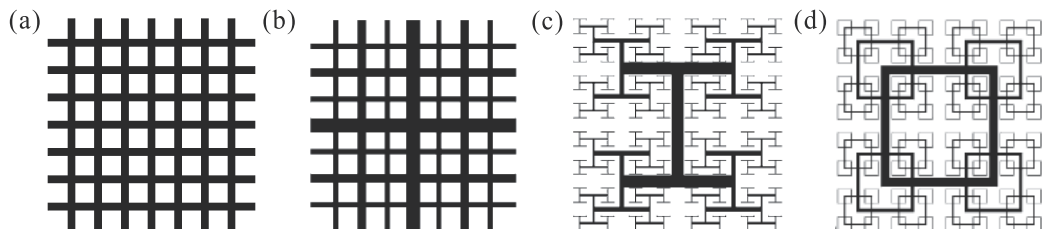


Fig. 9. Schematics of the turbulence-generating grids: (a) regular grid; (b) fractal cross grid; (c) fractal I grid; (d) fractal square grid (after Hurst & Vassilicos 2007)

Grid type	$D_f$	$N$	$\sigma$	$t_r$
Regular	2.0	1	0.36	1
Fractal I	2.0	4	0.36	8.5
Fractal cross	2.0	4	0.36	8.5
Fractal square	2.0	4	0.36, 0.44	5.0, 8.5, 13.0, 15.0

Table 3. Specifications of the turbulence-generating grids

important flows (e.g., Nagata & Komori 2000, 2001; Ito et al. 2002) are not very large. Since future advancements in supercomputers can be anticipated fairly confidently, it can be assumed that DNS of complex geometry at high Reynolds numbers should soon become possible.

In this section, we describe the numerical method for performing DNS of grid-generated turbulence with scalar transfer. The DNS code for fractal grid turbulence has also been independently developed by Laizet & Vassilicos (2010) using a different approach. The numerical code is applied to DNS of a turbulent field with scalar transfer downstream of regular and fractal grids, and the characteristics of flow and scalar fields are presented.

### 3.2 Turbulence-generating grids

Figure 9 shows the schematics of turbulence-generating regular and fractal grids. The regular grid consists of a square bar, square mesh, and biplane construction. In the present DNS, all bars of the fractal grid have square cross-sections, although all these bars have the same thickness in the direction of a mean flow in the previous experiments (Hurst & Vassilicos 2007; Seoud & Vassilicos 2007; Mazellier & Vassilicos 2010). The grid parameters are listed in Table 3. Here,  $D_f$  is the fractal dimension;  $N$ , the fractal iteration;  $\sigma$ , the solidity; and  $t_r$ , the thickness ratio of the largest bar thickness to the smallest bar thickness,  $t_{max}/t_{min}$ . The values of  $D_f$  and  $N$  for the fractal grids are the same as those used in previous experiments (Hurst & Vassilicos 2007; Seoud & Vassilicos 2007; Mazellier & Vassilicos 2010). Details on the fractal grids are provided in Hurst & Vassilicos (2007).

### 3.3 Computational domain

Figure 10 shows the computational domain. Here,  $L_x, L_y$ , and  $L_z$  are normalized by the effective mesh size,  $M_{eff}$  (refer to Hurst & Vassilicos 2007 for further details on  $M_{eff}$ ). The domain size and number of mesh points are listed in Table 4. The turbulence-generating grid is numerically constructed at  $5M_{eff}$  downstream from the entrance. In runs Tests 1 ~ 3, only the smallest grid (the smallest component of the fractal grid) is placed in the middle of the domain at  $x/M_{eff} = 0$ , as shown in Fig. 10 (b), to determine the minimum number of mesh points in the  $y$  or  $z$  direction for reproducing the suitable wakes of the smallest grid bars. The domain size for runs Tests 1 ~ 3 is  $2M_{eff} \times 2M_{eff}$  in cross section (which corresponds to  $(1/8)^2$  of that for the actual fractal grids, i.e., runs SFG1~3, SFGm1~3). The length and thickness of the smallest bar used in runs Tests 1 ~ 3 are  $M_{eff}$  and  $0.1M_{eff}$ , respectively. In run Test 1, only two mesh points are arranged on the bar in the  $y$  or  $z$  direction. In runs Tests 2 and 3, three and five mesh points, respectively, are arranged on the bar in the  $y$  or  $z$  direction. Note that more mesh points (which are identical for all runs) are arranged on the bar in the streamwise ( $x$ ) direction as shown in section 3.5.2. The number of mesh points for other runs are determined after performing runs Tests 1 ~ 3. The dependence of mesh points on the wakes is discussed in section 3.8.1.

Run	grid	$L_x$	$L_y, L_z$	$N_x$	$N_y, N_z$	$Re_M$	$Pr$
Test1	Fractal square ( $N = 1$ )	38.4	2	512	20	2,500	-
Test2	Fractal square ( $N = 1$ )	38.4	2	512	40	2,500	-
Test3	Fractal square ( $N = 1$ )	38.4	2	512	80	2,500	-
RG1	Regular ( $S_\theta = \text{const}$ )	115.2	8	1,280	160	2,500	0.71
RGm1	Regular (s.m.l.)	64.0	8	768	160	2,500	0.71
CFG	Fractal cross	115.2	16	1,280	320	2,500	-
IFG	Fractal I	115.2	16	1,280	320	2,500	-
SFG1	Fractal square ( $S_\theta = \text{const}$ ) ( $t_r = 8.5, \sigma = 0.36$ )	115.2	16	1,280	320	2,500	0.71
SFG2	Fractal square ( $t_r = 15.0, \sigma = 0.36$ )	115.2	16	1,280	416	2,500	-
SFG3	Fractal square ( $t_r = 8.5, \sigma = 0.44$ )	115.2	16	1,280	256	2,500	-
SFGm1	Fractal square ( $t_r = 5.0, \sigma = 0.36$ , s.m.l.)	64.0	16	768	256	2,500	0.71
SFGm2	Fractal square ( $t_r = 8.5, \sigma = 0.36$ , s.m.l.)	64.0	16	768	320	2,500	0.71
SFGm3	Fractal square ( $t_r = 13.0, \sigma = 0.36$ , s.m.l.)	64.0	16	768	416	2,500	0.71

Table 4. Computational conditions. (s.m.l.: scalar mixing layer)

### 3.4 Governing equations

The governing equations are the forced incompressible Navier-Stokes equations (19), the continuity equation (20), the forced transport equation for scalar fluctuations (21) in case of the linear scalar gradient, and the forced transport equation for instantaneous scalar (22) in case of the scalar mixing layer:

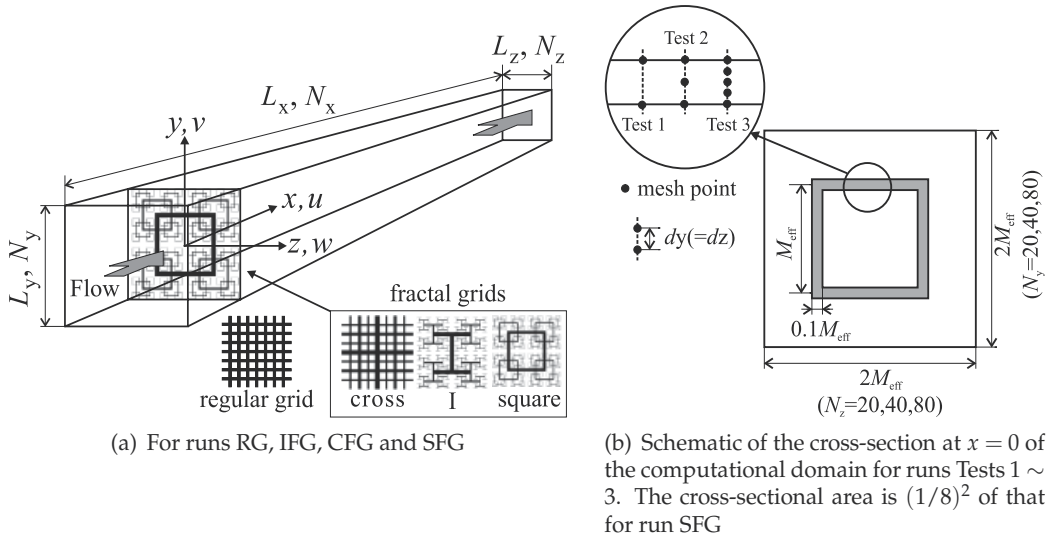


Fig. 10. Schematic of computational domain

$$\frac{\partial U_i}{\partial t} + U_j \frac{\partial U_i}{\partial X_j} = -\frac{\partial P}{\partial X_i} + \frac{1}{Re_M} \frac{\partial^2 U_i}{\partial X_j \partial X_j} + F_i, \quad (19)$$

$$\frac{\partial U_i}{\partial X_i} = 0, \quad (20)$$

$$\frac{\partial \theta}{\partial t} + U_j \frac{\partial \theta}{\partial X_j} + U_2 S_\theta = \frac{1}{Re_M Pr} \frac{\partial^2 \theta}{\partial X_j \partial X_j} + F_\theta, \quad (21)$$

$$\frac{\partial T}{\partial t} + U_j \frac{\partial T}{\partial X_j} = \frac{1}{Re_M Pr} \frac{\partial^2 T}{\partial X_j \partial X_j} + F_T, \quad (22)$$

where  $S_\theta$  is the constant scalar gradient. The equations are normalized using  $U_0$ ,  $M_{eff}$ , and the characteristic value of scalar  $\Delta T$ . Here  $\Delta T$  is chosen as the scalar difference within the vertical length  $M_{eff}$  in case of the linear scalar gradient and is chosen as the scalar difference between the upper and lower streams in case of the scalar mixing layer. In Equations (19) and (21), the force terms,  $F_i$ ,  $F_\theta$ , and  $F_T$ , are introduced for satisfying the boundary conditions on the grid surface when using the immersed boundary method (Fadlun et al. 2000).

### 3.5 Boundary conditions

#### 3.5.1 Boundary conditions at the boundary of domain

The uniform flow  $U_0$  is given as an inflow, in which no velocity or scalar fluctuations are provided. The periodic boundary conditions are imposed for all variables in the vertical and spanwise directions. The convective outflow condition:

$$\frac{\partial \beta}{\partial t} + U_c \frac{\partial \beta}{\partial X_1} = 0, \quad (23)$$

is applied for velocities and scalar at the exit, where  $\beta$  denotes the instantaneous velocity or instantaneous scalar or scalar fluctuation, and  $U_c$  denotes the convection velocity, which is set equal to  $U_0$ . For pressure, the Neumann condition is applied at the inlet and the Dirichlet-Neumann condition is applied at the exit.

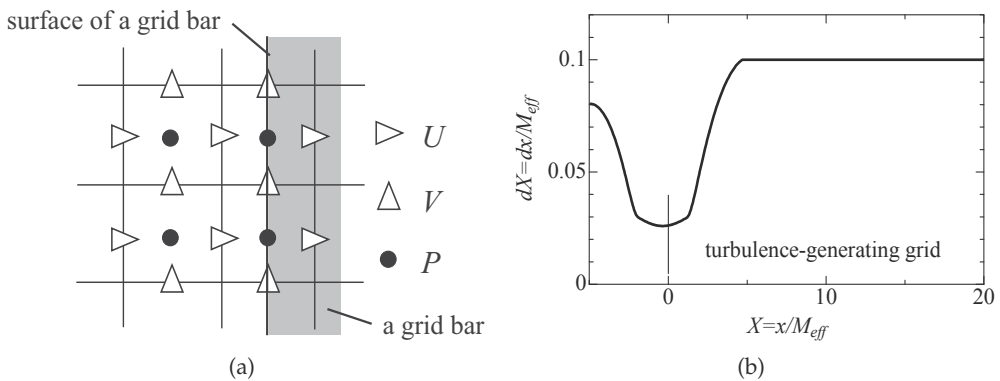


Fig. 11. (a) Schematic of surface layout and (b) streamwise variation of streamwise mesh size  $dX$

### 3.5.2 Boundary conditions on the grid surface

The immersed boundary method (Fadlun et al. 2000) is used to satisfy the boundary conditions on the grid surface. This method employs the force term  $F_i$  to satisfy the specified Dirichlet conditions on the solid surface. The direct forcing method (Fadlun et al. 2000) has been adopted in the present DNS. To solve Equations (19) and (20) using the fractional step method, the Poisson equation should be solved. Ikeno & Kajishima (2007) stated that existing schemes for the immersed boundary method violate the wall condition during time advancement due to the inconsistency between the pressure and the velocity interpolated to represent the solid wall; they developed a modified pressure equation based on the interpolated pressure gradient. However, in this method, an iterative process is required to solve the Poisson equation, which requires extensive computational resources. Fortunately, turbulence-generating grids have surfaces parallel and perpendicular to the Cartesian grid system; therefore, we reduced the pressure inconsistency problem by adopting the mesh arrangement shown in Fig. 11 (a). Since the definition points of the pressure exist on the grid surface, the pressure does not require interpolation, and can be directly determined from the Poisson equation. Most definition points for the velocities are also arranged on the grid surface to directly specify the nonslip wall conditions. The staggered mesh arrangement is used in this study to prevent spurious pressure oscillations.

With these mesh arrangements for the grid surface, we can reproduce suitable wakes behind the smallest bars. It should be noted that suitable wakes were not reproduced when other mesh arrangements were used for the present mesh sizes (spatial resolutions) and Reynolds number. In addition, spatial resolutions around the turbulence-generating grids were ensured by concentrating the grid points in the streamwise ( $x$ ) direction, as shown in Fig. 11 (b). This grid system is used for all runs listed in Table 4. Around the turbulence-generating grid,  $dX$  is about  $1/4$  of the far downstream value. These mesh arrangements prevent numerical instability around the grid bars. It should be noted that numerical filters and non-physical numerical viscosity, which are often used to prevent numerical instability, were not used in the present DNS.

### 3.6 Numerical methods

The numerical methods used here are similar to those described in section 2, with some modifications as described below. The third-order Runge-Kutta method is used for time advancement. The Poisson equation for pressure is solved using the diagonal matrix algorithm (DMA) along the streamwise ( $x$ ) direction and the fast Fourier transform (FFT) along the vertical ( $y$ ) and spanwise ( $z$ ) directions. The pressure and convection terms along the  $y$  and  $z$  directions in Equations (19) and (21) are discretized by the fully conservative 4th-order central scheme (CDS4) (Morinishi et al. 1998), and those along the  $x$  direction, by the fully conservative 6th-order central scheme (CDS6) (Morinishi et al. 1998). The viscous and diffusion terms along the  $y$  and  $z$  directions in Equations (19) and (21) are calculated by the Fourier spectral method, and those along the  $x$  direction are discretized by the 8th-order central compact scheme (CCS8) on a cell-centered mesh (Lele 1992).

### 3.7 Flow conditions

The mesh Reynolds number  $Re_M(= U_0 M_{eff}/\nu)$  is set at 2,500 for all cases. This value is much smaller than that used in previous experiments on fractal grid turbulence (Hurst & Vassilicos 2007; Seoud & Vassilicos 2007; Mazellier & Vassilicos 2010) owing to limitations in computer resources; however, it is the same as that used in Komori & Nagata (1996) and

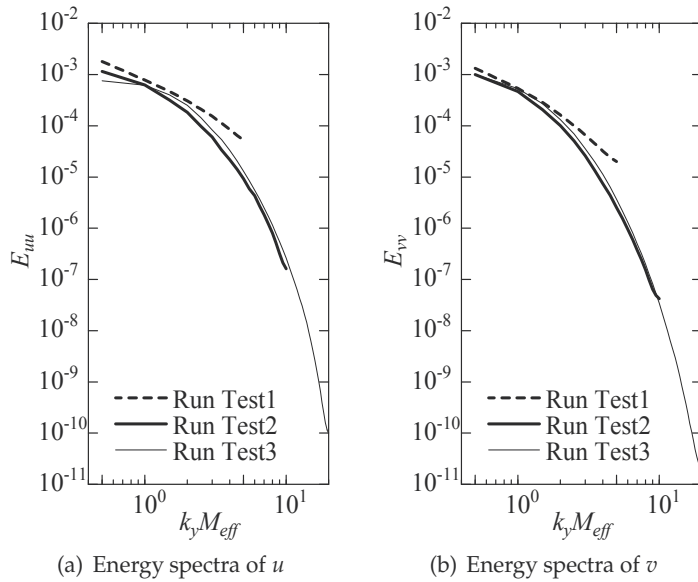


Fig. 12. Energy spectra of  $u$  and  $v$  at  $x/M_{eff} = 8$  for runs Tests 1 ~ 3. In runs Tests 1 ~ 3, two, three, and five mesh points are respectively arranged on the bar in the  $y$  or  $z$  direction

Nagata & Komori (2000, 2001). For a linear scalar gradient (runs RG1 and SFG1), the constant scalar gradient  $S_\theta$  is set to  $1/16$  for both regular and fractal grid turbulence. Therefore, the normalized maximum scalar difference in the vertical direction is 1.0 for the fractal grid turbulence (run SFG1) and is  $1/2$  for the regular grid turbulence (run RG1). For a scalar mixing layer (runs RGM1 and SFGM1 ~ SFGM3), the initial nondimensional scalar is  $T = 1$  and  $T = 0$  in the upper and lower half streams, respectively. Therefore, scalar mixing layers that initially have a step profile develop downstream of the grids, as in the previous experiments (e.g. Huq & Britter 1995; Komori & Nagata 1996; Nagata & Komori 2000, 2001; Suzuki et al. 2010a). The Prandtl number  $Pr$  is set at 0.71, considering heat transfer in an air flow. It should be noted that it is impossible to perform DNS of high-Schmidt-number scalar fields because the smallest scale of the scalar field (i.e., the Batchelor scale),  $\eta/\sqrt{Sc}$ , is considerably small at a high Schmidt number; here,  $\eta$  is the Kolmogorov scale and  $Sc$  is the Schmidt number ( $Sc \approx 2,100$  in our previous experiments using Rhodamine B (Suzuki et al. 2010a)).

### 3.8 Results and discussions

#### 3.8.1 Grid dependence on wakes of grid bars

Figure 12 shows the energy spectra of  $u$  and  $v$  at  $x/M_{eff} = 8$  for runs Tests 1 ~ 3. In run Test 1, the spectra obviously differ from those for runs Tests 2 and 3. Therefore, at least three mesh points should be arranged in the vertical (or spanwise) direction to accurately reproduce the wakes of the smallest grid bars. It should be noted that this result is for the smallest bars (corresponding to  $j = N - 1 = 3$  in runs CFG, IFG, SFG1 ~ 3, and SFGM1 ~ 3) of the actual fractal grid; naturally, more mesh points are arranged on the larger bars for iterations of  $j = 0$  (the largest component of the fractal grid) ~ 2 (the second smallest component of the fractal grid). In addition, the results depended on the resolution of time advancement as well as the number of mesh points: proper wakes were not reproduced when the 2nd and 3rd order Adams-Bashforth schemes were employed.

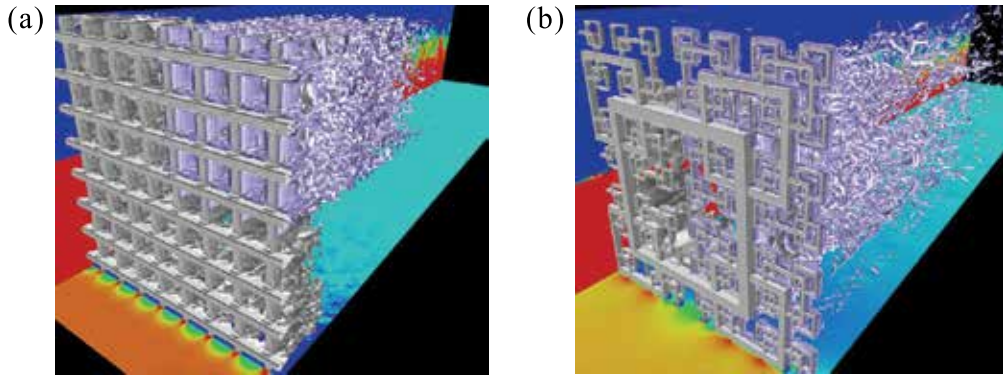


Fig. 13. Instantaneous flow fields around turbulence-generating grids: (a) regular grid (run RGM1); (b) fractal square grid (run SFGm2)

### 3.8.2 Instantaneous and mean flow fields

Figure 13 shows the snapshots of the instantaneous flow fields near the grids. The grid is visualized using the isovelocity surface in case of instantaneous streamwise velocity  $U = 0$ . The isosurfaces of the second invariant of the velocity gradient tensor  $Q$ , contour of pressure  $P$  (on the bottom plane near  $y = -8M_{eff}$ ), and contour of scalar for the mixing layer (on the side plane near  $z = -8M_{eff}$ ) are drawn. Here,  $Q$  is defined as

$$Q = \frac{1}{2} (W_{ij}W_{ij} - S_{ij}S_{ij}), \quad (24)$$

where,

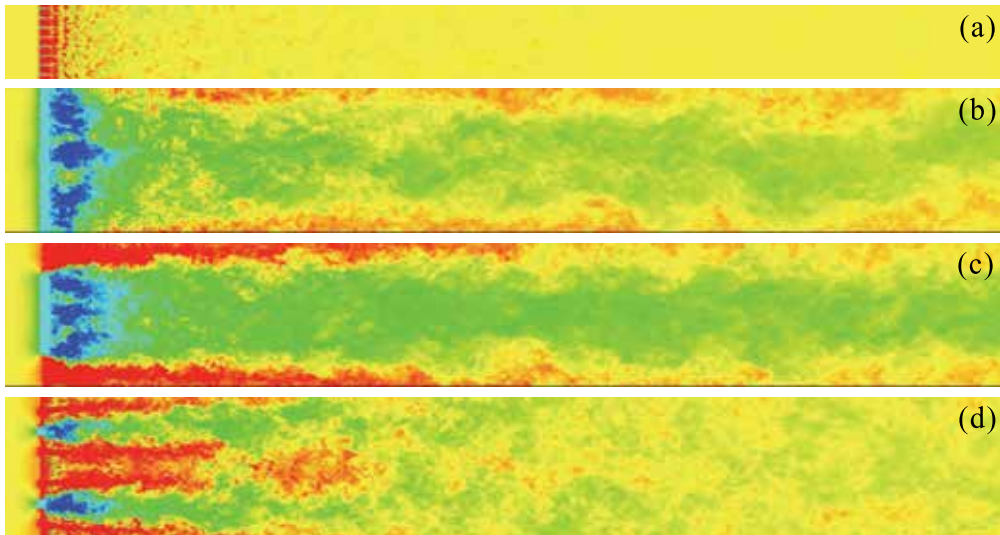
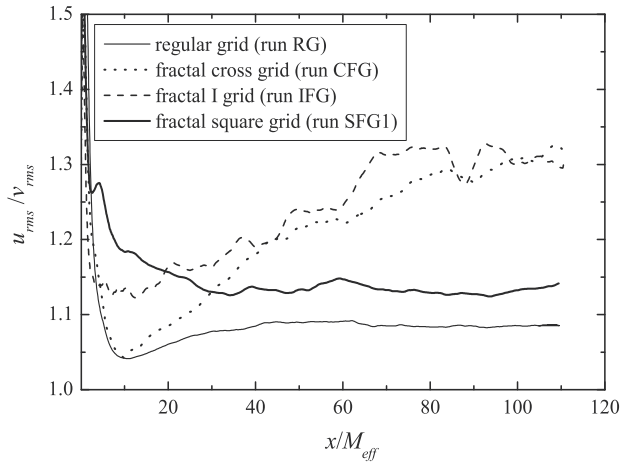
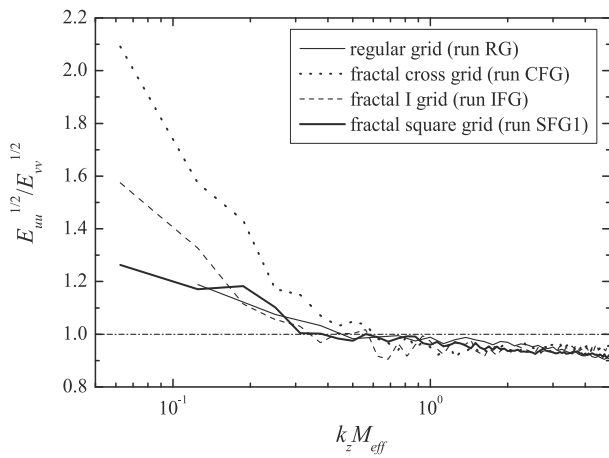


Fig. 14. Instantaneous flow fields downstream of (a) regular grid (run RG1), (b) fractal cross grid (run CFG), (c) fractal I grid (run IFG), and (d) fractal square grid (run SFG1). White: high speed ( $U = 1.5$ ), black: low speed ( $U = -1.5$ )



(a) Large-scale anisotropy: ratio of  $u_{rms}$  and  $v_{rms}$



(b) Small-scale anisotropy: ratio of square-root of spectra of  $u_{rms}$  and  $v_{rms}$

Fig. 15. Isotropy of turbulence

$$W_{ij} = \frac{1}{2} \left( \frac{\partial u_j}{\partial x_i} - \frac{\partial u_i}{\partial x_j} \right), \quad S_{ij} = \frac{1}{2} \left( \frac{\partial u_j}{\partial x_i} + \frac{\partial u_i}{\partial x_j} \right). \quad (25)$$

It can be observed that the regular and fractal grids are adequately constructed using the present method and that the grid turbulence is generated downstream of the grids.

Figure 14 shows the snapshots of the instantaneous velocity field at  $z = 0$  plane. Here, the left side of the figure indicates the upstream. The instantaneous contours of streamwise velocity in the entire computational regions are depicted. It can be observed that all the fractal grids generate high turbulence intensities compared with the regular grid turbulence. It is inferred from Fig. 14 that as compared with the fractal cross and the I grids, the fractal square grid returns the optimal homogeneity in the downstream region: in Figs. 14 (b) and (c) (in case of the fractal cross and I grids), significant velocity defects can be observed near the central region even in the far downstream region. In fact, mean velocity profiles show significant velocity defects even in the far downstream region of the fractal cross and I grids (refer to Nagata et al. 2008 for statistics). Note that periodic boundary conditions are applied to  $y$  and  $z$  boundaries, and therefore, no effects of side walls on the flow field exist.

### 3.8.3 Isotropy of turbulence

When grid-generated turbulence is experimentally used in fundamental researches as a way of producing quasi homogeneous isotropic turbulence, the degree of isotropy as well as homogeneity should necessarily be important. To evaluate the isotropy of turbulence, Fig. 15 (a) shows the streamwise profiles of the ratio of rms velocities  $u_{rms}/v_{rms}$ , which serves as a measure of large-scale anisotropy. The ratio  $u_{rms}/w_{rms}$  is identical to  $u_{rms}/v_{rms}$  in the fractal-generated turbulence with the symmetrical fractal cross and square grids, as in the case of the mean velocity profile. Figure 15 (a) shows that acceptable isotropy of  $u_{rms}/v_{rms} \sim 1.15$  is attained in the far downstream region of the fractal square grid, whereas large anisotropy is observed in the downstream regions of the fractal cross and I grids. Figure 15 (b) shows the ratio of the spectra,  $E_{uu}(k_z)^{1/2}/E_{vv}(k_z)^{1/2}$ , where  $k_z$  is the spanwise wavenumber. It is found

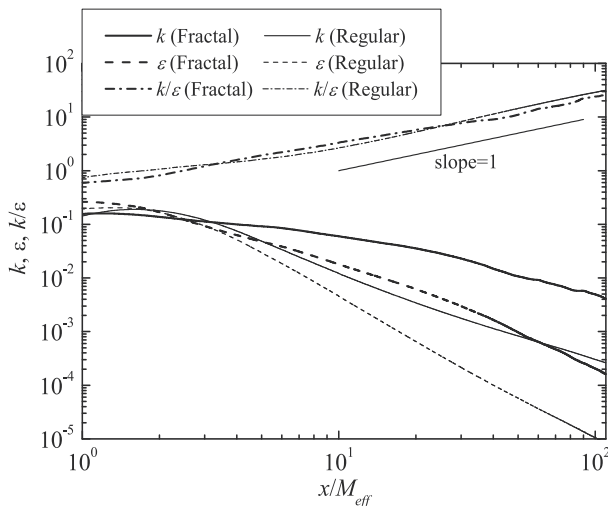


Fig. 16. Streamwise variations of turbulence kinetic energy  $k$ , dissipation rate  $\varepsilon$ , and timescale  $k/\varepsilon$  downstream of regular and fractal square grids (runs RG1 and SFG1)

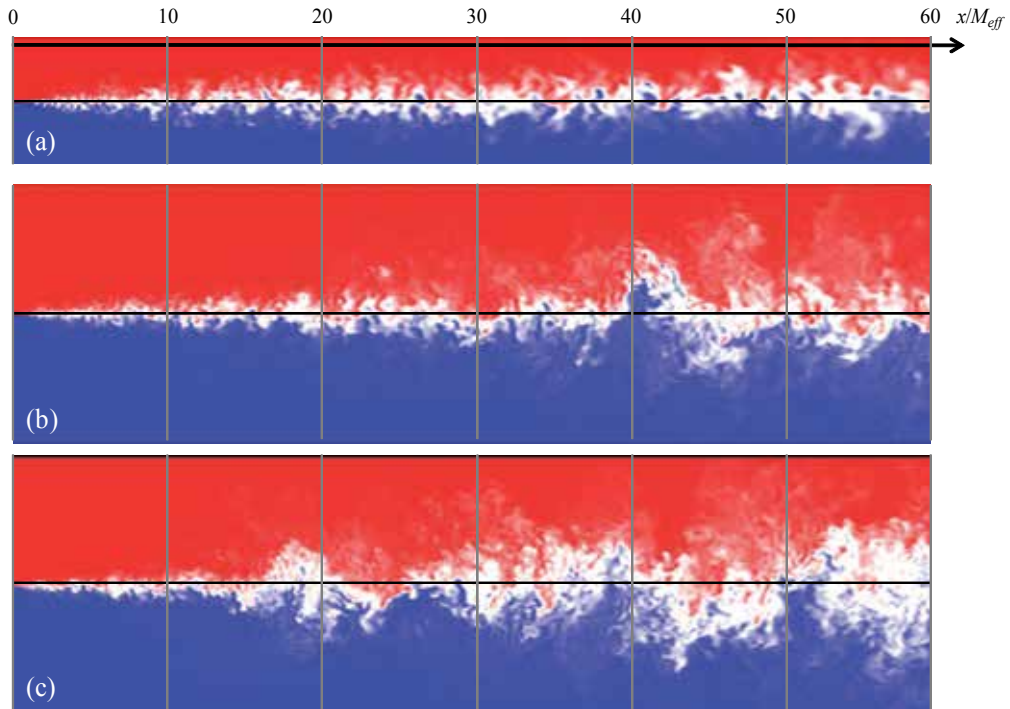


Fig. 17. Instantaneous scalar fields at  $z = 0$  in (a) regular grid turbulence (run RGm1), (b) fractal grid turbulence at  $t_r = 5.0$  (run SFGm1), and (c) fractal grid turbulence at  $t_r = 8.5$  (run SFGm2). In all figures, red:  $T = 1$ , white:  $T = 0.5$ , blue:  $T = 0$

that the anisotropy of the fractal-generated turbulence with the fractal square grid is mainly due to the anisotropy at a large scale; the acceptable isotropy is attained for fractal-generated turbulence with a fractal square grid in intermediate to smallest scales. The result qualitatively agrees with that of Seoud & Vassilicos (2007). It should be noted that even at the large scale, the anisotropy is less than 1.3 for the fractal square grid; this value is comparable to that in the regular grid turbulence.

The correlation coefficients of the Reynolds stresses (not shown) are small in the downstream region of the fractal square grid, whereas the maximum values are large (approximately 0.5) even in the far downstream regions of the fractal cross and I grids.

The above results suggest that the fractal square grid generates quasi homogeneous isotropic turbulence in the far downstream region of the grid. On the other hand, homogeneous isotropic turbulence could not be generated using the fractal cross and I grids under the present fractal parameters and mesh Reynolds number. Therefore, after this section, we will only show the results for the fractal square grid and regular grid for comparison.

### 3.8.4 Turbulence statistics

Figure 16 shows the streamwise variations of turbulence kinetic energy  $k = \frac{1}{2} \langle u_i u_i \rangle$ , dissipation rate  $\varepsilon$  of  $k$ , and timescale of  $k/\varepsilon$  downstream of regular and fractal square grids (runs RG1 and SFG1, respectively). Here,  $k$  and  $\varepsilon$  are normalized by  $U_0^2$  and  $U_0^3/M_{eff}$ , respectively. Note that profiles are averaged over the  $y - z$  plane. As shown in previous experiments (Hurst & Vassilicos 2007; Seoud & Vassilicos 2007; Mazellier & Vassilicos 2010;

Suzuki et al. 2010a),  $k$  is much larger in the fractal grid turbulence than in the regular grid turbulence. Figure 16 shows that  $\varepsilon$  is also much larger in the fractal grid turbulence than in the regular grid turbulence. However, the normalized timescale  $k/\varepsilon$  was almost identical for the regular and fractal grid turbulence. In both flows, the timescale is proportional to  $x/M_{eff}$  in the decaying region, which agrees with the relationship derived from the transport equation of  $k$  for decaying homogeneous isotropic turbulence, i.e.  $dk/dt = -\varepsilon$ .

Other turbulence statistics for the flow field downstream of these grids have been shown in Nagata et al. (2008) and Suzuki et al. (2010b).

### 3.8.5 Scalar fields

Figures 17 and 18 show the instantaneous scalar fields and instantaneous fluctuating scalar fields, respectively, for scalar mixing layers in regular grid turbulence (run RGm1) and fractal grid turbulence (runs SFGm1 and SFGm2) at  $z = 0$ . The result for run SFGm3 is similar to those for runs SFGm1 and SFGm2 (Suzuki et al. 2009). The interval between the vertical gray lines in Figs. 17 and 18 corresponds to a distance of  $10M_{eff}$ . Figure 17 shows that the width of the mixing layer is considerably larger for fractal grid turbulence (Figs. 17 (b) and (c)) than for regular grid turbulence (Fig. 17 (a)). In fact, half widths of mean scalar and scalar variance profiles are larger for fractal grid turbulence than for regular grid turbulence (Suzuki et al. 2010c). Thus, as confirmed in our experiment (Suzuki et al. 2010a), for the same  $Re_M$ , turbulent mixing is enhanced to a greater extent in the case of fractal grid turbulence than in the case of regular grid turbulence. The fluctuating scalar fields (Fig. 18) also show that

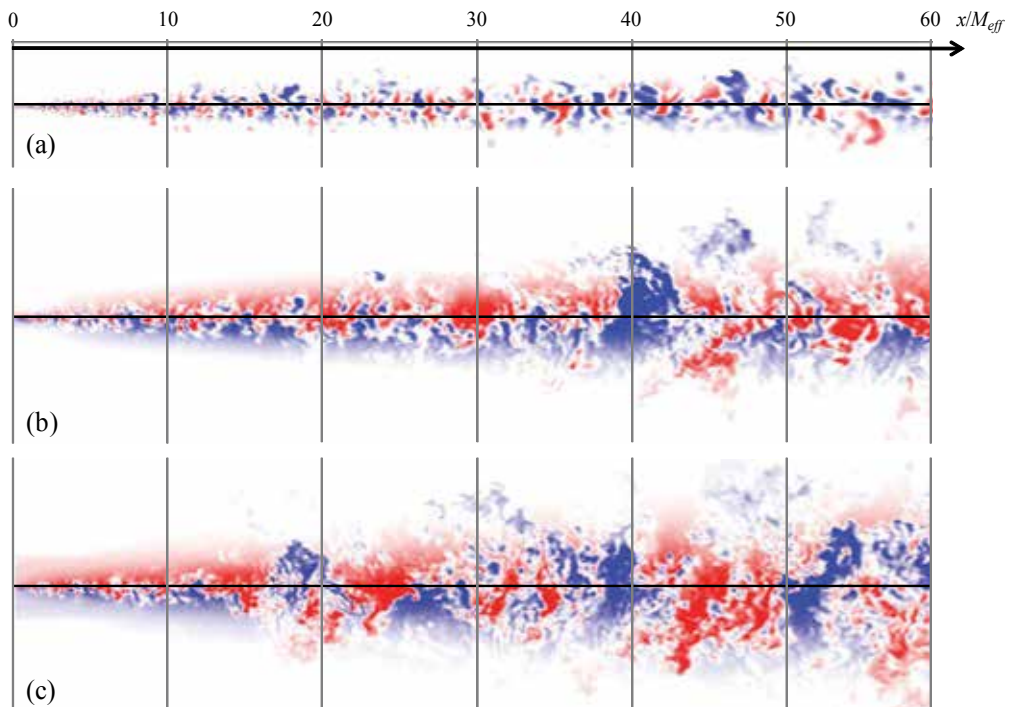


Fig. 18. Instantaneous fluctuating scalar fields at  $z = 0$  in (a) regular grid turbulence (run RGm1), (b) fractal grid turbulence at  $t_r = 5.0$  (run SFGm1), and (c) fractal grid turbulence at  $t_r = 8.5$  (run SFGm2). In all figures, red:  $\theta = 0.3$ , white:  $\theta = 0$ , blue:  $\theta = -0.3$

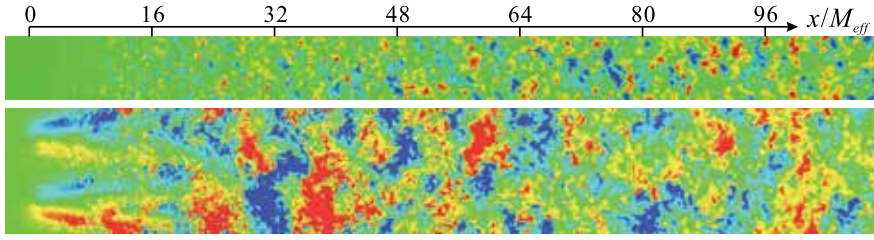


Fig. 19. Instantaneous fluctuating scalar fields at  $z = 0$  (with a linear scalar gradient): upper, in regular grid turbulence (run RG1); lower: in fractal grid turbulence (run SFG1)

turbulent mixing is highly enhanced in case of fractal grid turbulence. Further, Figs. 17 and 18 suggest that smaller-scale scalar fluctuations exist in case of fractal grid turbulence. The intense mixing of scalar can also be found for the linear mean scalar profile (runs RG1 and SFG1), as shown in Fig. 19. Figure 20 shows the streamwise variations of scalar variance  $k_\theta = \frac{1}{2} \langle \theta^2 \rangle$ , scalar dissipation rate  $\varepsilon_\theta$ , and timescale  $k_\theta / \varepsilon_\theta$  downstream of the regular and fractal grids with a linear scalar gradient (runs RG1 and SFG1, respectively).  $k_\theta$  is normalized by  $\Delta T^2$ , and  $\varepsilon_\theta$ , by  $\Delta T^2 U_0 / M_{eff}$ . The quantities are averaged over the  $y - z$  plane. For regular grid turbulence,  $k_\theta$  increases and  $\varepsilon_\theta$  decreases in the downstream direction after  $x / M_{eff} = 3$ , while both  $k_\theta$  and  $\varepsilon_\theta$  decrease in the far downstream region after  $x / M_{eff} = 40$  in the fractal grid turbulence. Thus, after  $x / M_{eff} = 80$ ,  $k_\theta$  becomes larger in the regular grid turbulence than in the fractal grid turbulence. The timescale for scalar fluctuations in the regular grid turbulence is almost identical to  $k / \varepsilon$  after  $x / M_{eff} = 6$ , where grid turbulence is fully developed. The term "fully developed" is used here in the context that turbulence intensities have peaks, after which they begin to decay. In contrast,  $k_\theta / \varepsilon_\theta$  in the fractal grid turbulence is considerably smaller than that in the regular grid turbulence. It has been shown that the large convection from upstream causes the different behaviors in scalar variance and timescale in the fractal grid turbulence (Nagata et al. 2009).

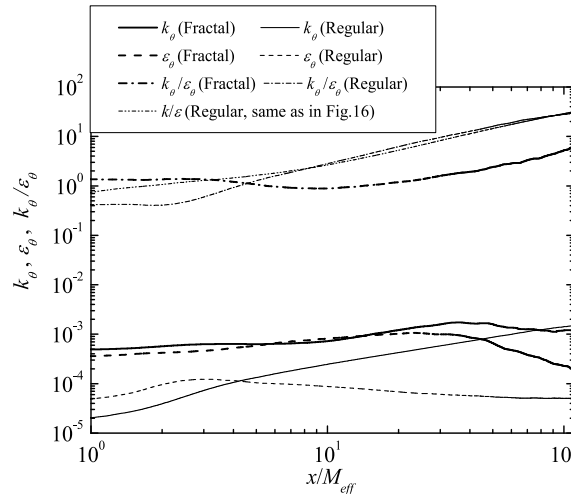


Fig. 20. Streamwise variations of scalar variance  $k_\theta$ , scalar dissipation rate  $\varepsilon_\theta$ , and timescale  $k_\theta / \varepsilon_\theta$  downstream of regular and fractal grids with a linear scalar gradient (runs RG1 and SFG1)

## 4. Conclusions

A direct numerical simulation (DNS) code was developed for computing turbulent flows with scalar transfer around complex geometries with a spectral-like accuracy. This code is based on the fully conservative higher-order finite-difference schemes for nonlinear terms, the higher-order compact schemes for higher differentiation terms, and the immersed boundary method for numerical building of three-dimensional complex geometries, and is highly optimized for a vector-type supercomputer (NEC SX-8). In the first part of this chapter, we present the results for the canonical channel flow with a scalar transfer obtained using our DNS code and compare them with those obtained using the spectral method. The results show that various turbulence quantities, including spectra, are in excellent agreement with those obtained using the spectral method. Further, our code is applied to turbulent fields with scalar transfer around and downstream of regular and fractal grids as an example of flow around complex geometries. The results show that suitable turbulence and scalar fields are reproduced around and downstream of complex geometries, i.e., regular and fractal grids. Unfortunately, the application of DNS to complex geometries is currently limited to the moderate Reynolds number and the small Prandtl number ( $\sim O(1)$ ) owing to limitations in computer resources. However, with future advancements in supercomputers, DNS of complex geometry at higher Reynolds numbers and higher Prandtl (or Schmidt) numbers should soon become possible.

## 5. Acknowledgements

The authors acknowledge Professor J. Christos Vassilicos of Imperial College London and Professor Yohei Morinishi of Nagoya Institute of Technology for providing many valuable comments and suggestions for this study. They also acknowledge Dr. Takashi Kubo (Meijo University) and Mr. Osamu Terashima (Nagoya University) for their help in this study. A part of this study was carried out under the Collaborative Research Project of the Institute of Fluid Science, Tohoku University, and the Research Cooperative Program between the Japan Society for the Promotion of Science and The Royal Society. A part of this study was supported by Grants-in-Aid (Nos. 20008010, 21656051, 22360076, 22360077) from the Japanese Ministry of Education, Culture, Sports, Science and Technology.

## 6. References

- Budwig, R., Tavoularis, S. & Corrsin, S. (1985). Temperature Fluctuations and Heat Flux in Grid-Generated Isotropic Turbulence with Streamwise and Transverse Mean-Temperature Gradients. *Journal of Fluid Mechanics*, Vol. 153, pp. 441-460.
- Fadlun, E. A., Verzicco, R., Orlandi, P. & Mohd-Yusof, J. (2000). Combined Immersed-Boundary Finite-Difference Methods for Three-Dimensional Complex Flow Simulations. *Journal of Computational Physics*, Vol. 161, pp. 35-60.
- Gad-el-Hak, M. & Morton, J. B. (1979). Experiments on the Diffusion of Smoke in Isotropic Turbulent Flow. *AIAA Journal*, Vol. 17, pp. 558-562.
- Gibson, C. H. & Schwarz, W. H. (1963). The Universal Equilibrium Spectra of Turbulent Velocity and Scalar Fields. *Journal of Fluid Mechanics*, Vol. 17, pp. 558-562.
- Huq, P. & Britter, R. E. (1995). Mixing Due to Grid-Generated Turbulence of a Two-Layer Scalar Profile. *Journal of Fluid Mechanics*, Vol. 285, pp. 17-40.
- Hurst, D. & Vassilicos, J. C. (2007). Scalings and Decay of Fractal-Generated Turbulence. *Physics of Fluids*, Vol. 19, 035103.

- Ikeno, T. & Kajishima, T. (2007). Finite-Difference Immersed Boundary Method Consistent with Wall Conditions for Incompressible Turbulent Flow Simulations. *Journal of Computational Physics*, Vol. 226, pp. 1485-1508.
- Ito, Y., Nagata, K. & Komori, S. (2002). The Effects of High-Frequency Ultrasound on Turbulent Liquid Mixing with a Rapid Chemical Reaction. *Physics of Fluids*, Vol. 14, pp. 4362-4371.
- Iwamoto, K., Suzuki, Y. & Kasagi, N. (2002). Reynolds Number Effect on Wall Turbulence: Toward Effective Feedback Control. *International Journal of Heat and Fluid Flow*, Vol. 23, pp. 678-689.
- Jayesh, Yoon, K. & Warhaft, Z. (1991). Turbulent Mixing and Transport in a Thermally Stratified Interfacial Layer in Decaying Grid Turbulence. *Physics of Fluids A*, Vol.3, No.5, pp. 1143-1155.
- Kasagi, N., Tomita, Y. & Kuroda, A. (1992). Direct Numerical Simulation of Passive Scalar Field in a Turbulent Channel Flow. *Journal of Heat Transfer*, Vol. 114, pp. 598-606.
- Komori, S., Nagata, K., Kanzaki, T. & Murakami, Y. (1993). Measurements of Mass Flux in a Turbulent Liquid Flow with a Chemical Reaction. *AIChE Journal*, Vol. 39, pp. 1611-1620.
- Komori, S. & Nagata, K. (1996). Effects of Molecular Diffusivities on Counter-Gradient Scalar and Momentum Transfer in Strongly Stable Stratification. *Journal of Fluid Mechanics*, Vol. 326, pp. 205-237.
- Laizet, S. & Vassilicos, J. C. (2010). A Numerical Strategy to Combine High-Order Schemes, Complex Geometry and Parallel Computing for High Resolution DNS of Fractal Generated Turbulence. *Computers & Fluids*, Vol. 39, pp. 471-484.
- Lele, S. K. (1992). Compact Finite Difference Schemes with Spectral-Like Resolution. *Journal of Computational Physics*, Vol. 103, pp. 16-42.
- Lienhard V, J. H. & Van Atta, C. W. (1990). The Decay of Turbulence in Thermally Stratified Flow. *Journal of Fluid Mechanics*, Vol. 210, pp. 57-112.
- Mazellier, N. & Vassilicos, J. C. (2010). Turbulence without Richardson-Kolmogorov Cascade. *Physics of Fluids*, Vol. 22, 075101.
- Morinishi, Y., Lund, T. S., Vasilyev, O. V. & Moin, P. (1998). Fully Conservative Higher Order Finite Difference Schemes for Incompressible Flow. *Journal of Computational Physics*, Vol. 143, pp. 90-124.
- Nagata, K. & Komori, S. (2000). The Effects of Unstable Stratification and Mean Shear on the Chemical Reaction in Grid Turbulence. *Journal of Fluid Mechanics*, Vol. 408, pp. 39-52.
- Nagata, K. & Komori, S. (2001). The Difference in Turbulent Diffusion between Active and Passive Scalars in Stable Thermal Stratification. *Journal of Fluid Mechanics*, Vol. 430, pp. 361-380.
- Nagata, K., Wong, H., Hunt, J. C. R., Sajjadi, S. G. & Davidson, P. A. (2006). Weak Mean Flows Induced by Anisotropic Turbulence Impinging onto Planar and Undulating Surfaces. *Journal of Fluid Mechanics*, Vol. 556, pp. 329-360.
- Nagata, K., Suzuki, H., Sakai, Y., Hayase, T. & Kubo, T. (2008). Direct Numerical Simulation of Turbulence Characteristics Generated by Fractal Grids. *International Review of Physics*, Vol. 2, pp. 400-409.
- Nagata, K., Suzuki, H., Sakai, Y. & Hayase, T. (2009). Turbulence Structure and Scalar Transfer in Fractal Generated Turbulence. *Proceedings of Japan-Korea CFD Workshop*, CD-ROM.
- Nagata, K., Hunt, J. C. R., Sakai, Y. & Wong, H. (2010). Distorted Turbulence and Secondary Flow near Right Angled Plates. *Journal of Fluid Mechanics*, in press.

- Nakamura, I., Sakai, Y. & Miyata, M. (1987). Diffusion of Matter by a Non-Buoyant Plume in Grid-Generated Turbulence. *Journal of Fluid Mechanics*, Vol. 178, pp. 379-403.
- Proud, O., Fincham, A. M. & Sommeria, J. (2005). Decaying Grid Turbulence in a Strongly Stratified Fluid. *Journal of Fluid Mechanics*, Vol. 522, pp. 1-33.
- Seoud, R. E. & Vassilicos, J. C. (2007). Dissipation and Decay of Fractal-Generated Turbulence. *Physics of Fluids*, Vol. 19, 105108.
- Sreenivasan, K. R., Tavoularis, S., Henry, R. & Corrsin, S. (1980). Temperature Fluctuations and Scales in Grid-Generated Turbulence. *Journal of Fluid Mechanics*, Vol. 100, pp. 597-621.
- Stapountzis, H., Sawford, B. L., Hunt, J. C. R. & Britter, R. E. (1986). Structure of the Temperature Field Downwind of a Line Source in Grid Turbulence. *Journal of Fluid Mechanics*, Vol. 165, pp. 401-424.
- Stillinger, D. C., Helland, K. N. & Van Atta, C. W. (1983). Experiments on the Transition of Homogeneous Turbulence to Internal Waves in a Stratified Fluid. *Journal of Fluid Mechanics*, Vol. 131, pp. 91-122.
- Suzuki, H., Nagata, K., Sakai, Y., Hayase, T. & Kubo, T. (2009). DNS of Passive Scalar Field with Mean Gradient in Fractal-Generated Turbulence. *Proceedings of 6th International Symposium on Turbulence and Shear Flow Phenomena*, Vol. 1, pp. 55-60.
- Suzuki, H., Nagata, K., Sakai, Y. & Ukai, R. (2010a). High Schmidt Number Scalar Transfer in Regular and Fractal Grid Turbulence. *Physica Scripta*, in press.
- Suzuki, H., Nagata, K., Sakai, Y. & Hayase, T. (2010b). Direct Numerical Simulation of Regular and Fractal-Grid Turbulence Using the Immersed Boundary Method and Fully Conservative Higher-Order Finite-Difference Schemes. *International Review of Physics*, Vol. 4, No. 2, pp. 83-90.
- Suzuki, H., Nagata, K., Sakai, Y. & Hayase, T. (2010c). Direct Numerical Simulation of Turbulent Mixing in Regular and Fractal Grid Turbulence. *Physica Scripta*, in press.
- Warhaft, Z. & Lumley, J. L. (1978). An Experimental Study of the Decay of Temperature Fluctuations in Grid-Generated Turbulence. *Journal of Fluid Mechanics*, Vol. 88, pp. 659-684.

# Preliminary Plan of Numerical Simulations of Three Dimensional Flow-Field in Street Canyons

Liang Zhiyong, Zhang Genbao and Chen Weiya  
*College of Science Donghua University  
China*

## 1. Introduction

Along with the rapid development of urban construction, the rapid increase the number of motor vehicles, so that the city's air pollution worsened in some areas of serious deterioration in air quality. With the increased concern over pollutants in urbanized cities, extensive investigation such as field measurements, laboratory-scale physical modelling and computational fluid dynamics techniques (CFD), have been launched in recent years to study the wind flow in street canyons<sup>[1]</sup>. The major parameters affecting pollutant transport are ambient conditions(wind speed and direction), building geometry(height, width, and roof shape), street dimensions(width), model of dimensions etc, and these factors should be considered. But with the limit of computational techniques, based on the three-dimensional numerical simulation is not widely carried out, particularly for some of the complex structure of the street (as a crossroads) study of literature is more rare, most studies(e.g., Kim and Baik (2001), Chan et al.(2002)) employ high-quality two-dimensional numerical simulations approach<sup>[2]</sup>. However, with the ever-increasing computational power, it is now feasible to employ three-dimensional numerical simulations technique to simulate building-scale flow and dispersion in real street canyons.

## 2. Computational model and boundary conditions

### 2.1 Computational model

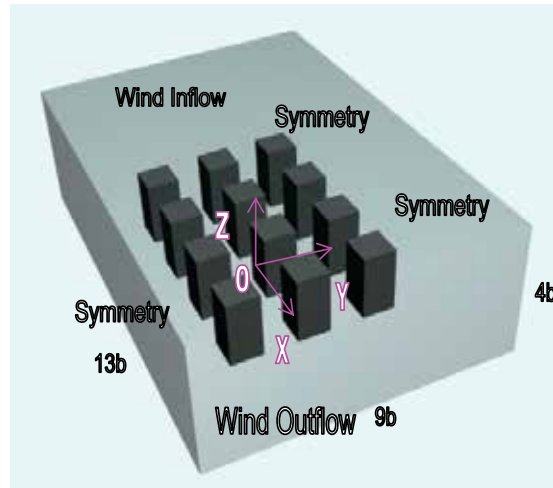
The three-dimensional computational domain consists of two parallel arranged in a string of street in the streamwise direction. The origin of coordinates is located in the center of the bottom of the buildings. (Fig.1). The flow properties of the street canyon of the domain are presented in the following discussion.  $h$  and  $b$  denotes the height and the width of the street canyon, respectively. The height of the street canyon of aspect ratio ( $H=h=2b$ ) and the free-stream inflow speed  $U$  are considered as the reference length and velocity scales, respectively. The Reynolds number is prescribed at  $9.0 \times 10^5$ . The flow is treated as an incompressible, isothermal, and pseudo steady-state turbulence<sup>[2]</sup>.

### 2.2 Boundary conditions

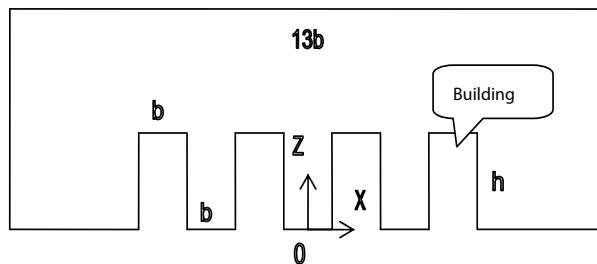
In the three-dimensional computational domain, the solid boundaries at the bottom and around the building are assumed as no-slip wall conditions. The inlet boundary condition in

the upstream direction:  $u=U, v=0, \omega=0$ . The outlet boundary condition in the downstream direction:  $\frac{\partial u}{\partial x}=0, \frac{\partial u}{\partial y}=0, \frac{\partial u}{\partial z}=0$ . Other boundaries are considered as symmetry conditions:  $u=U, v=0, \omega=0$ . (Fig.1)

### 3. Figures



(a) Stereogram



(b) Projection of X-Y plane

Fig. 1. Computational model and Boundary conditions

### 4. Equations

In the use of software “Fluent” to model calculation, the first step needs to build a variety of Street Canyon models and a reasonable mesh in pre-processor Gambit, and then the definition of the boundary conditions and the physical model can be used to solve the model in fluent software.<sup>[3]</sup>

The three-dimensional computational domain chooses hex and wedge grids. The total numbers of the grids is 2,755,206. The precision  $\epsilon$  takes  $10^{-6}$ . This simulation carries on by the parallel computer in Donghua University. The coming velocity:  $U = 2.0 \text{ m/s}$ .

In this paper the results are based on the numerical solution to the governing fluid flow and transport equations, which are derived from basic conservation principles as follows:

The mass conservation equation<sup>[4]</sup>:

$$\frac{\partial \bar{u}_i}{\partial x_i} = 0 \tag{1}$$

( $\bar{u}_i$  mean velocity component in the  $(x, y, z)$  directions ( $ms^{-1}$ ))

The momentum conservation (Navier–Stokes) equation<sup>[4]</sup>:

$$u_j \frac{\partial \bar{u}_i}{\partial x_j} = \left( \frac{\rho - \rho_n}{\rho_n} \right) g_i - \frac{1}{\rho} \frac{\partial \bar{p}}{\partial x_i} + \frac{\partial}{\partial x_j} \left( \nu \frac{\partial \bar{u}_i}{\partial x_j} - \bar{u}_i'' u_j'' \right) \tag{2}$$

( $\bar{u}_i$  mean velocity component in the  $(x, y, z)$  directions ( $ms^{-1}$ );  $\bar{u}_i''$  mean velocity fluctuation in the  $(x, y, z)$  directions ( $ms^{-1}$ );  $\nu$  mean kinematic viscosity ( $ms^{-1}$ );

$g$  mean acceleration due to gravity ( $ms^{-2}$ ))

The realizable  $k - \varepsilon$  equations<sup>[4]</sup>:

$$\bar{u}_i \frac{\partial k}{\partial x_i} = \frac{1}{\rho} \frac{\partial}{\partial x_i} \left[ \left( \mu + \frac{\mu_t}{\sigma_k} \right) \frac{\partial k}{\partial x_i} \right] + \frac{1}{\rho} P_k - \varepsilon + \frac{1}{\rho} G_b \tag{3}$$

$$\bar{u}_i \frac{\partial \varepsilon}{\partial x_i} = \frac{1}{\rho} \frac{\partial}{\partial x_i} \left[ \left( \mu + \frac{\mu_t}{\sigma_k} \right) \frac{\partial \varepsilon}{\partial x_i} \right] + C_1 S_\varepsilon - C_2 \frac{\varepsilon^2}{k + \sqrt{\nu \varepsilon}} + \frac{1}{\rho} C_{\varepsilon 1} \frac{\varepsilon}{k} C_{\varepsilon 3} G_b \tag{4}$$

( $G_b = \beta g \frac{\mu_t}{Pr_t} \frac{\partial \bar{\theta}}{\partial x_i}$ ;  $\mu_t = \rho C_\mu \frac{k^2}{\varepsilon}$ ;  $P_k = \nu_t \times \frac{\partial \bar{u}_i}{\partial x_j} \left( \frac{\partial \bar{u}_i}{\partial x_j} + \frac{\partial \bar{u}_j}{\partial x_i} \right)$ ;  $\sigma_k = 1.0$ ;  $C_{\varepsilon 1} = 1.44$ ;  $C_{\varepsilon 3} = \tanh|v/u|$ ;

$\beta$  mean the thermal expansion coefficient)

### 5. Conclusion

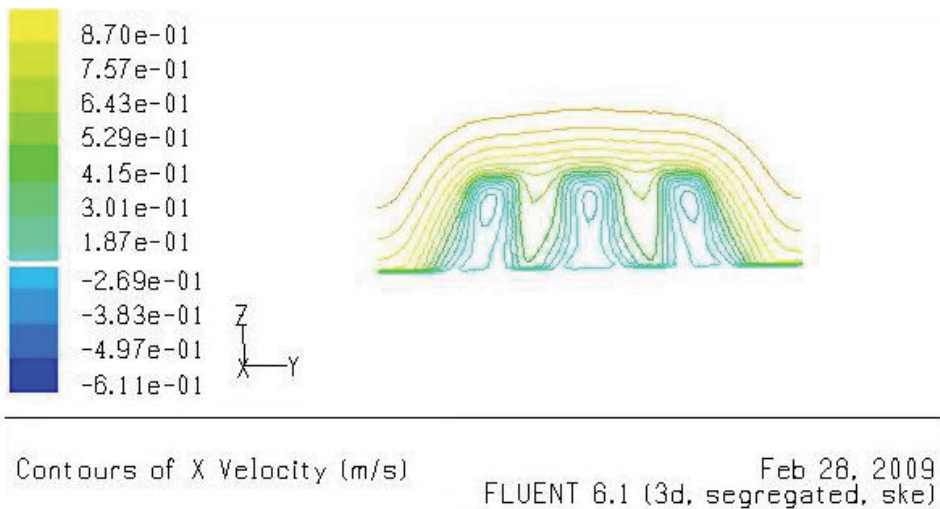


Fig. 2. Velocity distribution in y-z plane at  $x = 0.0$  and a Reynolds number is  $9.0 \times 10^5$

Fig. 2 depicts clearly a large vorticity in the back of the buildings in the direction of the wind. More detailed analysis reveals that some of the second vorticity, which are recent Oval, can be clearly observed in the back of the buildings. In addition, flow lines are basically as the same as the profile of the streets.

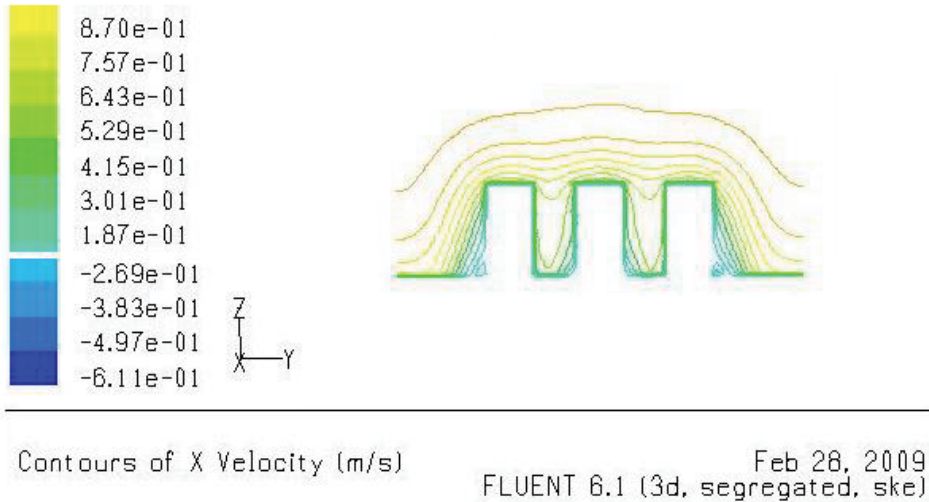


Fig. 3. Velocity distribution in y-z plane at  $x = 1.0$  and a Reynolds number is  $9.0 \times 10^5$

Fig. 3 shows that in a cross-section of the building, none of vorticity can be found in the streets, but a small vorticity is observed in the bottom of the both sides of buildings. In addition, flow lines are basically as the same as the profile of the streets.

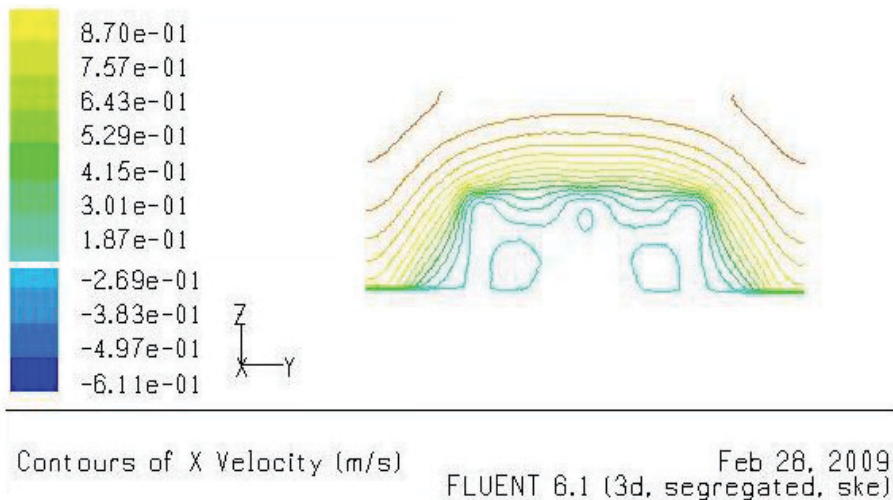


Fig. 4. Velocity distribution in y-z plane at  $x = 2.0$  and a Reynolds number is  $9.0 \times 10^5$

Fig. 4 depicts clearly some recent circle vorticities in the back of the buildings in the direction of the wind. In the back of the buildings of both sides, a large vorticity is found and in the middle of the back of the building, a vorticity is observed at the top of the streets. In addition, flow lines are basically as the same as the profile of the streets.

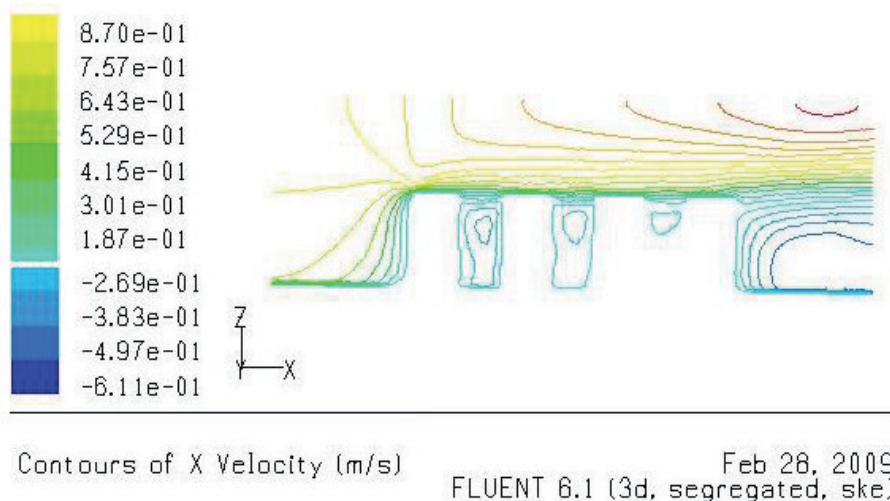


Fig. 5. Velocity distribution in x-z plane at  $y = 0.0$  and a Reynolds number is  $9.0 \times 10^5$

As shown in Fig. 5, some strong vorticities are found in the every target streets. The flow lines are raised when it first reaches the urban building. The flow lines at roof level are almost parallel to the ground after the flow passed several urban buildings with identical height. The flow under this configuration is found to be stable within the whole simulation period, as also stated by Gerdes and Olivari (1999).<sup>[5]</sup>

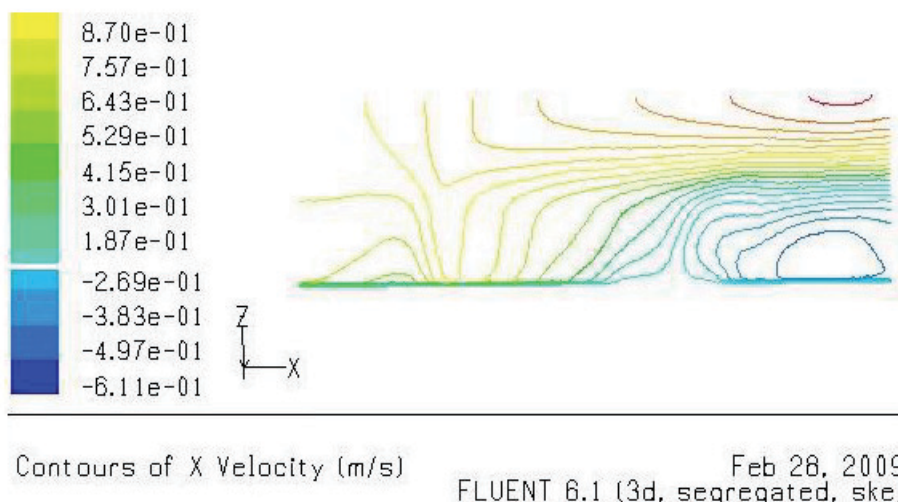


Fig. 6. Velocity distribution in x-z plane at  $y = 1.0$  and a Reynolds number is  $9.0 \times 10^5$

As shown in Fig. 6, there is no vorticity, in the direction of the wind, the speed lines are sparse, while the flow lines are intensive in the leeward direction, The flow lines at roof level is almost parallel to the ground after the flow passed several urban buildings with identical height.

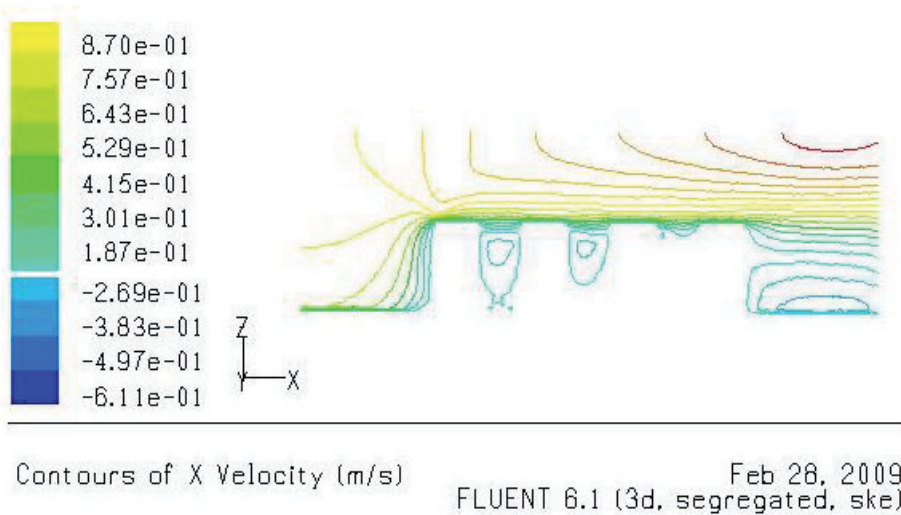


Fig. 7. Velocity distribution in x-z plane at  $y = 2.0$  and a Reynolds number is  $9.0 \times 10^5$

As shown in Fig. 7, some strong vorticities are found in the every target streets. The first street in the direction of wind has a large vorticity, in the first two streets, there are respectively two vorticities (a large vorticity, a small vorticity), and the vorticity can not be found in the last street. But some vorticities can be found on the lower part of the building in the leeward direction at the bottom of the streets.

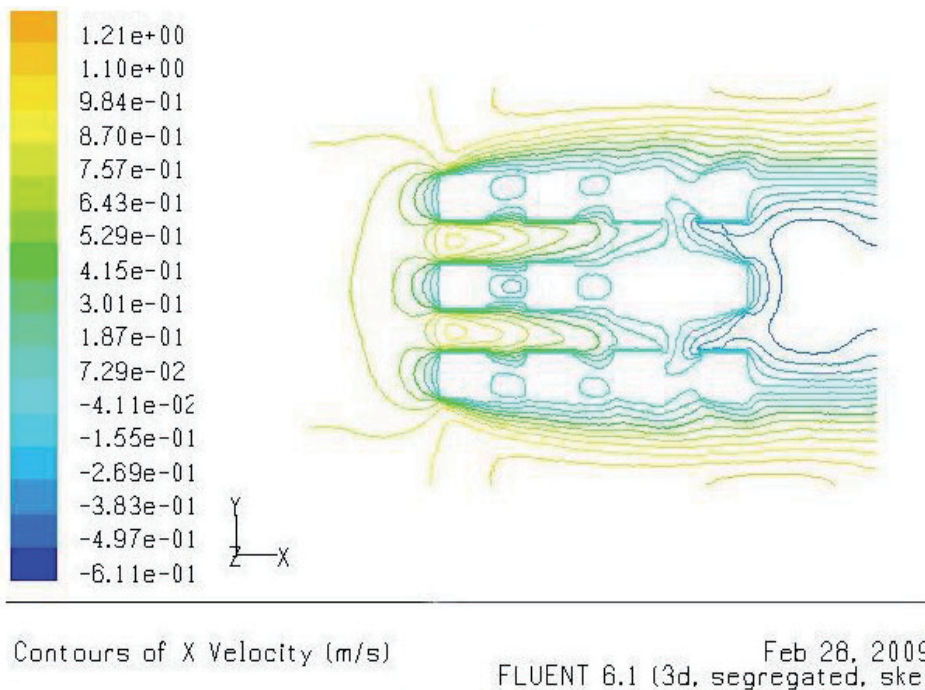


Fig. 8. Velocity distribution in x-y plane at  $z = 0.5$  and a Reynolds number is  $9.0 \times 10^5$

As described in Fig. 8, some strong vorticities are found in the every target streets. The number of vorticity in the direction of the wind is more than that in the leeward direction, some large recent oval vorticity can be found in the back of the buildings in the direction of the wind. It is found that the wind is difficult to go through the streets.

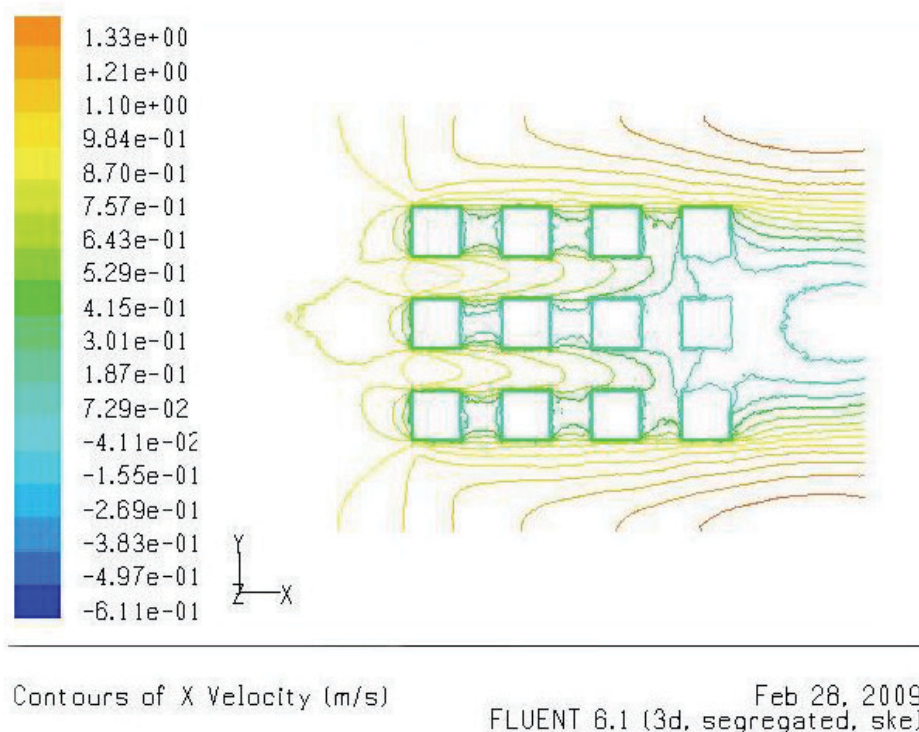


Fig. 9. Velocity distribution in x-y plane at  $z = 2.0$  and a Reynolds number is  $9.0 \times 10^5$

As described in Fig. 9, some strong vorticities are found in the every target streets. With the high degree increasing, there is a clear vorticity on the back part of the building in the leeward direction. In addition, flow lines are basically as the same as the profile of the streets.

As described in Fig. 10, none of strong vorticity is found on this cross-section. The contours of x velocities are not found above the streets, so the flow of this part, to the basic, is unchanged.

Three-dimensional flow-field is investigated in street canyons at a Reynodes number of  $9.0 \times 10^5$  using a realizable  $k - \epsilon$  model, and we get the results (depicted in the front). The present model can exactly describe the flow-field in street canyons and we can get the results in any directions. The results of the present numerical model show that X velocity in the upstream directions is as same as that outside the street canyon, but X velocity is lower in most parts of inside the street canyons, and the air inside and outside streets is difficult to be exchanged In this paper only the velocities in X direction could be shown, other results are not mentioned. The pollution in the streets does not considered. So, More works need to be done to perfect our research.

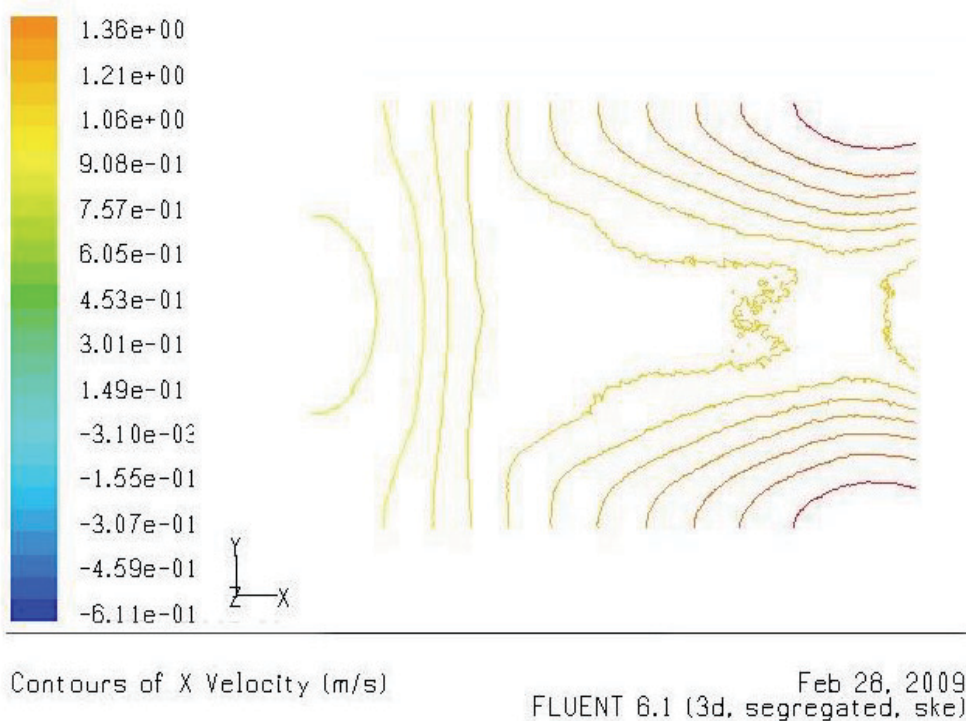


Fig. 10. Velocity distribution in x-y plane at  $z = 3.0$  and a Reynolds number is  $9.0 \times 10^5$

## 6. References

- [1] Recent progress in CFD modelling of wind field and pollutant transport in street canyons, Xian-Xiang Li<sup>a</sup>, Chun-Ho Liu<sup>b</sup>, Dennis Y.C. Leung<sup>a</sup>, K.M. Lam<sup>c</sup>, Atmospheric Environment 40 (2006) 5640-5658
- [2] Development of a  $k-\varepsilon$  model for the determination of air exchange rates for street canyons, Xian-Xiang Li, Chun-Ho Liu, Dennis Y.C. Leung, Atmospheric Environment 39 (2005) 7285-7296, Atmospheric Environment 40 (2006) 5640-5658
- [3] Pollutant dispersion in urban street canopies, Jiyang Xia, Dennis Y.C. Leung, Atmospheric Environment 35 (2001) 2033-2043
- [4] Computational Fluid Dynamics The Basics with Applications, John D. Anderson, JR, 1995 by McGraw-Hill Companies, Inc.
- [5] On the prediction of air and pollutant exchange rates in street canyons of different aspect ratios using large-eddy simulation, Chun-Ho Liu<sup>a</sup>, Dennis Y.C. Leung<sup>a</sup>, Mary C. Barth<sup>b</sup>, Atmospheric Environment 39 (2005) 1567-1574.

# Advanced Applications of Numerical Weather Prediction Models – Case Studies

P.W. Chan  
*Hong Kong Observatory*  
*Hong Kong, China*

## 1. Introduction

Numerical weather prediction (NWP) models are widely used nowadays in weather forecasting services. The models that are commonly considered include the global models and the mesoscale models with horizontal resolutions in the order of several kilometres to a couple of tens of kilometres. Performance of NWP models with even higher spatial resolutions is studied extensively recently with the objective of making location-specific forecasts. This paper describes some attempts of modelling the weather conditions in Hong Kong, a subtropical, coastal city, with a horizontal resolution of a kilometre or less, and presents the applications of the model results in the forecasting of hazardous weather. The following aspects are included:

- a. Turbulence forecasts – Turbulence could be hazardous to the aircraft (HKO, IFALPA and GAPAN, 2010). At the Hong Kong International Airport (HKIA), terrain disruption of the prevailing wind is the main case of airflow disturbances experienced by the pilots. Simulations of the wind flow down to a horizontal resolution of 50 m have been tried out to study the possibility of providing an indication of the occurrence of terrain-induced turbulence. Moreover, the simulated turbulence intensity is compared with the measurements by sophisticated remote-sensing meteorological instruments, including minisodar, radar wind profilers and Light Detection And Ranging (LIDAR) systems.
- b. Wind gust forecast – Strong gust could occur in association with the passage of subtropical squall lines. Terrain effect may also bring about gustiness of the wind. A physical-based approach has been attempted in simulating the gusts in intense convective weather and terrain-induced airflow disturbances. The simulations are carried out with a horizontal resolution of 0.2 to 1 km. In the selected case studies, the simulated gusts are comparable with the actual observations by the dense network of ground-based anemometers in Hong Kong.
- c. Strong wind and heavy rain forecast – High winds associated with tropical cyclones and rainstorms due to summer monsoon are hazardous weather to the general public. This paper also discusses the possibility of improving the forecasting of such weather phenomena by using numerical simulations of high spatial resolutions (1 – 2 km) and sophisticated algorithms of assimilating actual observations into the NWP models. In particular, the inclusion of radar data brings about significant improvement in the forecasting of high winds and heavy rain of tropical cyclones.

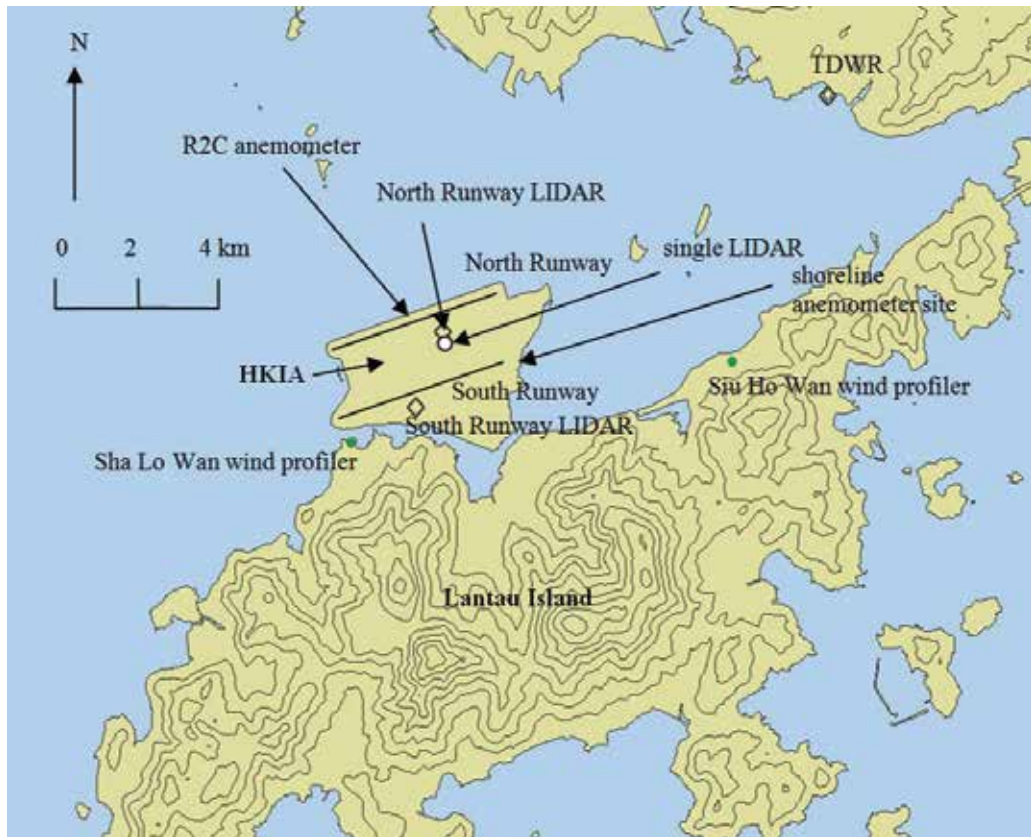


Fig. 1. Locations of the meteorological instruments mentioned in this Chapter. The terrain around HKIA is also shown. Height contours: 100 m. The single LIDAR at the airport (before relocation to become the south runway LIDAR in 2008) is shown as a white dot.

## 2. Turbulence forecasts

HKIA is situated in an area of complex terrain (Figure 1). To the south of the airport is the mountainous Lantau Island with peaks rising to about 1000 m AMSL and valleys as low as 400 m in between. Turbulent airflow due to terrain disruption could occur in the airport area when the winds from east to southwest climb over Lantau Island. Low-level turbulence (below 1600 feet or 500 m) is an aviation hazard to the aircraft flying into or out of HKIA. It brings about rapid bumps or jolts to the aircraft. In severe turbulence cases, abrupt changes in the altitude and attitude of the aircraft may occur and the pilot may suffer a momentary loss of control.

The Hong Kong Observatory (HKO) provides turbulence alerting services to HKIA. In accordance with the practice of the International Civil Aviation Organization (ICAO), turbulence intensity is expressed in terms of the cube root of the turbulent kinetic energy (TKE) dissipation rate, or eddy dissipation rate (EDR) (ICAO 2007). An  $EDR^{1/3}$  between 0.3 and  $0.5 \text{ m}^{2/3}\text{s}^{-1}$  refers to moderate turbulence, and  $EDR^{1/3}$  of  $0.5 \text{ m}^{2/3}\text{s}^{-1}$  or above is severe turbulence. Studies have been carried out to measure EDR using remote-sensing instruments such as LIDAR systems (Chan 2006) and radar wind profilers (Chan and Chan

2004) in the airport area for improving the detection of low-level turbulence that may be encountered by the aircraft. The locations of the equipment could be found in Figure 1.

Forecasting of turbulence intensity distribution around HKIA using NWP models would be useful in providing short-term turbulence warnings to the pilots (e.g. in the next several hours). This section examines the feasibility of numerical simulation of the EDR field using the Regional Atmospheric Modelling System (RAMS) (Cotton et al. 2003) in typical cases of turbulent airflow at HKIA by comparison to the EDR measurements from remote-sensing instruments. Numerical simulation of terrain-induced turbulence over Lantau Island has been studied in Clark et al. (1997) with a horizontal resolution of 62 m in a tropical cyclone case. The horizontal resolution of the innermost grid in the present study is of similar magnitude (50 m) and severe turbulence associated with a typhoon is also studied. However, this paper includes the following new features:

- a. Instead of initializing the numerical model with a single upper-air ascent and adding excitation artificially into the model, RAMS in this study is nested with the output of an operational mesoscale meteorological model in order to assess the possibility of forecasting the occurrence of severe turbulence over HKIA in an operational model setup;
- b. Instead of comparing the model results with the measurements by an aircraft along a flight leg only, more extensive comparison is made in the present study, viz. with the EDR map obtained from a Doppler LIDAR and EDR profile measured by a radar wind profiler; and
- c. The impact of different turbulence parameterization schemes on the numerical simulation results is studied.

The latest version of RAMS, viz. version 6, is used in this study. It is nested with the operational Regional Spectral Model (ORSM) of HKO, which has a horizontal resolution of 20 km (Yeung et al. 2005). Four nesting runs are performed with RAMS using the following horizontal resolutions: 4 km, 800 m, 200 m and 50 m (known as grids 1 to 4 respectively). Technical details of the model setup could be found in Chan (2009). The innermost domain (Figure 2(a)) focuses on the area to the west of HKIA, which is downwind of the mountains on Lantau Island in east to southwesterly flow.

In grids 1, 2 and 3, Mellor-Yamada 2.5-level closure scheme (Mellor & Yamada 1982) is used. For grid 4, Deardorff (1980) scheme is employed. It is applied to both vertical and horizontal mixing, so that the turbulence so simulated is isotropic and the diffusion coefficients are the same in all directions. The prognostic TKE equation is solved. The dissipation term in the TKE equation, viz. the EDR ( $\epsilon$ ), is given by:

$$\epsilon = \frac{C_D E^{3/2}}{l} \quad (1)$$

where  $l$  is a subgrid-scale mixing length which depends on the atmospheric stability (see Deardorff (1980) for details),  $E$  the TKE and  $C_D = 0.19 + 0.51l / (\Delta x \Delta y \Delta z)^{1/3}$  ( $\Delta x$  is the grid size in the x-direction, etc.).

A case of the passage of Typhoon Imbudo to the southwest of Hong Kong on 24 July 2003 is considered here. This was the day with the largest number of severe turbulence reports from aircraft since the opening of HKIA in 1998 (Chan & Mok 2004). Imbudo brought gale-force southeasterly wind to the airport area. The result of RAMS 3-hour simulation initialized at

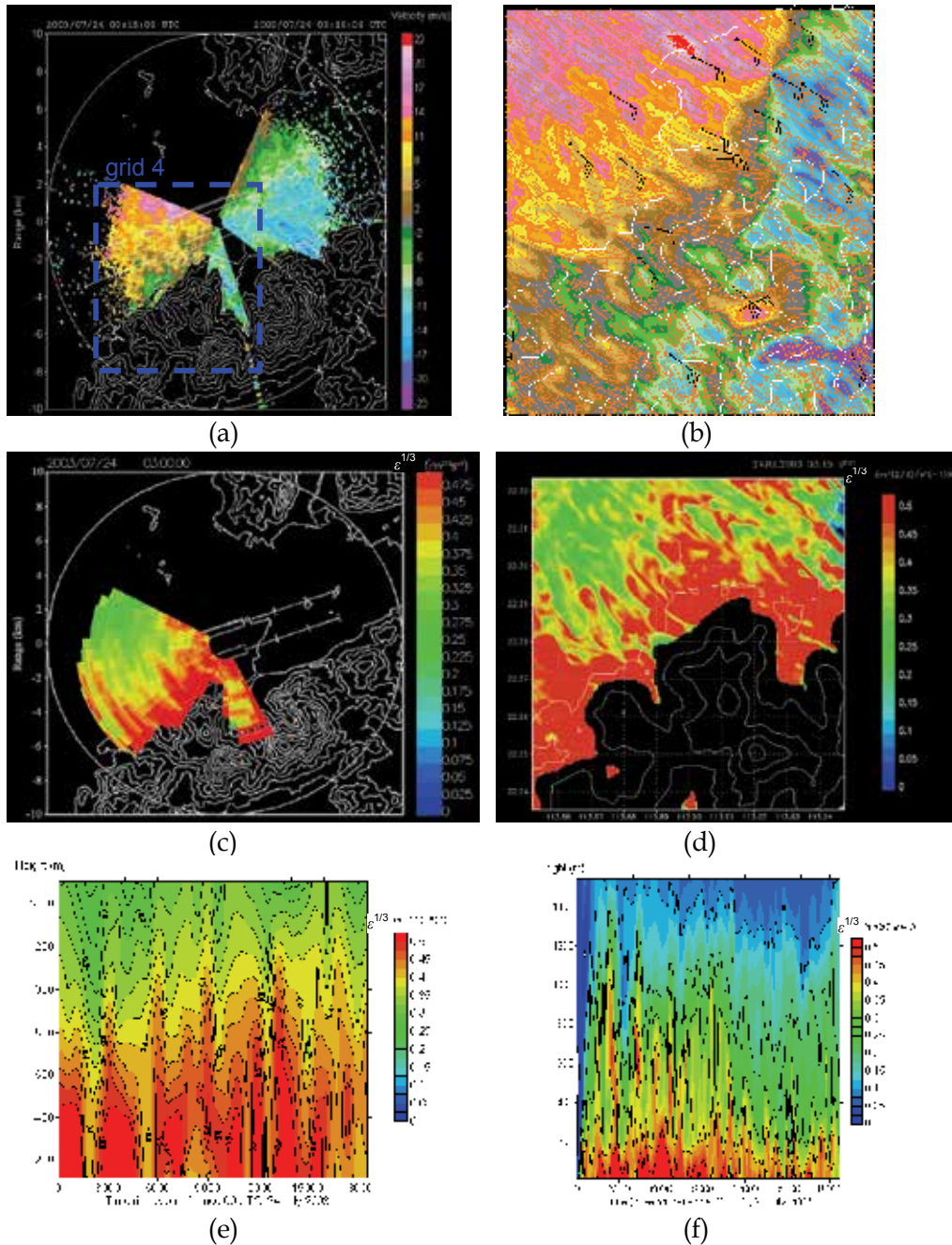


Fig. 2. LIDAR's radial velocity imagery from 1-degree conical scan at 03:15 UTC, 24 July 2003 (a) and the corresponding EDR map based on LIDAR data (c). The RAMS simulation results at the same time of (a) and (c) at 50 m AMSL are given in (b) and (d) respectively. (e) is the observed turbulence intensity from SLW wind profiler, and the simulated results are in (f).

00 UTC of 24 July (Figure 2(b)) is similar to the LIDAR's radial velocity imagery at 03:ISUTC, 24 July, (Figure 2a) except that the blobs of reverse flow (coloured green in Figure 2(a)) to the west of HKIA extended further downstream of Lantau Island in reality. There were streaks of severe turbulence (coloured red in Figure 2(c)) extending for about 4 km from the mountains on Lantau Island. These streaks are well captured in the model prediction (Figure 2(d)).

The model-simulated turbulence intensity has about the same magnitude as the measurement from the wind profiler in the first couple of hundred metres above ground (c.f. Figures 2(e) and 2(f)). Further aloft, it decreases too rapidly with height when compared to actual observations. Fast and Shaw (2002) reported similar discrepancies in the RAMS simulations for the Vertical Transport and Mixing (VTMX) campaign at Salt Lake Valley, U.S.A. using Mellor-Yamada 2.5-level closure scheme. They conjectured that the differences might be due to over-prediction of vertical mixing near the ground and under-prediction of TKE aloft in the model simulations. The latter behaviour was also observed in simulations using the Deardorff scheme (Trini Castelli et al. 2005). Nonetheless, in the present simulations, it is interesting to note that the model simulated results suggest that moderate to severe turbulence can penetrate to a height of about 1000 m at times, similar to the wind profiler observations.

### 3. The use of other turbulence parameterization schemes

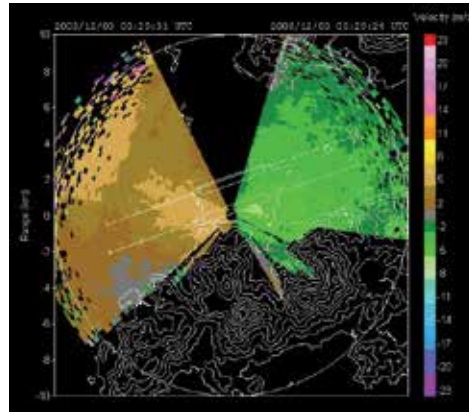
Apart from Deardorff (1980) scheme, other turbulence parameterization schemes that are developed recently are also available RAMS version 6. It would be interesting to study other the model simulation results depend on the selection of the turbulence scheme. One such scheme is the TKE-mixing length (e-l) scheme. In this scheme, the diffusion coefficient of momentum  $K_m$  is determined as:

$$K_m = c_\mu E^{1/2} l \quad (2)$$

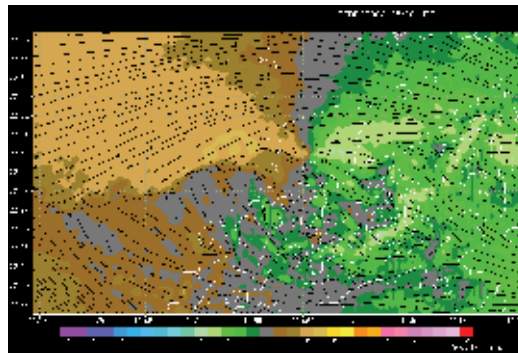
where  $c_\mu$  is a closure empirical constant. Following Xu and Taylor (1997), it has a value of 0.41. This constant is in turn related to the corresponding empirical constant of dissipation term of TKE  $\epsilon_\mu = c_\mu^3$ . In the present study,  $c_\mu$  is made variable between 0.1 and 0.7 and the resulting EDR<sup>1/3</sup> field is compared with the actual measurements (mainly vertical EDR profiles from the two radar wind profilers near HKIA) to find out a suitable value for this empirical constant.

Moderate easterly winds prevailed along the southern coast of China on 3 December 2008. From the radiosonde ascents at 00 and 12 UTC on that day (not shown), temperature inversion (of a few degrees) or an isothermal was depicted between about 600 m and 900 m above ground. From the LIDAR's velocity imagery (Figure 3(a)), easterly flow prevailed in the area of the airport. However, a region of weaker and possibly reverse flow appears to the southwest of HKIA (shown as grey in Figure 3(a)). The occurrence of such a region is possibly related to the airflow disruption by the complex terrain of Lantau Island in a stable boundary layer.

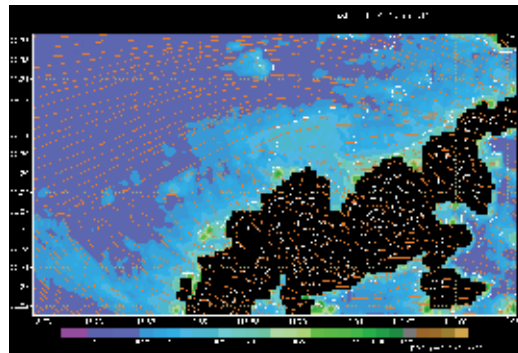
The model simulation starts at 00 UTC, 3 December 2008 and the results at 05:30 UTC on that day are analyzed here. The model-simulated wind field using the e-l scheme with  $c_\mu = 0.4$  is shown in Figure 3(b). It could be seen that, apart from the generally easterly flow, there is an area of southerly flow to the west of the HKIA. The occurrence of the latter is generally consistent with the Doppler velocity field measured by the LIDAR (Figure 3(a)), though the spatial extent of the southerly flow (arising from terrain disruption) may be exaggerated.



(a)



(b)



(c)

Fig. 3. The winter monsoon case at 05:30 UTC, 3 December 2008. (a) is the velocity imagery from the south runway LIDAR. The model-simulated winds (resolved along the LIDAR's radials) at a height of 50 m are shown in (b). The  $EDR^{1/3}$  field at the same time from model simulation is given in (c).

The model-simulated  $EDR^{1/3}$  field at that time is given in Figure 3(c). More turbulent air is forecast downstream of Lantau Island. The result appears to be reasonable considering the mechanical generation of turbulence as the airflow impinges on Lantau terrain.

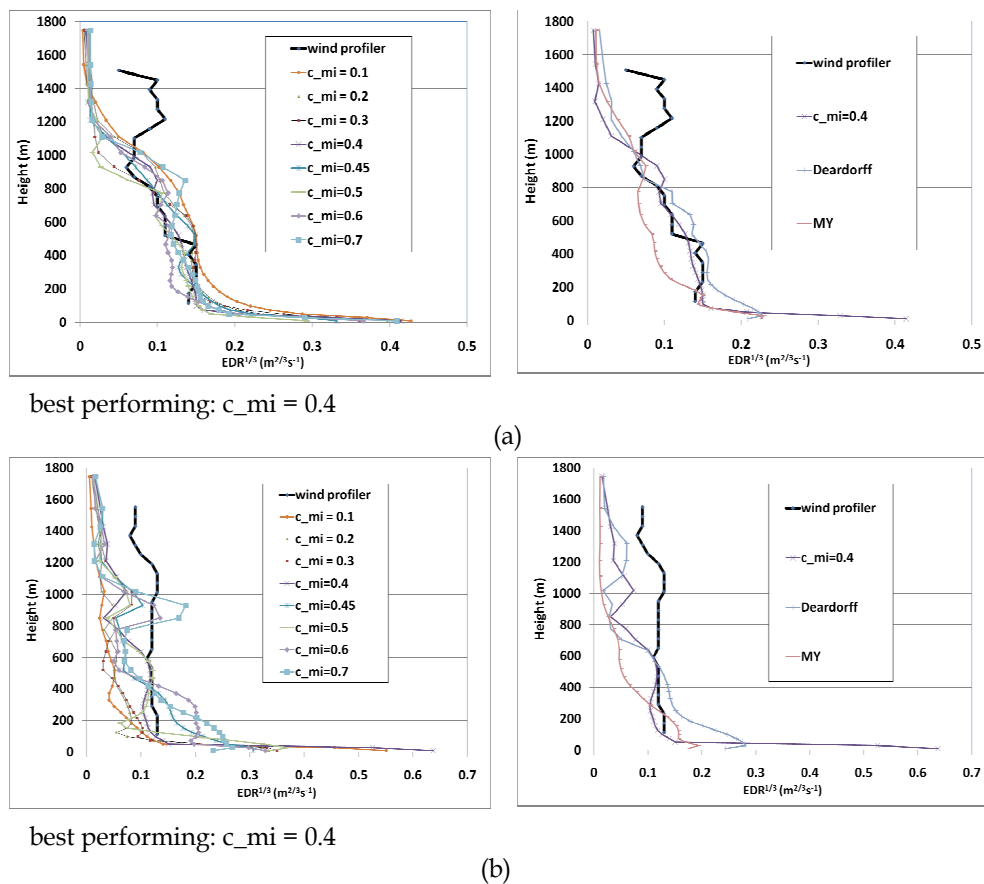
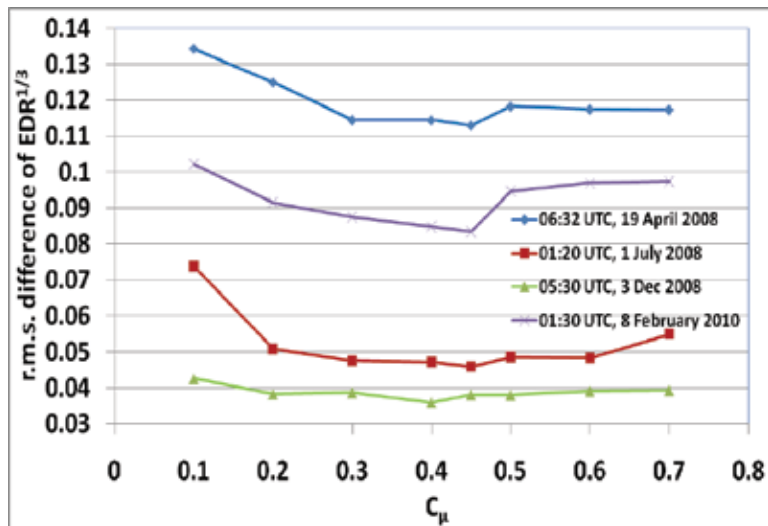


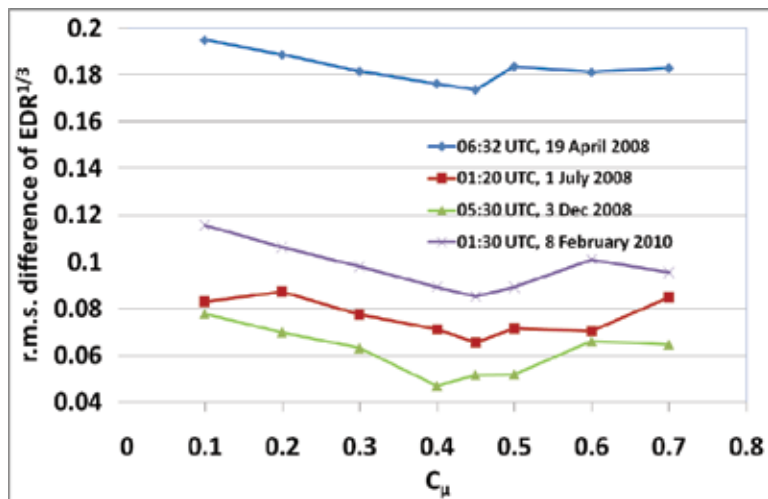
Fig. 4. The  $EDR^{1/3}$  profiles from the wind profiler at (a) Sha Lo Wan and (b) Siu Ho Wan in comparison with the model-simulated profiles using the various turbulence parameterization schemes:  $c_{mi}$  is the  $c_p$  value in e-l scheme, Deardorff means Deardorff turbulence scheme, and MY is the Mellor-Yamada 2.5 scheme available in RAMS 6.0.

The  $EDR^{1/3}$  profiles at Sha Lo Wan (SLW) and Siu Ho Wan (SHW) are qualitatively compared with model-simulation results in Figures 4(a) and (b) respectively. The locations of these two wind profilers could be found in Figure 1. The e-l scheme and Deardorff scheme give  $EDR^{1/3}$  values that are generally consistent with the actual observations up to about 1000 m. At higher altitudes, the forecast  $EDR^{1/3}$  values fall with height too rapidly. On the other hand, the Mellor-Yamada scheme in generally gives too small  $EDR^{1/3}$  values in various altitudes. It is interesting to note that, for e-l scheme, if  $c_p$  is taken to have a too low value (e.g. 0.1), the resulting  $EDR^{1/3}$  curve is quite close to the wind profiler data at SLW, but not at SHW.

The root-mean-square (r.m.s.) differences between the model-simulated results and the actual measurements of  $EDR^{1/3}$  between 120 m and 1500 m (the first and the last range gates of the wind profilers in low mode) have been calculated as a function of  $c_p$ . The results for SLW and SHW are given in Figures 5(a) and (b) respectively. It could be seen that:



(a)



(b)

Fig. 5. The r.m.s. difference between model-simulated and actual measurement of  $EDR^{1/3}$  as a function of  $c_{\mu}$  value in e-l scheme for the wind profiler at (a) Sha Lo Wan and (b) Siu Ho Wan. Four cases are considered in the figure.

- i. The “optimal”  $c_{\mu}$  value giving the smallest r.m.s differences is about 0.4 to 0.45. This is consistent with the results in the literature (between 0.40 and 0.55).
- ii. The r.m.s. differences are much greater for the tropical cyclone case (19 April 2008) than the other cases, such as the moderate wind case (3 December 2008).

	Mellor-Yamada	Deardorff	e-l scheme (best performing)
19 April 2008	0.172	0.123	0.113
1 July 2008	0.102	0.041	0.046
3 December 2008	0.043	0.034	0.036
8 February 2010	0.154	0.121	0.083

## (a) Sha Lo Wan

	Mellor-Yamada	Deardorff	e-l scheme (best performing)
19 April 2008	0.199	0.173	0.174
1 July 2008	0.103	0.073	0.066
3 December 2008	0.071	0.060	0.047
8 February 2010	0.127	0.120	0.085

## (b) Siu Ho Wan

Table 1. The r.m.s. differences between the model-simulated  $EDR^{1/3}$  profiles and the actual measurements from the wind profiler at (a) Sha Lo Wan and (b) Siu Ho Wan for the various turbulence parameterization schemes.

The r.m.s. differences for e-l scheme are compared quantitatively with those for Deardorff scheme and Mellor-Yamada scheme, as shown in Table 1. It could be seen that, using an optimal value of  $c_{\mu}$ , the use of e-l scheme with a variable asymptotic mixing length gives results that are comparable with the best turbulence parameterization scheme, namely, Deardorff scheme, as found out in the previous study of Chan (2009). The major challenge for e-l scheme would then be the instability in strong wind situation (e.g. tropical cyclone case). On the other hand, Mellor-Yamada scheme generally gives too small  $EDR^{1/3}$  values and thus the r.m.s. differences are the largest among the three schemes.

For e-l scheme and Deardorff scheme, the r.m.s differences with actual observations are generally in the order of  $0.03 - 0.07 \text{ m}^{2/3}\text{s}^{-1}$  in moderate wind situation. This is still less than  $0.1 \text{ m}^{2/3}\text{s}^{-1}$ . As such, the forecast  $EDR^{1/3}$  fields by these turbulence parameterization schemes could be useful in the monitoring of low-level turbulence in an area of complex terrain, which is a safety hazard to the aircraft. On the other hand, the performance in tropical cyclone cases is more questionable. The simulation results for Deardorff scheme could still be useful for the monitoring of low-level turbulence in the first few hundred metres or so, as discussed in Section 2 and Chan (2009).

In Chan (2009), a fixed vertical gridding is used for all model simulations, namely, with a stretching ratio of 1.15 according to the vertical gridding method of RAMS. As an illustration of the potential effect of vertical gridding on the simulation results of turbulence intensity profile, a case study is considered in this paper, namely, moderate southerly winds in the morning of 1 July 2008 under the summer monsoon. Moreover, for simplicity, only the Deardorff scheme is used in this case study. Three vertical griddings have been used, namely, with a stretching ratio of 1.15, 1.35 and 1.55.

The  $EDR^{1/3}$  distribution obtained from LIDAR data at 01:18 UTC, 1 July 2008 is shown in Figure 6(a). Due to the mountains on Lantau Island, the area of moderate turbulence extends up to about 6 km downstream of this island. However, at the same time there are some “narrow streaks” of lower turbulence, reaching the level of light turbulence only (coloured

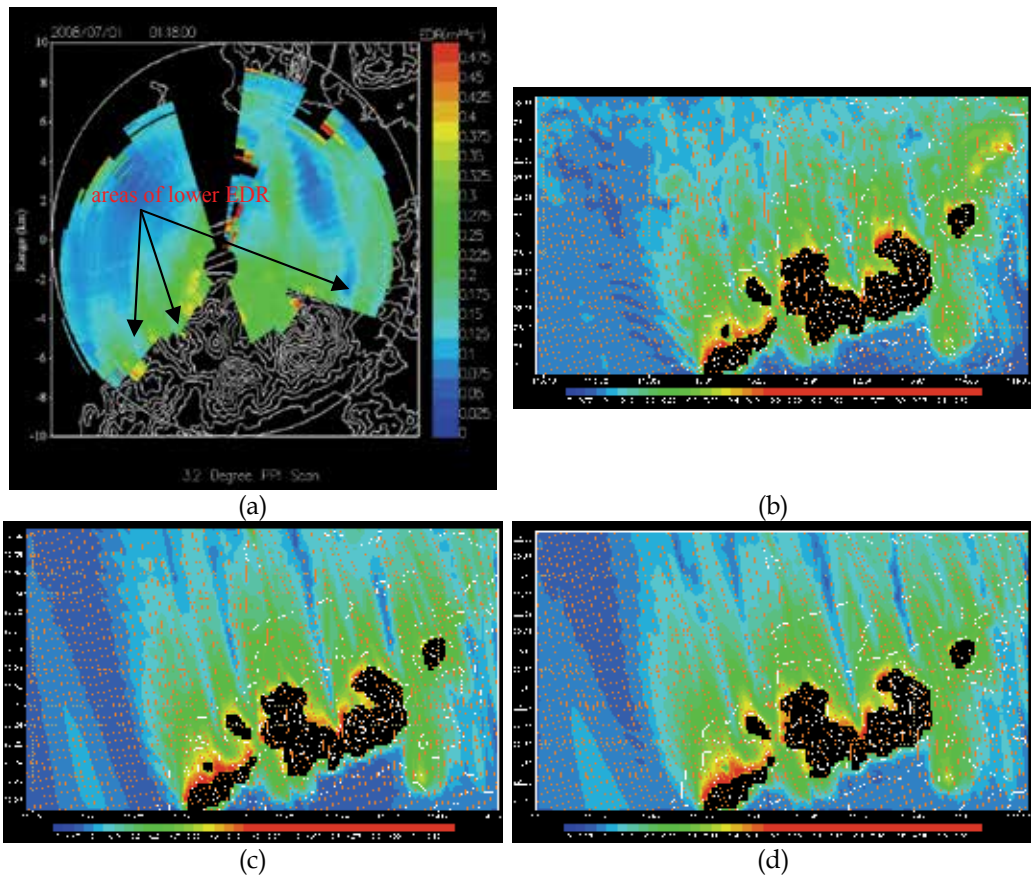
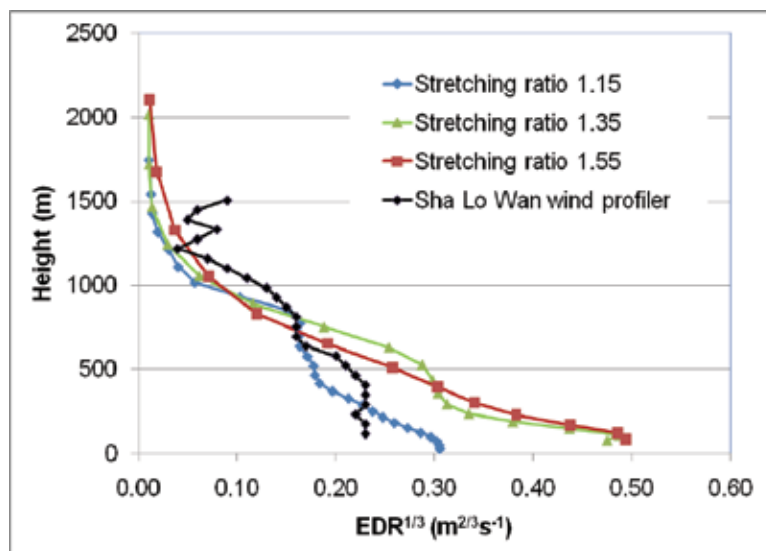


Fig. 6. (a) is the LIDAR-estimated  $EDR^{1/3}$  distribution in the vicinity of the airport at 01:18 UTC, 1 July 2008. The model-simulated results are given in (b), (c) and (d), corresponding to the use of vertical grids with the stretching ratio 1.15, 1.35 and 1.55 respectively.

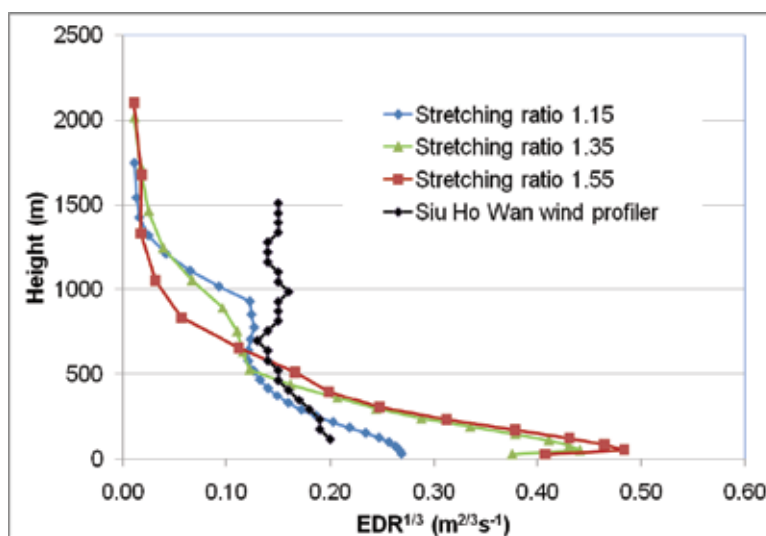
blue in Figure 6(a)). They appear to originate from the gaps of Lantau Island. As such, the mechanical turbulence associated with the cross-mountain flow brings about moderate turbulence to the areas in the vicinity of the airport, but at the same time the airflow through the gaps has light turbulence only.

The above features of turbulence distribution could largely be reproduced from RAMS simulations. The simulated  $EDR^{1/3}$  patterns with different vertical griddings are very similar, as shown in Figures 6(b) to (d). The height of about 300 m is considered in the model simulations, which is about the height of the location of light turbulence gap flow to the east of the airport.

Though the general turbulence patterns are largely the same, the magnitudes of the simulated  $EDR^{1/3}$  values could be quite different with the use of the different vertical griddings. The forecast  $EDR^{1/3}$  profiles from the three grids are compared with the actual measurements from SLW and SHW wind profilers in Figure 7. It could be seen that the vertical gridding used in the study so far and in Chan (2009), namely, a stretching ratio of 1.15, gives the best comparison results with the actual data. With coarser vertical grids, the  $EDR^{1/3}$  values tend to be over-forecast.



(a)

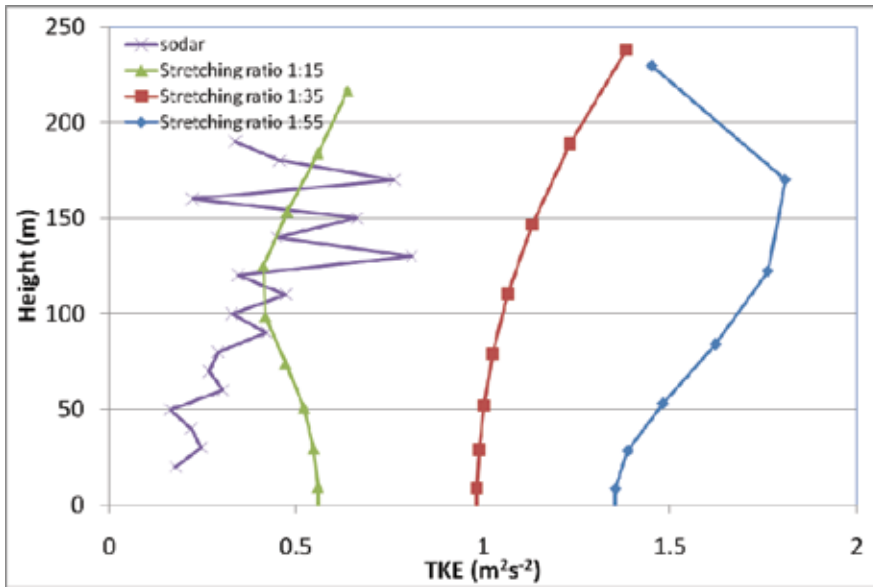


(b)

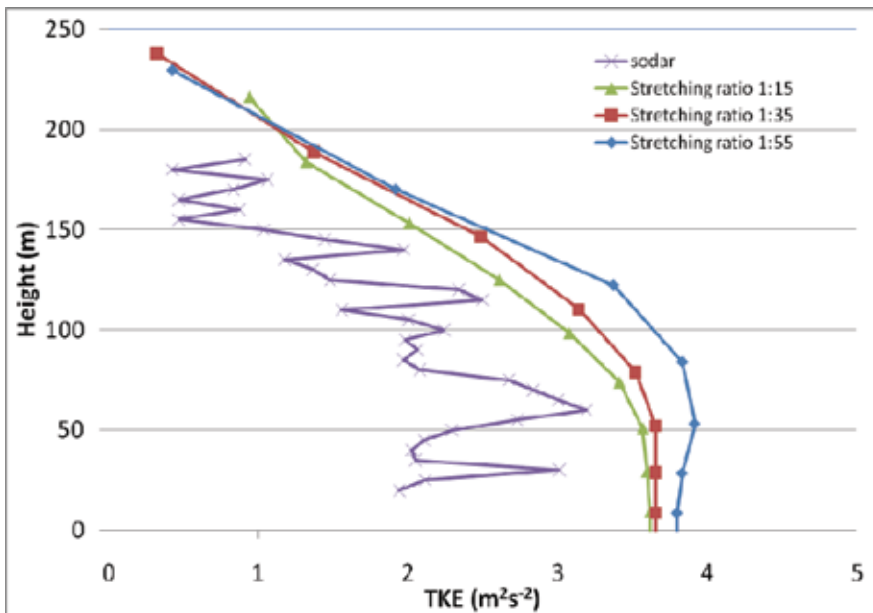
Fig. 7. Comparison between  $EDR^{1/3}$  obtained from the wind profiler and the simulation results for (a) Sha Lo Wan, and (b) Siu Ho Wan. The model simulations include the use of vertical co-ordinates with stretching ratios 1.15, 1.35 and 1.55.

The studies so far concentrate on  $EDR^{1/3}$ , which is the intentionally adopted metric for turbulence intensity in aviation application. Other metrics have been considered for aviation purpose, such as TKE. The performance of RAMS in the simulation of TKE has also been examined in a couple of examples. Deardorff scheme is employed in all the simulations.

The first example is the spring-time easterly wind case on 8 February 2010. The model-simulated TKE profiles at shoreline anemometer site (location in Figure 1) with different vertical griddings (namely, stretching ratios of 1.15, 1.35 and 1.55) are shown in Figure 8(a).



(a)



(b)

Fig. 8. TKE profile measured by the sodar at shoreline anemometer site and compared with the model simulated results: (a) 03 UTC, 8 February 2010, and (b) 07 UTC, 5 March 2010.

It appears that, with the use of a coarser grid, the TKE tends to be higher within the first couple of hundred metres or so above ground.

In order to assess the quality of the model-simulated TKE, the actual measurements by the minisodar at shoreline anemometer site has been considered. Data are available up to about

200 m above sea level, and they are plotted in Figure 8(a). Simulation is carried out starting from 00 UTC, 8 February 2010 and the simulation results after three hours are used. The simulated TKE profile with a vertical gridding of the stretching ratio of 1.15 seems to be generally consistent with the actual measurements. This comparison result supports the use of the stretching ratio of 1.15 for the vertical gridding in the simulation study for easterly flow.

Another case is considered here, namely, stronger turbulence in the southerly wind case of 5 March 2010. Simulation is carried out starting from 00 UTC, 5 March 2010 and the simulation results after 7 hours are considered. The sodar-measured profile and the model-simulated profile of TKE are compared in Figure 8(b). Again, the actual profile appears to be captured well by the model simulation (Deardorff scheme, stretching ratio of 1.15 for the vertical gridding), though the simulated results have higher values of TKE. The simulation results based on the stretching ratio of 1.15 for vertical gridding have the best comparison with the actual observations, which supports the selection of this stretching ratio value.

The minisodar with a measurement range of 200 m has been working at the airport since January 2010. More data would be collected for assessing the performance of RAMS simulations of TKE, e.g. in summer monsoon and tropical cyclone situations.

#### 4. Wind gust forecast

Wind gust is an important element in the forecasting of local weather. It could have significant impact on the safety of the public and the operation of certain business such as container port and construction work. The destruction associated with the gusts may be much larger than the mean wind itself, particularly in conditions when the mean wind is light. People working in the exposed area may need to take prompt action within a short period of time in order to protect themselves against the impact of gusty winds. For instance, on 9 May 2005, a squall line along coastal area of southern China brought strong gusts to Hong Kong. At the container port of the territory, some empty containers were blown to collapse under the gust, causing one death and two injuries. In aviation meteorology, gust could have great impact on the operation of the airport, particularly in strong crosswind situation when the pilots may need to make difficult decisions in attempting to land on a runway. Accurate forecast of the gust, such as in tropical cyclone situation, would facilitate the smooth operation of the airport in strong crosswind and minimize air traffic disruption.

Traditionally, wind gust estimate is mainly based on climatological information of the wind excess due to gust on top of the mean wind in different weather conditions. In a subtropical coastal area like Hong Kong, gust climatology may be formulated in synoptic patterns like northeast monsoon in the winter, strong easterly winds under stable boundary layer in the spring, southwest monsoon in the summer, intense convective weather like squall lines, and tropical cyclone situations. Wind gust forecasting is more challenging at HKIA due to the complex terrain in the vicinity. Winds from east to southwest may be disrupted by the terrain and give rise to strong gusts in favourable weather condition. As a result, gust forecasting not only needs to consider the synoptic weather pattern, but also takes into account the mesoscale and even microscale features as well such as convective rain cells and terrain-induced airflow disturbances.

This section aims to study the possibility of using a more objective estimation method of wind gust given the complicated condition at HKIA. The basis is a NWP model with high

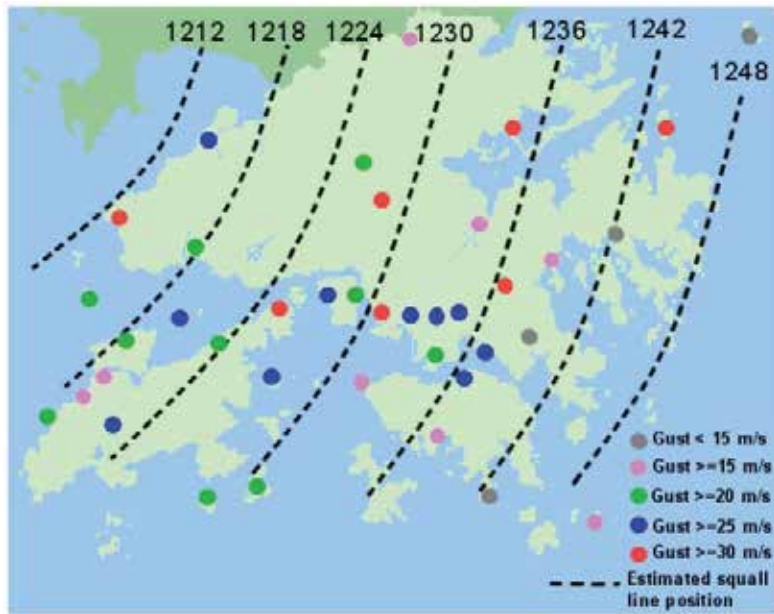
spatial resolution, and a physical approach to wind gust estimate. The RAMS version 4.4 is employed. It has been found to give satisfactory results in the simulation of microscale airflow disturbances and turbulent winds arising from the complex terrain of Lantau Island. In the simulation of a squall line case, the horizontal resolution down to 1.33 km is employed in the present study in order to resolve the convection explicitly. For terrain-disrupted airflow, the resolution is increased further to 200 m so that the complex terrain of Lantau Island could have a reasonable representation in the numerical model. The wind gust estimate is based on turbulent kinetic energy and vertical air motion from the RAMS simulation results (Brasseur 2001).

A trough of low pressure affected the inland area of southern China in the morning of 9 May 2005. A squall line developed in the strong southwesterly flow ahead of the trough and moved southeastward to Hong Kong. It swept across the territory between noon and 1 p.m. (Hong Kong time, which is 8 hours ahead of UTC), bringing gusts of about 20 m/s to HKIA and more than 30 m/s to some other places in Hong Kong (Figure 9(a)). The largest gust was recorded at the container terminal at Kwai Chung (location in Figure 9(a)), reaching 37.6 m/s. A more detailed account of the event could be found in Lam and Lam (2006).

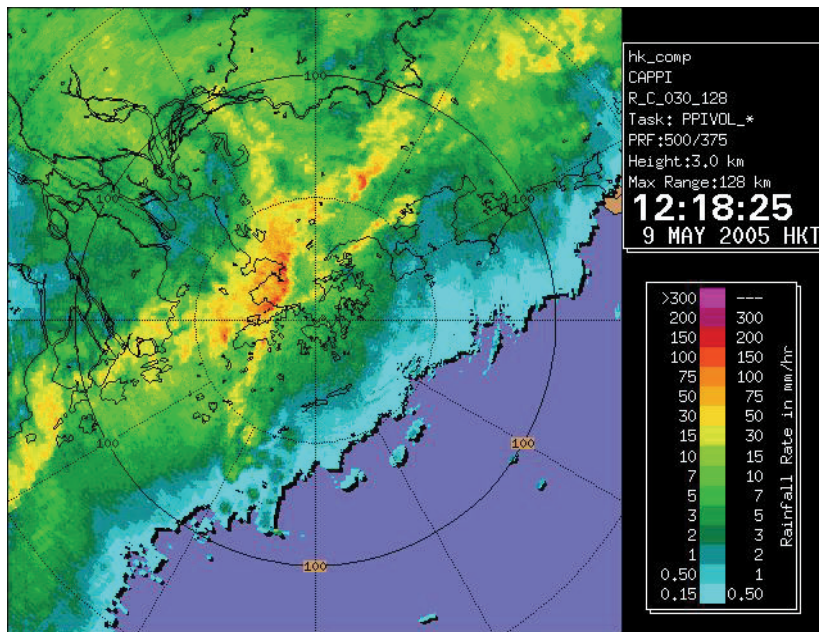
On the radar display, a bow-shaped echo was observed when the squall line moved across Hong Kong (Figure 9(b)). Strong southwesterly wind prevailed at the surface ahead of this intense radar echo with northwesterly flow at its rear (not shown). The passage of the squall line at a location showed up as a rapid change of the wind direction (from southwesterly to northwesterly) and a sharp peak in the wind speed (associated with the squall) in a matter of several minutes. In a typical wind trace of an anemometer (not shown), the southwesterly flow ahead of the squall line was rather gusty, with a mean wind of about 10 m/s and the gust reaching 16 m/s or so. The squall line moved past that anemometer at about 12:18 p.m. and the gust reached a maximum of 21 m/s in the northwesterly flow. The wind remained northerly for about half an hour afterwards, and became significantly weaker and less gusty. The temperature also dropped from a high of 27°C to about 21°C. This was the period when the cold pool behind the squall line affected the territory. Starting from around 1:20 p.m., winds turned to southeasterly and the temperature rose again after the passage of the cold pool.

The RAMS simulation reproduces reasonably well the southeastward movement of the squall line. In the “radar” plot of the simulated surface rainfall (Figure 10(a)), an intense, bow-shaped “echo” is forecast to sweep across Hong Kong between noon and 1 p.m. of 9 May 2005, consistent with the actual observations. The updraft in this “echo” reaches a maximum of about 16 m/s (Figure 10(b)), which is the magnitude to be expected in such a severe squall event.

At the surface, the model successfully simulates the strong southwesterly flow ahead of the squall line and the northwesterly flow at the rear of it. For instance, northwesterly wind of 15 m/s (29 knots) is predicted over HKIA after the passage of the squall line (Figure 11(a)), consistent with the actual measurements. At the location of the R2C anemometer at HKIA (location in Figure 1), the wind direction change and the peak in wind speed associated with the squall line are reasonably well forecast (Figure 11(b)). However, some discrepancies are observed between the actual and the forecast wind fields: (a) the arrival time of the squall line is later by about half a hour in the simulation, and (b) the cold pool behind the squall line is more widespread (not shown) and affects Hong Kong for much longer time in the model, e.g. the wind at HKIA (Figure 11(b)) remains to be southwesterly to northwesterly for a couple of hours after the passage of the squall line.

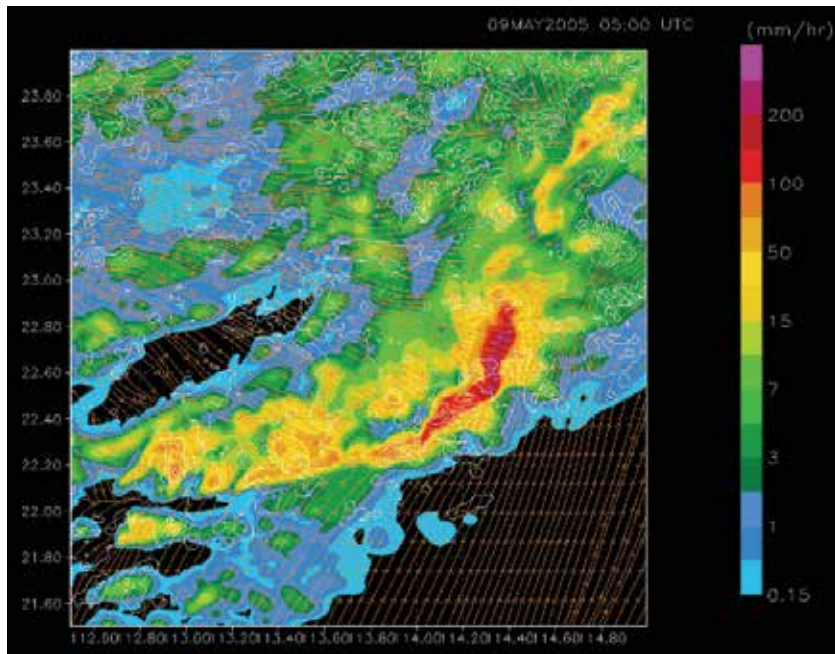


(a)

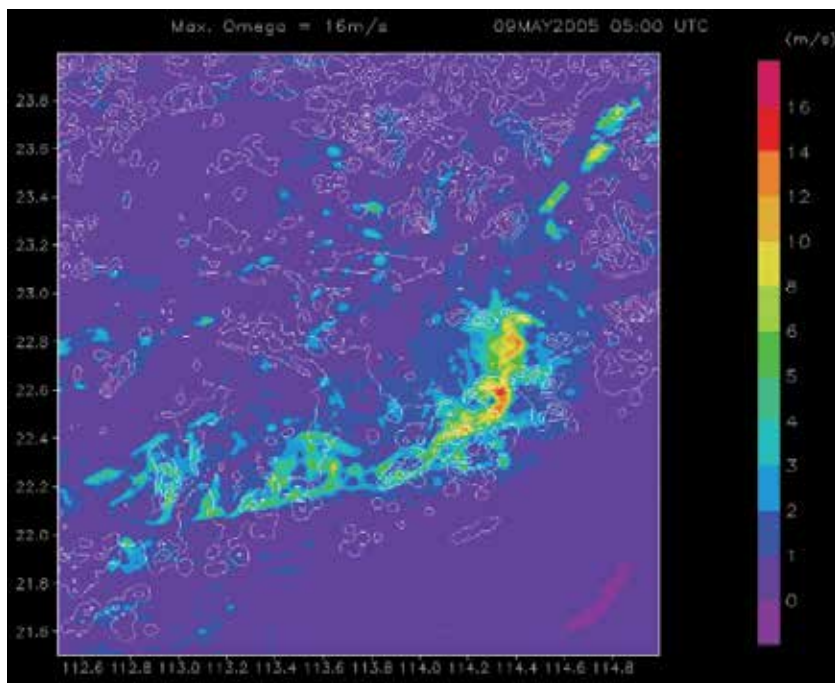


(b)

Fig. 9. (a) shows the location of the squall line in the 9 May 2005 event and the gust measured at various places in Hong Kong due to the squall line. The numbers at the broken curves are in Hong Kong time. (b) is the 128-km range radar picture of Hong Kong at 12:18 p.m., 9 May 2005, showing the passage of the squall line across the territory.

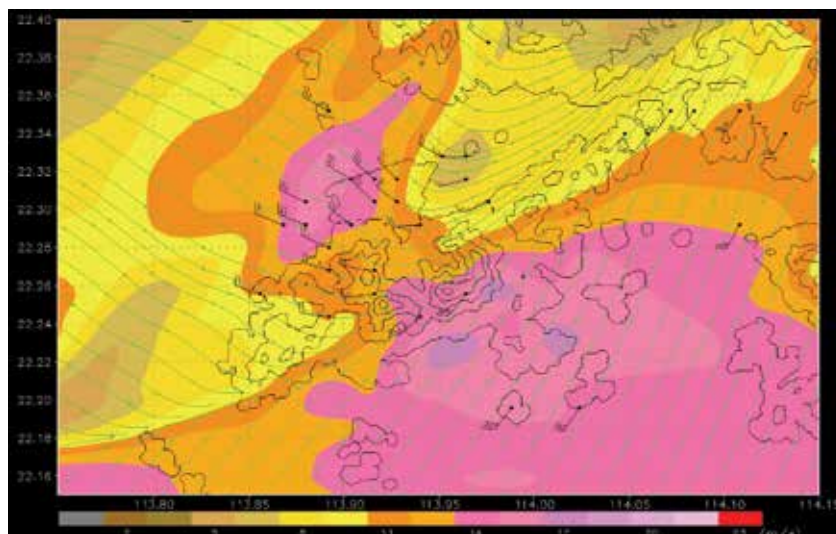


(a)

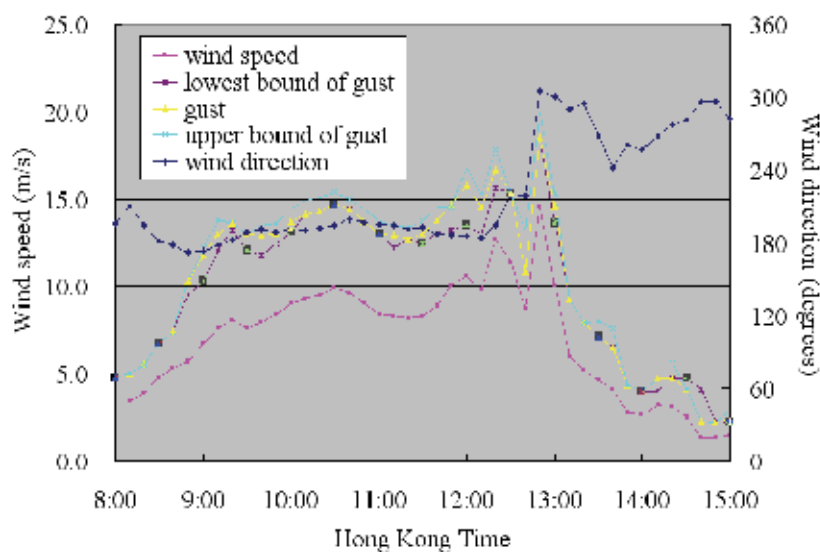


(b)

Fig. 10. (a) is the “radar” plot of the simulated surface rainfall in Grid 2 of RAMS simulation at 1 p.m., 9 May 2005. (b) is the maximum updraft strength simulated using RAMS



(a)



(b)

Fig. 11. (a) is the simulated surface wind magnitude (colour shaded), streamlines (green lines) and winds at the anemometer locations (wind barbs) at 12:50 p.m., 9 May 2005. (b) is the simulated surface wind speed and direction from RAMS and the wind gust estimate from the Brasseur (2001) method at the location of R2C anemometer at HKIA.

Within the Hong Kong territory, the upper bound of the wind gust has a maximum value of 30 m/s based on the simulation results. Though it is smaller than the actual maximum gust observed (37.6 m/s), the gust estimate nonetheless provides a useful indication about the gust that could be attained in the present severe squall event (see the magnitude of gust in various places in Hong Kong in Figure 9(a)). Lam and Lam (2006) found that GUSTEX of

Geerts (2001) gave a wind gust estimate of 25.2 m/s for the present event, which is even smaller than the gust estimated from the Brasseur (2001) method based on RAMS simulation. They proposed a modified GUSTEX using the wind at 700 hPa and the estimated gust value is closer to reality.

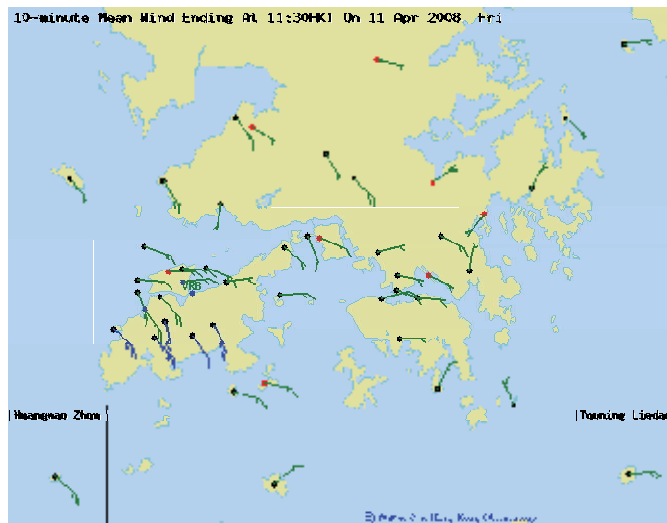
An experiment has also been carried out by retaining the default setting of cloud-top turbulent mixing in the simulation. The convective development turns out to be weaker. The maximum updraft is 12 m/s only, which is smaller than that in the model run without the cloud-top mixing. The arrival time of the squall line at Hong Kong is also later by an hour, with weaker northwesterly wind behind the squall line (14 m/s). The cloud-top turbulent mixing appears to have significant effect on the development of convection, the speed of propagation as well as the strength of rear inflow of the squall line in the simulation.

We then turn to the forecasting of gusts in terrain-disrupted airflow. A typical example is studied here. A ridge of high pressure developed over southeastern China later on 10 April 2008 and extended southwards on the following day. Surface easterlies strengthened at HKIA at about 6 a.m. on 11 April. Low level winds veered to the south at around 600 m as depicted by wind profiler data. The cool easterlies were shallow and a low level inversion developed between 400 and 800 m after the onset of easterlies (not shown). From the vertical profile of low level winds in the upstream and downstream of the Lantau Island (not shown), strengthening of low level southeasterly winds from around 10 m/s to 15 m/s was found between 200 m and 800 m when they passed over the hills over Lantau Island with height close to that of the inversion. The timing and strength of the strong low level southeasterlies matched with those of the observed maximum gusts at HKIA during 9 a.m. to 1 p.m. on 11 April.

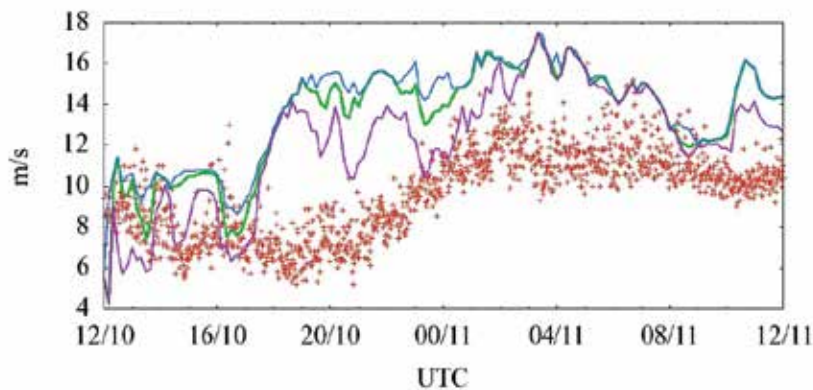
The strong southeasterlies on the hill tops were rather localised over the Lantau Island (Figure 12(a)). The Froude number in this case was found to be 0.7 - 1 (taking the mean wind speed of 10 m/s, the Brunt-Väisälä frequency of 0.02 /s, and the height of hills on the Lantau Island ranging from about 500 m to 900 m). The flow on the upwind side was subcritical. Thinning and acceleration of airflow occurred on the upslope side and attained maximum at the crest when the Froude number was close to 1. In case the Froude number equals to 1 at the crest, the flow will become supercritical and continue to accelerate as it descends the lee side until it adjusts back to the ambient subcritical conditions. The effect of topography apparently plays a significant role to the gusty condition in this type of east to southeasterly flow in the presence of a low level inversion close to the hill top.

The model forecast increasing mean wind and gust about four hours earlier than observed at HKIA in the morning of 11 April (Figure 12(b)). However, the model forecast maximum gust attained at around noon on that day is consistent with the observed data, though the strength is over-estimated by about 2 m/s.

The sensitivity of gust forecasts to the choice of turbulence parameterization scheme has also been studied. In the simulation of strong east to southeasterly flow on 10 - 11 April 2008, gust forecasts from the model run utilizing Deardorff (1980) as the turbulence parameterization scheme are different from those obtained using Mellor-Yamada Level 2.5 turbulence closure scheme. In particular, the peak of maximum gust occurred at around midnight of 10 April could be depicted by the upper bound forecast from the model run using Deardorff scheme, but not the one using Mellor-Yamada Level 2.5 turbulence closure scheme.



(a)



(b)

Fig. 12. (a) is the wind distribution at the surface in Hong Kong at 11:30 a.m., 11 April 2008. (b) is the time series of 24-hour maximum gust forecast by 200-m RAMS with model initial time at 8 p.m. on 10 April 2008: model forecast in green curve, upper bound in blue curve and lower bound in pink curve. This is compared with the maximum value of 1-minute gust (red crosses) among the six anemometers inside HKIA. Local time = UTC + 8 hours.

In the present formulation of the wind gust estimate (see Cheung et al., 2008, for details), the upper bound of gust forecast is given by the maximum wind speed in the boundary layer whose depth is taken as the height where TKE is 0.01 of the surface value. The discrepancy mentioned above for the two turbulence parameterization schemes suggests that they may produce rather different vertical profiles of TKE. The vertical profiles of TKE and wind speed at HKIA extracted from model forecasts at midnight of 10 April 2008 is shown in Figure 13(a). The Mellor-Yamada scheme forecasts the boundary layer top at around 500 m, while that of the Deardorff scheme is around 1400 m. Consequentially, winds of larger speed at higher levels have been taken as the gust upper bound based on the Deardorff scheme (see Figure 13(b)).

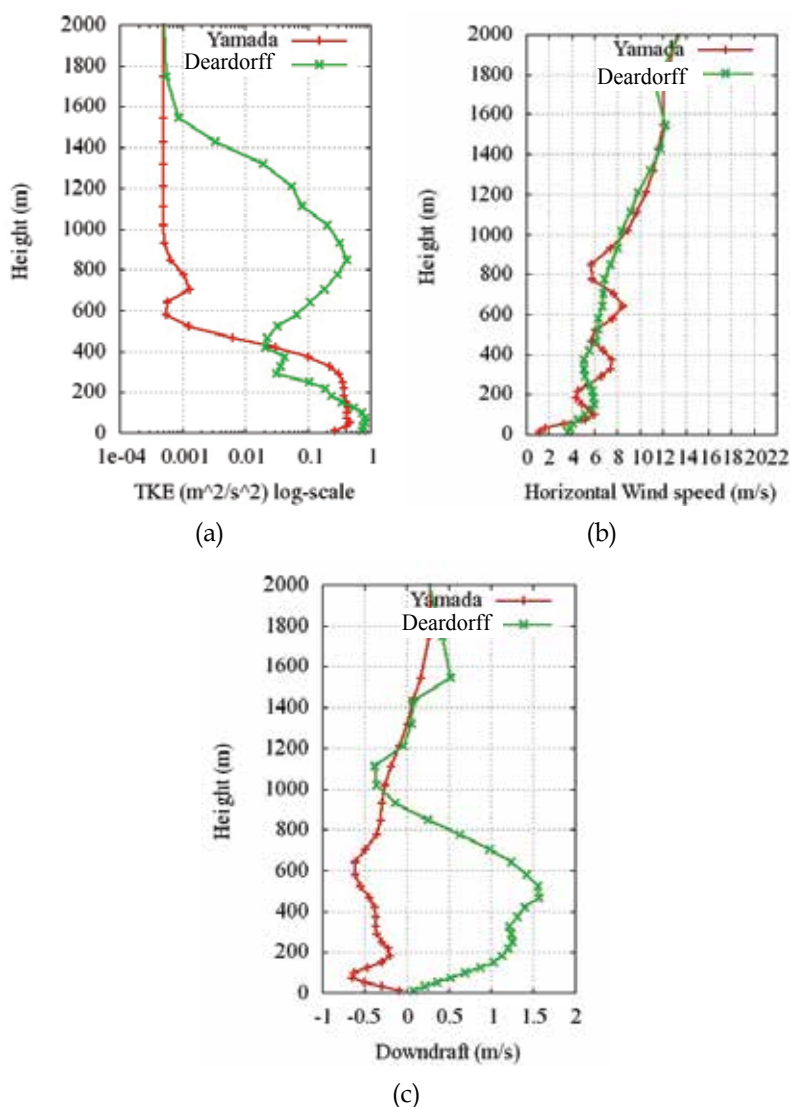


Fig. 13. Vertical profiles of (a) TKE, (b) horizontal wind speed, and (c) downdraft at HKIA at the midnight of 10 April 2008. The TKE plot is in log-scale, red for Deardorff scheme and green for Mellow-Yamada scheme

The vertical profiles of downdraft for the two schemes are also shown in Figure 13(c). The Deardorff scheme successfully depicts the downdraft associated with the accelerated descent of the supercritical air flow from around 500 m while the Mellow-Yamada scheme has no such indication. It should be noted that the downdraft is also considered in the gust estimation as described in Cheung et al. (2008). Further tests would be necessary to obtain more conclusive results for the performance of two turbulence schemes in different types of weather conditions and their impact on the model gust forecasts.

## 5. High winds and heavy rain associated with tropical cyclones – impact of assimilation of radar data

In every summer, tropical cyclones bring about hazardous weather to south China coastal areas, including strong winds and heavy rain associated with the outer rain bands. Accurate forecasting of the winds and rain caused by tropical cyclones would be very useful for the provision of timely warnings for the general public. Nowadays, NWP models, from synoptic scale to mesoscale scale, are widely used in the weather services in forecasting the heavy rain and strong wind areas brought by tropical cyclones. The performance of NWP models is gradually improved with the physical parameterizations becoming more and more sophisticated. At the same time, the assimilation of remote-sensing data covering the tropical cyclones, such as radar and satellite observations, could also help initializing the NWP models.

In this section, the impact of radar data on the model forecasting of strong wind and heavy rain areas of tropical cyclones is studied. One tropical cyclone event over the northern part of the South China Sea and south China coastal areas in 2008 is considered, namely, Severe Tropical Storm Kammuri in August. At the first step, only the data from a single radar in Hong Kong are used in the analysis. Such data, including the Doppler velocity and reflectivity measurements, are used in a variety of ways, namely, by assimilation using a 3D variational scheme (3DVAR) of the NWP model at the initial time only, by 3DVAR assimilation in a cycling run at two separate times (with 3 hours apart), and in a cycling run but with 3DVAR assimilation of the radar-retrieved 2D wind field. The study aims at finding out which assimilation method has the strongest positive impact on the simulation results, in terms of the forecasting of strong winds and heavy rain areas of the cyclones. The model under consideration is Weather Research and Forecasting (WRF) model version 2.2.

The radar considered in this study is the one located at Tate's Cairn in Hong Kong (22°21'36"N 114°12'54"E). It is an S-band radar at around 585 m AMSL on top of a hill with a Nyquist velocity of 35.8 m/s. It scans at 12 different elevation angles from 0.5° to 34.7°. The volume scan takes about 6 minutes to complete. Before the variational analysis, the radar data are interpolated into a Cartesian grid. The grid has 640 × 640 points with a size of 800 m. In the vertical, the radar data extend from the ground up to 5000 m with a resolution of 500 m.

The Doppler velocity and reflectivity data of Tate's Cairn radar are assimilated into WRF using WRF VAR version 2.1 (Barker et al., 2004). The conventional weather observations, such as surface SYNOP and upper air TEMP/PILOT data, are also included in the analysis. WRF VAR is a variational data assimilation scheme to ingest both conventional and non-conventional data through the iterative minimization of a prescribed cost (or penalty) function. Differences between the analysis and the observations are penalized (damped) according to their perceived error. For simplicity, the errors of radial velocity and reflectivity are taken to be 1 m/s and 1 dBZ respectively. Details of the model setup could be found in Cheung and Chan (2010).

As an experiment, apart from the direct ingestion of Doppler velocity and reflectivity data from the radar, the 2D wind field under the coverage of the radar is retrieved from the Doppler velocity data of the radar and ingested into WRF through WRF VAR. For this purpose, the two-step variational method as described in Yang and Qiu (2006) is employed. In the assimilation into WRF, the 2D wind profile at a grid point is taken to be an "upper-air ascent", similar to the radiosonde measurement.

In the morning of 6 August 2008, Kammuri was located at about 130 km south of Hong Kong and moved to the northwest steadily across the south China coastal waters. It brought about gale-force east to southeasterly winds to Hong Kong. Moreover, the outer rain bands associated with Kammuri affected the coast of Guangdong.

Model simulations start at 00 UTC, 6 August 2008. For cycling run, the first simulation is made at 21 UTC, 5 August 2008 and run for three hours before data assimilation and another model run at 00 UTC, 6 August. The WRF-simulated surface wind magnitude and the streamlines for the various data assimilation runs after 6 hours are shown in Figures 14(a) to (d). The cold-start runs (a) and (b) forecast very strong winds over the territory and seas to the south, reaching 23 m/s or more. On the other hand, the cycling runs (c) and (d) give generally lower wind speeds. In particular, there is just a small area of 23 m/s wind speed (coloured red) in the cycling simulation with the direct assimilation of radar velocity and reflectivity data (Figure 14(c)). Unfortunately there were no surface observations over the seas for direct comparison with the model simulation results. However, if we consider the wind observations over Hong Kong only (Figure 14(e)), the strongest winds seem to be in the order of 17 - 20 m/s (35 - 40 knots) only, and there is no extensive area of surface wind magnitude reaching 23 m/s. Winds of the strength similar with that over Hong Kong were also recorded at Huang Mao Zhou, an island over the northern part of the South China Sea to the south of Hong Kong (not shown).

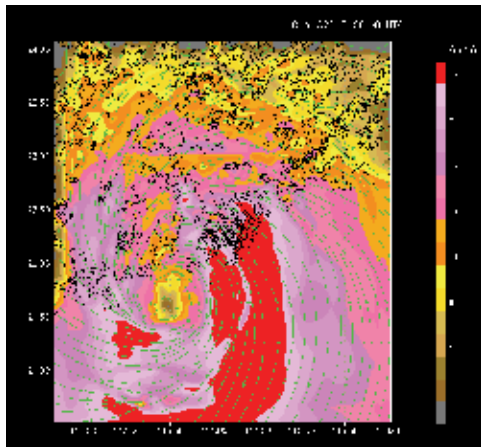
The rain forecasts of the various model runs are given in Figures 15(a) to (d). Among these runs, the cycling simulation Figure 15(c) gives the stronger rain bands (simulated radar reflectivity of about 40 dBZ) located just to the north of Hong Kong, so that the territory is just clear of the influence of heavier rain. This is the most consistent with the actual radar observation (Figure 15(e)). However, in all simulations, the radar-echo-free area associated with the eye of the tropical cyclone appears to be too large.

It could be seen from the present case that the assimilation of radar data through an advanced data assimilation scheme helps improve the forecasting of high winds and heavy rain of a tropical cyclone. More tropical cyclone cases are under study to see the impact of radar data more systematically.

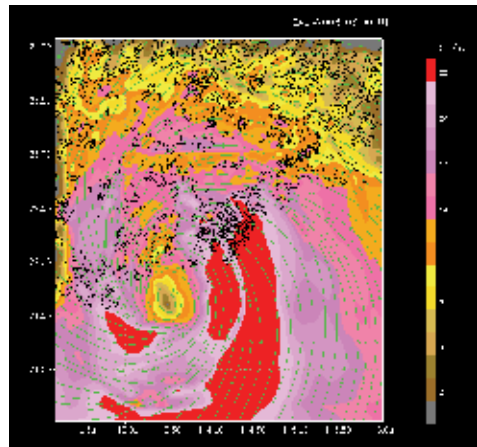
## 6. Conclusion

This paper discusses some advanced applications and setup of NWP model in the forecasting of hazardous weather. It is first shown that the use of sub-kilometre simulation and the development of sophisticated turbulence parameterization schemes help the forecasting of turbulence for aviation application, as well as the provision of wind gust estimate in intense severe weather as well as terrain-disrupted airflow. The sub-kilometre simulation is crucial in explicitly forecasting the convection and resolving the complex terrain near the Hong Kong International Airport in fine details in order to capture the terrain-induced airflow disturbances. The forecast results are also shown to be rather sensitive to the choice of turbulence parameterization scheme. In particular, the inclusion of a TKE equation appears to be important in giving a reasonable simulation of the TKE and its dissipation rate.

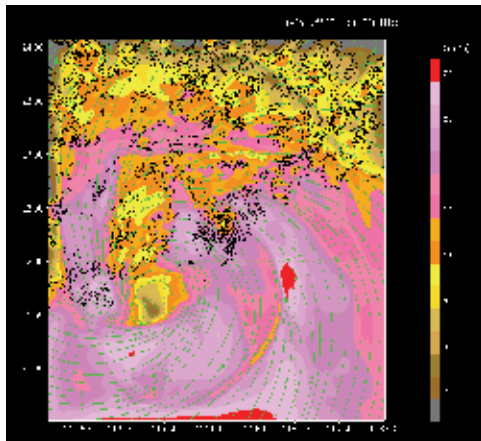
The assimilation of non-conventional meteorological data, namely, radar data, is shown to improve the forecasting of high winds and heavy rain in a tropical cyclone case. This may be achieved through the use of sophisticated data assimilation scheme, such as 3DVAR of radar reflectivity and radial velocity, or simply direct assimilation of the radar-based 2D wind field retrieved separately.



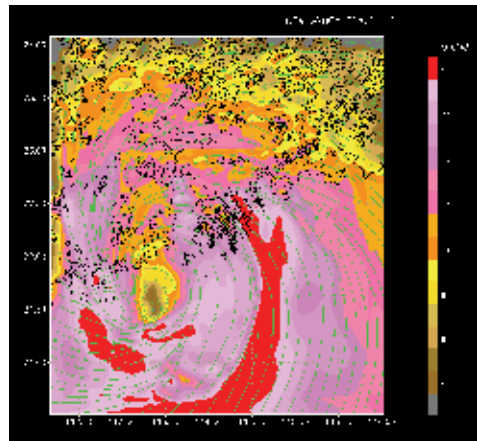
(a) cold start, no radar data



(b) cold start, with the assimilation of radar data



(c) cycling run, direct assimilation of radar data



(d) cycling run, assimilating radar retrieved winds



(e) actual surface wind observations in Hong Kong

Fig. 14. The simulated surface wind magnitude (coloured contours) and streamlines for the four different model runs (a) to (d) at 06 UTC, 6 August 2008. (e) shows the actual surface wind data in Hong Kong at the same time.

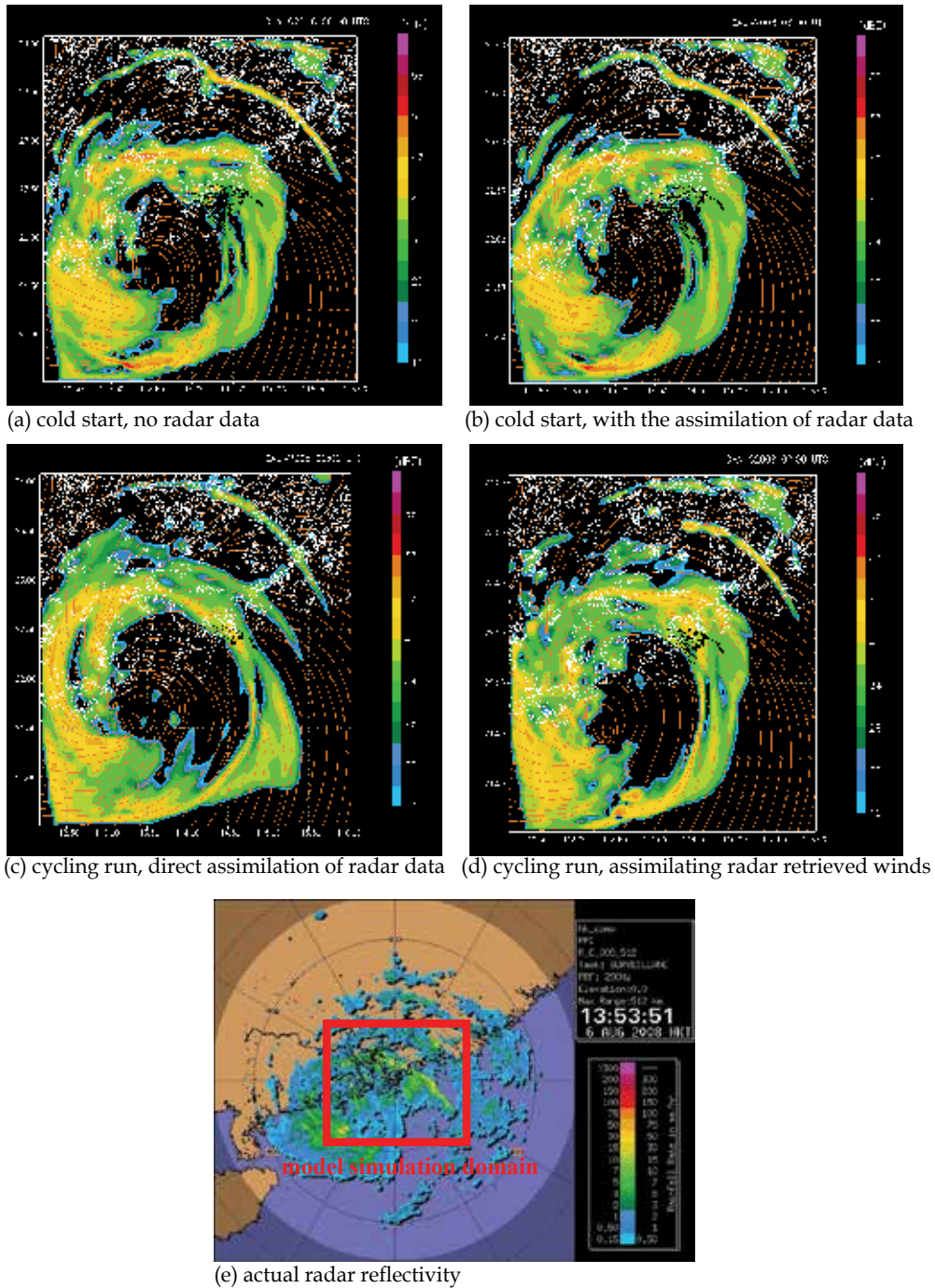


Fig. 15. The simulated radar reflectivity (coloured contours) and streamlines for the four different model runs (a) to (d) at 06 UTC, 6 August 2008. (e) shows the actual radar reflectivity at the same time.

The operational mesoscale model of the Hong Kong Observatory has just been upgraded to a non-hydrostatic model. The horizontal resolution gets down to 2 km at the present, and would become sub-kilometre scale in the future. Assimilation of remote-sensing meteorological data, such as radars and satellites, is under development in the operational data assimilation suite. With the use of such a model setup for some time, more experience would be accumulated on kilometre scale to sub-kilometre scale simulation, advanced data assimilation, and the selection of the appropriate model physics. The results of the operational runs would be reported in the papers in the future.

## 7. References

- Barker, D.M.; Huang, W., Guo, Y.R., & Xiao, Q.N. (2004). A three-dimensional (3DVAR) data assimilation system for use with MM5: Implementation and initial results. *Mon. Wea. Rev.*, 132, 897-914.
- Brasseur, O. (2001). Development and application of a physical approach to estimating wind gusts. *Mon. Wea. Rev.*, 129, 5-25.
- Chan, P.W. (2006). Generation of eddy dissipation rate map at the Hong Kong International Airport based on Doppler LIDAR data. *12th Conference on Aviation, Range, and Aerospace Meteorology*, Atlanta, GA, U.S.A.
- Chan, P.W. (2009). Atmospheric Turbulence in Complex Terrain: Verifying numerical model results with observations by remote-sensing instruments. *Meteorol. Atmos. Phys.*, 103, 145-157.
- Chan, P.W.; & Chan, S.T. (2004). Performance of eddy dissipation rate estimates from wind profilers in turbulence detection. *11th Conference on Aviation, Range, and Aerospace Meteorology*, Hyannis, MA, U.S.A.
- Chan, S.T.; & Mok, C.W. (2004). Comparison of Doppler LIDAR observations of severe turbulence and aircraft data. *11th Conference on Aviation, Range, and Aerospace Meteorology*, Hyannis, MA, U.S.A.
- Cheung, P.; Lam, C.C., & Chan, P.W. (2008). Numerical simulation of wind gusts in terrain-disrupted airflow at the Hong Kong International Airport. *13th Conference on Mountain Meteorology*, Whistler, BC, Canada.
- Cheung, T.C.; & Chan, P.W. (2010). Improving wind and rain simulations for tropical cyclones with the assimilation of Doppler radar data. *The Open Atmospheric Science Journal*, 4, 57-63.
- Clark, T.L.; Keller, T., Coen, J., Neilley, P., Hsu, H., & Hall, W.D. (1997). Terrain-induced turbulence over Lantau Island: 7 June 2004 Tropical Storm Russ case study. *J. Atmos. Sci.*, 54, 1795 – 1814.
- Cotton, W.R.; Pielke Sr., R.A., Walko, R.L., Liston, G.E., Tremback, C., Jiang, H., McAnelly, R.L., Harrington, J.Y., Nicholls, M.E., Carrio, G.G., & McFadden, J.P. (2003). RAMS 2001: Current status and future directions. *Meteor. Atmos. Phys.*, 82, 5-29.
- Deardorff, J.W. (1980). Stratocumulus-capped mixed layers derived from a three-dimensional model. *Bound.-Layer Meteor.*, 18, 495-527.
- Fast, J.D.; & Shaw, W.J. (2002). An evaluation of mesoscale model predictions of turbulence kinetic energy and dissipation. VTMX Science Meeting, Salt Lake City, U.S.A., 17 – 19 September 2002 (<http://www.pnl.gov/vtmx/presentations2002.html>).
- Geerts, B. (2001). Estimating downburst-related maximum surface wind speeds by means of proximity soundings in New South Wales, Australia. *Wea. Forecasting*, 16, 261-269.

- HKO; IFALPA, & GAPAN (2010). *Windshear and Turbulence in Hong Kong – information for pilots*. 3rd Edition.
- ICAO (2007). *Meteorological Service for International Air Navigation, Annex 3 to the Convention on International Civil Aviation (16th Edition)*, International Civil Aviation Organization.
- Lam, C.C.; & Hilda Lam (2006). Analysis of high wind gusts associated with thunderstorms, tropical cyclones and monsoons. *20th Guangdong – Hong Kong – Macao Seminar on Meteorological Technology* (in Chinese with English abstract).
- Mellor, G. L.; & Yamada, T. (1982). Development of a turbulence closure model for geophysical fluid problems. *Rev. Geophys. Space Phys.*, 20, 851–875.
- Trini Castelli, S.; Ferrero, E., Anfossi, D., & Ohba, R. (2005). Turbulence closure models and their application in RAMS. *Environmental Fluid Mechanics*, 5, 169–192.
- Xu, D.; & Taylor, P.A. (1997). On turbulence closure constants for atmospheric boundary-layer modelling: neutral stratification. *Boundary-Layer Meteorology*, 84, 267–287.
- Yang, Y.; & Qiu, C.J. (2006). Analysis on mesoscale circulation within a heavy rain system using Doppler radar data. *Plateau Meteorology*, 25, 925–931 (in Chinese with English abstract).
- Yeung, L.H.Y.; Chan, P.K.Y., & Lai, E.S.T. (2005). Impact of radar rainfall data assimilation on short-range quantitative precipitation forecasts using four-dimensional variational analysis technique. *32nd Conference on Radar Meteorology*, American Meteorological Society, New Mexico, U.S.A.

# Hygrothermal Numerical Simulation: Application in Moisture Damage Prevention

N.M.M. Ramos, J.M.P.Q. Delgado, E. Barreira and V.P. de Freitas  
*LFC – Building Physics Laboratory, Civil Engineering Department  
Faculty of Engineering, University of Porto  
Portugal*

## 1. Introduction

### 1.1 Background

Building pathologies originated by moisture are frequently responsible for the degradation of building components and can affect users' health and comfort. The solutions for treating moisture related pathologies are complex and, many times, of difficult implementation. Several of these pathologies are due to innovative techniques combined with new materials of poorly predicted performance. The knowledge of the physical processes that define hygrothermal behaviour allows for the prediction of a building response to climatic solicitation and for the selection of envelope solutions that will lead to required feasibility.

Over the last five decades, hundreds of building energy software tools have been developed or enhanced to be used. A list of such tools can be obtained in the US Department of Energy Webpage (2007). This directory provides information for more than 345 building software tools for evaluating energy efficiency, renewable energy and sustainability in buildings.

The problem of moisture damage in buildings has attracted interest from the early days of the last century, but it was during the past decades that the general topic of moisture transport in buildings became the subject of more systematic study, namely with the development of the modelling hygrothermal performance. In the field of building physics the hygrothermal models are widely used to simulate the coupled transport processes of heat and moisture for one or multidimensional cases. The models may take into account a single component of the building envelope in detail or a multizonal building.

In literature, there are many computer-based tools for the prediction of the hygrothermal performance of buildings. These models vary significantly concerning their mathematical sophistication and, as shown Straube and Burnett (1991), this sophistication depends on the degree to which the model takes into consideration the following parameters: moisture transfer dimension; type of flow (steady-state, quasi-static or dynamic); quality and availability of information and stochastic nature of various data (material properties, weather, construction quality, etc.).

All the hygrothermal simulation tools presented later in this paper are based on one of the following numerical methods for space and time discretization:

- a. Finite Difference Methods (FDM) and Finite Control Volume (FCV) methods;
- b. Finite Element Method (FEM);
- c. Response Factor and Transfer Function method.

## 1.2 HAM models

Different models for the coupled heat, air, moisture and salt transport have been developed and incorporated into various software programs used in the field of porous building materials and in the closely related field of wetting and drying of soils.

The HAM models (heat, air and moisture) combine the flow equations with the mass and energy balances. Transient, one-dimensional models for combined heat, air and moisture transport in building components have been reasonably well established for about two decades now. In 1996 the final report of Volume 1 - Modelling, of the Annex 24 of the International Energy Agency (IEA), elaborated by Hens (1996), showed that 37 programs had been developed by researchers of 12 countries, 26 of which were non-steady state models. In the last ten years, many programs indicated in this work have developed new versions and improved the conditions of analysis and therefore sensitized the values of results.

More recently, a review of hygrothermal models for building envelope retrofit analysis made by Canada Mortgage and Housing Corporation (2003) has identified 45 hygrothermal modelling tools, and in the last four years, 12 new hygrothermal models were developed, most of them during Annex 41 (Rode and Grau, 2004).

Most of the 57 hygrothermal models available in literature are not readily available to the public outside of the organization where they were developed. In fact, only the following 14 hygrothermal modelling tools are available to the public in general. The programs available for the public in general were analyzed in detail (Delgado *et al.* (2010)), namely the input of material properties and the boundary conditions (inside and outside).

**1D-HAM** - a one-dimensional model for heat, air and moisture transport in a multi-layered porous wall. The program uses a finite-difference solution with explicit forward differences in time. Analytical solutions for the coupling between the computational cells for a given air flow through the construction are used. The moisture transfer model accounts for diffusion and convection in vapour phase, but not liquid water transport. Heat transfer occurs by conduction, convection and latent heat effects. Climatic data are supplied through a data file with a maximum resolution of values per hour over the year. The program accounts for surface absorption of solar radiation (Hagentoft and Blomberg, 2000).

**BSim2000** - a one-dimensional model for transport of heat and moisture in porous building materials. BSim2000, the successor of the MATCH program, is a computational design tool for analysis of indoor climate, energy consumption and daylight performance of building. The software can represent a multi-zone building with heat gains, solar radiation through windows, heating, cooling, ventilation and infiltration, steady state moisture balance, condensation risks. A new transient moisture model for the whole building was also developed as an extension of BSim2000. One of the limitations is that liquid moisture transfer in constructions is not yet represented (Rode and Grau, 2004).

**DELPHIN 5** - a one or two-dimensional model for transport of heat, air, moisture, pollutant and salt transport in porous building materials, assemblies of such materials and building envelopes in general. The Delphin program can be used in order to simulate transient mass and energy transport processes for arbitrary standard and natural climatic boundary conditions (temperature, relative humidity, driving rain, wind speed, wind direction, short and long wave radiation). This simulation tool is used for:

- a. Calculation of thermal bridges including evaluation of hygrothermal problem areas (surface condensation, interstitial condensation);

- b. Design and evaluation of inside insulation systems;
- c. Evaluation of ventilated facade systems, ventilated roofs;
- d. Transient calculation of annual heating energy demand (under consideration of moisture dependent thermal conductivity);
- e. Drying problems (basements, construction moisture, flood, etc);
- f. Calculation of mold growth risks and further applications.

A large number of variables as moisture contents, air pressures, salt concentrations, temperatures, diffusive and advective fluxes of liquid water, water vapour, air, salt, heat and enthalpy which characterize the hygrothermal state of building constructions, can be obtained as functions of space and time (Nicolai, Grunewald and Zhang, 2007).

**EMPTIED** - a one-dimensional model for heat, air and moisture transport, with some considerations for air leakage included (Rousseau, 1999). The software makes enough simplifying assumptions to be practical for designers to use in order to compare the relative effects of different climates, indoor conditions, wall materials and air tightness on wall performance. EMPTIED calculates temperatures assuming steady-state conditions for the duration of each bin, neglecting latent heat and heat transported by moving air. The program uses monthly bin temperature data and outputs plots of the monthly amount of condensation, drainage and evaporation. It is recommended for simple analysis of air leakage. EMPTIED has limitations that should be kept in mind. Initial moisture contents cannot be specified. Wind, sun and rain are not taken into account. Air movement is taken to be the same through every layer, there are no convection loops within layers or between the exterior and vented cavities. The maximum amount of moisture a material can store safely is assumed to be the same amount at which condensation will start to occur on the surface.

**GLASTA** - a one-dimensional model for heat and moisture transport in porous media. It is based on the Glaser method, but includes a model for capillary distribution within the layers of the assembly and may be suitable for assessing drying potential. The program calculates monthly mean values of temperature and vapour pressure or relative humidity and climatic database for more than 100 European locations are presented (see Physibel, 2007).

**hygIRC-1D** - a one-dimensional simulation tool for modelling heat, air and moisture movement in exterior walls. This program is an advanced hygrothermal model that is an enhanced version of the LATENITE model developed jointly by Institute for Research in Construction and the VTT (Finland). The hygIRC program can be used to model common wall systems. The hygIRC model simulates heat, air and moisture conditions within the retrofitted walls to determine how the retrofits affect the durability of the wall system. This information can be used as a means to confirm the integrity of several specific retrofit measures developed for high-rise wall structures before they are recommended to the building industry (Karagiosis, 1993 and Djebbar *et al.*, 2002a,b).

**HAMLab** - a one-dimensional heat, air and moisture simulation model. This hygrothermal model is a collection of four tools and functions in the MatLab/Simulink/FemLab environment that includes: HAMBASE (used for: indoor climate design of multizone buildings; energy and (de)humidification simulation; rapid prototyping; and HAM building model component to be used with HAMSYS, for the design of HVAC systems), HAMSYS (used for: HVAC equipment design; and controller design), HAMDET (used for: HAM simulation of, up to 3D, building constructions; and airflow simulation in rooms and around buildings) and HAMOP (used for: design parameters optimization; and optimal operation). All tools have been validated, except HAMOP, by comparison with experimental data obtained in the laboratory and in field studies (van Schijndel, 2005).

The main objective of HAMBASE is the simulation of the thermal and hygric indoor climate and energy consumption. In SimuLink, the HAMBASE model is visualised by a single block with input and output connections. The interface variables are the input signal of the HAMBASE SimuLink model and the output signal contains for each zone the mean comfort temperature, the mean air temperature and RH. In HAMBASE model the diffusion equations for heat and moisture transfer in the walls are modelled with a finite difference scheme and solved with an implicit method.

**HAM-Tools** - a one-dimensional heat, air and moisture transfer simulation model. The main objective of this tool is to obtain simulations of transfer processes related to building physics, i.e. heat and mass transport in buildings and building components in operating conditions. Using the graphical programming language Simulink and Matlab numerical solvers, the code is developed as a library of predefined calculation procedures (modules) where each supports the calculation of the HAM transfer processes in a building part or an interacting system. Simulation modules are grouped according to their functionality into five sub-systems: Constructions, Zones, Systems, Helpers and Gains (Kalagasidis, 2004). The software is an open source, new modules can be easily added by users and moreover they are free of charge and can be downloaded from the internet.

**IDA-ICE** - a tool for building simulation of energy consumption, indoor air quality and thermal comfort. It covers a large range of phenomena, such as the integrated airflow network and thermal models, CO<sub>2</sub> and moisture calculation and vertical temperature gradients. For example, wind and buoyancy driven airflows through leaks and openings are taken into account via a fully integrated airflow network model. IDA ICE may be used for the most building types for the calculation of:

- a. The full zone heat and moisture balance, including specific contributions from: sun, occupants, equipment, lighting, ventilation, heating and cooling devices, surface transmissions, air leakage, cold bridges and furniture;
- b. The solar influx through windows with a full 3D account of the local shading devices and those of surrounding buildings and other objects;
- c. Air and surface temperatures;
- d. The operating temperature at multiple arbitrary occupant locations, e.g. in the proximity of hot or cold surfaces. The full non-linear Stephan-Boltzmann radiation with the view factors is used to calculate the radiation exchange between surfaces;
- e. The directed operating temperature for the estimation of asymmetric comfort conditions;
- f. Comfort indices, PPD and PMV, at multiple arbitrary occupant locations;
- g. The daylight level at an arbitrary room location;
- h. The air, CO<sub>2</sub> and moisture levels, which both can be used for controlling the VAV (Variable Air Volume) system air flow;
- i. The air temperature stratification in displacement ventilation systems;
- j. Wind and buoyancy driven airflows through leaks and openings via a fully integrated airflow network model. This enables one to study temporarily open windows or doors between rooms;
- k. The airflow, temperature, moisture, CO<sub>2</sub> and the pressure at arbitrary locations of the air-handling and distribution systems;
- l. The power levels for primary and secondary system components;
- m. The total energy cost based on time-dependent prices.

To calculate moisture transfer in IDA-ICE, the common wall model RCWall should be replaced with HAMWall, developed by Kurnitski and Vuolle (2000). It can be used either as a single independent model or as a component of a bigger system. HAMWall model can be used also as a single program. The moisture transfer is modelled by one moisture-transfer potential, the humidity by volume. The liquid water transport is not modelled and hysteresis is not taken into account. By using this moisture transfer model it is possible to study the following cases:

- a. The effect of structures on the indoor air quality and thermal comfort;
- b. The effect of moisture buffering building materials and furniture to dampen the fluctuation of air humidity;
- c. Making the hygrothermal analysis by taking into account the changes in the indoor climate;
- d. To study the influence of the ventilation system caused under or over pressure on the hygrothermal conditions in the building envelope;
- e. To study the influence of moisture on the heating and cooling load and on the performance of heating and cooling equipment.

**MATCH** - a one-dimensional model for heat and moisture transport in composite building structures. A modified version of the program also calculates air flow (Rode, 1990). The program uses both the sorption and suction curves to define the moisture storage function and the sorption isotherm in the hygroscopic regime. MATCH uses a Finite Control Volume method to calculate the transient evolution of both the thermal and the moisture related variables, and the moisture transport is assumed to be by vapour flow only, defined by the vapour permeability of the material. In the capillary regime the suction curve is used together with the hydraulic conductivity to model moisture transport. Some applications of the program are:

- a. Determining of moisture transport in and through building constructions;
- b. Calculating the temperature and moisture profiles transiently by considering the thermal and hygroscopic capacities.

By dividing the time into small steps, it is possible to take into account the effect on constructions of short, intensive temperature gradients, such as when they are exposed to solar radiation. MATCH can be used successfully for the analysis and design of protected membrane roofs and walls with non-absorbent cladding. The program has been validated by comparison with experimental data obtained in the laboratory and in field studies.

**MOIST** - a one-dimensional model for heat and moisture transport in building envelopes. It models moisture transfer by diffusion and capillary flow, and air transfer by including cavities that can be linked to indoor and outdoor air (Burch and Chi, 1997). The program enables the user to define a wall, cathedral ceiling or low-slope roof construction, and to investigate the effects of various parameters on the moisture accumulation within layers of the construction, as a function of time of year for a selected climate. Most of the material data required by the program are coefficients of curve-fits to specific equations for each property. The equilibrium moisture curves had to be severely approximated, close to the saturation point. Some applications of the MOIST program are:

- a. Predicting the winter moisture content in exterior construction layers;
- b. Predicting the surface relative humidity at the construction layers in hot and humid climates, thereby analysing the potential for mould and mildew growth;
- c. Determining the drying rates for materials containing original construction moisture;

- d. Investigating the performance of cold refrigeration storage rooms;
- e. Analysing the effect of moisture on heat transfer.

Finally, MOIST is a one-dimensional model, doesn't include exterior wetting of a construction by rain and the insulating effect and change in roof absorptance from a snow load. Moreover, the model does not include heat and moisture transfer by air movement (the construction is assumed to be air tight) and the weather data for European cities are not available and cannot be generated (only has weather data of USA and Canada).

**MOISTURE-EXPERT** - one or two-dimensional model for heat, air and moisture transport in building envelope systems (Karagiozis, 2001). The program is, basically, software developed by Oak Ridge National Laboratory and Fraunhofer Institute for Building Physics, to adapt the original European version of WUFI software for USA and Canada. The model treats vapour and liquid transport separately. The moisture transport potentials are vapour pressure and relative humidity, and the energy transport potential is the temperature. The model includes the capability of handling temperature dependent sorption isotherms and liquid transport properties as a function of drying or wetting processes. It is a highly complex program, typically requiring more than 1000 inputs for the one-dimensional simulations. Inputs include: exterior environmental loads, interior environmental loads, material properties and envelope system and subsystem characteristics.

**UMIDUS** - a one-dimensional model for heat and moisture transport within porous media, in order to analyze hygrothermal performance of building elements when subjected to any kind of climate conditions (Mendes et al., 1999). Diffusion and capillary regimes are modelled, so moisture transport occurs in the vapour and liquid phases. The model predicts moisture and temperature profiles within multi-layer walls and low-slope roofs for any time step and calculates heat and mass transfer. The program needs to be validated.

**WUFI** - a one or two-dimensional model for heat and moisture transport developed by Fraunhofer Institute in Building Physics (IBP). It was validated using data derived from outdoor and laboratory tests, allows calculation of the transient hygrothermal behaviour of multi-layer building components exposed to natural climate conditions (Kuenzel and Kiessl, 1997). Heat transfer occurs by conduction, enthalpy flow (including phase change), short-wave solar radiation and long-wave radiative cooling (at night). Convective heat and mass transfer is not modelled. Vapour-phase transport is by vapour diffusion and solution diffusion, and liquid-phase water transport is by capillary and surface diffusion.

As the purpose of most hygrothermal models is usually to provide sufficient and appropriate information needed for decision-making, four items should be considered when choosing software for modelling a single component of the building envelope or a multizonal building:

- a. The software must be in the public domain (freeware or commercially) available;
- b. Suitability of the software for the single component or a multizonal building analysis under consideration must be assured;
- c. The programs must be of reasonably recent vintage or with recent further development;
- d. The software must be "user friendly".

Finally, as the programs have different hygrothermal potentialities, strengths and weaknesses, such as the ability to model heat and moisture transfer by air movement, 2-D or 3-D phenomena, or the capability to simulate high number of zones in a reasonable execution time, the investigators need to select the hygrothermal simulation tools that suit better to their problems.

### 1.3 Numerical simulations data

The hygrothermal performance of a building can be assessed by analysing energy, moisture and air balances. The hygrothermal balances consider the normal flows of heat by conduction, convection and radiation; moisture flows by vapour diffusion, convection and liquid transport; and airflows driven by natural, external or mechanical forces.

The prediction of the hygrothermal performance of the building enclosure typically requires some knowledge of:

**Geometry of the enclosure** - The enclosure geometry must be modelled before any hygrothermal analysis can begin. In simple methods the geometry is reduced to a series of one-dimensional layers. The enclosure geometry includes all macro building details, enclosure assembly details and micro-details.

**Material Properties** - Material properties and their variation with temperature, moisture content and age, as well as their chemical interaction with other materials are also critical. Some material properties needed in hygrothermal simulation are: bulk density, porosity, specific heat capacity, thermal conductivity, sorption isotherm, vapour permeability and diffusivity, suction pressure, liquid diffusivity, specific moisture capacity, etc.

**Boundary Conditions** - The boundary conditions imposed on a mathematical model are often as critical to its accuracy as the proper modelling of the moisture physics. In general, the following environment needs to be known: (i) interior environment, including the interaction of the enclosure with the interior environment; (ii) exterior environment, including the interaction of the building with the exterior environment and (iii) boundary conditions between elements. The correct treatment of the interfacial flows at boundaries between control volumes of different type is an important point in successful modelling.

#### 1.3.1 Material properties

**Bulk density ( $\rho$ )** - Several standards can be applied for the experimental determination of this property, as EN ISO 10545-3 (1995) for ceramic tiles, EN 12390-7 (2000) for concrete, EN 772-13 (2000) for masonry units. The samples must be dried until constant mass is reached. The samples volume is calculated based on the average of three measurements of each dimension.

**Bulk porosity ( $\varepsilon$ )** - The standards EN ISO 10545-3 (1995) for ceramic tiles and ASTM C 20 (2000) for fired white ware products, could be used to measure the bulk porosity of building materials. The samples are dried until constant mass is reached ( $m_1$ ). After a period of stabilization, the samples are kept immersed under constant pressure. Weigh of the immersed sample ( $m_2$ ) and the emerged sample ( $m_3$ ) the bulk porosity is given by:  
$$\varepsilon = (m_3 - m_1) / (m_3 - m_2).$$

**Specific heat capacity ( $c_p$ )** - This test method employs the classical method of mixtures to cover the determination of mean specific heat of thermal insulating materials. The materials must be essentially homogeneous and composed of matter in the solid state (see ASTM C 351-92b (1999)).

The test procedure provides for a mean temperature of approximately 60°C (100 to 20°C; temperature range), using water as the calorimetric fluid. By substituting other calorimetric fluids the temperature range may be changed as desired. All the samples shall be dried to constant mass in an oven at a temperature of 102 to 120°C and the method is to add a measured material mass, at high temperature, to a measured water mass at low temperature in order to determine the resulting equilibrium temperature. The heat absorbed by water

and container is so calculated and this value equalised to the amount of heat released expression in order to calculate the specific heat desired.

**Thermal conductivity ( $\lambda$ )** - The standards ISO 8302 (1991), EN 12664 (2001), EN 12667 (2001) and EN 12939 (2001) can be applied to determine the thermal conductivity of building materials using the Guarded Hot Plate method. The method uses two identical samples of parallel faces. After the system stabilization, a constant flux is obtained, perpendicular to the samples dominant faces. Knowing the temperature in opposite faces allows determining the thermal conductivity of the samples.

**Moisture storage functions** - The sorption curve of a material can be determined using different methods. Gravimetric type methods are usually preferred for building materials following, for instance, the standard EN ISO 12571 (2000). According to this document, the sorption curves are determined by stabilizing material samples in different conditions of relative humidity and constant temperature. The obtained values allow knowing the moisture content of the material at hygroscopic equilibrium with the surrounding air.

The moisture content in the over-hygroscopic region is usually defined using suction curves that can be determined using pressure plate measurements.

**Water vapour permeability ( $\delta_p$ )** - Vapour permeability is usually determined using the cup test method. The sample is sealed in a cup containing either a desiccant (dry cup) or a saturated salt solution (wet cup). The set is put inside a climatic chamber where the relative humidity value is regulated to be different from the one inside the cup. The vapour pressure gradient originates a vapour flux through the sample. The standard EN ISO 12572 (2001) can be used as a reference.

**Water absorption coefficient (A)** - The standard EN ISO 15148 (2002) can be applied in the determination of the water absorption coefficient by partial immersion. The side faces of the samples are made impermeable to obtain a directional flux. After stabilization with the room air, the samples bottom faces are immersed ( $5 \pm 2$  mm) and weighed at time intervals defined according to a log scale during the first 24 h period and after that every 24 h. This property is derived from the linear relation between mass variation and the square root of time. When that relation is not verified, only the values registered at 24 h are used.

The liquid conductivity,  $K$ , can be related to the moisture diffusivity,  $D_w$ , and is highly dependent on moisture content. This implicates that its determination implies the knowledge of moisture content profiles on the material. These profiles can be estimated from the water absorption coefficient.

**Reference values** - The standards EN ISO 10456 (2007) and EN 12524 (2000) present tabulated design values of hygrothermal properties for a wide range of building materials (see Table 1).

Materials	$\rho$ kg/m <sup>3</sup>	$\varepsilon$ (%)	$c_p$ J/(kgK)	$\lambda$ W/(mK)	$\delta_p \times 10^{12}$ kg/(msPa)	A kg/(m <sup>2</sup> s <sup>0.5</sup> )
Stone	1600-2800	0,5-20	1000	0,5-3,5	2,0	0,01-0,025
Lime plaster	1600	26	1000	0,8-1,5	4,5-13	0,01-0,25
Concrete	2000-2400	16	1000	1,15-2,0	0,7-13	0,01
Brick	1000-2400	28	920	0,34-1,04	2,4	0,05

Table 1. Example of material properties values.

### 1.3.2 Boundary conditions

A critical aspect in the design of envelope elements is the inclusion of the exterior and interior hygrothermal environmental loads (see Table 2). The most important exterior environmental loads are: (1) ambient temperature; (2) ambient relative humidity; (3) diffuse solar radiation; (4) direct solar radiation; (5) cloud index; (6) wind speed; (7) wind direction and (8) horizontal rain.

Name	Type	Boundary Conditions (outside)										B.C. (inside)			
		1	2	3	4	5	6	7	8	9	10	A	B	C	D
1D-HAM	1D-HAM	X	X	X	X				X			X	X		
Bsim2000	1D-HM	X	X	X	X	X	X		X	X		X	X	X	
DELPHIN 5	1/2D-HAMPS	X	X	X	X	X	X	X	X			X	X	X	
EMPTYED	1D-HAM	X	X	X								X	X	X	
GLASTA	1D-HM	X	X		X				X			X			
hygIRC-1D	1D-HAM	X	X		X	X	X	X		X	X	X	X		X
HAMLab	1D-HAM	X	X			X	X		X	X		X	X		
HAM-Tools	1D-HAM	X	X	X	X	X	X	X	X	X		X	X	X	
IDA-ICE(*)	1D-HAM	X	X	X	X	X	X		X			X	X		
MATCH	1D-HAM	X	X		X	X		X	X	X		X	X		
MOIST	1D-HM	X	X		X	X	X			X		X	X		
MOIST-EXP.	1/2D-HAM	X	X	X	X	X	X	X	X	X	X	X	X	X	X
UMIDUS	1D-HM	X	X		X	X	X					X	X		
WUFI (**)	1/2D-HM	X	X		X	X	X	X	X	X		X	X		

(\*) IDA-ICE version with HAMWall; (\*\*) WUFI family: WUFI-Plus, WUFI-2D, WUFI-Pro and WUFI-ORNL/IBP. A free research and education version of WUFI-ORNL/IBP for USA and Canada is available.

#### List of symbols:

- |   |   |
|---|---|
| 1 - Temperature   | 8 - Long-wave exchange  |
| 2 - RH / Humidity ratio / Dew point / Vapour pressure/concentration | 9 - Cloud index   |
| 3 - Air pressure  | 10 - Water leakage  |
| 4 - Solar radiation   | A - Temperature   |
| 5 - Wind speed  | B - RH / Humidity ratio / Dew point / Vapour pressure/concentration |
| 6 - Wind direction  | C - Air pressure  |
| 7 - Horizontal rain   | D - Interior stack effect (T and RH)                                |

Table 2. Some information of the 14 hygrothermal models available to the public in general.

## 2. Case Study 1 – Interstitial condensations

### 2.1 Steady-state vs. transient simulations

Interstitial condensation, originating undesired liquid water inside components, can lead to degradation of variable severity depending on the type of materials that are affected. This

process depends on components characteristics and boundary conditions (interior and exterior).

Relevant standardization in the field of hygrothermal behaviour and energy performance is being developed by the International Organization for Standardization (ISO) and by the European Committee for Standardization (CEN), which established the technical committee CEN/TC 89 - Thermal Performance of Buildings and Building Components. This committee aims to study heat and moisture transfer and its effect on buildings behaviour.

This case study intends to evaluate, for the problem of interstitial condensation in building components, what is the structure of standardization for the available numerical simulation and connected experimental determination of material properties (see Ramos *et al.* (2009)). Two numerical models of different complexity are then analysed using an example. The simpler model is supported by the software Condensa 13788 developed in collaboration with the Building Physics Laboratory - FEUP, based on the Glaser model, and it allows for analysis under steady state conditions. The more complex model is supported by the software WUFI 5.0 developed by the Fraunhofer Institute of Building Physics, allows for analysis under transient conditions.

The model used by WUFI 5.0 is based on the standard EN 15026 (2007). It allows for a detailed knowledge of the hygrothermal state of the building component. It is possible to evaluate, for the simulation period, the hourly evolution of the component total moisture content. The variation of the moisture content, temperature and relative humidity for each layer or for a chosen location in the component is also available, not only through the simulation period, but also for the component profile for a specific point in time. Although its complexity, the model neglects:

- a. Convective transport (heat and moisture);
- b. Some of the liquid transport mechanisms, as seepage flow through gravitation, hydraulic flow through pressure differentials and electro-kinetic and osmotic effects;
- c. The interdependence of salt and water transport;
- d. The resistance of the interface between two capillary-active materials;
- e. The enthalpy flows resulting from the transport of liquid water due to temperature differential.

The software Condensa 13788 applies the model defined by the standard EN ISO 13788 (2002), allowing for the calculation of temperature, vapour pressure and saturation pressure in defined interfaces of a component, for monthly periods. The Glaser model simplifies the heat and moisture transport process assuming:

- a. Condensation only occurs in interfaces and there is no redistribution of liquid water;
- b. The dependence of thermal conductivity on moisture content is negligible;
- c. Capillary suction and liquid moisture transfer are negligible;
- d. The heat and moisture transport by convection are neglected;
- e. One-dimensional moisture transfer is assumed;
- f. Boundary conditions are constant over the months (average value);
- g. The effects of solar and long-wave radiation and rain are neglected.

## 2.2 Numerical results

Figures 1 and 2 show a schematic representation of the façade under study and the internal and external boundary conditions used in this application, respectively.

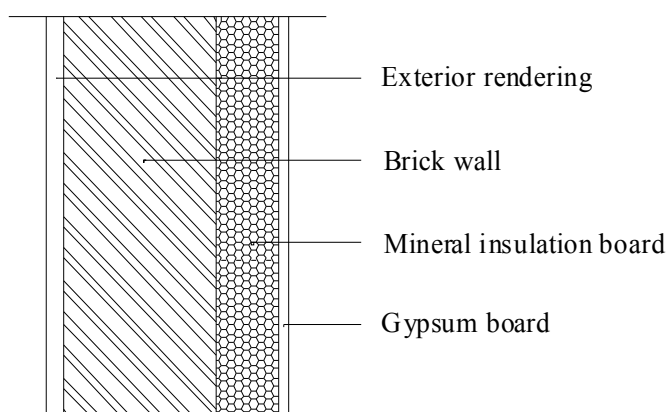


Fig. 1. Building component under study – exterior wall with interior insulation.

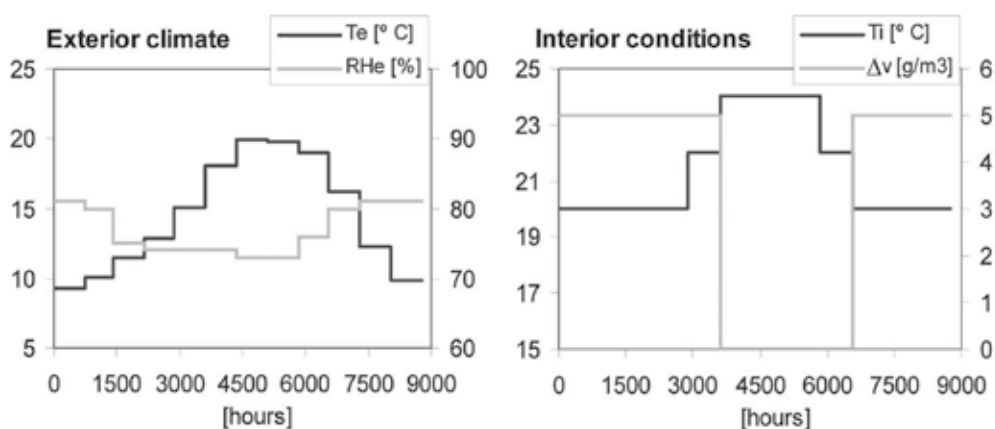


Fig. 2. Boundary condition for simulation.

### 2.2.1 Simulation with Condensa 13788

Condensa 13788 allows the risk assessment for interstitial condensation according to the standard EN13788 (2002). The material properties (see Table 3) necessary for the simulation with Condensa 13788 are the thermal conductivity ( $\lambda$ ) and the water vapour diffusion resistance factor ( $\mu$ ), derived from vapour permeability.

Materials	$d$ [m]	$\lambda$ [W/(mK)]	$\mu$ [-]
Exterior rendering	0,02	1,2	25
Brick wall	0,2	0,6	10
Mineral insulation board	0,08	0,043	3,4
Gypsum board	0,0125	0,2	8,3

Table 3. Material properties required by Condensa 13788.

Condensa 13788 assumed one-dimensional, steady-state conditions. Moisture transfer is assumed to be pure water vapour diffusion, described by the following equation,

$$g = \frac{\delta_a}{\mu} \cdot \frac{\Delta P}{\Delta x} = \delta_a \frac{\Delta P}{s_d} \quad (1)$$

where  $s_d$  is the water vapour diffusion-equivalent air layer thickness,  $\delta_a$  is the water vapour permeability of air with respect to partial vapour pressure,  $\delta_a = 2 \times 10^{-10} \text{ kg}/(\text{m.s.Pa})$ , and  $P$  is the water vapour pressure. The density of heat flow rate is given by,

$$q = \lambda \frac{\Delta T}{d} = \frac{\Delta T}{R} \quad (2)$$

where  $T$  is the temperature in Celsius,  $R$  is the thermal resistance and  $d$  is the material layer thickness.

Figure 3 presents an example of Condensa 13788 graphical output indicating the interface where condensation/drying occur for each month.

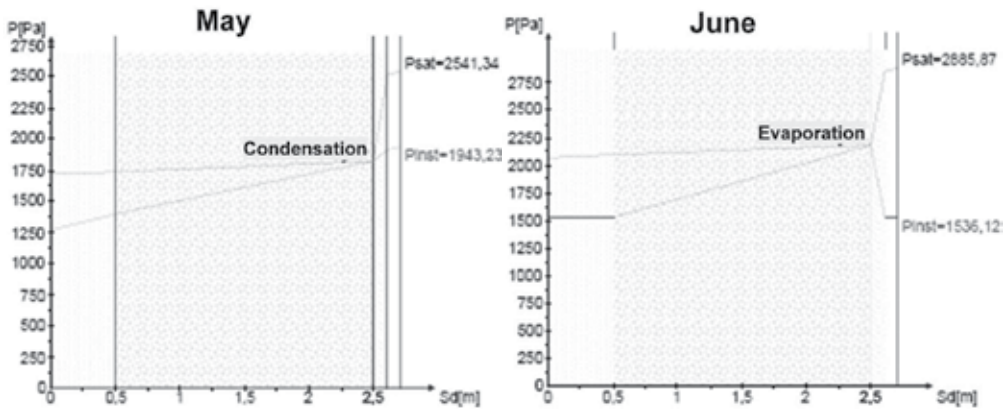


Fig. 3. Condensa 13788 graphical output.

Table 4 presents the simulation results, where  $gc_1$  represents the flux of condensation/drying for each month and  $Ma_1$  stands for the amount of water resulting from accumulated condensation/drying on the interface. The results indicate that the wall would go back to dry state in an annual cycle. With the information from  $Ma_1$  it would also be possible to determine if the condensed flux would originate pathologies in the wall layers. However, that evaluation is not simple since the actual amount of water in each layer next to the condensation interface is unknown. This aspect can lead a designer to be too conservative and adopt a strategy of full elimination of condensation risk.

Month	Time [h]	$\theta_e$ [°C]	$\varphi_e$ [%]	$P_e$ [Pa]	$\theta_i$ [°C]	$\Delta v$ [g/m <sup>3</sup> ]	$P_i$ [Pa]	$gc_1$ [kg/(m <sup>2</sup> s)]	$Ma_1$ [kg/m <sup>2</sup> ]
October	744	16,2	80	1472,50	20,0	5	2145,29	1,96E-07	0,5242
November	720	12,3	81	1158,12	20,0	5	1826,40	2,48E-07	1,1659
December	744	9,9	81	987,48	20,0	5	1652,99	2,69E-07	1,8876
January	744	9,3	81	948,44	20,0	5	1613,26	2,75E-07	2,6243
February	672	10,1	80	988,45	20,0	5	1654,19	2,55E-07	3,2405
March	744	11,5	75	1017,19	20,0	5	1684,55	1,70E-07	3,6956
April	720	12,9	74	1100,52	20,0	5	1769,50	1,34E-07	4,0422
May	744	15,1	74	1269,40	22,0	5	1943,23	6,58E-08	4,2185
June	720	18,1	74	1536,12	24,0	0	1536,12	-6,81E-07	2,4526
July	744	19,9	73	1695,44	24,0	0	1695,44	-7,44E-07	0,4597
August	744	19,8	73	1684,97	24,0	0	1684,97	-7,42E-07	0
September	720	19,0	76	1669,08	22,0	0	1669,08	0,00E+00	0

Table 4. Condensa 13788 simulation results.

### 2.2.2 Simulation with WUFI 5.0

The WUFI 5.0 allows for the calculation of the transient hygrothermal behaviour of multi-layer building components exposed to natural climate conditions (see Kuenzel and Kiessl (1996)). This program is a one-dimensional model for heat and moisture transport analysis of building envelope components, based on the finite volume method.

The governing equations for moisture and energy transfer are, respectively,

$$\frac{\partial w}{\partial \varphi} \frac{\partial \varphi}{\partial t} = \nabla (D_\varphi \nabla \varphi + \delta_p \nabla (\varphi p_{\text{sat}})) \quad (3)$$

$$\frac{\partial H}{\partial T} \frac{\partial T}{\partial t} = \nabla (\lambda \nabla T) + h_v \nabla (\delta_p \nabla (\varphi p_{\text{sat}})) \quad (4)$$

where  $w$  is water content (kg/m<sup>3</sup>),  $\varphi$  is the relative humidity (%),  $t$  is the time (s),  $D_\varphi$  is the liquid conduction coefficient (kg/ms),  $\delta_p$  is the vapour permeability (kg/m.s.Pa),  $p_{\text{sat}}$  is the saturation vapour pressure (Pa),  $H$  is the enthalpy (J/m<sup>3</sup>),  $T$  is the temperature (K) and  $h_v$  is the latent heat of phase change (J/kg). The water vapour diffusion resistance factor,  $\mu$ , used by WUFI is given by,

$$\mu = \frac{\delta_a}{\delta_p} = \frac{2.0 \times 10^{-7} T^{0.81} / P_n}{\delta_p} \quad (5)$$

where  $P_n$  is the normal atmospheric pressure (Pa).

European standard EN 15026:2007 provides minimum criteria for simulation software used to predict one-dimensional transient heat and moisture transfer in multi-layer building components exposed to transient climate conditions on both sides, and WUFI 5.0 complies

with all requirements of this European standard. WUFI program requirements of material properties include: bulk density ( $\text{kg}/\text{m}^3$ ), porosity ( $\text{m}^3/\text{m}^3$ ), heat capacity ( $\text{J}/\text{kgK}$ ), water content ( $\text{kg}/\text{m}^3$ ) *vs.* relative humidity, liquid transport coefficient (suction and redistribution) ( $\text{m}^2/\text{s}$ ) *vs.* water content ( $\text{kg}/\text{m}^3$ ), heat conductivity ( $\text{W}/\text{mK}$ ) *vs.* water content ( $\text{kg}/\text{m}^3$ ) and diffusion resistance factor *vs.* relative humidity (%).

The application of WUFI 5.0 in the case study provides the variation with time of the moisture content in the building element and in each layer (see Figure 4). It is also possible to know the moisture content profile at a given point in time (see Figure 5).

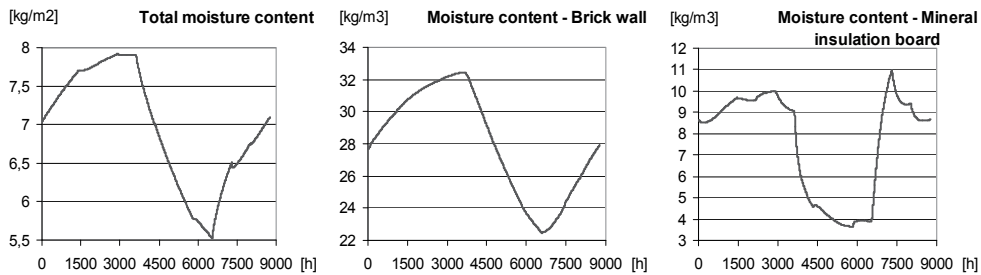


Fig. 4. Component moisture content variation over time in WUFI 5.0 simulation.

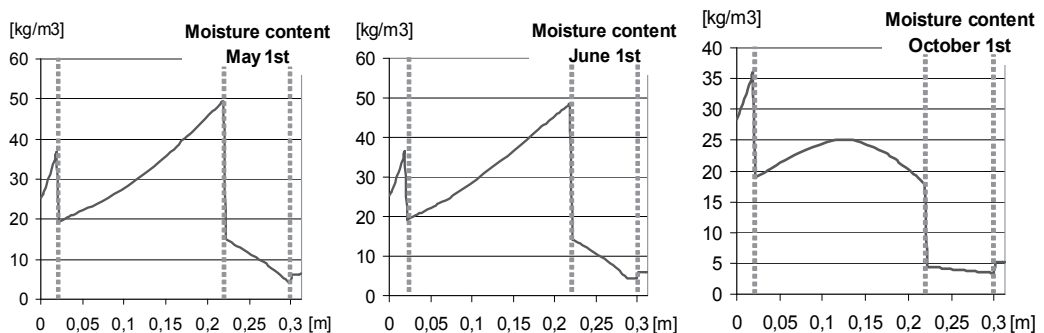


Fig. 5. Component moisture content profiles in WUFI 5.0 simulation.

### 2.3 Discussion

Using two simulation programmes of different complexity degree allows for the following discussion:

- The application of Condensa 13788 is less demanding regarding material properties. Admitting steady state condition, moisture retention curves are not necessary. It must be understood that if properties must be introduced in a model as moisture dependent the data availability decreases. Characterization of moisture dependency properties is of slow and complex experimental determination and is not easy to find in literature for all materials;
- Results interpretation, in the case of Condensa 13788 demand less basic building physics knowledge to perform interstitial condensation risk assessment;
- The results from WUFI 5.0 allow for extensive knowledge on each layer's moisture content development over time. This type of information is important for component

optimization since it supports a detailed risk control strategy. As an example, it's possible to evaluate the increase of thermal conductivity of the mineral wool layer, due to the increase in moisture content during winter;

- d. Both programmes indicated that, for the case study, interstitial condensation or the increase in moisture content would not cause severe damage, since the component would regain equilibrium during summer. But the more detailed simulation pointed out the decrease of insulating capacity during winter (see Figure 6). This is due to the moisture content increase in mineral wool which implies an increase of thermal conductivity.

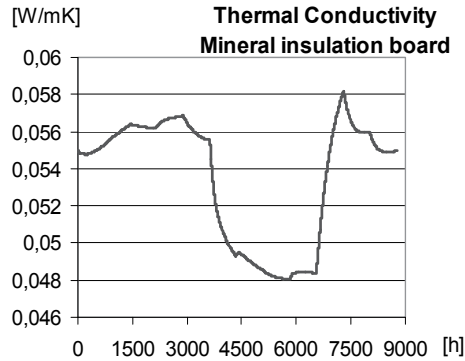


Fig. 6. Thermal conductivity variation over time in WUFI 5.0 simulation.

### 3. Case Study 2 – External condensations

#### 3.1 Overview of the analysed models

One important characteristic of HAM models is the ability to simulate the radiative balance in the exterior surface. In fact, most models use a simplified method to assess surface temperature on the exterior layer that only considers explicitly the effect of solar radiation. The effect of the long-wave radiation exchange is modelled as a constant parameter, independent of the surface itself, and is included in the heat transfer coefficient value. Solar radiation, considered as a source of heat that increases the surface temperature during the day, depends on short-wave radiation absorptivity,  $\alpha_s$ , and on the solar radiation normal to component surface,  $I_s$  (Hagentoft, 2001)

$$q_s = \alpha_s \times I_s \quad (6)$$

The heat flux,  $q_{cr}$ , between the surface and the exterior air is given by their temperature differences,  $T_s$  and  $T_a$ . The heat transfer coefficient,  $h$ , consists in 2 parts, one dealing with convection,  $h_c$ , and the other with long-wave radiation,  $h_r$ .

$$q_{cr} = h \times (T_a - T_s) \quad (7)$$

$$h = h_c + h_r \quad (8)$$

The radiative heat transfer coefficient,  $h_r$ , specifies the long-wave radiation exchange between the building surface and other terrestrial surfaces (sky included), that is governed

by the Stefan-Boltzmann Law ( $\sigma$  is the Stefan-Boltzmann constant). As all surrounding surfaces of the building have similar temperatures, the heat flux,  $q_r$ , dependent on the fourth power of the temperature, can be linearized in good approximation. Since normally the temperatures of the terrestrial surfaces are not known, they are assumed to be identical to the air temperature. Furthermore, it is also assumed that all objects have similar emissivities,  $\varepsilon$ , as long as they are non-metallic, which is usually the case in the context of building physics. Three of the four powers of the temperature are lumped together with the radiative heat transfer coefficient and a simple linear relationship analogous to the convective heat transfer is obtained (Hagentoft, 2001).

$$q_r = \varepsilon_t \times \sigma \times T_a^4 - \varepsilon_s \times \sigma \times T_s^4 \approx h_r \times (T_a - T_s) \quad (9)$$

$$h_r = 4 \times \varepsilon \times \sigma \times T_0^3 \quad (10)$$

where  $T_0$  is an average temperature depending on the surface, the surrounding surfaces and the sky.

Although these temperatures change in time, in most formulations they are assumed as constant. Providing that outside surfaces have similar emissivity, a constant value for the radiative heat transfer coefficient may be adopted. This simplification is quite appropriate for most hygrothermal simulations, however to assess the undercooling phenomenon in walls covered with external thermal insulation composite systems – ETICS more accuracy in the exterior layer is needed. The low thermal capacity of the external rendering and its thermal decoupling emphasises the influence of boundary conditions, mainly temperature and radiation.

It is known that undercooling phenomenon, which occurs mostly during the night, is caused by long wave radiation exchange between the exterior surface and its surroundings. The radiant balance of a building façade is affected by the building's radiation, the sky's radiation and terrestrial surface's radiation (Barreira *et al.*, 2009). A building, being a grey body, emits long wave radiation that can be calculated using the Stefan-Boltzmann Law. On the other hand, the façade absorbs part of the long wave radiation emitted by surrounding surfaces and by the sky. Terrestrial radiation is the sum of long wave radiation emitted by the terrestrial surfaces (ground, other building façades, obstacles, etc.) that also behave as grey bodies and whose temperature is similar to the building's temperature. Therefore, terrestrial surfaces and the building emit long wave radiation at identical intensities.

Atmosphere may behave in two distinct manners. If the sky is cloudy, the atmosphere behaves like a grey body whose temperature is identical to the building's, and emits radiation in a continuous spectrum at intensity similar to that of terrestrial surfaces. If the sky is clear, the atmosphere stops emitting continuously for all wavelengths and the atmosphere's emitted radiation decreases considerably. The radiation emitted by the surface is, therefore, greater than the one that reaches the surface, causing a heat loss.

This negative balance that is not compensated by solar radiation during the night causes the building's surface temperature to decrease, which is maintained until heat transport by convection and by conduction compensate for the loss by radiation. Condensation takes place whenever the surface temperature is lower than the dew point temperature.

For this reason, the influence on the exterior surface temperature of the numerical treatment of the radiative balance will be analyzed in detail in the following paragraphs.

In this case study, three hygrothermal models, WUFI 5.0, hygIRC-1D and HAM-Tools, were used to compare the results of a case study under natural conditions. These simulations used real climatic variables and actual material properties to determine temperature dynamics.

The governing equations of WUFI 5.0 for moisture and energy transfer are given by Eqs. (3) and (4), respectively. The hygIRC-1D governing equations for moisture, heat, air mass and momentum balance are, respectively,

$$\frac{\partial w}{\partial t} + \nabla(u\rho_v + K\rho_w g) = \nabla(D_w \nabla w + \delta_p \nabla p_{sat}) + m_s \quad (11)$$

$$c_p \rho \frac{\partial T}{\partial t} + \nabla(u\rho_a c_{pa} T) = \nabla(\lambda \nabla T) + L_v (\nabla(\delta_p \nabla p_{sat})) - L_{ice} \left( w \frac{\partial f_l}{\partial t} \right) + Q_s \quad (12)$$

$$\nabla(\rho_a u) = 0 \quad (13)$$

$$-\nabla \left( p_a \frac{k_a}{\eta} \nabla P \right) = 0 \quad \text{with} \quad u = -\frac{k_a}{\eta} \nabla P \quad (14)$$

where  $u$  is the air velocity,  $\rho_v$  is the water-vapor density,  $K$  is the liquid-water permeability,  $\rho_w$  is the density of water,  $g$  is the acceleration due to gravity,  $D_w$  is the moisture diffusivity,  $m_s$  is the moisture source,  $c_p$  is the effective heat capacity,  $\rho$  is the dry density of the material,  $\rho_a$  is the density of air,  $c_{pa}$  is the specific capacity of air,  $L_v$  is the latent heat of evaporation/condensation,  $L_{ice}$  is the latent heat of freezing/melting,  $f_l$  is the fraction of water frozen,  $Q_s$  is the heat source,  $k_a$  is the air permeability and  $\eta$  is the dynamic viscosity.

Finally, HAM-Tools governing equations for moisture and energy transfer are,

$$\frac{\partial w}{\partial t} = -\frac{\partial}{\partial x} \left( K \frac{\partial s}{\partial x} - \delta_p \frac{\partial p}{\partial x} + g_a u \right) \quad (15)$$

$$\rho c_p \frac{\partial T}{\partial t} = -\frac{\partial}{\partial x} \left( -\lambda \frac{\partial T}{\partial x} + g_a c_{pa} T + g_v L_v \right) \quad (16)$$

where  $s$  is the suction pressure,  $g_a$  is the air flux density and  $g_v$  is the water vapour flux density.

Regarding the treatment of the radiation effect on the exterior surface, all the three models use an explicit balance of the long-wave radiation, defining the surface emission,  $I_e$ , and the radiation arriving to it,  $I_l$ . They are combined with the shortwave radiation components into a collective heat source at the surface which may have positive or negative value, depending on the overall radiation balance: a positive value leads to heating up the component and a negative value leads to cooling it. With this methodology, the exterior heat transfer coefficient only contains the convective part.

$$q = \alpha_s \times I_s + \varepsilon_{l,surf} \times I_l - I_e \quad (17)$$

In Eq. (17), the two first items give the total amount of radiation (short and long) arriving to the surface, as according to Kirchoff Law the emissivity of a surface,  $\varepsilon_{l,surf}$ , is equal to its long-wave absorptivity. The last item is the radiation emitted by the building surface.

The total solar radiation,  $I_s$ , is described as a function of the direct solar radiation normal to component surface,  $I_{s,dir}$ , of the diffuse solar radiation,  $I_{s,dif}$ , affected by the atmospheric field of view,  $g_{atm}$ , and of the solar radiation reflected by the ground,  $I_{s,ref}$ , affected by the field of view of the ground,  $g_{ter}$ .

$$I_s = I_{s,dir} + g_{atm} \times I_{s,dif} + g_{ter} \times I_{s,ref} \quad (18)$$

The total long-wave radiation arriving to the surface,  $I_l$ , depends on the downward atmospheric radiation,  $I_{l,atm}$ , affected by the atmospheric field of view,  $g_{atm}$ .

$$I_l = g_{atm} \times I_{l,atm} \quad (19)$$

The sky radiation is ruled by the Planck Law, considering the concept of effective sky temperature, which can be defined as the temperature of a blackbody that emits the same amount of radiation as the sky (Martin and Berdahl, 1984). The effective sky temperature depends on several atmospheric conditions, which are rarely available. For that reason, it is assumed that the sky behaves like a grey body, ruled by Stefan-Boltzmann Law, considering the sky emissivity and the air temperature near the ground (Finkenstein and Haupl, 2007). The downward atmospheric radiation in a specific location may be obtained through measurement, using pyrgeometers, or by empirical models (detailed methods are not commonly used because they require the knowledge of atmospheric conditions). According to Finkenstein and Haupl (2007), those empirical models provide satisfactory results for clear sky but the approaches for cloudy sky still point to very different results. The long-wave radiation emitted by the surface,  $I_e$ , depends on the surface emissivity,  $\varepsilon_{l,surf}$ , and temperature,  $T_{surf}$ , as it is ruled by the Stefan-Boltzmann Law.

$$I_e = \varepsilon_{l,surf} \times \sigma \times T_{surf}^4 \quad (20)$$

From the above equations, the direct solar radiation normal to component surface,  $I_{s,dir}$ , is automatically calculated by each model from the direct solar radiation in an horizontal surface, included in the climatic data, using information about the sun position. The diffuse solar radiation,  $I_{s,dif}$  is obtained directly from the climatic data. The solar radiation reflected,  $I_{s,ref}$ , is calculated using solar radiation data (direct in an horizontal surface and diffuse) and the short wave radiation reflectivity of the ground.

The differences between the three models, regarding the heat exchange by radiation in the exterior surface, are related with the way the long-wave radiation emitted by the sky is obtained and the effect of the ground in the balance.

WUFI 5.0 allows two different approaches to obtain the atmospheric long-wave radiation,  $I_{l,atm}$ , necessary for the calculation: it may be read directly from the climatic file, if it has this information available, or it may be calculated using the cloud index data. This model also considers the emission and reflection of long-wave radiation by the ground, adding to eq. (19) two extra items: the long-wave radiation emitted by the ground, calculated by the Stefan-Boltzmann Law assuming that the ground has the same temperature as the air and inputting the ground long-wave emissivity, and the atmospheric long-wave radiation reflected by the ground, calculated using the atmospheric long-wave radiation,  $I_{l,atm}$ , and the long-wave radiation reflectivity of the ground.

HygIRC-1D calculates the atmospheric long-wave radiation,  $I_{l,atm}$ , necessary for the simulation, using the cloud index information available in the climatic file. The effect of the ground (emission and reflection of long-wave radiation) is not taken into account.

HAM-Tools reads the atmospheric long-wave radiation,  $I_{l,atm}$ , necessary for the calculation directly from the climatic file. The effect of the ground (emission and reflection of long-wave radiation) is not included in the mathematical treatment.

### 3.2 Input data

Figure 7 is a schematic of the test façade analysed numerically and Table 5 presents the material properties used in this application. The construction type chosen for comparison of the three hygrothermal models was a wall with external thermal insulation systems (ETICS) exposed to solar radiation.

Wall components	$L$ (cm)	$\rho$ (kg/m <sup>3</sup> )	$\varepsilon$ (m <sup>3</sup> /m <sup>3</sup> )	$\lambda$ (W/mK)	$c_p$ (J/kgK)	$\mu$ (-)
Resin finishing coat	0.5	1800	0.12	0.70	840	1000
EPS (Expanded polystyrene)	4	15	0.95	0.04	1500	30
Concrete C12/15	20	2200	0.18	1.6	850	92
Cement plaster - stucco	1.5	1985	0.30	1.20	840	25

Table 5. Material properties of wall components used in the hygrothermal models.

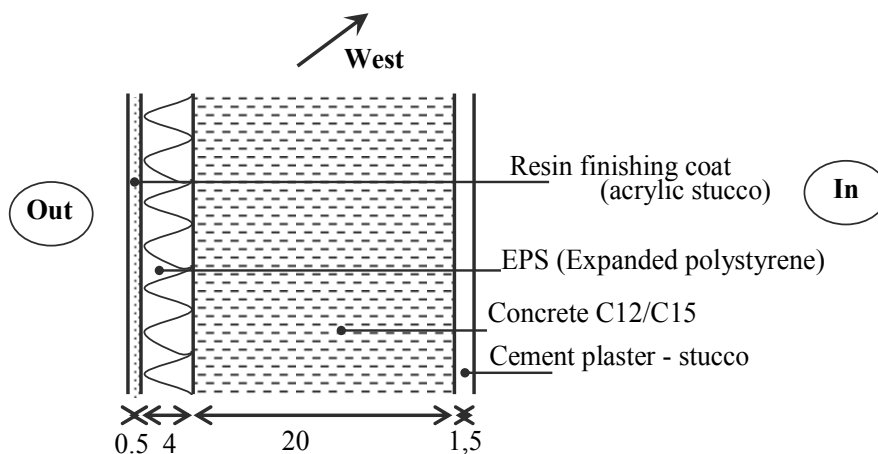


Fig. 7. Wall construction details (dimensions in cm).

The exterior and interior  $S_d$  value used was zero (no coating) and the interior heat transfer coefficient was constant and equal to  $8 \text{ W/m}^2\text{K}$ . The exterior heat transfer coefficient only contained the convective part and was considered independent from the wind (constant value of  $17 \text{ W/m}^2\text{K}$ ).

All the calculations were done with climate data for Porto city obtained with METEONORM 6.0 (METEOTEST 2008). METEONORM is a software tool that consists of a set of meteorological databases and a series of conversion utilities that prepare and format weather data for use with major hygrothermal modelling software packages. METEONORM calculates hourly values of all parameters using a stochastic model and the

resulting weather data files are produced in a variety of formats. The weather data inputted to the models was temperature ( $^{\circ}\text{C}$ ), relative humidity (-), wind direction ( $^{\circ}$ ), wind speed (m/s), global solar radiation in a horizontal surface ( $\text{W}/\text{m}^2$ ) and diffuse solar radiation in a horizontal surface ( $\text{W}/\text{m}^2$ ). WUFI 5.0 also required information about air pressure (hPa), downward atmospheric radiation in a horizontal surface ( $\text{W}/\text{m}^2$ ) and cloud index (two climatic files were created, one with downward atmospheric radiation and other with cloud index). HygIRC-1D also included information about the cloud index variation and HAM-Tools also demanded data about the air pressure (hPa) and the downward atmospheric radiation in a horizontal surface ( $\text{W}/\text{m}^2$ ). In the climatic files rain was inputted equal to zero. The conditions of indoor air were constant, with  $RH=60\%$  and  $T=20^{\circ}\text{C}$  (comfort values). The short wave radiation absorptivity and the long-wave radiation emissivity considered were 0.4 (stucco-normal bright) and 0.9, respectively, and the initial conditions within the element were  $RH=70\%$  and  $T=15^{\circ}\text{C}$ . The ground short-wave reflectivity was 0.2 and for WUFI 5.0 the ground long-wave emissivity was 0.9 and the ground long-wave reflectivity was 0.1.

The condensation on surface was assessed by comparing the surface temperature with the dew point temperature of outdoor air. Whenever the surface temperature drops below the dew point temperature condensations occur. The risk of condensation was evaluated by the monthly accumulated value of the positive differences between the dew point temperature of outdoor air and the surface temperature.

### 3.3 Numerical results and discussion

In this case study simulations were done with three hygrothermal models to analyse the influence of the numerical treatment of the radiative balance in the exterior surface temperature of the wall in Figure 7. All input parameters, including material properties, climatic data, and initial conditions, were made to vary as little as possible between the models in order to ensure a fair comparison.

WUFI 5.0 requires as material properties bulk density ( $\text{kg}/\text{m}^3$ ), porosity ( $\text{m}^3/\text{m}^3$ ), heat capacity ( $\text{J}/\text{kgK}$ ), water content ( $\text{kg}/\text{m}^3$ ), liquid transport coefficient (suction and redistribution) ( $\text{m}^2/\text{s}$ ), heat conductivity ( $\text{W}/\text{mK}$ ) and diffusion resistance factor.

HygIRC-1D requires similar material properties as WUFI 5.0 but uses different units. The material properties required for simulation are: air permeability ( $\text{kg}/\text{mPas}$ ), thermal conductivity ( $\text{W}/\text{mK}$ ), dry density ( $\text{kg}/\text{m}^3$ ), dry heat capacity ( $\text{J}/\text{kgK}$ ), sorption curve moisture content ( $\text{kg}/\text{kg}$ ), suction pressure (Pa), water vapour permeability ( $\text{kg}/\text{mPas}$ ), liquid moisture diffusivity ( $\text{m}^2/\text{s}$ ) and water content ( $\text{kg}/\text{kg}$ ). The liquid moisture diffusivity was assumed the same as the liquid transport coefficient by suction used in WUFI 5.0. The water content was converted from  $\text{kg}/\text{m}^3$  to  $\text{kg}/\text{kg}$  simply by dividing by the density of the material, and to  $\text{m}^3/\text{m}^3$  by dividing by the density of the material and multiplying by the density of water ( $1000\text{ kg}/\text{m}^3$ ). The water vapour permeability and the suction pressure,  $s$ , were calculated using the water vapour diffusion resistance factor and the Kelvin equation (Galbraith *et al.*, 1997), respectively.

The properties required by HAM-Tools are the density of the dry material ( $\text{kg}/\text{m}^3$ ), open porosity (-), specific heat capacity of the dry material ( $\text{J}/\text{kgK}$ ), thermal conductivity ( $\text{W}/\text{mK}$ ), sorption isotherm, moisture capacity, water vapor permeability ( $\text{kg}/\text{msPa}$ ) and liquid water conductivity (s).

It was possible to obtain similar temperatures on surface using all the models. The existing differences may be related with the calculations of the solar radiation normal to the surface

that influences mostly the surface temperature during the day, but also after the sunset and at dawn. The differences can also be related with the formulation used to calculate the radiation emitted by the sky (WUFI 5.0\_a and HAM-Tools use downward atmospheric radiation in a horizontal surface calculated by meteorological software and WUFI 5.0\_b and HygIRC-1D calculate themselves the radiation using cloud index information). Differences in the governing equations and the conversion of the material properties may also have some effects on surface temperatures.

Figure 8 shows the variation in time of the calculated surface temperatures during a winter day (23<sup>rd</sup> of January) and Figure 9 shows the accumulated degrees of condensation (or the sum of the positive differences between dew point temperature and the surface temperature) for the same day. It is possible to see that surface temperature drops below dew point temperature during the early morning hours for all models, due to the low thermal capacity of the system that allows the dissipation of the heat stored during the day in a few hours after sunset. Condensation occurs during this period of time.

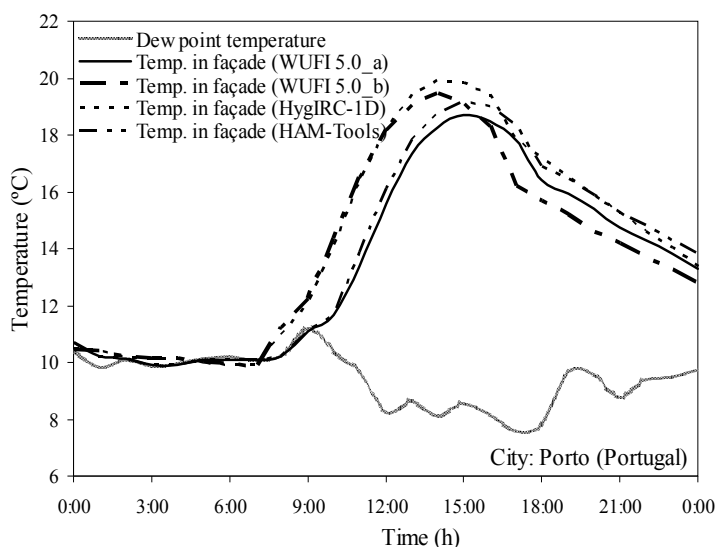


Fig. 8. Surface temperatures obtained by each hygrothermal model for Porto (23-January).

There is however small differences between the models that induce the results presented in Figure 9. Comparing WUFI 5.0\_a and WUFI 5.0\_b, of which only difference is the long-wave radiation used (in WUFI 5.0\_a the radiation used was calculated by meteorological software and in WUFI 5.0\_b was calculated by the equations included in the model using cloud index information), it shows that the values inputted for the long-wave radiation influence considerably the surface temperature and consequently the surface condensation. Figure 10 shows that the model used to calculate the atmospheric radiation induces significant differences in the obtained values. This is related with the difficulty in modelling atmospheric radiation with cloudy sky, referred previously. As radiation used in WUFI 5.0\_a is higher than the one used in WUFI 5.0\_b, surface temperatures are also higher and condensation reduce.

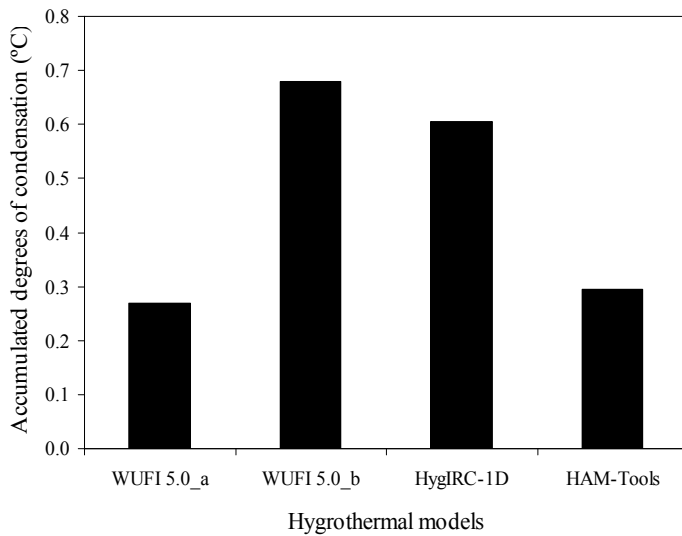


Fig. 9. Sum of positive differences between  $T_{dp}$  and  $T_{surf}$  for Porto (23-January).

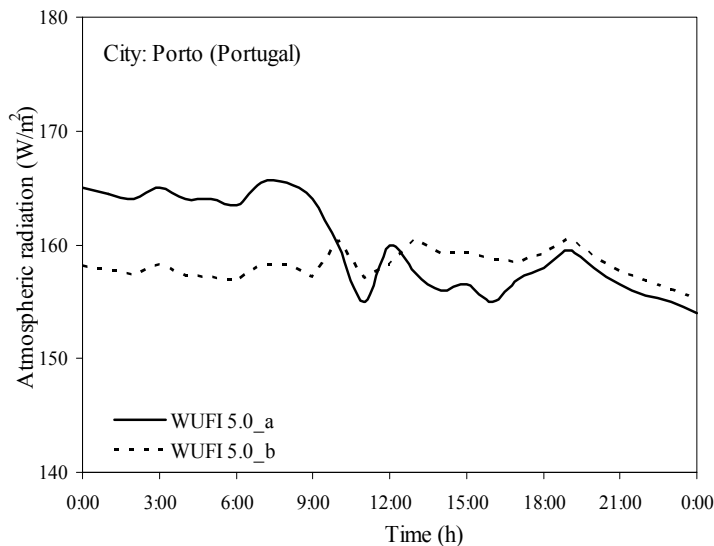


Fig. 10. Atmospheric radiation in a vertical plane in Porto (23-January).

WUFI 5.0\_b and HygIRC-1D present very similar variation of the surface temperature, especially during the night. This points to the similarity of the models, not only in terms of governing equations but also in terms of boundary conditions. The effect of the ground included in WUFI 5.0\_a may not have much influence in the phenomenon or it may compensate some differences existing between the two models. The similar values obtained for the surface temperature are also shown in Figure 9, where the condensation values are also similar. WUFI 5.0\_a and HAM-Tools both use the atmospheric radiation calculated by the meteorological software and their results are quite similar. The considerations made previously for WUFI 5.0\_b and HygIRC-1D can also be applied to this case.

Figure 11 displays monthly accumulated degrees of condensation. The results show that the most pronounced condensations occur during the late summer, fall and winter months. This is related with the climatic conditions in Porto, a coastal town, namely its high relative humidity and mild temperatures all year-round. However, it should be remarked, once more, that the effect of long-wave radiation is quite clear, as WUFI 5.0\_a and HAM-Tools have similar results and WUFI 5.0\_b and HygIRC-1D also have similar results, but these two groups don't match. In fact, the last two (WUFI 5.0\_b and HygIRC-1D) have quite higher condensation as radiation is lower.

Figure 11 also shows that there are very few accumulated degrees of condensation in every month, using any program, and this is due to the small differences between the dew point temperature and the surface temperature, which are, on average, around 0.2° C per hour. On the other hand, condensation occurs, on average, only half a hour per day during the year.

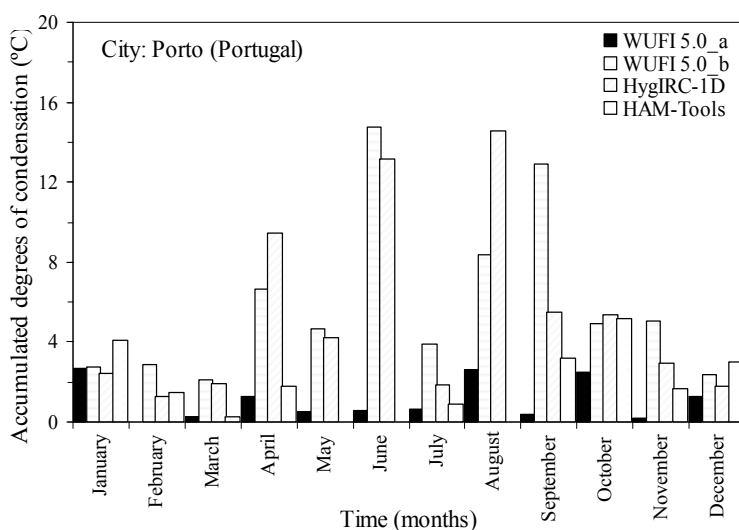


Fig. 11. Sum of positive differences between  $T_{dp}$  and  $T_{surf}$  for Porto.

#### 4. Conclusion

This book chapter presented a brief review of heat, air, and moisture (HAM) analysis methods commonly used in numerical simulation and methods that allow for their determination. The review has shown that there are numerous hygrothermal models with a range of capabilities and that these models are important tools to better understand the real problems and to provide correct solutions.

Hygrothermal simulation can be implemented with different complexity degrees. An important difference between models is the ability to tackle transient behaviour, since steady state conditions will frequently be a rough approximation to reality. Standardization also supports hygrothermal simulation contributing to higher feasibility of model application by designers.

A case study of interstitial condensation risk assessment allowed for comparison between two different complexity models. Although more advanced models are a better support for component optimization, they are more demanding regarding user ability to interpret

results and material data availability. If a designer is defining, for instance, a solution for improving the thermal resistance of an existing building element he must therefore decide which type of modelling should be applied to solve a specific problem. A possible approach could be to start with the simpler model and evaluate if the intended solution has any risk of interstitial condensation. This first approach should be developed on the safe side, using worst case scenario boundary conditions. If risk of condensation is detected and cost optimization is relevant, more complex modelling can be produced, allowing, for instance, for a suitable design of a vapour barrier.

In the second case study, the numerical results show that these programs are useful tools to simulate the undercooling phenomenon and assessing the exterior condensation on façades, providing that all relevant components of radiation exchange at the exterior surface are included in calculations. The models present similar results except when different inputs of long-wave radiation are used. In fact, it seems to be the key factor for the differences observed in the calculated values. Using cloud index information or measured long-wave radiation, even in the same model, provided the most significant differences.

Using accumulated degrees of condensation, a comparative measure of the risk of condensation on exterior surfaces can be obtained. Since very small differences between surface and dew point temperature contribute to this indicator, the calculations are therefore demanding in terms of required precision.

## 5. References

- ASTM, C 20 (2000). *Test method for water absorption, bulk density, apparent porosity and apparent specific gravity of fired white ware products*, ASTM International, USA.
- ASTM, C 351-92b (1999). *Test method for mean specific heat of thermal insulation*, ASTM International, USA.
- Barreira, E.; Freitas, V.P. & Ramos, N. (2009). Risk of ETICS defacement – A sensitivity analysis of the demand parameters, *Proceedings of the 4<sup>th</sup> International Building Physics Conference*, pp. 317-324, Istanbul, Turkey.
- Burch, D.M. & Chi, J. (1997). *MOIST: A PC program for predicting heat and moisture transfer in building envelopes*, Release 3.0, NIST special publication 917.
- Canada Mortgage and Housing Corporation (2003). *Review of hygrothermal models for building envelope retrofit analysis, Research highlights*, Technical series 03-128.
- Condensa 13788 (2010). <http://www.condensa13788.com/>, accessed in 2010.
- Delgado, J.M.P.Q.; Ramos, N.M.M.; Barreira, E. & Freitas, V.P. (2010). A Critical Review of Hygrothermal Models used in Porous Building Materials. *Journal of Porous Media*, Vol. 13, No. 3, pp. 221-234.
- Djebbar, R.; Kumaran, M.K.; Van Reenen, D. & Tariku, F. (2002a). *Hygrothermal modeling of building envelope retrofit measures in multiunit residential and commercial office buildings*, Client Final Rep. No. B-1110.3, IRC/NRC, National Research Council, Ottawa, 187.
- Djebbar, R.; Kumaran, M.K.; Van Reenen, D. & Tariku, F. (2002b). Use of hygrothermal numerical modeling to identify optimal retrofit options for high-rise buildings. *Proceedings of the 12<sup>th</sup> International Heat Transfer Conference*, Paper No. NRCC-45215, Grenoble, France.
- EN 772-13 (2000). *Methods of test for masonry units. Determination of net and gross dry density of masonry units (except for natural stone)*, British Standards, London, UK.

- EN 12390-7 (2000). *Testing hardened concrete. Density of hardened concrete*, British Standards, London, UK.
- EN 12524 (2000). *Building materials and products – Hygrothermal properties – Tabulated design values*, British Standards, London, UK.
- EN 12664 (2001). *Thermal performance of building materials and products – Determination of thermal resistance by means of guarded hot plate and heat flow meter methods – Dry and moist products of medium and low thermal resistance*, British Standards, London, UK.
- EN 12667 (2001). *Thermal performance of building materials and products – Determination of thermal resistance by means of guarded hot plate and heat flow meter methods – Products of high and medium thermal resistance*, British Standards, London, UK.
- EN 12939 (2001). *Thermal performance of building materials and products – Determination of thermal resistance by means of guarded hot plate and heat flow meter methods – Thick products of high and medium thermal resistance*, British Standards, London, UK.
- EN 15026 (2007). *Hygrothermal performance of building components and elements - Assessment of moisture transfer by numerical simulation*, British Standards, London, UK.
- EN ISO 8302 (1991) *Thermal insulation - Determination of steady-state thermal resistance and related properties-Guarded hot plate apparatus*, International Standards Organization, Geneva, Switzerland.
- EN ISO 10456 (2007). *Building materials and products – Procedures for determining declared and design thermal values*, International Standards Organization, Geneva, Switzerland.
- EN ISO 10545-3 (1995). *Ceramic tiles: Determination of water absorption, apparent porosity, apparent relative density and bulk density*, International Standards Organization, Geneva, Switzerland.
- EN ISO 12571 (2000). *Hygrothermal performance of building materials and products – Determination of hygroscopic sorption properties*, International Standards Organization, Geneva, Switzerland.
- EN ISO 12572 (2001). *Hygrothermal performance of building materials and products - Determination of water vapour transmission properties*, International Standards Organization, Geneva, Switzerland.
- EN ISO 13788 (2002). *Hygrothermal performance of building components and building elements - Internal surface temperature to avoid critical surface humidity and interstitial condensation - Calculation methods*, International Standards Organization, Geneva, Switzerland.
- EN ISO 15148 (2002). *Hygrothermal performance of building materials and products - Determination of water absorption coefficient by partial immersion*, International Standards Organization, Geneva, Switzerland.
- Finkenstein, C. & Haupl, P. (2007). Atmospheric long wave radiation being a climatic boundary condition in hygrothermal building part simulation, *Proceedings of the 12<sup>th</sup> Symposium for Building Physics*, vol. 2, pp. 617-624, Dresden, Germany.
- Galbraith, G.H.; McLean, R.C. & Guo. J.S. (1997). The selection of appropriate flow potentials for moisture transport models, *Proceedings of the 5<sup>th</sup> International Building Performance Simulation Association Conference*, Prague, Czech Republic.
- Hagentoft, C.E. (2001). *Introduction to Building Physics*, Studentlitteratur Ab, Sweden.
- Hagentoft, C.E. & Blomberg, T. (2000). *1D-HAM coupled heat, air and moisture transport in multi-layered wall structures*, Manual of version 2.0, Lund-Gothenburg Group for Computational Building Physics.
- Hens, H. (1996). *Heat, Air and Moisture Transfer in Insulated Envelope Parts. Modelling, Final Report*, vol. 1, Part 1, International Energy Agency, IEA ANNEX 24, K.U.-Leuven.

- Kalagasidis, A.S. (2004). *HAM-Tools: An Integrated Simulation Tool for Heat, Air and Moisture Transfer Analyses in Building Physics*, PhD Thesis, Chalmers University of Technology, Gothenburg, Sweden.
- Karagiozis, A. (1993). *Overview of the 2-D hygrothermal heat-moisture transport model LATENITE*, Internal IRC/BPL Rep., National Research Council Canada, Ottawa.
- Karagiozis, A. (2001). Advanced Hygrothermal Modelling of Building Materials using Moisture-Expert 1.0, *Proceedings of the 35<sup>th</sup> International Particleboard-Composite Materials Symposium*, Pullman Washington.
- Kehrer, M. & Schmidt, T. (2008). Radiation effects on exterior surfaces, *Proceedings of the 8<sup>th</sup> Symposium on Building Physics in the Nordic Countries*, Vol. 1, pp. 207-212. DTU, Copenhagen, Denmark.
- Kuenzel, H.M. & Kiessl, K. (1997). Calculation of Heat and Moisture Transfer in Exposed Building Components. *International Journal of Heat and Mass Transfer*, Vol. 40, No. 1, pp. 159-167.
- Kurnitski, J. & Vuolle, M. (2000). Simultaneous calculation of heat, moisture and air transport in a modular simulation environment, *Proceedings of the Estonian Academy of Sciences Engineering*, Vol. 6, pp. 25.
- Martin, M. & Berdahl, P. (1984). Summary of results from the spectral and angular sky radiation measurement program. *Solar Energy*, Vol. 33, No. 3-4, pp. 241-252.
- Mendes, N.; Ridley, I.; Lamberts, R.; Philip, P.C. & Budag, K. (1999). UMIDUS-A PC program for the prediction of heat and moisture transfer in porous buildings elements. *Building Energy Simulation*, Vol. 20, No. 4, pp. 2-8.
- Meteotest (2007). *Meteororm - Version 6.0*. Meteotest, Bern, Switzerland.
- Nicolai, A.; Grunewald, J. & Zhang, J.S. (2007). *Salztransport und Phasenumwandlung - Modellierung und numerische Lösung im Simulationsprogramm Delphin 5*, *Bauphysik* 3, pp. 231-239.
- Physibel (2007). GLASTA Diffusion - Condensation - Drying extended Glaser method. Retrieved October 19, 2007, from <http://www.physibel.be/v0n2gl.htm>.
- Ramos, N.M.M.; Delgado, J.M.P.Q.; Barreira, E. & Freitas, V.P. (2009). Hygrothermal Properties Applied in Numerical Simulation: Interstitial Condensation Analysis. *Journal of Building Appraisal*, Vol. 5, No. 2, pp. 161-170.
- Rode, C. (1990). *Combined heat and moisture transfer in building constructions*, Ph.D. Thesis, Technical University of Denmark, Thermal Insulation Laboratory, 1990.
- Rode, C. & Grau, K. (2004). *Calculation tool for whole building hygrothermal analysis building simulation 2000*, IEA Annex 41 meeting, Zurich, Switzerland.
- Rousseau, J. (1999). *Envelope moisture performance through infiltration, exfiltration and diffusion-EMPTIED*, CMHM Technical Series 99-123.
- Straube, J. & Burnett, E.F.P. (1991). *Overview of hygrothermal (HAM) analysis methods*, HR Trechsel, editor. ASTM manual 40-moisture analysis and condensation control in building envelopes.
- US Department of Energy Webpage (2009). Building energy software tools directory. Retrieved October 19, 2009, from: <http://www.eere.energy.gov/buildings>.
- van Schijndel, A.W.M. (2005). *Integrated heat, air and moisture modelling and simulation in HAMLab*, IEA ECBCS Annex 41, working meeting, Trondheim, Norway.
- WUFI Pro IBP (2008). WUFI Pro 5.0 on line help.

# Computational Flowfield Analysis of a Planetary Entry Vehicle

Antonio Viviani<sup>1</sup> and Giuseppe Pezzella<sup>2</sup>

<sup>1</sup>*Seconda Università degli Studi di Napoli, via Roma 29, 81031 Aversa,*

<sup>2</sup>*Centro Italiano Ricerche Aerospaziali, via Maiorise, 81043 Capua  
Italy*

## 1. Introduction

Computational Fluid Dynamics (CFD) analysis represents a key technology within planetary entry vehicle design. Safe landing of vehicles re-entering from space requires, in fact, an accurate understanding of all physical phenomena that take place in the flowfield past the hypersonic vehicle to assess its aerodynamics and aerothermodynamics performance. CFD allows to significantly reduce the number of in-flight and plasma wind-tunnel (PWT) experimental test campaigns and to account for real-gas flow features, which are difficult to reproduce in ground-test facilities. Flight measurements collected during re-entry have demonstrated that real gas effects strongly influence both aerodynamics and aerothermal loads of hypervelocity vehicles. On the other hand, trajectory calculation for atmospheric re-entry involves determination of vehicle aerodynamics and aerothermodynamics. As a consequence, accurate modeling of flow physics, in particular flow chemistry is fundamental to reliably design re-entry vehicles.

In this chapter, we stress this point with an application to a capsule-type crew return vehicle (CRV) for the International Space Station (ISS) support servicing.

However, high accuracy in modeling flow and chemistry coupling may produce only a small increase in the numerical results accuracy, despite the high modeling efforts and the increased computational cost. So, one must balance the theoretical and computer time effort needed to use a more general and sophisticated model against the expected accuracy of results. The question then arises as to what extent the number of reactions, coefficients, reaction mechanism, etc. influence the flow. To answer this question, a step-by-step numerical investigation has been carried out to examine the influence of the chemical reactions, its mechanisms and kinetics, and of thermal non-equilibrium on the air flows past the CRV, in the framework of a low Earth orbit (LEO) scenario. Two-dimensional axisymmetric and three-dimensional Navier-Stokes computations are performed, for perfect gas and reacting gas mixture in thermal and chemical non-equilibrium, and for several chemical reaction mechanisms. In particular, simulations are computed with different wall-surface boundary conditions: non-catalytic wall (NCW), partially catalytic wall (PCW), fully catalytic wall (FCW) to underline the effect of the heat shield catalyticity on the vehicle aerodynamic heating. The work confirms that high-temperature transport phenomena markedly influence the vehicle flowfield and, in turn, the vehicle aerodynamics and aerothermodynamics, but it also stresses that, with an acceptable loss of results accuracy, we

do not need to use models of such high complexity, and therefore considerable computing time can be saved.

## 2. Real gas effects and re-entry hypersonic flight

During atmospheric descent, re-entry vehicles encounter several flow regimes and thermochemical phenomena: they fly from free molecular to fully continuum phases and, when in continuum, from laminar to fully turbulent flows. When freestream enthalpy is large enough the flow passing through the bow shock dissociates resulting in a several species reacting mixture flow around the vehicle. The thermal and chemical characteristics of the gas in the shock layer are altered depending on the atomic and molecular structure of the air species (Sarma, 1995). For instance, when flow velocity is low, energy is absorbed only into particles vibration and rotation degrees of freedom (dof). But as velocity sufficiently increases, the thermal energy of the gas becomes comparable with the energy associated with a whole range of gas phase chemical processes, such as the excitation of molecular modes of vibration; the dissociation of oxygen and nitrogen; the formation of other chemical species through recombination reactions; the ionisation of both molecular and atomic species.

As a consequence, the flowfield chemical composition around the re-entry vehicle varies spatially and temporally and, because shock layer molecules continuously exchange their energy between the translational and internal dof, the air can result in a thermal-and/or chemical non-equilibrium mixture. Then, the microscopic structure of the mixture species, affecting the ways in which energy may be redistributed, influences the specific heat ratio ( $\gamma$ ), the chemical reaction rates, and the transport properties. These quantities, in turn, affect the dynamics of the flow as well as shock and expansion waves (i.e. pressure, temperature, and velocity distributions), the chemical energy diffused to the surface (i.e. the chemical contribution to the heat flux at the wall), the boundary layer structure (i.e. the heat flux and shear stress). In particular, the flow chemical dissociation results in a large density ratio ( $\varepsilon$ ) across the strong bow shock, which markedly influences the capsule's aerodynamics. In fact,  $\varepsilon$  influences the shock shape, the stand-off distance, and the wall-surface pressure that, at the stagnation point (e.g.,  $C_{p_{\max}}$ ), reads:

$$C_{p_{\max}} = C_{p_{t2}} = \frac{P_{t2} - P_{\infty}}{q_{\infty}} = \left( \frac{P_{t2}}{P_{\infty}} - 1 \right) \frac{2}{\gamma M_{\infty}^2} \cong 2 - \varepsilon \quad (1)$$

where  $\varepsilon$ , in the hypersonic limit, is:

$$\varepsilon = \lim_{M_{\infty} \rightarrow \infty} \frac{\rho_1}{\rho_2} = \frac{\gamma - 1}{\gamma + 1} \quad (2)$$

High temperature effects also modify the hypersonic capsule-vehicle aerodynamics and aerothermodynamics by means of a very abrupt change in the CRV trim angle of attack ( $\alpha_{\text{trim}}$ ). This is due to the shift of the sonic line position at the vehicle leeside because of the change in  $\gamma$ , thus affecting the CRV pitching moment ( $CM_Y$ ) (Hassan et al., 1993) and, hence, the capsule static stability that is a critical requirement for a re-entry vehicle, because static instability could lead to catastrophic failure if the thermal shield is not protecting the vehicle anymore. Real gas effects also influence vehicle aeroheating since thermal protection material (TPM) could promote the chemical recombination at wall of flowfield atomic

species thus increasing the overall heat flux up to two times or more than the value of a non-catalytic wall (Scott, 1997). For instance, the reactions considered above, taking place only in the gas phase, are termed as homogeneous chemical reactions and differ from the heterogeneous ones that, instead, occur near the vehicle wall involving gas and solid species. They can be catalyzed by the TPM and, being exothermic, contribute to the vehicle aeroheating. Thus, the TPM, promoting or preventing species recombination at wall, depending on its catalyticity, plays an important role in the aerodynamic heating. Neglecting conduction into the heatshield and radiation from the gas, the energy balance at the vehicle surface reads:

$$-\dot{q}_r = -\sigma \varepsilon T_w^4 = \lambda_{tr} \left( \frac{\partial T}{\partial n} \right)_w + \sum_{i=1}^{N_b} \lambda_{v,i} \left( \frac{\partial T_{v,i}}{\partial n} \right)_w + \rho \sum_{i=1}^{N_s} \left( \int_{T_o}^T C_{P_i} dT + \Delta h_{fi}^o \right) D_i \left( \frac{\partial Y_i}{\partial n} \right)_w \quad (3)$$

The first term, on the right-hand side, is the conductive heat-flux, the second one is the vibrational contribution, and the last one is the species diffusion contribution that strongly depends on the catalytic properties of thermal protection system (TPS). Therefore, the heatshield should be a poor catalyst (Anderson, 1973).

Of course the entire above mentioned scenario depends on the kind of re-entry (i.e. orbital or superorbital one). For example, flowfield computation involving ionized species, as for superorbital reentries, requires at least 11 chemical species with 20 reactions, whereas for lower velocity reentries, 5 non-ionized species and 17 reactions are sufficient (Sarma, 1995). Therefore, a reliable numerical simulation of re-entry flows can be very challenging, depending on the more or less correct and accurate modelling of the flowfield thermochemical processes. In this framework simulation problems may arise as the coupling of flow and chemistry leads to a stiff problem due to differences in reaction rate characteristic times (Anderson, 1989); dissociation rate coefficients can differ by orders of magnitude and, since reaction rates are very difficult to measure, different values may exist for the same coefficient. As a result, the appropriate set of reactions to be used represents a very relevant choice, especially if one considers that, in general, an increased model complexity does not entail a greater accuracy of numerical results, despite the higher computational cost needed for increased reactions set. Moreover, when one increases the number of chemical reactions, numerical results can be more influenced by the effect of the uncertainty in input data, such as species transport coefficients, relaxation times for thermal and chemical non-equilibrium. So, it could be important to simplify the reaction mechanisms, by reducing as much as possible the number of chemical reactions, without loss in accuracy but greatly reducing computing time.

### 3. CRV concept and re-entry flight scenario

The re-entry system is an Apollo-like capsule measuring about 5 m in diameter (D), with a nose radius ( $R_N$ ) of 6.05 m; the sidewall angle ( $\theta$ ) of 33 deg and the overall vehicle height of 3.8 m (see Fig. 1). The offset centre of gravity (cg) is located at  $x/D=0.26$  and  $y/D=-0.0353$ . This vehicle concept represents a scaled-up version of the ARD capsule, which is a flying test bed successfully experimented by ESA in October 1998 (Walpot, 2001).

The reference mission scenario considered for the CRV is the re-entry from the ISS orbit performed by a vehicle weighting about 9 ton, starting from the atmospheric entry interface ( $h_E=120$  km) with  $V_E=8$  km/s inertial, and  $\theta_E=-2$  deg. The re-entry flight scenario is given in

both altitude-velocity map and Mach-Reynolds plane in Fig. 2. These re-entry trajectories have been computed by means of the ENTRY (ENtry TRajectry) code developed at SUN (Viviani, 2006). The blue curve is a ballistic descent trajectory, while the red one refers to a lifting return since the capsule, flying trimmed at  $\alpha=20$  deg constant over the critical heating regime, is employing aerodynamic lift to sustain the descent flight path. As shown, the capsule, moving from a very rarefied atmosphere to a denser one, shifts from the free molecular flow (FMF) regime, where  $Kn_\infty \geq 10$  and individual molecular collisions are important, to the transition one, where  $10^{-3} < Kn_\infty < 10$  and slip effects are important, and then to the continuum regime where  $Kn_\infty \leq 10^{-3}$ . For instance, the similarity parameter that governs these different flow regimes is the Knudsen number (Bertin, 1994):

$$Kn_{\infty L_{ref}} = \frac{\lambda}{L_{ref}} = 1.25 \sqrt{\lambda} \frac{M_\infty}{Re_{\infty L_{ref}}} \quad (4)$$

where  $L_{ref}$  is the characteristic length of the body (e.g., the capsule diameter). Therefore, vehicle aerodynamics must also consider the effect of the Knudsen number. Re-entry trajectories of Fig.2 result in an aerothermal environment that must be accurately predicted for a reliable TPS design (Pezzella et al., 2007). To this end, trajectory freestream flight conditions have been used to perform numerical computations, as reported hereinafter.

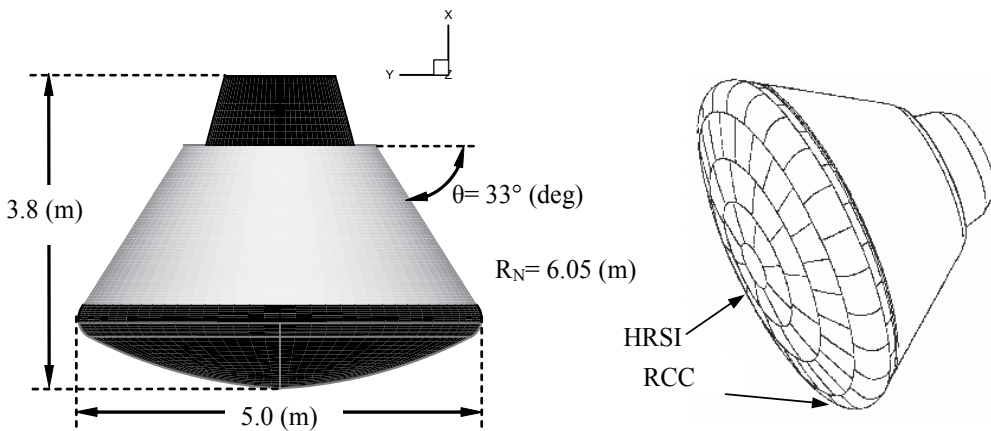


Fig. 1. CRV Vehicle configuration with quotes and TPS layout with high reusable surface insulator (HIRS) and reinforced carbon-carbon (RCC) tiles

#### 4. Design approaches and numerical tools

The preliminary AErodynamic DataBase (AEDB) of the CRV has been provided according to the space-based design approach (Prabhu, 2004), which dictates the generation of data set as function of a number of independent parameters (i.e.  $M_\infty$ ,  $Re_\infty$ ,  $\alpha$ ,  $\beta$ ).

On the other hand, the preliminary AeroThermodynamic DataBase (ATDB) has been computed following the trajectory-based design approach, which consists in performing aerothermal computations at a finite number of "critical" points of the nominal re-entry trajectory (Olynick, 1998).

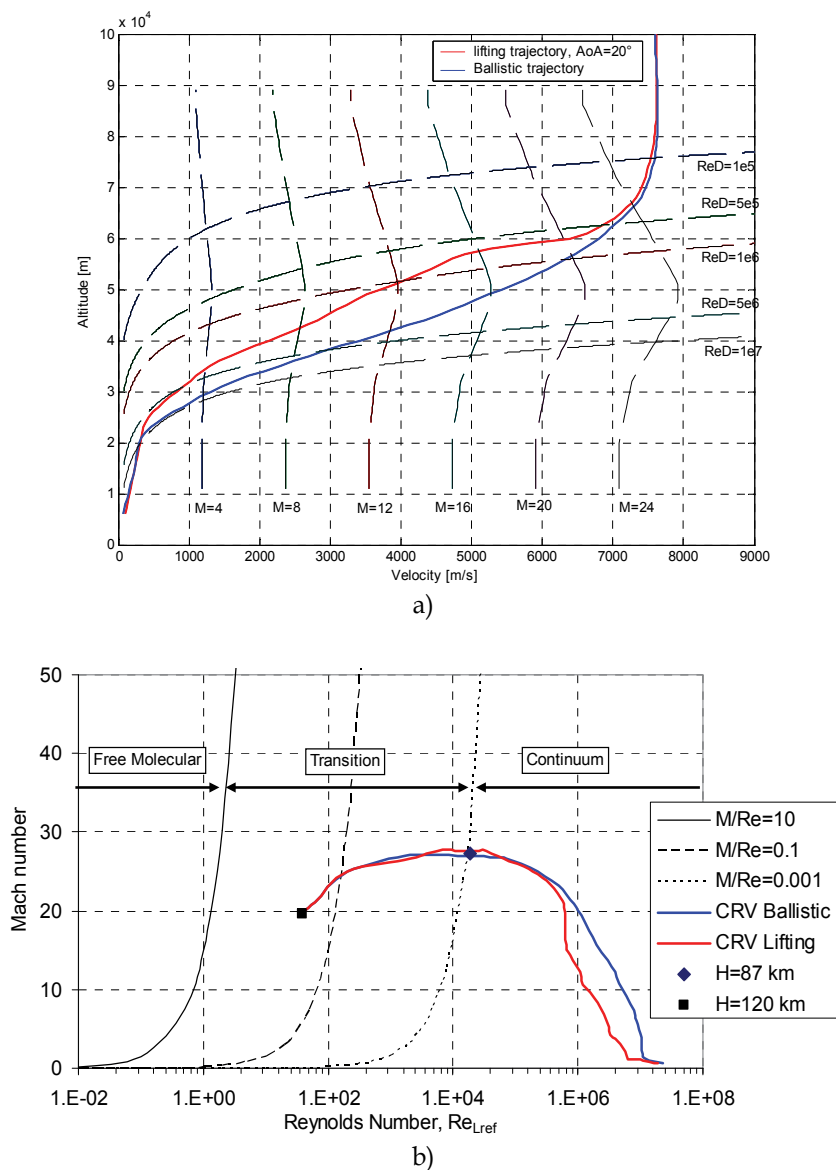


Fig. 2. Re-entry flight scenario; a) altitude-velocity map; b) Mach-Reynolds map with constant Knudsen numbers

Computational analysis of the CRV flowfield is performed by means of the solver code Fluent together with several user defined functions (UDF), developed by the authors, in order to manage vibrational relaxation, several catalytic models, radiative equilibrium at the wall and other boundary conditions. Computations have been carried out on multiblock structured grids. A close-up view of both 2-D and 3-D mesh can be seen in Fig. 3. The grid used for 3D calculations consists of 32 blocks with about 900.000 cells. For each computational case, a new grid has been created to properly accommodate for the detached bow shock location. See (Viviani et al., 2008) for further details on the computational grids.

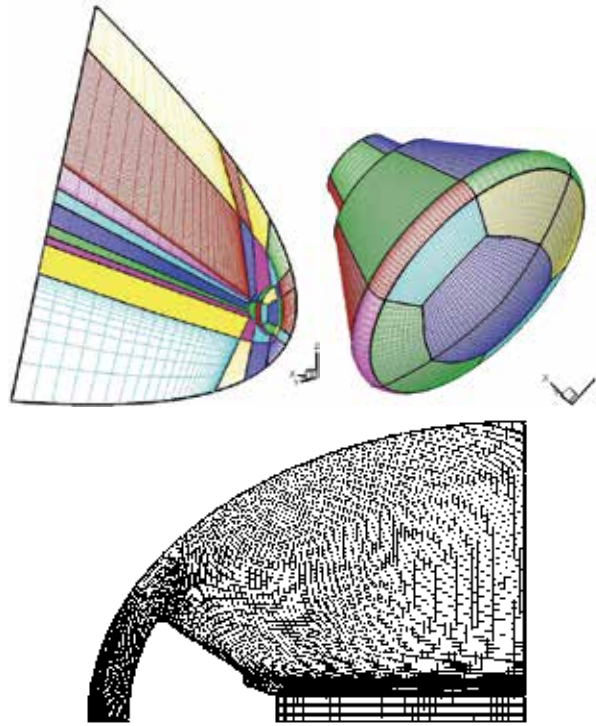


Fig. 3. Close-up view of 3-D (on top) and 2-D axi-symmetric computational mesh domains

## 5. The model and the numerical technique

The mathematical model describing the flowfield around a hypervelocity vehicle deals with balance equations for a multi-species chemically reacting gas mixture supplemented with an appropriate set of chemical reactions (i.e. the reactions mechanism) and with equations modelling species vibrations relaxation (i.e. thermal non-equilibrium).

### 5.1 Flowfield governing equations

The governing equations are made up of equations for mass conservation, total momentum balance, total energy (without the vibrational one) conservation, individual species balance and vibrational energy conservation. The full set of equations for a laminar viscous compressible continuum flow in thermal and chemical non-equilibrium, assuming the air as a mixture of  $N_S$  perfect gases and  $N_V$  vibrating species, written in the integral conservation is (Gnoffo et al., 1989):

$$\frac{\partial}{\partial t} \int_V \vec{W} dV + \int_S (\vec{F}_{inv} + \vec{F}_{vis}) \cdot \vec{n} dS + \frac{\Gamma}{R} \int_V (\vec{A}_{inv}^* + \vec{A}_{vis}^*) dV = \int_V \vec{\Omega} dV \quad (5)$$

where  $\vec{W} = [\rho, \rho u, \rho v, \rho w, e_t, \rho_1, \dots, \rho_{N_S-1}, \rho e_{v1}, \dots, \rho e_{vN_V}]$  is the unknown state vector of the conserved quantities, in which  $\rho$  is the fluid density,  $\rho u$ ,  $\rho v$  and  $\rho w$  are the momentum densities,  $e_t$  is the total internal energy per unit mass,  $\rho_i$  and  $e_{vi}$  are, respectively, the density and the vibrational energy of the  $i^{\text{th}}$  species while  $\rho e_{vi}$  takes into account for vibrational

energy conservation.  $\vec{F}$  and  $\vec{A}^*$ , splitted into an inviscid and a viscous part, are the flux vector and the axis-symmetric terms matrixes, respectively.  $\Gamma$  is equal to 1 for axis-symmetric flows and 0 for 2D and 3D flows.  $\vec{\Omega} = [0, 0, 0, 0, 0, \Omega_1, \dots, \Omega_{N_s-1}, \Omega_{v1}, \dots, \Omega_{vN_v}]^T$  is the source terms vector. It defines the mass and energy exchange among the species as a result of the chemical reaction rate and the energy transfer due to the internal energy excitation processes (Bertin, 1994). Finally,  $V$  is the arbitrary control volume cell,  $S$  is its closed boundary control surface and  $\vec{n}$  is the outward normal unit vector (Anderson, 1989).

Eq.(5) can be written in differential form as follows:

*Continuity:*

$$\frac{\partial \rho}{\partial t} + \vec{\nabla} \cdot (\rho \vec{V}) = 0 \quad (6)$$

*Momentum:*

$$\frac{\partial (\rho \vec{V})}{\partial t} + \vec{\nabla} \cdot (\rho \vec{V} \vec{V}) + \vec{\nabla} p = 2 \vec{\nabla} \cdot \left[ \mu (\vec{\nabla} \vec{V})_o^s \right] \quad (7)$$

*Energy:*

$$\frac{\partial (\rho e_t)}{\partial t} + \vec{\nabla} \cdot [(\rho e_t + p) \vec{V}] = \vec{\nabla} \cdot \left[ \lambda \nabla T + 2 \mu (\vec{\nabla} \vec{V})_o^s \cdot \vec{V} + \sum_i h_i \vec{J}_i \right] - \sum_i h_i \dot{\omega}_i - \sum_j \dot{e}_{vj} \quad (8)$$

*Species:*

$$\frac{\partial (\rho Y_i)}{\partial t} + \vec{\nabla} \cdot (\rho \vec{V} Y_i) + \vec{\nabla} \cdot \vec{J}_i = \dot{\omega}_i \quad (9)$$

*Vibrational energy:*

$$\frac{\partial (\rho e_{vj})}{\partial t} + \vec{\nabla} \cdot (\rho \vec{V} e_{vj}) = \dot{e}_{vj} \quad (10)$$

In these equations,  $\vec{V}$  is the velocity vector,  $Y_i$  is the mass fraction of the  $i^{\text{th}}$  species and,  $\dot{\omega}_i$  is the rate of change of  $\rho_i$  due to chemical reactions,  $J_i$  is the diffusive flux of  $i^{\text{th}}$  species, which arises due to concentration gradients,  $M_i$  and  $h_i$  are, respectively, the molecular weight and enthalpy of  $i^{\text{th}}$  species,  $p$  is the pressure,  $\mu$  is the viscosity and  $\lambda$  is the thermal conductivity. For each species the perfect gas model applies and the Dalton's law holds:

$$p = \sum_i p_i \quad (11)$$

where  $p_i$  is the partial pressure of the  $i^{\text{th}}$  species of the mixture. As a consequence, the following relation for density reads:

$$\rho = \frac{p}{R_0 T \sum_i Y_i / M_i} \quad (12)$$

where  $R_0$  is the universal gas constant. The internal energy of the mixture is defined as:

$$e = \sum_i (Y_i e_i) \quad (13)$$

where  $e_i$ , the internal energy of the single component gas, is the sum of the energies representing the different degrees of freedom of the molecules. Finally, the enthalpy is:

$$h = \sum_i (Y_i h_i) \quad (14)$$

Computation of the diffusive fluxes requires knowledge of the transport coefficient.

## 5.2 Transport properties

For pure species from kinetic theory of gases (Anderson, 1989) follows that:

*Viscosity:*

$$\mu_i = \frac{2.6693 \times 10^{-6} \sqrt{M_i T}}{\sigma_i^2 \Omega_{\mu i}} \quad (15)$$

*Thermal conductivity:*

$$\lambda_i = \frac{15}{4} \left( \frac{\mu_i R_0}{M_i} \right) \left( \frac{4}{15} \frac{c_{pi} M_i}{R_0} + \frac{1}{3} \right) \quad (16)$$

*Mass diffusivity:*

$$D_{ij} = \frac{0.0188 \times T^{\frac{3}{2}} \sqrt{(M_i + M_j) / M_i M_j}}{p \sigma_{ij}^2 \Omega_{Dij}} \quad (17)$$

Global transport properties of the gas mixture rely on semi-empirical rules such as Wilke's mixing rule for viscosity  $\mu$  and thermal conductivity  $\lambda$ :

$$a = \frac{\sum_i \chi_i a_i}{\sum_j \chi_j \left\{ \frac{1}{\sqrt{8}} \left( 1 + \frac{M_i}{M_j} \right)^{\frac{1}{2}} \left[ 1 + \left( \frac{a_i}{a_j} \right)^{\frac{1}{2}} \left( \frac{M_i}{M_j} \right)^{\frac{1}{4}} \right]^2 \right\}} \quad a = \mu, \lambda \quad (18)$$

where  $\chi_i$  is the mole fraction of species  $i$  and  $a_i$  (equal to  $\mu_i$  or  $\lambda_i$ ) is obtained by kinetic theory of gases. For the diffusion coefficient of the  $i$ th species in the mixture the multicomponent diffusion coefficient is applied:

$$D_i = \frac{(1 - \chi_i)}{\sum_j \frac{\chi_j}{D_{i,j}}} \quad (19)$$

with  $D_{i,j}$  evaluated by kinetic theory. Finally, vibrational relaxation is modelled using a Landau-Teller formulation, where relaxation times are obtained from Millikan and White, assuming simple harmonic oscillators (Bertin, 1994).

### 5.3 Chemical species and reactions mechanism

Within a LEO re-entry scenario (e.g., no flowfield ionization occurs), the gas is approximated as a finite-rate chemistry mixture of  $N_2$ ,  $O_2$ ,  $N$ ,  $O$ ,  $NO$  species (Gnoffo et al., 1999). The elementary reactions mechanism, governing the species in high-temperature air, deals with three dissociation reactions and two exchange reactions, as reported in Tables 1a, 1b; there  $M$ , namely reacting partner or third body, can be any of the five reacting species, thus providing or removing collision energy. Efficiencies of the third body are also reported in Tables 1a, 1b, since they are employed in computations to increase CPU time efficiency. The reactions mechanism results in a system of 17 chemical reactions, with 17 forward and backward reactions rate coefficients.

No	Reaction	$A_{f,r}$ ( $m^3/kgmole\ s$ )	$\bar{T}$ (k)	$\beta_{f,r}$	$E_{a,f,r}$ (J/kgmole)	Third body efficiency
1	$O_2 + M = 2O + M$	$3.60 \times 10^{15}$	T	-1.0	$4.947 \times 10^8$	$O_2=9, N_2=2, O=25,$ $N=NO=1$
2	$N_2 + M = 2N + M$	$1.90 \times 10^{14}$	T	-0.5	$9.395 \times 10^8$	$O_2=1, N_2=2.5,$ $O=N=NO=1$
3	$N_2 + N = 3N$	$4.085 \times 10^{19}$	T	-1.5	$9.395 \times 10^8$	-
4	$NO + M = N + O + M$	$3.90 \times 10^{17}$	T	-1.5	$6.277 \times 10^8$	$O_2=N_2=1, O=N=NO=20$
5	$NO + O = O_2 + N$	$3.20 \times 10^6$	T	1.0	$1.638 \times 10^8$	-
6	$N_2 + O = NO + N$	$7.00 \times 10^{10}$	T	0.0	$3.159 \times 10^8$	-

Table 1a. Reaction rate parameters in Eq. (21), Dunn & Kang model (Gnoffo et al., 1989)

No	Reaction	$A_{f,r}$ ( $m^3/kgmole\ s$ )	$\bar{T}$ (k)	$\beta_{f,r}$	$E_{a,f,r}$ (J/kgmole)	Third body efficiency
1	$O_2 + M = 2O + M$	$1.00 \times 10^{19}$	$T_a$	-1.5	$4.947 \times 10^8$	$O_2=N_2=NO=0.2, O=N=1$
2	$N_2 + M = 2N + M$	$3.00 \times 10^{19}$	$T_a$	-1.6	$9.412 \times 10^8$	$O_2=N_2=NO=0.233,$ $O=N=1$
3	$NO + M = N + O + M$	$1.10 \times 10^{14}$	$T_a$	0.0	$6.277 \times 10^8$	$O_2=N_2=0.05,$ $O=N=NO=1$
4	$NO + O = O_2 + N$	$2.40 \times 10^6$	T	1.0	$1.598 \times 10^8$	-
5	$N_2 + O = NO + N$	$1.80 \times 10^{11}$	T	0.0	$3.193 \times 10^8$	-

Table 1b. Reaction rate parameters in Eq. (21), Park model (Park et al., 1993)

Of the simpler sets of homogeneous reactions, it is standard to use the following three chemical reactions, known as Zeldovich process (Sarma, 1995):



It considers only Oxygen dissociation, due to collisions with molecular Nitrogen, and two exchange reactions. This model can be explained considering that the gas is so hot that the Oxygen completely dissociates, while the Nitrogen does neither dissociate completely nor as fast as the Oxygen. Finally, exchange reactions are important because they determine the

speed of Nitrogen dissociation. Chemical reactions proceed with forward rates,  $k_{f,r}$  that appear in the source terms ( $\dot{\omega}_i$ ) of the species transport equation, Eq. (9). They are expressed in the Arrhenius form as:

$$k_{f,r} = k_{f,r}(\bar{T}) = k_f (T^a T_v^b) = A_{f,r} \bar{T}^{\beta_{f,r}} \exp\left(-\frac{E_{a,f,r}}{R_o \bar{T}}\right) \quad (21)$$

where  $\bar{T}$  and the constants depend on the model kinetics (see Tables 1a, 1b).

The Dunn-Kang model uses one temperature to describe all the energy modes (e.g.  $\bar{T} = T$ , thermal equilibrium), while the Park model assumes that  $\bar{T}$  can be  $T$ ,  $T_v$ , or  $T^a T_v^b$  (namely rate controlling temperature) depending on the reaction (see Table 1b). So Park's two-temperature model provides more accurate results because it uses  $T$  to describe translational and rotational energy modes and  $T_v$  for vibrational and electron-translational modes.

#### 5.4 Boundary conditions

Eq. (3) states that the properties of a surface are emissivity ( $\epsilon$ ) and wall catalyticity (i.e.  $k_{wi}$ ). As atoms of dissociated flow strike vehicle surface, the catalyticity property of the wall is implemented by means of a production term (i.e.  $\dot{\omega}_{wi} \neq 0$ ) in the boundary layer problem to solve. Then, steady-state mass atomic conservation at the wall states that the production of  $i^{\text{th}}$  species, due to the catalytic recombination rate, must be balanced by the rate of diffusion to the surface:

$$(\dot{\omega}_a)_w = -(\rho_a v_a)_w \quad (22)$$

The source term  $\dot{\omega}_a$  is given by Goulard's relationship:

$$\dot{\omega}_a = k_{wa} (\rho_w Y_{iw})^p \quad (23)$$

where  $p$  is the reaction order and  $k_{wi}$  is the catalytic reaction rate (Anderson, 1989). The diffusive flux  $\rho_a v_a$  is expressed by means of Fick's law and then:

$$(\dot{\omega}_a)_w = k_{wa} (\rho Y_i)_w^p = \left( \rho D_a \frac{\partial Y_i}{\partial n} \right)_w \quad (24)$$

When the TPM does not promote any particular reaction (i.e.,  $\dot{\omega}_{wi} = 0$ ), the TPS surface is called NCW (i.e.  $k_{wi}=0$ ); on the opposite situation, when the TPM can activate any reactions, the TPS surface is called FCW (i.e.  $k_{wi} \rightarrow \infty$ ). Between these two limit cases (i.e.  $0 < k_{wi} < \infty$ ), the vehicle surface is considered as PCW and the heat fluxes to the vehicle greatly differ depending on the value of  $k_{wi}$ . Furthermore, when a low conductive TPS protects the vehicle, the radiative equilibrium condition holds at vehicle surface. To account for this condition, during numerical simulations, the wall temperature is calculated by Stephan-Boltzman law and is implemented by means of a Newton-Raphson approach.

#### 5.5 Numerical technique

The governing equations, together with the proper boundary conditions, are discretized using a cell-centered finite volume formulation on a structured multiblock grid (see Fig. 3). For the single-mesh cell, the discretized equation reads:

$$\frac{d\vec{W}_c}{dt} + \frac{1}{V_c} \sum_{f=1}^6 (\vec{F}_{c_{inv}} + \vec{F}_{c_{vis}})_f \cdot \vec{n} + \frac{\Gamma}{r} (\vec{A}_{c_{inv}}^* + \vec{A}_{c_{vis}}^*) = \vec{H}_c \quad (25)$$

where  $f$  is the index of the cell face and  $c$  refers to the single cell of the computational domain. The inviscid fluxes at cell interfaces are calculated by using a flux difference splitting (FDS) Riemann solver, since upwind methods are particularly suitable for high speed flows. However, second order accuracy is not automatically reached. For this reason, a second order essentially non oscillatory (ENO) technique for the reconstruction of cell interface values is employed (Anderson, 1995). The viscous fluxes are calculated by central differencing, i.e. computing the gradients of flow variables at cell interfaces by means of Gauss theorem. The method is second order accurate in space. Time integration is performed by employing both an explicit single-stage (Euler forward) algorithm and an explicit five stage Runge-Kutta scheme, coupled with an implicit evaluation of the chemical and vibrational source terms, under the hypothesis of time marching approach to reach the steady solution for the flow.

## 6. Reliability of numerical study

A reliable flow simulation dictates the validation of the theoretical models describing the high temperature effects in a hypersonic flow by means of PWT and free flight experimental data. To this end, in order to assess the reliability of present results a numerical rebuilding of ELECTRE (Muylaert et al., 1999) and ARD (Walpot, 2001) test campaigns were performed. Experimental and numerical comparisons of results for both the test models were reported.

### 6.1 ELECTRE test article in HEG wind-tunnel

ELECTRE test article (see Fig. 4) consists of a blunt conical surface 0.4 m long, semiaperture cone angle of  $4.6^\circ$  deg, and hemispherical nose radius of 0.035 m. It was tested in flight and in PWT, becoming a standard reference model to study non-equilibrium hypersonic flow past blunt-body configurations (Muylaert et al., 1999). The CFD computational domain, shown in Fig.4, consists of  $60 \times 120$  cells with a minimum normal wall spacing of  $10^{-5}$ m which a grid sensitivity analysis has shown to be necessary to obtain a sufficient resolution of the flowfield features.

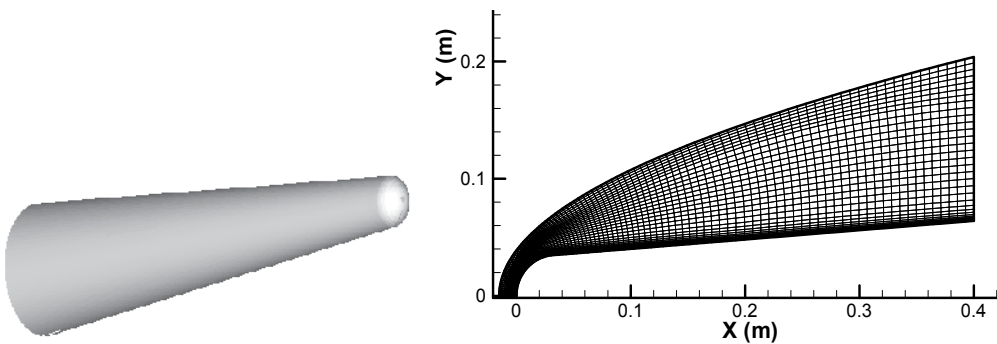


Fig. 4. ELECTRE test article geometry and axi-symmetric mesh domain

Test conditions are summarized in Tab.2. They correspond to operating conditions of the HEG PWT located at DLR Gottingen at which two different test cases were run considering alternatively the specimen wall as NC, and FC for N and O species.

$T_\infty$ (K)	$P_\infty$ (Pa)	$\rho_\infty$ (kg/m <sup>3</sup> )	$V_\infty$ (m/s)	$M_\infty$ (-)	$Re_\infty/m$ (1/m)	$Y_O$ (-)	$Y_N$ (-)	$Y_{NO}$ (-)	$Y_{O_2}$ (-)
790	430	1640x10 <sup>-6</sup>	5919	9.7	270x10 <sup>3</sup>	0.179	1.0x10 <sup>-6</sup>	3.3x10 <sup>-2</sup>	3.6x10 <sup>-2</sup>

Table 2. Reference calibration point conditions of the HEG nozzle (Muylaert et al., 1999)

As an early assessment of work several engineering evaluations have been accomplished by means of ENTRY as, for example, pressure coefficient and convective heat transfer distributions on the test article wall. ENTRY quickly evaluates the pressure distribution by using the surface impact method, typical of hypersonics:

$$C_p = C_{pt2} \sin^2 \theta \quad (26)$$

where  $C_{pt2}$  is the stagnation-point pressure coefficient that depends on the flow theory one considers, while  $\theta$  is the local slope body angle (Bertin, 1994). For example, Newtonian flow theory states that  $C_{pt2}$  is equal to 2 while in the case of Modified Newtonian theory (see Eq.(1)) it reads:

$$C_{pt2} = \left( \frac{P_{t2}}{P_\infty} - 1 \right) \frac{2}{\gamma M_\infty^2} \quad (27)$$

For the aeroheating, ENTRY evaluates the convective heat transfer around both hemispherical nose and spherically capped cone, according to the Lees theory (Lees, 1956). Lees approach shows that, for a blunt cone with nose radius  $R_N$  and semiaperture vertex angle  $\theta_c$ , at any point on the cone surface, the ratio of heat transfer to the stagnation value  $\dot{q}_{co}$  reads:

$$\begin{aligned} \text{Nose} \quad \frac{\dot{q}_w(\theta)}{\dot{q}_{co}} &= \frac{2\theta \sin \theta \cos^2 \theta}{\sqrt{D(\theta)}} \\ \text{Cone skirt} \quad \frac{\dot{q}_w(s')}{\dot{q}_{co}} &= A(\theta_c) \frac{s'}{R_N} \left[ B(\theta_c) + \left( \frac{s'}{R_N} \right)^3 \right]^{\frac{1}{2}} \end{aligned} \quad (28)$$

Eq.(28) is valid for  $s'/R_N \geq \cot \theta_c$ , where  $s'$  is the curve length measured along the cone surface of the effective sharp-nosed cone and, for high flight Mach number:

$$\begin{aligned} A(\theta_c) &\approx \frac{\sqrt{3}}{2} \sin \theta_c \sqrt{\frac{\pi}{2} - \theta_c} \\ B(\theta_c) &\approx \frac{3}{16} \frac{1}{\sin^4 \theta_c} \left[ \frac{D(\theta)}{\theta} \right]_{\theta=\frac{\pi}{2}-\theta_c} - \cot^3 \theta_c \\ D(\theta) &\approx \theta^2 - \frac{1}{2} \theta \sin 4\theta + \frac{1}{8} (1 - \cos 4\theta) \end{aligned} \quad (29)$$

CFD aerothermodynamic computations have been performed with different wall catalytic boundary conditions for the test article. The computations refer to fully laminar non-equilibrium flow conditions with model temperature fixed to  $T_w=300$  K. The flowfield past the test bed is shown in Fig.5, where the Mach number contour field is plotted, comparing the results for perfect gas (upper side) and real gas model (lower side).

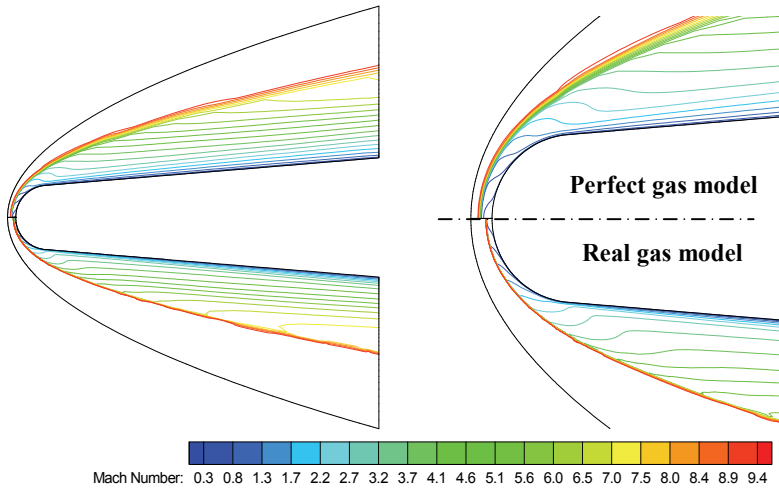
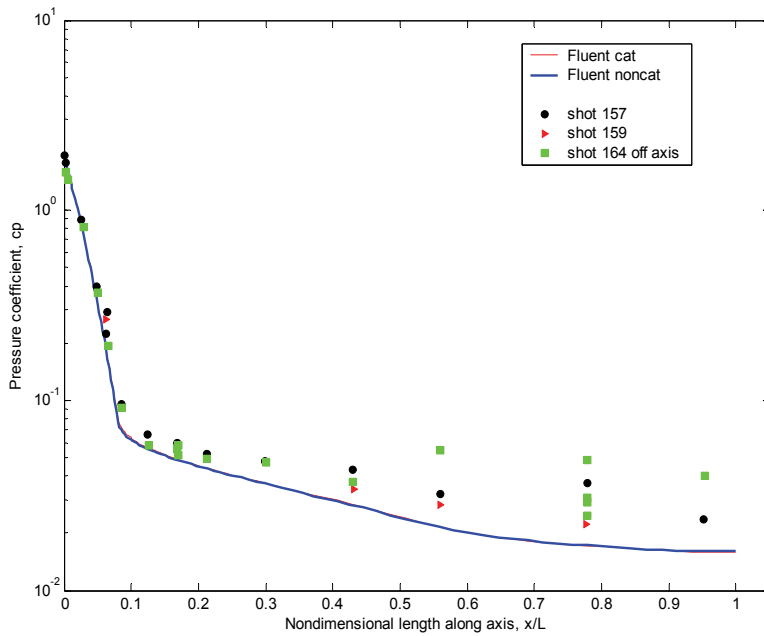


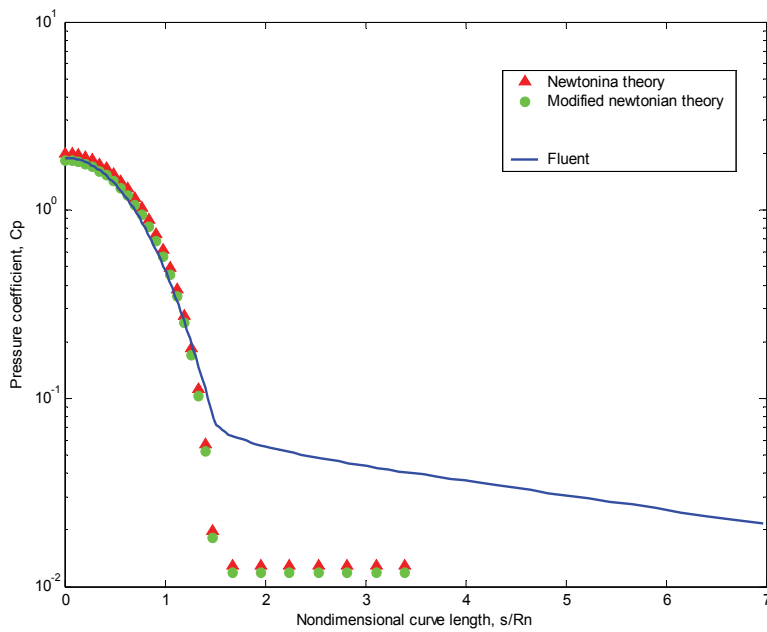
Fig. 5. Mach number contours field. Comparison between perfect gas (top) and real gas model. Detail on the nose region of the test bed (right)

Pressure coefficient and wall heat flux distributions for different wall catalytic conditions are reported respectively in Fig. 6 and Fig. 7, where CFD results were compared with engineering and available experimental results (i.e. shot157, shot159, shot164) (Muylaert et al., 1999).

The  $C_p$  comparison of numerical, experimental and engineering results shows good agreement in the first part of the test specimen, with differences only at the model end. In particular, Fig. 6 highlights that no differences exist between NC and FC wall boundary conditions, as expected. Moreover, ENTRY results (see Fig. 6-b) compare well with the Modified Newtonian theory, where the  $C_{p12}$  has been evaluated using the inflow specific heat and Mach number as provided by CFD analyses. As shown, the pressure on the probe nose decreases with curve length from the stagnation point, becoming constant on the conical skirt (e.g.,  $\theta=\theta_c=\text{const}$  in Eq.(26)). Modified Newtonian theory, however, loses in accuracy as highlighted by CFD since the surface pressure depends on many factors such as the interaction of compression and of expansion waves which originate from body curvature, reflection from the bow shock and slip lines due to the rotationality introduced by the curved bow shock wave. In particular, as the cone is very slender, the surface pressure in the expanding flow decreases so slowly that the asymptotic (sharp cone) value is not reached, resulting in an underexpanded flow. The heat flux distribution (see Fig. 7) shows an agreement with the numerical FC solution (the red curve) on the nose of the test article while on the rear part of cone there is a mismatch between experimental data and CFD results, as already seen in the case of  $C_p$ . Both these mismatches could be probably caused by flowfield perturbations due to the support arm, located at the end of the test bed. Anyway Fig.7-b shows that CFD results compare well with Lees theory.



a)



b)

Fig. 6. a)  $C_p$  comparison between numerical, engineering, and experimental data, b) detail on the nose probe (Muylaert et al., 1999)

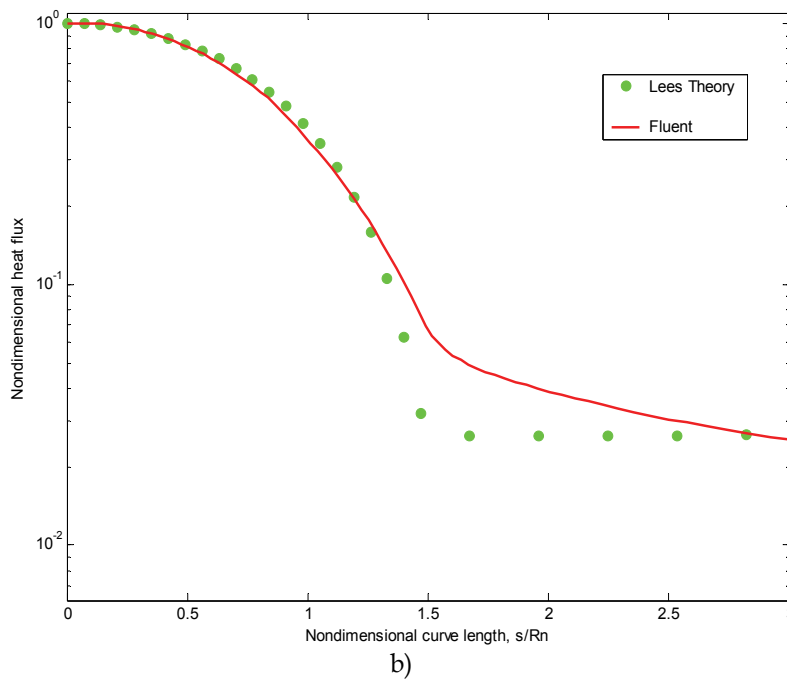
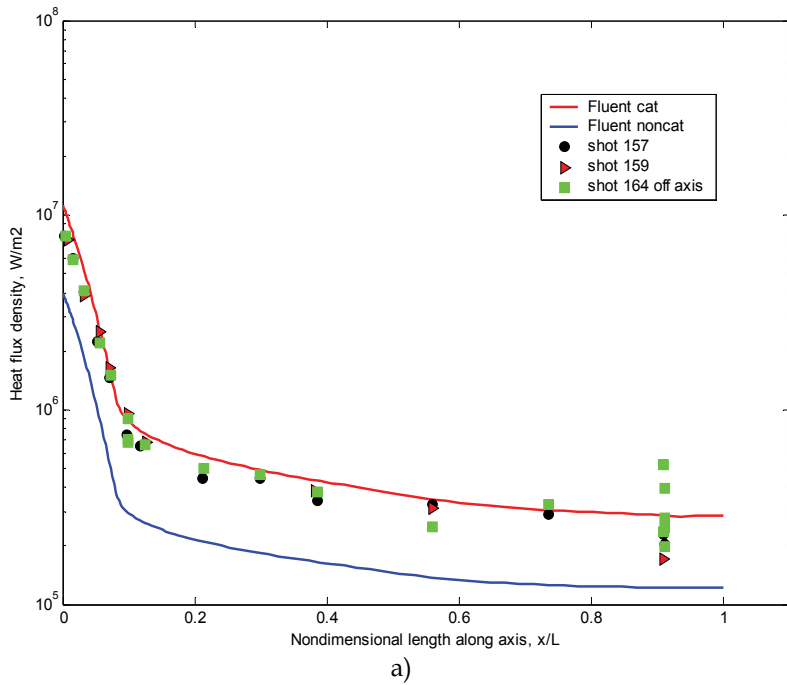


Fig. 7. Heat flux; a) comparison between numerical, engineering, and experimental data; b) detail on the nose probe (Muylaert et al., 1999)

## 6.2 ARD model in S4 wind-tunnel

S4 test campaigns provide pressure profiles on the forebody centerline of the atmospheric re-entry demonstrator (ARD) capsule (see Fig.1) at the freestream conditions of Tab. 3 (Walpot, 2001).

$P_0$ (bar)	85	25
$T_0$ (k)	1151	1108
$Re_{D_\infty}$	967237.3	319208
$M_\infty$	9.92	9.72
$P_\infty$ (Pa)	211.3	71.17
$T_\infty$ (k)	55.7	55.7
$T_{wall}$ (k)	300	300
$X_{cg}/D$	0.26	0.26
$Y_{cg}/D$	0.0353	0.0353
AoA (deg)	-20	-20

Table 3. ONERA S4 exit conditions (Walpot, 2001)

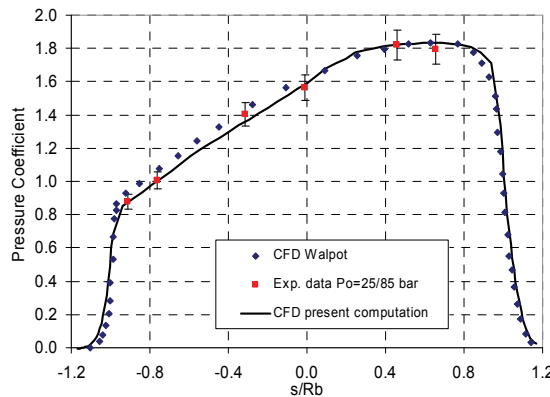


Fig. 8. Pressure coefficient: comparison between present results and data in (Walpot, 2001)

Results of present computations in terms of  $C_p$  on forebody centerline are summarized and compared with experimental data in Fig. 8, where CFD data provided by Walpot are also reported as further benchmark (Walpot, 2001). As one can see, experimental and numerical data compare well, thus confirming the reliability of numerical results.

## 7. CRV flowfield computational analysis

Axi-symmetric and fully three-dimensional simulations were performed at the freestream conditions listed in Table 4, with the far field composed of 79%  $N_2$  and 21%  $O_2$ .

In order to appreciate how vehicle flowfield depends on real gas effects, numerical computations have been performed in a step-by-step approach. For instance, starting with the perfect gas model, flowfield computation accounts for the chemistry considering first the flow in equilibrium conditions and then in non-equilibrium ones. In the latter case, the effects of both reaction mechanism and chemical kinetics are considered, for example, by means of Zeldovich reaction mechanism, and Dunn-Kang and Park kinetic models. Finally,

thermal non-equilibrium and wall catalyticity are accounted for, providing a complete overview of high temperature effects on CRV aerodynamics and aerothermodynamics.

Altitude (Km)	Mach (-)	Pressure (Pa)	Temperature (k)	AoA (deg)
50	10	79.78	270.65	0
57	19	32.78	255.27	10
57	19	32.78	255.27	17.5
57	19	32.78	255.27	21
57	19	32.78	255.27	28
57	16	32.78	255.27	28
57	12	32.78	255.27	28

Table 4. Freestream conditions of CFD computations

All the computations considered in this work have been performed by means of an Intel Core Duo E7300 at 2.66 GHz.

### 7.1 Axi-symmetric computations

A general overview of the flowfield past the vehicle is shown in Fig. 9, where contours of pressure and translational temperature in the forebody flowfield are plotted. They refer to a perfect gas computation performed at  $M_\infty=19$ ,  $H=57$  km and  $\alpha=0$  deg (e.g., peak heating conditions of the ballistic trajectory of Fig. 2).

Figure 10 shows a comparison of the non-dimensional temperature profile between perfect gas (PG), equilibrium gas (EG), chemical non-equilibrium gas with NCW and chemical non-equilibrium gas with FCW, as evaluated along with the stagnation line. As clearly shown, the temperature is large enough to cause the complete Oxygen dissociation in the shock layer while Nitrogen partially dissociates. Moreover, differences can be found in temperature peak, stand-off distance and also in the equilibration trend for translational temperature. In particular, in the case of chemical non-equilibrium computation, the temperature profile on the stagnation line exhibits a sharp discontinuity at the shock wave and a large overshooting value due to the finite rate dissociation of molecules.

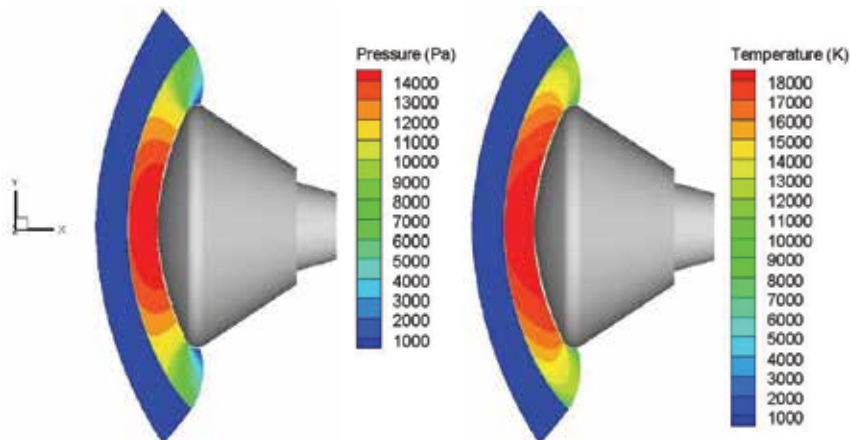


Fig. 9. Contours of static pressure (left) and temperature for  $\alpha=0$  deg,  $M_\infty=19$ , and  $H=57$  km

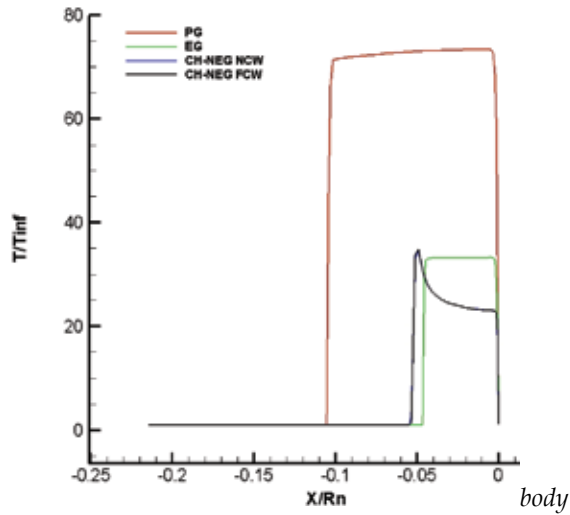


Fig. 10. Comparison of static temperature for  $\alpha=0$  deg,  $M_\infty=19$ , and  $H=57$  km, along with the stagnation line for different chemical models

Figure 10 also shows that the shock layer becomes thinner because high temperature phenomena absorb heat, thus decreasing the effective specific heat ratio  $\gamma$ . As a result, the gas compressibility changes, which lead to changes in the shock wave shape around the vehicle. In particular, as the green curve highlights, this phenomenon occurs more prominently in the equilibrium flow than in a non-equilibrium one.

When we account for the influence of chemical kinetics, we have provided in Fig. 11 the comparison of non-dimensional temperature profiles, along the stagnation line, for the results of Dunn-Kang and Park models.

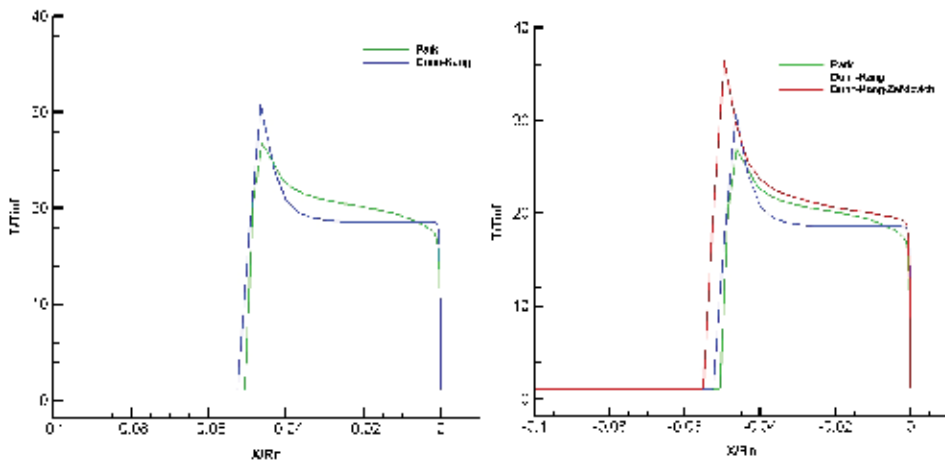


Fig. 11. Comparison of translational temperature, along the stagnation line, for different chemical models and reaction mechanisms, for  $\alpha=0$  deg,  $M_\infty=19$ , and  $H=57$  km.

As shown, chemical kinetics slightly changes both stand-off distance and the peak temperature. Differences are also in the shape of temperature profiles in the shock layer,

because for the Dunn-Kang model the flow equilibrates before reaching the boundary layer, differently from the case of Park model. As to the effects of the reaction mechanism, Fig. 11 (right side) also reports the effect of the Zeldovich's model on translational temperature along the stagnation line. As one can see, this reaction mechanism over-estimates both temperature peak and stand-off distance. In particular, the temperature profile of complete reaction mechanism (the blue curve), shows that flowfield in the shock layer tends toward equilibrium faster than Park and Zeldovich results.

The effects of vibrational relaxation can be appreciated in Fig. 12, where the comparison between translational temperature distributions, along the stagnation line, is reported for Park kinetics.

Results shows only slight differences between the case of thermal equilibrium and non-equilibrium computation. When vibrational equilibrium holds (green curve) there is no incubation time for vibration to relax, as highlighted by the temperature rise of the curve. Therefore, we can conclude that at the peak heating the flowfield around the capsule is characterized by an almost thermal equilibrium conditions (remember that capsule features a large forebody radius,  $R_N=6.05$  m). Hence, chemistry is active just behind the shock and energy goes only in chemistry thus yielding lower translational temperature in the shock layer. In fact, even if the exact functional dependence is unknown, it is agreed that a reaction mechanism depending only on T over-predicts the amount of dissociation.

Thermal equilibrium conditions are also confirmed by results summarized in Fig. 12 (right side), where the comparison between the translational and vibrational non-dimensional temperatures is reported.

As we can see, temperature profiles are almost overlapping except across the shock, with the vibrational temperature of molecular nitrogen that slightly lags behind the others (e.g., the energy transfer takes a certain number of collisions to proceed). In particular,  $O_2$ , NO and  $N_2$  quickly equilibrate.

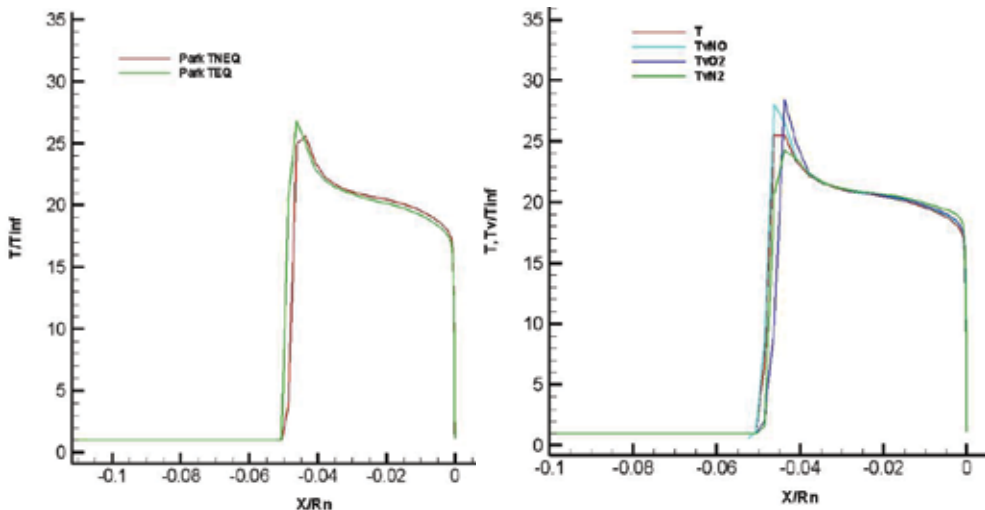


Fig. 12. Translational and vibrational temperatures along with the stagnation line for  $\alpha=0$  deg,  $M_\infty=19$ , and  $H=57$  km for NCW. Comparison between thermal equilibrium (TEQ) and non-equilibrium (TNEQ) conditions for Park kinetics

### 7.2 Three-dimensional computations

In the framework of 3-D CFD computations, several AoAs have been considered (see Tab.4). Figure 13 shows the static temperature contours on capsule symmetry plane and two flowfield cross sections and the static pressure contours on the CRV surface at  $M_\infty=19$  and  $\alpha=20$  deg, considering the flow as a reacting gas mixture. As shown, the CRV bow shock structure around the descent vehicle can be appreciated as well. Figure 14 reports the flowfield contours of Oxygen (O) and Nitrogen (N) mass fraction (on the right side) for  $M_\infty=19$ ,  $H=57$  km, and  $\alpha=20$  deg. As expected, the oxygen is fully dissociated.

Concerning capsule static stability, the transition in sonic line location is shown in Fig. 15 to Fig. 17 for different AoA and Mach numbers. Figure 15 reports sonic line location for four cases, involving two different Mach numbers (e.g., 10 and 19) and all the AoA considered in the computations. As shown, the sonic line location and its shape markedly depend on freestream Mach number, altitude and AoA, thus highlighting that capsule attitude conditions are highly influenced during descent.

In order to appreciate the effect of finite rate chemistry, the sonic line comparison between PG and RG computations both for  $M_\infty=16$  and  $M_\infty=19$  is summarized in Fig. 16.

In both cases for the PG solution the flowfield around almost all the capsule heat shield is entirely subsonic with consequent high pressure distribution. Therefore, as the sonic line shifts due to the chemical reactions, the flow becomes entirely supersonic and the pressure decreases, thus confirming that pitching moment ( $CM_y$ ) and  $\alpha_{trim}$  are affected by real gas effects. In particular, differences between the green and blue lines on the capsule afterbody, underline that at  $M_\infty=19$   $CM_y$  is affected by the chemical kinetics while no influences are expected when CRV is flying at  $M_\infty=16$  (see left side of Fig. 16).

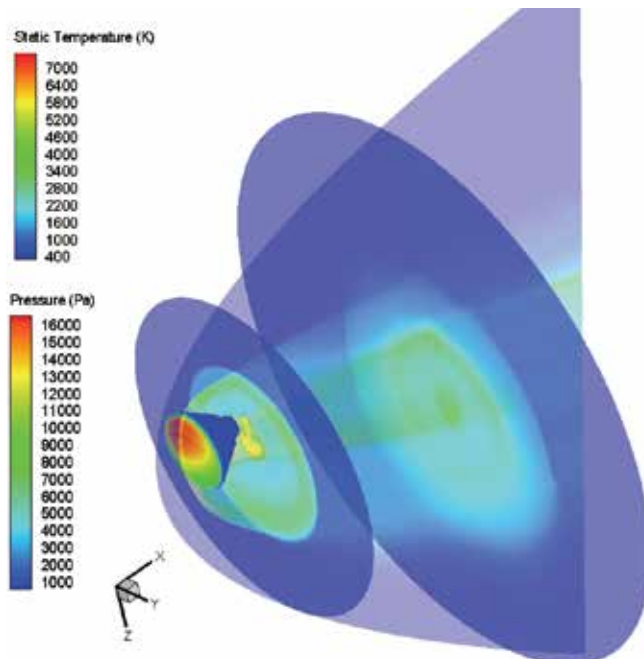


Fig. 13. Static temperature on CRV symmetry plane and two cross sections at  $M_\infty=19$ ,  $H=57$  km and  $\alpha=20$  deg. Static Pressure contours on capsule forebody

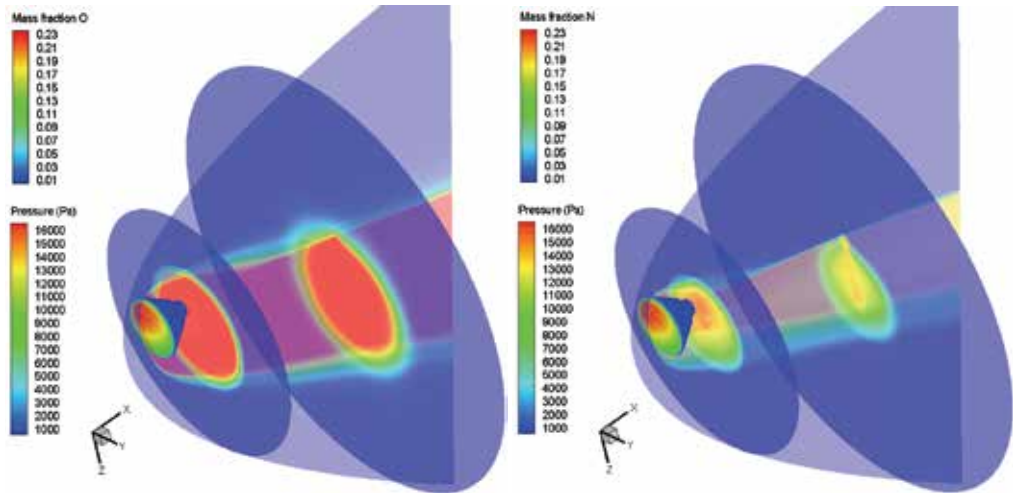


Fig. 14. Flowfield contours of Oxygen and Nitrogen (right) mass fraction for  $M_\infty=19$ ,  $H=57$  km, and  $\alpha=20$  deg on CRV symmetry plane and two cross sections. Static Pressure contour on capsule forebody

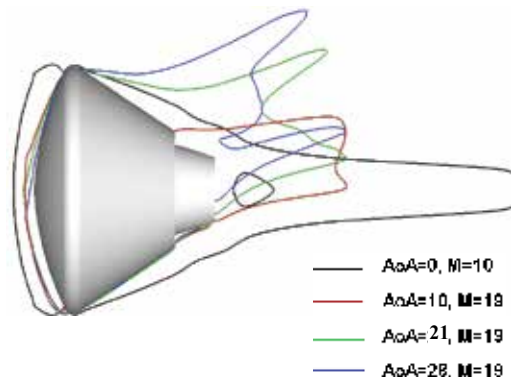


Fig. 15. Sonic line location in the capsule pitch plane for different AoA and Mach number

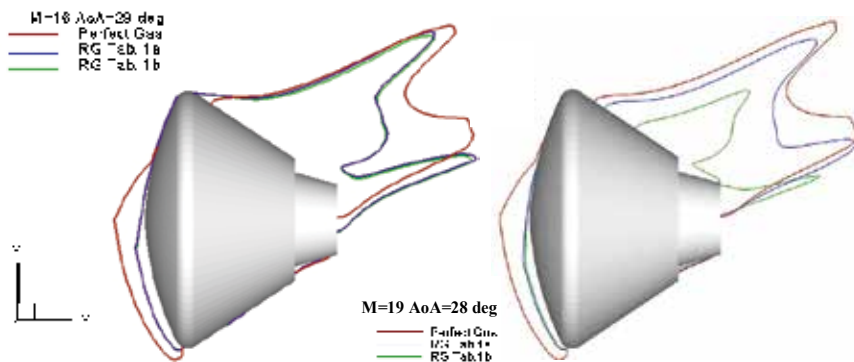


Fig. 16. Sonic line location in the capsule pitch plane for  $M_\infty=16$ ,  $M_\infty=19$ ,  $H_\infty=57$  km and  $\alpha=28$  deg. Comparison between PG and RG computations

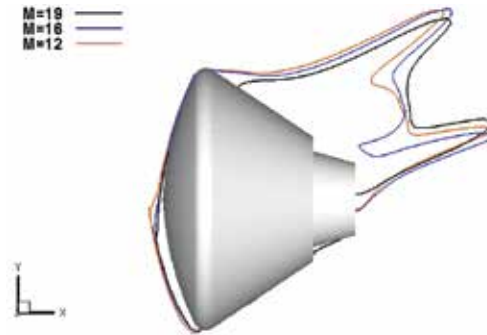


Fig. 17. Sonic line location in the capsule pitch plane at  $\alpha=28$  deg and  $H_\infty=57$  km. Comparison among  $M_\infty=12, 16$  and  $19$

Finally, Fig. 17 shows the sonic line for  $M_\infty=12, 16$ , and  $19$  at the same  $\alpha$ , thus highlighting the effect of the Mach number. Therefore, region of vehicle static instability could be expected during re-entry, depending on the capsule's c.g. location.

## 8. CRV aerodynamic analysis

Aerodynamic features of primary interest for an axi-symmetric vehicle are lift ( $C_L$ ), drag ( $C_D$ ), and pitching moment ( $CM_y$ ) coefficients, which are calculated according to Eq. (30).

$$C_i = \frac{F_i}{\frac{1}{2} \rho_\infty v_\infty^2 S_{ref}} \quad i = L, D \quad C_{M_j} = \frac{M_j}{\frac{1}{2} \rho_\infty v_\infty^2 L_{ref} S_{ref}} \quad j = Y \quad (30)$$

where  $L_{ref}=5.0$  m (i.e., CRV diameter-longitudinal reference length);  $S_{ref}=(\pi D^2)/4=19.6$  m<sup>2</sup> (i.e. CRV maximum cross-section area). Pole coordinates for the  $CM_y$  calculation are (1.3,-0.1765,0) m (i.e., vehicle cg). Based on the reentry scenario of Fig. 2 the AEDB has been generated for FMF, transitional regime and continuum flow. No lateral directional analysis has been taken into account in this work. CRV aerodynamic appraisal within FMF and transitional regime entails Direct Simulation Monte Carlo Method (DSMC) computations and a very simple relationship to bridge the transitional flow regime from continuum to FMF one (Pezzella et al., 2009). CRV continuum aerodynamics refers to both engineering-based analysis and CFD-based analysis.

### 8.1 Engineering-based aerodynamics of CRV

As an early assessment of the CRV continuum aerodynamics several engineering evaluations have been accomplished by ENTRY considering that when the capsule travels at hypersonic velocities the aerodynamic forces are dominated by pressure effects. Viscous and other effects, such as base drag, represent only about ten percent of the total. So the flow may be approximated as inviscid and surface inclination methods (SIM), like Modified Newtonian theory (MN), can be used (Bertin, 1994). To this end let us consider Fig.18 where the capsule's outer mold line (OML) is shown.

Assuming that the freestream particles impact only on the frontal area of the body and cannot curl around it, combining Eq. (26) and Eq. (1), MN theory suggests that the pressure coefficient ( $C_p$ ) becomes:

$$C_p = (2 - \varepsilon) \sin^2 \theta \quad (31)$$

By integrating Eq. (31) over the whole vehicle surface one is able to evaluate aerodynamic forces acting on the vehicle, both for zero lift and AoA cases.

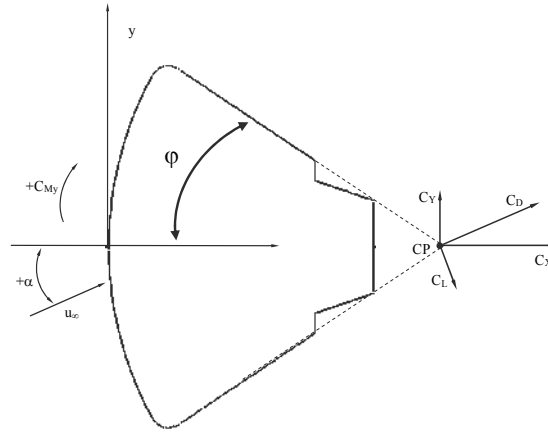


Fig. 18. Capsule OML used for surface impact method aerodynamics

### 8.1.1 Zero lift aerodynamics

The zero lift drag coefficient of the CRV is given by:

$$C_{D0} = \frac{2\pi}{S_{ref}} \int_0^\varphi C_p r^2 \sin \varphi \cos \varphi d\varphi = \frac{(2 - \varepsilon)}{2} (1 + \cos^2 \varphi) \quad (32)$$

where  $\varphi$  is the capsule frustum angle (i.e. 33 deg).

### 8.1.2 AoA aerodynamics

When the capsule is flying at an AoA the pressure coefficient on vehicle's wall facing flow, reads:

$$C_p = (2 - \varepsilon) (\hat{u} \cdot \hat{n})^2 = (2 - \varepsilon) (\cos \alpha \cos \theta + \sin \alpha \sin \theta)^2 \quad (33)$$

So, when  $\alpha < \theta$  (i.e. the sidewall surface is shadowed) the axial and normal force coefficients are, respectively:

$$C_x = \frac{(2 - \varepsilon)}{2} \left[ \cos^2 \alpha (1 + \cos^2 \varphi) + \frac{1}{2} \sin^2 \alpha \sin^2 \varphi \right] \quad (34)$$

$$C_y = \frac{(2 - \varepsilon)}{2} \cos \alpha \sin \alpha \sin^2 \varphi \quad (35)$$

Therefore, the capsule lift to drag ratio (E) is:

$$E = \frac{C_L}{C_D} = \frac{C_Y \cos \alpha - C_X \sin \alpha}{C_Y \sin \alpha + C_X \cos \alpha} \quad (36)$$

By imposing the pitch moment balance around the vehicle heat shield nose we have:

$$CM_Y = -\frac{x_{cp}}{L_{ref}} C_Y = -\frac{(2-\varepsilon)}{2L_{ref}} x_{cp} \cos \alpha \sin \alpha \sin^2 \varphi \quad (37)$$

where  $x_{cp}$  is the abscissa of the vehicle center-of-pressure (cp) that, as said before, is expected to be influenced by the real gas effects, thus affecting capsule trim angle and in turn its descent flight due to the lower aerodynamic efficiency of vehicle (Park et al., 1992). Then, for very high Mach numbers, say larger than five, SIM states that the aerodynamic characteristic of the capsule does not depend on vehicle velocity, but rather on the  $\alpha$  and the geometric angle of the body shape  $\varphi$ . Further expressions to compute lift and drag coefficients are:

$$C_D = C_{D_0} + 12(1 - C_{D_0}) \sin^2 \frac{\alpha}{2} - 6(6 - 5C_{D_0}) \sin^4 \frac{\alpha}{2} + 4(6 - 5C_{D_0}) \sin^6 \frac{\alpha}{2} \quad (38)$$

$$C_L = \left[ 2(1 - C_{D_0}) - (3 - \frac{5}{2} C_{D_0}) \sin^2 \alpha \right] \sin \alpha \quad (39)$$

## 8.2 CFD-based aerodynamics of CRV

Curves of aerodynamic efficiency and pitching moment coefficient are shown in Fig. 19. Note that,  $CM_Y$ , shows that the pitching moment derivative  $CM_\alpha$  is negative in the AoA range of 150-180 deg, signifying that the CRV is statically stable for this range of  $\alpha$  (provided that the capsule cg is close to the moment reference point).

Other numerical data, provided in (Crowder et al., 1969), are also reported to highlight the accuracy of results. As to the effect of chemical kinetics on CRV aerodynamics, Fig. 20 shows that at  $M_\infty=16$  no differences are expected for aerodynamic forces, passing from Dunn-Kang to Park kinetics. On the contrary, at  $M_\infty=19$  both  $C_L$  and  $C_D$  increase ranging from PG through DK and Park kinetics. Differences of about 2% and 5% are observed concerning the value of  $C_L$  and  $CM_Y$ , respectively. These conclusions for  $M_\infty=19$  are confirmed by the displacement of the abscissa of the vehicle centre-of-pressure ( $x_{cp}$ ) non-dimensionalized with respect to its value for MN (Viviani et al., 2010). The increase in  $C_p$  at the stagnation region and its decrease over the remaining region lead to a forward (toward nose) shift of centre-of-pressure, or equivalently, positive (nose-up) pitching moment, as the flow  $\gamma$  decreases.

Figure 20 also shows that at  $M_\infty=16$ , the  $x_{cp}$  in the case of PG solution decreases of about 10% with respect to the MN estimation and there are no differences between the values provided by both the chemical models. At  $M_\infty=19$ , instead, even if the value of  $x_{cp}$  in the case of PG solution decreases again of about 10% with respect to the MN estimation, the two chemical models provide values that differ from each other of about 2%. Note that the latter difference may be dangerous if neglected when designing vehicle thermal shield layout. Analyses of the effect of chemical kinetics on capsule aerodynamics at  $\alpha=28$  deg versus Mach number, can be found in (Viviani et al., 2010).

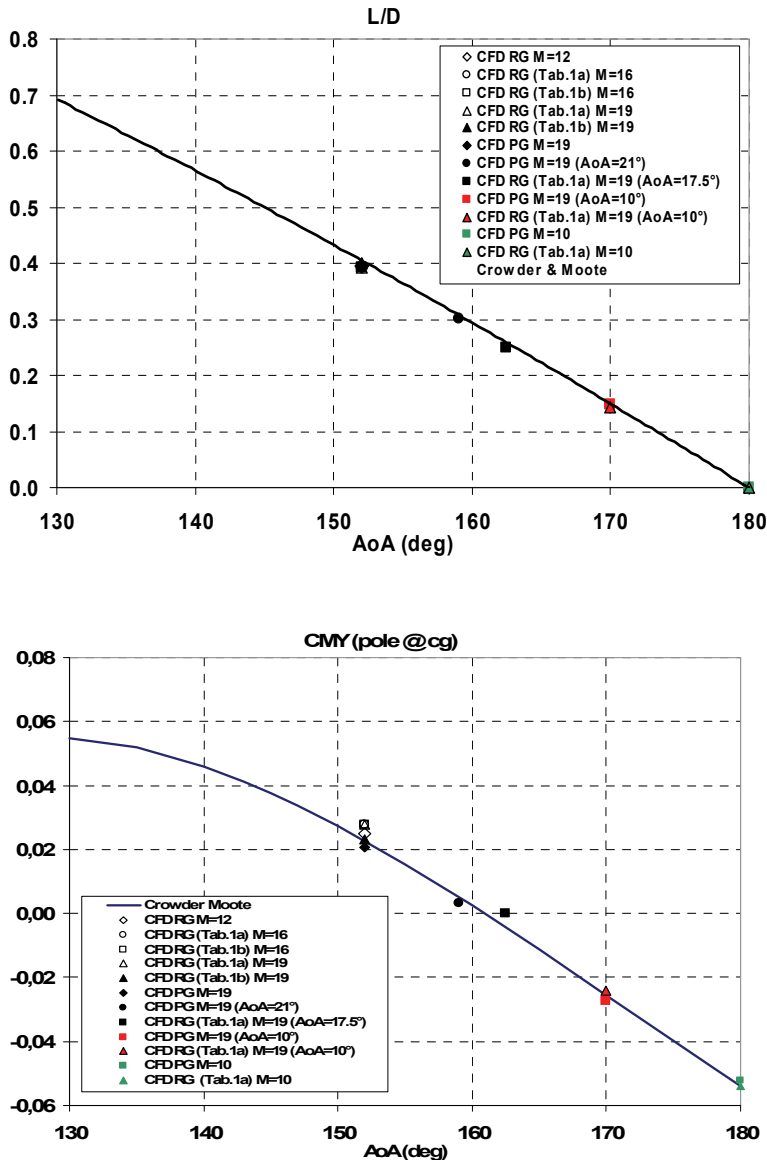


Fig. 19. Capsule L/D and  $CM_y$  versus  $\alpha$ . Comparison among present and literature data (Crowder et al., 1969)

Finally, Fig. 21 shows, in a step-by-step approach, the effects of reaction mechanism on CRV aerodynamics when the capsule is flying at  $\alpha=28$  deg,  $M_\infty=19$  and  $H=57$  km.

As shown, the results for Zeldovich model compare globally well with those of the complete reaction mechanism, i.e. 17 reactions. Such a result is very interesting considering that Zeldovich results differ from those of full reaction mechanism of 1% only for all the aerodynamic coefficients. In this case, in fact, the CPU time efficiency increases of about 40%. Therefore, the gain in terms of solution speed up is very high if compared to the loss in

accuracy of 1% only. The same consideration can be made in the case of aerodynamic results obtained in the case of  $O_2$ ,  $N_2$  and  $NO$  dissociation only, even if here the  $CM_y$  differs of about 5%. When results refer to  $O_2$  and  $N_2$  dissociation only, CPU time efficiency increases of about 45% but the  $CM_y$  accuracy evaluation is in the range of 10%. Finally, when aerodynamic coefficients account for only  $O_2$  dissociation the speed up efficiency reaches about 65%, whereas when flow dissociation is neglected (e.g., PG solution) the gain is nearly 70%. In this case, however,  $CM_y$  differs of about 15% and 25%, respectively. As a result, Fig. 21 highlights that CPU speed up depends on the accuracy expected in vehicle pitching moment assessment. Therefore, this confirms that  $CM_y$  is one of the most critical parameters within vehicle aerodynamic design.

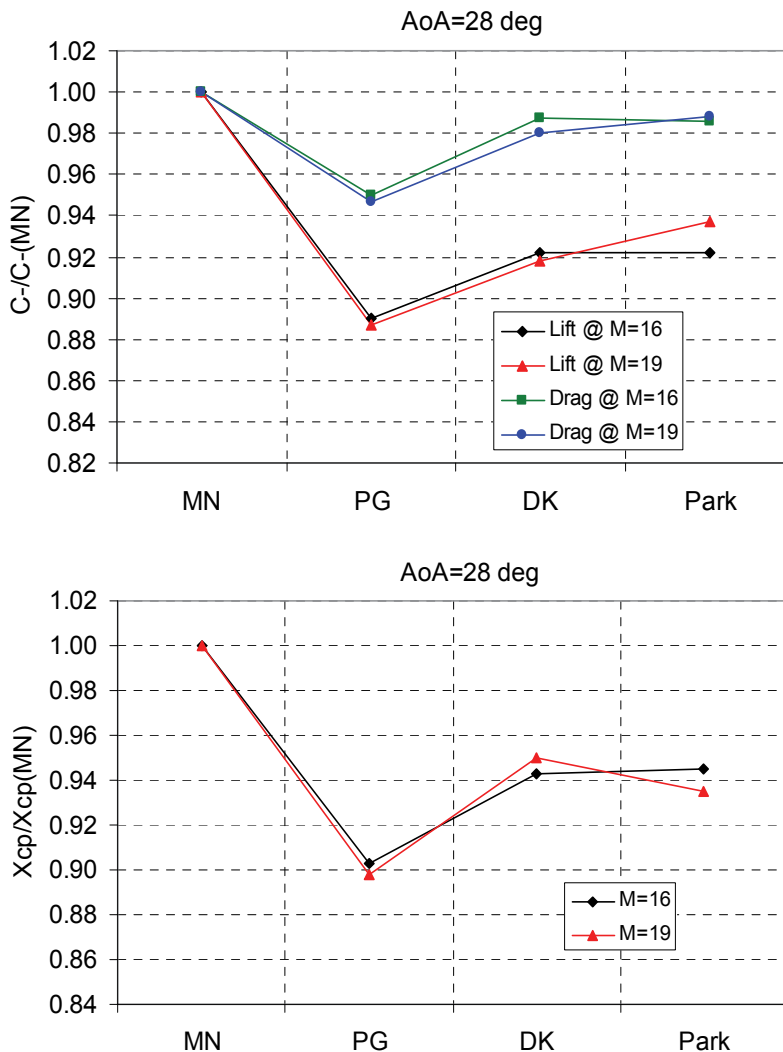


Fig. 20. Effect of chemical reactions on CRV aerodynamics at  $\alpha = 28$  deg for  $M_\infty = 16$  and  $M_\infty = 19$ . Comparison among MN, PG, Dunn-Kang and Park computations

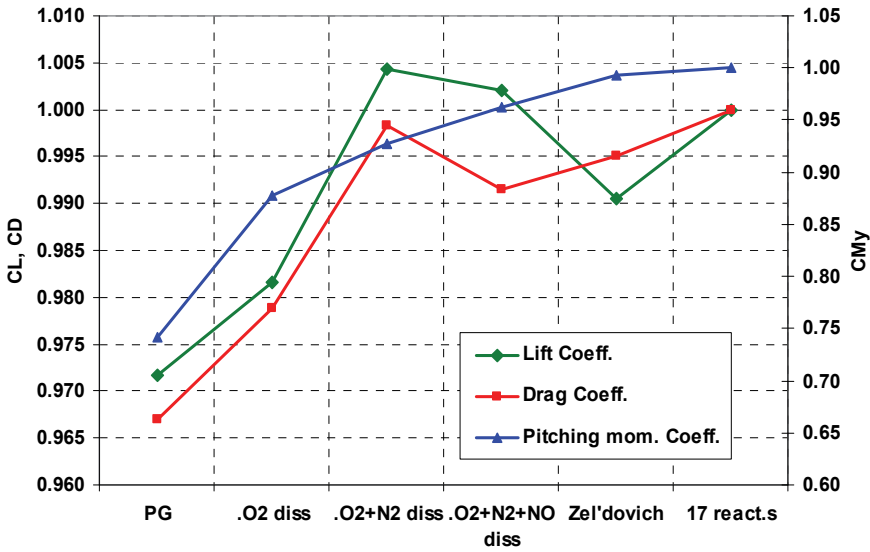


Fig. 21. Effects of reaction mechanism on CRV aerodynamics at  $\alpha=28$  deg,  $M_\infty=19$  and  $H_\infty=57$  km

**8.3 Free molecular flow and transitional aerodynamics of CRV**

Drag coefficients, evaluated by means of DSMC simulations, have been reported and compared in Fig. 22, with those assessed through a quick engineering estimation provided by a bridging relationship between FMF results and continuum ones. For instance, a very simple relationship to bridge the transitional flow regime from continuum regime to FMF reads:

$$C_{D\text{Transitional}} = C_{D\text{Continuum}} + (C_{D\text{FMF}} - C_{D\text{Continuum}}) \cdot \bar{C}_D \tag{40}$$

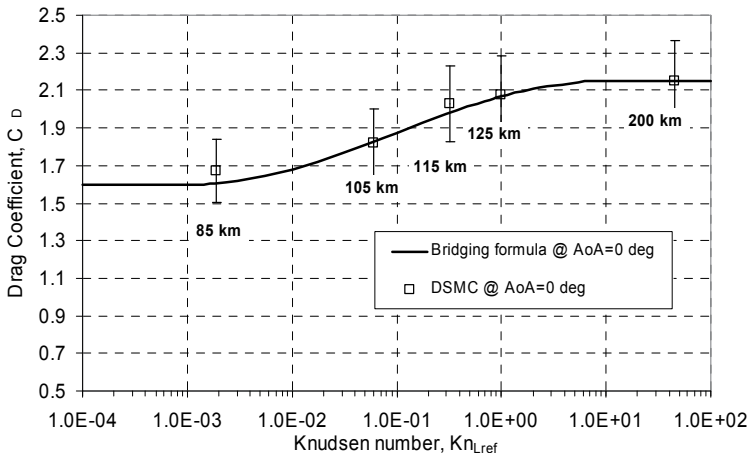


Fig. 22. Drag coefficients vs Knudsen number for  $\alpha=0$  deg (Pezzella et al., 2009)

where the normalized coefficient  $\bar{C}_i$  uses Knudsen number as the independent parameter:

$$\bar{C}_D = \frac{C_D - C_{D\text{Continuum}}}{C_{DFM} - C_{D\text{Continuum}}} = F(Kn_\infty) = \text{sen}^2 \left[ \frac{\pi}{8} (3 + \text{Log}_{10} Kn_\infty) \right] \quad (41)$$

$10^{-3} < Kn_\infty < 10$  and  $C_{D\text{Continuum}}$  and  $C_{DFM}$  are the aerodynamic drag coefficient in continuum and FM flow regimes, respectively.

The effect of rarefaction on the aerodynamic drag is clearly shown considering that  $C_D$  at  $\alpha=0$  deg increases of about 24% passing from 85 km to 125 km, whereas the drag at  $H=200$  km is 25% higher than the one at 85 km.

## 9. CRV aerothermodynamic features

The CRV aeroheating analysis reveals two critical regions on the vehicle surface (Viviani et al., 2007). They are the stagnation point (capsule flying at  $\alpha=0$  deg) and the vehicle side corner (capsule flying at  $\alpha \neq 0$  deg).

Several Navier-Stokes computations have been performed assuming the chemically reacting gas model, considering alternatively the heat shield surface as NC, PC and FC wall. The computations refer to fully laminar flow conditions with capsule surface temperature fixed at 300 K or in radiative equilibrium conditions. Note that, due to relatively low entry velocities (e.g., no radiation heat flux applies) only convective heat flux are taken into account. Moreover no heat shield ablation and recession were assumed for simplicity.

In order to illustrate the high temperature real gas effects in air, Fig. 23 shows the comparison of heat flux on the forebody centerline, in the cases of PG, EG and chemical non-equilibrium gas; for the latter case, the results for NCW and FCW are also reported. All these heat flux profiles are evaluated for cold wall conditions (e.g.,  $T_w=300$  K).

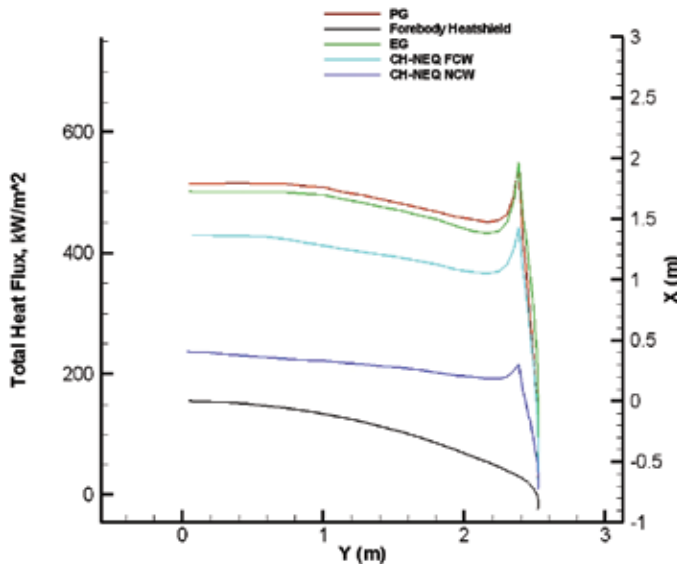


Fig. 23. Real gas effect on CRV forebody heat flux at  $\alpha=0$  deg,  $M_\infty=19$  and  $H_\infty=57$  km.  $T_w=300$  K

As shown, the wall heat flux is higher in the case of chemical equilibrium condition and it is closer to the heat flux for PG simulation. This can be explained considering that as the wall is cold, the chemical equilibrium leads to the recombination of dissociated atoms.

When the boundary layer (BL) is in chemical non-equilibrium, CFD simulations confirm that the higher heat flux is attained for FCW. As shown, this value is lower than that for EG, but it is very large compared with the case of NCW, as expected. Therefore, we can conclude that if the gas in the BL is in equilibrium (e.g., fast recombination) then a surface catalyst will not have any effect on the formation of molecules. In this case, in fact, atoms recombine and liberate their energy of dissociation to the gas in the BL. This added heat tends to increase the heat flux to the surface via thermal conduction, thus indicating that the recombination of atoms is more important than in the case of a FCW. For this reason, we regard the equilibrium condition as the reference condition in much of the state of the art TPS design activities.

The equilibrium condition hypothesis, however, may lead to an excessively conservative assessment of vehicle aeroheating. Therefore, realistic heat flux assessment over vehicle surface demands non-equilibrium flowfield computations with a full reaction mechanism, as wall catalyticity plays a significant role when assessing vehicle aeroheating.

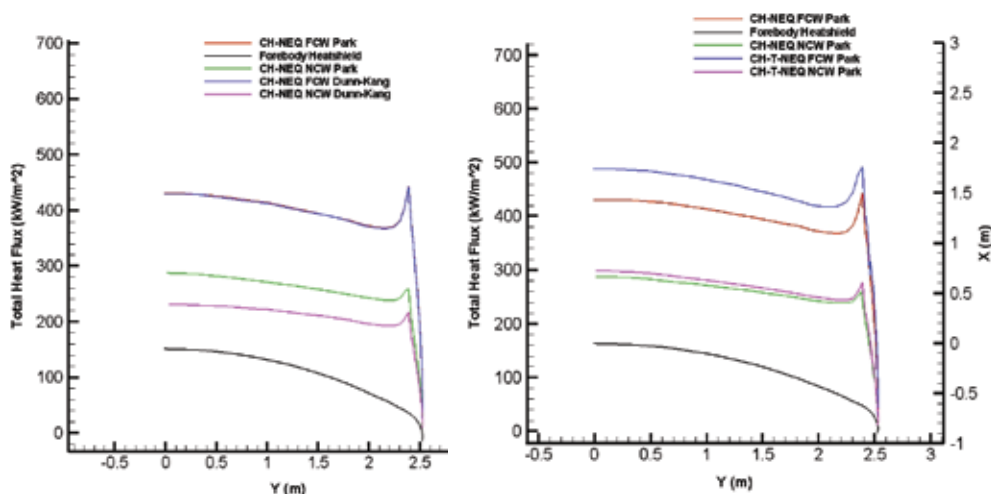


Fig. 24. Effects of chemical kinetics (left side) and of vibrational relaxation (right side) on capsule forebody total heat flux at  $\alpha = 0$  deg,  $M_\infty = 19$  and  $H_\infty = 57$  km for  $T_w = 300$  K

As far as effect of chemical kinetics is concerned, Fig. 24 shows that in the case of a FCW a large part of  $\dot{q}_c$  is due to the energy released by the recombination of atoms so that the influence of chemical kinetics is small. On the contrary the differences in the heat flux profile, as evaluated for NCW, underline that the role of reaction rate may be very important in order to assess vehicle aerodynamic heating. Therefore, we can conclude that the chemical model is negligible for a catalytic wall and is significant in the non-catalytic case. Of course the latter conclusion is expected depending on freestream conditions. For instance, at high altitude the shock layer has not dissociated since pressure and density are low. Therefore, the number of particle collisions is low so that the chemical reactions are not significantly activated (e.g., the flow is nearly frozen): there is not much energy involved in dissociation. Most of the energy is in translational modes. As flying altitude decreases the

density suddenly increases and the chemical reactions are activated. At very low altitude, the shock layer is so dense that the BL is close to equilibrium (e.g., atoms recombine in the BL before they have a chance to strike the wall). Hence, the BL is heated and there is more potential for heat transfer by conduction (i.e., reactions rate comeback to have a little effect). Figure 24 also displays the effect of vibrational relaxation on the wall heat flux. As shown, the heat flux profile in the case of FCW conditions depends on vibrational relaxation more than in the case of NCW (Viviani et al., 2007).

In order to illustrate the magnitude of the effects of catalytic activity on TPS, Fig. 25 shows the comparison of the heat flux along the forebody centreline at wall radiative equilibrium conditions, between the cases of FCW, PCW and NCW, in the case of lifting re-entry (3D computations). As one can see, the overheating caused by the catalytic action is potentially very large compared with the case of NCW. In particular, the largest difference occurs at the sphere-cone junction (corner fillet) where large changes in the flow gradients along the surface occur. Therefore, the corner radius is the dominant geometric feature for the convective heating (instead of heat shield radius of curvature), and it is confirmed that significant reduction in convective heat flux occurs if the thermal shield is built with a non-catalytic TPM.

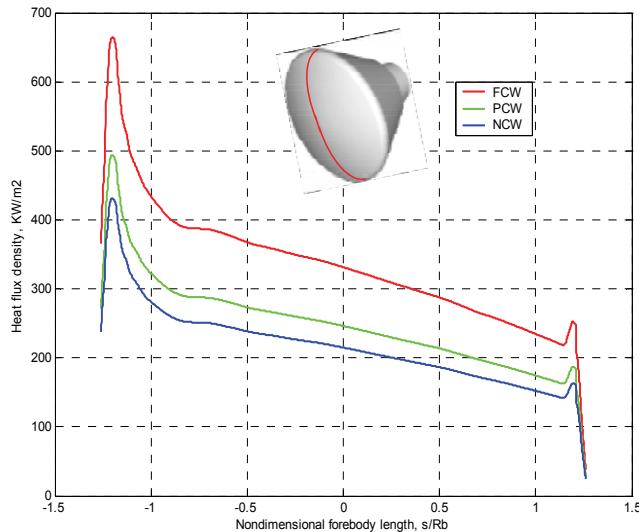


Fig. 25. Heat flux on the forebody OML. Nondimensional surface distance measured from centerline. Lifting trajectory. Vehicle trimmed at  $\alpha=20$  deg

## 10. Conclusions

Real gas effects on the design of a Crew Return Vehicle for the International Space Station have been taken into account. CFD analysis has been performed to simulate the re-entry of an Apollo-shaped capsule in order to determine the effect of thermal and chemical non-equilibrium on flowfield past the vehicle. Numerical results confirm that high temperature air conditions strongly affects both the aerodynamics and the aerothermodynamics of capsule. In particular, a comparison is made between CFD computations for perfect gas and reacting gas mixture, in order to bring into evidence the effects of finite rate chemistry, the

role of reaction mechanism with the related chemical kinetics and, finally, the influence of wall catalyticity. Model simplification is also investigated by considering a restricted set of predominant chemical reactions such as those of the Zeldovich model. Results comparisons for CRV aerodynamics confirm the strong effect of the real gas behavior on the capsule static stability. In particular, aerodynamic coefficients obtained with the Zeldovich model are within 1% of that of a solution with complete reaction mechanism, but the simulation speed up efficiency is of about 40 %. Therefore, the gain in terms of solution speed up is very high if compared with the loss in accuracy of 1% only. Anyway, in the framework of vehicle aerodynamics, the CPU speed up depends on the accuracy expected in vehicle pitching moment assessment thus confirming that the CM<sub>y</sub> is one of the most critical vehicle design parameters.

On the contrary as far as vehicle aerothermodynamic is concerned a reliable heat flux assessment over vehicle surface demands flowfield computations with a full reaction mechanism as wall catalyticity plays a significant role in the assessment of vehicle aeroheating.

Finally, the work underlines that the exact prediction of the heat transfer and chemical environment is crucial for the design of the vehicle TPS. In fact, the possibility of reducing the heat loads on the surface of space vehicles has been highlighted.

## 11. References

- Anderson, J. D. (1989). *Hypersonic and High Temperature Gas Dynamics*, McGraw-Hill Book Company, ISBN 0-07-001671-2, New York.
- Anderson, J. D. (1995). *Computational Fluid Dynamics: The Basics with Applications*, McGraw-Hill Book Company, ISBN 0-07-001685-2, New York.
- Anderson, L. A. (1973). Effects of Surface Catalytic Activity on Stagnation Heat Transfer Rates. *AIAA Journal*, Vol. 11, No.5, page numbers (649-656), doi: 10.2514/3.6806.
- Bertin, J. J. (1994). *Hypersonic Aerothermodynamics*, AIAA Education series, ISBN 1-56347-036-5, Washington.
- Crowder R. S.; Mootte J. D., (1969). Apollo Entry Aerodynamics. *Journal of Spacecraft and Rockets*, Vol. 6, No. 3, page numbers (302-307), doi: 10.2514/3.29589.
- Gnoffo, P. A.; Weilmuenster K. J.; Hamilton, H. H.; Olynick, D. R.; Venkatapathy, E. (1999). Computational Aerothermodynamic Design Issues for Hypersonic Vehicles. *Journal of Spacecraft and Rockets*, Vo. 36, No. 1, page numbers (21-43). doi: 10.2514/2.3430.
- Gnoffo, P. A.; Gupta, R. N.; Shinn, J. (1989). Conservation Equations and Physical Models for Hypersonic Air Flows in Thermal and Chemical Non-equilibrium. *NASA TP 2867*.
- Hassan, B.; Candler, G. V.; Olynick, D. (1993). Thermo-Chemical Non-equilibrium Effects on the Aerothermodynamics of Aerobraking Vehicles. *Journal of Spacecraft and Rockets*, Vol. 30, No. 6, page numbers (647-655). doi: 10.2514/3.26369.
- Lees, L., (1956). Laminar Heat Transfer over Blunt-Nosed Bodies at Hypersonic Flight Speeds", *Jet Propulsion*, Vol. 26, page numbers (259-269).
- Muylaert, J.; Walpot, L.; Wennemann, D. (1999). A Review of European Code-Validation studies in High-Enthalpy Flow. *Philosophical Transactions. The Royal Society. London*. A 357, page numbers (2249-2278).
- Olynick, D. (1998). Trajectory-Based Thermal Protection System Sizing for an X-33 Winged Vehicle Concept. *Journal of Spacecraft and Rockets*, Vol. 35, No. 3, page numbers (249-257). doi: 10.2514/2.3338.

- Park, C.; Lee Seung-Ho. (1993) Validation of Multi-Temperature Nozzle Flow Code Noznt. *Proceedings of the 28<sup>th</sup> AIAA Thermophysics Conferences*, Orlando (FL), USA. paper AIAA-93-2862.
- Park, C.; Yoont S. (1992). Calculation of Real-Gas Effects on Blunt body Trim Angles. *AIAA Journal*, Vol. 30, No. 4, page numbers (1146-1146). doi: 10.2514/3.48931.
- Pezzella, G.; Battista, F.; Schettino, A.; Marini, M.; De Matteis, P. (2007). Hypersonic Aerothermal Environment Preliminary Definition of the CIRA FTB-X Re-entry Vehicle. *Proceedings of the West-East High Speed Flow Field Conferences*; Moscow, RUSSIA. Nov. (19-22).
- Pezzella, G.; Votta, R. (2009). Finite Rate Chemistry Effects on the High Altitude Aerodynamics of an Apollo-Shaped Reentry Capsule", *16<sup>th</sup> AIAA/DLR/DGLR International Space Planes and Hypersonic Systems and Technologies Conference*, Bremen, Germany, Oct. 19-22. AIAA-2009-7306.
- Prabhu, D. K. (2004). System Design Constraints-Trajectory Aerothermal Environments. *RTO AVT/VKI Lecture Series in Critical Technologies for Hypersonic Vehicle Development*. Rhode St. Genèse, Belgium. May (10-14).
- Sarma, G. S. R. (1995). Aerothermochemistry for Hypersonic Technology. *VKI Lecture series 1995-04*. Rhode St. Genèse, Belgium.
- Scott, C. D. (1987). The Effects of Thermochemistry, Non-equilibrium, and Surface Catalysis in the Design of Hypersonic Vehicles. *1<sup>th</sup> Joint Europe-US Short Course on Hypersonic*. GAMNI-SMAI. Paris, France Dec. (7-11).
- Viviani, A.; Pezzella, G.; Cinquegrana, D. (2006). Aerothermodynamic Analysis of an Apollo-like Re-entry Vehicle. *Proceedings of the 14<sup>th</sup> AIAA/AHI Space Planes and Hypersonic Systems and Technologies Conferences*. 6-9 November, Canberra (AU); paper AIAA-2006-8082.
- Viviani, A.; Pezzella, G.; Borrelli, S. (2008). Effect of Finite Rate Chemical Models on the Aerothermodynamics of Re-entry Capsules. *Proceedings of the 15<sup>th</sup> AIAA Space Planes and Hypersonic Systems and Technologies Conferences*. 28 April-1 May, Dayton (OH); paper AIAA-2008-2668.
- Viviani, A.; Pezzella, G. (2007). Catalytic Effects on Non-Equilibrium Aerothermodynamics of a Re-entry Vehicle. *Proceedings of the 45<sup>th</sup> AIAA Aerospace Sciences Meeting and Exhibit*. 8-11 January, Reno, NE (USA); paper AIAA-2007-1211.
- Viviani, A., Pezzella, G. (2007). Influence of Surface Catalyticity on Re-entry Aerothermodynamics and Heat Shield. *Proceedings of the 39<sup>th</sup> AIAA Thermophysics Conference*. 25-28 June, Miami, FL (USA); paper AIAA-2007-4047.
- Viviani, A., Pezzella G. (2010). Computational Flowfield Analysis over a Blunt-Body Reentry Vehicle. *Journal of Spacecraft and Rockets*. Vol.47, No. 2, page numbers (258-270). ISSN 0022-4650. doi: 0.2514/1.40876.
- Walpot, L. (2001). Numerical Analysis of the ARD Capsule in S4 Wind Tunnel. *ESA SP.487*.

# Numerical Simulation of Liquid-structure Interaction Problem in a Tank of a Space Re-entry Vehicle

Edoardo Bucchignani, Giuseppe Pezzella and Alfonso Matrone  
*Centro Italiano Ricerche Aerospaziali, via Maiorise, 81043 Capua  
Italy*

## 1. Introduction

The current perspectives in the aerospace sector require a particular attention for the analysis of several phenomena involving the coupling between the mechanical behaviour and the other physics fields such as the fluid-structure interaction problem. This issue is particularly felt in the design of Reusable Launch Vehicle (RLV) since, during reentry, such kind of vehicles carries large quantities of Main Engine Cut Off (MECO) residual propellants. The management of the residual propellant remaining in the reusable stage after MECO during a nominal mission is a crucial point for the design with respect to: dimensioning and weight, landing safety issues, and post-landing procedures.

Generally speaking, the motion of a fluid inside the RLVs' tank (e.g. propellant sloshing) can affect the stability of the spacecraft and, when it is too much violent, could damage the structure, generating the vehicle failure. As a consequence, the structural design of propellant tanks should take adequately into account for the propellant slosh load in combination with all other loads and inputs. Therefore, there is a need for explaining what happens with a fluid subjected to loading environment of a typical RLV reentry trajectory (Bucchignani et al. 2008). Sloshing of propellants describes the free-surface oscillations of a fluid in a partially filled tank. These oscillations are due to lateral and longitudinal or angular motions of the spacecraft, as well as, when there are no tank disturbances, to the interchange of kinetic energy and the potential energies due to gravitational and surface tension forces (NASA, 1968). In particular, these free oscillations may persist since the damping provided by the wiping of the fluid against the tank's wall is negligible. Therefore, forced oscillations result in large free-surface waves. The magnitude of propellant sloshing depends upon the following parameters: acceleration field, propellant properties, tank geometry, effective dumping, height of propellant in the tank, and perturbing motion of the tank (NASA, 1968).

In recent times, the phenomenon of sloshing in partially filled tanks has been widely investigated by means of analytical methods or experimental techniques. The problem of small horizontal oscillations has been extensively investigated in the past, using analytical and experimental methods (Faltinsen et al., 2000) (Faltinsen et al., 2001). It has been shown that the response is the same as that of the undamped Duffing equation and changes from soft-spring (decreasing amplitude with increasing frequency) to hard-spring (increasing

amplitude with increasing frequency) behaviour as the ratio width–depth passes through a certain value. This value has analytically been determined (Faltinsen, 1974) and is given by  $L/H = 0.3374$ . On the other side, there is a lack in numerical simulations based on Computational Fluid Dynamics (CFD) codes, because they often require large amount of computational resources.

The goal of this chapter is to describe an innovative numerical method, based on a *multiphysics* approach, aimed to the simulation of an unsteady RLV-like tank configuration, such as liquid Oxygen (LO<sub>2</sub>) and/or liquid Hydrogen (LH<sub>2</sub>), subject to a typical reentry loading environment. The flow-field pressure and the stress field in the tank structure have been evaluated considering the motion of an incompressible fluid with a mobile free surface, in a tank with deforming walls under the action of the liquid pressure. An unsteady Finite Element formulation is used, instead, for modelling the tank. The global solution procedure uses a *multiphysics approach*, which allows to simultaneously simulate all the fields involved in order to capture the physical effects arising from the interaction phenomena. In particular, the coupling algorithm, based on a *semi-implicit staggered method*, belongs to the class of the partition treatment techniques, which allow solving the fluid and structural fields by means of two distinct models.

This paper is structured as follows: after a short overview of the theory of non-linear *sloshing* in par. 1.1, in Sec. 2 the mathematical model is discussed; Section 3 is dedicated to the numerical implementation and finally in Section 4 results related to several unsteady numerical simulations of the motion of a LO<sub>2</sub> and/or LH<sub>2</sub> propellant in a tank made of Aluminium-Lithium alloy (Al 2195) are presented: the main aim is the estimation of the pressures exerted by the sloshing fluid on the tank with the consequent stress field in the structure.

### 1.1 Theory of non-linear sloshing

The fluid motion in a partially filled tank forced to oscillate in a frequency domain close to its natural frequencies can be rather violent. The ratio between maximum free surface amplitude and characteristic tank motion amplitude is then high and significant non-linearities occur. The theoretical predictions by Faltinsen (Faltinsen et al., 2000) can be used as a basis for our studies. It is assumed that the tank is forced to oscillate with amplitude  $L \varepsilon \sin \omega t$  in the horizontal x-direction. The non-dimensional parameter  $\varepsilon$  assumes usually values between 0 and 0.05 and it is defined in order to express the smallness of the motion. Let  $\omega=2\pi/T$  be the circular frequency of the excitation signal. The wave amplitude response  $A$  of the lowest primary mode and the excitation period  $T$  are coupled by a cubic secular equation:

$$\left[ (T/T_1)^2 - 1 \right] (A/L) + m_1 (A/L)^3 = P_1 H \quad (1)$$

where  $T_1$  is the highest natural period of the tank,  $L$  is the tank width,  $H$  is the water depth,  $m_1$  is a function of  $H/L$  and  $T/T_1$ .  $P_1 H$  is a dimensionless excitation amplitude. It can be observed that this response is equal to the one of Duffing equation (Zeeman, 2000) and changes from soft-spring (decreasing amplitude with increasing frequency) to hard-spring (increasing amplitude with increasing frequency) behaviour as the ratio width–depth passes through a certain value, given by  $L/H = 0.3374$ . Fig. 1 shows typical hard-spring behaviour.

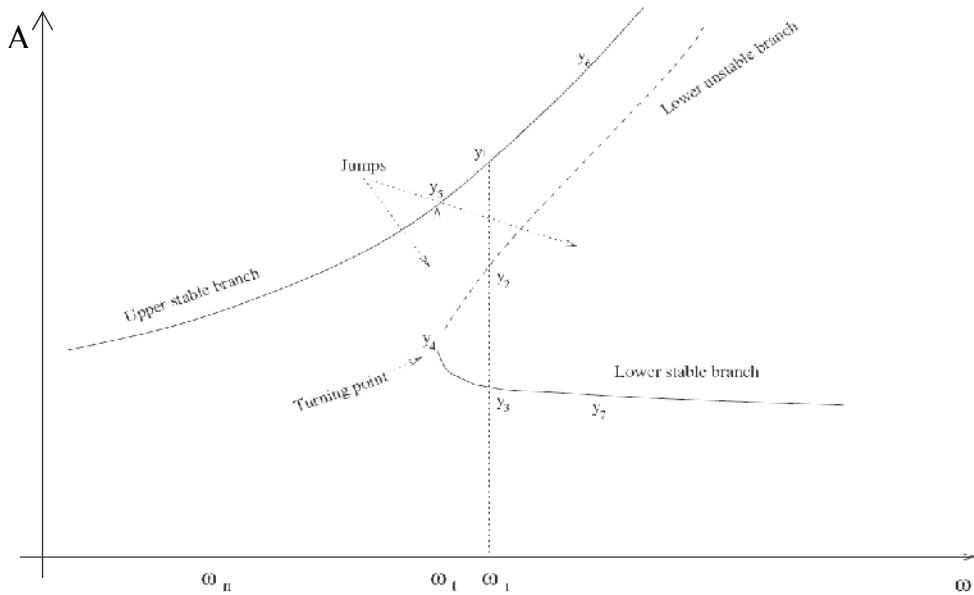


Fig. 1. The typical hard-spring behaviour

There exists a particular value of  $\omega$  (i.e.  $\omega_t$ ) such that the discriminant of the cubic equation is zero. For  $\omega < \omega_t$  the secular equation has only one real root. For  $\omega > \omega_t$  (e.g.,  $\omega_1$ ) there will be three real valued solutions. What solution the physical system will select depends on how the value  $\omega_1$  is approached. If one starts to oscillate the tank with a much lower frequency, the solution will be  $y_1$ . If one does the opposite, the solution will be  $y_3$ . The physical system never select  $y_2$  because it is an unstable solution. If we approach  $\omega_t$  from below and continue increasing  $\omega$ , the solution will suddenly jump from  $y_6$  to  $y_7$ . On the other hand, if one starts with a high frequency and decreases the frequency, the solution will follow the lower stable branch and suddenly jump from  $y_4$  to  $y_5$ .

The first (upper) branch implies stable solutions. The second (lower) branch displays stable and unstable steady-state solutions with a turning point between them. The turning point defines a jump from the lower to the upper branch. Another jump from the upper to the lower jump occurs as  $A/L$  increases along the upper branch. It defines a downshift of maximum wave amplitude response. This pair of jumps constitutes the hysteresis between two stable solutions.

## 2. Mathematical model

### 2.1 Fluid dynamics

The evolutions of waves on the surface of a fluid enclosed in a box are described by means of the equations governing the motion of the flow with appropriate boundary conditions. As we are considering structures with characteristic dimensions larger than those of characteristic wavelengths, the viscous effects and surface tension have been neglected, whilst non-linear free surface effects have been taken into account. It has also been assumed that the amplitude of the oscillations is small if compared with the wavelength of the perturbation and with the depth of the box. All the physical quantities are referred to a

coordinate system rigid with the tank, so in the case of a moving tank the apparent forces must be taken into account. The equation governing the motion of an irrotational incompressible flow is the classical Laplace equation:

$$\nabla^2 \phi = \frac{\partial^2 \phi}{\partial x^2} + \frac{\partial^2 \phi}{\partial z^2} = 0 \quad (2)$$

where  $\phi$  is the potential velocity and the components of the velocity vector  $\mathbf{u}(u,w)$  are given by:

$$u = \frac{\partial \phi}{\partial x} \quad w = \frac{\partial \phi}{\partial z} \quad (3)$$

Let  $\eta(x,t)$  be the function describing the wave height measured with respect to the undisturbed configuration (Fig.2). The boundary conditions are imposed in the following way:

- on the rigid walls, the compatibility condition on the velocity field is:

$$\mathbf{u} \cdot \mathbf{n} = \mathbf{u}_s \cdot \mathbf{n}$$

where  $\mathbf{n}$  is the outer normal to the boundary and  $\mathbf{u}_s$  is the velocity deformation of the wall.

- on the free surface, a cinematic and a dynamic conditions are imposed. The first one states that the velocity of the surface must be equal to the vertical component of velocity:

$$\frac{\partial \eta}{\partial t} + \frac{\partial \phi}{\partial x} \frac{\partial \eta}{\partial x} - \frac{\partial \phi}{\partial z} \Big|_{z=\eta} = 0 \quad (4)$$

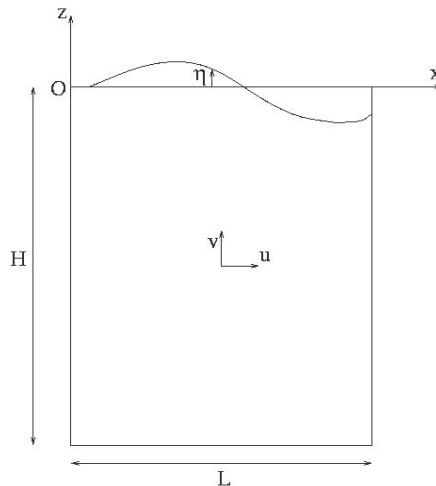


Fig. 2. Reference System for the Fluid

The dynamic condition states that the pressure on the free surface is equal to the external one (e.g., tank pressure). The Bernoulli theorem can be successfully used: if the volume

forces are reduced to the weight and the external pressure is set equal to zero, we obtain (Faltinsen et al., 2001):

$$\frac{\partial \phi}{\partial t} + \frac{1}{2} \left[ \left( \frac{\partial \phi}{\partial x} \right)^2 + \left( \frac{\partial \phi}{\partial z} \right)^2 \right] + g\eta + \frac{\partial \phi_c}{\partial t} = 0 \quad (5)$$

where  $g$  is the gravitational acceleration,  $\frac{\partial \phi_c}{\partial t}$  is the acceleration of the tank with respect to

an inertial coordinate system. This last term vanishes if the tank is motionless.

The Laplace equation and the boundary conditions have been set in non-dimensional form assuming the width of the tank  $L$  as reference length and a reference time equal to  $(L/g_0)^{1/2}$  ( $g_0$  is the gravity acceleration at earthly level). At the end of each time step, the liquid pressure on the solid walls is evaluated using the Bernoulli equation:

$$p = -\frac{\partial \phi}{\partial t} - \frac{1}{2} \left[ \left( \frac{\partial \phi}{\partial x} \right)^2 + \left( \frac{\partial \phi}{\partial z} \right)^2 \right] - gz - \frac{\partial \phi_c}{\partial t} \quad (6)$$

## 2.2 Structure

When the walls of a tank are thin, their vibrations under the effects of variable liquid pressure cannot be neglected. In this case it is essential to develop a mathematical model that keeps into account the deformations of the walls.

It is assumed that the tank is made up of an elastic isotropic material and that the constitutive law is the Hook's one.

The governing equations for the structure are the usual undefined equilibrium relations for continuous media. Under these hypotheses, a Finite Element discretization of the tank can be performed. If the displacement of the structure changes in the time, it is necessary to keep into account the inertial forces and the frictional resistances opposing the motion. These can be due to microstructure movements, air resistance etc. As a consequence, the equilibrium general condition for the structure in a Finite Element formulation assumes the following expression:

$$M\ddot{\vec{d}} + C\dot{\vec{d}} + K\vec{d} = \vec{f} \quad (7)$$

where  $\vec{d}$  is the displacement vector,  $M$ ,  $C$ ,  $K$  are respectively the mass matrix, the damping matrix and the stiffness matrix;  $\vec{f}$  is the force vector. All the matrices are obtained by assembling related to each element ( $M^e$ ,  $C^e$  and  $K^e$ ).  $K^e$  is obtained according with reference (Golub et al., 1990) as:

$$K^e = \int_s B^T D B ds \quad (8)$$

where  $B$  is the strain-displacement matrix and  $D$  is the material matrix (depending on the Young modulus  $E$  and on the Poisson coefficient  $\nu$  of the material).  $M^e$  is given by:

$$M^e = \int_s N^T \rho N ds \quad (9)$$

where  $\rho$  is the density and  $N$  is the shape function matrix. The definition of  $C^e$  is in practice difficult and therefore it is assumed that  $C^e$  is a linear combination of stiffness and mass matrices, that is:

$$C^e = \alpha M^e + \beta K^e \quad (10)$$

where  $\alpha$  and  $\beta$  are determined experimentally.

### 3. Numerical methodology

The flowfield has been solved using a time-dependent algorithm, in order to obtain accurate true transient solutions. A Fully Implicit approach has been adopted for the time integration in order to guarantee high stability to the method. As shown in (Guj et al., 1993) this kind of approach represents a useful compromise among numerical efficiency, robustness and flexibility in applications. Particular care has been adopted for the treatment of the non-linear conditions on the free surface (Zienkiewicz et al., 1977) (Zienkiewicz et al., 1977). Linearization has been performed by *freezing* one of the terms at the previous time step.

$$\frac{\partial \eta}{\partial t} + \frac{\partial \phi^*}{\partial x} \frac{\partial \eta}{\partial x} - \frac{1}{2} \left( \frac{\partial \phi^*}{\partial z} + \frac{\partial \phi}{\partial z} \right) = 0 \quad (11)$$

$$\frac{\partial \phi}{\partial t} + \frac{1}{2} \frac{\partial \phi^*}{\partial x} \frac{\partial \phi}{\partial x} + \frac{1}{2} \frac{\partial \phi^*}{\partial z} \frac{\partial \phi}{\partial z} + \frac{1}{2} g(\eta + \eta^*) = -\frac{\partial \phi_c}{\partial t} \quad (12)$$

Where all the quantities are considered at the current time step, with the exception of the quantities marked with a \* that are considered at the previous time step.

Few remarks can be made on this use of quantities evaluated at the previous time step. For what concerns the terms  $\partial \phi / \partial z$  and  $\eta$  respectively in the first and second equation, the discrete form is obtained following the well known Crank-Nicholson formula (Crank et al., 1947). Concerning the quadratic terms, since they are all non-linear, a linearization is required in order to approach the resulting algebraic problem with a linear solver. In this case one of the factors has been frozen at the previous time step, reducing the problem to a linear one (Galpin et al., 1986).

This technique guarantees a good coupling between all the equations.

As a result of the simplifying assumptions, the lack of viscosity may cause an undesirable contribution from the high frequency components to the numerical solution of the problem. This contribution is undesirable because the high frequency modes are poorly represented in the discretized system. As a consequence, a dispersion error may develop in the numerical solution. This effect may occur when the liquid is in the resonance zone or when the excitation level is relatively high. Numerical dissipation could be used to damp out the high frequency wave components propagating near the free surface, as proposed in (El-Zeiny, 2000). This strategy, however, has not been considered in the present work, as our goal is the investigation of the system for small amplitude oscillations. The Laplace equation has been discretized using a Finite Volume technique on a grid made up of quadrilateral elements. The computational grid is updated at each time step, in order to take into account the variation of the domain shape due to the movement of the free surface and of the solid walls. A transient procedure requires particular care, as the mass conservation could be

violated. The staggering of the variable location provides the maximum accuracy of the discretized derivatives and ensures the discrete conservation of mass at each time step. In fact, as shown in reference (Guj et al., 1993), it is possible to obtain mass conservation to round off error if the horizontal velocity is located at the middle of the vertical face of the computational cell and the vertical velocity is located at the middle of the horizontal face. As a consequence, the potential  $\phi$  is naturally located at the centre of the cell.

For what concerns the boundary conditions, spatial derivatives are discretized using two-point backward differences, while time derivatives are discretized using three-point backward differences. At each time step the original system of partial differential equations gives rise to a large linear system of equations of the type  $Ax=b$ , where  $x$  is the unknown vector. The coefficient matrix  $A$  has a large sparse structure. The solution of this linear system via a direct method is not recommended due to the size of the problem, so an iterative procedure has been preferred: the Bi-CGSTAB algorithm (Van der Vorst, 1992) (Gluck et al., 2001), associated with a ILU decomposition of the matrix  $A$  as preconditioner has been employed. The Bi-CGSTAB algorithm is an iterative method belonging to the class of the Krylov subspace methods; it has been chosen for its good numerical stability and speed of convergence even in dealing with non-symmetric problems, as shown in references (Stella et al., 1996).

The spatial discretization of the structure has been performed using triangular elements with linear shape functions. The discretization of the time derivatives has been performed using Finite Difference approximations with a three-point formula for the second-order derivative and a two-point formula for the first-order derivative. Also in this case, the large sparse linear systems arising from discretization at each time step are solved using the Bi-CGSTAB algorithm without preconditioning.

### 3.1 Coupling between fluid and structural fields: the Multiphysics approach

Multiphysics (Bucchignani et al., 2008) is the science that simultaneously studies two or more different physical problems which interact dynamically. Each interacting physical entity is named *component*. The collection of the single components constitutes the *dynamical system* to be studied.

Other investigators (Felippa, 2001) prefer the term *coupled field problems*, by idealizing the interacting components as fields. Generally, the denomination *Multiphysics* tends to be applied to computational physics problem, whereas coupled field problems to mechanics.

The numerical simulation of components (or fields) of a system (or a coupled problem) as isolated entities has been pursued and refined within of each separate discipline. The challenge of these last years is to solve simultaneously the whole system in order to capture the physical effects arising from the interaction. This approach requires innovative mathematical modelling, new numerical methods and a strong interdisciplinary approach.

The fields of a coupled problem are usually governed by partial differential equations in space and time. Three approaches to the time advancing of the whole system can be followed:

1. **Elimination:** At each time step one or more fields can be eliminated by appropriate techniques such as integral transform, and the remaining component solved by a standard time integration scheme.
2. **Partitioned integration:** The system components are treated as isolated entities which separately advance in time. Interaction effects are viewed as *forcing effects* during the time advancing. This approach can be of two types:

- **Loose or weak coupling.** Data generated by a system during its time advancing are used as input data from the other(s) system (one way interaction)
  - **Tight or strong coupling:** At each time step data generated by the single systems are exchanged among them (mutual interaction).
3. **Monolithic or simultaneous integration:** The whole system is treated as monolithic entity, that is the fields are coupled at the fundamental equation level and advance simultaneously in time.

The methodology proposed here for the solution of the fluid-structure interaction problems is based on a partitioned approach with a strong coupling. One of the advantages of the Partitioned methods is the software reuse to solve each field involved in the simulation (Felippa et al., 2001), whereas a monolithic approach requires the development of an unified mathematical model and therefore a dedicated software.

Another important advantage in the specific case is that a partitioned treatment preserves the different approaches used for CFD, that is based on an “eulerian” formulation, and Computational Structural Dynamics (CSD), which adopts a “Lagrangian” point of view.

The coupling between fluid and structure is obtained by using a semi-implicit *staggered algorithm* (Felippa et al., 2001) (Matthies et al., 2003).

A staggered method introduces an external (physical) time loop and considers the two solvers as partitions or sub-systems of the whole system to be solved. They can be classified as follows: explicit, when both solvers use the values computed at the previous time step; semi-implicit, when one of the two subsystems uses the values computed by the other solver; implicit, when both solvers use the values at the current time. In the latter case some linearization procedures have to be used.

In the applications of interest, there are other important problems to be considered, such as the data transfer between the different grids, the fluid domain deforming, which could be well represented by an ALE formulation, the relationship between the external time step and those used by each solver, which are limited by their stability regions.

Structural motions are typically dominated by low frequency vibration modes, which means that large time step can be used. On the other hand, the thermo fluid dynamics response must be captured in a smaller time scale because of unsteady effects involving shock, vortices, turbulence and chemical reactions. Thus, the use of a smaller time step for the fluid is natural. This device is called sub-cycling. The ratio of structural to fluid time steps may range from 10:1 through 1000:1, depending on the problem characteristics and the use of explicit or implicit fluid solver (Strain, 1999).

The semi-implicit staggered approach proposed in this work can be illustrated as follows:

```

do n= 1, ntime
| Call fluid (F(n-1),S(n-1),F(n))
| Call transf
| Call struct (S(n-1), F(n),S(n))
| Call grid_deforming
End do

```

where **fluid** and **struct** represent, respectively, the fluid and the structural solvers, **transf** the subroutine for the data transfer between fluid and structural fields and **grid-deforming** the subroutine which updates the fluid domain on the basis of the solid deformations. Details about these subroutine are given in the following.

As described above, in a general approach the CFD and CSD solvers use different formulations and discretizations. The two computational grids are not continuously interconnected, in the sense that the nodes on the interface of the fluid domain do not coincide with the ones of the interface of the solid domain (see Fig.3). Therefore, the data exchange between the two solvers is not immediate, but requires some interpolation operations. The data transfer from CFD to CSD is realized by evaluating the forces acting on the nodes of the solid interface starting from the values of the pressure in the nodes of the liquid interface. This operation must be performed carefully, in such a way that the global energy of the system is conserved.

To this end it is worth noting that the lateral sloshing of liquid propellant in a tank results in a distributed pressure loading on the walls, which is of importance for detailed structural design. Indeed, the forces acting on the CSD nodes are:

$$F_i = \int_S -N_i p_i n ds \tag{13}$$

where the pressure  $p_i$  in the CSD nodes is the integral of the liquid pressure on the faces of the CSD cells (Fig.4):

$$p_i = \frac{1}{\Delta x} \int_{x_i - \Delta x/2}^{x_i + \Delta x/2} p(x) dx \tag{14}$$

Otherwise, in many practical problems the liquid pressure distribution is rather regular and so it is convenient to have an analytical representation of the pressure distribution by means of a polynomial interpolation; in this case a second-order polynomial is adopted.

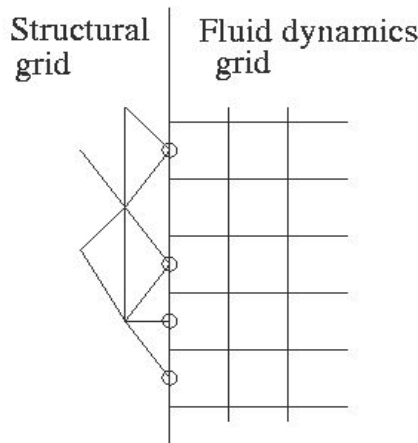


Fig. 3. Solid-fluid interface

The data transfer from CSD to CFD is less difficult and is performed by a simple data interpolation on the deformations. This is due to a better regularity of the physical phenomenon of structural deformation with respect to the pressure fluctuations.

The time-stepping algorithm works as follows. First, the partition method that we have developed performs a fluid dynamics simulation and the pressures on the solid walls and

displacements of the points of the free surface are evaluated. Then, data are transferred to the CSD solver and the structural simulation is performed, in order to evaluate the deformations of the tank. These values are transferred to the CFD solver to update the boundary conditions. Besides, it is now possible to draw the new shape of the CFD domain and to update the computational grid, performing a new time step and continuing the time marching procedure with a new CSD simulation (performed on the grid which has been updated on the basis of the previous deformations).

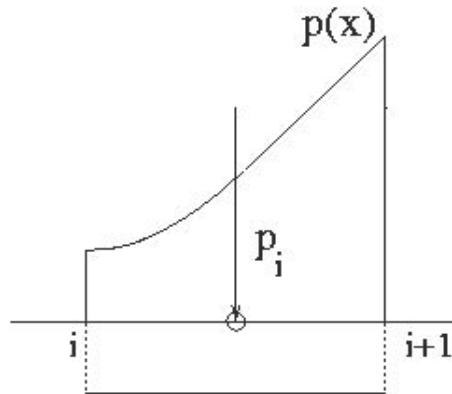


Fig. 4. Pressure distribution on a cell face

#### 4. Numerical results

As practical applications, several unsteady numerical simulations of the motion of a  $\text{LO}_2$  and/or  $\text{LH}_2$  propellant in a tank made of Aluminium-Lithium alloy (Al 2195) have been performed in order to estimate the pressures exerted by the sloshing fluid on the tank with the consequent stress field in the structure.

It is worth nothing that  $\text{LO}_2$  and  $\text{LH}_2$  propellant have been chosen considering that for RLV the higher thrust-to-weight ratio of other propellants such as  $\text{LO}_2$ -Kerosene are offset by their lower specific impulse, which leads to a higher propellant demand, higher launch mass and hence to a higher residual propellant.

The reentry trajectory, provided in Fig. 5, has been considered as a typical RLV flight scenario to take into account in the numerical simulations.

Among the specific critical issues that can be envisaged within RLV design, two basic ones are of general interest in the framework of fluid-structure interaction. They are:

1. the propellant management, since it influences the operability of a RLV considering the automatic fly-back and landing needs. Indeed, a large quantity of propellants filling the tanks determines high safety constraints.
2. the alternative between an aeroshell or loads-carrying tanks structures may heavily affect the vehicle design in terms of: launch mass, complexity, safety and operability.

Therefore, it can be influence sloshing analysis.

The post-MECO propellant management issue is even more important in case of mission abort, since the time available to expel the residual propellant in atmosphere may be extremely short.

#### 4.1 RLV reentry flight scenario

Figure 5 shows the nominal reentry scenario investigated to assess the fluid-structure interaction issue (Spies, 2003).

The RLV mission starts from launch site, where the two-stage-to-orbit (TSTO) vehicle lifts-off with all the engines running. Hence the upper stage separates from the booster and after MECO, it transports the payload into the final target orbit. At the end of mission, the reusable launcher follows a gliding downrange re-entry flight to a landing site.

When entering the densest layers of the atmosphere, the aerodynamic forces rapidly increase and, finally, stabilize the vehicle attitude at an angle of attack of about 30÷40 deg. In this trajectory phase, certain constraints typically apply. For instance, the dynamic pressure is confined below certain limits, the heat flux at stagnation point does not exceed the allowable value for the vehicle thermal protection system (TPS), the total load factor is smaller than the one bearable by the launcher structure design, etc. Those trajectory constraints identify the admissible flight envelope, well known as reentry corridor of the RLV, thus defining the most severe dimensioning criteria of the launcher.

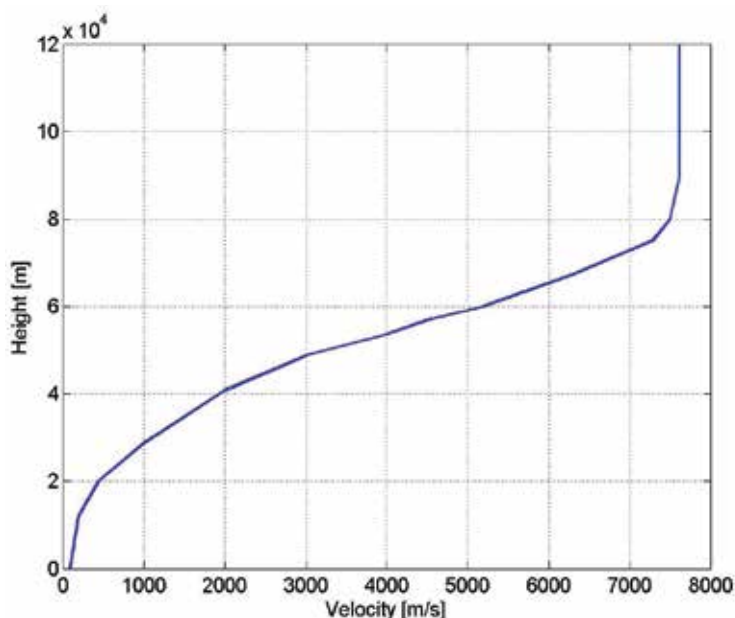


Fig. 5. Typical RLV re-entry trajectory in the Altitude-velocity map (Spies, 2003)

During reentry, the launcher decelerates taking advantage of aerodynamic forces (e.g., lift and drag) by flying at an angle of attack (AoA)  $\alpha$ , thus performing a gliding descent.

The free body diagram of the RLV is recognized in Fig.6.

Then, at the peak deceleration region, it must be noted that by imposing the equilibrium both in the axial (A) and lateral (L) direction, it results that:

$$\begin{cases} A_A = |\bar{a}_A - \bar{g} \sin \varphi| \cong |(0.1 \div 0.3) \bar{g}_o| \\ A_L = |\bar{a}_L + \bar{g} \cos \varphi| \cong |(2.0 \div 3.0) \bar{g}_o| \end{cases} \quad (15)$$

where the value of the gravity acceleration at the flight altitude  $H$  is determined according with the well known formula:

$$g = g_0 \left( \frac{R_{Earth}}{R_{Earth} + H} \right)^2 \quad (16)$$

where  $g_0$  is sea level acceleration (e.g., 9.81 m/s<sup>2</sup>),  $R_{Earth}$  is the Earth's radius (e.g., 6378 km). Note that, the gliding descent helps to mitigate the acceleration environment that the vehicle has to withstand during descent.

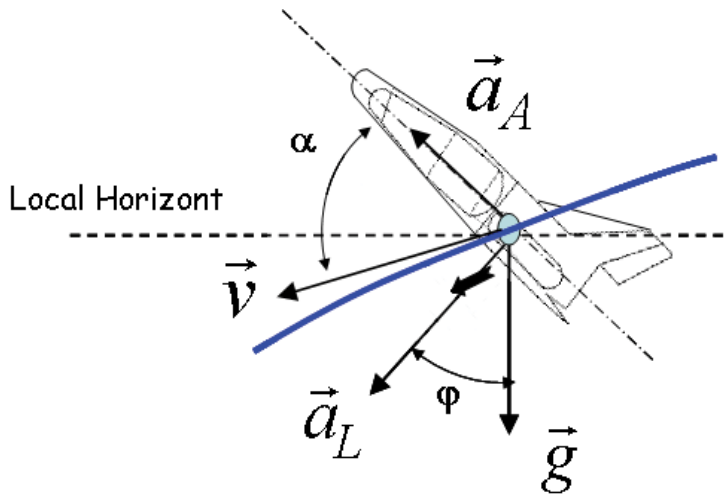


Fig. 6. Typical RLV free body diagram

So, as the lowest sloshing frequency corresponds to the lateral excitation of the tank (lateral sloshing), the design considerations are generally governed by the lateral slosh (NASA, 1968). In this case the linear theory of sloshing in rigid tanks states that, on the tank is applied a time dependent pressure, which is a function ( $f_1$ ) of:

$$p = f_1(p_{Tank}, y, \rho \eta A_A \sin \omega t) \quad (17)$$

where  $\omega$  is the fundamental lateral frequency (sloshing frequency),  $p_{Tank}$  is the tank pressurization,  $\rho$  is the fluid density, and  $y$  is the free-surface height.

For a rigid cylindrical tank, the second-mode sloshing mass is only about few percent of the first-mode sloshing mass; therefore, the second and higher mode sloshing effects are generally negligible (NASA, 1968). This means that the resulting fluid force decreases rather substantially in the higher modes of oscillation.

In particular, in the case of rigid cylindrical tank with a flat bottom, the frequency rad/s of free-surface motion is a function ( $f_2$ ) of:

$$\omega_n = f_2 \left( \epsilon_n \frac{h |\vec{a}_A|}{R_{Tank}} \right) \quad (18)$$

where  $\varepsilon_n$  is a coefficient that take into account for the slosh mode,  $h$  is the height of quiescent fluid surface and  $R_{Tank}$  is the tank radius. For example, when  $h \gg R_{Tank}$  we have that (NASA, 1968):

$$\omega_n \cong \sqrt{\varepsilon_n \frac{|\bar{a}_A|}{R_{Tank}}} \quad (19)$$

Moreover, Eq. (19) can be used to estimate the natural sloshing frequency of tanks of many other shapes, filled to various heights (NASA, 1968).

For what concerns numerical simulations, the test cases presented herein assume that the undeformed tank and flow are the ones shown in Fig. 7 (Bucchignani et al., 2008).

The external dimensions are  $L=5$  m and  $H=1$  m in the case of  $LO_2$  tank while  $L=15$  m and  $H=3$  m for the  $LH_2$  tank. The walls are made up of Al 2195 (e.g., Young module:  $E=84000$  MPa at 20 K, 83100 MPa at 80 K, and 76000 MPa at 300 K; Poisson module:  $\nu=0.33$ , and density  $\rho_{Al2195}=2700$  Kg/m<sup>3</sup>) and are characterized by a thickness section  $s=0.1$  m ( $LO_2$ ) and  $s=0.3$  m ( $LH_2$ ). The frictional resistance opposing the motion is neglected. The density of  $LO_2$  is  $\rho_{LO_2}=1300$  Kg/m<sup>3</sup>, while the one of  $LH_2$  is  $\rho_{LH_2}=3$  Kg/m<sup>3</sup>.

The fluid dynamics domain, in the undisturbed configuration, ranges from 0.1 m to 4.9 m in the horizontal direction, and from 0.1 m to 0.8 m in the vertical direction for the  $LO_2$  sloshing.

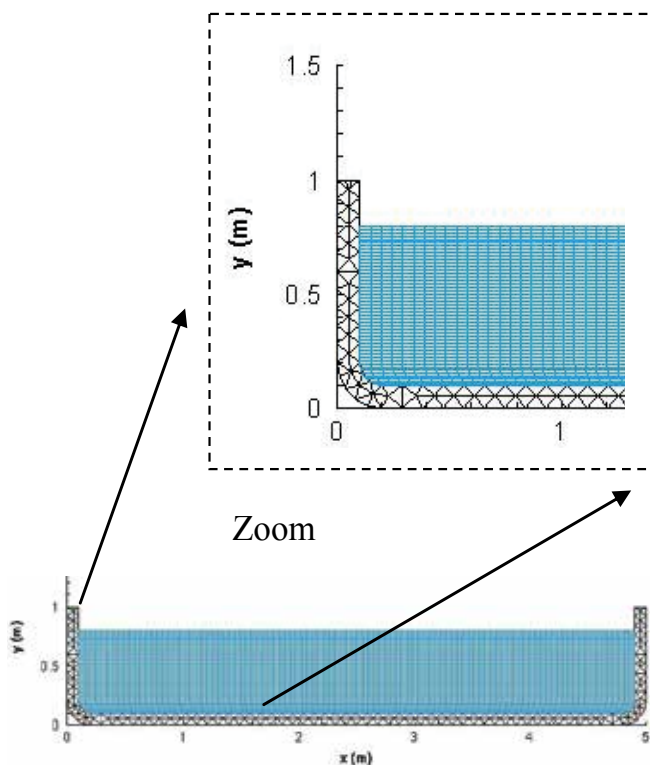


Fig. 7. The computational grid for the structure-flow in the case of  $LO_2$  test case

For the CFD solver, a grid with 101 by 51 nodes has been adopted, while for the CSD solver an unstructured grid of 238 nodes and 312 elements is used. These grids (undisturbed configurations - see Fig.7) have been generated by means of the commercial code ANSYS ICEM CFD 10.

The time step is set equal to  $10^{-3}$  (non-dimensional units).

Figure 8 shows the deformed grid as evaluated automatically by the code during the time stepping.

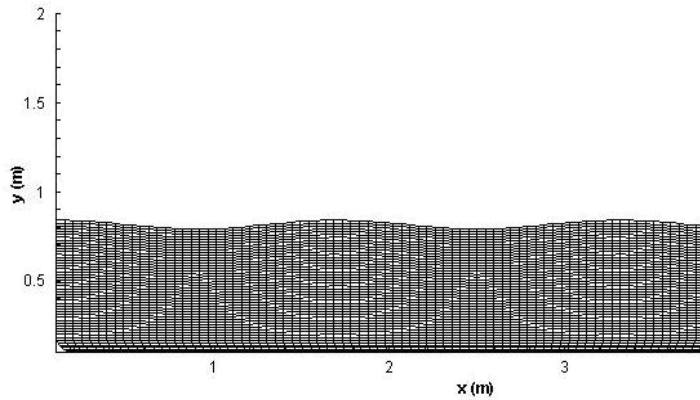


Fig. 8. The computational grid for the fluid

The deviation with respect to tank pressure  $p_{\text{Tank}}=120$  kPa for  $\omega=2\pi$  is recognized in Fig. 9 (up) and Fig. 9 (down) for  $\text{LO}_2$  and  $\text{LH}_2$  simulation, respectively. These results refer to the time  $t=3$  [min].

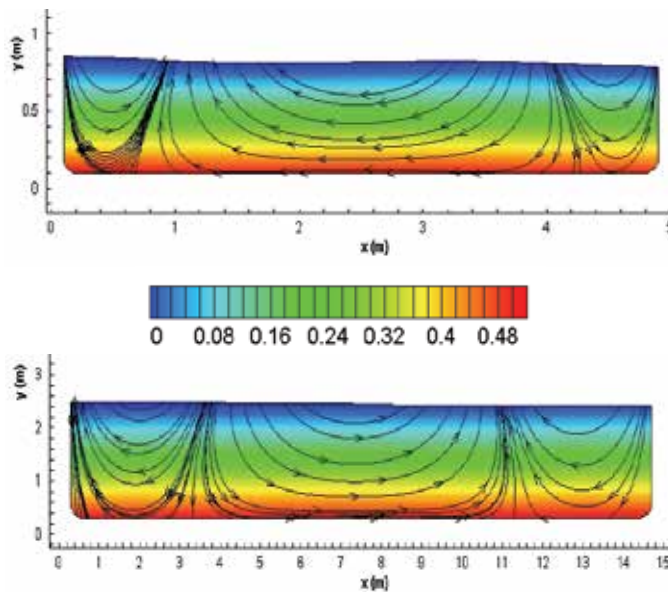


Fig. 9. Streamlines at a fixed time step superimposed on the pressure field in the plane of oscillation.  $\text{LO}_2$  simulation (up) and  $\text{LH}_2$  (down)

This distributed pressure loading on the walls is of importance for detailed structural design, since it resulted in a stress field in the tank structure, as recognized in Fig. 10 for the case of LH<sub>2</sub>, and in Fig.11 for the case of LO<sub>2</sub> (Bucchignani et al., 2008).

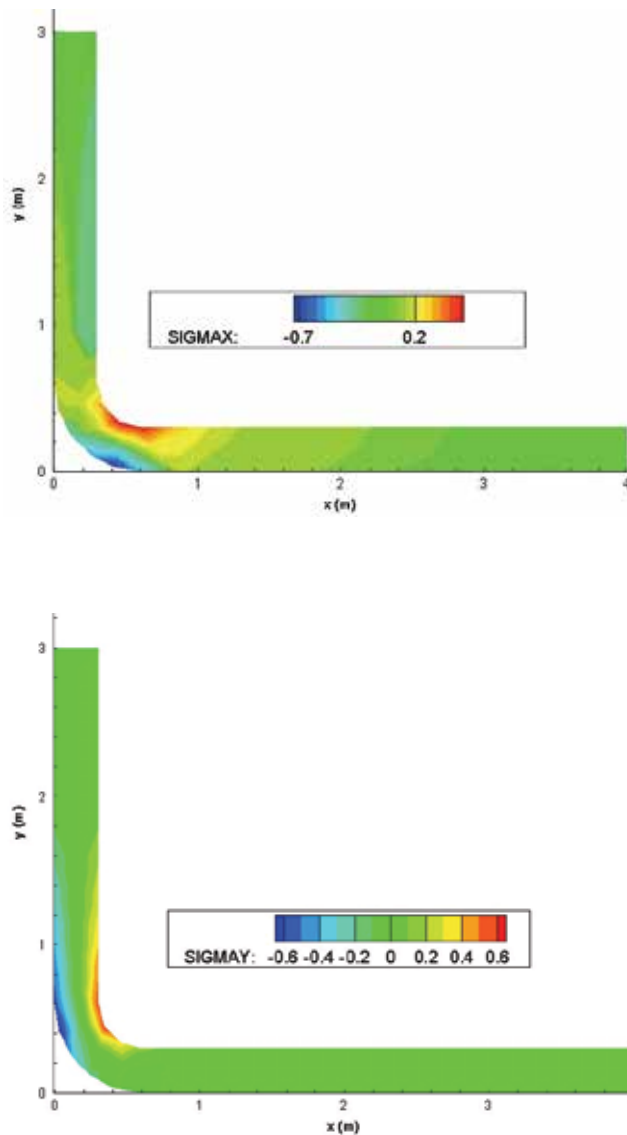


Fig. 10.  $\sigma_x$  and  $\sigma_y$  tensions field (MPa) in the plane of oscillation. LH<sub>2</sub> simulation

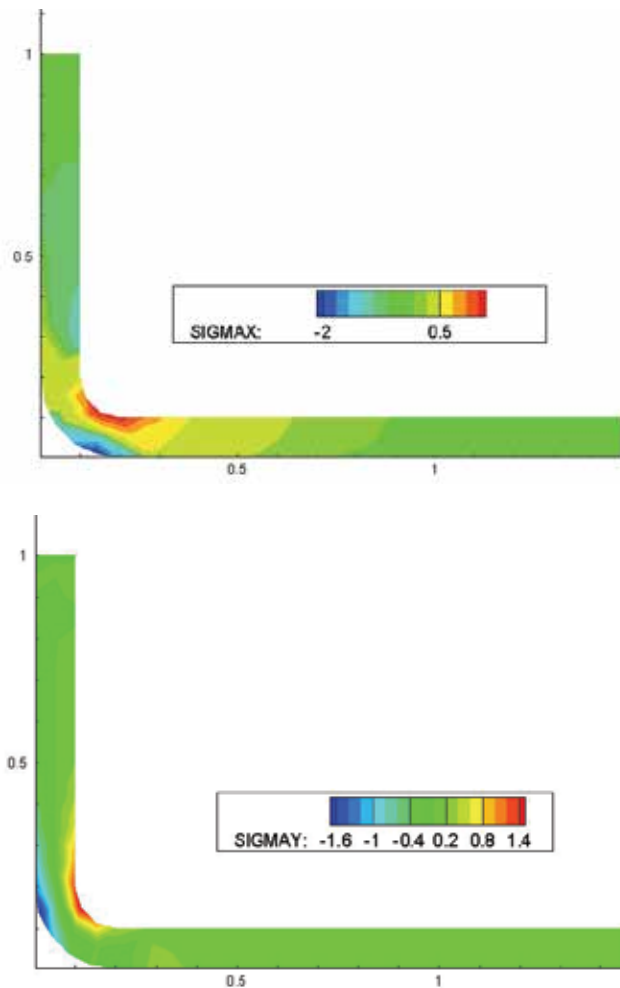


Fig. 11.  $\sigma_x$  and  $\sigma_y$  tensions field (MPa) in the plane of oscillation. LO<sub>2</sub> simulation

## 5. Conclusions

A software environment for the analysis of coupled liquid-structure fields has been developed. A staggered partitioned procedure has been employed using finite volume (FV) for the fluid and finite element (FE) for the structure.

A tank configuration typical of RLV has been considered. It is filled with liquid propellant such as LH<sub>2</sub> and/or LO<sub>2</sub>. Stress distributions in the structure and flow field in the liquid phase have been shown as well as transient history of structure displacement. Maximum stress as a function of maximum acceleration has also been shown and compared with structure limit.

In the future, it is our intention to implement a sub-cycling strategy in order to reduce the computational time, and to develop a fully implicit staggered scheme based on a Newton-Krylov algorithm.

## 6. References

- Bucchignani, E., Stella, F., Paglia F. (2004). A Partition method for the solution of a coupled liquid structure interaction problem. *Applied Numerical Mathematics*, Vol. 51, No. 4, page numbers (463-475), ISSN:0168-9274.
- Bucchignani, E.; Pezzella, G.; Matrone, A. (2008). Numerical Simulation of Liquid-Structure Interaction Problems in a Tank for Aerospace Applications. *Sixth European Symposium on Aerothermodynamics for Space Vehicles*. Palais des Congrès, Versailles, France. 3-5 November 2008.
- Cranck, J.; Nicholson, P. (1947). A practical method for numerical evaluation of solutions of partial differential equations of the heat conduction type, *Proc. The Cambridge Philosophical Soc.* Vol. 43, No. 50, page numbers (50-67).
- El-Zeiny, A. (2000). Nonlinear Time-Dependent Seismic Response of Unanchored Liquid Storage Tanks, PhD Thesis, Irvine, University of California, 2000.
- Faltinsen, O. (1974). A nonlinear theory of sloshing in rectangular tanks, *Journal of Ship Research*. Vol. 18, No. 4, page numbers (224-241).
- Faltinsen, O.; Rognebakke, O.; Lukowsky, I.; Timokha, A. (2000). Multidimensional modal analysis of nonlinear sloshing in a rectangular tank with finite water depth. *Journal of Fluid Mechanics*. Vol. 407, page numbers (201-234).
- Faltinsen, O.; Timokha, A. (2001). An adaptive multimodal approach to nonlinear sloshing in a rectangular tank. *Journal of Fluid Mechanics*, Vol. 432, page numbers (167-200). ISSN:0022-1120.
- Felippa, C.A.; Park, K.C.; Farhat, C. (2001). Partitioned analysis of coupled mechanical systems, *Computer methods in applied mechanics and engineering*, Vol. 190, No. 24-25, page numbers (3247-3270). ISSN: 0045-7825.
- Galpin, P.F.; Raithby, G.D. (1986). Treatment of non-linearities in the numerical solution of the incompressible Navier-Stokes Equations. *International Journal of Numerical Methods in Fluids*. Vol. 6, No. 7, page numbers (409-426).
- Gluck, M.; Breuer, M.; Durst, F.; Halfmann, A.; Rank, E. (2001). Computation of fluid-structure interaction on lightweight structures, *Journal of Wind Engineering and Industrial Aerodynamics*, Vol. 89, page numbers (1351-1368). ISSN:0167-6105.
- Golub, G.; van Loan, C. (1990). *Matrix computations*, The John Hopkins University Press. Baltimore, Maryland 21218-4363. ISBN:0-8018-5414-8.
- Guj, G.; Stella, F. (1993). A Vorticity-Velocity method for the numerical solution of 3D incompressible flows, *Journal of Computational Physics*, Vol. 106, No. 2, June 1993, page numbers (286-298). ISSN: 0021-9991.
- Matthies, H. G.; Steindorf, J. (2003). Partitioned Strong coupling algorithms for fluid-Structure Interaction., *Computers and Structures*, Vol. 81, No. 8-11, page numbers (805-812)
- NASA (1968). Propellant slosh loads. *NASA SP-8009*.
- Spies, J. (2003). RLV Hopper: Consolidated System Concept, *Acta Astronautica*. Vol. 53, No. 4, page numbers (709-717). ISSN: 0094-5765.
- Stella, F.; Bucchignani, E. (1996). True transient vorticity-velocity method using preconditioned Bi-CGSTAB, *Numerical Heat Transfer Part B*. Vol. 30, page numbers (315-339).
- Strain (1999). Three Methods for Moving Interfaces. *Journal of Comp. Physics*, 151, page numbers (616-648).

- Van der Vorst, H. (1992). Bi-CGSTAB, a fast and smoothly converging variant of Bi-CG for the solution of nonsymmetric linear systems, *SIAM J. Sci. Stat. Comput.* Vol. 13, No. 2, page numbers (631-644).
- Zienkiewicz, O.; Taylor, R.L. (1977). *The Finite Element Method Vol.1*, McGraw-Hill Book Company.
- Zienkiewicz, O.; Taylor, R.L. (1991). *The Finite Element Method Vol.2* (Fourth Edition), McGraw-Hill Book Company.
- Zeeman, E. (2000). Duffing's equation: catastrophic jumps of amplitude and phase, Lectures available at: <http://www.math.utsa.edu/~gokhman/ecz/duffing.html>.

# Three-Dimensional Numerical Simulation of Injection Moulding

Florin Ilinca and Jean-François Héту  
*National Research Council, Industrial Materials Institute  
Canada*

## 1. Introduction

Injection moulding of polymeric materials is an important manufacturing process used to produce cost effective parts for a large number of industries. Very often, moulded parts must satisfy stringent quality requirements in terms of mechanical behaviour and dimensional characteristics. Numerical simulations are cost effective and provide quick solutions, thus being an inevitable tool for the design and evaluation of the processing parameters. Numerical investigations are able to estimate aspects of the physical model which otherwise would be difficult to quantify. *What if?* tests give information on the effect of process parameters on the final part and provide setup conditions to obtain the optimal process and final part characteristics.

The injection moulding cycle can be described as being formed by three main stages: filling, packing-holding and cooling. During the initial filling stage, when the molten polymer fills the cavity, compressibility effects are small and the flow is usually considered incompressible. During this phase, non-isothermal effects are important, even if they are concentrated in boundary layers close to the mould-cavity interface. Once the entire cavity is filled, the process enters the packing-holding stage during which a much larger pressure is applied on the material. At this point a compression occurs and the solution behaviour is driven by the polymer compressibility. The compression phase is very short but results in dramatic changes on the nature of the polymer flow in the cavity. Velocities may take values comparable with those during the filling stage, while the pressure increase propagates into the entire cavity. As soon as the pressure reaches its maximum value, the velocity amplitude falls. It is the beginning of the holding stage during which compressibility effects are still important. The inflow of material must compensate for the decrease of the specific volume from cooling. The polymer in the gate then freezes and the mass of polymer in the cavity is set. The physics during the remaining cooling phase are modeled by the energy and state equations.

Co-injection moulding involves injection of skin and core polymer melt into a mould cavity such as the core material is embedded within the solidified layers of the skin material. The process has the potential of providing optimal properties of the moulded part by using a proper combination of the skin and core materials. It may also reduce part weight, part cost, injection pressure, residual stresses and warpage when comparing with the traditional single material injection moulding. Co-injection moulding popularity increased over the last years as recent developments in machines, materials and design concepts made the process more flexible and useful. In gas-assisted injection moulding, gas is injected into the cavity in the place of a second polymer melt. Gas-assisted injection demands lower injection-packing

pressure, smaller cooling times and less moulding material resulting in smaller part weight. Gas-assisted moulded parts present more uniform properties, reduced shrinkage, warpage and residual stresses. Therefore, better final products are produced at lower costs.

A faithful model and numerical simulation of the material behaviour during injection is extremely important in order to predict with confidence the characteristics of the final product. Most of the work done to simulate the injection moulding process was performed by using the Hele-Shaw approximation (Kamal et al., 1975; Hieber & Shen, 1980; Chen & Liu, 1994; Chen & Hsu, 1995; Chen et al., 1995; Han & Im, 1997; Gao et al., 1997; Schlatter et al., 1999). Such approach is unable to predict fountain flow, transverse pressure gradients, and simplifies the modeling near corners, bifurcations and changes in the part thickness. In recent years there is increased interest in the 3D modeling for an accurate representation of the material behaviour (Hétu et al., 1998; Ilinca & Hétu, 2001; Ilinca et al., 2002; Kim & Turng, 2004; Polynkin et al., 2005). This chapter presents a full 3D numerical approach to solve the injection moulding process. The methodology is perfectly well suited for three-dimensional parts for which simplifying lubrication hypothesis are inappropriate, for modeling multi-material injection or processes presenting jetting and folding of the material inside the cavity. In addition to traditional injection moulding applications, examples are shown for the simulation of gas-assisted injection moulding, co-injection moulding and injection moulding of metallic powders. Numerical solutions of the transient, three-dimensional, free surface flow and heat transfer equations describing the material behaviour during injection are obtained by a stabilized finite element method on unstructured grids and compared with experimental data.

## 2. Numerical modelling

### 2.1 Assumptions

The constitutive equations represent the thermal and mechanical behaviour of isotropic amorphous polymers during the filling stage of the injection moulding process. We resume here the main considerations behind the choice of model equations described in this section. The maximum pressure drop encountered during the filling of most plastic parts is about  $10^6$  to  $10^7 Pa$ . Considering that the compressibility coefficient of most polymer melts is of the order of  $10^{-9} Pa^{-1}$ , one can conclude that compressibility effects can be neglected. During the filling stage the polymer melt is thus considered incompressible. Second, the mechanical behaviour of an amorphous polymer in shear dominated flows (such as in injection moulding and co-injection) can be described reasonably well by a generalized Newtonian fluid model. This assumption has been validated numerically by (Baaijens & Douven, 1991) who showed that flow kinematics predicted by viscoelastic approach do not significantly differs from the one obtained using a generalized Newtonian approach. This is also in agreement with experimental observations of (Janeschitz-Kriegl, 1983) and (Wimberger-Friedl & Janeschitz-Kriegl, 1988).

Polymer melts have a surface tension  $\sigma$  between 20 and  $50 mN/m$  (Wu, 1991) and viscosities are of the order of  $10^3 Pa \cdot s$ . Velocities at the interface are of the order of  $0.02 m/s$  leading to a Capillary number  $Ca = \eta V / \sigma$  of the order of  $O(10^3)$ . Similar dimensional analysis leads to Reynolds numbers (ratio of inertia to viscous forces) in the range of  $10^{-4}$  to  $10^{-2}$ . One can conclude that viscous forces dominate and that both inertia and surface tensions can be neglected in the momentum equation. Meanwhile, given the small thermal conductivity of polymers, the Peclet number takes very large values, in the range of  $10^3$  to  $10^5$ , and the inertia has to be taken into account in the energy equation.

**2.2 Governing equations**

The equations governing the incompressible melt flow are the Stokes and continuity equations

$$0 = -\nabla p + \nabla \cdot [2\eta\dot{\gamma}(\mathbf{u})], \tag{1}$$

$$-\nabla \cdot \mathbf{u} = 0, \tag{2}$$

where  $\dot{\gamma}(\mathbf{u}) = (\nabla\mathbf{u} + \nabla\mathbf{u}^T)/2$  is the strain rate tensor. Heat transfer is modeled by the energy equation:

$$\rho c_p \left( \frac{\partial T}{\partial t} + \mathbf{u} \cdot \nabla T \right) = \nabla \cdot (k\nabla T) + 2\eta\dot{\gamma}^2. \tag{3}$$

In the above equations,  $t$ ,  $\mathbf{u}$ ,  $p$ ,  $T$ ,  $\rho$ ,  $\eta$ ,  $c_p$  and  $k$  denote time, velocity vector, pressure, temperature, density, viscosity, specific heat and thermal conductivity respectively. During the packing phase the compressibility of the polymer should be taken into account. The set of equations in this case includes the state equation as described in (Ilinca & Héту, 2001).

**2.3 Front tracking method**

The position of the polymer/air and skin/core polymer interfaces is tracked using a level-set method (Ilinca & Héту, 2002). The approach defines smooth functions  $F_i$  such that the critical value  $F_c$  represents the position of the interface. We consider  $i = 1$  for the polymer/air interface and  $i = 2$  for the skin/core interface. A front tracking value greater than  $F_c$  denotes a region filled by the respective polymer, while a smaller than  $F_c$  value corresponds to an unfilled region. For co-injection and gas-assisted injection two interfaces are present and the various combinations are summarized in Table 1. The front tracking technique identifies the skin, core and empty regions. Core breakthrough is also predicted.

At each time step the level-set functions tracking the polymer/air and skin/core interfaces are obtained by solving pure advection equations using the velocity field provided by the solution of the momentum-continuity equations:

$$\frac{\partial F_i}{\partial t} + \mathbf{u} \cdot \nabla F_i = 0 \tag{4}$$

**2.4 Boundary conditions**

Appropriate boundary conditions complete the statement of the problem. On the entry section both velocity and temperature are imposed. Filling is performed at constant flow rate as given by the velocity of the screw. Co-injection is performed using different barrel/screw plasticizing units, therefore the injection speed and temperature may be different for the skin and core materials. A free boundary condition is imposed on the unfilled part of the cavity walls allowing for the formation of the typical fountain flow, whereas no-slip boundary conditions are imposed on the filled part of the boundary. When the cavity is completely filled, the simulation stops as the no-slip boundary condition cannot allow more material to enter the cavity. The heat transfer between the cavity and the mould is given by

$$q = h_c(T - T_{mould}) \quad \text{on } \Gamma_{mould} \tag{5}$$

	$F_1 \geq F_c$	$F_1 < F_c$
$F_2 \geq F_c$	Core polymer	Core breakthrough skin material
$F_2 < F_c$	Skin polymer	Empty (air)

Table 1. Definition of filled (skin/core) and empty regions for co-injection

where  $h_c$  is a surface heat transfer coefficient and  $T_{mould}$  is the mould temperature. For the front tracking function, homogeneous Neumann boundary conditions are considered on all boundaries, except for the entry where Dirichlet conditions are imposed. Entry values change in time and indicate whether skin or core polymers are injected.

### 3. Finite element solution procedure

Model equations are discretized in time using a first order implicit Euler scheme. Linear continuous shape functions are used for all variables. At each time step, the global system of equations is solved in a partly segregated manner. The solution algorithm solves separately the systems of equations as follows:

For time smaller than the injection time:

1. Solve the incompressible momentum-continuity equations ( $\mathbf{u} - p$ ).
2. Solve the energy equation ( $T$ ).
3. Solve the front tracking equation  $F_1$  (polymer/air interface) if skin material is injected, or equations ( $F_1, F_2$ ) if core material is injected.

Check convergence. If converged goto the next time step, otherwise repeat steps 1 to 3.

Steps 1 to 3 are solved using the last known values of the dependent variables and iterations are made to obtain converged solutions of the coupled system of equations. The finite element formulations of the equations are discussed hereafter.

#### 3.1 Momentum-continuity equations

The Stokes equations (1) and (2) are solved using a Galerkin Least-Squares (GLS) method (Franca & Frey, 1992). This method contains an additional pressure stabilization term compared with the standard Galerkin method. In such a way, the use of linear elements for both the velocity and pressure is permitted. The GLS variational formulation of the momentum-continuity equations is:

$$\int_{\Omega} 2\eta \dot{\gamma}(\mathbf{u}) : \dot{\gamma}(\mathbf{v}) d\Omega - \int_{\Omega} p \nabla \cdot \mathbf{v} d\Omega + \int_{\Omega} \nabla \cdot \mathbf{u} q d\Omega + \sum_K \int_{\Omega_K} \{ \nabla p - \nabla \cdot [2\eta \dot{\gamma}(\mathbf{u})] \} \cdot \tau_u \nabla q d\Omega_K = 0 \quad (6)$$

where  $\mathbf{v}$  and  $q$  are velocity and pressure test functions respectively. The stabilization parameter  $\tau_u$  is defined as:

$$\tau_u = \frac{m_k h_K^2}{4\eta} \quad (7)$$

where  $h_K$  is the size of the element  $K$  and  $m_k$  is a coefficient commonly considered 1/3 for linear elements.

#### 3.2 Energy equation

For polymers, the Prandtl number takes large values. Therefore, during the filling, the energy equation is dominated by the convection. However, cooling generated by the heat lost through walls, coupled with a low material diffusivity, generates high temperature gradients in direction normal to the wall. The solution algorithm must correctly represents

both advective and diffusive mechanism. Here a GLS/GGLS method is used to solve for the temperature. The GLS (Franca & Frey, 1992) term stabilizes the convection, whereas the GGLS contribution (Franca & Dutra do Carmo, 1989) deals with the presence of sharp boundary layers.

The GLS/GGLS formulation of equation (3) is:

$$\begin{aligned}
& \int_{\Omega} \rho c_p \left( \frac{T - T_0}{\Delta t} + \mathbf{u} \cdot \nabla T \right) w d\Omega + \int_{\Omega} k \nabla T \cdot \nabla w d\Omega - \int_{\Omega} 2\eta \dot{\gamma}^2 w d\Omega \\
& + \sum_K \int_{\Omega_K} \left[ \rho c_p \left( \frac{T - T_0}{\Delta t} + \mathbf{u} \cdot \nabla T \right) - \nabla \cdot (k \nabla T) - 2\eta \dot{\gamma}^2 \right] \tau_T \rho c_p \mathbf{u} \cdot \nabla w d\Omega_K \quad (8) \\
& + \sum_K \int_{\Omega_K} \nabla \left[ \rho c_p \left( \frac{T - T_0}{\Delta t} + \mathbf{u} \cdot \nabla T \right) - \nabla \cdot (k \nabla T) - 2\eta \dot{\gamma}^2 \right] \tau_{\nabla} \nabla w d\Omega_K \\
& = \int_{\Gamma_{mould}} h_c (T - T_{mould}) w d\Gamma
\end{aligned}$$

Note that the stabilization terms are integrated only over the element interiors. The stabilization parameter  $\tau_T$  is defined as in (Ilinca et al., 2000):

$$\tau_T = \left[ \left( \frac{2\rho c_p}{\Delta t} \right)^2 + \left( \frac{2\rho c_p |\mathbf{u}|}{h_K} \right)^2 + \left( \frac{4k}{m_k h_K^2} \right)^2 \right]^{-1/2} \quad (9)$$

The definition of the stabilization parameter  $\tau_{\nabla}$ , as from reference (Franca & Dutra do Carmo, 1989), is:

$$\tau_{\nabla} = \frac{h_K^2}{6} \bar{\xi} \quad (10)$$

where

$$\bar{\xi} = \frac{\cosh(\sqrt{6\alpha}) + 2}{\cosh(\sqrt{6\alpha}) - 1} - \frac{1}{\alpha} \quad (11)$$

$$\alpha = \frac{(\rho c_p / \Delta t) h_K^2}{6k} \quad (12)$$

### 3.3 Front tracking equations

The front tracking equations are discretized using an SUPG finite element method. SUPG provides smooth solutions when the convective part of the equation is dominant, as is in the present case. The variational formulation is given by

$$\int_{\Omega} \left( \frac{\partial F}{\partial t} + \mathbf{u} \cdot \nabla F \right) v d\Omega + \sum_K \int_{\Omega_K} \left( \frac{\partial F}{\partial t} + \mathbf{u} \cdot \nabla F \right) \tau_F (\mathbf{u} \cdot \nabla v) d\Omega_K = 0. \quad (13)$$

In the absence of diffusion the stabilization coefficient  $\tau_F$  is defined as

$$\tau_F = \frac{h_K}{2|\mathbf{u}|}. \quad (14)$$

The front tracking functions are discretized using linear elements. They are reinitialized after each time step to insure mass conservation of the skin and core polymers (Ilinca & Hétu, 2002).

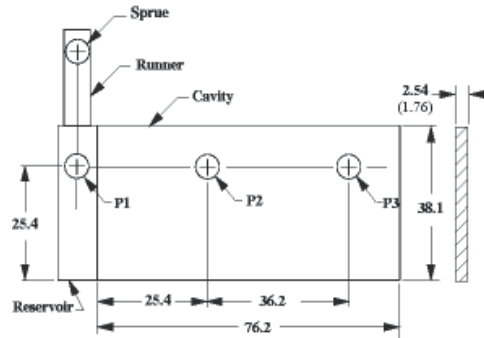


Fig. 1. Geometry of the cavity and location of control points P1, P2 and P3

## 4. Numerical applications

### 4.1 Filling and post-filling analysis of a plate

The first application is the simulation of the filling and post-filling stages of a polystyrene part (Ilinca & Héту, 2001). The cavity is a rectangular plate (76.2mm by 38.1mm) of uniform thickness (either 2.54mm or 1.76mm) as shown in Figure 1.

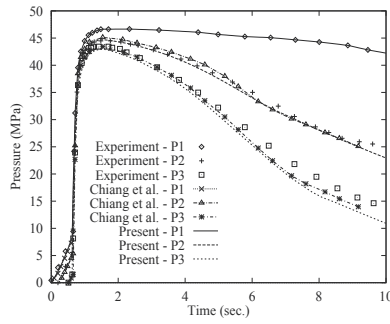
This problem was the object of a numerical and experimental investigation in (Chiang et al., 1991a;b). The problem was also simulated numerically using the Hele-Shaw model by Chen & Liu (1994) and by Han & Im (1997). Conditions for numerical simulations followed those used by (Chiang et al., 1991b). The parameters were varied in order to evaluate their influence on the numerical results. Tests were performed using different values for the packing pressure, cavity thickness, melt temperature and mould temperature. The computational conditions are summarized in Table 2. Experimental data at point P1 were used as inlet conditions for the numerical simulation. Material properties for the numerical simulation are given in (Ilinca & Héту, 2001). The heat transfer coefficient used on the cavity-mould interface is  $h_c = 2000 \text{ W/m}^2 \cdot ^\circ\text{C}$ .

Pressure solutions at points P2 and P3 are presented in Figure 2. Comparison is made for all cases with the experimental and numerical data of Chiang et al. (1991b). Case 1 is used as a reference. In case 2 the packing pressure is reduced to half the reference value and the results are presented in Figure 2(b). For this case, the pressure decreases at the same rate as for case 1 (Figure 2(a)) but because of the smaller packing pressure, it falls to zero earlier in time and therefore at higher temperature. The net result will be that the final shrinkage of the part will be more important when the packing pressure is smaller.

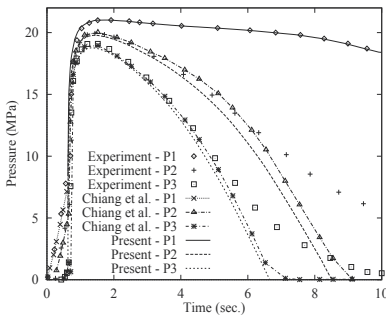
Figure 2(c) shows the results for case 3 for which the melt temperature was increased to  $230^\circ\text{C}$ . The 3D solution is almost superimposed over the experimental data and the results

Condition	Case 1	Case 2	Case 3	Case 4	Case 5
Cavity thickness (mm)	2.54	2.54	2.54	1.76	1.76
Melt temperature ( $^\circ\text{C}$ )	200	200	230	200	200
Fill time (s)	0.69	0.69	0.69	0.48	0.48
Hydraulic hold pressure (MPa)	6.9	3.45	6.9	6.9	6.9
Holding time (s)	> 15	> 15	> 15	> 15	> 15
Mould temperature ( $^\circ\text{C}$ )	32	32	32	32	60

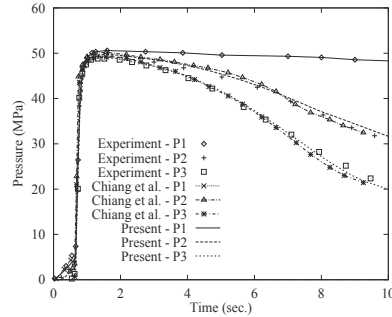
Table 2. Processing conditions for the rectangular plate



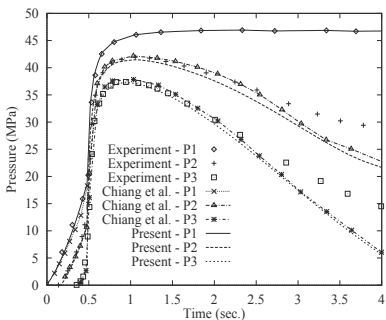
(a) Case 1



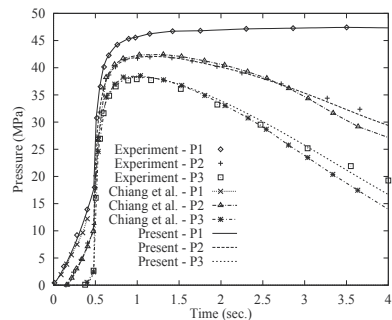
(b) Case 2



(c) Case 3



(d) Case 4



(e) Case 5

Fig. 2. Pressure traces at control points P1, P2 and P3

of Chiang et al. (1991b). Because of the higher melt temperature, the polymer is less viscous than for case 1. The pressure decreases then at a smaller rate. Note that for point P1 the maximum pressure is about 5 MPa greater than for case 1. Increasing the melt temperature has a comparable effect as increasing the packing pressure.

Conditions of case 4 correspond to a thinner cavity. Pressure traces for this case are presented in Figure 2(d). The time taken by the melt temperature to decrease below the no-flow temperature is reduced from about 10s on the thicker plate to less than 4s on the thinner plate. The numerical results are closer to the experimental data during the first two seconds of packing and larger differences are apparent on the later stage of the holding phase.

Simulation for case 5 (Figure 2(e)) reproduces the conditions of case 4 but with the mould

temperature increased from 32<sup>0</sup>C to 60<sup>0</sup>C. Because of the lower cooling rate the pressure decreases more slowly. A good agreement is observed between experimental measurements, 2.5D numerical results (Chiang et al., 1991b) and present 3D predictions. We may conclude that the present numerical approach performs well and produces prediction in good agreement with experiments.

#### 4.2 Co-injection of a center gated rectangular plate

For this application the mould cavity is a centrally gated rectangular plate with dimensions of 76x164x7mm. Experimental trials were carried out in a 150-ton Engel co-injection machine (Ilinca et al., 2006). The horizontal and vertical barrel/screw plasticizing units are used to feed the skin and core materials, respectively, to the co-injection head. The materials are injected sequentially in the mould through a single nozzle equipped with a check valve, which controls the amount of material entering the mould. A given percentage of the skin material is first injected in the cavity, followed by the injection of the core material. The material used for both skin and core is an injection grade polycarbonate Caliber 200-14 supplied by The Dow Chemical Company. For visualization purposes, a red pigment is added to the core material. Numerical results for the same part injected with an ABS polymer are reported in (Ilinca & Héту, 2002) and (Ilinca & Héту, 2003). The polymer viscosity is modeled with the Cross-WLF model:

$$\eta(T, \dot{\gamma}, p) = \frac{\eta_0(T, p)}{1 + \left( \frac{\eta_0(T, p) |\dot{\gamma}|}{\tau^*} \right)^{1-n}} \quad (15)$$

$$\eta_0(T, p) = D_1 \exp \left[ - \frac{A_1 (T - T^*)}{A_2 + (T - T^*)} \right], \quad (16)$$

where

$$T^*(p) = D_2 + D_3 p, \quad (17)$$

$$A_2(p) = \tilde{A}_2 + D_3 p. \quad (18)$$

The rate of deformation  $|\dot{\gamma}|$  is computed from the strain rate tensor as  $|\dot{\gamma}| = \sqrt{2\dot{\gamma} : \dot{\gamma}}$ . Model constants used for the numerical simulation are summarized in Table 3. Density, specific heat and thermal conductivity were considered constant, equal to 1162 kg/m<sup>3</sup>, 2000 J/(kg ·<sup>0</sup>C), and 0.25W/(m ·<sup>0</sup>C) respectively.

Numerical solutions were obtained on a mesh having 44,850 nodes and 199,440 tetrahedral elements. Given the segregated nature of the solution algorithm, the maximum CFL number at the melt/air interface is limited to unity, and a typical solution needs about 150 time steps for the filling period. Computations were carried out for different skin/core ratio, skin/core injection temperatures and skin/core injection speeds and the results were compared with the moulded parts. Process conditions and simulation results are summarized in Table III. The temperature of the injected melt was set at either 300<sup>0</sup>C or 250<sup>0</sup>C, while the mould temperature was set at 90<sup>0</sup>C. Screw speed was considered either 20mm/s or 50mm/s. At the lower injection speed, filling of the plate takes 3.5s, while at the faster speed it takes 1.4s. The reference case

Model constant	Value
$n; \tau^*(Pa)$	0.18; 5.766 · 10 <sup>5</sup>
$D_1(Pa \cdot s); D_2(^0C); D_3(^0C/Pa)$	3.46 · 10 <sup>6</sup> ; 175.0; 0.0
$A_1; \tilde{A}_2(^0C)$	11.59; 33.98

Table 3. Cross-WLF model constants for PC200

Case	Skin/core ratio, vol. %	Skin/core inj. speed, mm/s	Skin/core temperature, °C	Delay time, s	Core Length/Width, mm
Ref.	80/20	20/20	300/300	0	47.2/30.0
A	A(1): 90/10 A(2): 70/30 A(3): 60/40	20/20	300/300	0	29.2/23.4 61.2/32.8 72.9/30.0
B	80/20	B(1): 20/50 B(2): 50/20 B(3): 50/50	300/300	0	46.7/29.8 45.0/29.6 44.3/29.4
C	80/20	20/20	C(1): 300/250 C(2): 250/300 C(3): 250/250	0	44.8/30.4 51.8/28.9 48.4/29.7
D	80/20	20/20	300/300	D(1): 1 D(2): 2 D(3): 4	50.5/30.1 52.3/30.3 56.0/30.6

Table 4. Operating conditions and simulation results

has a skin/core ratio of 80/20 and the same injection temperature (300°C) and injection speed (20 mm/s) for both skin and core.

Figure 3 compares the moulded part with the 3D solution for the reference case. Front view and isometric view are shown. The skin polymer is plotted in transparency in order to allow for the core to be visible. The core material advances more rapidly in the direction corresponding to the plate length. Because the plate fills first in the width, the core penetrates less in this direction. The 3D solution of the co-injection process is able to predict the core shape in all directions. Most important, the residual skin thickness is computed and critical regions can be identified. In this case thin polymer skin is predicted in the region of the gate. The hot polymer is directed into the opposite wall and the skin thickness is very small at this location. Far from the center, the core polymer penetrates by the mid-plane and the skin thickness is almost the same on top and bottom of the part.

Figure 4 illustrates the change in the solution when the ratio skin/core ratio varies from 90/10 to 60/40. As more core material is injected in the cavity the core penetrates deeper inside the skin. Core penetration changes mostly in the length of the plate as the filling during core injection occurs mostly in this direction.

Experimental and numerical core penetration in length and width directions are compared in Figure 5. The effect of changing the skin/core ratio, the injection speed, the injection temperature and the core injection delay is investigated. As expected, Figure 5(a) indicates that a deeper core penetration is observed for a higher ratio core/skin materials. The effect of the injection speed is shown in Figure 5(b). By increasing the injection speed the temperature of the polymer increases because of the shear heating and also because of the smaller cooling time. The net effect is that a faster filling (i.e. higher temperature) determines a higher core thickness and therefore a shorter core penetration length. A similar effect is observed when the skin/core temperature is varied (Figure 5(c)). The mean injection temperature is computed by using 80% of the skin value and 20% of the core value. A lower temperature determines a thinner core (thicker skin) and hence a deeper core penetration. Note however that changes in skin and core temperature have opposite effects. A lower core temperature determines a higher viscosity core. Therefore, the core is thicker and the penetration length is

shorter. Meanwhile, lower skin temperature determines a thicker skin and therefore deeper core penetration. Changing the core injection delay (Figure 5(d)) has a similar effect on the solution. Increasing the delay is equivalent to a lower skin temperature and hence deeper core penetration.

This results indicate a good agreement between experiment and simulation except for cases C(2) and C(3) which present core instability in the experiment. Both numerical simulation and experiment indicate that core penetration increases at longer filling times (Figure 5(b)), at higher core temperature (reference case compared with C(1) and C(2) compared with C(3)), at smaller skin temperature (reference case compared with C(2) and C(1) compared with C(3)), and at larger core injection delay (Figure 5(d)).

#### 4.3 Gas-assisted injection of a thin plate with a flow channel

We consider here the gas-assisted injection of a rectangular plate with a flow channel on the longitudinal axis. This problem was the object of an experimental and numerical study by Gao et al. (1997). The moulded plate is 100mm wide, 384mm long and 2.5mm thick. The channel present along the centerline of the part is 325mm long, 6mm wide and 9mm deep. Material properties correspond to a high density polyethylene (HDPE). The viscosity dependence upon the shear rate and temperature is described by the modified Carreau-WLF model (Ilinca & Héту, 2003):

$$\eta = \frac{\eta_0 A_t}{(1 + \lambda A_t \dot{\gamma})^n} \quad (19)$$

$$\ln(A_t) = \frac{8.81(T_{ref} - T_s)}{101.6 + T_{ref} - T_s} - \frac{8.81(T - T_s)}{101.6 + T - T_s} \quad (20)$$

Material properties and viscosity model constants are given in Table 5.

Computations were done in order to quantify the solution dependence on various parameters as melt temperature, mould temperature, gas pressure, polymer/gas volume ratio, and gas injection delay. Numerical simulations for the same conditions but using a Cross-WLF viscosity model are given in (Ilinca & Héту, 2002). The computational parameters, namely

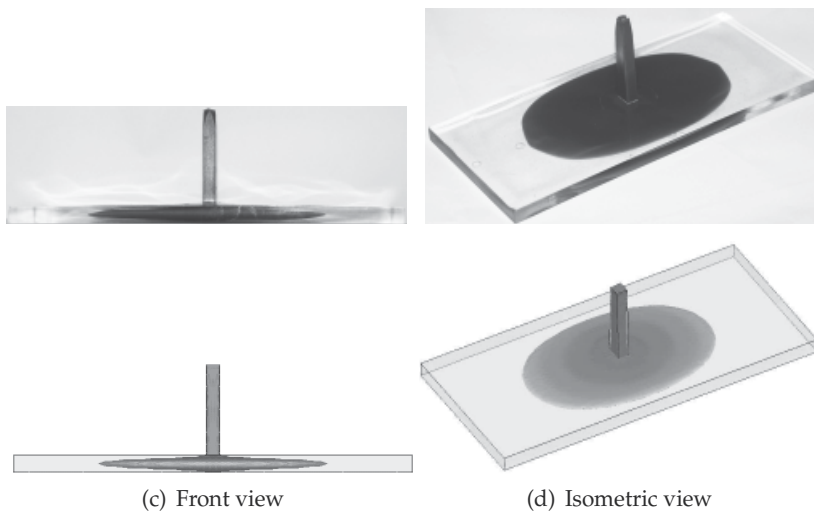


Fig. 3. Experimental (top) and simulated (bottom) results for the reference case

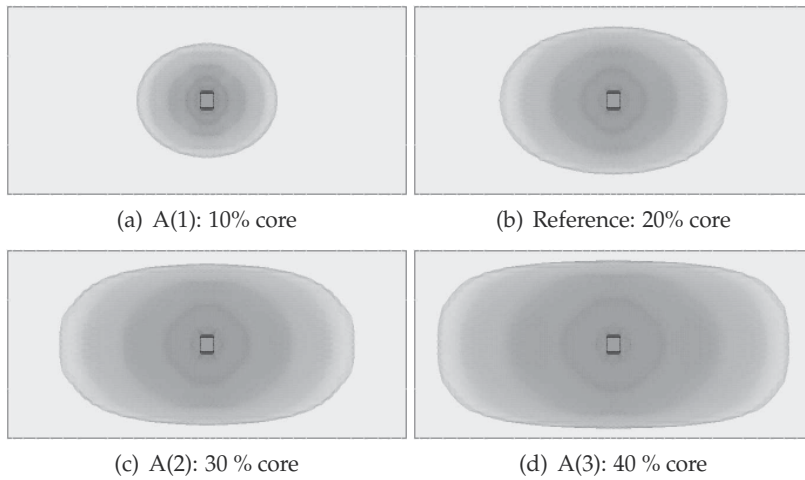


Fig. 4. Numerical solutions for different ratios skin/core polymers

melt temperature, mould temperature, gas pressure, and gas volume, are summarized in Table 6. For each case, three series of computations were performed: (a) gas injected with no delay, (b) with one-second delay, and (c) with four seconds delay, respectively. For the given

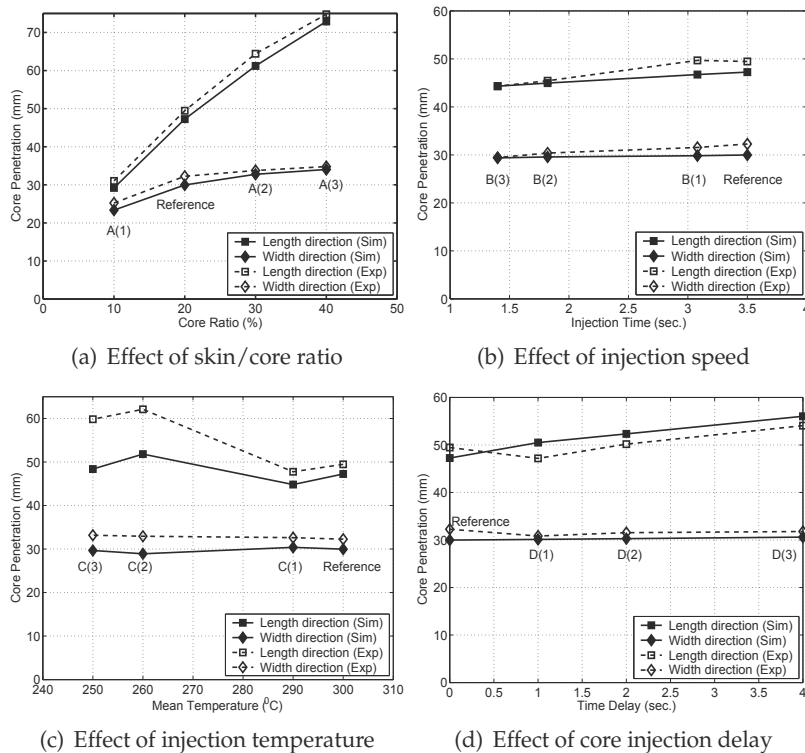


Fig. 5. Comparison of numerical and experimental core penetration

Density, $\rho$ ( $kg/m^3$ )	850.0
Specific heat, $c_p$ ( $J/kg/K$ )	4000.0
Thermal conductivity, $k$ ( $W/m/K$ )	0.35
Zero shear rate viscosity, $\eta_0$ ( $Pa \cdot s$ )	501.97
Relaxation time, $\lambda$ (s)	0.00422
Power law index, $n$	0.698
Reference temperature, $T_{ref}$ ( $^{\circ}C$ )	232.3
Standard temperature, $T_s$ ( $^{\circ}C$ )	-66.0
No flow temperature, ( $^{\circ}C$ )	133.0

Table 5. Material properties for HDPE

polymer injection speed, complete filling of the part would take 1 second. The cavity/mould heat transfer coefficient was taken  $h_c = 4000 W/(m^2 \cdot ^{\circ}C)$ . The results for the gas injection time and the length of the gas core are also listed in Table 6.

Case A is considered as a reference on which the other cases are compared. This way, the effect of different parameters on the solution behaviour is quantified. Figure 6 shows the solution at the end of the gas injection for case A. The plot was made in transparency in order to make visible the gas region inside. Gas corresponds to the darkest region and mainly follows the central channel. When gas injection is delayed, the cooling of the plate is such that the gas does not penetrate laterally in the thin plate region. Therefore, gas penetration in the flow leader is more profound. The length of the gas core is 42% longer when gas injection is delayed by four seconds than with no delay. The gas injection time is also affected. When part temperature decreases, the viscosity increases, causing a slower polymer flow. For a gas delay time of four seconds, the gas injection time increases by a factor of almost three compared to the case without delay time. For case B, the melt temperature is increased to  $270^{\circ}C$ . The polymer being at higher temperature becomes less viscous. Therefore, the gas penetrates more in the

Case	$T_{melt}$ ( $^{\circ}C$ )	$T_{mould}$ ( $^{\circ}C$ )	$p_{gas}$ (MPa)	Gas vol. %	Gas inj. delay (s)	Gas inj. time (s)	Gas core length (mm)
A	240	35	17.25	8	A(1): 0	0.48	223.6
					A(2): 1	0.68	255.7
					A(3): 4	1.22	316.8
B	270	35	17.25	8	B(1): 0	0.36	220.4
					B(2): 1	0.51	252.2
					B(3): 4	0.92	315.0
C	240	75	17.25	8	C(1): 0	0.43	207.3
					C(2): 1	0.57	233.2
					C(3): 4	0.86	268.0
D	240	35	34.5	8	D(1): 0	0.17	217.7
					D(2): 1	0.25	251.5
					D(3): 4	0.45	311.5
E	240	35	17.25	10	E(1): 0	0.51	279.2
					E(2): 1	0.69	316.5
					E(3): 4	1.13	363.2*

Table 6. Operating conditions and simulation results (\* indicates gas fingering)

thin regions of the plate. Results listed in Table 6 indicate that melt temperature influences less the length of the gas core but has larger impact on the gas penetration time. Meanwhile, when increasing the mould temperature (case C) the time injection delay exhibits little changes, while the length of the gas core varies more significantly. The explanation of this behaviour is that gas injection time is determined by the core polymer viscosity, which depends on the melt temperature. The length of the gas core depends on the skin polymer thickness, which is influenced mostly by the mould temperature. Case D is completed in order to evaluate the influence of the gas pressure. The gas pressure is increased to  $34.5\text{MPa}$ , twice the pressure for the reference case. The gas pressure determines little changes on the length of the gas channel for the case with one-second delay. Remark that the gas injection takes more time at lower gas pressure. We expect that for a gas pressure below a critical value, the gas injection becomes so long that the cooling of the polymer causes an incomplete filling as reported in (Ilinca & Héту, 2002). For case E, the volume of gas injected is increased from 8% to 10%. As expected, the length of the gas core increases by almost 25% (see case A(1) compared with E(1), and A(2) compared with E(2)). The gas injection time exhibit little changes. For case E(3), the gas occupies the entire length of the channel when only 98.2% of the part is filled. At this point, the gas penetrates into the thin plate near the end of the central channel producing gas fingering.

Figure 7 illustrates the shape of the gas bubble at different positions along the flow leader. The solution on the top is for case A(1), followed by the solutions for cases A(2) and A(3). When the gas is injected with no delay it penetrates slightly in the thin plate. Increasing the gas injection delay results in lower temperatures and hence, higher viscosities. Therefore, the gas enters mostly through the flow leader and penetration into the thin section is eliminated.

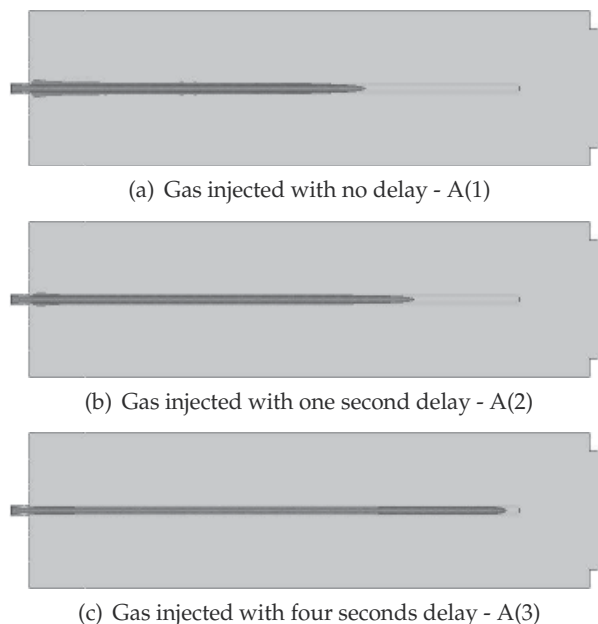


Fig. 6. Gas penetration for case A

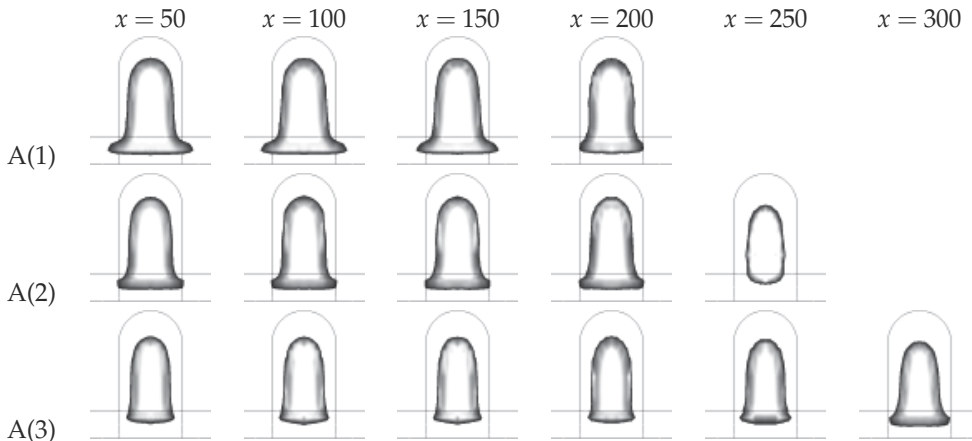


Fig. 7. Gas penetration

#### 4.4 Powder segregation in piston driven flow

In powder injection moulding the material is a feedstock composed of a metal or ceramic powder and a polymeric binder. To model segregation in powder injection moulding in addition to the momentum-continuity and energy equations we solve for a transport equation describing the behaviour of the solid fraction (Phillips et al., 1992; Ilinca & Héту, 2008a;b). This test case consists of displacing a fixed volume of suspension down a pipe by means of a piston. The material exhibits a similar behaviour in injection moulding where the suspension pushed by a piston forms a free surface (Ilinca & Héту, 2008b). The uniformity of the suspension downstream of the piston will then affect the distribution of particles inside the moulded part. An experimental study of this problem was performed by Subia et al. (Subia et al., 1998). The piston radius is  $2.54\text{cm}$  and the pipe was filled with material on a length of  $30\text{cm}$ . In the initial state the suspension is homogeneous and contains 50% of spherical particles having  $3178\mu\text{m}$  in diameter. The piston moves from left to right at a speed of  $0.0625\text{cm/s}$ , while the pipe was held stationary as shown in Figure 8.

A first computation was carried out on a fixed mesh by considering that the pipe moved from right to the left and the pistons were maintained fixed. This way a reference solution was obtained using an Eulerian approach. The mesh for this simulation has 52,569 nodes and is formed by 257,280 tetrahedral elements. Particle segregation for different positions of the piston is shown in Figure 9. The solid fraction decreases in front of the piston and is higher in the second half of the domain along the pipe axis. This is in agreement with experimental observation (Subia et al., 1998). The mean solid fraction on sections normal to the pipe axis was computed and plotted along the pipe axis in Figure 10. The results are compared with

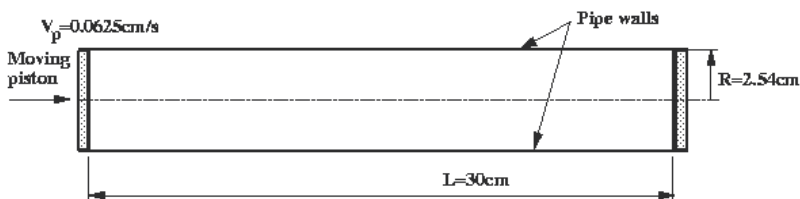


Fig. 8. Piston driven flow: Problem definition

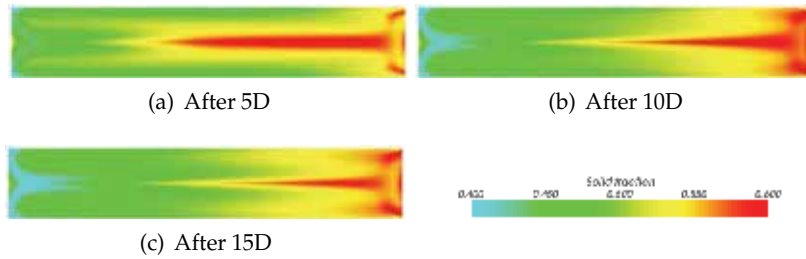


Fig. 9. Distribution of solid fraction for various piston displacements (Eulerian approach)

experimental data collected after the piston was displaced with 5 piston diameters. The numerical solution recovers correctly the segregation behaviour, but slightly underestimates the change in the solid fraction. However, the agreement with previously published numerical results (Fang et al., 2002) is very good. Simulation indicates that the segregation in front of a moving piston evolves quite rapidly and that an almost developed flow is attained after a 10D piston displacement.

This problem describes well the behaviour of the material in front of the plunger during injection moulding. However, simulation of the piston movement in material processing would not be possible in an Eulerian frame of reference, since the model includes both the moving piston and stationary parts as the mould cavity. Therefore the more general Arbitrary Lagrangian Eulerian (ALE) formulation is used as described in (Ilinca & Héту, 2008b). The ALE simulation was carried out on a mesh with 104,489 nodes and 499,200 tetrahedral elements. There were 16 elements in radial direction, 48 elements along the piston circumference and 160 elements along the pipe axis. Results using the ALE formulation for the piston driven flow with a free surface are shown in Figures 11 and 12. Figure 11 illustrates the solid fraction distribution in a cross-section along the pipe axis. It shows also the change in the computational domain (gray rectangles) and the form of the free surface on the right hand end of the filled region. The results are very close to those given by the Eulerian approach (Figures 9 and 10). Small differences are observed at the right end of the computational domain, where a non-planar free surface is present in the ALE solution and a flat no-slip surface is present in the Eulerian case. The agreement between the two sets of computations indicates that the ALE approach performs well and can be used for injection moulding applications.

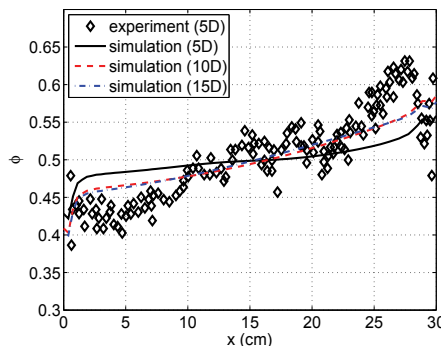


Fig. 10. Mean solid fraction along the tube axis using an Eulerian approach (experimental data from (Subia et al., 1998))

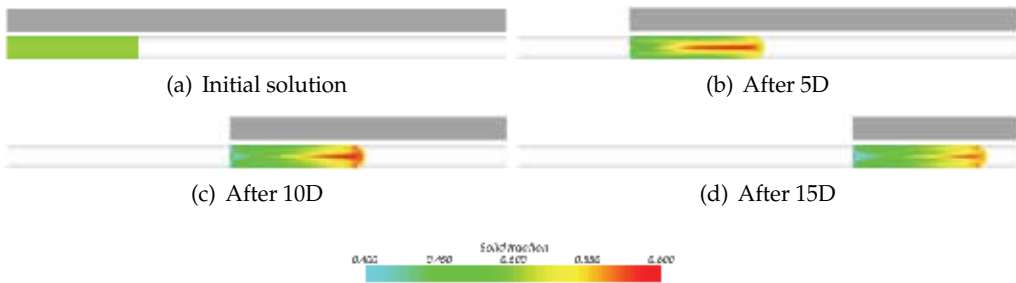


Fig. 11. Computational domain and distribution of solid fraction for various piston displacements (ALE formulation)

The particle migration towards the center of the flow through a tube and the buildup of higher solid particle concentration in the vicinity of the free surface is well documented by experimental observation (Karnis & Mason, 1967; Seshadri & Sutera, 1967; Ramachandran & Leighton, 2007). Tang et al. (2000) associated the observed instability of the fluid/air interface under specific conditions to the particle accretion in the meniscus region. In the present piston driven flow the particle concentration is significantly higher in the right handside of the tube. To illustrate this phenomenon we divided the flow domain shown in Figure 8 into two equal size sub-domains: one for  $x < L/2$  and the other for  $x > L/2$  ( $x = L/2$  denotes the middle of the fluid region). One can observe that the region near the center of the pipe has higher flow rate and also higher particle concentration. Thus, even if the net flow exchange between the left and right sub-domains is zero, there is a non-zero particle flux across the surface between the two sub-domains at  $x = L/2$  as shown in Figure 13(a). The mean volumetric particle concentration in the left and right sub-domains is shown in Figure 13(b). A positive particle flux indicates that more particles are transported from the left towards the right sub-domain than in the opposite direction. Therefore the mean volumetric particle concentration increases in the right side. This happens until  $t = 1000s$ , from which point the left/right particle migration reverses and the net particle flux is from the right towards the left side.

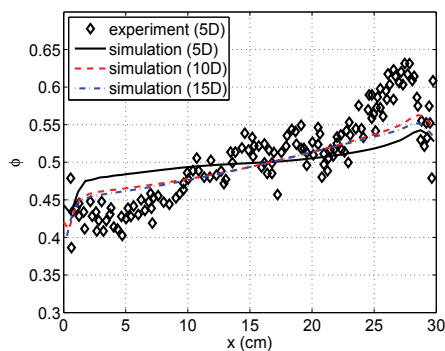


Fig. 12. Mean solid fraction along the tube axis using an ALE approach (experimental data from (Subia et al., 1998))

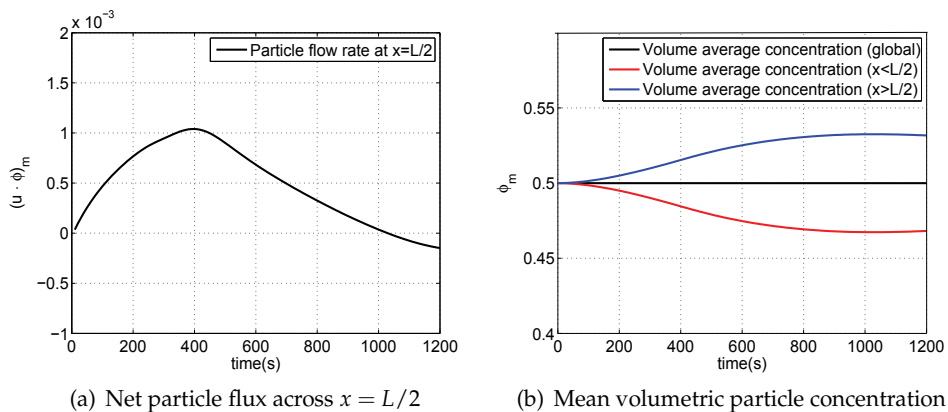


Fig. 13. Particle migration from one side to the other of the flow domain

#### 4.5 Segregation during mould filling

In this application the ALE formulation is used to predict powder segregation during the injection moulding of a rectangular plate (Ilinca & Héту, 2008a). The plate is  $8\text{ cm}$  by  $6\text{ cm}$  and has  $4\text{ mm}$  in thickness. The filling piston has a radius of  $1\text{ cm}$  and his displacement is  $13.2\text{ cm}$ . Filling of the plate is made through a circular gate with a radius of  $2\text{ mm}$ . The suspension contains particles of  $100\mu\text{ m}$  in diameter and the initial solid fraction is uniform at  $50\%$ . Complete filling of the plate takes  $10.0\text{ s}$ . The filling pattern and the solid fraction distribution is shown in Figure 14 after  $1.8\text{ s}$ ,  $4.0\text{ s}$ ,  $7.2\text{ s}$  and respectively  $10.0\text{ s}$ .

The figure shows a cut along the symmetry plane parallel to the longest side of the plate in order to see the solid fraction distribution inside the part. The images show both the complete domain, where the displacement of the piston during the filling is clearly seen, and details of the flow inside the plate. Segregation of solid particles is apparent inside the pipe as previously observed for the piston driven flow case. This causes the material to enter the gate with a non-uniform solid fraction. Additional segregation is observed inside the gate where shear rates are highest. The moulded part has higher solid fraction in the mid-plane and on the boundaries of the plate (far from the gate) and lower solid fraction on the upper and lower surfaces. The particle concentration at the end of the filling time for various locations inside the gate and along the plate is shown in Figure 15. Figure 15(a) shows the solution at gate inlet and outlet, as well as midway between the two locations. The gate length is  $5\text{ mm}$ . Note that particle concentration increases near the gate axis, where velocities are higher. At the exit from the gate the particle concentration decreases significantly near the walls. Particle distribution across the thickness of the plate at  $1$ ,  $2$ , and respectively  $3\text{ cm}$  from the gate (in the center plane parallel to the longest side) are shown in Figure 15(b). In all sections the concentration is higher in the center and lower at the walls.

#### 5. Conclusion

A three-dimensional finite element algorithm for the solution of injection moulding is presented. Numerical solutions are validated against experimental data for the filling-packing of a rectangular plate and then the methodology is applied to co-injection, gas-assisted injection and powder injection moulding. The algorithm is very robust and provide accurate

solutions. It is able to recover three-dimensional phenomena as the thickness distribution of skin and core polymers in co-injection and the gas penetration for gas-assisted injection. For powder injection moulding the segregation of solid particles is solved using a diffusive flux model. For the piston driven flow the ALE formulation is shown to provide similar results as an Eulerian approach on a fixed mesh, thus indicating that the procedure performs well. Application to the mould filling of a rectangular plate shows the ability to use this method to the solution of powder injection moulding.

## 6. References

- Baaijens, F.P.T. & Douven, L.F.A. (1991). Calculation of flow-induced residual stresses in injection moulded products. *Applied Scientific Research*, Vol. 48, pp. 141-157.
- Chen, B.S. & Liu, W.H. (1994). Numerical simulation of the post-filling stage in injection molding with a two-phase model, *Polymer Engineering and Science*, Vol. 34, pp. 835-847.
- Chen, S.C. & Hsu, K.F. (1995). Numerical Simulation and Experimental Verification of Melt Front Advancements in Coinjection Molding Process. *Numerical Heat Transfer, Part A*, Vol. 28, p.503.
- Chen, S.C.; Cheng, N.T. & Hsu, K.S. (1995). Simulations of gas penetration in thin plates designed with a semicircular gas channel during gas-assisted injection moulding,

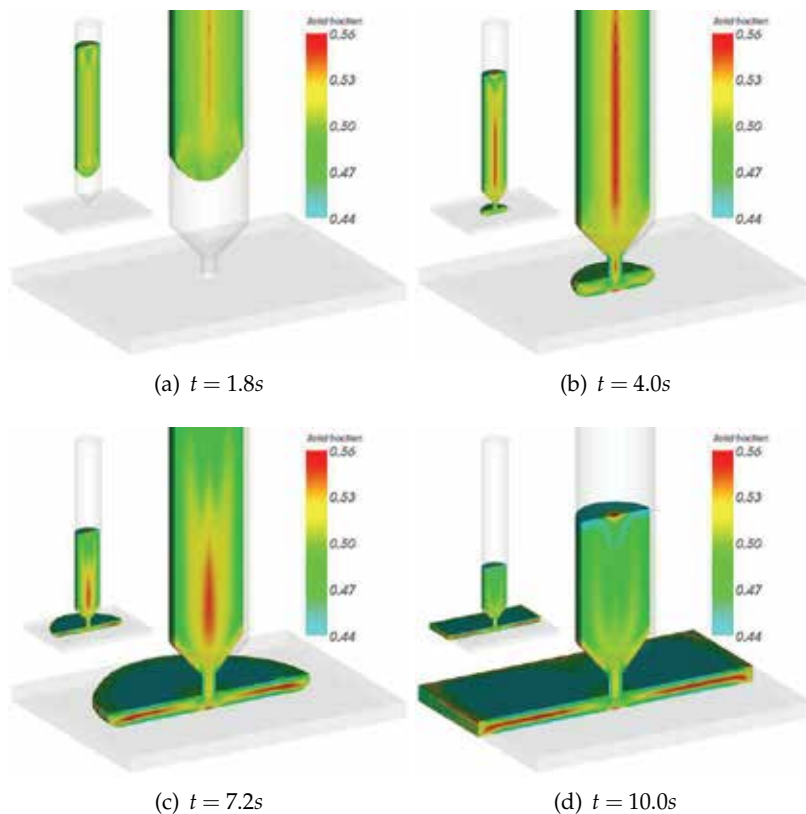


Fig. 14. Distribution of solid fraction for the injection of a plate.

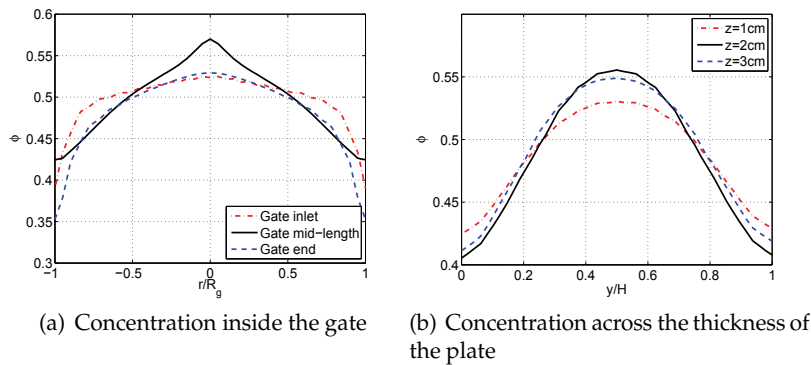


Fig. 15. Distribution of solid fraction for the injection of a plate.

*Int. J. Mech. Sci.*, Vol. 38, pp. 335–348.

- Chiang, H.H.; Hieber, C.A. & Wang, K.K. (1991). A unified simulation of the filling and postfilling stages in injection molding. Part I: Formulation. *Polymer Engineering and Science*, Vol. 31, pp. 116–124.
- Chiang, H.H.; Hieber, C.A. & Wang, K.K. (1991). A unified simulation of the filling and postfilling stages in injection molding. Part II: Experimental verification. *Polymer Engineering and Science*, Vol. 31, pp. 125–139.
- Fang, Z.; Mammoli, A.A.; Brady, J.F.; Ingber, M.S.; Mondy, L.A. & Graham, A.L. (2002). Flow-aligned tensor models for suspension flows, *Int. J. of Multiphase Flow*, Vol. 28, pp. 137–166.
- Franca, L.P. & Dutra do Carmo, E.G. (1989). The Galerkin Gradient Least-Squares Method. *Computer Methods in Applied Mechanics and Engineering*, Vol. 74, p.41.
- Franca, L.P. & Frey, S.L. (1992) Stabilized finite element methods: II. The incompressible Navier-Stokes equations. *Computer Methods in Applied Mechanics and Engineering*, Vol. 99, p.209.
- Gao, D.; Nguyen, K.; Garcia-Rejon, A.; Salloum, G. (1997). Numerical modelling of the mould filling stage in gas-assisted injection moulding, *Int. Polym. Proc.*, Vol. 12, pp. 267–277.
- Han, K.-H. & Im, Y.-T. (1997). Compressible flow analysis of filling and post-filling in injection molding with phase-change effect, *Composite Structures*, Vol. 38, pp. 179–190.
- Hétu, J.-F., Gao, D.M., Garcia-Rejon, A. & Salloum, G. (1998). 3D finite element method for the simulation of the filling stage in injection molding. *Polymer Engineering and Science*, Vol. 38, pp. 223–236.
- Hieber, C.A. & Shen, S.F. (1980). A finite-element/finite-difference simulation of the injection-molding filling process. *J. Non-Newtonian Fluid Mechanics*, Vol. 7, pp. 1–32.
- Ilinca, F., Hétu, J.-F. & Pelletier, D. (2000). On Stabilized Finite Element Formulations for Incompressible Advective-Diffusive Transport and Fluid Flow Problems. *Computer Methods in Applied Mechanics and Engineering*, Vol. 188, pp. 235–255.
- Ilinca, F. & Hétu, J.F. (2001). Three-dimensional filling and post-filling simulation of polymer injection molding. *International Polymer Processing*, Vol. 16, p.291.
- Ilinca, F. & Hétu, J.-F. (2002). Three-Dimensional Finite Element Solution of Gas-Assisted Injection Moulding, *Int. J. Num. Methods Engng.*, Vol. 53, pp. 2003–2017.
- Ilinca, F., Hétu, J.-F., Derdouri, A. & Stevenson, J. (2002). Metal Injection Molding: 3D Modeling of Nonisothermal Filing. *Polymer Engineering and Science*, Vol. 42,

- pp. 760–770.
- Ilinca, F. & Héту, J.F. (2002). Three-dimensional numerical modeling of co-injection molding. *International Polymer Processing*, Vol. 17, pp. 265–270.
- Ilinca, F. & Héту, J.-F. (2003). Three-dimensional simulation of multi-material injection molding: Application to gas-assisted and co-injection molding. *Polymer Engineering and Science*, Vol. 43, pp. 1415–1427.
- Ilinca, F.; Héту, J.-F. & Derdouri, A. (2006). Numerical investigation of the flow front behaviour in the co-injection moulding process. *International Journal for Numerical Methods in Fluids*, Vol. 50, pp. 1445–1460.
- Ilinca, F. & Héту, J.F. (2008). Three-dimensional numerical simulation of segregation in powder injection molding. *International Polymer Processing*, Vol. 23, pp. 208–215.
- Ilinca, F. & Héту, J.-F. (2008). Three-dimensional free surface flow simulation of segregating dense suspensions. *International Journal for Numerical Methods in Fluids*, Vol. 58, pp. 451–472.
- Janeschitz-Kriegl, H. (1983). *Polymer melt rheology and flow birefringence*, Springer-Verlag, pp. 424–448.
- Kamal, M.R., Kuo, Y. & Doan, P.H. (1975). The injection molding behavior of thermoplastics in thin rectangular cavities. *Polymer Engineering and Science*, Vol. 15, pp. 863–868.
- Karnis, A. & Mason, S.G. (1967). The flow of suspensions through tubes: VI. Meniscus Effects, *J. Colloid and Interface Sc.*, Vol. 23, pp. 120–133.
- Kim, S.-W. & Turng, L.-S. (2004). Developments of three-dimensional computer-aided engineering simulation for injection moulding. *Modeling and Simulation in Materials Science and Engineering*, Vol. 12, pp. 151–173.
- Phillips, R.J., Armstrong, R.C., Brown, R.A., Graham, A.L. & Abott, J.R., (1992). A constitutive equation for concentrated suspensions that accounts for shear-induced particle migration, *Physics of Fluids, A*, Vol. 4, pp. 30–40.
- Polynkin, A., Pittman, J.F.T. & Sienz, J. (2005). Gas assisted injection molding of a handle: Three-dimensional simulation and experimental verification. *Polymer Engineering and Science*, Vol. 45, pp. 1049–1058.
- Ramachandran, A. & Leighton Jr., D.T. (2007). The effect of gravity on the meniscus accumulation phenomenon in a tube, *J. Rheol.*, Vol. 51, pp. 1073–1098.
- Schlatter, G.; Davidoff, A.; Agassant, J.F. & Vincent, M. (1999). An Unsteady Multifluid Model: Application to Sandwich Injection Molding Process. *Polymer Engineering and Science*, Vol. 39, p.78.
- Seshadri, V. & Suter, S.P. (1967). Concentration changes of suspensions of rigid spheres flowing through tubes, *J. Colloid and Interface Sc.*, Vol. 27, pp. 101–110.
- Subia, S.R.; Ingber, M.S.; Mondy, L.A.; Altobelli, S.A. & Graham, A.L. (1998). Modelling of concentrated suspensions using a continuum constitutive equations, *Journal of Fluid Mechanics*, Vol. 373, pp. 193–219.
- Tang, H.; Grivas, W.; Homentcovski, D.; Geer, J. & Singler, T. (2000). Stability considerations associated with the meniscoid particle band at advancing interfaces in Hele-Shaw suspension flows, *Physical Review Letters*, Vol. 85, pp. 2112–2115.
- Wimberger-Friedl, R. & Janeschitz-Kriegl, H. (1988). Residual birefringence in injection molded compact discs. *First international conference on electrical, optical and acoustic properties of polymers*, 22/1–22/10, Canterbury, UK, 1988.
- Wu, S. (1991). Surface and interfacial tensions of polymers, oligomers, plasticizers and organic pigments. *Polymer Handbook*, Ed. J.Brandup, EH Immergut EA Grulke, pp. 521–541.

# Numerical Simulation of Fluid Flow and Hydrodynamic Analysis in Commonly Used Biomedical Devices in Biofilm Studies

Mohammad Mehdi Salek and Robert John Martinuzzi  
*University of Calgary  
Canada*

## 1. Introduction

Biofilms are microbial communities which can form on most biotic or abiotic surfaces including glass, metal, plastic, rocks, and live tissues. These colonies begin with individual planktonic bacterial cells that attach to a surface and then start to generate a sticky Extracellular Polymeric Substance (EPS). This complex polysaccharide matrix contributes to a modification of the phenotypic status of bacteria and protects them against the detrimental changes in the microenvironment surrounding the biofilms. These phenotypic changes typically confer increased resistance to antibiotics or to the host defence system in patients. This enhanced tolerance is associated with significant problems, such as hospital acquired infections, equipment damage, and energy losses (Trachoo, 2003; Percival et al., 2004), making biofilms a major concern in different industries.

In health care, biofilms are responsible for 65% of hospital acquired infections, adding more than \$1 billion annually for treatment costs in United States (Percival et al., 2004). Hospital acquired infections are the fourth leading cause of death in the U.S. accounting for 2 million death annually (Wenzel, 2007). Almost all types of biomedical devices and tissue engineering constructs are susceptible to biofilm formation (Bryers & Ratner, 2004; Bryers, 2008). Biofilms are particularly associated with a variety of bloodstream infections related to indwelling medical devices (e.g. urinary and cardiovascular catheters, vascular and ocular prostheses, prosthetic heart valves, cardiac pacemakers, cerebrospinal fluid shunts and other types of surgical devices). They are also responsible for chronic infections and recalcitrant diseases such as cystic fibrosis and periodontal diseases (Castelli et al., 2006; MacLeod et al., 2007; Meda et al., 2007; Presterl et al., 2007; Murray et al., 2007; Bryers, 2008; Phillips et al., 2008).

In industrial applications, biofilms can clog filters, block pipes and induce corrosion. They are responsible for billions of dollars yearly in equipment damage, energy losses, and water system contamination (Geesey & Bryers 2000). Additional costs associated with biofilm contaminations include disinfection, preventive maintenance, mitigation and replacement of contaminated materials.

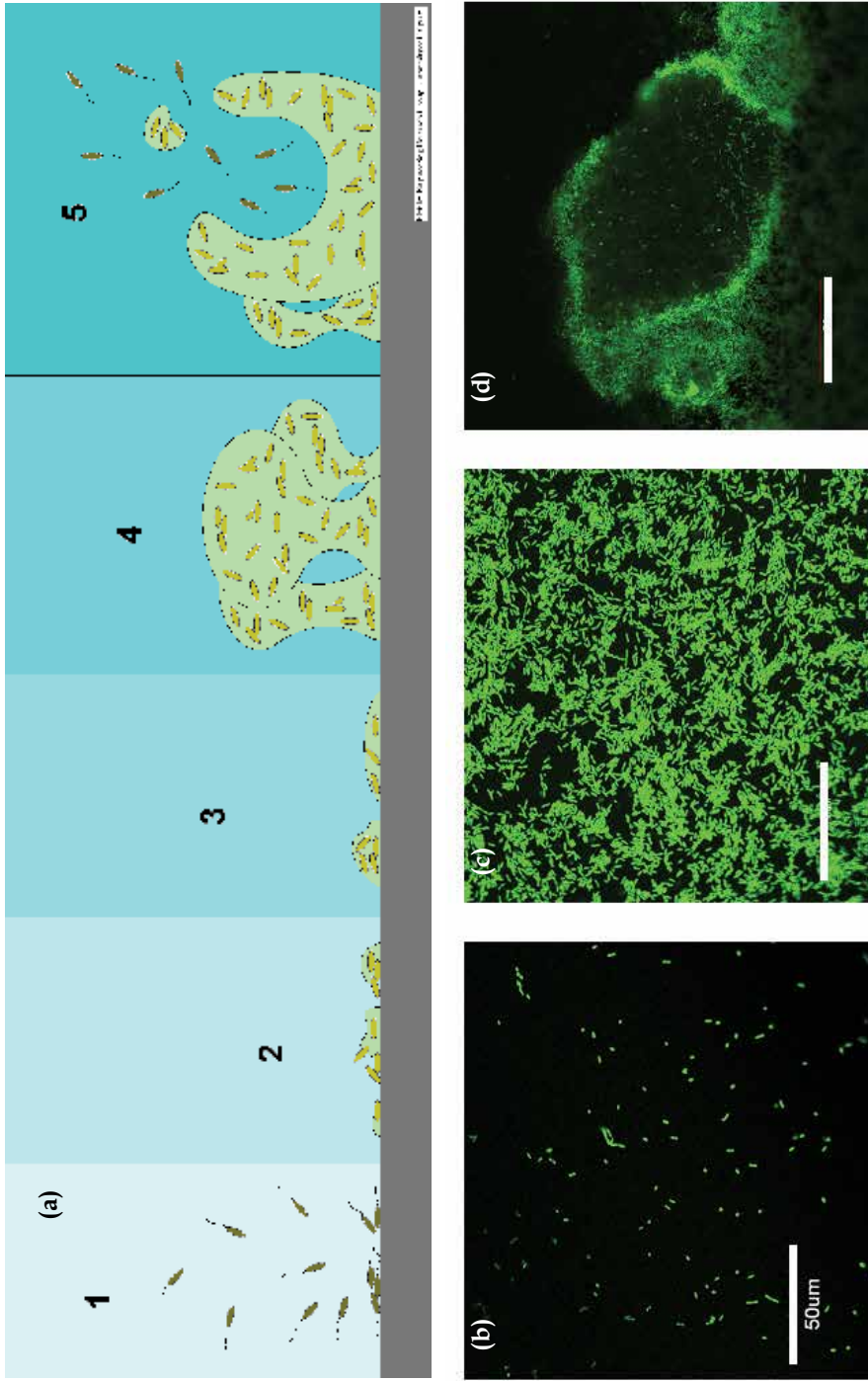


Fig. 1. a) Biofilm development process; b) Representative Confocal Scanning Laser Microscopy (CSLM) image of *Pseudomonas aeruginosa* O1 biofilms corresponding to step 1 and 2; c) corresponding dispersal structure corresponding to step 5 (Salek et al., 2009). All bars are 50  $\mu\text{m}$

Biofilm formation and behaviour is a result of several generally coupled physical, chemical and biological processes as illustrated in Fig. 1:

1. Transport of bacterial cells from the bulk liquid to the surfaces and then adhesion to the wall. The process of attachment is either reversible or irreversible. If the adhesion is reversible, the bacterial cells can still be detached by small shear forces or their own motility (Marshall, 1985).
2. After the attachment, bacterial cells start to produce EPS. This polymeric matrix acts like glue holding the biofilms together.
3. The next step is surface colonization and biofilm growth through a combination of cell division, cellular growth, EPS production and attachment/sequestering of new cells.
4. Biofilms develop to form morphologically more complex structures.
5. The final stage of biofilm formation is dissemination and recolonization. There are two important mechanisms here:
  - i. Biofilm detachment due to nutrient depletion and hydrodynamic forces. It occurs when external forces through the shear stress are larger than the internal strength of the micro-colonies (Horn et al., 2003).
  - ii. Seeding dispersal in which single cells may be released from the colony

All these stages are influenced by transport processes and thus the interaction with the fluid environment. While the fluid (e.g. blood, water or oil) is a source of nutrients, it also governs the transport of signaling molecules or of the bacteria and can provide the mechanical stimulus for regulating gene expression. Hence, the hydrodynamics of the fluid over biofilms is one of the more important factors affecting biofilm formation, structure and activity (Christensen, 1989; Stoodley et al., 1999; Purevdorj et al., 2002; Manz et al., 2003; Chen, 2005; Gjersing et al., 2005; Salek et al., 2009). The flow field affects each process of biofilm formation by changing the substrate concentration around the colonies, which influences the transport of bacteria and nutrients, and regulates the physiological properties of these complex structures by changing the mechanical shear stresses at the fluid-biofilm interface.

A broad range of techniques and models have been developed for in-vitro studies of the biofilm behavior under different environmental conditions. Among these, different types of tube flow cells are widely used to manipulate the hydrodynamics of flow around the biofilms (Manz et al., 2003; Gjersing et al., 2005). Tube flow cells and parallel plate flow chambers are commonly used in biofilm and microbiology studies to manipulate the hydrodynamics of flow surrounding the biofilms. Tube flow cells can be incorporated into different flow systems working over a wide range of flow regime from laminar to turbulent, and therefore they can be easily used to study the influence of flow velocity on biofilms structure and behavior (Stoodley et al., 2001b). Hosoi et al. (1986) investigated the effects of fluid velocity and shear on the biofilm formation in round pipes and found that an optimum shear to maximize the biofilm accumulation existed. Manz et al. (2003) imaged the velocity distribution over the biofilms in round tubes and showed that the local shear stress calculated from the measured velocity profiles at the biofilm interface was higher than the average wall shear stress calculated on the base of the mean flow velocity. This coupling between the stress field and biofilm growth illustrates the need for a detailed knowledge of the near-wall flow even in for the apparently simple round tube flow cell.

Albeit round tubes provide simpler hydrodynamic conditions, square or rectangular flow cells are often preferred for experiments to provide optical or microelectrode access (Gjersing et al., 2005). Stoodley et al. (2001a), for example, used square tubes to study biofilm properties under different fluid shear and environment conditions. They found that the hydrodynamic shear and local ionic environment influenced biofilm structure, cohesive

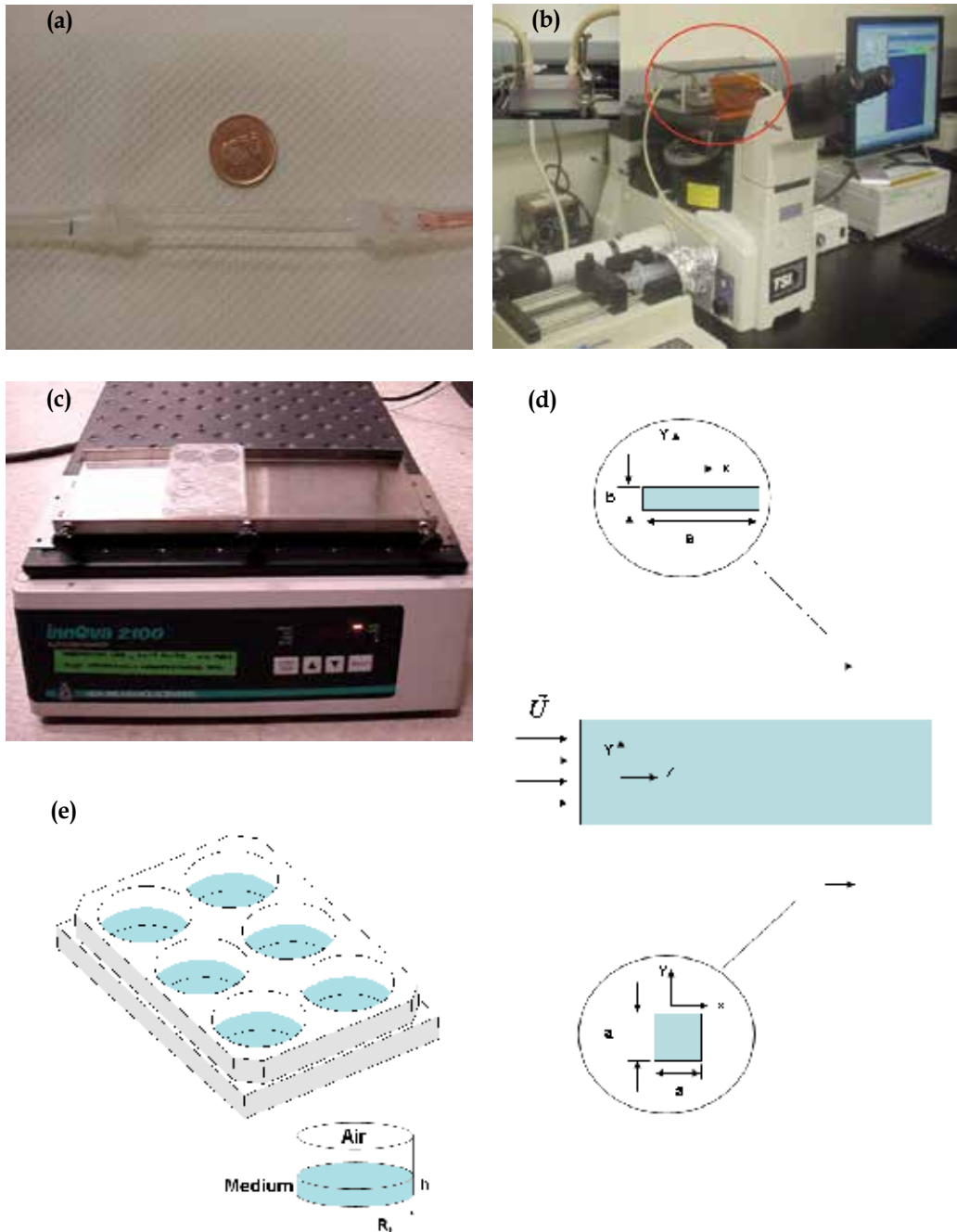


Fig. 2. Biomedical devices used in biofilm studies, Biofilm Engineering Research Group, University of Calgary (a) Glass tube flow cell; (b) Micro parallel-plate chamber located on a micro-PIV system; (c) 6-well plate mounted on an orbital shaker; (d) Schematic of rectangular and square flow cells; (e) Schematic of the 6-well plate

strength and material properties. Ebrahimi et al., (2005) showed that substrate limitation can reduce growth in the corners of rectangular channels. Gjersing et al. (2005) employed magnetic resonance microscopy to characterize the advective transport through a square duct geometry with biofilms covering the circumference. They observed that the presence of secondary flows can alter the mass transport in the reactor. Salek et al. (2009) studied the effects of non-uniform local hydrodynamic conditions arising in square and rectangular glass flow cells on PAO1 biofilm formation and structure. Their study showed that even under nominally uniform flow conditions, the spanwise changes in the hydrodynamic parameters can effectively change the biofilm colonization, structure and antimicrobial response.

Whereas flow cells are well suited for controlling hydrodynamic conditions, their use is generally impractical when many concurrent microbial tests over a range of flow conditions are required. High-throughput devices, commonly used to study microbial biofilms (Sillankorva et al., 2008; Sousa et al., 2008), are very practical when many parallel tests are needed in a short time period. They are widely used for rapid testing of antibiotic susceptibility and conducting many replicates. But the hydrodynamics inside these devices is not well understood. Therefore, they have been rarely used to study the biofilms under controlled hydrodynamic conditions.

The main purpose of the present work is to develop and apply different computational techniques to simulate and analyse the flow field and local hydrodynamics over the biofilm culture area in different biomedical devices as are typically used in biofilm studies (Fig. 2). In the first part, the influence of the flow cell geometry on the hydrodynamics and mass transport acting locally on biofilms is investigated computationally for different types of flow cells. In the second part of this chapter, the unsteady oscillating flow arising in high-throughput devices is investigated. To this end a numerical simulation of the flow in an agitated well plate and MBEC™ device, commonly used high-throughput devices for biofilm studies, is presented.

## 2. Hydrodynamic characteristics of tube flow cells and parallel plate flow chambers

Results obtained in flow cells used in different microbiology studies are sometimes contradictory. It is thus hypothesized that the differences in the biofilms responses can be directly related to the hydrodynamic changes caused by the flow cell geometry (Salek & Martinuzzi, 2007; Salek et al., 2009). In this part, the shear stress and mass transport, the most important parameters in biofilm studies, are investigated in different types of flow cells. The effects of flow cell configuration, flow velocity and substrate diffusivity on shear stress and mass distribution are presented.

### 2.1 Numerical method and study parameters

The coupled three-dimensional (3D) steady-state Navier-Stokes and continuity equations for incompressible flow

$$\rho(\vec{v} \cdot \nabla)\vec{v} = -\nabla p + \mu \nabla^2 \vec{v} \quad (1)$$

$$\nabla \cdot \vec{v} = 0 \quad (2)$$

were solved where  $\vec{v}$ ,  $\mu$ ,  $\rho$  and  $p$  are velocity, dynamic viscosity, density and pressure respectively.

At the inlet, a uniform axial velocity was assumed, corresponding to the average bulk velocity:

$$U_m = \frac{Q}{A} \quad (3)$$

where  $A$  is the cross sectional flow areal and  $Q$  is the total volumetric flow rate. This inlet condition is a reasonable assumption when the length of tubes is sufficient to allow fully developed flow. At the outlet, a fully developed flow condition (zero velocity gradients in the axial direction) was imposed. A no slip boundary condition was imposed at the walls. This boundary condition implies a zero-velocity at the walls (for a clean flow cell). For further details please refer to (Salek & Martinuzzi, 2007) and (Salek et al., 2009).

The configuration of any physical system can be described as a function of relevant system parameters such as forces, fluxes and geometry, which are characterized in terms of non-dimensional numbers.

The non-dimensional form of shear stress can be defined in terms of Darcy-Weisbach friction factor and Reynolds number (Spiga et al., 1994; Salek et al., 2009):

$$\bar{\tau} = \frac{\tau_w}{\mu U_m / 8D_h} = f \cdot \text{Re}_D \quad (4)$$

Where the friction factor,  $f$ , and Reynolds number,  $\text{Re}_D$ , are:

$$f = \frac{8\tau_w}{\rho U_m^2} \quad (5)$$

$$\text{Re}_D = \frac{\rho U_m D_h}{\mu} \quad (6)$$

in which  $\tau_w$  is the wall shear stress.  $D_h$  is the hydraulic diameter :

$$D_h = \frac{4A}{\Gamma} \quad (7)$$

where  $\Gamma$  denotes the wetted perimeter of the tube.

The friction factor is given by:

$$f = \frac{K}{\text{Re}_D} \quad (8)$$

where  $K$  is a constant depending only on the tube geometry. For laminar flow,  $K = 64$  in round tubes. In rectangular tubes,  $K$  is calculated according to the following equation [Tsanis et al., 1982; Leutheusser, 1984]:

$$K = (96\alpha^2 / (\alpha + 1)^2) \left( 1 - ((192 / \pi^5 \alpha)) \right. \\ \left. (\tanh(3\pi\alpha / 2) + 3^{-5} \tanh(3\pi\alpha / 2) + \dots) \right)^{-1} \quad (9)$$

in which  $\alpha = a/b$  is the aspect ratio of the channel of width  $a$  and height  $b$ . In parallel plate flow chambers, the two-dimensional limit  $K = 96$  is approached as  $\alpha \gg 1$ .

In previous biofilm studies in either laminar or turbulent regimes (Cao and Alaerts 1995; Stoodley et al. 2001a,b; Dunsmore et al. 2002), the wall shear stress and friction factor for a rectangular channel were approximated (as an average) based on the round tube results. In laminar flow, the average shear stress at the wall is estimated as:

$$\tau_{wD} = \frac{8\mu U_m}{D_h} \quad (10)$$

However, the latter equation is erroneously used for typical geometric configurations of small aspect ratio. For example, for a square cross-section flow cell ( $\alpha = 1$ ) and a two-dimensional high aspect ratio flow cell ( $\alpha = \infty$ ),  $K = 56$  and  $K = 96$  respectively. This leads to 70% changes in the average wall shear stress under nominally uniform flow conditions (i.e. the same bulk velocity and hydraulic diameter). Different flow cells with different geometric configurations are compared in (Salek et al., 2009).

Although the analyses mentioned above are done for a clean reactor, they can be used for early biofilm formation (i.e. thin layer with a relatively simple structure). From a fluid mechanics point-of-view, the adhered bacterial cells and small micro-colonies can be viewed as small surface roughness elements, or protrusions, embedded deeply in the low momentum wall layer. Under these conditions, Miksis and Davies (1994) have shown that the macroscopic wall shear stress can be approximated by the no slip boundary condition at the average roughness height, and therefore the flow prediction in a clean reactor can be a good guide in the study of early stages of biofilm formation (Salek et al., 2009). For older biofilms with morphologically complex structures an effective slip condition should be defined at the solid boundaries (Miksis & Davies, 1994). Moreover, if the roughness is

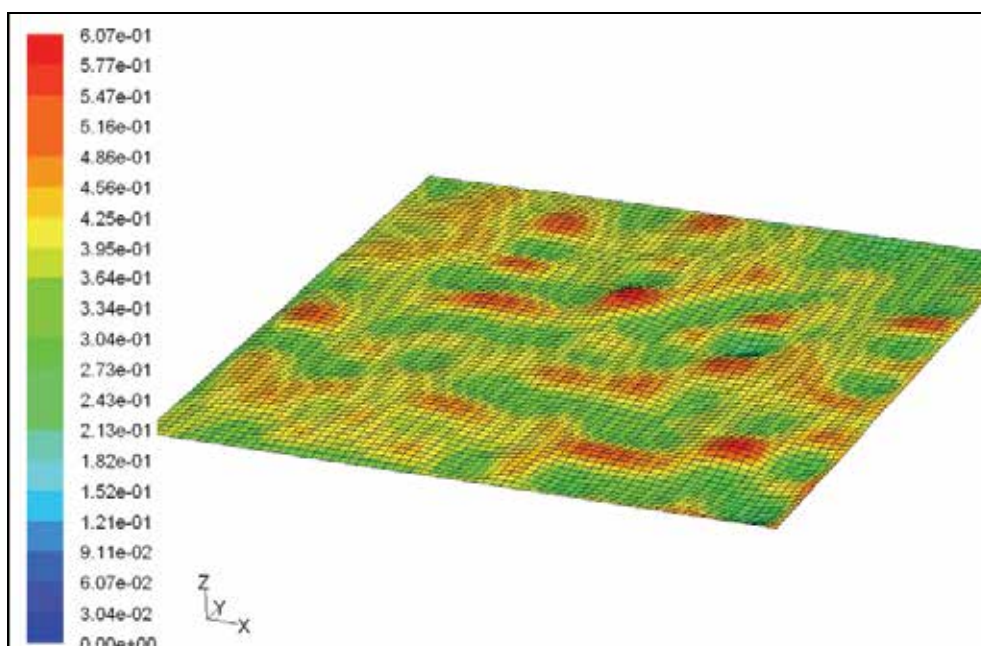


Fig. 3. Wall shear stress distribution over the reconstructed Endothelial Cells in a  $\mu$ -channel as determined by CFD (unit is in Pa). Reprinted from (Dol et al., 2010), ASME. Note that shear stress distribution correlates well with local roughness height

comparable to the height of flow cell, the actual surface should be modeled (e.g. endothelial cell cultures in micro-flow chambers, shown schematically in figure 3, from (Dol et al., 2010). This figure shows that when the roughness height is not negligible within the flow cell, the surface shear stress distribution can not be adequately represented by a global average.

In spite of the fact that biofilm formation is a dynamic process of growth and detachment, models under steady conditions can provide useful insights on the effects of flow cell configuration on substrate concentration distribution (Salek & Martinuzzi, 2007). To this end, the substrate concentration was numerically simulated inside the flow cells by solving the mass transport equation (Salek & Martinuzzi, 2007):

$$\vec{v} \cdot \nabla C = D \nabla^2 C \quad (11)$$

where  $C$  and  $D$  are the substrate concentration and diffusivity, respectively. Oxygen was assumed as the substrate and a uniform distribution of biofilms (consuming the oxygen from the medium) was assumed on the walls. A uniform concentration of oxygen ( $C_{in}$ ) at the inlet and no streamwise gradient of mass ( $\partial C / \partial z = 0$ ) at the outlet were assumed as the mass boundary conditions here. The consumption of oxygen by biofilms was assumed to follow the Monod kinetics (Picioreanu et al., 2000; Rittmann et al., 2001). The microbial activities within the biofilms consume the substrate from the bulk flow, and then create a substrate flux from the bulk liquid to the biofilms at the walls. This substrate flux is a function of substrate concentration right at the top of the biofilm surfaces and was set at the walls:

$$D \frac{\partial C(x, 0, z)}{\partial y} = \eta \hat{q}_{\max} X_f L_f \frac{C(x, 0, z)}{K_s + C(x, 0, z)} \quad (12)$$

$$D \frac{\partial C(x, b, z)}{\partial y} = \eta \hat{q}_{\max} X_f L_f \frac{C(x, b, z)}{K_s + C(x, b, z)} \quad (13)$$

$$D \frac{\partial C(0, y, z)}{\partial x} = \eta \hat{q}_{\max} X_f L_f \frac{C(0, y, z)}{K_s + C(0, y, z)} \quad (14)$$

$$D \frac{\partial C(a, y, z)}{\partial x} = \eta \hat{q}_{\max} X_f L_f \frac{C(a, y, z)}{K_s + C(a, y, z)} \quad (15)$$

$K_s$ ,  $\hat{q}_{\max}$ ,  $X_f$ ,  $L_f$ , and  $\eta$  are the half maximum rate concentration, maximum specific rate of substrate utilization, biofilm density, biofilm thickness, and effectiveness factor respectively. In fact,  $\eta$  is the ratio of the real flux to the flux occurring when the biofilm is fully penetrated at the top surface concentration. The effectiveness factor shows the effect of internal mass transport resistance. In our study, the biofilms were idealized with uniform thickness and density (Rittmann et al., 2001). Oxygen was modeled as a continuum species in a bulk flow.

The governing equations were solved using the Computational Fluid Dynamics (CFD) code FLUENT 6.2. Distributions of substrate concentration were solved with a species transport model. An external C++ user defined function (UDF) linked to FLUENT was used to define

and discretize the mass boundary condition at the wall. This was done by defining the mass flux using the values of mass concentration on the wall face and in the adjacent cell, and then overwriting the value of concentration on the face according to the concentration of the adjacent cell and desired flux.

The non-dimensional substrate concentration is defined as:

$$\bar{C} = \frac{C}{C_{in}} \quad (16)$$

And the mass Peclet number, which measures the ratio of convective to diffusive mass flux, is defined as:

$$Pe = \frac{U_m D_h}{D} \quad (18)$$

The other important non-dimensional parameter in mass transfer is the Damkohler number (Tilles et al., 2001; Zeng et al., 2006):

$$Da = \frac{\eta X_f q_{max} L_f D_h}{C_{in} D} \quad (19)$$

$Da$  is the ratio of substrate reaction rate at the wall to substrate diffusion from the medium. Biofilms with higher activity present higher  $Da$ . Damkohler was kept constant at 0.5 in our study.  $K_s$  was assumed constant except in the model verification section, where it was set to zero to simplify the boundary condition.

## 2.2 Model verification

The area weighted average of the wall shear stress in the fully developed regions in each flow cells was compared with the values obtained by the shear equation considering the geometry configuration. The results were in good agreement (not shown here). The mass transport model used in this study was verified through the comparison of the analytical solution for oxygen transport with the results gained at the bottom of a two-dimensional (2D) flow cell. No flux at one wall and a constant substrate flux at the other wall were assumed. The flow velocity was constant and uniform through the flow cell. To simplify the boundary condition just in model verification, we put  $K_s = 0$  which means that the substrate flux is constant at the maximum value. The analytical solution for the oxygen concentration along the bottom wall is obtained by the following equation (Carslaw et al., 1959; Tilles et al., 2001):

$$\begin{aligned} C / C_{in} = & 1 - z \frac{l}{b U_m} \frac{\eta X_f q_{max} L_f}{C_{in}} - \frac{\eta X_f q_{max} L_f b}{3 C_{in} D} \\ & + \frac{2}{\pi^2} \frac{\eta X_f q_{max} L_f b}{C_{in} D} \sum_{n=1}^{\infty} \frac{(-1)^n}{n^2} \cos(n\pi) \exp\left[-\frac{D l \pi^2 n^2 z}{U_m b^2}\right] \end{aligned} \quad (20)$$

Figure 4 compares the calculated mass distribution at the base with the analytical solution showing a good agreement. As will be discussed later, at lower mass Peclet number less

substrate is provided by the biofilms and nutrient depletion can happen through the flow cell ( $C \approx 0$ ).

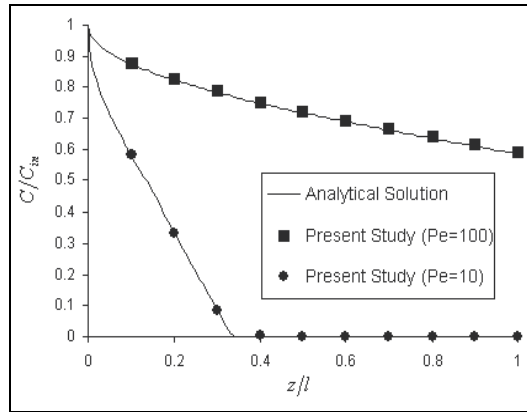


Fig. 4. Oxygen concentration at the substratum in a 2D flow cell model (Salek et al., 2007, ASME)

### 2.3 Shear stress and substrate concentration distribution

Figure 5(a) and (b) show the non-dimensional velocity profiles along the centerline of rectangular and square flow cells. These non-dimensional velocities are only a function of position and are independent of Reynolds number.

The shear (strain) rate contours in rectangular and square flow cells are shown in Figures 5(c) and (d) respectively. There are no secondary flows and the only shear component corresponds to the streamwise velocity. In Newtonian fluids, shear stress is proportional to shear rate ( $\dot{\gamma}$ ) with a constant viscosity:

$$\tau_w = \mu \dot{\gamma} \quad (21)$$

The shear rate is higher at the walls where the bacteria try to attach and colonize the surface. Figure 5(e) shows the non-uniform shear stress in rectangular (aspect ratio=5) and square flow cells. In each flow cell the non-dimensional wall shear stress distribution is a function of spanwise location in the flow cell and is independent of Re. It is clear that the flow cells with higher aspect ratio can provide a uniform shear stress distribution (i.e. no spanwise shear gradient) over a large part of their surfaces. Thus, most of the bacterial biofilm formation and challenges with antimicrobials will be exposed to similar hydrodynamic conditions. Hence, results would generally be representative of the nominal (average) conditions. However, this is not true for square flow cells. Clearly the distributions differ (figure 5(e)) from each other and also from their mean (e.g. 81 for rectangular flow cell and 56 for square flow cell). For the square flow cell, significant spanwise gradients exist and there is no region of uniform shear distribution. Essentially, the nominal or mean levels are not representative of the flow conditions to which bacteria are exposed. Thus,  $D_h$  is an insufficient parameter to relate low aspect ratio flow cells. These differences in wall shear stress distribution can lead to misleading interpretation in results and may account for some of the inconsistencies observed in the literature.

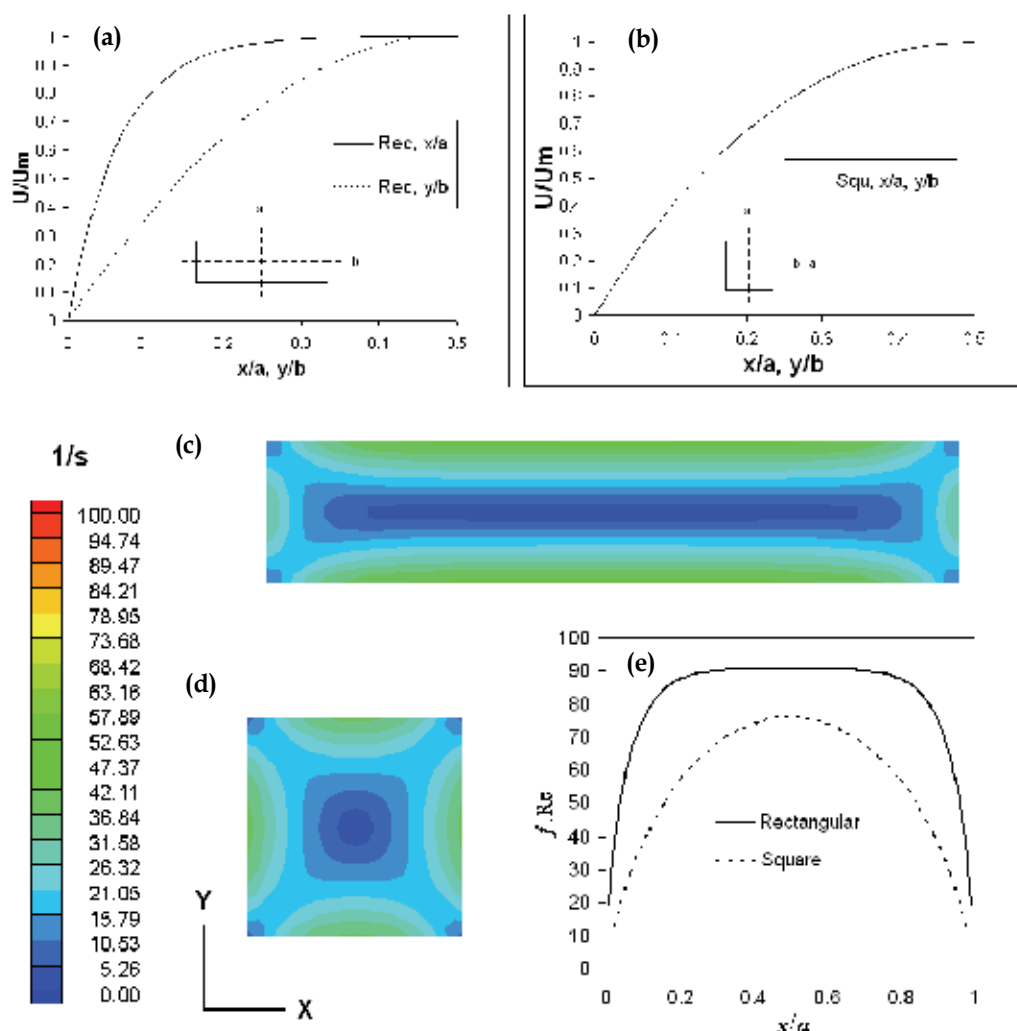


Fig. 5. Non-dimensional velocity profile along two centerlines in (a) rectangular and (b) square flow cell; Strain rate contours (1/s) (c) square tube flow cell; (d) rectangular (aspect ratio=5) tube flow cell; (e) Non-dimensional shear stress at the base of square and rectangular flow cells (Salek & Martinuzzi, 2007, ASME)

Shear plays an important role in bacterial attachment (Li et al., 1996; Thomas et al., 2002; Nejadnik et al., 2008) and biofilms morphology (Cao and Alaerts, 1995). When a cell is able to attach and resist the detachment under the shear forces, the adhesion is called stable which depends on the local fluid dynamics and the local interactions between the cell and the surface (Dickinson et al., 1995). It is been reported in the literature that in laminar flow the attachment process to the mammalian cells occurs at the shear levels between 0.25 and  $0.6 N/m^2$  (Olivier et al., 1993; Chisti, 2001); however, microbial attachment can occur at much higher shear levels (Duddridge et al., 1982). When adhered to the surfaces, bacteria can withstand higher stresses (Dickinson et al., 1995). The motile bacteria can attach more

strongly to surfaces at higher flow velocities (McClaine et al., 2002). On the other hand, it is been recently shown that the spanwise wall shear stress gradients arising in rectangular and square tube flow cells could affect the biofilm development and structure through the flow cells (Salek et al., 2009). Using the non-circular flow cells can lead to contradictory results if the presence of this spanwise shear gradient is not considered. If the non-uniform hydrodynamic condition in spanwise direction is significant, the biofilm distribution, maturity and expressed response can vary according to the location within the flow cell. In high aspect ratio flow cells, the areas with non-uniform hydrodynamics are limited to a small portion of the surfaces at the corners which makes them suitable to study the effects of shear stress level on cell adhesion and biofilm development.

Figure 6 shows the substrate concentration at different planes of a flow cell for different Peclet numbers. The distribution of substrate concentration is a function of convection, diffusion, which depends on the substrate diffusivity, and reaction rate, which depends on the biofilms characteristics. The effects of these parameters can be presented in terms of non-dimensional numbers,  $Pe$  and  $Da$ . In order to show the effects of flow cell geometry, we have isolated the other effects, and hence the biofilms characteristics and  $Da$  were assumed to be constant.

Figure 6(a) shows the substrate concentration at the base. In each cross section the substrate concentration is lower at the corners due to lower local convective mass flux. For higher  $Pe$ , the relative difference between the substrate concentration at the corner and at the middle is smaller (results not shown here). The local difference in mass concentration can cause different phenotypic biofilm responses. Piciooreanu et al., (2001) numerically showed that the mushroom-like biofilm structures are due to both biofilm detachment and nutrient depletion. Both nutrient concentration and shear stress vary through each cross section which can effectively change the structure of the biofilms in different locations (Salek & Martinuzzi, 2007; Salek et al., 2009).

The present simulations can, when considering low  $Pe$  cases, explain some discrepancies seen in the literature. For example, despite of low shear stress in the corners of square channel, which reduce biofilm detachment and can increase the attachment, Ebrahimi et al., (2005) observed thicker biomass formed in the middle of honeycomb packaging channels than in the corner. They attributed these differences to local substrate limitation at the corner, and concluded that at the middle biofilms receive more nutrients. This is correct when the biofilm growth is just limited to the microbial metabolism; however, the biofilm development can be due to both increased attachment of cells and bacterial growth (Brading et al., 1995).

The substrate concentration decreases along the channel which is due to the substrate consumption by the biofilms. At lower  $Pe$  numbers this reduction is more sensible (e.g. figure 6(d)). An appropriate  $Pe$  should be chosen in long tubes to prevent substrate depletion. In fact,  $Pe$  is the ratio of convective to diffusive mass fluxes. Figure 6(b) and (c) indicates that at smaller mass Peclet numbers, the bulk concentration is influenced more by the substrate consumption at the flow cell surfaces. This is clear, because smaller  $Pe$  means weaker convective terms which can not provide enough substrate for the biofilms. In the flow with small  $Pe$ , the substrate utilization is faster than the transport of substrate, leading to greater concentration gradient through the flow cell which forms different areas of growth for the biofilms. Rich media with higher  $Pe$ , provide a more uniform environment in which the effects of nutrient availability are less pronounced. For higher  $Pe$  cases, the differences observed at the corner and middle of the flow cells should thus show more

clearly the effect of shear stresses. Inconsistencies observed in the literature can often be traced to uncontrolled variations in Pe (Salek & Martinuzzi, 2007).

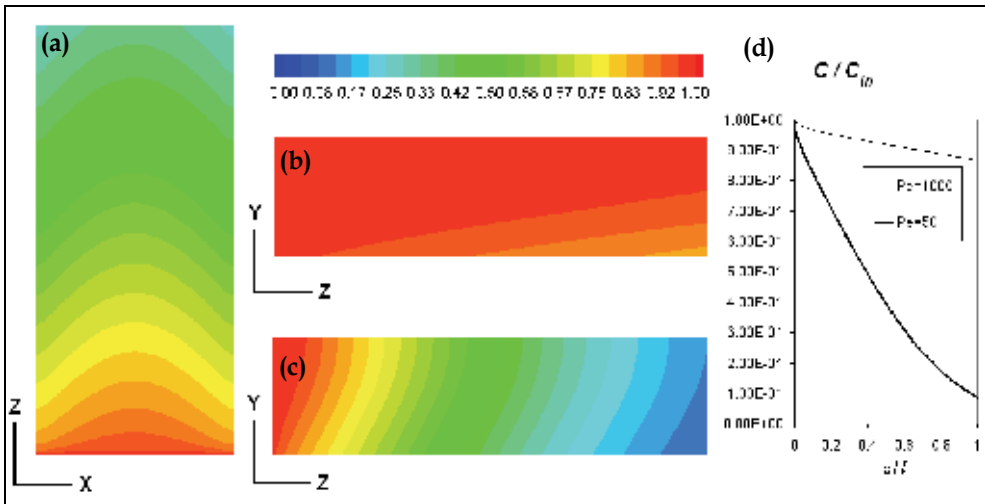


Fig. 6. Substrate concentration in the square flow cell (a) at the base at Pe=100; (b) and (c) at the mid plane at Pe= 1000 and 50 respectively; (d) at the base (Salek & Martinuzzi, 2007, ASME)

### 3. Unsteady flow in high-throughput 6-well plates

Devices for high-throughput assays have repeating geometric patterns, generally a well, in order to conduct many tests in parallel. When these plates are placed on an orbital shaker, the movement of the table induces the same motion in each well. The purpose of this section is to analyse the induced fluid motion in an individual well under varying acceleration conditions simulating the movement of an orbital shaker. Understanding of the fluid mechanics in these containers helps to interpret and correlate the biofilms results to hydrodynamic parameters in a well-controlled manner.

#### 3.1 Numerical method

The unsteady two-phase flow (i.e. air and water) inside an individual well of a 6-well plate was simulated using the Computational Fluid Dynamics (CFD) code FLUENT 6.3 for different rotational speeds and volumes of fluid.

The three-dimensional unsteady Navier-Stokes and continuity equations for incompressible flow were solved in each single-phase region.

$$\frac{\partial \rho}{\partial t} + \nabla \cdot (\rho \vec{v}) = 0 \tag{22}$$

$$\frac{\partial}{\partial t} (\rho \vec{v}) + \nabla \cdot (\rho \vec{v} \vec{v}) = -\nabla p + \nabla (\mu \nabla \vec{v}) + \rho F \tag{23}$$

where  $v$ ,  $\rho$ ,  $\mu$ ,  $p$  and  $F$  are velocity, density, dynamic viscosity, pressure and external force (per unit mass) for the corresponding single-phase, respectively.

To capture the free surface, the volume of fluid (VOF) method was selected, in which the volume fraction of each phase in each control volume is determined. Then, based on the volume fraction of each phase, the properties (e.g. dynamic viscosity and density) of control volumes are calculated. The system of equation is then closed by solving the continuity equation for the volume fraction. Just one set of momentum equation should be solved through the domain and then the obtained velocities are shared among the phases. The geometric reconstruct scheme was employed for the calculation of transient VOF model and interface tracking. For more information please see (Salek et al., 2010a; Salek et al., 2010b).

The influence of surface tension was assumed negligible which is valid when the gravitational forces and inertial forces on the liquid phase are significantly larger than the capillary forces. These forces are expressed through the Bond and Webber non-dimensional numbers:

$$Bo = \frac{(\rho_{water} - \rho_{air})g(2R)^2}{\sigma} \quad (24)$$

$$We = \frac{\rho_{water}\Omega^2(2R)^3}{\sigma} \quad (25)$$

In the present work, Bo and We are typically of the order of 100 (i.e. Bo, We  $\gg$  1).

The orbital shaker imparts a two-dimensional, in-plane movement to the 6-well plates mounted on the table. In an orbital motion, all points undergo a circular motion horizontally with a fixed radius of gyration.

There are two methods to introduce the orbital motion numerically to an individual well (Salek et al., 2010b). While these are mathematically equivalent, the numerical implementation and the behaviour of the solution differ.

In the first method, the equations of motions are solved in a stationary frame of reference. In this case, the dynamic mesh technique is used in which the entire mesh moves with the imposed velocity by the shaker ( $\vec{v} = \vec{U}$ ). An external C++ user defined function (UDF) linked to FLUENT was used to define the transient boundary condition for the moving well. In this method the only external force would be the gravity.

In the second method, the equations of motions are solved in a moving reference frame. In this method, the reference frame is translating with the speed of orbital shaker, and instead, the solid boundaries have zero velocity relative to the frame ( $\vec{v} = 0$ ). The influence of the plate motion is introduced through additional momentum source terms which are the acceleration of moving reference frame, the angular acceleration effect, Coriolis and centripetal acceleration appearing in the following equation respectively:

$$\vec{F} = \vec{g} - \frac{d\vec{U}}{dt} - \frac{d\omega}{dt} \times R_p - 2\omega \times v_{rel} - \omega \times (\omega \times R_p) \quad (26)$$

In the case of orbital motion all those terms are zero except the acceleration of moving reference frame.

Both methods were implemented to verify the validity of the original assumptions. While the simulation results were in agreement within the numerical accuracy, it was found that a coarser grid and bigger time step could be used applying the dynamic mesh technique, and hence the convergence rate was much faster (Salek et al., 2010b). In moving reference frame technique, the grids and time step needed to be 2x and 6x finer respectively.

### 3.2 Model verification

The motion of the free surface obtained from the CFD was compared with the captured SONY digital camera snapshots. The results were in good agreement (not shown here).

The average wall shear stress was validated experimentally using an optical shear rate (MicroS Sensor, Scientific Measurement Enterprise). The predicted shear rates agreed well with the experiments (Fig. 7(a)). The comparison of the results and the principles of sensors have been described in detail in (Salek et al., 2010a; Salek et al., 2010b).

### 3.3 Free surface flow and wall shear stress analysis in agitated 6-well plates

The instantaneous free-surface and wall shear stress field have been shown in figure 8. Generally, the shape of the free-surface resembles an inclined horseshoe over the elevated fluid region which undergoes a solid body rotation at the same rate as shaker's frequency. At higher frequencies, the interface is more inclined and rotates faster about the centre axis of the plate.

At 100 RPM, the fluid covers the entire bottom surface; but, in 200 RPM a small portion of the surface is exposed to the air. This can effectively change the wall shear stress magnitude due to big differences in the viscosity of air and water.

The wall shear stress at the bottom surface where the biofilms colonization occurs has been selected as the main hydrodynamic parameter here. Although the well itself does not rotate, the whole shear stress field rotates with the same frequency of the shaker. Hence the local wall shear stress at any point on the well culture area fluctuates with the same frequency of the shaker. The wall shear stress distribution is not symmetric about the center of rotation, but it is correlated with the shape of free-surface. The free surface can be characterized by a traveling wave which completes a full revolution in each period of rotation. The minimum and maximum local wall shear stress leads and lags the wave crest respectively (Salek et al., 2010b).

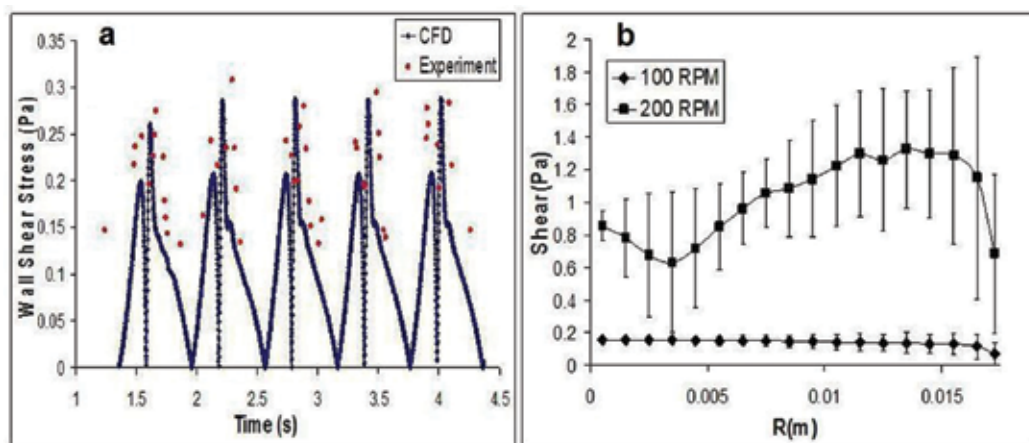


Fig. 7. (a) Time series of numerical and experimental wall shear stress component magnitude for 5 cycles at  $r=12\text{mm}$  from the center and 100 RPM; (b) Radial distribution of the mean wall shear stress magnitude at 100 and 200 RPM (Reprinted from (Salek et al., 2010a), IEEE)

Figure 7 (b) shows the radial distribution of the mean wall shear stress component magnitude (i.e time averaged at a point) at 100 and 200 RPM. It is clear that the wall shear level increases at higher rotational speeds. The shear distribution shows little variations across the plate for 100 RPM, except close to the distal corners in which the mean shear magnitude and the standard deviation of the fluctuations of the shear level magnitude are

decreased and increased respectively for both 100 and 200 RPM. This variation at the corner is due to secondary recirculation (Fig. 9) and wall effects (Salek et al., 2010b).

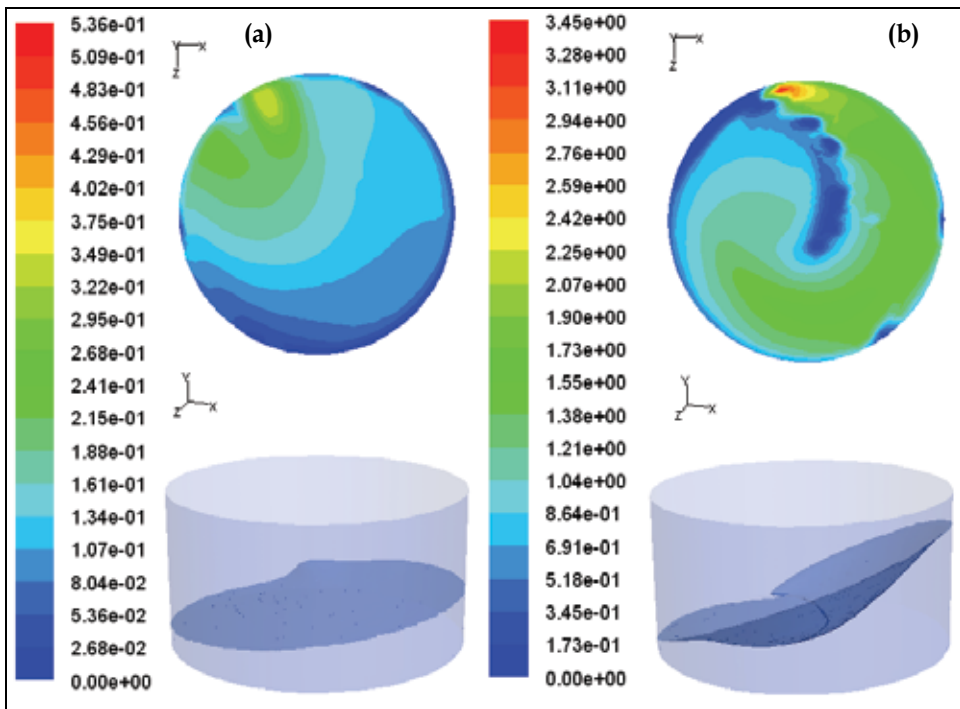


Fig. 8. Wall shear stress magnitude at the bottom wall and free-surface (a) 100rpm, 4ml, (b) 200rpm, 4ml (Reprinted from (Salek et al., 2010a), IEEE)

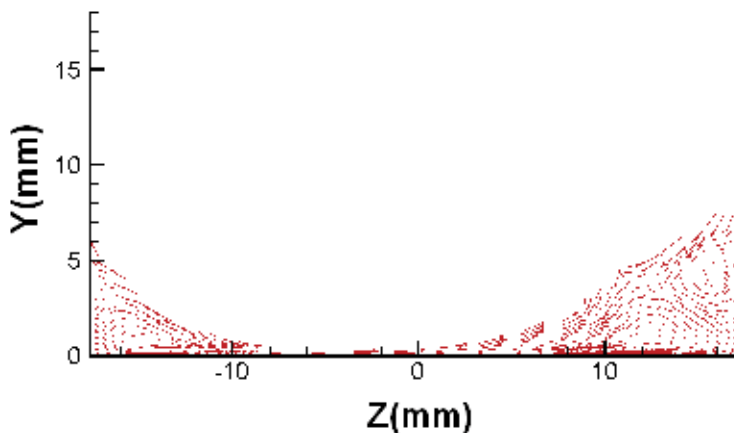


Fig. 9. Vector plots of flow in liquid phase with free-surface inside an individual well, 200rpm, 4ml

The oscillating flow behavior arising in 6-well plates can represent the physiological flows observed in vivo. Both increased shear stress levels and flow oscillation associated with plate motion were observed to contribute to biofilms formation (Kostenko et al., 2010).

#### 4. Conclusions

In the first part of this chapter, the hydrodynamics and nutrient availability were numerically simulated inside long rectangular and square flow cells. The local substrate concentration and wall shear stress are significantly different from the mean values and are changed through the rectangular and square flow cells depending on the flow cell geometry configuration. According to the present results, high aspect ratio flow cells (e.g. parallel plate flow chambers) at higher Peclet numbers provide a more uniform environment in the flow cells.

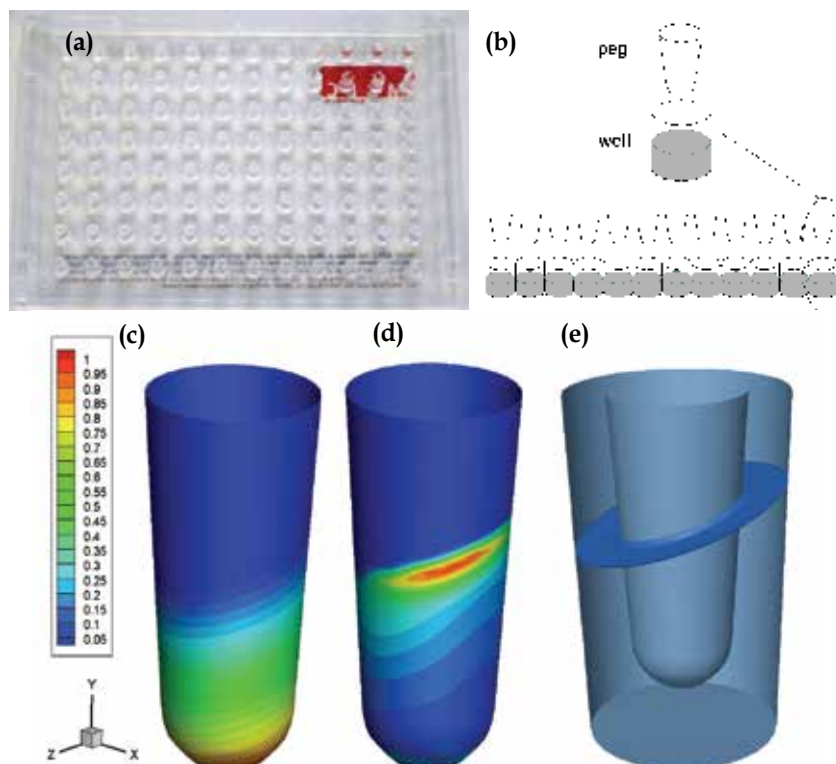


Fig. 10. (a) MBEC™ device, broadly used high-throughput device in the study of biofilms susceptibility to antibacterial agents (Ceri et al., 1999); (b) Schematic of MBEC™ device and peg and well; (c) Contours of non-dimensional static pressure over the peg; (d) Contours of non-dimensional wall shear stress over the peg; (e) Free surface flow

In the second part of this chapter, we confirmed the possibility of applying high-throughput devices to mimic physiologically relevant flow conditions to simulate the culture areas in practical applications. By controlling the hydrodynamics of the flow inside these plates, they can be more beneficial in the pathogenesis studies of biofilm infections, specially bloodstream infections.

The current methodology can be extended to other types of high-throughput devices (e.g. Fig10) as well; however, new source terms or forces may have to be considered due to the small size of some of these devices.

## 5. References

- Brading, M.G.; Boyle, J. & Lappin-Scott, H.M. (1995) Biofilm formation in laminar flow using *Pseudomonas fluorescens* EX 101, *Journal of Industrial Microbiology*, 15, pp. 297-304.
- Bryers, J.D. (2008) Medical Biofilms. *Biotechnol. Bioeng*, 100, pp. 1-18.
- Bryers, J.D. & Ratner, B.D. (2004) Bioinspired implant materials befuddle bacteria. *ASM News*, 70, pp. 232-237.
- Cao, Y.S. & Alaerts, G.J. (1995) Influence of reactor type and shear stress on aerobic biofilm morphology, population and kinetics. *Wat. Res.* 29, pp. 107-118.
- Carlsaw, H.S. & Jaeger, J.C. (1959) *Conduction of Heat in Solids*, second ed., Oxford University press, Oxford.
- Castelli, P.; Caronno, R.; Ferrarese, S.; Mantovani, V.; Piffaretti, G.; Tozzi, M.; Lomazzi, C.; Rivolta, N. & Sala, A. (2006) New trends in prosthesis infection in cardiovascular surgery. *Surg Infect* 7 (Suppl 2): pp. 45-47.
- Ceri, H.; Olson, M.E.; Stremick, C.; Read, R.R.; Morck, D. & Buret, A. (1999) The Calgary biofilm device: new technology for rapid determination of antibiotic susceptibilities of bacterial biofilms, *Journal of Clinical Microbiology*, 37, pp. 1771-6.
- Chen, M.J.; Zhang, Z. & Bott, T.R. (2005). Effects of operating conditions on the adhesive strength of *Pseudomonas fluorescens* biofilms in tubes. *Colloids and surfaces. B: Biointerfaces*, 43, pp. 61-71.
- Chisti, Y. (2001) Hydrodynamic Damage to Animal Cells, *Crit. Rev. Biotechnol.*, 21, 2, pp. 67-110.
- Christensen, B.E. & Characklis W.G. (1989). In: *Biofilms*, Characklis, W.G., & Marshall, K.C., (Ed.), (Chapter 4), Wiley Interscience, New York, USA.
- Dickinson, R. & Cooper, S. (1995) Analysis of Shear-Dependent Bacterial Adhesion Kinetics to Biomaterial Surfaces, *AIChE Journal*. 41, 9, pp. 2160-2173.
- Dol, S.S.; Salek, M.M.; Viegas, K.; Martinuzzi, R.J. & Rinker, K. (2010) Micro-PIV and CFD Studies Show Non-Uniform Wall Shear Stress Distributions Over Endothelial Cells. *Proceedings of ASME 2010, 8th International Conference on Nanochannels, Microchannels, and Minichannels*, Montreal, Canada, Aug 1-4, 2010.
- Duddridge, J.E.; Kent, C.A. & Laws, J.F. (1982) Effect of surface shear stress on the attachment of *Pseudomonas fluorescens* to stainless steel under defined flow conditions, *Biotechnol Bioeng.*, 24, pp. 153-64.
- Dunsmore, B.C.; Jacobsen, A.; Hall-Stoodley, L.; Bass, C.J.; Lappin-Scott, H.M.; Stoodley, P. (2002) The influence of fluid shear on the structural and material properties of sulphate-reducing bacterial biofilms. *J Ind Microbiol Biotechnol* 29, pp. 347-353.
- Ebrahimi, S.; Picioareanu, C.; Xavier, J.B.; Kleerebezem, R.; Kreutzer, M.; Kapteijn, F.; Moulijn, J.A. & van Loosdrecht, M.C.M. (2005) Biofilm growth pattern on honeycomb monolith packings: Effect of shear rate and substrate transport limitations, *Catalysis Today*, 105, pp. 448-454.
- Geesey, G.G. & Bryers J.D. (2000). Biofouling of engineered materials and systems, In: *Biofilms II: Process Analysis and Applications*, Bryers J.D., (Ed.), (237-279), Wiley-Liss, Inc., New York, USA.
- Gjersing, E.L.; Codd, S.L.; Seymour, J.D. & Stewart, P.S. (2005). Magnetic Resonance Microscopy Analysis of Advective Transport in a Biofilm Reactor. *Biotechnol Bioeng*, 89, 7, pp. 822-834.
- Horn, H.; Reiff, H. & Morgenroth, E. (2003) Simulation of growth and detachment in biofilm systems under defined hydrodynamic conditions, *Biotechnol. Bioeng*, 81, 5, pp. 607-617.

- Hosoi, Y.; & Murakami, H., (1986). Effect of the Fluid Velocity on the Biofilm Development, *Proceedings of the Water Forum 86: World Water Issues in Evolution*, pp.1718-1725, Long Beach, California, August 1986.
- Kostenko, V.; Salek, M.M. ; Sattari, P. & Martinuzzi, R.J. (2010). Staphylococcus aureus Biofilm Formation and Susceptibility to Antibiotics in Response to Oscillatory Shear Stresses of Physiological Levels. *FEMS Immunology and Medical Microbiology*, 59, pp. 421–431.
- Leutheusser, H.J. (1984) Velocity distribution and skin friction resistance in rectangular ducts, *Journal of Wind Engineering and Industrial Aerodynamics*, 16, pp. 315-327.
- Li, Z.; Ho'o'k, M.; Patti, J.M. & Ross., J.M. (1996) The effect of shear stress on the adhesion of *Staphylococcus aureus* to collagen I, II, IV and VI. *Ann. Biomed. Eng.* 24 (Suppl. 1): S-55.
- MacLeod, S.M. & Stickler, D.J. (2007) Species interactions in mixed-community crystalline biofilms on urinary catheters. *Med. Microbiol.*, 56, 11, pp. 1549-57.
- Manz, B.; Volke, F.; Goll, D. & Horn H. (2003). Measuring local flow velocities and biofilm structure in biofilm systems with magnetic resonance imaging (MRI). *Biotechnol Bioeng.* 84, pp. 424-432.
- Marshall, K.C. (1985) Mechanisms of bacterial adhesion at solid-water interfaces. In: *Bacterial adhesion*, Savage, D.C., Fletcher, M. (Ed.), pp. 133–161, Plenum Press, New York.
- McClaine, J.W. & Ford, R.M. (2002) Characterizing the adhesion of motile and nonmotile *Escherichia coli* to a glass surface using a parallel-plate flow chamber. *Biotechnol. Bioeng.* 78, pp. 179-189.
- Meda, M.S.; Lopez, A.J. & Guyot, A. (2007) Candida inferior vena cava filter infection and septic thrombophlebitis. *Br J Radiol.*, 80, 950, pp. 48-9.
- Miksis, M.J. & Davis, S.H. (1994) Slip over rough and coated surfaces. *J Fluid Mech*, 273, pp. 125–139.
- Murray, T.S.; Egan, M. & Kazmierczak, B.I. (2007) Pseudomonas aeruginosa chronic colonization in cystic fibrosis patients. *Curr Opin Pediatr.*, 19, 1, pp. 83-8.
- Nejadnik, M.R. ; van der Mei, H.C. ; Busscher, H.J. and Norde, H. J. (2008) Determination of the shear force at the balance between bacterial attachment and detachment in weak-adherence systems, using a flow displacement chamber. *Appl. Environ. Microbiol.* 74, pp. 916-919.
- Olivier, L.A. & Truskey, G.A. (1993) A Numerical Analysis of Forces Exerted by Laminar Flow on Spreading Cells in a Parallel Plate Flow Chamber Assay, *Biotechnol. Bioeng.*, 42, pp. 963–973.
- Percival, S.L. & Bowler, P.G. (2004). Biofilms and their potential role in wound healing, *Wounds*, 16, 7, pp. 234-240.
- Phillips, P.L.; Sampson, E.; Yang Q.; Antonelli, P. ; Progulske-Fox, A. & Schultz, G. (2008) Bacterial biofilms in wounds. *Wound Healing South Afr*, 1, pp. 10-12.
- Picioleanu, C.; Van Loosdrecht, M.C.M. & Heijnen, J.J. (2001) Two-dimensional model of biofilm detachment caused by internal stress from liquid flow, *Biotechnology and Bioengineering*, 72, pp. 205–218.
- Picioleanu, C.; Van Loosdrecht, M.C.M. & Heijnen, J.J. (2000) A theoretical study on the effect of surface roughness on mass transport and transformation in biofilms. *Biotechnol. Bioeng.* 68, pp. 355–369.
- Presterl, E.; Lassnigg, A.; Eder, M.; Reichmann, S.; Hirschl, A.M. & Graninger, W. (2007) Effects of tigecycline, linezolid and vancomycin on biofilms of viridans streptococci isolates from patients with endocarditis. *Int J Artif Organs*, 30, 9, pp. 798-804.

- Purevdorj, B.; Costerton, J.W. & Stoodley, P. (2002) Influence of hydrodynamics and cell signaling on the structure and behavior of *Pseudomonas aeruginosa* biofilms, *Appl. Environ. Microbiol.* 68, pp. 4457–4464.
- Rittmann, B.E. & McCarty, P.L. (2001) *Environmental Biotechnology: Principles and Applications*. McGraw-Hill Book Co, New York.
- Salek, M.M. & Martinuzzi, R.J. (2007) Numerical simulation of fluid flow and oxygen transport in the tube flow cells containing biofilms, *Proceedings of 5th Joint ASME/JSME Fluid Engineering Conference*, pp. 1-8, San Diego, USA, July 30-August 2, 2007.
- Salek, M.M.; Jones, S. & Martinuzzi R.J. (2009) The influence of flow cell geometry related shear stresses on the distribution, structure and susceptibility of *Pseudomonas aeruginosa* 01 biofilms. *Biofouling*, 25, pp. 711-725.
- Salek, M.M. ; Sattari, P. & Martinuzzi, R.J. (2010a) What Do Biofilms Sense in Agitated Well Plates? A Combined CFD and Experimental Study on Spatial and Temporal Wall Shear Stress Distribution, *IEEE Proc. of the 36th Annual Northeast Bioengineering Conference*, Columbia University, New York City, NY, USA, March 26-28, 2010.
- Salek, M.M. ; Sattari, P. & Martinuzzi, R.J. (2010b) Numerical and Experimental Investigation of Flow and Wall Shear Stress Pattern inside Part-Filled Moving 6-well Plates, unpublished data.
- Sillankorva, S.; Neubauer, P. & Azeredo, J. (2008) *Pseudomonas fluorescens* biofilms subjected to phage phiIBB-PF7A. *BMC Biotechnology*, 8 : 79.
- Sousa, C.; Henriques, M.; Azeredo, J.; Teixeira, P. & Oliveira, R. (2008) *Staphylococcus epidermidis* glucose uptake in biofilm versus planktonic cells. *World J. Microbiol. Biotechnol.* , 24, pp. 423-426.
- Spiga, M. & Morini, G.L. (1994) A symmetric solution for velocity profile in laminar flow through rectangular ducts, *Int. Comm. Heat Mass Transfer*, 21, pp. 469-475.
- Stoodley, P.; Dodds, I.; Boyle, J.D. & Lappin-Scott, H.M. (1999) Influence of hydrodynamics and nutrients on biofilm structure. *J Appl Microbiol*, 85 pp. 19-28.
- Stoodley, P.; Jacobsen, A.; Dunsmore, B.C. ; Purevdorj, B.; Wilson, S.; Lappin-Scott, H.M. & Costerton, J.W. (2001a) The influence of fluid shear and AICI<sub>3</sub> on the material properties of *Pseudomonas aeruginosa* PAO1 and *Desulfovibrio* sp. EX265 biofilms, *Water Sci Technol*, 43, pp. 113–120.
- Stoodley, P.; Hall-Stoodley, L. & Lappin-Scott, H.M. (2001b) Detachment, surface migration, and other dynamic behavior in bacterial biofilms revealed by digital time-lapse imaging. *Methods in Enzymology*, 337, pp. 306-319.
- Thomas, W.E.; Trintchina, E.; Forero, M.; Vogel, V. and Sokurenko, E. V. (2002) Bacterial adhesion to target cells enhanced by shear force, *Cell*, 109, 7, pp. 913– 923.
- Tilles, A.W.; Baskaran, H.; Roy, P.; Yarmush, M.L. & Toner, M. (2001) Effects of oxygenation and flow on the viability and function of rat hepatocytes cocultured in a microchannel flat-plate bioreactor, *Biotechnol. Bioeng.*, 73, pp. 379-389.
- Trachoo, N. (2003) Biofilms and the food industry. *Songklanakarinn J. Sci. Technol.*, 25, 6, pp. 807-815.
- Tsanis, I.K. & Leutheusser, H.J. (1982) Non Uniform Laminar Free Surface Flow. *Journal of the Engineering Mechanics Division* , ASCE, 108, pp. 386-398.
- Wenzel, R.P. (2007) Health care-associated infections: Major issues in the early years of the 21st century. *Clin Infect Dis* 45 (Suppl 1): S85–S88.
- Zeng, Y.; Lee, T.S.; Yu, P.; Roy, P. & Low H.T. (2006) Mass Transport and Shear Stress in a Microchannel Bioreactor: Numerical Simulation and Dynamic Similarity, *J. Biomech Eng.* 128, 2, pp. 185-193.

# Comparison of Numerical Simulations and Ultrasonography Measurements of the Blood Flow through Vertebral Arteries

Damian Obidowski and Krzysztof Jozwik  
*Technical University of Lodz,  
Institute of Turbomachinery, Medical Apparatus Division  
Poland*

## 1. Introduction

Vertebral arteries are a system of two blood vessels through which blood is carried to the rear region of the brain. This region of the human body has to be very well supplied with blood. Blood is delivered to the brain through carotid arteries as well. Due to their position and shape, vertebral arteries are a special kind of blood vessels. They have their origin at a various distance from the aortic ostium, can branch off at different angles, and have various lengths, inner diameters and spatial shapes. The above-mentioned variations are connected with inter-patient differences in the human anatomy. In the upper part of vertebral arteries, there is a marked arch curvature, owing to which turning the head is not followed by obliteration of these vessels. Contrary to other arteries, vertebral arteries join at their ends to form one vessel, a comparatively large basilar artery. This junction can be characterized by a varied geometry as well. For individual geometrical configurations of the vertebral artery system, there are also differences in the diameter of the left and right artery. All the above-mentioned differences result from a unique individual anatomical structure and do not follow from any pathology (Daseler & Anson 1959; Jozwik & Obidowski 2008; Jozwik & Obidowski 2010).

Some symptoms occurring in patients may suggest that the cause of an ailment lies in an incorrect blood supply to the rear region of the brain, and thus in an incorrect blood flow through vertebral arteries. The direct cause of such a phenomenon can result from arterial occlusion. The ultrasonography is employed to check the flow correctness. It is rather difficult to conduct this imaging procedure, but if it is performed by an experienced specialist, then the results obtained can be considered reliable. It happens, however, that the measured values of the maximum and minimum velocity in the left and right artery, which characterize the blood flow, differ significantly. Hence, the diagnosis of arteriosclerosis in these vessels is well based. It can be an indication for a surgical procedure (Mysior 2006). A significantly large percentage of cases diagnosed in such a way are not related to changes in the artery structure, and thus surgery would be irrelevant. If a structure and a shape of vertebral arteries, their individual variations are considered, then differences in the blood flow and a lack of relation between these differences and artery diameters can result from flow phenomena only.



inner diameters (left to right and patient to patient), and thus in flow fields. Such variations in inner diameters do not exceed the range of 2 – 6 mm. However, for a particular patient anatomy, the inner diameter, except for stenosis occurring in arteries, of an individual vertebral artery can be treated as constant along the artery. Nevertheless, it is impossible to formulate explicit relations describing the dependence between the left and right artery inner diameter. Each configuration of diameters (whose values fall within the range mentioned) is possible (Daseler & Anson 1959; Sokołowska 1988).

### 3. Model of the selected structure geometry

For the system of the vertebral artery structure occurring most frequently in the human anatomical structure, three models of its geometry have been developed (see Fig. 2). Each model has one inlet (aortic ostium) and six outlets (cross-sections of main arteries in the considered region). Owing to a significant differentiation in individual human anatomy (Daseler and Anson 1959; Ravensbergen et al.1974), which consists in a varied arrangement, length, kind of junctions, inner diameters and other geometrical parameters of the blood vessels under consideration, averaged data included in anatomical atlases, scientific publications, results of tomographic, magnetic resonance and ultrasonography imaging (Daseler and Anson 1959; Bochenek and Reicher 1974; Daniel 1988; Michajlik and Ramotowski 1996; Sinelnikov 1989; Vajda 1989) have been employed in the models developed. The models of vertebral arteries do not account for a part of secondary vessels branching off from the arteries under analysis before they join to form the basilar artery. Diameters of these vessels are relatively very small and their effect on the flow is insignificant.

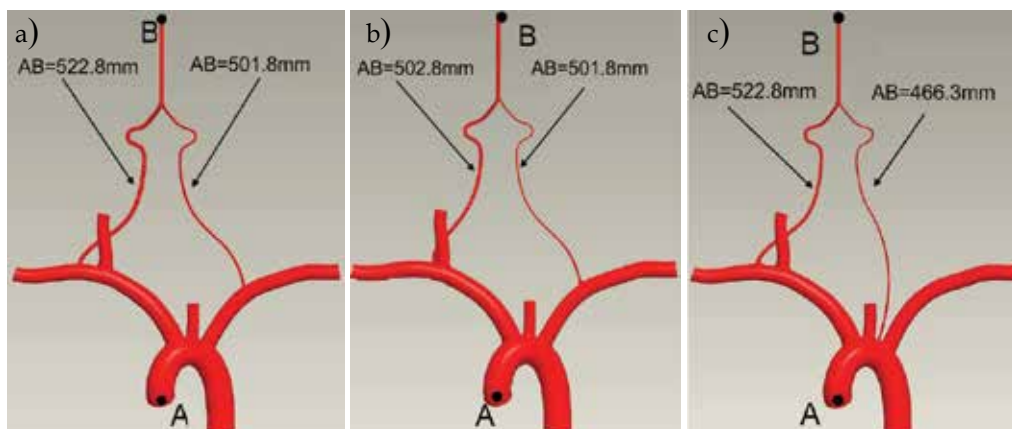


Fig. 2. Developed models of the selected geometry of the vertebral artery region of the circulatory system (Obidowski 2007)

The 3D shape of arteries has been taken into account in the three models prepared. These models differ as far as the place the left and right artery starts, the spatial shape and the length of individual arteries are concerned. For each model further on referred to as model 1, 2 and 3, differences in the total length of the left and right artery occur that are equal to, respectively: for model 1 – left artery – 501.8 mm, right artery – 522.8 mm, for model 2 – left artery – 501.8 mm, right artery – 502.8 mm, for model 3 – left artery – 466.3 mm, right artery

– 522.8 mm. These differences result from various places the left or right vertebral artery originates. Model 3, in which the left artery starts directly on the aortic arch, differs mostly. Moreover, it has been assumed that artery diameters can vary within the range of the values quoted above, but they are constant along their length. Taking into consideration changes in the inner diameter with a step equal to 1 mm and the fact that an arbitrary combination of the left and right artery diameter can occur, 25 cases of geometry for each model system and three different system geometries have been obtained, giving altogether 75 cases to be analysed. To simulate the flow, walls of all vessels considered have been assumed rigid and not subject to deformations with changes in the blood pressure. The diameters of the remaining artery vessels in the segments under consideration are listed in Table 1.

Artery	Diameter [mm]
Aorta	28.5
Brachiocephalic trunk artery	20 at bifurcation ÷ 14 at the outlet cross-section
Right carotid artery	14 at bifurcation ÷ 12 at the outlet cross-section
Left carotid artery	12 at bifurcation ÷ 11.5 at the outlet cross-section
Left subclavian artery	16 at bifurcation ÷ 15.5 at the outlet cross-section
Basilar artery	3 ÷ 8.5 depending on the vertebral artery diameter
Vertebral arteries	2 ÷ 6 depending on the case studied

Table 1. Values of diameters used to model the geometry (Bochenek 1974; Daniel 1988; Mysior 2006; Vajda 1989 et al.)

For each case of the system geometry, a computational mesh built of tetrahedral elements, condensed in the region of vertebral arteries, has been generated. Additionally, prism elements have been introduced in the vicinity of walls to define flow parameters at vessel walls more precisely. A sample mesh can be found in (Obidowski 2007, Jozwik and Obidowski 2010). The mesh independence tests have not yielded any significant differences that could affect the results of the computations conducted. Thus, due to time-consuming transient simulations, a middle-size density has been employed. The average size of the mesh used is approx. 1 million elements.

#### 4. Blood flow parameters and boundary conditions

Blood is the medium owing to which each place in our organism is supplied with products indispensable for life and simultaneously purified from waste or toxic substances. From the viewpoint of flow, blood parameters are very difficult to describe. Even for a particular individual, values of the parameters alter, and these alterations depend on numerous factors connected with sex, age, diet and physical conditions, etc. Moreover, variations in values of blood flow parameters occur both slowly (e.g., along with the patient's ageing), as well as very fast (e.g., as an effect of irritation). The blood flow in human body is a cyclic flow with a strong asymmetry of changes within one cycle. In addition, owing to damping properties of blood vessel walls, amplitude and pressure variations versus time undergo changes depending on a position and a distance of the point under consideration from the heart. A proper model of blood, as well as properly imposed boundary conditions exert a direct

influence on the quality and accuracy of computations (Ballyk et al. 1994; Chen & Lu 2006; Gijssen et al. 1999; Johnston et al. 2004; Obidowski 2007, Walburn & Schneck 1976). On the other hand, taking into account a relatively wide range of alternations in values of these parameters, the blood model should reflect its behaviour in the flow and not necessarily render exactly the values of individual quantities that describe blood flow characteristics.

#### 4.1 Model of blood

From the viewpoint of flow, the fundamental blood parameters are as follows:

- density,
- viscosity,
- heat conductivity.

For the phenomena and the region under consideration, the last parameter can be neglected. Changes in blood density depend on age and sex of the person first of all and their values fall within the range of 1030 - 1070 kg/m<sup>3</sup> (Bochenek et al. 1974, Michajlik et al. 1996). For the needs of this simulation, the constant density of blood equal to 1055 kg/m<sup>3</sup> has been assumed.

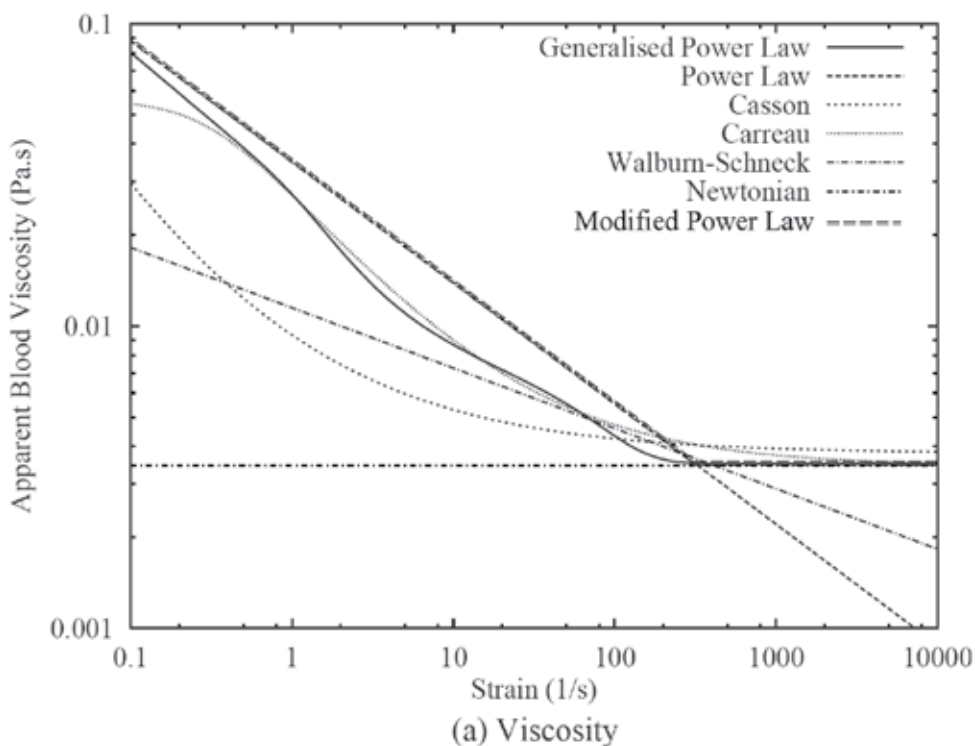


Fig. 3. Apparent blood viscosity as a function of strain for different blood models (Johnston et al. 2004)

Blood is a non-Newtonian fluid with a state memory. It means that the dynamic viscosity coefficient does not depend on the kind of liquid only, but also on flow parameters and a tendency in their variations. In the literature, numerous models describing a relation between the blood viscosity coefficient and blood flow parameters can be found. To describe

the flow occurring in vicinity of the aortic ostium, the Newton's model is appropriate. On the other hand, the blood flow in small vessels needs a more complex blood model (Ballyk et al. 1994; Chen and Lu 2006; Gijssen et al. 1999; Johnston et al. 2004; Obidowski 2007, Walburn and Schneck 1976). For the purpose of this study, a modified Power Law model has been employed. This model reflects the behaviour of the Newtonian fluid for large Reynolds numbers and simultaneously renders the flow nature at the viscosity of blood vessels of low diameters and low velocities. The model is expressed by the following system of equations:

$$\left\{ \begin{array}{l} \mu = 0.554712 \text{ for } \left( 2 \frac{\partial U_i}{\partial x_j} S_{ij} \right)^{\frac{1}{2}} < 1e^{-9} \\ \mu = \mu_0 \left( \left( 2 \frac{\partial U_i}{\partial x_j} S_{ij} \right)^{\frac{1}{2}} \right)^{n-1} \text{ for } 1e^{-9} \leq \left( 2 \frac{\partial U_i}{\partial x_j} S_{ij} \right)^{\frac{1}{2}} < 327 \\ \mu = 0.00345 \text{ for } \left( 2 \frac{\partial U_i}{\partial x_j} S_{ij} \right)^{\frac{1}{2}} \geq 327 \end{array} \right. \quad (1)$$

where:  $\mu_0 = 0.0035 \text{ Pa s}$ ,  $n = 0.6$  and  $\left( 2 \frac{\partial U_i}{\partial x_j} S_{ij} \right)^{\frac{1}{2}}$  - shear strain rate.

Characteristic curves as a function of strain are presented in Fig. 3. The same curves show variations in other blood models known from the literature (Johnston et al. 2004; Gijssen et al. 1999; Walburn & Schneck 1976).

#### 4.2 Boundary conditions

For the system under consideration, boundary conditions referring to time-variable parameters at the inlet and in six outlet cross-sections (see Fig. 4) should be assumed. Velocity variations versus time, as well as pressure variations can be approximated with a Fourier series. The Fourier series employed to determine the velocity and pressure waves takes the following form:

$$F(t) = \frac{1}{2} a_0 + \sum_{n=1}^3 (a_n \cos(n\omega t + t_0) + b_n \sin(n\omega t + t_0)) \quad (2)$$

where  $a_0$ ,  $a_n$  and  $b_n$  are experimentally determined Fourier coefficients and  $t_0$  is a phase displacement. Thus, at the inlet, that is to say, at the aortic ostium, a uniform velocity distribution for the whole cross-section has been adopted. Six harmonics of the Fourier series allow one to generate a velocity profile used in the presented experiment as shown in Fig. 5, which is an approximation of experimental curves found in the literature (Traczyk 1980, Viedma 1997).

The time-variable static pressure has been taken as the parameter determining boundary conditions at outlets. The static pressure also changes periodically and a time displacement of these changes following from various paths of the pulse wave measured from the aortic

ostium should be taken into account for the assumed outlet cross-sections. The values of phase displacements for individual outlet cross-sections have been calculated on the basis of the length of centre lines and pulse wave propagation velocities in arteries. Wang has determined pulse wave propagation velocities in individual human arteries (Wang 2004). For the outlet cross-section of the basilar artery, the pressure has been determined on the basis of the averaged path along the left and right vertebral artery. The static pressure variations for individual outlets are shown in Fig. 6 (Jozwik & Obidowski 2009).

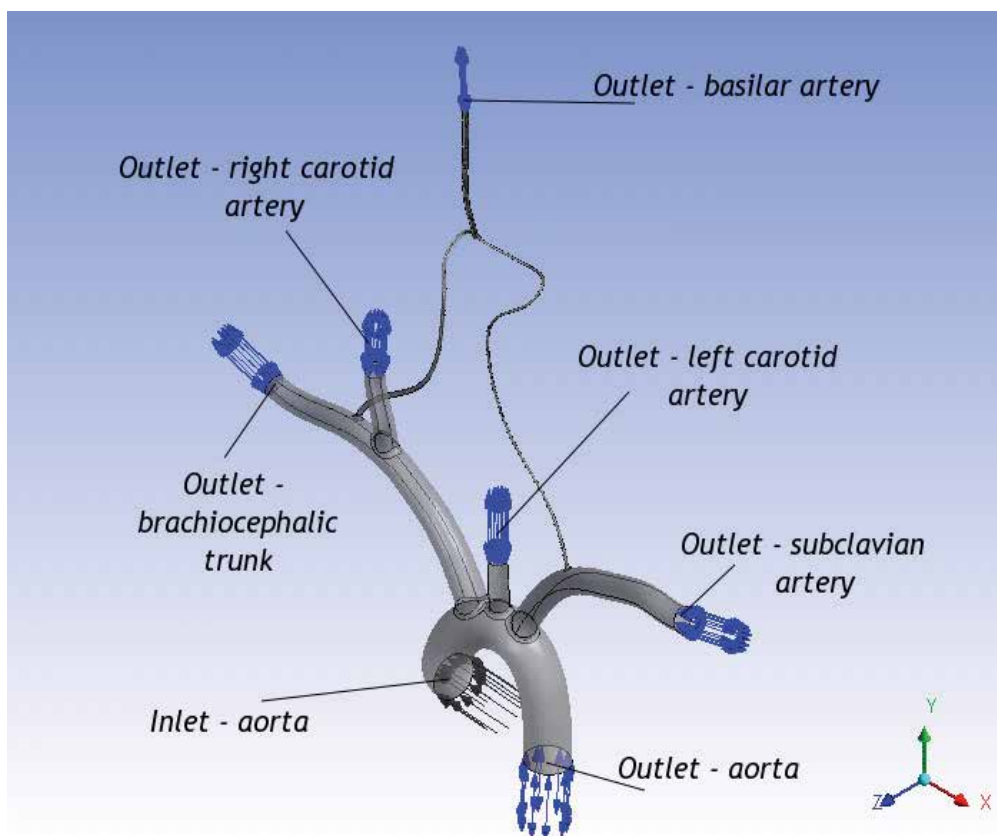


Fig. 4. Boundary conditions at the inlet and outlets of the modelled geometry of the vertebral arteries under investigation (Obidowski 2007)

The walls of vessels in which blood flows are supposed to be nondeformable. Owing to the flow nonstationarity that follows both from considerable values of velocity at the aortic ostium, numerous branches and narrowings, as well as from a pulsating nature of the flow, the flow is expected to be turbulent in many places of the system being modelled. A Shear Stress Transport (SST) model, belonging to the  $k-\omega$  model family, has been adopted as the turbulence model in the investigations.

This model renders correctly the character of the boundary flow for the flows characterized by low Reynolds numbers. Initially, the calculations were conducted for the flow under steady conditions.

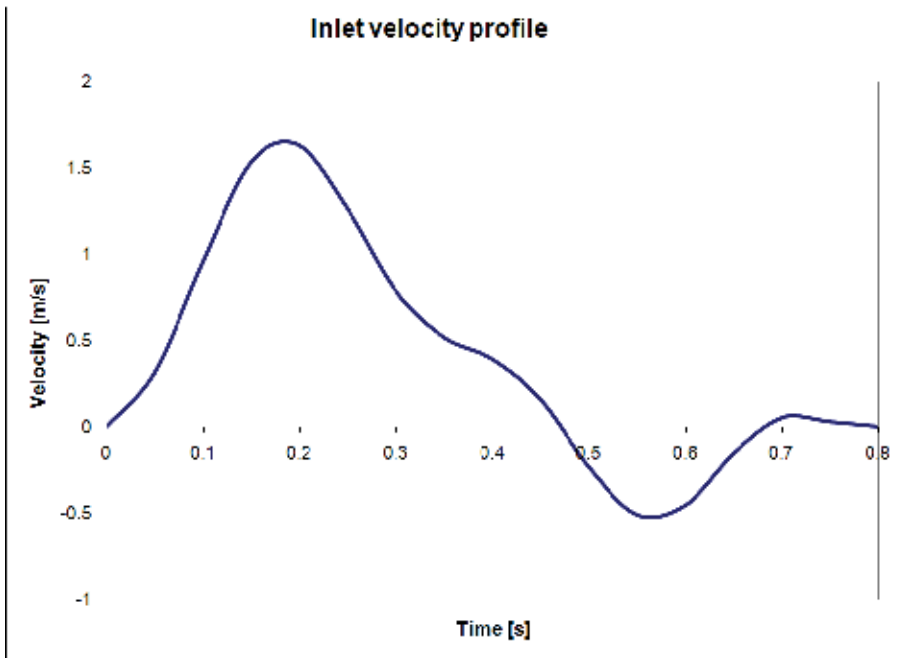


Fig. 5. Changes in velocity as a function of time for the inlet cross-section during one cycle of heart operation (Obidowski 2007)

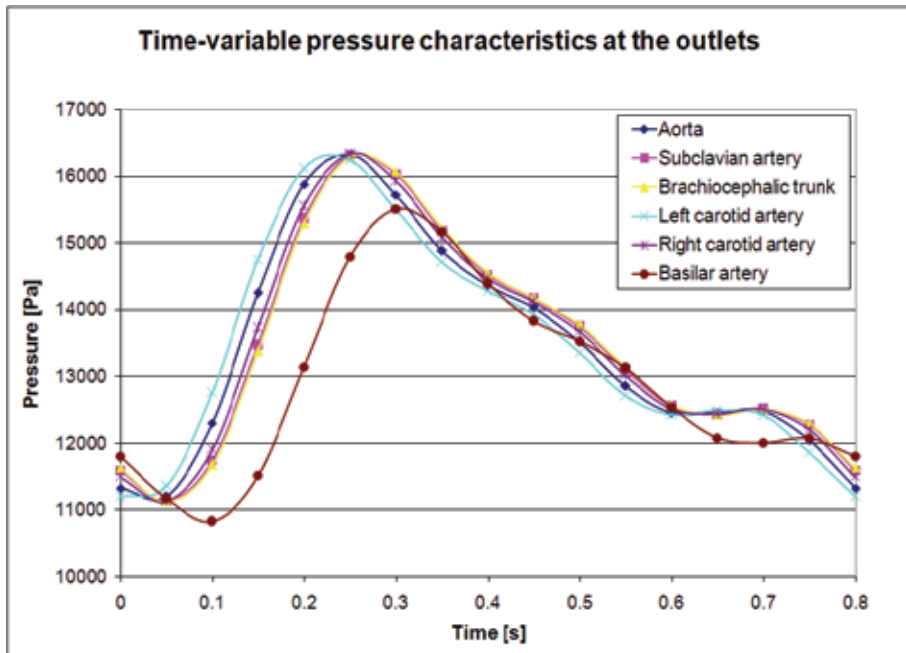


Fig. 6. Changes in pressure as a function of time for outlet cross-sections during one cycle of heart operation (Jozwik & Obidowski 2009)

The following values of parameters at the inlet and the outlet were taken, namely:

- velocity in the aortic ostium,  $v_{as} = 1.44$  m/s,
- all static pressures in all outlet cross-sections were assigned to averaged static pressures and were equal to 13 kPa.

The results obtained for steady flow calculations were taken as the initial ones for the unsteady flow, for which the calculations of five cycles of variations in parameters were conducted. Owing to this, the obtained results are independent of the assumed initial values from the steady flow conditions.

### 4.3 Governing equations

The ANSYS CFX v. 10.0 solver was used to obtain a solution to the described problem. The unsteady Navier-Stokes equations in their conservation form are a set of equations solved by ANSYS CFX (ANSYS CFX-Solver Theory Guide).

The continuity equation is expressed as:

$$\frac{\partial \rho}{\partial t} + \nabla \cdot (\rho \mathbf{U}) = 0 \quad (3)$$

Thus, the momentum equation takes the following form:

$$\frac{\partial (\rho \mathbf{U})}{\partial t} + \nabla \cdot (\rho \mathbf{U} * \mathbf{U}) = -\nabla p + \nabla \cdot \boldsymbol{\tau} + S_M \quad (4)$$

where the stress tensor,  $\boldsymbol{\tau}$ , is related to the strain rate by the following relation:

$$\boldsymbol{\tau} = \mu \left( \nabla \mathbf{U} + (\nabla \mathbf{U})^T - \frac{2}{3} \delta \nabla \cdot \mathbf{U} \right) \quad (5)$$

The total energy equation is represented by:

$$\frac{\partial (\rho h_{tot})}{\partial t} - \frac{\partial p}{\partial t} + \nabla \cdot (\rho \mathbf{U} h_{tot}) = \nabla \cdot (\lambda \nabla T) + \nabla \cdot (\mathbf{U} \cdot \boldsymbol{\tau}) + \mathbf{U} \cdot S_M + S_E \quad (6)$$

where  $h_{tot}$  is the total enthalpy, related to the static enthalpy  $h(T, p)$  by:

$$h_{tot} = h + \frac{1}{2} U^2 \quad (7)$$

The term  $\nabla \cdot (\mathbf{U} \cdot \boldsymbol{\tau})$  represents the work due to viscous stresses and is called the viscous work term. The term  $\mathbf{U} \cdot S_M$  refers to the work due to external momentum sources and is currently neglected.

An alternative form of the energy equation, which is suitable for low-velocity flows, is also available. To derive it, an equation for the mechanical energy  $K$  is required. This equation has the form:

$$K = \frac{1}{2} U^2 \quad (8)$$

The mechanical energy equation is derived by taking the dot product of  $\mathbf{U}$  with the momentum equation:

$$\frac{\partial(\rho K)}{\partial t} + \nabla \cdot (\rho U K) = -U \cdot \nabla p + U \cdot (\nabla \cdot \tau) + U \cdot S_M \quad (9)$$

In the present paper, the thermal energy equation is not taken into consideration as the blood flow in the short time is isothermal, thus energy dissipation and heat conductivity is neglected.

## 5. Results

For the 75 model geometrical cases investigated that cover changes in inner diameters of vertebral arteries of the three selected types of their spatial geometry, the results that allow for an analysis of velocity distributions during the whole cycle of heart operation in an arbitrary point of the modelled system have been obtained. The distance of the origin of vertebral arteries from the aortic ostium enables one to determine proper velocity profiles at the points crucial from the viewpoint of the investigations conducted. As an example, velocity profiles determined in the left and right vertebral artery during the first phase of the simulated cycle of heart operation (range of 0.15 – 0.30 s) are depicted in Fig. 7. One can see the velocity profile that suggests a laminar flow for small diameters, whereas for large diameters of blood vessels, the obtained profiles are deformed by unsteadiness of the phenomena and an effect of the duct curvature can be observed.

Determination of the flow structure versus time at the point where vertebral arteries join to form the basilar artery is more important for the investigation. Figures 8 and 9 show various velocity profiles in this point for five time instants of the heart operation cycle for the selected geometrical variants of three modelled structures and two different diameters of left and right arteries (Fig. 8 shows distributions for the diameter of the left artery equal to 3 mm and the right one – 5 mm and Fig. 9 presents the different situation – the diameter of the left artery equals 4 mm and of the right one – 2 mm). A very strong disproportion of the velocity of blood flowing into the basilar artery from the left and right artery and between the same arteries in different models can be observed. Of course, the result obtained refers to the selected geometry and is not characteristic of all cases under consideration. A possibility to compare changes in velocity of the left and right artery during one cycle of heart operation for the three selected geometries and three modelled structures of vertebral arteries is provided by the distributions shown in Fig. 10.

An effect of the velocity increase cannot be observed in the artery with an increasing diameter. Even for the identical diameter of both arteries, the velocity profile differs significantly. For the constant diameter of the arteries, both the left and the right one (see Fig. 10 b and c), a change in the diameter of the second artery affects differently a change in the velocity in the artery under consideration. In the left vertebral artery, the maximum velocity is attained for the same diameter of both the arteries (4 mm), whereas for the right artery, such behaviour was observed for the largest diameter of the left artery (6 mm). In this case, differences between the velocities occurring for individual diameters of the left artery under analysis are considerably lower. For the given low, constant diameter of the left artery equal to 2 mm (see Fig. 10 a), the maximum velocity occurs for two values of the right artery diameter (4 and 6 mm). Here, for the diameter of the right artery equal to 5 mm, a sharp decrease in the maximum velocity value in the left artery occurs. An effect of wave phenomena on the flow in arteries can be clearly seen.

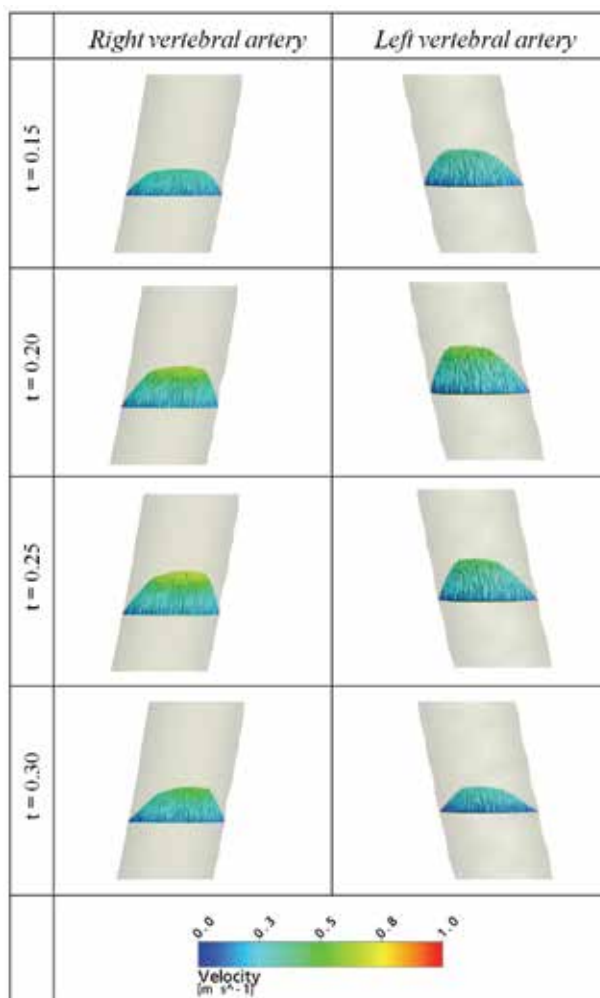


Fig. 7. Velocity distribution along the diameter of the left and right vertebral artery for one geometrical configuration at different instants of the heart operation cycle ( $t = 0.15$  s,  $t = 0.2$  s,  $t = 0.25$  s,  $t = 0.3$  s) (Obidowski 2007)

Some possibilities to compare the effect of diameters of the left and right vertebral artery on the values of velocity, which were obtained in these blood vessels during the simulations, are provided by a comparison of maximum velocities within the single heart cycle, measured in the centre part of the left and right artery for all the diameter configurations and for three modelled structures of these vessels analysed. This comparison is presented in Fig. 11 but only for the changes in the diameter from 2 to 5 mm as data from ultrasonography measurements were available only for this range. Moreover, the values of the maximum velocity for the defined diameters corresponding to the vessel diameters, calculated on the basis of the Hagen-Poiseuille equation, are shown. The equation is frequently used in medicine to compare the velocities in both the arteries (left and right) on the basis of the resistance assumed in vessels being a function of their diameters and a pressure drop in vertebral arteries.

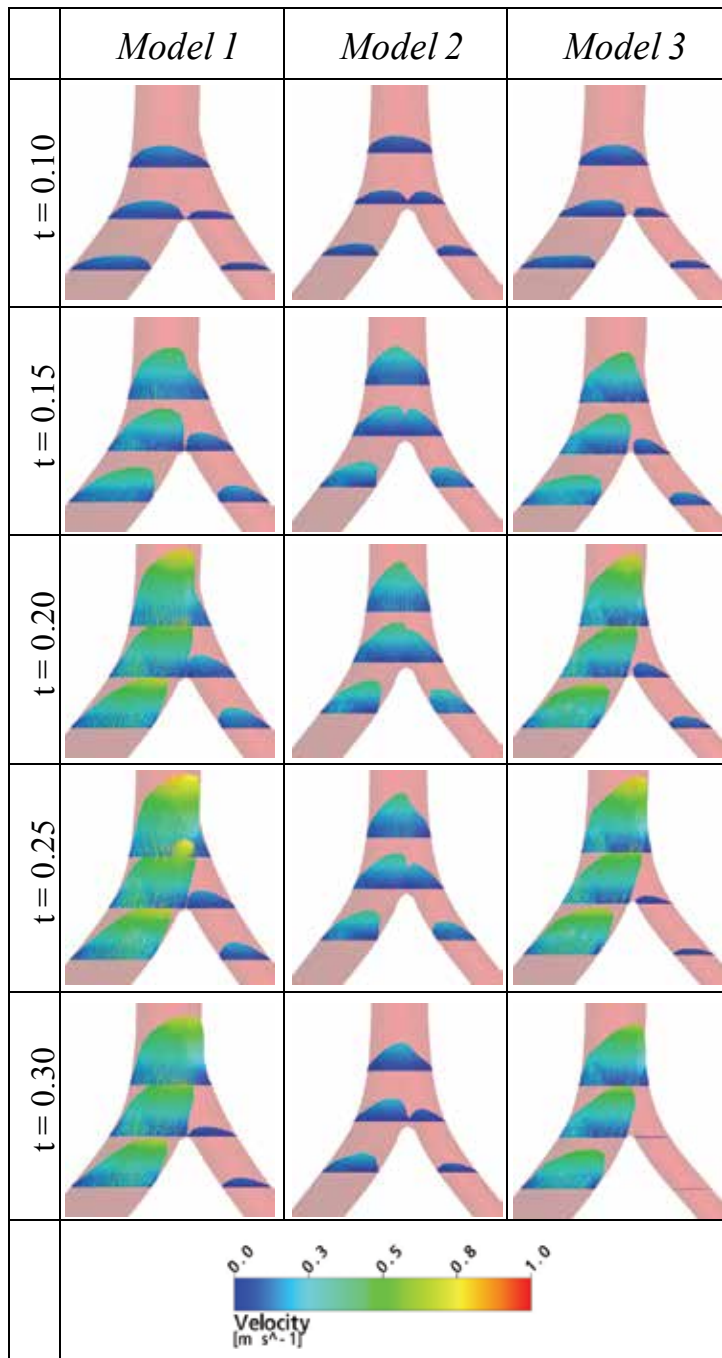


Fig. 8. Comparison of velocity profiles at the point vertebral arteries join to form the basilar artery for three spatial geometrical variants of the same diameter variant (left3right5) and for five time instants of the heart operation cycle ( $t = 0.1\ s$ ,  $t = 0.15\ s$ ,  $t = 0.2\ s$ ,  $t = 0.25\ s$ ,  $t = 0.3\ s$ )

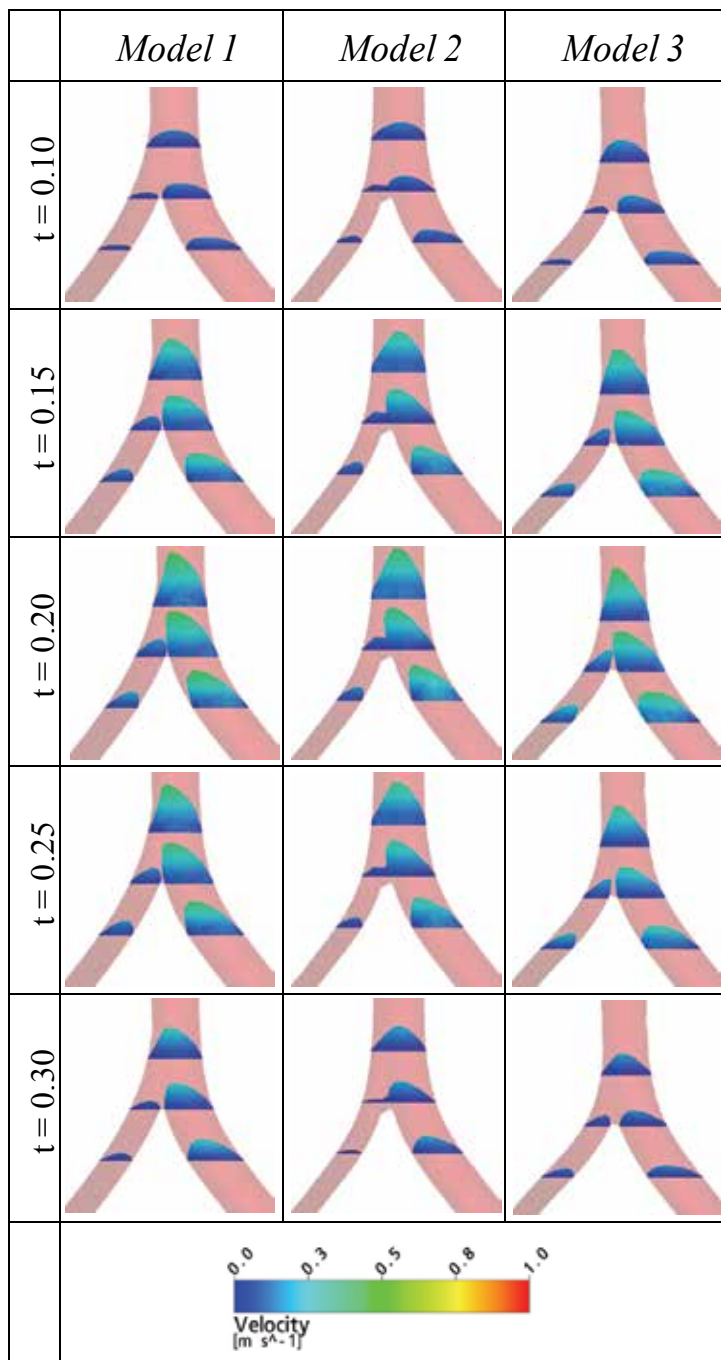


Fig. 9. Comparison of velocity profiles at the point vertebral arteries join to form the basilar artery for three spatial geometrical variants of the same diameter variant (left4right2) and for five time instants of the heart operation cycle ( $t = 0.1\ s$ ,  $t = 0.15\ s$ ,  $t = 0.2\ s$ ,  $t = 0.25\ s$ ,  $t = 0.3\ s$ )

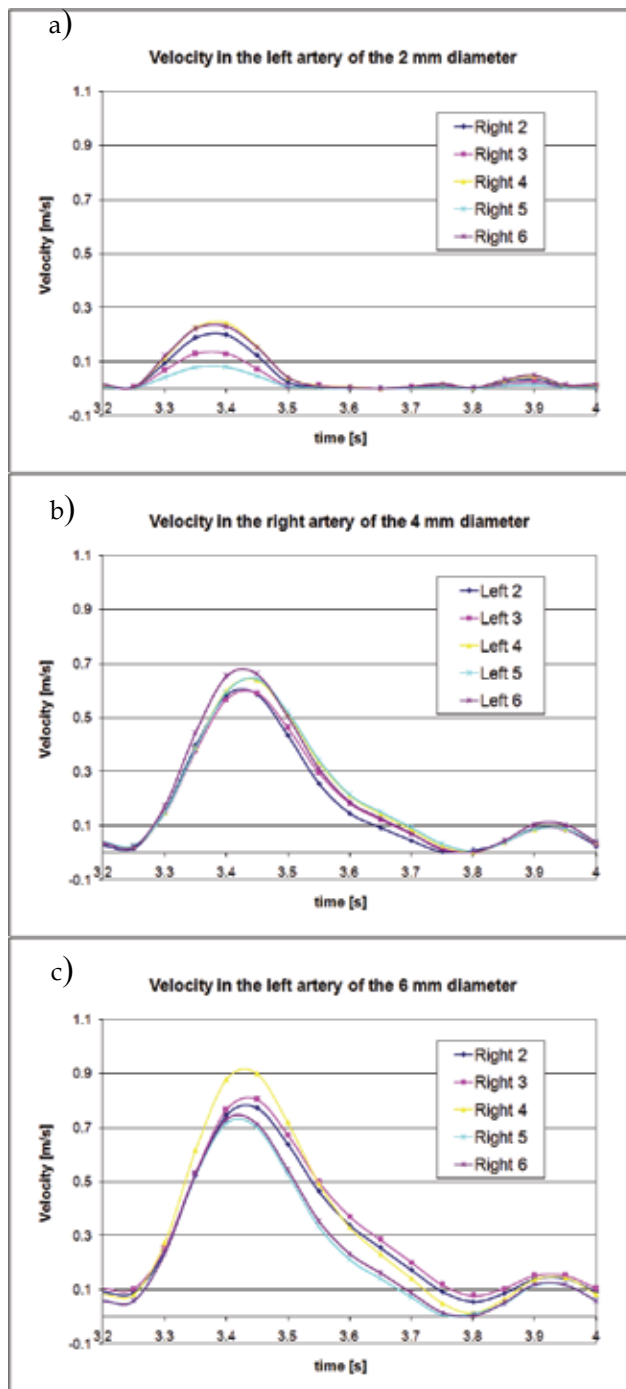


Fig. 10. Velocity distributions vs. time for one heart operation cycle in the left and right vertebral artery for three geometrical variants of blood vessels (left 2 mm, right 4 mm, left 6 mm) (Obidowski 2007)

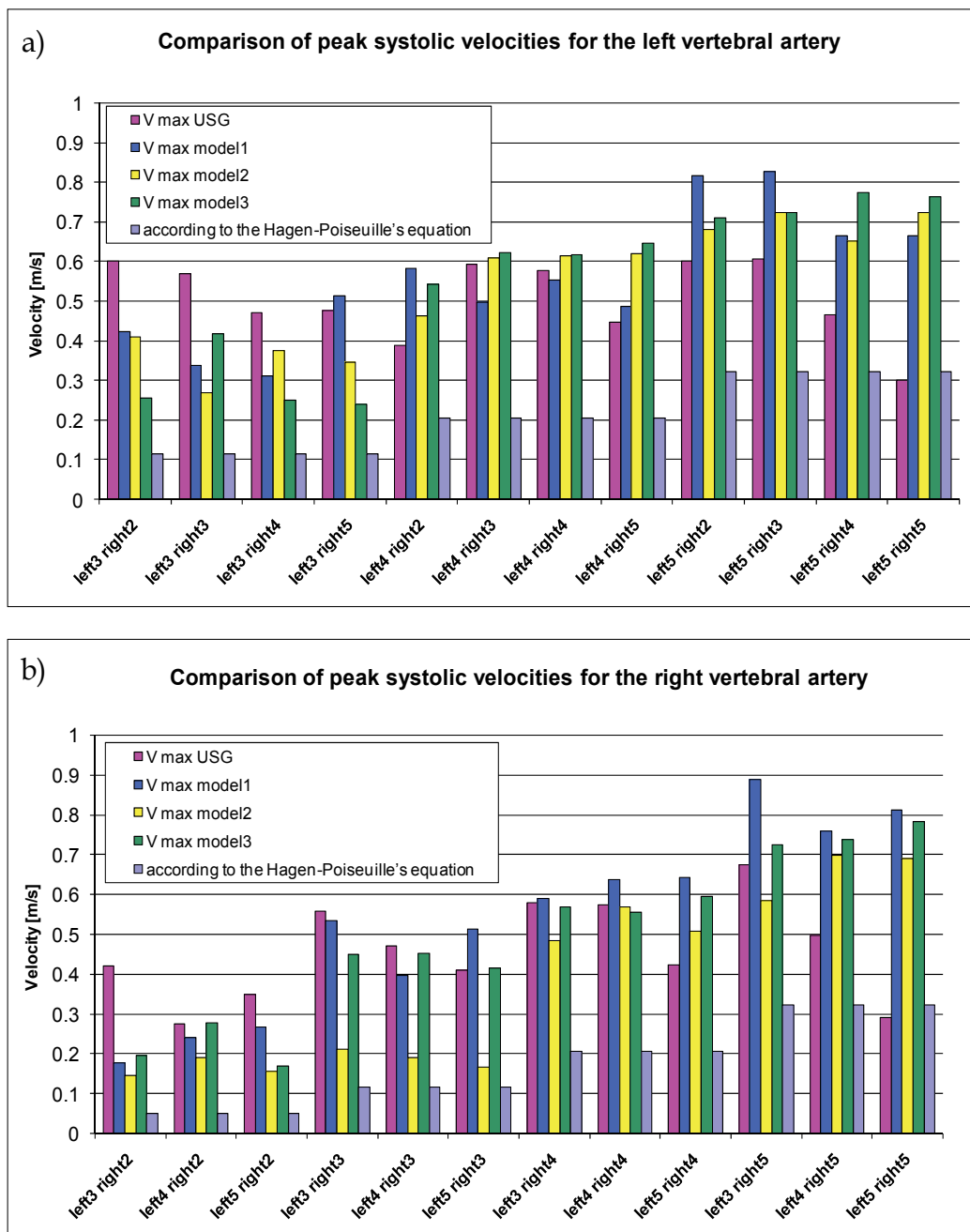


Fig. 11. Comparison of the maximum value of velocities obtained for the left and right vertebral artery for all investigated geometrical configurations of the system, ultrasonography measurements and calculated on the basis of the Hagen-Poiseuille equation (Obidowski 2007)

The same plot shows the maximum velocity values obtained from ultrasonography measurements in 520 people. The results have been averaged for all patients who had individual values of diameters of vertebral arteries, but without distinguishing the type of the spatial structure of arteries (Mysior 2006).

A good conformity between the results obtained from simulations and measurements (without distinguishing the type of geometry of arteries) occurs in the central region, which means a lack of conformity at the smallest diameters and for the two largest diameters. In case of large vertebral artery diameters, the results of measurements agree with those obtained on the basis of the Hagen-Poiseuille equation. For large diameters, an undisturbed laminar flow occurs, and thus the above-mentioned equation, which refers basically to such flows, yields correct results. A difference in the simulation results can follow from the fact that artery wall deformations have not been considered. It also refers to the case of the variant with the smallest diameters where the simulation results do not agree with the measurements. The vessel wall material is not subject to the Hook's law, and the relationship between the deformation and the pressure inside the vessel (or, strictly speaking, a difference in pressure between its inside and outside) is strongly nonlinear and dependent on the individual human anatomical structure. Thus, modelling the deformations in vertebral artery walls as a function of the flowing blood is extremely difficult if not impossible at all.

## 6. Discussion

The conducted numerical investigations confirm a possibility of modelling the geometry of the system of vertebral arteries together with vessels in their vicinity and of obtaining results that enable an analysis of the effect of an artery diameter on velocity distributions in vessels during the heart operation cycle for the selected, determined type of spatial geometry. The results obtained indicate explicitly that differences in the flow and instantaneous velocity values in vertebral arteries and in the point they join to form the basilar artery may not result from pathological changes in the artery system, but can follow from physical phenomena that occur in arteries as a consequence of the pulsating character of flow and the unique geometry, which is related to the individual human anatomical structure.

The presented results refer to selected models of the vertebral artery structure and do not account for changes in the length of individual arteries. Taking into account such a possibility of changes within one model of the system (not only vessel diameters are variable, but their length as well), the determination of the cause of disproportions found in the flow in vertebral arteries is very difficult and complex.

The maximum velocity in one vertebral artery is affected by the flow in the other one (see Fig. 11), thus the flow in the basilar artery strongly depends on the diameters and lengths of both vertebral arteries.

The results of calculations according to the Hagen-Poiseuille equation, commonly used in medicine for determination of the relation between flows in vertebral arteries, do not allow one even to predict the behaviour of the flow. All properties of the flow in such arteries are against the assumptions of the flow described by the above-mentioned equation. It is clearly visible that the results obtained in the presented investigations differ significantly from those calculated according to the Hagen-Poiseuille equation (see Fig. 11).

While analysing the obtained results, one should remember about the fact that rigid walls of vessels have been assumed. This assumption affects directly the lack of energy accumulation

during the cardiac contraction phase and its recovery during the heart relaxation. Moreover, rigid vessels do not cause damping of the phenomena occurring during the flow in vertebral arteries. Taking into account deformability of vessel walls through an introduction of their rigidity, it will be possible to obtain a better approximation. An influence of flexible walls of arteries should be especially observed in the values of minimum velocities of blood and in obtaining reverse flows in vertebral arteries. An influence of the brain supply by carotid arteries should be taken into account, as only completeness of the system will allow one to consider a possibility of occurrence of wave phenomena. As a result, these phenomena can be proven to follow from the pulsating flow and the vessel geometry.

In order to evaluate the simulation results, a model of the actual system of vessels for the selected patient should be developed. Flows in vertebral arteries and blood systolic and diastolic pressure should be measured for the selected geometry and, on this basis, the boundary and initial conditions for the simulation should be defined. Only thus prepared models and data will enable a correlation of the results of calculations and measurements.

## 7. Notations

$\alpha, \beta, \beta', \sigma_k, \sigma_m,$  - constants,

$k$  - turbulence kinetic energy,

$\omega$  - turbulence frequency,

$\mu$  - dynamic viscosity,

$\mu_t$  - turbulence viscosity,

$U$  - velocity vector,

$\rho$  - density,

$\nu_t$  - eddy viscosity,

$S$  - invariant measure of the strain rate,

$P_t$  - turbulence production due to viscous and buoyancy forces.

## 8. References

- Ballyk P.D., Steinman D.A. & Ethier C.R. (1994). Simulation of non-Newtonian blood flow in an end-to-end anastomosis, *J. Biorheology* Vol., No., 31, pp. 565-586.
- Bochenek A. & Reicher M. (1974). *Human anatomy*, volume III, PZWL, ed. V, Warsaw, (in Polish).
- Chen J. & Lu X.Y., (2006). Numerical investigation of the non-Newtonian pulsatile blood flow in a bifurcation model with a non-planar branch, *J. Biomechanics*, Vol., No., 39, pp. 818 - 832.
- Daniel B., (1988). *Atlas of human radiological anatomy*, PZWL, Warsaw, (in Polish).
- Daseler E. H. & Anson B. J., (1959). Surgical anatomy of the subclavian artery and its branches, *Surgery, Gynecology & Obstetrics*, pp. 149-174.
- Gijzen, F.J.H., van de Vosse, F.N. & Janssen, J.D. (1999). The Influence of the Non-Newtonian Properties of Blood on the Flow in Large Arteries: Steady Flow in a Carotid Bifurcation Model, *J. Biomechanics* Vol., No., 32, pp. 601-608.

- Gijssen, F. J. H., Allanic, E., van de Vosse, F. N., & Janssen, J. D., (1999). The Influence of the Non-Newtonian Properties of Blood on the Flow in Large Arteries: Unsteady Flow in a 90° Curved Tube, *J. Biomechanics*, Vol., No., 32, pp. 705–713.
- Johnston B. M., Johnston P. R., Corney S. & Kilpatrick D. (2004). Non-Newtonian blood flow in human right coronary arteries: steady state simulations, *J. Biomechanics* Vol. No., 37, pp. 709-720.
- Jozwik K. & Obidowski D., (2008). Geometrical models of vertebral arteries and numerical simulations of the blood flow through them, *Proceedings of BioMed2008, 3rd Frontiers in Biomedical Devices Conference & Exhibition*, pp. 5., BioMed2008-38048, ISBN 0-7918-3823-4, Irvine, California, USA, June 2008, ASME.
- Jozwik K. & Obidowski D., (2009). Numerical simulations of the blood flow through vertebral arteries. *J. Biomechanics*, Vol., No., 43, pp. 177-185.
- Michajlik A. & Ramotowski W. (1996). *Human anatomy and physiology*, PZWL, pp. 354-356 (in Polish).
- Mysior M., (2006). *Doppler ultrasound criteria of physiological flow in asymmetrical vertebral arteries*, PhD Thesis, Polish Mother Memorial Research Institute, Lodz, 2006 (in Polish).
- Obidowski D., (2007). *Blood flow simulation in human vertebral arteries*, PhD Thesis, Technical University of Lodz, Lodz, 2007 (in Polish).
- Obidowski D., Mysior M., Jozwik K., (2008). Comparison of Ultrasonic Measurements and Numerical Simulation Results of the Flow through Vertebral Arteries, *Proceedings of 4th Conference of the International Federation for Medical and Biological Engineering*, pp. 23-27, Belgium, Antwerp, November 2008, IFMBE Vol. 22, pp. 286-292, Springer-Verlag Berlin, Heidelberg, 2009.
- Ravensbergen J., Krijger J.K.B., Hillen B., Hoogstraten H.W. (1996). The Influence of the Angle of Confluence on the Flow in a Vertebro-Basilar Junction Model. *J. Biomechanics*, Vol., No., 29, pp. 281-299
- Sinelnikov R.D., (1989). *Atlas of human anatomy*, Mir Publishers, Moscow.
- Sokołowska J. - Pituchowa (eds.), (1988). *Human anatomy*, PZWL, Warsaw, (in Polish).
- Traczyk W., Trzebski A., (1980). *Human physiology with elements of clinical physiology*, PZWL, Warsaw 1980 (in Polish).
- Vajda J., (1989). *Atlas of human anatomy*, Akademia Kiodo, Budapest (in Polish).
- Viedma A., Jimenez-Ortiz C. & Marco V., (1997). Extended Willis circle model to explain clinical observations in periorbital arterial flow. *J. Biomechanics*, Vol., No., 30, pp. 265-272.
- Wang J.J. & Parker K.H. (2004). Wave propagation in a model of the arterial circulation. *J. Biomechanics*, Vol., No., 37, pp. 457-470.
- Walburn, F.J. & Schneck, D.J. (1976). A constitutive equation for whole human blood. *Biorheology* Vol., No., 31, pp. 201-218.

# Numerical Simulation of Industrial Flows

Hernan Tinoco<sup>1</sup>, Hans Lindqvist<sup>1</sup> and Wiktor Frid<sup>2</sup>

<sup>1</sup>*Forsmarks Kraftgrupp AB,*

<sup>2</sup>*Swedish Radiation Safety Authority  
Sweden*

## 1. Introduction

Computational Fluid Dynamics (CFD) is a numerical methodology for analyzing flow systems that may involve heat transfer, chemical reactions and other related phenomena. This approach employs numerical methods imbedded in algorithms to solve general conservation and constitutive equations together with specific models within a large number of control volumes (cells or elements) into which the associated computational domain of the flow system has been divided to build up a grid.

Numerical simulation of industrial flows using commercial CFD codes is now well developed in a number of technical fields. With the advent of powerful and low-cost computer clusters, events including both complex geometry and high Reynolds numbers, i.e. fully turbulent practical industrial applications, may today be accurately modeled. This technique constitutes a rather new tool for analyzing problems related to, for instance, design, performance, safety and trouble-shooting of industrial systems since time can now be treated fully as the primary independent variable.

The first commercial general-purpose CFD code, built around a finite volume solver, the Parabolic Hyperbolic Or Elliptic Numerical Integration Code Series (PHOENICS), was released in 1981. Initially, the solver was conformed to work only with structured, mono-block, regular Cartesian grids but it was subsequently broadened to admit even structured body-fitted grids. The multi-block grid option was developed many years later within this code which still preserves this restricting structured grid topology. Another well known commercial CFD code, FLUENT, was brought out onto the market in 1983 as a structured software that bore a resemblance to PHOENICS, but aimed towards modeling of systems with chemical reactions, specifically those related to combustion.

Hence, during the 1980s, CFD simulations were limited to rough time-independent models with very simplified geometry due to the grid-structured character of the software and the vast limitations in, at that time, normally available computer resources at the industry (see e.g. Tinoco & Hemström, 1990). It might be of some interest to point out that the top performance of a supercomputer at the end of the 1980s was of the order of 10 GFLOPS ( $10 \times 10^9$  Floating point Operations Per Second). The computers normally available at the industry had a thousandth to a hundredth of that performance, i.e. 10-100 MFLOPS. Today, a computer cluster containing a couple of hundred CPUs has a capacity of the order of TFLOPS.

At the beginning of the 1990s, important steps in software improvement took place through the development of grid-unstructured, parallelized algorithms (e.g. FLUENT UNS) that

enabled the possibility of an accurate geometrical representation of the modeled flow system (see e.g. Tinoco & Einarsson, 1997). At the same time, the communication through adequately formatted geometrical data between grid generators and CAD solid modelers was established and improved. This rather new link allowed the generation of unstructured grids more easily directly from appropriately simplified CAD geometry. However, a new problem arose with the use of CAD models, namely that of “dirty” geometries (see e.g. Beall et al., 2003) caused by relatively large tolerances, leading to gaps and overlaps, and by translating geometries from the native CAD format to another. In the section that follows, the issue of what is meant by grid quality will be assessed from different points of view, including that of the interaction with CAD geometries.

Even if the applications described in the present work have a slight emphasis towards the nuclear power industry, only single-phase phenomena will be discussed in following sections. Two-phase flow simulations are still considered by the authors to have a excessively high level of uncertainty and they have not reached the level of maturity of single-phase simulations. Two-phase phenomena suffer mainly from a deficit of comprehensive knowledge about the physics involved in the different processes included in two-phase flows. Consequently, the models available lack the CFD distinctive prediction capability because they are usually based on information gathered as relatively general correlations. A relevant example of the deficiencies of this field is that nobody has yet succeeded to measure the detailed structure a boundary layer modified by boiling at the wall.

## **2. Grid quality**

All geometries to be discussed in this work will be assumed to have been digitally expressed as CAD models, and all CAD models referred to herein are assumed to have been generated by solid modelers. Three-dimensional wireframe and surface models are not an alternative since they do not fulfill the fundamental requirements of an acceptable three-dimensional geometrical model. These models have no volume associated with them and, for instance, the curved surfaces involved have polyhedral approximations that may deteriorate the boundary layer resolution of a grid. A model of a shell may lead to the generation of negative grid volumes since, in this representation, the inner surface may cross the outer surface of the shell due to insufficient resolution of the geometrical model.

The grid is the most basic part of an industrial CFD analysis and reflects nearly all of the aspects to be considered in the flow problem, namely the objective of the analysis, the appropriateness of the geometry and flow domain included, the suitability of the boundaries chosen in connection to properly defined boundary conditions, the space-time resolution needed to cope with the flow characteristics (for instance turbulent, with heat transfer to boundaries, compressible with shocks, with chemical reactions, with two-phases, with free surface, etc.), the need of moving parts to capture the effect of, for instance, rotating pump impellers, closing valves, etc.

### **2.1 Geometrical fidelity, structured grids and multi-block strategy**

The absolutely first requirement to be fulfilled by the grid is the high degree of fidelity with which it has to represent the geometry of the flow system. This issue of geometrical fidelity is far from self-evident since, on the one hand, the geometry comprised in a CAD model may contain undersized “intended features” like chamfers and roundings that might need

to be suppressed due to irrelevance for the analysis and/or to grid size limits. On the other hand, the upper size limit for geometrical simplifications is subtle and has to depend on the purpose of the simulation: the elimination of geometrical details must not introduce unwanted flow effects or remove a detectable part of the flow effects to be analyzed.

Prior to the process of grid generation, importing models from a specific CAD platform may either provide too much detail, i.e. the “intended features” mentioned above, or deficient geometric representation with “artifact features” and other incompatibilities, such as the aforementioned gaps and overlaps, that invalidate the model (see e.g. Beall et al., 2003). These deficiencies lead to the problem of “dirty geometries” mentioned before which may nowadays be treated by making small changes to the model through the processes of “healing” gaps, “tweaking” geometries, “defeaturing” unwanted features, “merging” overlapping surfaces, i.e. a “repair” of the geometrical model. Still, this constitutes a rather serious problem for the design/analysis integration in the production line of the manufacturing industry.

The topological character of a structured grid may lead to undesirable oversimplifications of the geometry since it may be extremely difficult or impossible to sufficiently deform the structure of the grid to fit the geometry. A structured grid is laid out in a regular repeating pattern, a block, which accomplishes a mapping defining a transformation from the original curvilinear mesh onto a uniform Cartesian grid, as is shown in Fig. 1 for a two-dimensional case.

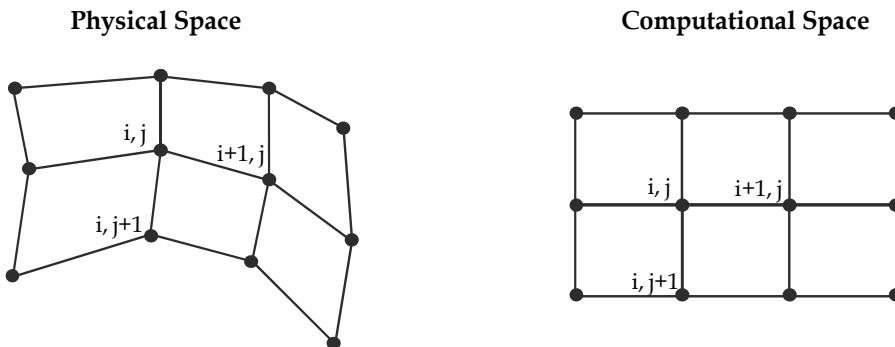


Fig. 1. Mapping associated with a two-dimensional structured grid.

For the pioneering codes of the beginning of the 1980s, this mapping allowed an easy identification of the neighbors of a specific point together with an efficient access to the information pertaining to these neighbors. Also, a complement for rough geometric fitting was available in PHOENICS through porosity, which allowed for a crude representation of curvilinear boundaries using rectangular grids but eliminated the possibility of a proper resolution of the corresponding boundary layer and the near wall flow.

Obviously, the calculations are facilitated by the use of structured grids since less computer resources are needed and the simulation may be speeded up utilizing simpler and more robust algorithms. On the other hand, a local refinement of the grid is impossible since the structure of the grid must be preserved, implying that the inclusion of an extra node results in the addition of a complete line or of a complete plane for, respectively, two- and three-dimensional grids. For instance, if an extra node is located between nodes  $(i, j)$  and  $(i+1, j)$  in the grid of Fig. 1, then a node between nodes  $(i, j+1)$  and  $(i+1, j+1)$  and a further node

between nodes  $(i,j-1)$  and  $(i+1,j-1)$  must be added. If not, the middle row would have one more node than the other rows, destroying by this the structure of the grid.

Another shortcoming of structured grids is their inability of accommodating a single block to a complex geometry such as the one associated with the unstructured surface grid shown in Fig. 2. Here, the geometry corresponds to that of the core shroud (moderator tank), with cover, of a Boiling Water Reactor (BWR). The three-leg pillars that hold the cylindrical drum of the steamdryer support (upper right corner of the view) may be observed at the edge of the cover. In the forefront, the piping of the core spray system and a feedwater sparger has been included in the figure. Steam separators that should have been connected to the outer side of the core shroud cover, have not been displayed in the view of Fig. 2 in order to avoid a forest of cylindrical shaped equipment that would have overloaded the view, rendering it thickly. Only the trace of the connecting circular holes is seen in the core shroud cover.

A strategy to overcome the limitations of a single block structured grid consists of dividing the computational domain in an appropriate number of regions, each one suitable for a single block, i.e. to increase the number of structured grids, one for each block. But now, the difficulties are moved to the issue of connecting the different blocks to build the complete domain. Several block connection methods are available: the point-to-point method, in which the blocks must match topologically and physically at the common boundary, the many-to-one-point method, in which the blocks must match physically at the common boundary, but be only topologically similar, and arbitrary connections, in which the blocks must match physically at the common boundary, but may have significant topological differences. Although the multi-block approach may increase the possibilities of achieving a higher geometrical fidelity of the simulated flow system, the block connection requirements may restrict the quality of the grids, which still are difficult to construct. Also, the price paid by increasing the degrees of freedom in block connectivity is a detriment to the accuracy of the solution and a deterioration in the solver robustness.

## 2.2 Unstructured grids, histogramming and polyhedra

In contrast to the limited possibilities of structured grids, Fig. 2 below constitutes a modest indication of how far it might be possible to get with the requirement of geometrical fidelity if an unstructured grid is used to fit a complex geometry. Unstructured grids lack the mapping of the structured grids and, therefore, the information about the connection of each node between physical space and computational space is kept within the algorithm of the unstructured solver, which has to work out the location of the neighbours of each node, i.e. the node at location "n" in memory may have no physical relation to the node next to it in memory, at location "n+1".

The disadvantages of unstructured grids are the need of larger computer resources and the use of more complex algorithms that may not be as effective as those used with structured grids under similar simulating conditions. Besides the aforementioned degree of geometrical fidelity, unstructured grids have the great advantages of being easily automatized in their generation, requiring limited time and effort in this process, and of readily being suitable for spatial refinement. Depending on the grid generator, a minor drawback with automatization might be the lack of user control when setting up the grid, since most of the user participation may be restricted to disposing the mesh at the boundary surfaces while the interior is automatically filled up by the software. Triangular and tetrahedral elements are not easily deformed, i.e. stretched or twisted, leading to a grid that may be rather isotropic, with elements of roughly the same size and shape. Rather than a

disadvantage, this property may turn out to be of assistance for maintaining almost everywhere in the computational domain a maximum element size of the grid that adequately matches the size of the time step needed for resolving the different structures of the flow to be simulated. Today's possibility of treating the time dependence of the flow with realistic accuracy is undoubtedly having an impact on the perception of grid quality, an subject that will be further discussed in this work.

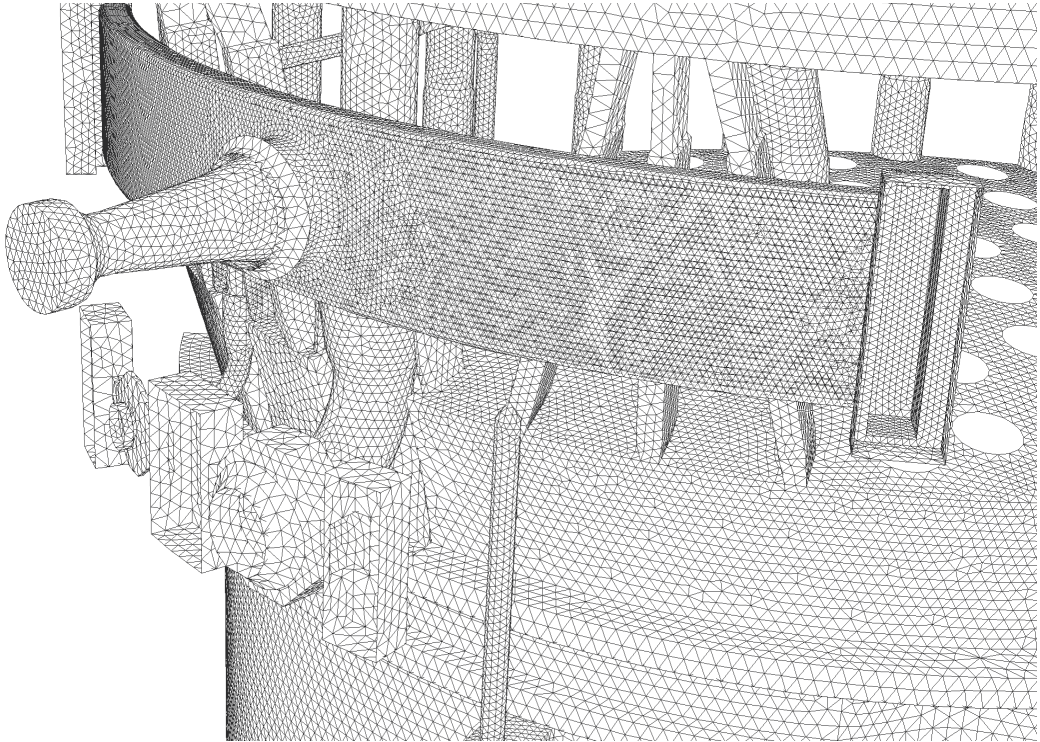


Fig. 2. Unstructured grid of the core shroud and cover of a BWR.

The traditional method for assessing grid quality, giving a statistical measure over the entire computational domain, consists in histogramming (Woodard et al., 1992). Several geometrical parameters are used to evaluate the quality of the individual elements, herein assumed, without losing generality, to be tetrahedra since similar parameter definitions may be obtained for any polyhedron. A few of such parameters are the minimum dihedral angle, the ratio between the areas of the largest and the smallest faces and the volume ratio between the smallest containing sphere and the largest contained sphere of the tetrahedron. The minimum dihedral angle, which is the angle between two planes, is determined by the scalar product of the combination of the four unity normal vectors corresponding to the faces of the tetrahedron. The ratio between areas is found by the combination of the normal vectors to each face obtained through the vector product of two of the three edges making up a face. Although the information provided by these two indicators about the shape of each element is similar, the evaluation of this area ratio is computationally far less demanding than determining the dihedral angles for each face. The aforementioned volume ratio is usually normalized by the value corresponding to a regular tetrahedron, which is

equal to 27 since the ratio of the radii of the spheres is 3. The ratio of the sphere radii, or its inverse value, is generally used as aspect ratios.

Another important parameter for evaluating element quality is skewness, being it a measure of the distortion of the element with respect to an ideal, equilateral element (i.e. regular tetrahedron, cube, etc.). A method to estimate skewness, only valid for tetrahedra, consists of the volume difference between the regular tetrahedron and the actual element shearing the same circumsphere, normalized by the volume of the regular tetrahedron. A more general method for skewness evaluation is the equiangle skew parameter defined by

$$Q_{EAS} = \max \left[ \frac{\theta_{\max} - \theta_e}{180^\circ - \theta_e}, \frac{\theta_e - \theta_{\min}}{\theta_e} \right], \quad (1)$$

where  $\theta_{\max}$  is the largest angle in face or cell,  $\theta_{\min}$  the smallest angle in face or cell and  $\theta_e$  the angle for equiangular face or cell, equal to  $60^\circ$  for tetrahedral and to  $90^\circ$  for hexahedral elements (see e.g. Fluent, 2006). With the above definition, the equiangle skew parameter will range between null and unity, being the maximum skewness value for an acceptable grid not larger than 0.9.

Not only single element quality but also local grid quality needs to be quantified in order to avoid large stretching and/or distorting of the grid. For instance, a doubling in the linear spacing will result in an eightfold increase in volume, leading to large changes in volume ratios. Even if these changes can be detected through analysis of the aforementioned volume parameter, and the grid rectified, the flow structures to be resolved need an even distribution of elements to maintain the accuracy of the simulation, as has already been mentioned. Therefore, a limit in the grid spacing of the order of 10 %, rather than the one normally accepted of about 20 %, should resolve this issue. The grid distortion can be estimated by means of a skewness parameter defined by the ratio between the area of a triangle formed with the center and the two nodes on each side of a chosen face, and the area of the face. If two elements are perfectly aligned, the area of the formed triangle is zero, indicating a local nonexistence of grid skewness.

Grid diagnosis using a methodology of the kind discussed above leads to the necessity of modifying the grid based not only on geometrical criteria but also on concrete physical criteria in order to objectively improve the quality of the grid to be used for the specific flow simulation. As was expressed at the beginning of this section, the grid reflects the simulation problem to be solved and should, consequently, be individual in its quality to conform to the associated physical problem. Therefore, the first, a priori, constructed grid following the aforementioned guidelines will seldom be optimal for the assigned task and will need to be customized through an iterative procedure to comply with the conditions of the physics involved in the simulation. A typical example of this situation is the need for grid refinement in order to capture shocks in aerodynamic applications (see e. g. Borouchaki & Frey, 1998, Acikgoz, 2007). The adaptation is normally achieved using the pressure gradient of the solution as an indicator and, in all probability, the adaptation procedure needs to be repeated several times in order to attain an optimal solution of the grid valid for the specific application.

A particular issue related to grid refinement, which needs special attention due to the connections to other physical phenomena like turbulence and heat transfer, is that of the near wall regions of the flow where large velocity gradients are present, i.e. the boundary layers. In turbulent flows, the wall region is dominated by the effect of shear stress and very

close to the wall, at the viscous sublayer, the scaling parameters are the kinematic viscosity of the fluid and the shear stress at the wall. The characteristic velocity and length scales there are the friction velocity, the square root of the quotient of the shear stress at the wall and the fluid density, and the viscous length scale, the quotient of the kinematic viscosity of the fluid and the friction velocity. Based on these scales, the non-dimensional normal distance to the wall may be expressed in wall units as

$$y^+ = \frac{u_\tau y}{\nu}, \quad (2)$$

where  $y$  is the dimensional normal distance to the wall,  $u_\tau$  the friction velocity and  $\nu$  the kinematic viscosity of the fluid. This distance in wall units is a dynamic measure of the relative importance of viscous and turbulence transport within the boundary layer that affects wall friction, heat transfer, buoyancy and other related physical phenomena. Depending on the degree of approximation of the simulation, a certain minimum value of  $y^+$  is required for the resolution of the computational cells adjacent to the wall in order to capture the correct wall phenomena to the desired level of accuracy.

Further considerations to be presented in the next sections establish that it is turbulence modeling that primarily defines the near wall grid resolution. Additional requirements not only on the normal distance to wall, may however arise due to, for instance, conjugate heat transfer (CHT), natural convection, etc. In the end, the near-wall resolution of the grid is, as the rest of it, solution dependent and has to be optimized by means of refinement through an iterative process.

Finally, some words should be added about the future of grid development. Tetrahedral grids have several already mentioned advantages, but need much larger number of elements for a given volume than grids using other geometrical elements as, for instance, hexahedra, resulting in higher requirements in memory storage and computing time. A tetrahedral control volume has only four neighbors, a property that may deteriorate the computation of gradients in all needed directions. If the neighbor nodes are inadequately located, for example all lying nearly in the same plane, the evaluated gradient normal to that plane may be marred by a large uncertainty. A solution to this and other problems with tetrahedral grids is the use of elements of more complex geometrical shape, i.e. polyhedra (see e.g. Peric, 2004). According to this reference, about four times fewer cells, half the memory and a tenth to a fifth of computing time are needed with polyhedral grids compared to tetrahedral grids for achieving the same level of accuracy of the solution. Two alternatives are now available for generating polyhedral grids, the first to generate the polyhedral grid from scratch and the second to convert tetrahedra to polyhedra from an already existing grid. The later possibility has been tested by the authors with clearly approved result that will be further commented in the next sections (see e.g. Figures 8 and 9).

As will be explained later on, a minimum spatial size of the grid is necessary for a required level of resolution of the turbulent, time dependent structures of the flow, and the feature of polyhedral grids of containing fewer, larger cells may not necessarily be a clear advantage in this kind of simulations. As in every new area of development, more quantitative examination of the properties of polyhedral grids, especially in turbulent, time dependent applications, is needed to get a complete understanding of the virtues of polyhedral elements in industrial simulations.

### 3. Time dependence and turbulence modelling

Time-independent or time-averaged solutions have constituted the traditional methodology of analysing industrial flow applications to obtain fundamental information such as flow direction, pressure drop, mean temperature, etc. Generally, the solutions have been obtained by solving time independent conservation equations, i.e. a steady state approximation, or by a rather short-time average of a rough time dependent solution. Rather often, the time average and steady state solutions of the same flow situation differ, casting a shadow of doubt about the existence and correctness of steady state solutions in industrial flow problems with complex geometries, even as initial guess to time dependent simulations.

As time has passed, the necessity to avoid more and more expensive experimental testing, replacing it by more cost-effective and faster numerical simulations has gradually oriented the CFD activities towards full time-dependent simulations, an evolution brought about mainly by the outstanding development of low-cost microprocessor clusters. Areas like flow induced effects on solid structures, i.e. vibrations, thermal fatigue, cavitation, etc., may now be investigated to a higher level of detail through more comprehensive CFD simulations of the process involved using better suited and more fundamental physical models, i.e. models based on the local flow properties instead of correlation governed global properties. However, this qualitative and quantitative improvement of the CFD analysis tool involves meeting a number of additional conditions, to be discussed throughout the rest of this work, together with a parallel experimental commitment to reinforce and further develop the knowledge about the physical phenomena to be simulated. As already mentioned, this commitment particularly concerns the field of two-phase flows but even issues like unsteady heat transfer to and from a solid boundary needs experimental clarification, as section 4 indicates. In any event, the first and probably rather fundamental condition, concerns the computational grid that now has to comply not only with the general requirements covered in the preceding section but also with those of a more advanced turbulence modelling.

#### 3.1 The numerical solution of the Navier-Stokes equations

The Navier-Stokes equations, describing the motion of Newtonian fluids, are nonlinear partial differential equations that still lack a general, continuously differentiable, analytical solution. Even the issue of the uniqueness of such a general solution has not yet been settled (see e.g. Doering, 2009). Therefore, in order to describe turbulence, which is a time dependent chaotic fluid behaviour, the Navier-Stokes equations are solved numerically through Direct Numerical Simulation (DNS, see e.g. Orszag, 1970) or by first averaging or filtering the equations and solving them numerically together with simpler mathematical models. The first solution approach is extremely time and resource consuming, becoming infeasible for the simulation of industrial flows, for which the only practical solution is to rely on some kind of turbulence model. A large group of models involves resolving of the Reynolds-averaged Navier-Stokes equations (RANS), i.e. a time average of the Navier-Stokes equations, strictly implying that the mean values of the dependent variables are time independent. Assuming that the temporal mean values of the dependent variables may be functions of time, i.e. temporally filtering the Navier-Stokes equations with a filter width which is not infinite but of the order of the turbulent integral timescale, the unsteady terms in the RANS equations are recovered, giving rise to a new group of turbulence models, Unsteady RANS (URANS) models. If the width of the temporal filter is further reduced

towards the Taylor microtimescale and beyond, a complete category of simulation forms, the Partially Resolved Numerical Simulation (PRNS) is obtained (see e.g. Liu & Shih, 2006). In this category, the dependent variables can develop from pure statistical means (RANS) through partially resolved large-scale variables (LES) to, eventually, completely resolved direct-simulated variable (DNS). Of course, depending on the simulation form, a turbulence model appropriate to the filter width must be numerically solved together with the filtered equations in a grid whose resolution is in accordance with the scale content of the resolved field. Figure 3 below shows the energy distribution of a normal turbulence spectrum as a function of the wave numbers in a log-log representation together with the lower scale limits of the resolved spectrum (higher limit of the wave number in light-blue broken lines) for the different groups of turbulence models belonging to the PRNS. In the case of Very Large Eddy Simulations (VLES), to be further discussed in what follows, and Large Eddy Simulations (LES), the limit lies within the inertial sub-range scales of motion where the energy spectrum is a universal function of the wave number, viscosity and dissipation rate (Kolmogorov, 1941, Ishihara et al., 2009).

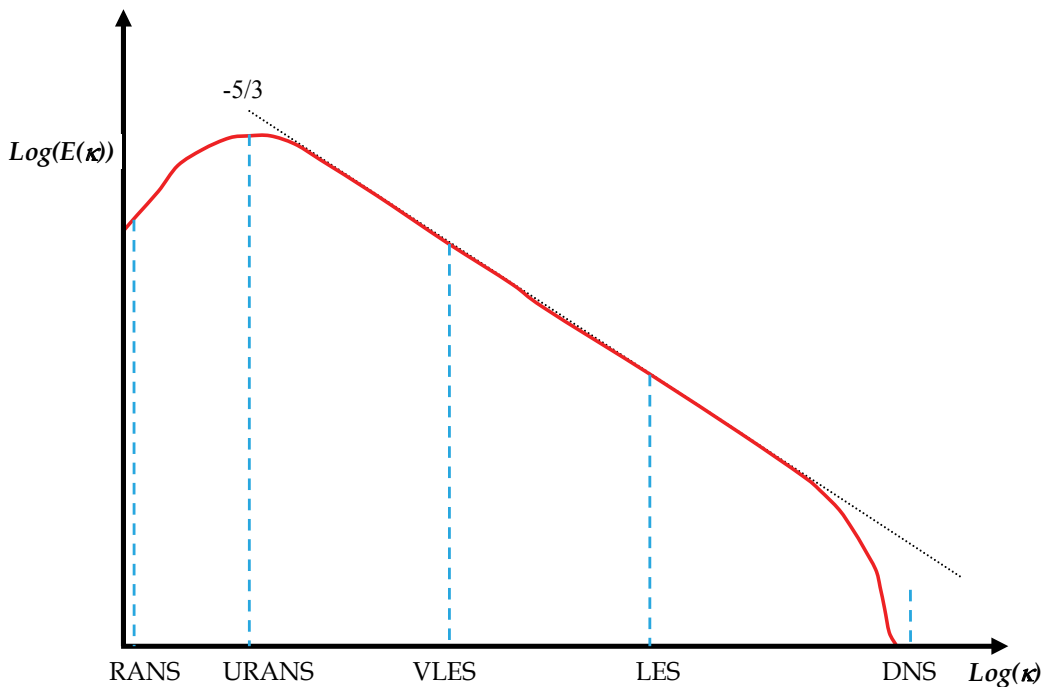


Fig. 3. Schematic view of RANS-DNS resolved energy spectra.

### 3.2 RANS and URANS modeling

RANS turbulence models may be classified by the number of partial differential equations to be solved, namely from zero, i.e. only algebraic equations are solved, through the very popular two-equation models based on the eddy viscosity concept of Boussinesq, like  $k-\varepsilon$  (Jones & Launder, 1973),  $k-\omega$  (Wilcox, 1988) and Shear Stress Transport (SST, Menter, 1994) models, to finally seven equations in the case of the Reynolds Stress Model (RSM, see e.g. Pope, 2000).

Retrieving the time dependent terms through a temporal filter of finite width in the RANS equations allows for time-resolved simulations of turbulent flows together with temporally extended RANS models, in other words URANS models. All empirical parameters and constants in the URANS models maintain the same forms and values as those assigned in the corresponding RANS models.

Time dependent simulations of flows where turbulence effects may be neglected, such as the one generated by a steam-line break in a BWR (Tinoco, 2002), are subjected to less rigorous conditions with respect to space and time resolution. Using a rather coarse grid, of about a few hundred thousand elements, with relatively small time steps may satisfy the Courant number condition ( $Cr < 1$ ) for stable computation of pressure wave propagation without losing too much accuracy. Also, in the case of steam line break, the total simulation time is of the order of some tenths of a second, implying a total number of time steps, about one tenth of a millisecond each, of the order of ten thousand. On the other hand, a turbulent simulation on a grid of many million elements may need a couple of minutes of simulation time, with time steps of the order of a millisecond or less, only for getting rid of the distorting effect of the initial conditions. Even though turbulence-free flow simulations may generate smaller data sets, they might share some problems with turbulent flow simulations in terms of the selection and processing of the data to be saved for further analysis. These issues regard, amongst others, the selection of the adequate variables to be saved for further analysis, the space locations where the variables have to be sampled, the specific views and the figures to choose for a visualization, etc. If the analysis concerns trouble-shooting, a new design or research, the simulation is probably run for the first time, with no or very limited information about the features of the flow to be simulated. Due to storage capacity, it is seldom possible to save a complete data set produced in a simulation of the type mentioned before. Hence, the data to be saved through scripts, to reduce their amount, may have to be defined iteratively since the data selection process depends on the simulation results but should be completed before running the full simulation. Furthermore, the subsequent analysis of the data as, for instance, time series, digital images, etc., is far from trivial and the issue will be further discussed in the rest of this chapter.

Time dependent turbulent flow simulations using URANS may give rather accurate results depending on the turbulence model, the grid resolution and the characteristics of the flow. In this chapter, the analysis of the behaviour of URANS models in time dependent simulations will be mainly concentrated to two-equation models and, in particular, to the SST model of turbulence, due to the rather convincing agreement between results and validation measurements experienced by the authors.

According to Menter (1994), the SST model is a zonal combination of the  $k-\varepsilon$  and  $k-\omega$  models. In contrast to the traditional concept (see Kline, 1989), zonal modelling means here that different models are employed in different regions, using "smart" functions for shifting between models, without the need of a prior knowledge of the flowfield for defining the boundaries for each model. According to this broader definition, model combinations ranging from wall functions and URANS models to Detached Eddy Simulations (DES), to be discussed later in this chapter, may be interpreted as zonal modelling.

The free stream constituent of the SST model, the  $k-\varepsilon$  model, solves one transport equation for the turbulent kinetic energy,  $k$ , and one for the energy dissipation rate,  $\varepsilon$ . It is one of the most widely used two-equation models and has been especially successful in modelling flows with strong shear stress. However, this model has a number of well known shortcomings, notably its lack of ability to correctly predict flow separation under adverse

pressure gradients together with the numerical stiffness of the damping-function-modified equations when integrated through the viscous sublayer. An accurate and robust alternative for dealing with the aforementioned limitations is the  $k-\omega$  model that solves instead a transport equation for the specific energy dissipation rate (or turbulent frequency)  $\omega$ . This model behaves significantly better under adverse pressure-gradient conditions and has a very simple formulation in the viscous sublayer, without damping functions and with unambiguous Dirichlet boundary conditions. Yet, this model has an important weakness with respect to non-turbulent free-stream boundaries, such as in a jet discharged to a quiescent environment: an unphysical, non-zero boundary condition on  $\omega$  is required and the computed flow strongly depends on the value specified. To take advantage of both models, the SST model solves the  $k-\omega$  model in the near wall region and the  $k-\varepsilon$  model in the bulk flow, coupled together through a blending function that ensures a smooth transition between the models.

After approximately ten years from its birth, a first review of a slightly modified model, was conducted by Menter et al. (2003), in which its strengths and weaknesses when applied to industrial problems, mostly connected to aeronautical issues, were discussed and analysed mainly within the context of time independent solutions. However, the time dependent hybrid DES formulation of Spalart et al. (1997), based on combination of the RANS-SST model and a LES formulation, was also examined due to its improved prediction capabilities, especially in unsteady flow with separation, but also due to one of the shortcomings of the method, i.e. premature grid-induced separation caused by grid refinement. DES, which is one of the alternatives for dealing with unsteady flow situations that cannot afford a proper LES requiring, for instance, a detailed resolution of the boundary layers, has been newly reviewed by Spalart (2009) and will be briefly discussed farther on.

Last year, a second review of the SST model, even this with industrial implications, was completed by Menter (2009), with a stronger accentuation on time dependent simulations. Also the SST model sensitized to unsteadiness through the Scale Adapted Simulation (SAS) approach (Menter et al., 2003, Menter & Egorov, 2004, Menter and Egorov, 2005), i.e. the SST-SAS model of turbulence, is examined and discussed. Some results obtained with the model are compared with both unsteady results obtained with the traditional SST model (SST-URANS) and results obtained with LES. The conclusion that may be drawn from these comparisons is that the spectrum of resolved scales produced in a SST-SAS simulation is broader than that in a URANS simulation but narrower than the corresponding in a LES, i.e. a SST-SAS simulation is equivalent to a VLES.

Over the years, the SST model has become one of the most popular two-equation models of turbulence, and a quite large number of time dependent simulations have been already reported in the literature. Some of the applications consist of cases with a rather academic emphasis, like the work of Davidson (2006) comparing the SST model with its VLES modification, the SST-SAS, in channel flow, in the flow through an asymmetric diffuser and in the flow over and around an axi-symmetric hill. As Davidson points out, URANS models are well dissipative, implying that they are not easily triggered into unsteady mode unless the flow instabilities are strong, like in vortex shedding behind bluff bodies (see e.g. Young & Ooi, 2004, Kim et al. 2005) or in high-Reynolds number jet flow (Tinoco & Lindqvist, 2009, Tinoco et al., 2010), and/or the mesh is fine enough to rule out steady solutions. This paper confirms the aforementioned conclusion about the behavior of the SST-SAS model of producing a simulation similar to VLES but, in some cases, like in the asymmetric diffuser, it may result in a poorer solution and, in some other cases, like in the axi-symmetric hill, it

may behave as poorly as the SST model. These results indicate that the SST-SAS model may not unambiguously tend to improve a URANS simulation by increasing the resolved scales and by, in this sense, approaching a LES since the additional terms, other parts of the model and/or a combination of both may obstruct a sound behavior. A further corroboration of a probable defective behavior of the SST-SAS model consists of its poor performance when used for modeling the OECD/NEA-Vattenfall T-junction Benchmark Exercise (see OECD, 2010, Mahaffy, 2010). A simpler and more straightforward approach to VLES based on the SST model, which incidentally performs rather well in the abovementioned exercise, will be presented, discussed and evaluated in this section.

Before leaving the general discussion about URANS, and the assessment of the SST model in particular, it may be of some interest to name some of its reported applications. Among those with a more academic taste, it is possible to list the following: synthetic jet flow (Rumsey, 2004, Vatsa & Turkel, 2004, King & Jagannatha, 2009), cavity flow (Hamed et al., 2003), base flow (Forsythe et al., 2002), bluff body flow (Young & Ooi, 2004, Kim et al. 2005, Uffinger et al., 2010), wave-maker flow (Lal & Elangovan, 2008), tip vortex flow (Duraisamy & Iaccarino, 2005), flow over airfoils and a turbine vane (Zaki et al., 2010). Also more complex problems, especially concerning the geometry and/or the modeling, have been tackled using the SST model of turbulence, such as fire flow in enclosures (Zhai et al., 2007), flow in a stirred tank (Hartmann et al. 2004), the cooling flow within a divertor magnetic coil of the fusion reactor ITER (Encheva et al., 2007), the flow around seabed structures (Hauteclouque et al., 2007), the flow in a centrifugal compressor stage (Smirnov et al., 2007) and the flow in nuclear reactors (Tinoco & Ahlinder, 2009, Tinoco & Lindqvist, 2009, Tinoco et al., 2010, Höhne et al. 2010). However, only few cases among the aforementioned examples have grids fine enough to overcome the dissipative character of the URANS approach and resolve details of the turbulent flow (Rumsey, 2004, Tinoco & Lindqvist, 2009, Tinoco et al., 2010). In spite of the large number of cells used in some cases, as in Tinoco & Ahlinder (2009) where more than 25 million cells are employed for the reactor model, the behavior of the flow is still inherently steady.

### 3.3 LES, DES and VLES

The evolution towards unsteady simulations in CFD has not been driven by a pure academic interest but rather by a concrete requirement in industrial simulations of finding the correct solution to troublesome problems. The paradigm of this kind of problems is the flow in a tee-junction connecting two pipes of, in general, different diameters with different flow rates and temperatures (see e.g. OECD, 2010). Figure 4 below shows a view along a longitudinal, vertical, central plane of the instantaneous temperature distribution obtained through a time dependent CFD simulation using a high quality grid with 11 million cells but with a rather low Reynolds number of about  $8 \times 10^3$ . This solution, which happens to be identical to its temporal mean value since the turbulence model performs in steady mode, does not allow for an analysis of the risk for thermal fatigue of the pipe wall since no temperature fluctuations are resolved. This case has shown to be ideal for LES, or to be precise DES, since simulations with coarse grids, containing as few as  $3 \times 10^5$  cells (see OECD, 2010), may deliver relevant information of the resolved flow away from the walls (see Fig. 6). To properly resolve the wall regions, including for this case the relevant effect of CHT, the grid requirements for LES increase explosively, with limits not only for the normal dimensions of the cells adjacent to the wall,  $y^+ \leq \sim 1$ , but also for streamwise dimensions,

$x^+ \leq \sim 20$ , and for the spanwise dimensions,  $z^+ \leq \sim 10$  (see Veber & Carlsson, 2010). Moreover, if the value of the Reynolds number corresponds to what is normal in industrial applications, i.e. of the order of million, the computational resources needed may become insurmountable (see e.g. Spalart, 2009).

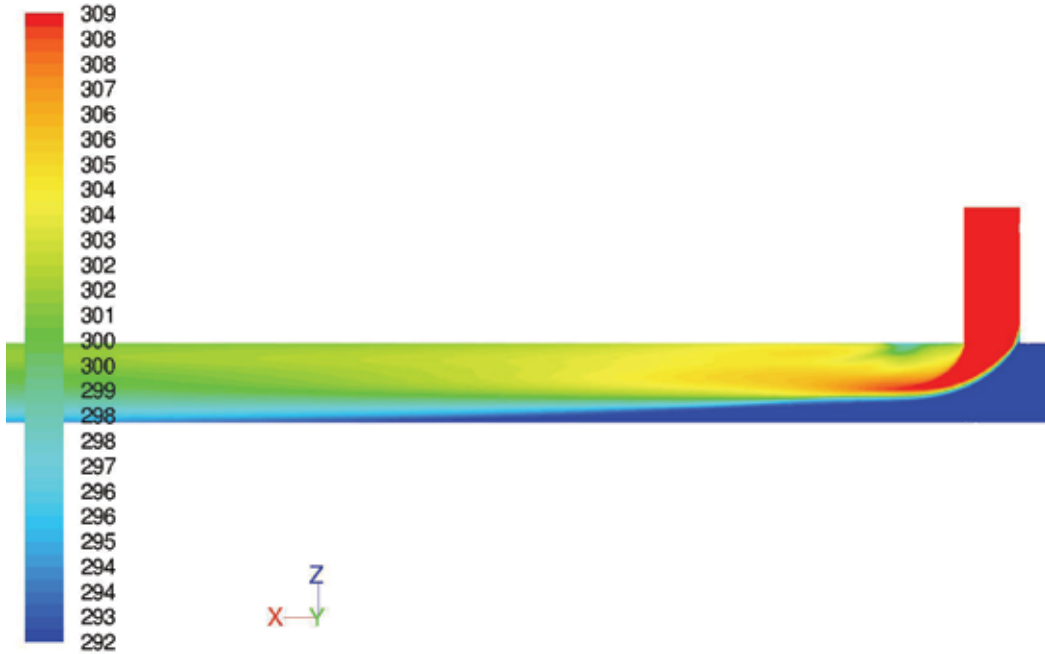


Fig. 4. SST solution of the instantaneous temperature distribution (K) along a longitudinal, vertical, central plane bisecting a tee-junction.

The preceding illustration about the need for unsteady analysis of industrial problems motivates a search for other less demanding alternatives to deal with the problems exemplified by the tee-junction. An option already mentioned in connection with zonal modeling is constituted by DES, which may be based on a combination of LES and URANS (see Spalart, 2009) but may also involve LES and simpler wall-modeling strategies like wall functions. The development of DES has been impelled by the belief that, separately, LES and URANS are incapable of solving the problems discussed above. This is a fact with modification since, as the rest of this section intends to show, a for VLES adjusted URANS may become the sought alternative for unsteady analysis of industrial problems. Different DES formulations using the SST model as the RANS component (Spalart, 1997, Morton et al., 2004, Li, 2007, Lynch & Smith, 2008, Gilling et al., 2009, Dietiker & Hoffmann, 2009, Zaki et al., 2010) have been applied to a wide variety of problems, again with an emphasis on aerodynamics, giving encouraging results. In any event, DES still demands significant computer and software resources and, at the same time, suffers from a number of pitfalls like the already mentioned premature grid-induced separation (Menter et al., 2003) and the more serious difficulties to demonstrate grid convergence and the absence of a theoretical order of accuracy (Spalart, 2009) together with the log-layer mismatch in channel flow simulation (Hamba, 2009). For instance, DES simulations

of the same case reported in the RANS simulations of Tinoco & Lindqvist (2009) and Tinoco et al. (2010), but with a 360° model containing slightly more than 70 million cells (see Veber, 2009), was run continuously during three month in a 256 Intel Xeon CPU machine and reached a simulation time of approximately one minute. An analysis of the temperature signals of some individual points showed temporal means that were not well converged, indicating that the computations would probably need to double the simulation time to reach the same level of convergence as that of the RANS simulations.

The Partially Resolved Numerical Simulation (PRNS) approach has been suggested by Liu & Shih (2006) and is motivated by the assertion that small-scale motions have small associated time scales, allowing for the use of temporal filtering for defining the resolved scales (see also Shih & Liu 2006, Shih & Liu, 2008, Shih & Liu 2009 and Shih & Liu, 2010). Other methodologies for achieving PRNS, not necessarily relying on temporal filtering, have been proposed in the literature, such as that of Ruprecht et al. (2003), that of Perot & Gadebusch (2007, 2009) or the one of Hsieh et al. (2010), but the abovementioned approach of Liu & Shih is the most attractive due to its inherent simplicity. Temporal filtering has been demonstrated by Fadai-Ghotbi et al. (2010) to offer a consistent formalism for a broad class of modeling methodologies that seamless unifies a URANS behavior of the simulation in some regions of the flow, e.g. wall regions, with a LES behavior in other regions where explicit resolution of large-scale structures is required. It is also concluded in this reference that the category of models that ranges from RANS to LES may be regarded as temporal filtered approaches depending on a filter width that needs not to be addressed explicitly. In the brief review of the approach of Liu & Shih (2006) that follows, the large-scale motions are defined using a temporal filter of fixed width, i.e. if  $\phi$  is a large-scale variable then

$$\bar{\phi}(t, x_i) = \int_{t-\Delta T/2}^{t+\Delta T/2} \phi(t', x_i) G(t-t') dt', \quad (3)$$

where  $G(t-t')$  is a normalized homogeneous temporal filter. The following top hat filter corresponds to this type of filter, i.e.

$$G(t-t') = \begin{cases} \frac{1}{\Delta_T}, & \text{if } |t-t'| \leq \frac{\Delta_T}{2} \\ 0, & \text{otherwise} \end{cases}, \quad \text{with } \int_{-\infty}^{\infty} G(t-t') dt' = 1. \quad (4)$$

Performing the filtering operation defined by Equation (3) on the Navier-Stokes and mass conservation equations, a set of exact equations for resolved, large-scale turbulence ( $\bar{\phi}$ ) is obtained

$$\begin{aligned} \rho_{,t} + (\rho \bar{u}_i)_{,j} &= 0, \\ (\rho \bar{u}_i)_{,t} + (\rho \bar{u}_i \bar{u}_j)_{,j} &= \bar{p}_{,i} - \tau_{ij,j} + 2\mu \left( \bar{S}_{ij} - \frac{1}{3} \delta_{ij} \bar{S}_{kk} \right)_{,j}. \end{aligned} \quad (5)$$

In these equations the notations “ $,t$ ” and “ $,j$ ” denote temporal and spatial derivatives, respectively,  $\rho$ ,  $u_i$ ,  $p$ ,  $\mu$ , are, respectively, density, velocity, pressure and dynamic viscosity, and  $S_{ij} = (u_{i,j} + u_{j,i})/2$  is the rate of strain tensor. The extra unknown term  $\tau_{ij}$  corresponds to the subscale stresses that have to be modelled in order to close the system of equations in

(5). In this case, Boussinesq's eddy viscosity concept will be adopted as the modelling approach, i.e.

$$\tau_{ij} = -2\mu_T \left( \bar{S}_{ij} - \frac{1}{3} \delta_{ij} \bar{S}_{kk} \right) + \frac{1}{3} \delta_{ij} \tau_{kk}, \quad (6)$$

where  $\mu_T$  is the turbulent eddy viscosity. The definition of turbulent viscosity corresponds to that of the SST model, a definition that involves  $k$ , the turbulent kinetic energy and  $\omega$ , the specific energy dissipation rate, implying that two additional equations (see e.g. ANSYS Fluent, 2006) are needed for completing the model characterization. The definition of the turbulent viscosity belonging to the SST model, including the VLES modification according to Liu & Shih (2006) that corresponds to the addition of a factor, the Resolution Control Parameter ( $RCP \leq 1$ ), is

$$\mu_t = (RCP) \frac{\rho k}{\omega} \frac{1}{\max\left(\frac{1}{\alpha^*}, \frac{SF_2}{a_1 \omega}\right)}, \quad (7)$$

where  $S \equiv (2S_{ij}S_{ij})^{1/2}$  is the strain rate magnitude,  $y$  the distance to the nearest wall and

$$\begin{aligned} F_2 &= \tanh(\Phi_2^2), \\ \Phi_2 &= \max\left(\frac{2\sqrt{k}}{0.09\omega y}, \frac{500\mu}{\rho y^2 \omega}\right), \\ \alpha^* &= \alpha_\infty^* \frac{\left(\alpha_0^* + \frac{Re_t}{R_k}\right)}{\left(1 + \frac{Re_t}{R_k}\right)}, \\ Re_t &= \frac{\rho k}{\mu \omega}, \\ \alpha_0^* &= \frac{\beta_i}{3}. \end{aligned} \quad (8)$$

The different constants in the expressions above adopt the following values:  $\alpha_\infty^* = 1$ ,  $R_k = 6$ ,  $a_1 = 0.31$  and  $\beta_i = 0.072$ .

The new factor,  $RCP$ , in the definition of the turbulent viscosity is defined as the ratio of two time scales, namely the filter width,  $\Delta_T$ , and the global turbulent time integral scale,  $T$ . According to the analysis of Liu & Shih (2006), an estimate of the lower limit of  $RCP$  may be obtained using instead a quotient of length scales, an equivalence supported by the study of Fadai-Ghotbi et al. (2010), giving in this case

$$RCP \geq (\Delta / \ell)^{4/3}, \quad (9)$$

where  $\Delta$  is the typical grid size and  $\ell$  is the turbulent integral length scale estimated through (see e.g. Wilcox, 1994)

$$\ell = \frac{\sqrt{k_{URANS}}}{\omega_{URANS}}, \quad (10)$$

where the index “URANS” means the typical values of the corresponding magnitudes obtained with a pure URANS simulation, i.e.  $RCP \equiv 1$ . In addition, the applications to be reported in what follows has been simulated assuming that the SST model of turbulence does not need to be modified when used together with the VLES approach<sup>1</sup>.

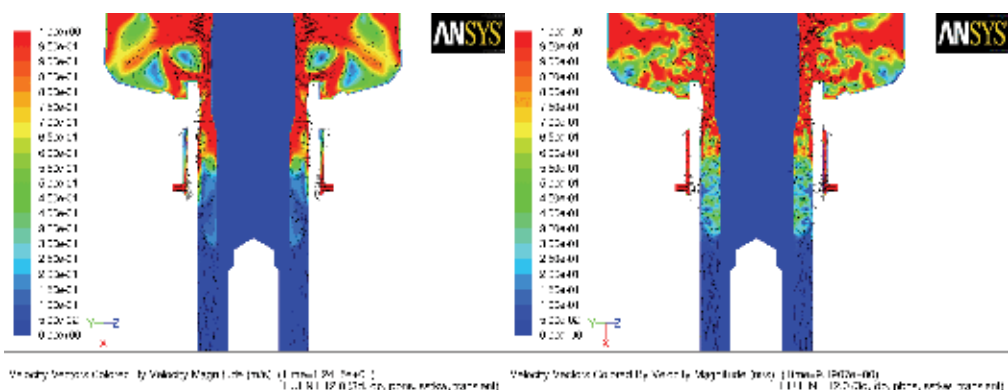


Fig. 5. Comparison of temperature and velocity fields, URANS to the left and VLES to the right ( $RCP = 0.38$ ), where finer structure may be observed.

The first case to be described here corresponds to the URANS simulation reported in Tinoco et al. (2010) concerning the mixing of cold and warm water within the annular space between a control rod and its corresponding guide tube. The URANS simulation is characterized by a high Reynolds number, strong disturbances and a high-resolution grid. Even if the numerical schemes of the FLUENT code are known to be rather dissipative, the simulated solution is strongly unsteady and exhibits rather large coherent structures caused by the inlet jets, as the example in the left view of Fig. 5 hints. Using the same grid and the same conditions, but smaller time steps, a simulation with the VLES approximation was tested with a value of  $RCP$  of 0.38, the same value as in Liu & Shih (2006), and the corresponding results are shown in the right view of Fig. 5. There, it is possible to observe structures of the URANS simulation accompanied with a rather wide range of smaller eddies indicating clearly that the simulated turbulence spectrum has been broadened. This test was discontinued due mainly to the increase in time involved in this type of simulation and to the lack of extensive validation of this rather novel approach. Also, the VLES approach gave a slightly poorer result in the test of CHT in a straight pipe, that will be reviewed in the next section (Tinoco et al., 2009).

The first real validation of the VLES approach carried out by the present authors consists of the simulation of the OECD/NEA-Vattenfall T-Junction Benchmark (OECD, 2010). Figure 6 below shows a comparison of the VLES simulation (right view), using  $RCP = 0.38$  and the same grid as in the URANS simulation shown in Fig. 4, with a DES simulation carried out in a coarser grid (left view). Both views in Fig. 6, which are instantaneous views of the

<sup>1</sup> During the process of editing the present chapter, it came to the knowledge of the authors that Nilsson & Gyllenram (2007) and Gyllenram & Nilsson (2008) have used an almost identical approach.

temperature field, differ radically from that of Fig. 4, showing that the unsteady solution is completely different in its behavior. Now, depending on the range of temperature differences and frequencies of the temperature fluctuations associated with the thermal striping phenomenon, the CHT to the wall may lead to high-cycle thermal fatigue (see e.g. Hosseini et al., 2009). Still, it is unclear if the unsteady CFD simulations may be able to accurately predict the thermal loading on the wall leading to thermal fatigue since no experiments on the heat flux to and out of a solid wall have yet been reported in the literature for validating this type of calculations. In the near future, experimental studies intended for CFD validation about the transient CHT between the flow inside the guide tube and the control rod will be carried out at Vattenfall Research and Development (VRD).

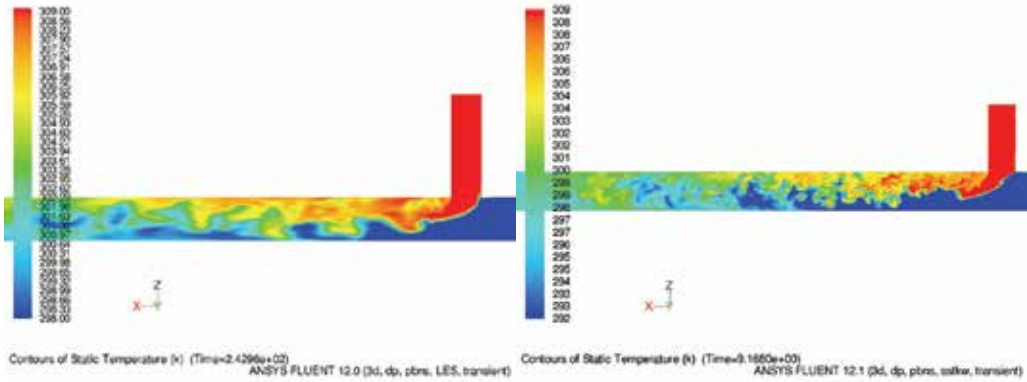


Fig. 6. Comparison of instantaneous temperature fields, DES to the left and VLES to the right ( $RCP = 0.38$ ), where finer structure may be observed due to finer grid.

### 3.3 Basic statistical validation examples

Even if the views in Fig. 6 give the impression of being physically correct, they constitute no quantitative proof of the accuracy of the simulation. In order to objectively validate the computational results against experimental values, a rather basic statistic comparison of not only the first order moments, the temporal mean values of the involved magnitudes, i.e. velocity and temperature, but also of the second order moments, the different variances or root-mean-square (rms) values, should be carried out. If  $\phi(x_i, t) = \{\phi_n(x_i, t_n), n = 1 \dots N\}$  is a turbulent stationary random variable given by its time series, then its temporal mean value is

$$\bar{\phi}(x_i) = \frac{1}{N} \sum_{n=1}^N \phi_n(x_i, t_n), \quad (11)$$

and its rms-value is

$$\phi_{rms}(x_i) = \sqrt{\frac{1}{N-1} \sum_{n=1}^N (\phi_n(x_i, t_n) - \bar{\phi}(x_i))^2}. \quad (12)$$

The sampling of the variable  $\phi(x_i, t) = \{\phi_n(x_i, t_n), n = 1 \dots N\}$  must fulfill some basic conditions like a broad population number (normally  $N \gg 10^3$ ) and a sampling rate (twice the Nyquist

frequency) which should be higher than twice the highest frequency contained in the fluctuations of  $\phi(x_i, t)$  (see e.g. Smith, 2007). Also, the sampling must take place when the simulation is statistically stationary, free from initial and other possible perturbations, i.e. the mean value of all variables associated with each point in the computational domain should have converged to a constant value.

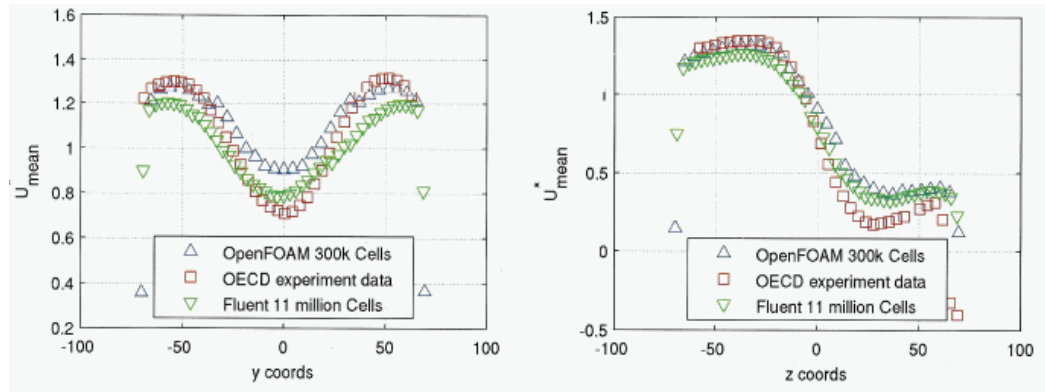


Fig. 7. Mean axial horizontal (left) and vertical (right) velocity profiles, 1.6-D downstream of the junction, for experiments (OECD, 2010), DES (OpenFoam) and VLES (FLUENT).

Figure 7 shows a comparison of the mean axial velocity profile, along a horizontal axis to the left and along a vertical axis to the right, at a section located 1.6 diameters (1.6-D) downstream of the tee-junction. The different values correspond to, respectively, experiments from the OECD/NEA-Vattenfall T-Junction Benchmark Exercise (OECD, 2010), DES with the open-source code OpenFoam (OpenCFD Ltd, 2004) and VLES with the FLUENT code. As may be observed from the results of this blind test, the agreement is fairly good for the temporal means of the axial velocity profile at this section, 1.6-D. For other sections and for the temporal mean of other components of the flow velocity, the agreement is similar but, for space reasons, these results have not been included in this work since they will be a part of the proceedings of the OECD/NRC & IAEA Workshop hosted by USNRC (OECD, 2010).

Figure 8 below shows the distribution of rms-value of axial velocity fluctuations along a horizontal axis to the left and along a vertical axis to the right, at a section located 1.6 diameters (1.6-D) downstream of the tee-junction. As in the preceding figure, the different values correspond to, respectively, experiments from the OECD/NEA-Vattenfall T-Junction Benchmark Exercise (OECD, 2010), DES with the open-source code OpenFoam and VLES with the FLUENT code.

As the results of Fig. 8 indicate, the agreement is fairly good even for the rms-values of the axial velocity fluctuations, as it is for other sections and for the second-order moments. Even if the preceding results are very encouraging regarding the performance of VLES, some general questions, to be discussed in what follows, are still not elucidated and need further investigation.

Figure 9 shows views of the mean axial velocity profile belonging to the same OECD case as in the preceding figures, and at the same section. In this figure, the blue curve corresponds to the experimental data and all other curves correspond to VLES simulations with different

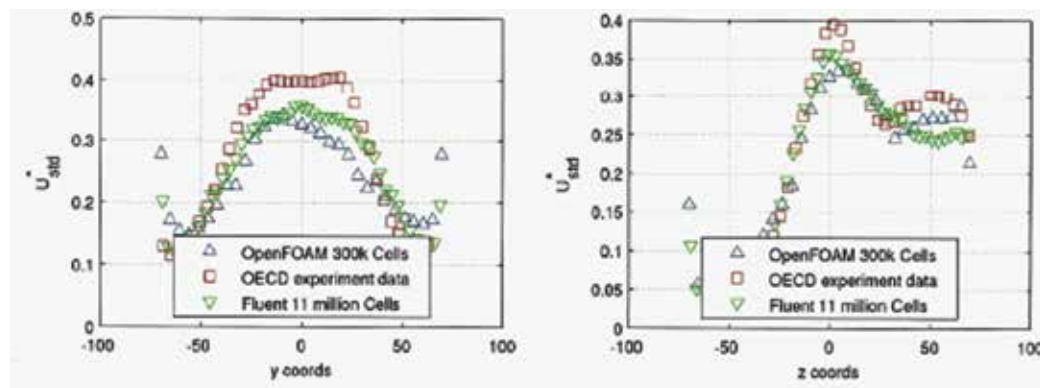


Fig. 8. Rms-value distribution of horizontal (left) and vertical (right) axial velocity fluctuations, 1.6-D downstream of the junction, for experiments (OECD, 2010), DES (OpenFoam) and VLES (FLUENT).

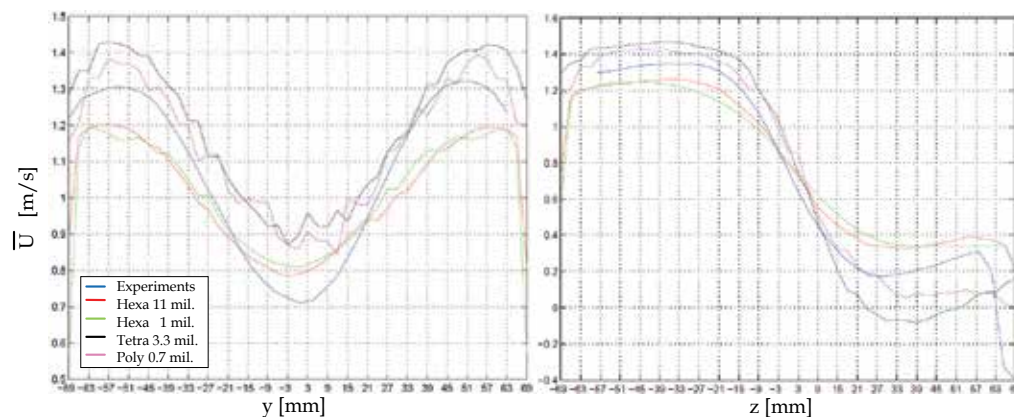


Fig. 9. Mean axial horizontal (left) and vertical (right) velocity profiles, 1.6-D downstream of the junction, for experiments (OECD, 2010) and four VLES (FLUENT) with different grids.

The red curve corresponds to the abovementioned simulation with an 11 million hexahedral grid, the green curve to one with a 1 million hexahedral grid, the black curve to one with a 3.3 million tetrahedral grid and the pink curve to a simulation with a 0.7 million polyhedral grid.

Figure 10 shows rms-values of axial velocity fluctuations belonging to the same OECD case as in the preceding figures. As in Fig. 9, blue corresponds to the experiments, red to VLES with 11 million hexahedra, green to VLES with 1 million hexahedra, black to VLES with 3.3 million tetrahedra and pink to VLES with 0.7 million polyhedra. According to these two last figures, the general agreement between experiments and simulations is rather good for the mean velocity profile but, surprisingly enough, the best agreement is reached with the tetrahedral and polyhedral grids. This is also true for the rms-value of the axial velocity fluctuations except for the results obtained with the 1 million hexahedral grid that give rather poor agreement. Similar comparisons from other sections and/or other magnitudes, not included here for space reasons, corroborate the trend observed through the two

preceding figures. The unexpected outcome of this simulation exercise with different grids brings the problem associated with a clear definition of high-quality grid to the fore. Two preliminary conclusions may be drawn from the present discussion: firstly, that the quality of the grid seems to be associated with the simulated problem, and secondly, that polyhedral grids seem to keep what they promise about quality.

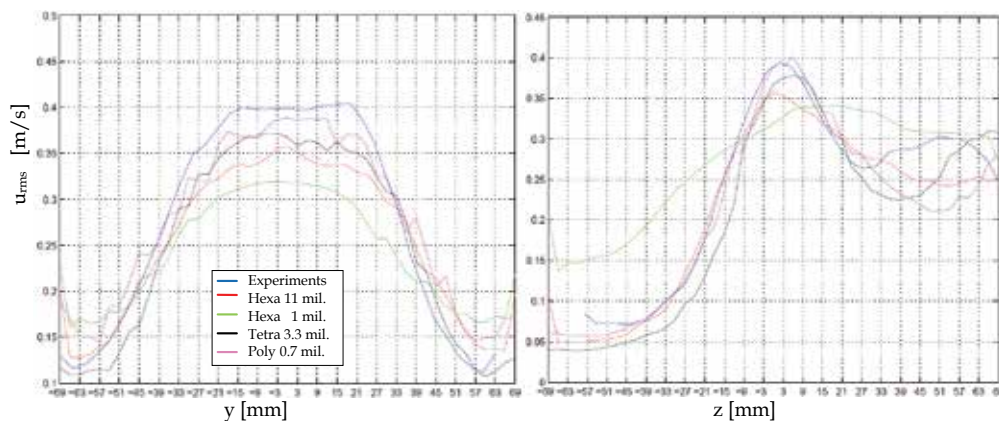


Fig. 10. Rms-value distribution of horizontal (left) and vertical (right) axial velocity fluctuations, 1.6-D downstream of the junction, for experiments (OECD, 2010) and four VLES (FLUENT) with different grids.

Finally, some other issues should be addressed in order to complete the view over numerical simulation of industrial flows using commercial codes. As the preceding paragraph suggests, the grid issue will probably need more time and effort to be resolved and, among other matters to be discussed, the definition of total simulation time needs perhaps a clarification. If the problem analyzed is statistically stationary, as it has been assumed until now, the convergence condition of the simulation is now twofold, first a solution convergence with each time step to minimize the numerical error and then a convergence of the solution to a statistically stationary solution. The later convergence implies a convergence of each point in the computational domain to a constant, time independent statistical mean. The corresponding boundary conditions of a statistically stationary simulation may contain time dependent constituents, like in the simulations of Davidson (2006) and Gilling et al. (2009) where synthetic turbulence is generated at the inlet, provided that the statistical temporal mean is constant.

Commercial codes are in general poorly adapted for running time dependant simulations since the sampling procedure is an operation not implemented at the same level as the case definition. User defined subroutines containing a number of suitable scripts are needed for generating text files of reduced size for sparing storage capacity since the normal data files produced by the code are too large. The capability for further statistical analysis of the sampled data in order to decide the degree of convergence of a time dependent simulation is practically non-existent in commercial CFD codes, and the user has to resort to other codes, like MATLAB (MathWorks, 2010), for the processing of the data.

Due to the amount of data that need to be processed, the selection and handling of images for the analysis of the time dependent simulation are crucial for understanding the problem studied and even for defining the simulation itself. As was mentioned before, the process of

defining the appropriate views in connection with the selection of a suitable combination of variables to be displayed is an iterative procedure that should be facilitated within the CFD code. In general, these options are, in the best case, insufficiently developed in the available commercial CFD codes and, as for the statistical data analysis, the user has to rely on additional software that may not be well adapted for the specific task. Probably, the visualization needs in industrial flow simulations may not be as advanced as those in scientific simulations of astrophysical phenomena (see e.g. Tohline, 2007) but a commercial CFD code containing tools similar to those used in science would undoubtedly win the appreciation of many industrial users. A complementary condition associated with visualization is that of a suitable format with satisfactory resolution quality, of the individual views and of the generated animated sequence that should produce the best possible result with minimized storage requirements.

#### 4. Heat transfer

Heat transfer, and more specifically CHT, deserves a special, although not necessary long, section for discussing its influence in industrial flow simulations since, depending on the case studied, it may constitute the cause of the problem. Indeed, together with cavitation and erosion-corrosion, thermal fatigue, both low cycle and high cycle, comprises one of the important mechanisms for damage generation of industrial equipment (see e.g. Zhu & Miller, 1998).

CFD simulation of heat transfer processes has progressively become an accepted tool for design, optimization, modification and safety analysis of industrial equipment. The applications of CHT reported in the literature range from cases of basic character such as the simulation of impinging cooling jets (Uddin, 2008, Zu et al., 2009) or nozzle flows (Marineau et al., 2006) to more applied cases like heat exchangers (Sridhara et al. 2005, Jayakumar et al., 2008), and to more advanced problems in nuclear reactors (Palko & Anglart, 2008, Tinoco & Lindqvist, 2009, Jo & Kang, 2010, Péniguel et al., 2010, Tinoco et al., 2010) and fusion reactors (Encheva et al., 2007).

Most of the examples mentioned above employ a URANS approach, implying that the Reynolds analogy between momentum transport and transport of heat through a turbulent Prandtl number is adopted in the simulations. Through this analogy, the turbulent transport of heat becomes locally isotropic and, normally, the turbulent Prandtl number is set to a constant value. However, even in flows of rather simple geometrical shape like a free impinging jet, the flow structure is complex, with clear anisotropic behavior near the wall, and with a turbulent Prandtl number which varies non-linearly over a rather definite range (Uddin, 2008). In this case, which is ill-suited for a URANS simulation, even a proper LES with the Smagorinsky-Lilly sub-grid model gives a Nusselt number distribution that fails to reproduce the location and intensity of the first maximum of the two-peaked experimental distribution (Uddin, 2008). In this work, the distance to the wall from cells adjacent to it is of the order of  $y^+ \approx 2 - 3$ , the streamwise dimension of the cells is  $r^+ \approx 36$  and the spanwise dimension  $r\Delta\theta^+ \approx 20$ . According to Tinoco et al. (2009) for pipe flow, and Veber & Carlsson (2010) for channel flow, the distance to the wall should be  $y^+ \leq 1$ , in order to be able to get the correct CHT. For channel flow, the streamwise dimensions should be  $x^+ \leq \sim 20$  and the spanwise dimensions  $z^+ \leq \sim 10$  (Veber & Carlsson, 2010). Probably similar requirements are to be fulfilled for the impinging jet flow but no study about the influence of the grid dimensions on CHT was carried out by Uddin (2008).

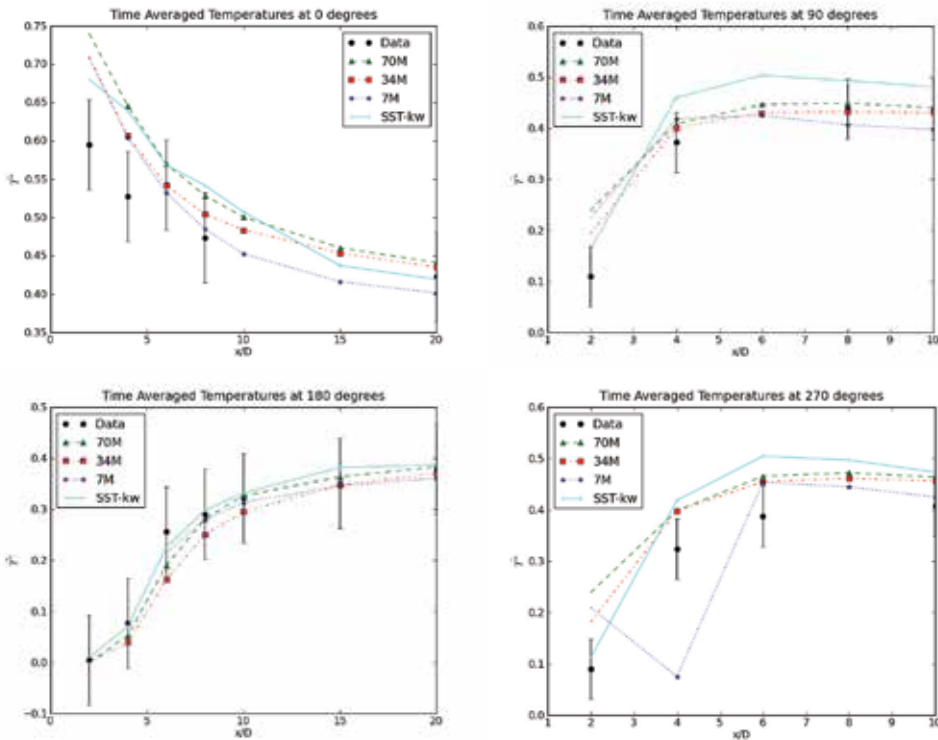


Fig. 11. Normalized axial mean temperature distribution at 1 mm from the wall for 4 azimuthal positions predicted using Fluent; LES with 3 grids (70 M, 34 M), VLES (SST-kw, 11 M) and experiments (OECD, 2010).

Curiously, a URANS simulation in steady mode of an impinging jet confined in a narrow gap using the SST model of turbulence gives satisfactory agreement with the experimental measurements of the Nusselt number distribution (Zu & Yan, 2009). In all probability, the walls of the cavity damp possible coherent structures that the jet might generate and the resulting Nusselt number distribution is flat, allowing even a URANS simulation to predict the distribution with an error of about 7 %. Even if a study of grid sensitivity was performed in connection with the URANS simulation, the grid resolution is not expressed in wall friction units, making very difficult to decide if the resolution corresponds to the aforementioned requirements that are even valid for steady simulations (Palko & Anglart, 2008).

The case reported in Tinoco & Lindqvist (2009) and Tinoco et al. (2010) corresponds to a URANS simulation of unsteady CHT that tries to follow at least the grid requirement related to the normal distance to the wall. Due to the wide range of Reynolds numbers of the flow, the condition is only partially fulfilled even in the region most exposed to thermal loads. In any event, the results of the simulation compare well with the experimental measurements (Angele et al., 2010) of the temperature distributions in the fluid but the predictions of the CHT have not yet been compared with experiments. The measurements of heat flux in and out of the solid are far from trivial since the risk for perturbing the magnitude to be measured by the measuring device is very high. However, as was mentioned before,

measurements of the unsteady CHT will be carried out in the near future at VRD using multiple temperature measurements in the solid. With this experimental basis, simulations using URANS, VLES and DES/LES will be validated since other experimental foundations of unsteady CHT are essentially non-existent.

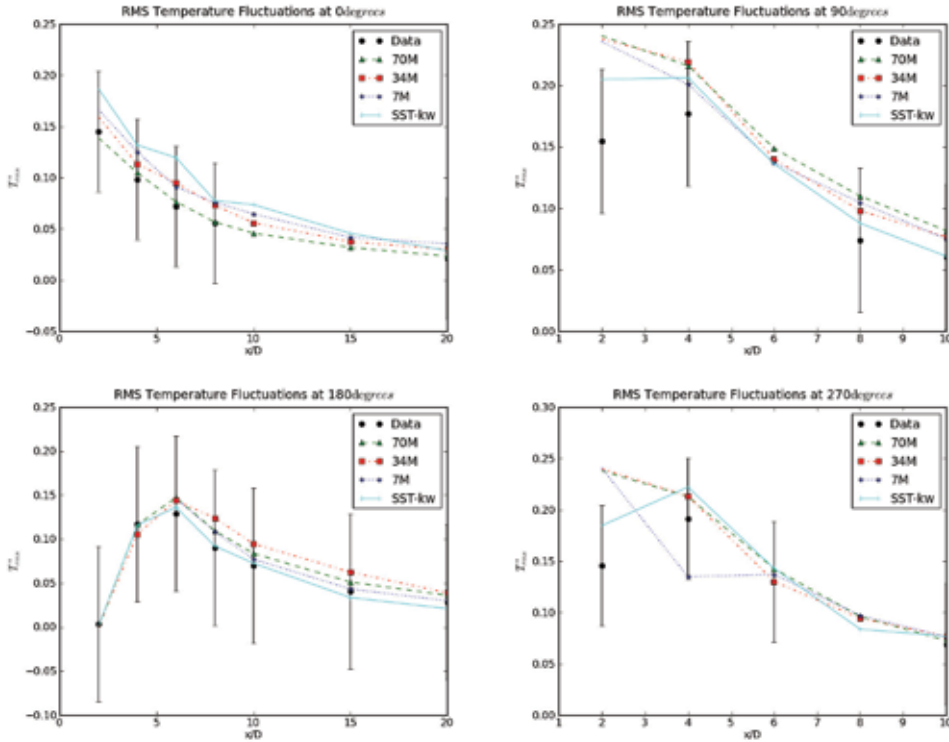


Fig. 12. Normalized axial distribution of rms-value of temperature fluctuations at 1 mm from the wall for 4 azimuthal positions predicted using Fluent; LES with 3 grids (70 M, 34 M), VLES (SST-kw, 11 M) and experiments (OECD, 2010).

Finally, some comments may be added about the simulation of turbulent heat transport within a fluid, excluding CHT. According to Fig. 4, the URANS approach to thermal mixing in a tee-junction lacks realism, at least for the grid, the numerical algorithm and the Reynolds number involved in the simulation. The corresponding VLES approach seems to capture the turbulent velocity field rather well, according to Figs. 8 and 9, indicating that the thermal mixing may be satisfactorily predicted. Surprisingly enough, the agreement between the predictions of the VLES approach with the 11 million grid together with a LES with three different grids and the experimental data (OECD, 2010) is not too good for the normalized (by temperature span) axial mean temperature distribution at the azimuthal positions of 0, 90 and 270 degrees for points located 1 mm from the wall, as Fig. 11 shows. This difference may be due to heat transfer effects since the pipes lack isolation. Heat transfer may affect to greater extent the upper part of the pipe that contains the warmer water with respect to the ambient temperature. A supporting indication is the fact that the temperature distribution at the azimuthal position of 180 degrees, i.e. the bottom of the pipe,

is very well predicted by simulations. This general trend is confirmed by the results of other simulations (see Mahaffy, 2010).

An additional indication of a systematic bias on the mean temperature measurements is constituted by the results shown in Fig. 12, where the normalized axial distribution of rms-value of temperature fluctuations is depicted. These rms-values are rather well predicted by the simulations, especially at the bottom of the pipe, i.e. at the azimuthal location of 180 degrees. The fact that temperature fluctuations mainly depend on the turbulence level, being less sensitive to heat transfer effects, may explain the aforementioned agreement displayed in Fig. 12. To sum up, and according to the results presented here about heat transfer and CHT, the VLES approach seems promising but the verifying simulations carried out in Tinoco et al. (2009) for steady CHT in a pipe indicate that the grid requirements for VLES of unsteady CHT may be similar, but not as severe, as those for a proper LES.

## 5. Verification and validation

The assessment of accuracy and reliability of numerical simulations, being not unique to the CFD methodology, is a necessary step in the process of solving a particular engineering or scientific problem. However, it might be of some interest to point out that accurate quantification of margins and uncertainties in CFD calculations is in particular important for two reasons. The first is due to the fact that CFD is often used as a replacement or complement to experimental investigation (in scaled or prototypic tests) of design or safety related problems. The other is that CFD is in many cases used to study three-dimensional fluid flow and heat transfer phenomena where there is a lack of previous experience (CFD application is outside the range of standard models and methods), for instance concerning mixing and stratification processes or heat transfer processes which require detailed investigation of phenomena in the fluid close to the solid wall (resolving boundary layers and turbulence modeling). Assessment of accuracy and reliability is in particular important when CFD is used in design and safety analyses of systems and processes which potentially can pose significant risk to the public and to the environment, such as nuclear power plants and some chemical industries. Actually, CFD applications in the field of nuclear reactor technology, both in the context of optimizing design and operation of power plants, as well as to solving safety issues, are rapidly growing in number. It is also a fact that rigorous requirements on accuracy assessment constitute today a limiting factor in the applicability of CFD for use in reactor safety cases.

Often the development of appropriate procedures and methodology for the assessment of accuracy and reliability of CFD simulations is driven by regulatory requirements. This is the case in the field of nuclear safety where high confidence in CFD simulations constitutes an obvious and necessary requirement. For example, in Sweden the regulatory authority, Swedish Radiation Safety Authority (SSM), requires that models, methods and data used to determine design and operating limits shall be validated and uncertainties shall be evaluated and analyzed. This applies to all kinds of deterministic analyses but, in the beginning, the requirement was intended for classical thermo-hydraulic codes used in the analysis of transients and accidents in nuclear power plants.

The process of assessment of credibility of CFD predictions usually contains two components, namely verification and validation. There are many definitions of these terms, which in some sense are variations around the same concept, with emphasis on certain

aspects of the verification and validation processes. In our opinion the following definitions are adequate (Oberkampf & Trucano, 2002):

- Verification: substantiation that a computerized model, i.e. computer code, represents a conceptual model within specified limits of accuracy.
- Validation: substantiation that a computerized model within its domain of applicability possesses a satisfactory range of accuracy consistent with the intended application of the model.

Popular, short descriptions of verification and validation also exist, namely that verification corresponds to “solving the equations right” and validation to “solving the right equations”. Interested readers are referred to the work of Roache (1997), Oberkampf & Trucano (2002), Roy (2005) and Stern et al. (2006) or the guidelines published by AIAA (1998), ERCOFTAC (2000), NEA (2007) and ASME (2009) for more information concerning verification and validation in CFD.

In the opinion of Oberkampf and Trucano (2002), the above definition of validation can be considered as somewhat vague. This definition, however, captures an essential aspect of CFD applications, namely that the requirement on the level of accuracy must be adapted to the parameters involved in the particular application and to the purpose of the simulations. For instance, in applications to problems in assessment of safety of nuclear power plants, the requirement on validation and accuracy must be, in general, high. However, even in this application field the requirement on validation is often a compromise based on the overall assessment of the problem, in which considerations including the purpose of the CFD analysis, simulations with less detailed codes and limited experimental validation must be weighted together to guide in the decision process. In some cases even qualitative insights into a particular problem provided by CFD results can be very useful. Hence, validation cannot be disconnected from a particular problem at hand but should be performed and evaluated in the context of what is reasonable and acceptable in each particular case. For instance, when CFD is used to provide input to structural mechanics codes for analysis of structural response to thermal loads (e.g. thermal fatigue), it is reasonable to adjust the requirement on the accuracy of CFD simulations to the desired accuracy in the input to structural analysis code.

Verification is achieved through comparison to exact analytical solutions, manufactured solutions or previously verified higher order simulations. The goal of verification is quantification of errors associated with insufficient spatial discretization convergence, insufficient temporal discretization convergence, lack of iterative convergence, and computer programming as well as with specification of initial and boundary conditions in an input model. According to the available standards and guidelines (AIAA 1998, NEA, 2007, ASME, 2009), verification testing relies on a systematic refinement of the grid size and time step to estimate the discretization error of the numerical solution. However, this procedure might give a wrong answer in the case of DES, as was commented before. In general, both the ASME standard and the aforementioned Guides assume steady solutions or time-averaged solutions, giving therefore no uncertainty estimation procedure for unsteady solutions containing statistical magnitudes for describing the simulation results. The new direction of industrial CFD towards full time-dependent simulations does not seem to have been noticed or forecasted by the different groups involved in developing guidelines and standards for verification and validation. Therefore, the comparison report

of the OECD/NEA-Vattenfall T-junction Bench mark Exercise (Mahaffy, 2010) is a very good example of the difficulties associated with the quality assessment of this type of simulations and, at the same time, it might constitute a first base in the development of criteria for error estimation, verification and validation.

Validation is achieved through the comparison between computational results and experimental data. Assessment of experimental uncertainties is a very important element of validation process. Considering that real engineering systems are often complex in terms of complicated geometry and many coupled physical phenomena, Oberkampf and Trucano (2002) have recommended a tiered approach to validation. The studied system is divided into four progressively simpler tiers that may lead to a minimization of the cancellation error problem.

- Complete systems
- Subsystems cases
- Benchmark cases
- Unit problems

In this approach, the validation starts from the unit problem, where only one phenomenon is investigated, often in simplified geometry but in well instrumented facility. The advantage of the tiered approach is that the four tiers together provide satisfactory validation even if complete validation on the subsystems or complete systems is practically impossible due to the lack of necessary measurements.

In the case of complex engineering systems, the selection of experiments used for validation might be guided by the PIRT process (Phenomena Identification and Ranking Table), a process originated as part of the U.S. Nuclear Regulatory Commission Code Scaling, Applicability and Uncertainty evaluation methodology (see e. g. NEA, 2007). In PIRT, phenomena and processes are ranked based on their influence on appropriate criteria, e.g. nuclear reactor safety criteria. Target variables should be selected by a panel of experts.

Statistical uncertainty analysis, using a Monte Carlo approach, which is often performed in numerical simulations, is in the case of CFD simulations of more complex systems practically impossible due to limitations in time and computer resources.

It is essential that the process and results of verification and validation are properly documented. Code verification should primarily be the responsibility of the code supplier (code developer), particularly if it concerns a commercial code, and should follow some general standard such the ASME standard V&V 20-2009 (ASME, 2009). As NEA's Guide suggests, every supplier of a commercial code should provide all users and even interested regulatory authorities, with a complete documentation of the verification. This demand seems legitimate because users have very seldom access to the source code of a commercial program that has to be used as a black box. At the same time, and owing to fact the user produces a solution, the verification of which is his responsibility, the user shares the responsibility of the verification of the code that generated the solution. Therefore, the user has the obligation of reporting the deficiencies detected through the use of the code, which should be of public knowledge to warn other users and to force the code supplier to deal with them. The burden of validation, which is a process that may involve expensive experimental activities, has to be shared by the complete CFD community, but principally by the industry that most directly harvests the fruits of well validated CFD simulations.

## 6. Acknowledgement

The authors want to thank Nicolas Forsberg from Forsmarks Kraftgrupp AB for allowing the use of his OpenFoam results in this paper.

## 7. References

- Acikgoz, N., (2007). Adaptive and Dynamic Meshing Methods for Numerical Simulations, Doctoral Thesis, Georgia Institute of Technology, Atlanta, GA, USA.
- AIAA, (1998), Guide for the Verification and Validation of Computational Fluid Dynamics Simulations, AIAA Guide G-077-1988, ISBN 1-56347-285-6, January 14, 1998.
- ASME, (2009). Standard for Verification and Validation in Computational Fluid Dynamics and Heat Transfer, *The American Society of Mechanical Engineers*, ASME V&V 20-2009.
- Angele, K., Cehlin, M., Högström, C-M., Odemark, Y., Henriksson, M., H., Lindqvist, H. & Hemström, B. (2010). Flow Mixing Inside a Control-Rod Guide Tube - Part II: Experimental Tests and CFD-Validation, *18<sup>th</sup> International Conference on Nuclear Engineering (ICONE 18)*, Xi'an, China.
- ANSYS Fluent (2006). "Fluent 6.3 Documentation", Fluent Inc., Lebanon, NH (2006).
- Beall, M. W., Walsh, J. & Shephard, M. S. (2003). Accessing CAD Geometry for Mesh Generation, *12<sup>th</sup> International Meshing Roundtable*, Sandia National Laboratories, New Mexico, USA.
- Borouchaki, H. & Frey, P. J. (1998). Adaptive Triangular-Quadrilateral Mesh Generation, *Int. J. Numer. Meth. Engng.*, Vol. 41, pp. 915-934.
- Davidson, L., (2006). Evaluation of the SST-SAS Model: Channel Flow, Asymmetric Diffuser and Axi-Symmetric Hill, *European Conference on Computational Fluid Dynamics, ECCOMAS CFD 2006*, TU Delft, The Netherlands.
- de Hauteclouque, G., Dix, J., Lamkin, D. & Turnock, S. (2007). Flow and Likely Scour Around Three Dimensional Seabed Structures Evaluated Using RANS CFD, University of Southampton, Ship Science Report No. 144, September 2007.
- Dietiker, J. F. & Hoffmann, K. A., (2009). Predicting Wall Pressure Fluctuations Over a Backward-Facing Step Using Detached Eddy Simulation, *J. of Aircraft*, Vol. 46, No. 6, pp. 2115-2120.
- Doering, C. R. (2009). The 3D Navier-Stokes Problem, *Annu. Rev. Fluid Mech.*, Vol. 42, pp. 109-128.
- Duraisamy, K. & Iaccarino, G., (2005). Curvature Correction and Application of the  $v^2-f$  Turbulence Model to Tip Vortex Flows, *Center for Turbulence Research, Annual Research Briefs 2005*, Stanford University, Stanford, California, USA.
- Encheva, A., Vayakis, G., Chavan, R., Karpouchov, A. & Moret, J. M., (2007). 3D Thermal and CFD Simulations of the Divertor Magnetic Coils for ITER, *NAFEMS World Congress 2007 (Simul. Technol. for the Eng. Analysis Community)*, Vancouver, Canada, 22 May 2007.
- ERCOFTAC, (2000). Best Practice Guidelines, *European Research Community On Flow, Turbulence And Combustion (ERCOFTAC), Special Interest Group on "Quality and Trust in Industrial CFD"*, Version 1.0 January 2000.

- Fadai-Ghotbi, A., Friess, C., Manceau, R., Gatski, T. B. & Borée, J., (2010). Temporal Filtering: A Consistent Formalism for Seamless Hybrid RANS-LES Modeling in Inhomogeneous Turbulence.
- Fluent, (2006). GAMBIT 2.3 User's Guide, Fluent Incorporated, Lebanon, NH, USA.
- Forsythe, J. R., Hoffmann, K. A., Cummings, R. M. & Squires, K. D., (2002). Detached-Eddy Simulation With Compressibility Corrections Applied to a Supersonic Axisymmetric Base Flow, *J. Fluids Engng.*, Vol. 124, pp. 911-923.
- Gilling, L., Sørensen, N. N. & Davidson, L., (2009). Detached Eddy Simulation of an Airfoil in Turbulent Inflow, 47<sup>th</sup> AIAA Aerospace Sciences Meeting Including The New Horizons Forum and Aerospace Exposition, AIAA Paper 2009-270, 5-8 January 2009, Orlando, Florida, USA.
- Gyllenram, W. & Nilsson, H., (2008). Design and Validation of a Scale-Adaptive Filtering Technique for LRN Turbulence Modeling of Unsteady Flow, *J. Fluids Engng.*, Vol. 130, pp. 051401-1 - 051401-10.
- Hamba, F., (2009). Log-Layer Mismatch and Commutation Error in Hybrid RANS/LES Simulation of Channel Flow, *Int. J. Heat Fluid Flow*, Vol. 30, pp. 20-31.
- Hamed, A., Basu, D. & Das, K. (2003). Detached Eddy Simulation of Supersonic Flow Over a Cavity, AIAA Paper 2003-0549, 41<sup>st</sup> AIAA Conference, Reno, Nevada, USA.
- Hartmann, H., Derksen, J. J., Montavon, C., Pearson, J., Hamill, I. S. & van den Akker, H. E. A. (2004). Assessment of Large Eddy and RANS Stirred Tank Simulations by Means of LDA, *Chem. Engng. Sci.*, Vol. 59, pp. 2419-2432.
- Hosseini, S. M., Yuki, K. & Hashizume, H., (2009). Experimental Investigation of Flow Field Structure in Mixing Tee, *J. Fluids Engng.*, Vol. 131, pp. 051103-1 - 051103-7.
- Hsieh K. J., Lien, F. S. & Yee, E. (2010). Towards a Unified Turbulence Simulation Approach for Wall-Bounded Flows, *Flow Turb. Combust.*, Vol. 84, pp. 193-218.
- Höhne, T., Krepper, E. & Rohde, U., (2010). Application of CFD Codes in Nuclear Reactor Safety Analysis, *Sci. Tech. Nuclear Inst.*, Vol. 2010, Article ID 198758, 8 pp.
- Ishihara, T., Gotoh, T. & Kaneda, Y. (2009). Study of High-Reynolds Number Isotropic Turbulence by Direct Numerical Simulation, *Annu. Rev. Fluid Mech.*, Vol. 41, pp. 165-180.
- Jayakumar, J. S. Mahajani, S. M., Mandal, J. C., Vijayan, P. K. & Bhoi, R., (2008). Experimental and CFD Estimation of Heat Transfer in Helically Coiled Heat Exchangers, *Chem. Eng. Research Design*, Vol. 86, No. 3, pp. 221-232.
- Jo, J. C. & Kang, D. G., (2010). CFD Analysis of Thermally Stratified Flow and Conjugate Heat Transfer in a PWR Pressurizer Surgeline, *J. Press. Vessel Tech.*, Vol. 132, pp. 021301-1 - 021301-10.
- Jones, W. P. & Launder, B. E., (1973), The Calculation of Low-Reynolds-Number-Phenomena with a Two-Equation Model of Turbulence, *Int. J. Heat Mass Transf.*, Vol. 16, pp. 1119-1130.
- Kim, S. E., Rhee, S. H. & Cokljat, D., (2005). The Prolate Spheroid Separates Turbulence Models, *Fluent News*, Spring 2005, pp.12-13.
- King, A. J. C. & Jagannatha, D., (2009). Simulation of Synthetic Jets With Non-Sinusoidal Forcing Functions for Heat Transfer Applications, 18<sup>th</sup> World IMACS/MODSIM Congress, Cairns, Australia, 13-17 July, 2009, pp. 1732-1738.
- Kline, S. J., (1989). Zonal Modeling, Stanford University, Thermosciences Division, Final Report, 1 Jan. 1986 - 31 Dec. 1988.

- Kolmogorov, A. N. (1941). The Local Structure of Turbulence in Incompressible Viscous Fluid for Very Large Reynolds Number, *Dokl. Akad. Nauk. SSSR*, Vol. 30(4), pp. 301-305.
- Lal, A. & Elangovan, M., (2008). CFD Simulation and Validation of Flap Type Wave-Maker, *World Academy of Sciences, Engng. Tech.*, Vol. 46, pp. 76-82.
- Li, Z., (2007). Numerical Simulation of Sidewall Effects on Acoustic Fields in Transonic Cavity Flow, University of Cincinnati, Department of Aerospace Engineering and Engineering Mechanics of the College of Engineering, Master of Science Thesis, March 2007.
- Liu, N. S. & Shih, T. H., (2006). Turbulence Modeling for Very Large-Eddy Simulation, *AIAA Journal*, Vol. 44, pp. 687-697.
- Lynch, G. E. & Smith, M. J., (2008). Hybrid RANS-LES Turbulence Models on Unstructured Grids, *38<sup>th</sup> Fluid Dynamic Conference and Exhibit*, *AIAA Paper 2008-3854*, 23-26 June 2008, Seattle, Washington, USA.
- Mahaffy, J., (2010). Synthesis of Results for the Tee-Junction Benchmark, *CFD4NRS-3, Experimental Validation and Application of Computational Fluid Dynamics and Computational Multi-Fluid Dynamics Codes to Nuclear Reactor Safety Issues*, OECD/NRC & IAEA Workshop hosted by USNRC, September 14-16 2010, Washington D.C., USA.
- Marineau E. C., Schetz, J. A. & Neel, R. E., (2006). Turbulent Navier-Stokes Simulations of Heat Transfer with Complex Wall Temperature Variations, *9<sup>th</sup> AIAA/ASME Joint Thermophysics and Heat Transfer Conference*, *AIAA Paper AIAA-2006-3087*, June 5-8, 2006, San Francisco, California.
- MathWorks, (2010). MATLAB Technical Documentation, <http://www.mathworks.se/>.
- Menter, F. R. (1994). Two-Equation Eddy-Viscosity Turbulence Models for Engineering Applications, *AIAA Journal*, Vol. 32, No. 8, pp. 1598-1605.
- Menter, F. R. (2009). Review of the Shear-Stress Transport Turbulence Model Experience From an Industrial Perspective, *Int. J. Com. Fluid Mech.*, Vol. 23, No. 4, pp. 305-316.
- Menter, F. R., Kuntz, M. & Langtry, R. (2003). Ten Years of Industrial Experience with the SST Turbulence Model, *4<sup>th</sup> International Symposium on Turbulence, Heat and Mass Transfer, ICHMT 4*, Antalya, Turkey.
- Menter, F. R., Kuntz, M. & Bender, R., (2003). A Scale-Adaptive Simulation Model for Turbulent Flow Prediction, *AIAA Paper 2003-0767*, Reno, Nevada, USA.
- Menter, F. R. & Egorov, Y., (2004). Revisiting the Turbulent Length Scale Equation, *IUTAM Symposium: One Hundred Years of Boundary Layer Research*, Göttingen, Germany.
- Menter, F. R. & Egorov, Y., (2005). A Scale-Adaptive Simulation Model Using Two-Equation Models, *AIAA Paper 2005-1095*, Reno, Nevada, USA.
- Morton S. A., Cummings, R. M. & Kholodar, D. B., (2004). High Resolution Turbulence Treatment Of F/A-18 Tail Buffet, *45<sup>th</sup> AIAA/ASME,ASCE/AHS/ASC Structures, Structural Dynamics & Materials Conference*, *AIAA Paper 2004-1676*, 19-22 April, 2004, Palm Springs, California, USA.
- Nilsson, H. & Gyllenram, W., (2007). Experiences with Open FOAM for water turbines applications, *Proceedings of the 1st OpenFOAM International Conference*, 26-27 November 2007, Beaumont House, Old Windsor, United Kingdom.

- NEA, (2007). Best Practice Guidelines for the Use of CFD in Nuclear Reactor Safety Applications, *Nuclear Energy Agency, Committee on the Safety of Nuclear Installations*, NEA/CSNI/R(2007)5, May 15, 2007.
- Oberkampf, W., L. & Trucano, T., G. (2002). Verification and Validation in Computational Fluid Dynamics, *Progress in Aerospace Sciences*, 38: 209-272.
- OECD, (2010). OECD/NEA-Vattenfall T-Junction Benchmark Exercise: Thermal Fatigue in a T-junction, *CFD4NRS-3, Experimental Validation and Application of Computational Fluid Dynamics and Computational Multi-Fluid Dynamics Codes to Nuclear Reactor Safety Issues*, OECD/NRC & IAEA Workshop hosted by USNRC, September 14-16 2010, Washington D.C., USA.
- OpenCFD Ltd, (2004). OpenFOAM open source CFD toolbox, <http://www.openfoam.com>.
- Orszag, S. A. (1970). Analytical Theories of Turbulence, *J. Fluid Mech.*, Vol. 41, pp. 363-386.
- Palko, D. & Anglart, H., (2008). Theoretical and Numerical Study of Heat Transfer Deterioration in High Performance Light Water Reactor", *Sci. Tech. Nucl. Instal.*, ID 405072.
- Péniguel, C., Rupp, I., Rolfo, S. & Guillaud, M., (2010). Thermal-Hydraulics and Conjugate Heat Transfer Calculation in a Wire-Wrapped SFR Assembly, *International Congress on Advances in Nuclear Power Plants, ICAPP '10*, June 13-17, 2010, San Diego, California, USA.
- Peric, M (2004). Flow Simulation Using Control Volumes of Arbitrary Polyhedral Shape, *ERCOFTAC Bulletin No. 62*, September, 2004, pp. 25-29.
- Perot, J. B. & Gadebusch, J., (2007). A Self-Adapting Turbulence Model for Flow Simulation at Any Mesh Resolution, *Phys. Fluids*, Vol. 19, pp. 115105-1 – 115105-11.
- Perot, J. B. & Gadebusch, J., (2009). A Stress Transport Equation Model for Simulating Turbulence at Any Mesh Resolution, *Teor. Comput. Fluid Dyn.*, Vol. 23, pp. 271-286.
- Pope, S. B. (2000). *Turbulent Flows*, Cambridge University Press, ISBN 0-521-59886-9, UK.
- Roache, P., J., (1997). Quantification of Uncertainty in Computational Fluid Dynamics, *Annu. Rev. Fluid. Mech.* 29: 123-160.
- Roy, C., J. (2005). Review of Code and Solution Verification Procedures for Computational Simulation, *Journal of Computational Physics*, 205, 131-156.
- Rumsey, C. L., (2004). Computation of a Synthetic Jet in a Turbulent Cross-Flow Boundary Layer, *NASA Report, TM-2004-213273*.
- Ruprecht, A., Helmrich, T. & Buntic, I. (2003). Very Large Eddy Simulation for the Prediction of Unsteady Vortex Motion, *Conference on Modelling Fluid Flow (CMFF'03)*, The 12<sup>th</sup> International Conference on Fluid Flow Technologies, Budapest, Hungary, September 3-6, 2003.
- Shih, T. H. & Liu, N. S. (2006). A Strategy for Very Large Eddy Simulation of Complex Turbulent Flows, *44<sup>th</sup> AIAA Aerospace Sciences Meeting and Exhibit, AIAA Paper 2006-175*, January 9-12, 2006, Reno, Nevada, USA.
- Shih, T. H. & Liu, N. S. (2008). Assessment of the Partially Resolved Numerical Simulation (PRNS) Approach in the National Combustion Code (NCC) for Turbulent Non-Reacting and Reacting Flows, *NASA Report NASA/TM-2008-215418*, October 2008.
- Shih, T. H. & Liu, N. S., (2009). A Very Large Eddy Simulation of the Non-Reacting Flow in a Single-Element Lean Direct Injection Combustor Using PRNS with Nonlinear Subscale Model, *NASA Report NASA/TM-2009-215644*, August 2009.

- Shih, T. H. & Liu, N. S., (2010). A Nonlinear Dynamic Subscale Model for Partially Resolved Numerical Simulation (PRNS)/Very Large Eddy Simulation (VLES) of Internal Non-Reacting Flows, *NASA Report NASA/TM-2010-216323*, May 2010.
- Smirnov, P., Hansen, T. & Menter, F. R., (2007). Numerical Simulation of Turbulent Flows in Centrifugal Compressor Stages with Different Radial Gaps, *Proceedings of GT2007, ASME Turbo Expo 2007: Power for Land, Sea and Air*, May 14-17, Montreal, Canada.
- Smith, S. W., (2007). *The Scientist and Engineer's Guide to Digital Signal Processing*, California Technical Publishing, California, USA.
- Spalart, P. R., Jou, W. -H., Strelets, M. & Allmaras, S. R. (1997). Comments on the Feasibility of LES for Wings, and on a Hybrid RANS/LES approach, 1<sup>st</sup> AFOSR International Conference on DNS/LES, August 4-8, 1997, Ruston, Los Angeles, In *Advances in DNS/LES*, Liu & Z. Liu Eds., Greyden Press, Columbus, Ohio, 1997.
- Spalart, P. R. (2009). Detached-Eddy Simulations, *Annu. Rev. Fluid Mech.*, 41, pp.181-202.
- Sridhara, S. N., Shankapal, S. R. & Umesh Babu, V. (2005). CFD Analysis of Fluid Flow and Heat Transfer in a Single Tube-Fin Arrangement of an Automotive Radiator, International Conference on Mechanical Engineering, ICME2005, December 28-30, 2005, Dhaka, Bangladesh.
- Stern, F., Wilson, R. & Shao, J. (2006). Quantitative V&V of CFD simulations and certification of CFD codes, *International Journal for Numerical Methods in Fluids*, 50: 1335-1355.
- Tinoco, H. (2002). Three-Dimensional Modeling of a Steam-Line Break in a Boiling Water Reactor, *Nuc. Sci. Engng.*, Vol. 140, No. 2, pp. 152-164.
- Tinoco, H. & Hemström, B. (1990). Numerical Modeling of Two-Phase Flow in the Upper Plenum of a BWR by a Three-Dimensional Two-Fluid Model, *International Symposium on Engineering Turbulence Modeling and Measurements*, pp. 927-936, ISBN13: 9780444015631, ISBN10: 0444015639, Dubrovnik, Yugoslavia, September 24-28, Elsevier, New York.
- Tinoco, H. & Einarsson, T. (1997). Numerical Analysis of the Mixing and Recombination in the Downcomer of an Internal Pump BWR, *Eighth International Topical Meeting on Nuclear Reactor Thermal-Hydraulics (NURETH 8)*, Kyoto, Japan.
- Tinoco, H, Darelus, A., Bernerskog, E., & Lindqvist, H., (2009). Forsmark 3 – System 30-222. Control rods. Time Dependent Flow Simulations of the Mixing Process Between the Crud-Cleaning Flow and the Bypass Flow Inside the Control Rod Guide Tube, FKA Report FT-2009-2732, 2009-09-02, Forsmark, Sweden.
- Tinoco, H. & Lindqvist, H., 2009. Thermal Mixing Instability of the Flow Inside a Control-Rod Guide Tube, *Thirteenth International Topical Meeting on Nuclear Reactor Thermal-Hydraulics (NURETH 8)*, Kanazawa, Japan.
- Tinoco, H. & Ahlinder, S. (2009). Mixing Conditions in the Lower Plenum and Core Inlet of a Boiling Water Reactor, *J. Engng. Gas Turb. Power*, Vol. 131, Paper No. 062903, pp. 1-12.
- Tinoco, H., Lindqvist, H., Odemark, Y., Högström, C-M. & Angele, K., (2010). Flow Mixing Inside a Control-Rod Guide Tube – Part I: CFD Simulations, *18<sup>th</sup> International Conference on Nuclear Engineering (ICONE 18)*, Xi'an, China.
- Tohline, J. E., (2007). Scientific Visualization: A Necessary Chore, *Computing in Science and Eng.*, Vol. 9, No. 6, pp. 76-81.

- Uffinger, T., Becker, S. & Ali, I., (2010). Vortex Dynamics in the Wake of Wall-Mounted Cylinders: Experiments and Simulation, *15<sup>th</sup> International Symposium on Applications of Laser Techniques to Fluid Mechanics*, Lisbon, Portugal, 5-8 July, 2010.
- Uddin, N., (2008). Turbulence Modeling of Complex Flows in CFD, Doctoral Thesis, Institute of Aerospace Thermodynamics, University of Stuttgart, August 2008, Germany.
- Vatsa, V. N. & Turkel, E. L., (2004). Simulation of Synthetic Jets in Quiescent Air Using Unsteady Reynolds Averaged Navier-Stokes Equations, *22<sup>nd</sup> AIAA Applied Aerodynamics Conference and Exhibit*, August 16-19, Providence, Rhode Island, USA.
- Veber, P. (2009). O3 - LES Analysis of the Mixing Region Between Bypass Flow and Crud-Cleaning Flow, (in Swedish), *Onsala Ingenjörbyrå*, Technical Note 01, 2009, Gothenburg, Sweden.
- Veber, P. & Carlsson, F., (2010). Heat Transfer Validation in Turbulent Channel Flow using Large Eddy Simulations, *Inspecta, Nuclear Technology 2010, Nordic Symposium*, December 1-2 2010, Stockholm, Sweden.
- Wilcox, D. C., (1988). Reassessment of the Scale-Determining Equation for Advanced Turbulence Models, *AIAA Journal*, Vol. 26, pp. 1299-1310.
- Wilcox, D. C., (1994). *Turbulence Modeling for CFD*, DCW Industries, Inc., ISBN 0-9636051-0-0, La Cañada, California, USA.
- Woodard, P. R., Batina, J. T. & Yang, H. T. Y., (1992). Quality Assessment of Two- and Three-Dimensional Unstructured Meshes and Validation of an Upwind Euler Flow Solver, NASA Technical Memorandum 104215.
- Young, M. E. & Ooi, A., (2004). Turbulence Models and Boundary Conditions for Bluff Body Flow, *15<sup>th</sup> Australian Fluid Mechanics Conference, The University of Sydney*, Sydney, Australia, 13-17 December 2004.
- Zaki, M., Menon, S. & Sankar, L., (2010). Hybrid Reynolds-Averaged Navier-Stokes and Kinetic Eddy Simulation of External and Internal Flows, *J Aircraft*, Vol. 47, No. 3, pp. 805-811.
- Zhai, Z., Zhang, Z., Zhang, W. & Chen, Q., (2007). Evaluation of Various Turbulence Models in Predicting Airflow and Turbulence in Enclosed Environments by CFD: Part-1: Summary of Prevalent Turbulence Models, *HVAC&R Research*, Vol. 13, No. 6, pp. 853-870.
- Zhai, Z., Zhang, Z., Zhang, W. & Chen, Q., (2007). Evaluation of Various Turbulence Models in Predicting Airflow and Turbulence in Enclosed Environments by CFD: Part 2 - Comparison with Experimental Data from Literature, *HVAC&R Research*, Vol. 13, No. 6, pp. 871-886.
- Zhu, D. & Miller, R. A., (1998). Investigation of Thermal High Cycle and Low Cycle Fatigue Mechanisms of Thick Thermal Barrier Coatings, *NASA Report NASA/TM-1998-206633*, February 1998.
- Zu, Y. Q., Yan, Y. Y. and Maltson, J. (2009). Numerical Study of Stagnation Point Heat Transfer by Jet Impingement in a Confined Narrow Gap, *J. Heat Transfer*, Vol. 131, pp. 094504-1 - 094504-4.

## **Part 2**

### **Transport of Sediments and Contaminants**



# Numerical Simulation of Contaminants Transport in Confined Medium

Mohamed Jomaa Safi and Kais Charfi  
*National Engineering School of Tunis  
Tunisia*

## 1. General introduction

Multiplication of the human activities and their diversity in all the sectors of the life such as industry, agriculture, transport, etc... had, as consequences, the increase in traditional pollution and appearance of new types, which have in turns generated diseases. Some polluting products such as CO<sub>2</sub>, waste water, etc form already part of our everyday life. In addition to these generated products, other natural products release a permanent radioactivity in the air and the water that the human ones consume daily. The accumulation of the amounts generate damages, sometimes in the short term. It is thus significant to understand the mechanisms of transport and circulation of these contaminants in our space of life to be able to bring an effective solution.

In this work, we are interested in the simulation of the transport of two pollutants which cohabit with the human ones.

The first is the Radon gas resulting from the disintegration of Uranium and Thorium and emanating from geological layers. This gas is also present in the subsoil waters which we consume and in the air and building materials of our houses.

The second pollutant is the waste water or brine rejected in the ground following the industrial water treatment or the desalination of brackish and sea water.

In the simulation, the transport of the two contaminants is investigated in time and space.

The Radon gas is transported by the air inside the habitat by diffusion-convection, and recirculation zones (accumulation of the amounts) due to the confinement appear with time. The effect of the temperature is demonstrated.

In the case of the brine, transport is done by water through porous heterogenous and anisotropic layers. The residence time of the contaminant in each layer depends on the thermo-physical properties and the importance of the flow.

In these two cases, the flow is modelled by the Navier-Stokes equations coupled with the energy and species equations to take into account the temperature and the dose effects.

For simplification, only the two-dimensional flow is considered.

## 2. Numerical method

These partial derivative equations need to be numerically solved. A panoply of methods is available in literature and CFD software makes it possible to simulate a large range of industrial problems. In order to reduce the number of nonlinear partial equations and

overcome the difficulties related to the pressure calculation, the stream function  $\psi$  and the vorticity function  $\Omega$  formulation is used with:

$$u = -\frac{\partial\Psi}{\partial y}, \quad v = \frac{\partial\Psi}{\partial x}, \quad \Omega = \frac{\partial v}{\partial x} - \frac{\partial u}{\partial y}$$

In our case, the equations are solved using a difference finite scheme based on a compact Hermetian method where the function and its first and second derivatives are considered as unknowns. This method allows to reach a good accuracy: fourth order  $O(h^4)$  for  $\psi$  and second order  $O(h^2)$  for  $\Omega$ ,  $T$  and  $C$ . The Alternate Direction Implicit technique (A.D.I) is used to integrate the parabolic equations. This scheme is well described in the literature and has been widely used for natural convection and recirculation flow and was proposed by (Loc & Daube, 1978) to solve the Navier-Stokes equations and by (Safi & Loc, 1994) to solve coupled problems. This procedure has the advantage that the resulting tri-diagonal matrix instead of a matrix with five occupied diagonals can easily be solved by factorization algorithm. Some difficulties were encountered in implementing the vortices boundary conditions. Different approximations were tested and the Padé approximation was employed to overcome the numerical instability (Safi & Loc, 1994). The convergence criterions were defined by the following relations:

$$\text{MAX}|\Psi_{ij}^{n+1/2} - \Psi_{ij}^n| + \text{MAX}|\Psi_{ij}^{n+1} - \Psi_{ij}^{n+1/2}| < \chi \quad \text{for } \Psi$$

$$\text{MAX}|(\Omega, T, C)_{ij}^{n+1} - (\Omega, T, C)_{ij}^n| < \chi \quad \text{for } \omega, T \text{ and } C$$

$\chi$  is equal to  $10^{-6}$  for the stream function  $\Psi$  and  $10^{-4}$  for the  $\Omega$ ,  $T$  and  $C$ .

### Nomenclature

- A: Aspect ratio of the cavity= H/L
- c: Specific heat at constant pressure
- C: Dimensionless concentration
- D: Massic diffusivity
- $D_p$ : Massic diffusivity of porous media
- $D_T$ : Thermal diffusivity of solute concentration
- g: Gravitational acceleration
- H: Height of the cavity
- K: Permeability of porous media
- L: Reference width of the cavity
- Le: Lewis number
- Nu: Average Nusselt number
- Gr: Gradshof number
- $Da=K/H^2$ : Darcy number
- $N=\alpha\Delta C_0/\beta\Delta T_0$ : Floatability number
- $Ra^T=GrPr$ : Thermal Rayleigh number
- $Ra^s=NRa^T$ : Solutal Rayleigh number

Pe= RePr : Peclet number

Pr: Prandlt number

Re: Reynolds number

R<sub>i</sub>: Richardson number

R<sub>d</sub>: effective Mass diffusivity ratio,  $R_d = \varepsilon + (1 - \varepsilon)R_{d_p}$

R<sub>d<sub>p</sub></sub>: Mass diffusivity ratio

R<sub>v</sub>: effective Viscosity ratio,

$R_v = \nu_e / \nu$ , where  $\nu_e = f(\nu, \varepsilon) = \nu f(\varepsilon)$

t: dimensionless time

t<sub>0</sub>: reference time

t<sup>\*</sup>: dimensional time

(u,v) : dimensionless velocity

(x,y): dimensionless coordinate system

### Greek Letters

$\alpha$ : Mass expansion coefficient

$\beta$ : Thermal expansion coefficient

$\Delta C$ : Concentration difference,  $C^* - C_2^*$

$\Delta C_{ref}^*$ : Reference concentration difference,  $C_1^* - C_2^*$

$\Delta\psi$ : Laplacien of stream function

$\varepsilon$ : Porosity

$\nu$ : Kinematic viscosity

$\nu_e$ : Effective cinematic viscosity

$\psi$ : Stream function

$\Omega$ : Vorticity =  $\frac{\partial v}{\partial x} - \frac{\partial u}{\partial y}$

### Subscripts

e: Effective

p: Refers to porous media

## First example: The indoor diffusion-convection of the radon gas

### 1. Introduction

Among the sources of natural radioactivity to which the man is exposed, is the radon gas emanating from the disintegration of Uranium and Thorium and other rocks. This gas is present in all the atmosphere under the effect of meteorology and in most the ground water. Owing to the fact that it emanates from the rocks, most of the applied and fundamental studies concentrated on its transport through these rocks considered as porous body (Durani & LLic, 1997; Tomozo & al, 2008).

Research on fine scales concerning multiphase transport to determine the coefficient of emanation of this gas starting from the rocks was carried out (Nielson & Rogers, 1994).

Few works related to the direct effect of the temperature on the diffusion or the convection of this gas especially in closed mediums like the dwelling or the factory exist whereas the principal producers of phosphate, significant source of radon emanation, are located in North Africa where the solar radiation exceeds sometimes 1000W/m<sup>2</sup>. Over more, the settlements of the workmen of the mines which were built last century around these mines

and with the stones coming from the same site are transformed into villages and cities cohabiting the phosphate and the radon.

In this study we choose the radon 222 whose half life time is only of 3.8 days in order to simulate the physical process during disintegration of this gas.

## 2. Physical model

We consider a parallelepiped room whose walls are uniform including the ground and the ceiling. This symmetry of boundary conditions allows to consider only one vertical medium plane ( $X, Y, Z=1/2$ ).

We consider a source of radon(S), placed at the middle of X to an  $H/3$  height (Fig.1) and at constant concentration C.

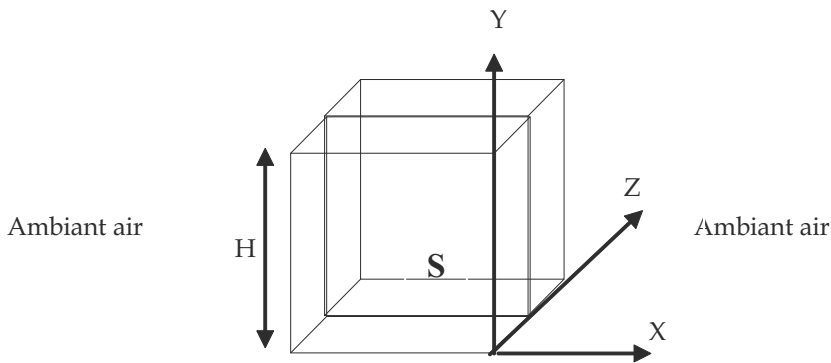


Fig. 1. Geometrical configuration of the physical model

Taking into account the thermo physical properties of radon, we can consider that it moves with the air at the same velocity and with the same properties especially viscosity but at a different concentration. For better determination of the temperature effect, only the natural convection is thus considered. The effect of the climate is limited to the temperature of the outer jacket of the habitat.

Thus the transport equations are written in a two dimensional geometry (vertical medium plane):

- Mass conservation equation:

$$\frac{\partial U}{\partial x} + \frac{\partial V}{\partial y} = 0$$

- Momentum equation:

$$\rho \frac{\partial \vec{U}}{\partial t} + \rho (\vec{U} \nabla) \vec{U} = -\nabla p + \mu \nabla^2 \vec{U} + \rho \vec{g}$$

- Energy equation

$$\rho c \frac{\partial T}{\partial t} + \left( \frac{\partial UT}{\partial x} + \frac{\partial VT}{\partial y} \right) = \lambda \nabla^2 T$$

- Concentration Equation:

$$\frac{\partial c}{\partial t} + \left( \frac{\partial U c}{\partial x} + \frac{\partial V c}{\partial y} \right) = \nabla(D \nabla c) - \lambda c + \lambda c^{source}$$

Where:

C is the Radon concentration expressed as radioactivity (Bq/m<sup>3</sup>),

$\left( \frac{\partial U c}{\partial x} + \frac{\partial V c}{\partial y} \right)$  is the advection term,  $\nabla(D \nabla c)$  is the diffusion term,  $-\lambda c$  is the decay term,

$\lambda c^{source}$  is the source term, and  $\lambda = \frac{\ln 2}{T_{vie}^{(1/2)}}$  is the radon decay constant (1/s).

We notice that the concentration is not directly related to the temperature because we neglected the Dufour effect. However the two parameters are dependent each from the other through the velocity.

As mentioned above, streamline function  $\Psi$  and vorticity function  $\Omega$  were used to replace velocity components U, V and the pressure P.

To generalize this study independently of dimensions and time ( by applying physical simulation), the transport equations inside the habitat are written in the following dimensionless form:

$$\Delta \Psi = \Omega \quad (1)$$

$$\frac{\partial \Omega}{\partial t} + \left( \frac{\partial u \Omega}{\partial x} + \frac{\partial v \Omega}{\partial y} \right) = \frac{\text{Pr}}{R_t} \Delta \Omega + \frac{\text{Pr} Ra^T}{R_t^2} \left( \frac{\partial T}{\partial x} - N \frac{\partial C}{\partial x} \right) \quad (2)$$

$$\frac{\partial T}{\partial t} + \left( \frac{\partial u T}{\partial x} + \frac{\partial v T}{\partial y} \right) = \frac{\nabla^2 T}{R_t} \quad (3)$$

$$\frac{\partial C}{\partial t} + \left( \frac{\partial u C}{\partial x} + \frac{\partial v C}{\partial y} \right) = \frac{\nabla^2 C}{R_t Le} - \ln 2 C + \ln 2 \frac{C^{source}}{\Delta C_0} \quad (4)$$

The boundary conditions on the walls were fixed as following:

- C=0 which means that the walls from where radon can exit towards outside remains at the low concentration,
- u=v=0 ; due to the adherence ,
- $\Psi=0$  expresses conservation the flow rate inside the habitat ( there's no momentum change with the outside), and  $\Omega$  is calculated using Padé approximation.

Consequently, the phenomenon of diffusion-convection of radon depends on of the following dimensionless parameters:

- Lewis number  $Le = D_T / D_0$
- Prandlt number  $Pr = \nu / D_T$
- Thermal Rayleigh number  $Ra^T = \frac{\beta g \Delta T_0 H^3}{\nu D_0}$  with  $\Delta T_0 = 10 \text{ K}$ ( temperature difference to which natural convection is due)
- Floatability number :  $N = \alpha \Delta C_0 / \beta \Delta T_0$

With:

$\alpha=0.103\text{m}^3\text{Kg}^{-1}$ : mass expansion

$\beta=310^{-3}\text{K}^{-1}$ : thermal expansion

$D_T=410^{-6}\text{m}^2\text{s}^{-1}$ : thermal diffusion

$D_0=1.808\cdot 10^{-5}\text{m}^2\text{s}^{-1}$ : mass diffusion

$\Delta C_0=(C^S-C_0)=1000-10(\text{Bqm}^{-3})$  (difference between initial and source dose),

- Solutal Rayleigh number  $Ra^S=NRa^T$ ,

-  $R_t = \frac{t_0}{T_{vie}^{(1/2)}}$  with  $T_{vie}^{(1/2)} = 4$  days (half life time of the radon gaz), and

-  $t_0 = \frac{H^2}{D_T} = \frac{3^2}{410^{-6}} = 2.2510^6\text{s} = 26.04$  days

### 3. Results

Numerical simulation was carried out in a square cavity with a uniform grid of  $41 \times 31$  nodes. Physical parameters were limited to the above values of  $\Delta C$  and  $\Delta T$ . Consequently we obtain:  $Pr=2.5$ ,  $Le=0.221$ ,  $Ra^T=2.027\cdot 10^{11}$ ,  $N=0.5510^{-23}$ ,  $R_t=6.51$ . Notice that  $C=1000\text{Bq}/\text{m}^3$  is considered as amount of alert in all the countries. The amounts maxima authorized are  $150\text{Bq}/\text{m}^3$  in U.S.A and  $400$  in E.U.

In this study, different boundary conditions were considered.

#### 3.1 Isothermal diffusion of radon

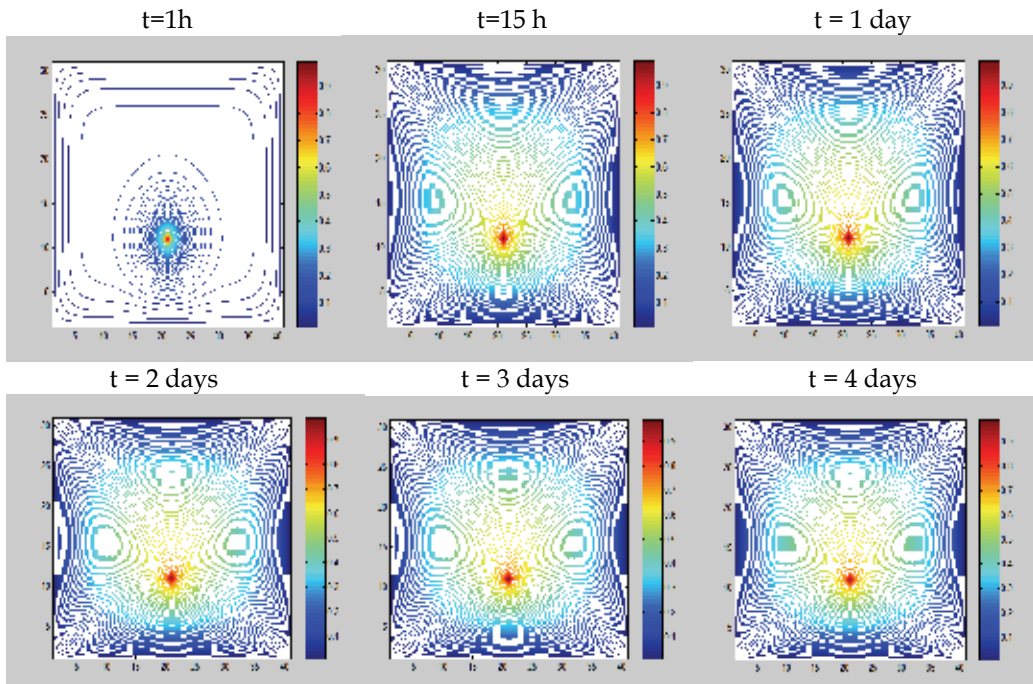


Fig. 2. Iso-concentration lines of radon gas diffusion

We considered the case of a body source located at the middle of the room at 1m from the floor of the house (H/3). This source released a constant intensity of radon towards the rest of the room space including the walls, the floor and the roof. The whole system was considered at the same temperature. The numerical results are expressed in terms of iso-contours of concentration (Fig.2) which illustrate the different steps of the transfer inside the room.

At  $t=1$  hour, the concentration is still located in the vicinity of the source.

At  $t=5$ h, the gas occupied the whole of the room with a maximum concentration around the source. We still have a diffusion transfer.

At  $t=15$ h, over than 50% of the space had a higher concentration, and a weak recirculation zones appear in the vicinity of the walls. This phenomena announces the beginning of the convective movement.

Since  $t=15$  h to  $t=4$  days, the recirculation zones extended slowly from the wall region towards the rest of the room and concentration tends to be uniform in a large region. This mixing convective movement is very weak and a quasi steady state is reached.

### 3.2 Temperature effect

Temperature may occur in three ways (a) double diffusion phenomena, (b) transport by natural convection (c) and transport by forced convection.

In the present study, two geometrical configurations are considered.

#### 3.2.1 Lateral thermal gradient

This configuration simulates the difference of temperature between two walls (East-West or North –South) due to, for example, heating by solar radiation.

Results are represented by the isotherm and iso-concentration contours (Fig.3).

At  $t=1$  hour, heat is transferred to the colder wall in a vertical front way. The most important thermal layer remains against the hot wall. The parallel vertical isotherms indicate that the transfer is occurring by pure diffusion. As a consequence, the radon is smoothly diffused in all the directions and the maximum concentration is found to be around the source.

At  $t=15$ h, the temperature front continue to move towards the cold wall and a recirculation zone appears entraining the gas in a rotational movement.

At  $t=1$  day, the thermal front reaches 1/4 of the distance between the two lateral walls.

During the remaining three days, and due to natural convection, temperature and concentration continue to be transported inside at low velocities but faster than in the isothermal case.

#### 3.2.2 Vertical gradient

This configuration simulates the temperature difference between the floor and the roof. Such a gradient occurs, for example at noontime due to heating by vertical solar radiation or by heating from below during the cold season. The last case was investigated.

Results are represented by the isotherm and iso-concentration contours (Fig.4).

At  $t=1$  hour, thermal front moves faster than in the previous cases. This is due to the buoyancy effect and to the fact that lateral walls were taken adiabatic. The concentration is spread faster but still in closed contours indicating the diffusion regime.

At  $t=5$ h, the temperature front reaches the cold side and recirculation zones appeared against the walls as in the precedent case at  $t=15$ h. We deduced that the transfer in this case is accelerated by about 10 hours.

At  $t=1$  day, a quasi-linear thermal stratification appeared, such a phenomena is not advised for habitants and simultaneously the recirculation zones decreased in density. Since that time and until  $t=4$  days, temperature and concentration continue to spread slowly. A quasi state regime with weak vortices oscillating in density settles.

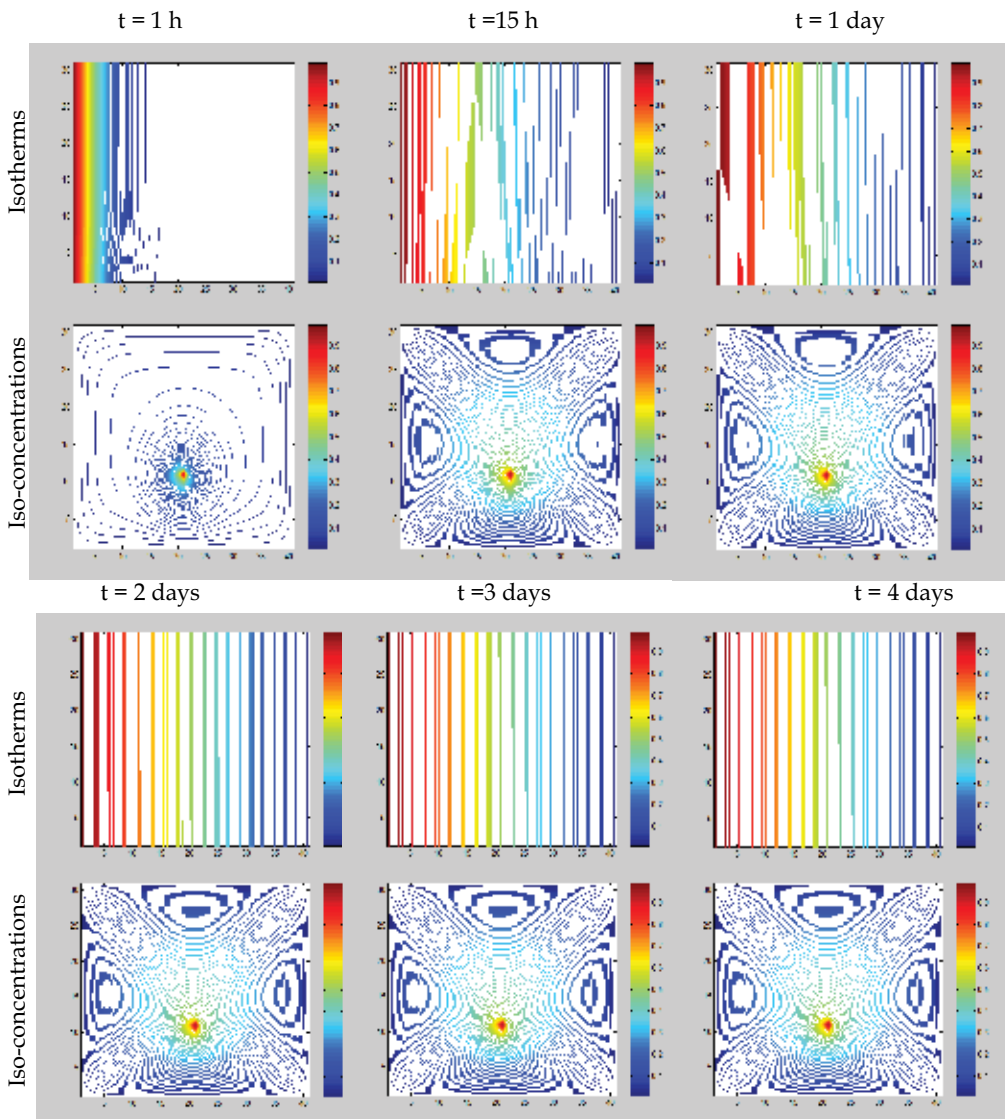


Fig. 3. Diffusion-convection of radon gas under lateral thermal gradient

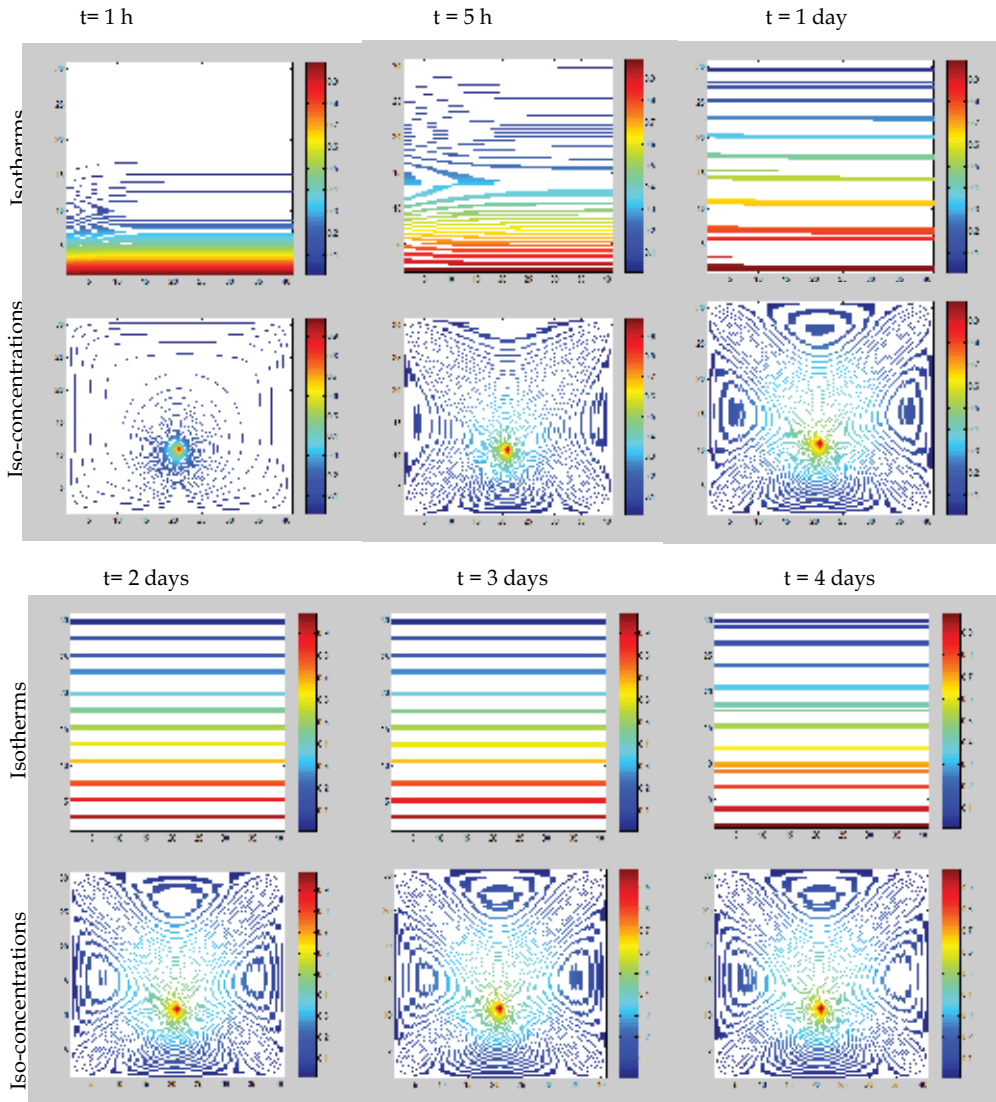


Fig. 4. Diffusion-convection of radon gas under vertical thermal gradient

#### 4. Conclusion

A numerical simulation of the transport of radon gas concentration, temperature and momentum in a room has been investigated numerically.

These simulations, allow us to predict the space-time evolution of the concentration, the temperature and the streamline fields. In the present work, although the source dose is important, the transport is influenced especially by the thermal buoyancy effect.

The results show that:

1. thermal natural convection, makes the transport of radon gas faster due to the air movement,

2. this acceleration is more important when a vertical gradient is applied to the room opposite walls.
3. by changing the concentration, we concluded that the dose variation doesn't affect the flow behaviour significantly.
4. The intrusion of radon from outside through windows will be investigate as well as the ventilation of the habitat.

## **Second example: Flow and concentration transport through saturated porous layers**

### **1. Introduction**

Some people still imagine, like one century ago, that the oceans and the ground are infinitely large to contain all the solid pollutants and liquids which they produce.

This false belief brought the inhabitants of the coast to discharge their contaminants in the sea and those of the remote zones to throw their contaminants at free surface or to bury them basement.

Last century, the American manufacturers of textile, oil and mines, poured, without any concern, million m<sup>3</sup> of waste water coming from dyeing, hydrocarbons and the factories of washing of the mines. Today the consequences are catastrophic as in Texas where: contamination of the tablecloths, desertification and lack of drinking water recall to the order. In California, due to an excess in desalting brackish tablecloths and to discharging the very concentrated brine into the soil; salty small-lakes appeared in under ground contaminating any form of life. These catastrophes gave birth for a certain regulation on the rejections.

Today, with the appearance of other essential activities for the human ones, pollution took other forms. Being limited only to the sector of water, source of the life, two forms of pollution are generated: the waste water and the brine resulting from desalination. To face the water shortage, many countries are recurring more and more to brackish and sea water desalination.

In the case of desalination of sea water, the brine is rejected on the coast with a salinity able to be four times initial salinity, with chemicals resulting from the pre-treatment and sometimes (thermal desalination) with an increase in temperature of + 10K. It results destruction of the phone and the flora. It is currently the case with the countries of the gulf and the Canary Islands. In the remote zones, R.O technique is usually used to desalt ground water at a salinity varying from 3 to 6 g/l. The desalt water is used to supply fresh water to the local population and to irrigate greenhouses, while the concentrated brine is released in the environment or injected into the ground without any regulation. As a consequence, the local agriculture is suffering and ground water quality is degrading.

The waste water which constitutes the second source of water after that of the seas constitutes also the second form of pollution. It is rejected after treatment in the coast or into the ground. Even in the best cases where water is treated secondary, bacteria and especially viruses persist and are transported in the receiving mediums to proliferate unless this water undergoes a very expensive tertiary treatment which is not obligatory in any country. This water is more dangerous than the brines because it transports with it several types of chemicals and in significant amounts. In coastal regions which receive the two thirds of the world population, certain regulations impose the use of the emissary to

discharge the contaminated water far from the coast. This solution is very expensive and when it is applied, it is not optimized because one badly knows the mechanisms of diffusion and dispersion of water in the sea. In addition, the interaction near field-far - field (coast-broad) is still badly known. This requires the establishment of accurate models and of large-scale digital simulations. In the remote zones, the situation is more complicated because the receiving medium is not transparent and the in situ experiments are very expensive and hazardous. The prediction by the digital simulation, after characterizations of the medium and the waste water, makes it possible to approximate the residence time of these contaminants and to reduce the in situ experiments.

Some people use the phenomenon of Riverbank to filter their liquid pollutants. The Germans used this process to recover the permeate in the water of the Rheine river. This process cannot be an effective solution for all the types of waste water. Its efficiency depends on several parameters. The Riverbank filtration represents a natural process to use in first stage in the water treatment. This process is always in direct contact by the contamination of the organic, inorganic substances, viruses polluting and bacteria which can modify the quality of drinking water (Sontheimer, 1980; Jacobs et al, 1988; Magee et al, 1991; Matsunga et al, 1993). Contaminant transport in Riverbank filtration has been investigated by several researchers using different model. A kinetic model was proposed (Song & Yavuz, 2002) to simulate this phenomenon in the presence of dissolved organic matter and bacteria. This model can help to understand the behaviour of contaminants in riverbank filtration.

As a first step towards the design of an efficient system, we investigated a *numerical simulation* of brine discharge. The soil is simulated by *stratified porous layers* of different thickness and geological properties (porosity, permeability, etc...). The discharge is assumed to be at the surface in vertic direction. The mechanism of flow transport and concentration becomes strongly coupled and the prediction of its behaviour depends on the accuracy of the numerical scheme. Christophe Filder et al (2001) have already studied numerically the behaviour of a panache resulting from an injection located in a heterogeneous vertical porous medium of two superimposed layers of the same thickness and different permeabilities.

## 2. Physical model equations

The system should be represented by a stack of 5 layers with different interface boundary layers (Fig.1).

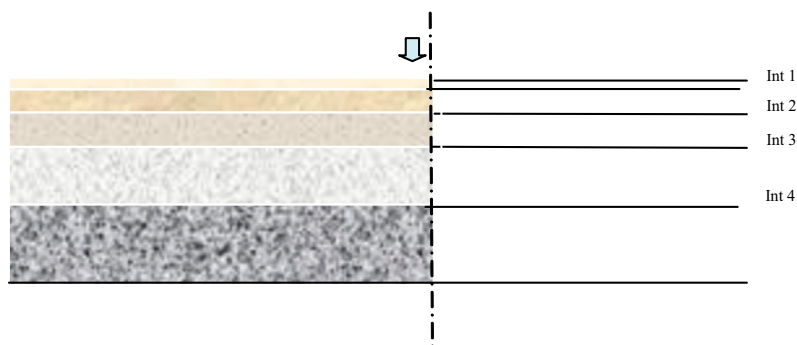


Fig. 1. Physical Model

The flow in such a configuration is three dimensional and need long time computing. As a first step for further complicated flows, we make the following assumptions (which could in fact be realistic):

1. The layers are homogeneous but different each from the other.
2. The bottom and the surface are permeable.
3. The liquid waste at high concentration is still considered as Newtonian fluid.
4. Geological layers are represented by porous media, we assume isotropic.

With assumptions, the flow could be considered two dimensional and Boussinesq approximation is valid. Hence the transfer phenomenon is described by Navier-Stokes and concentration equations including the Darcy-Brinkman-Forchheimer formulation.

To reduce the number of unknowns and overcome the resolution of the presence equation, the streamline and vorticity formulation is used as in the first example.

The consequent set of dimensionless equations is:

$$\Delta\Psi = \Omega \quad (1)$$

$$\frac{1}{\varepsilon} \frac{\partial \Omega}{\partial t} + \frac{1}{\varepsilon^2} \left( \frac{\partial u \Omega}{\partial x} + \frac{\partial v \Omega}{\partial y} \right) = \frac{R_v}{\text{Re}} \Delta \Omega + \left( \frac{\Omega}{\text{Re} Da} + \frac{b}{Da^{1/2}} \left( \frac{\partial |u|v}{\partial x} - \frac{\partial |u|u}{\partial y} \right) \right) - \text{Ri} \left( \frac{\partial C}{\partial x} \right) \quad (2)$$

$$\varepsilon \frac{\partial C}{\partial t} + \left( \frac{\partial u C}{\partial x} + \frac{\partial v C}{\partial y} \right) = \frac{Rd}{\text{LePe}} \Delta C \quad (3)$$

The following parameters were defined to obtain the dimensionless above equations:

$$(u, v) = \left( \frac{U^*}{V_1^*}, \frac{V^*}{V_1^*} \right), \quad (x, y) = \left( \frac{X^*}{H}, \frac{Y^*}{H} \right), \quad C = \frac{C^* - C_2^*}{\Delta C_{ref}} \quad (4)$$

$$\text{and } t = \frac{t^*}{t_0} \text{ where } t_0 = \frac{H}{V_1^*} \quad (5)$$

The Forchheimer coefficient  $b$  was taken equal to  $0.55\sqrt{Da}$  (Hwa-Chong Tien & Kwang\_Sheng Chiang, 2001).

It results that the flow depends on the following dimensionless parameters:

$$Da = \frac{K}{H^2}$$

$$\text{Re} = \frac{V_1 H}{\nu}$$

$$\text{Gr} = \frac{g \alpha \Delta C_{ref}^* H^3}{\nu^2}$$

$$\text{Ri} = \frac{\text{Gr}}{\text{Re}^2}$$

$$\text{Pr} = \frac{\nu}{D_T}$$

$$\text{Pe} = \text{RePr}$$

$$\text{Le} = \frac{D_T}{D}$$

Da, b and  $\varepsilon$  depend mostly on the porous matrix structure and are influenced by the properties of the solid and fluid. However,  $R_d$  and  $R_v$  are functions of both the solid and fluid thermo physical properties, and may also be governed by the hydrodynamic and thermal dispersion. The variation in  $R_d$  and  $R_v$  is not still fully understood. Those two parameters has been considered in this study as constant equal to 1 as considered by most of authors.

### 3. Results and discussion

Numerical simulations are investigated for a rectangular cavity with 5 m deep and 200 m large hence the aspect ratio is equal to 40. The porosity, The Darcy number and the thickness (from top to bottom) of each layer are respectively equal to: (0.8,  $0.3210^{-7}$ , 0.6m); (0.7,  $0.2810^{-7}$ , 0.8m); (0.6,  $0.2410^{-7}$ , 1m); (0.5;  $0.210^{-7}$ , 1.2m); and (0.4,  $0.1610^{-7}$ , 1.4m).

The waste was injected vertically at the mid plane through a nozzle of 0.20m diameter and the exit was set along the horizontal boundaries.

Due to the symmetry of the geometry only the mid-domain is considered so the waste injection became located at the top corner and the aspect ratio is reduced to 10. As a waste water, we considered a brine rejected by a small thermal desalination plant producing  $1\text{m}^3/\text{h}$  fresh water at conversion rate of 20% (the maximum reached by thermal technology).

To ensure good accurate a grid of  $1001 \times 51$  nodes was chosen and a convergence criteria was satisfied by the two following relations:

$$\text{MAX} \left| (\Omega, C)_{ij}^{n+1} - (\Omega, C)_{ij}^n \right| < 10^{-3} \quad \text{MAX} \left| \Psi_{ij}^{n+1/2} - \Psi_{ij}^n \right| + \text{MAX} \left| \Psi_{ij}^{n+1} - \Psi_{ij}^{n+1/2} \right| < 10^{-6} \quad ,$$

where n denotes the number of time increments and the residue  $10^{-3}$  was taken for  $\Omega$ ,  $\Psi$ , and C.

In order to achieve real time simulations, the set of equations was solved in transient regime. This required small time steps to ensure numerical stability and good convergence. The flow was simulated for 7 days, indeed calculation required a long time computing.

The transport phenomena was simulated for: Reynolds number  $\text{Re}=50$ , Prandlt number  $\text{Pr}=5$ , Lewis number  $\text{Le}=78.55$ , and Schmidt number  $\text{Sc} = 770$ .

Results of the computations are presented in the form of contours plots of stream function and concentration at different times for an aspect ratio equal to 10.

It was found (Fig.2) that:

- In the beginning, small vortices appear in the entrance and the exit, the most area of the system is of laminar flow with parallel streamlines. The concentration is located in the vicinity of the inlet. The parallel contours indicate that the transfer is due to diffusion.

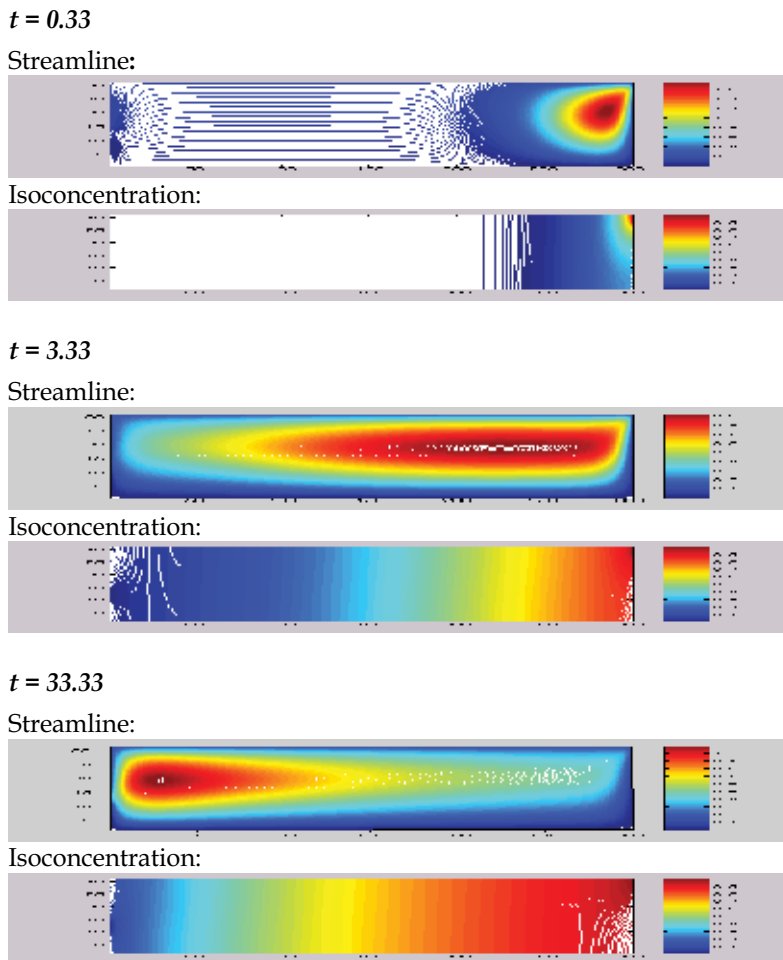
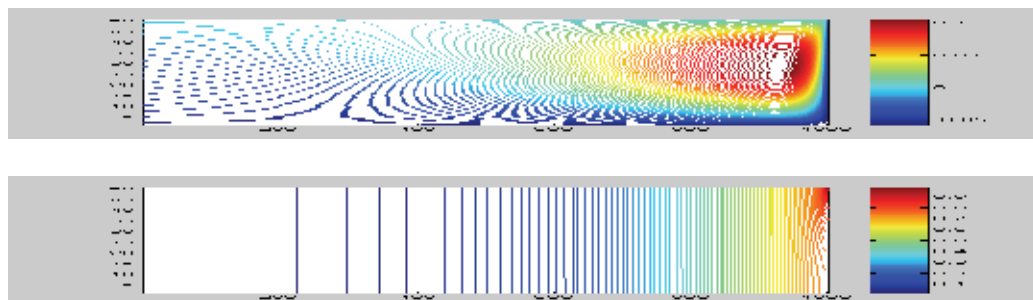


Fig. 2. Streamlines and Iso-concentrations evolution for  $A=10$ ,  $Re=50$ ,  $Ri=8 \cdot 10^4$ ,  $Pr=5$ ,  $Le=78.75$

- After some time, the vortex near the entry extended in the horizontal direction and a recirculation zone took place inducing the acceleration of the diffusion of concentration. At the same time the vortices at the exit grew and form a single vortex moving in the opposite direction of the main flow. This movement announced the development of a convection regime.
- As far as time increases, the recirculation zone extend towards the exit and hence, due to the presence of the backward movement, a chain of vortices took place increasing the dissipation of concentration.
- At  $t=33,33$ , a single cell occupied the whole system with a small outflow rate whereas the concentration continue to spread over the whole surface in a weak manner expressing the diffusion regime of concentration. This is due probably to the value of Richardson number which is much greater than 1 (threshold of appearance of the stratification).

It means that for a high concentration, Reynolds should be important to avoid stratification and to create forced convection in order to dissipate the brine quickly.

In order to reduce the computing time and especially to overcome the interface conditions, a second study was carried out to replace the 5 layers by a single one but at equivalent properties. The results showed a good agreement between the two models. Hence, one may use the equivalent model to save time and memory during computation.



Streamlines and Iso-concentrations for a one equivalent layer after 1 day

#### 4. Conclusion

The flow and concentration transport through saturated porous layers was investigated numerically using a numerical approach which considers the whole components as one domain to overcome the boundary conditions at the interfaces. The Naviers- Stockes equations and Darcy-Brinkman-Forscheimer formulation were used for modelling the transfer in each component going from the fluid to the porous media by changing the thermo physical properties of porous layers. The transient study of the flow allows to understand the evolution of the physical phenomena and thus the mechanism of transport.

In this physical problem we notice that some of the recirculation zones which appear could constitute stagnation region and increase the residence time, so we should increase the Reynolds number. Moreover, for a quick approximation, one can replace a stack of layers by only one equivalent layer having equivalent properties gaining by consequent much computing time.

Further investigations with small Ri values will be achieved.

#### 5. References

- Chritophe, F.; Constantin, O. & Michel, B. (2001). Infiltration d'une solution saline dans un milieu poreux hétérogène en présence d'un gradient hydraulique, *XV<sup>ème</sup> Congrès Français de Mécanique*, Nancy, Spetembre 2001.
- Durrani, S.A. & Ilic, R. (1997). Radon Measurements by Etched Track Detectors: *Applications in Radiation Protection, Earth Sci. Environ.* (World Scientific, Singapore).
- Hwa-Chong, T. & Kwang- Sheng, C. (1999). Non Dary flow and heat transfer in a porous insulation with infiltration and natural convection, *J. of Marine Scien technology*, 7., 2., (125-131).

- Jacobs, L.A.; Von Gunten, H.R.; Keil, R. & Kusly, M. (1988). Geochemical changes along a river-groundwater infiltration flow path: Glattfelden, Switzerland. *Geochimica et Cosmochimica Acta*, 52, 11, (November 1988), (2693-2706)
- Nielson, K.K & Rogers, V.C. (1994). A sensitive effluent method for measuring radon gas emanation from low-emanating materials, *Nucl. Instrum. Methods Phys. Res.*, A353, (519-523).
- Magee, B.R.; Lion, L.W. & Lemley, A.T. (1991). Transport of dissolved organic macromolecules and their effect on the transport of phenanthrene in porous media, *Environ. Sci. technol.*, 25, (324-331).
- Matsunga, T.; Karametaxas, G.; Von Gunten, H.R. & Lichtner, P.C. (1993). Redox chemistry of iron and manganese minerals in river recharged aquifers: a model interpretation of a column experiment, *Geochim. Cosmochim. Acta*, 57, (1691-1704).
- Safi, M.J & Loc, T.P. (1994). Development of thermal stratification in two-dimensional cavity: a numerical study, *In. J. Heat Mass Transfer*, 37, 14, (2017-2024).
- Song-Bae, K. & Yavuz, C.M. (2002). Contaminant transport in riverbank filtration in the presence of dissolved organic matter and bacteria: a kinetic approach, *Journal of hydrology*, 266, (269-283).
- Sontheimer, H. (1980). Experience with riverbank filtration along the Rhine River. *J. AWWA*, 72, 7, (386-390).
- Sasaki, T.; Gunji, Y. & Iida, T. (2008). Theoretical Basis for Measuring Small Radon Diffusion Coefficients for a Radium-Bearing Porous Material Generated by Precipitation of Iron (III) Hydroxide. *Journal of nuclear science and technology*, 45, 7, (647-652).
- Loc, T.P. & Daube, O. (1978). A combined second and fourth order method for the numerical solution of steady and unsteady Navier-Stokes equations, *International Conference on numerical Methods in Laminar and turbulent flow*, Swansea .

# Experimental and Theoretical Modelling of 3D Gravity Currents

Michele La Rocca<sup>1</sup> and Allen Bateman Pinzon<sup>2</sup>

*Sediment Transport Research Group (GITS-UPC)*

<sup>1</sup>*University Roma TRE, Dep. of Civil Engineering Sciences, Rome,*

<sup>2</sup>*Politechnical University of Catalunya, Dep. of Hydraulic, Maritime and Environmental Eng., Barcelona,*

<sup>1</sup>*Italy*

<sup>2</sup>*Spain*

## 1. Introduction

When two liquid bodies with different density come in contact in non-equilibrium conditions, a flow is caused, known as gravity or density current. In the environment, as well as in the industrial framework, this kind of flow is very common and the scientific-technical interest of the investigation on it is very high. The paper of Huppert (2006) and the book of Ungarish (2009b) give excellent reviews on the state of the art of the topic, while a huge collection of artificial, as well as natural, gravity currents and a qualitative description of their key features is given in the book of Simpson (1997).

The investigation on gravity currents dates back to several decades ago (first important works are those of Von Karman, 1940; Yih, 1947; Prandtl, 1952 and Keulegan, 1957), nevertheless many aspects still need a better understanding. These aspects should be investigated in order to widen the knowledge on the considered phenomenon and are generally related to the geometry of the fluid domain and the use of particular fluids, like e.g. mixtures of liquid and sediments.

Early studies on gravity currents were based on analytical and experimental methods and were concerned with 2D gravity currents: i.e. gravity currents whose description can be made in a vertical  $x$ - $z$  plane. The seminal work of Benjamin (1968) formulates a fundamental theory, based on the perfect-fluid hypothesis and simple extensions of it (like the classical theory of hydraulic jumps), which gives a relationship between the thickness of the gravity current and the velocity of the front. The Benjamin's theory is a milestone and analytical investigations on gravity currents, even the most recent (Shin et al., 2004; Lowe et al., 2005; Ungarish & Zemach, 2005; Ungarish, 2008; Ungarish, 2009) cannot disregard it.

Laboratory gravity currents can be realized in very different ways (Simpson, 1997), depending on which features have to be investigated. The basic experimental setup, which permits to investigate the propagation's features of the gravity current, is the lock exchange release experiment. This experiment consists in leaving two liquid bodies of different density in non-equilibrium condition, typically removing a sliding gate which originally separated them. The consequence is a flow of heavier liquid (the gravity current) under the

lighter liquid. The advancing velocity of the gravity current's front, its thickness and the relation between them are the major issues. The work of Huppert & Simpson (1980) is one of the first works which gives an empirical relation between the velocity and the thickness of the gravity current's front. The validity of the empirical relation of Huppert and Simpson is confirmed by the fact that many experimental results, also of earlier experimental works (Simpson & Britter, 1979), agree well with it. Other experimental studies, as the work of Rottmann & Simpson (1983), highlight also the different phases of the gravity current's evolution (slumping phase, self-similar phase, viscous phase). More complex geometries and fluids are accounted for in recent experimental studies: it is the case of axisymmetric gravity currents (i.e. gravity currents whose description can be made in a radial-vertical  $r$ - $z$  plane), in fixed and rotating frames, (Hallworth et al., 2001; Hallworth et al., 2003; Patterson et al., 2006; and Ungarish, 2007a) and the case of gravity currents realized with mixtures of water and sediments or with solutions of particular substances and water, which realize a high density difference (Bonnecaze et al., 1993; Lowe et al., 2005). In comparison with 2D and axisymmetric gravity currents, the case of fully 3D gravity currents, whose spatial description needs all of the three spatial coordinates, has been investigated more rarely in the scientific literature. The works of Ross (2002) and La Rocca et al. (2008) are interesting examples

With the increasing development of computational resources, numerical investigations on gravity currents have developed to a considerable extent. There are two main approaches on which numerical investigations are based. The first is represented by the vertically averaged equations of motion (shallow water equations). This approach is justified by the fact that the longitudinal extension of the gravity current has (except for the very initial phase of motion) an order of magnitude  $L$  larger than its thickness  $h$ . The shallow water approach gives a "technical" description of the gravity current, based on the thickness and the vertically averaged horizontal velocity of this latter, while the fine details of motion are ignored. The first interesting work is that of Rottman & Simpson (1983), focused on 2D gravity currents. Since then, this approach has been giving interesting results, as the works of Bonnecaze et al. (1993), Klemp et al. (1994), D'aleccio et al. (1996), Ungarish & Zemach (2005) and Ungarish (2007a) show. The approach based on the vertically averaged equations has been successfully applied to gravity current realized in axisymmetric domains (Hallworth et al., 2003; Ungarish, 2007b; Ungarish, 2010) and to fully 3D gravity currents (La Rocca et al., 2008). Despite of its limitations, the shallow water approach gives reliable insights and fairly accurate predictions (sometimes even better than those obtained by full Navier-Stokes simulations) except for a very short initial phase (Ungarish, 2007b). Additionally, the shallow water solutions reveal features that appear relevant to the more complex two-dimensional simulations (Klemp et al., 1994).

The second numerical approach is based on the complete equations of motion and gives a detailed description of the gravity current motion. It is a recent approach, due to the large computational resources needed, but it has already achieved a considerable development. Some interesting works are those of Härtel et al. (2000a) and Härtel et al. (2000b), who computed a high-resolution direct numerical simulation (DNS) of the flow at the gravity current's head; Birman et al. (2005), who made a DNS of 2D non-Boussinesque gravity currents (i.e., occurring in fluids with large density differences). Hallworth et al. (2001) solved the Navier Stokes equations in a rotating axisymmetric domain. Patterson et al. (2006) characterized the flow structure of the head of an axisymmetric gravity current

evolving in a circular sector of about  $10^\circ$ , and was able to distinguish different stages of the gravity current evolution.

This brief analysis of the recent literature highlights that the attention dedicated to the investigation on fully 3D gravity currents, with constant or variable density, has not had the same extent than that dedicated on 2D and axisymmetric gravity currents.

This chapter is then aimed to give a contribution for the widening of the knowledge on gravity currents, presenting some recent numerical and experimental results obtained on fully 3D gravity currents, with constant and variable density. The structure of the chapter is as follows. After a brief qualitative description of the phenomenon, different mathematical models, corresponding to the case of constant and variable density, are formulated. Then, the main numerical method is explained and the experimental setup is described. At last, after the validation of the mathematical models and the numerical method, experimental and numerical results, obtained for 3D gravity currents with constant and variable density, are presented.

**2. Description of the phenomenon**

Gravity currents are characterised by a very complex dynamics and a variety of phenomena (Simpson, 1997), represented schematically in Fig. 1.

The gravity current shown in Fig. 1 is generated on an erodible bed after that the two liquid bodies with different densities  $\rho_1, \rho_2$  ( $\rho_1 > \rho_2$ ) are put in contact in non equilibrium condition. After some time, the gravity current assumes the characteristic tapered form shown in Fig. 1: the front advances with velocity  $u_f$  and has a conventional thickness  $h_f$ . The drawing shown in Fig. 1 is not arbitrary and can be compared with the experimental gravity current shown in Fig. 4, realised by means of a lock exchange release experiment at the hydraulic lab of the DEHMA of the Politechnical University of Catalunya, in a transparent channel (length  $L=2$  m, width  $b=0.2$  m, height  $H=0.35$  m), with salty ( $\rho_1=1100$   $\text{kgm}^{-3}$ ) and fresh water ( $\rho_2=1000$   $\text{kgm}^{-3}$ ), on a fixed bed. The initial height of the lock was  $h_1=0.28$  m.

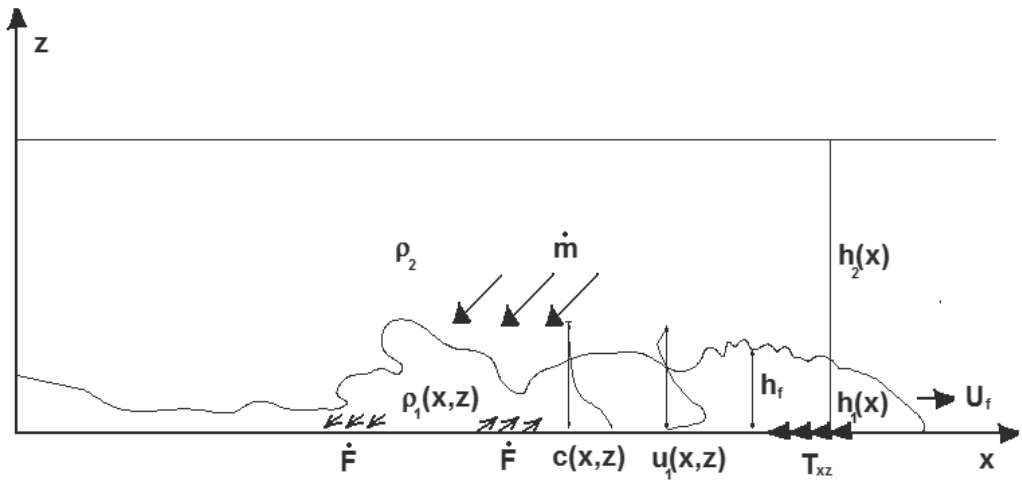


Fig. 1. Sketch of the gravity current

The gravity current represented in Fig.1 flows under a layer of lighter liquid (density  $\rho_2$ ), whose thickness  $h_2$  is larger than that of the gravity current  $h_1$ : quite a common situation. The surface between the gravity current and the liquid layer, represented by a continuous line in Fig. 1, is, in fact, a conventional surface. Increasing  $z$ , there is actually a gradual change, although rather abrupt for  $z \sim h_1$ , of all the quantities characterizing the gravity current.

The gravity current can exchange mass with the lighter liquid by entraining a mass per unit time  $\dot{m}$  of lighter liquid. This entrainment of liquid dilutes the density  $\rho_1$ , while causing an increase of the gravity current's volume. An exchange of mass, represented by the term  $\dot{F}$ , can occur also with the bottom, if the gravity current consists of a mixture of liquid and sediment with concentration  $c$ . This exchange of mass causes a variation of the density  $\rho_1$ , by means of a variation of the concentration of sediment  $c$ , and consists in the settling down and re-suspension of sediment. The settling down is caused by the sediment's weight, while the re-suspension is caused by the drag stress exerted by the current on the bottom. This latter, on the other hand, acts on the gravity current by means of a friction stress  $T_{xz}$ , which depends on the roughness of the bottom.

All of the quantities which characterize the gravity current depend on the spatial coordinates and time. In particular, in Fig. 1 are shown the profiles of the concentration and the gravity current's velocity  $c$  and  $u_1$ . Fig. 1 can give an idea of the complexity of the phenomena involved in the gravity current dynamics.

Fig.1 and Fig.4 refer to a 2D gravity current. In Figures 2, 3, the more complex structure of the dynamics of a 3D gravity current can be appreciated. In Figg. 2, 3 are shown the top and side view of the 3D gravity current respectively.

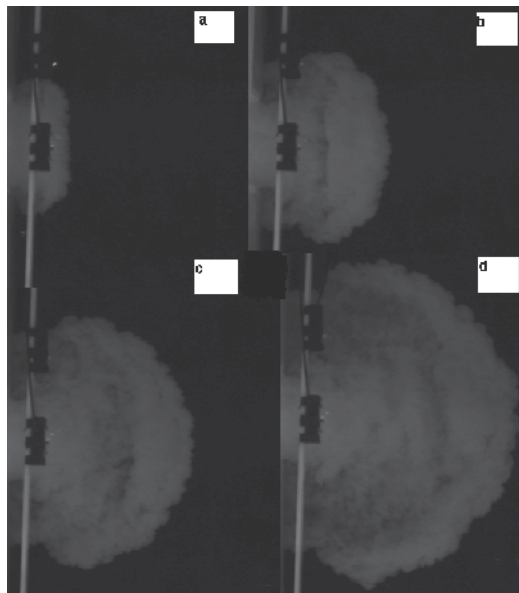


Fig. 2. Top view of a 3D gravity current. a) 2 s; b) 4 s; c) 6 s; d) 8 s after the complete removal of the lock

The gravity currents shown in Figures 2 and 3 were realized by means of a lock exchange experiment performed at the hydraulic lab of the Dep. of Civil Eng. Sciences of the

University Roma TRE. A transparent rectangular tank, made of two equal square tanks (side  $L=1$  m), was used. A wall, with an opening with width  $b=0.2$  m and closed by a sliding lock, divided the two square tanks. The case shown in Fig. 2 was realized with salty ( $\rho_1=1015$   $\text{kgm}^{-3}$ ) and fresh water ( $\rho_2=1000$   $\text{kgm}^{-3}$ ). The initial height of the lock was  $h_1=0.15$  m.

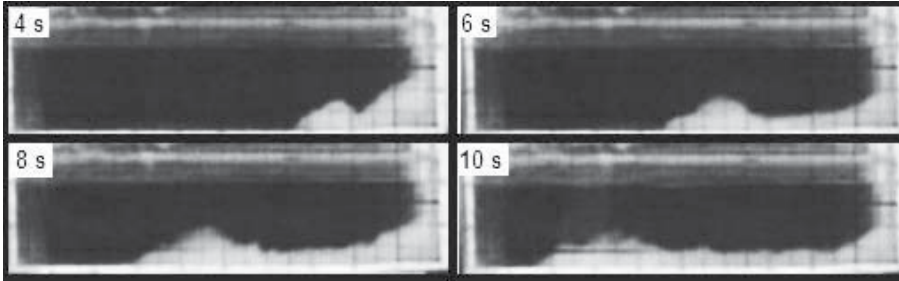


Fig. 3. Side view of a 3D gravity current, 4s, 6s, 8s, 10s after the complete removal of the lock. The case shown in Fig. 3 was realized with salty ( $\rho_1=1018$   $\text{kgm}^{-3}$ ) and fresh water ( $\rho_2=1000$   $\text{kgm}^{-3}$ ). The initial height of the lock was  $h_1=0.20$  m.

### 3. Mathematical models

#### 3.1 Derivation of the shallow water equations for two superimposed liquid layers

Consider two layers of liquids (Fig. 1), whose densities and thicknesses are respectively  $\rho_1, \rho_2$  ( $\rho_1 > \rho_2$ ),  $h_1, h_2$ . As shown in Fig. 1, the lighter layer is superimposed on the heavier layer and hereinafter reference will be made to the upper or lighter layer and to the lower or heavier layer indifferently.

The densities of the layers will be able to vary slightly, due to the possible mixing between the layers, which occurs across the separation surface between them, and to the sedimentation and re-suspension phenomena. Standard scaling arguments (Pedloski, 1987) and formal perturbative expansions (Stoker, 1957) show that, if the ratio  $\delta=h/L$  (being  $h, L$  a vertical and a horizontal spatial scale respectively) is such that:  $\delta < 1$ , the vertical component of the momentum balance equation of the  $i^{\text{th}}$  layer ( $i=1,2$ ) is reduced to:

$$\frac{\partial p_i}{\partial z} = -\rho_i g \tag{1}$$

from which, assuming that the density  $\rho_i$  does not depend on the vertical coordinate  $z$ , the following hydrostatic pressure distributions can be obtained in each layer:

$$p_2 = P_s + \rho_2 g(h_1 + h_2 + z_f - z), \quad p_1 = P_s + \rho_2 g h_2 + \rho_1 g(h_1 + z_f - z) \tag{2}$$

The pressure  $P_s$  is a reference pressure, defined on the upper surface. If this latter is a free-surface,  $P_s$  vanishes. The pressure distributions (2) are a reliable approximation of the actual pressure distribution, at least to order  $O(\delta)$  (D'Alessio et al., 1996).

Consider the mass balance equation in each layer and integrate it with respect to the vertical coordinate  $z$ . Making use of the Leibniz rule and of suitable conditions on the separation surface and on the bottom (D'Alessio, 1996), the following result is obtained:

$$\begin{cases} \frac{\partial \rho_1 h_1}{\partial t} + \frac{\partial(\rho_1 U_1 h_1)}{\partial x} + \frac{\partial(\rho_1 V_1 h_1)}{\partial y} = \dot{m} \\ \frac{\partial \rho_2 h_2}{\partial t} + \frac{\partial(\rho_2 U_2 h_2)}{\partial x} + \frac{\partial(\rho_2 V_2 h_2)}{\partial y} = -\dot{m} \end{cases} \quad (3)$$

All of the quantities appearing in equations (3) are vertically averaged quantities, defined as:

$$\begin{cases} \int_{z_f}^{h_1+z_f} \rho_1 dz = \rho_1 h_1, & \int_{z_f}^{h_1+z_f} \rho_1 u_1 dz = \rho_1 U_1 h_1, & \int_{z_f}^{h_1+z_f} \rho_1 v_1 dz = \rho_1 V_1 h_1 \\ \int_{h_1+z_f}^{h_1+h_2+z_f} \rho_2 dz = \rho_2 h_2, & \int_{h_1+z_f}^{h_1+h_2+z_f} \rho_2 u_2 dz = \rho_2 U_2 h_2, & \int_{h_1+z_f}^{h_1+h_2+z_f} \rho_2 v_2 dz = \rho_2 V_2 h_2 \end{cases} \quad (4)$$

where  $z_f$  is the bottom elevation. In this framework  $z_f$  is assumed as a known function of the spatial coordinates and does not depend on time. The bottom profile is given by:  $z_f=0$ , if the bottom is flat.

The mass flux between the two liquid layers is accounted for by means of the source term  $\dot{m}$  at RHS of equations (3). It is worth observing that the source term appears with positive sign in the mass equation of the first layer and with negative sign in the mass equation of the second layer, then showing consistently that the mass lost by a layer is gained by the other layer and preserving the mass conservation for the fluid system as a whole.

Consider the horizontal components of the momentum equation in each layer and integrate them with respect to the vertical coordinate  $z$ , accounting for the hydrostatic pressure distribution (2). Making use of the Leibniz rule and of the abovementioned conditions on the separation surface and on the bottom, the following result is obtained:

$$\begin{cases} \frac{\partial \rho_1 U_1 h_1}{\partial t} + \frac{\partial}{\partial x} \left( \left( \rho_1 U_1^2 + P_s + \rho_2 g h_2 + \rho_1 g \frac{h_1}{2} \right) h_1 \right) + \frac{\partial \rho_1 U_1 V_1 h_1}{\partial y} = \dot{m} u_{s1} + S_{xss} - S_{xb} - \frac{\partial \tau_{xx}^1}{\partial x} - \frac{\partial \tau_{xy}^1}{\partial y} - \tau_{xss} + \tau_{xb} \\ \frac{\partial \rho_1 V_1 h_1}{\partial t} + \frac{\partial \rho_1 U_1 V_1 h_1}{\partial x} + \frac{\partial}{\partial y} \left( \left( \rho_1 V_1^2 + P_s + \rho_2 g h_2 + \rho_1 g \frac{h_1}{2} \right) h_1 \right) = \dot{m} v_{s1} + S_{yss} - S_{yb} - \frac{\partial \tau_{yx}^1}{\partial x} - \frac{\partial \tau_{yy}^1}{\partial y} - \tau_{yss} + \tau_{yb} \\ \frac{\partial \rho_2 U_2 h_2}{\partial t} + \frac{\partial}{\partial x} \left( \left( \rho_2 U_2^2 + P_s + \rho_2 g \frac{h_2}{2} \right) h_2 \right) + \frac{\partial \rho_2 U_2 V_2 h_2}{\partial y} = -\dot{m} u_{s2} + S_{xus} - S_{xss} - \frac{\partial \tau_{xx}^2}{\partial x} - \frac{\partial \tau_{xy}^2}{\partial y} - \tau_{xus} + \tau_{xss} \\ \frac{\partial \rho_2 V_2 h_2}{\partial t} + \frac{\partial \rho_2 U_2 V_2 h_2}{\partial x} + \frac{\partial}{\partial y} \left( \left( \rho_2 V_2^2 + P_s + \rho_2 g \frac{h_2}{2} \right) h_2 \right) = -\dot{m} v_{s2} + S_{yus} - S_{yss} - \frac{\partial \tau_{yx}^2}{\partial x} - \frac{\partial \tau_{yy}^2}{\partial y} - \tau_{yus} + \tau_{ys} \end{cases} \quad (5)$$

The momentum fluxes exchanged by the liquid layers due to the mass flux  $\dot{m}$  are accounted for by means of the horizontal components of the liquid velocity on the separation surface:  $u_{s1}, v_{s1}, u_{s2}, v_{s2}$ . The quantities  $S_{xss}, S_{xb}, S_{xus}$  and  $S_{yss}, S_{yb}, S_{yus}$  are the horizontal components of the pressure forces on the separation surface (ss), the bottom (b) and the upper surface (us). They are defined as:

$$\begin{cases} S_{xss} = (P_s + \rho_2 g h_2) \frac{\partial}{\partial x} (h_1 + z_f), S_{xb} = (P_s + \rho_2 g h_2 + \rho_1 g h_1) \frac{\partial z_f}{\partial x}, S_{xus} = P_s \frac{\partial}{\partial x} (h_1 + h_2 + z_f) \\ S_{yss} = (P_s + \rho_2 g h_2) \frac{\partial}{\partial y} (h_1 + z_f), S_{yb} = (P_s + \rho_2 g h_2 + \rho_1 g h_1) \frac{\partial z_f}{\partial y}, S_{yus} = P_s \frac{\partial}{\partial y} (h_1 + h_2 + z_f) \end{cases} \quad (6)$$

The quantities  $\tau_{ij}^k, k=1,2; i=x,y; j=x,y$  represent the vertically average viscous and turbulent stresses and the dispersive stresses. The quantities  $\tau_{xss}, \tau_{xb}, \tau_{xus}$  and  $\tau_{yss}, \tau_{yb}, \tau_{yus}$  are the horizontal components of the stress  $\tau$  on the separation surface ( $\tau_{xss}, \tau_{yss}$ ), the bottom ( $\tau_{xb}, \tau_{yb}$ ) and the upper surface ( $\tau_{xus}, \tau_{yus}$ ). Equations (3) and (5) are put in the most general form, from which it is possible to derive all of the shallow water approximations concerning the motion of two liquid layers with slightly varying densities.

### 3.2 The case of two immiscible liquids with constant density

The case of two immiscible liquids with constant densities is representative for gravity currents realized with water and a soluble matter (e.g. NaCl), when the Richardson number

$$Ri = \frac{\rho_1 - \rho_2}{\rho_2} \frac{gh}{U^2} \quad (7)$$

has an order of magnitude larger than 1 (Fischer et al., 1979). Indeed, the Richardson number, calculated with the velocity and thickness scales  $U, h$ , is the ratio of the order of magnitude of hydrostatic forces to the order of magnitude of inertial forces: if the former dominate, i.e. if  $Ri > 1$ , mixing between the two liquid layers is hindered by the stratification and can be neglected. The gravity currents realized with water and a soluble matter are known as conservative gravity currents, because the matter dissolved in water is conserved, and are distinguished from those realized with mixtures of water and sediments, whose density can change due to sedimentation and re-suspension processes. Variations of density in conservative gravity currents are possible only due to the entrainment of lighter liquid, which occurs at the separation surface, as shown in Fig. 4, where the red ellipses indicate the part of the gravity current affected by the entrainment of lighter liquid.

As a consequence of the immiscibility hypothesis, the mass flux  $\dot{m}$  is zero. Moreover, it is a usual assumption to neglect the stresses  $\tau_{ij}^k, k=1,2; i=x,y; j=x,y$  (Ungarish, 2009). This assumption is based on the estimate of the Reynolds number of the current and on the difficulty in modeling dispersive stresses. The Reynolds number of the current is defined by:

$$Re = \frac{h}{\nu} \sqrt{\frac{\rho_1 - \rho_2}{\rho_1} gh} \quad (8)$$

and is usually very high, due to the small value of the kinematic viscosity and the moderate values of the gravity current's height. As an example, the value of the Reynolds number of the gravity current shown in Fig. 4, assuming  $h=0.1$  m,  $\nu=10^{-6}$  m<sup>2</sup>s<sup>-1</sup>, is equal to:  $Re = 3 \times 10^4$ , showing that the gravity current is in turbulent motion. Only the stresses  $\tau_{xb}, \tau_{yb}$  will be retained. Indeed, they are exerted on the lower layer by the bottom and are surely more important than the stresses acting on the separation surface  $\tau_{xss}, \tau_{yss}$  and the stresses acting on the upper surface  $\tau_{xus}, \tau_{yus}$ . These latter vanish if the upper surface is a free surface.

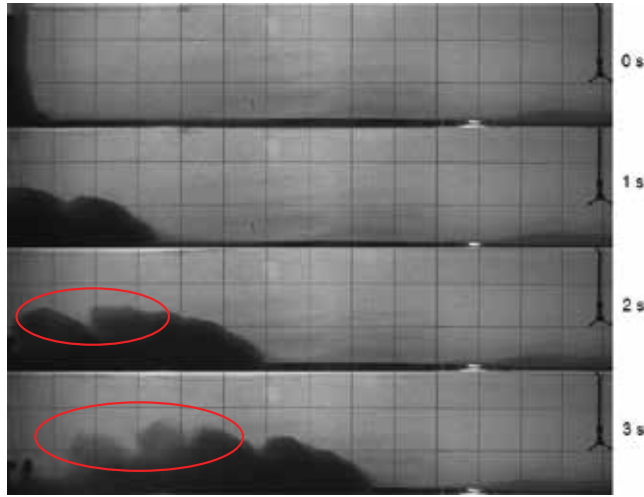


Fig. 4. Experimental profile of a 2D gravity current

$$\left\{ \begin{array}{l}
 \frac{\partial h_1}{\partial t} + \frac{\partial(U_1 h_1)}{\partial x} + \frac{\partial(V_1 h_1)}{\partial y} = 0 \\
 \frac{\partial h_2}{\partial t} + \frac{\partial(U_2 h_2)}{\partial x} + \frac{\partial(V_2 h_2)}{\partial y} = 0 \\
 \frac{\partial U_1 h_1}{\partial t} + \frac{\partial}{\partial x} \left( U_1^2 h_1 + g \frac{h_1^2}{2} \right) + \frac{\partial U_1 V_1 h_1}{\partial y} + \frac{\rho_2}{\rho_1} g h_1 \frac{\partial h_2}{\partial x} = -\frac{h_1}{\rho_1} \frac{\partial P_s}{\partial x} - g h_1 \frac{\partial z_f}{\partial x} + \frac{\tau_{xb}}{\rho_1} \\
 \frac{\partial V_1 h_1}{\partial t} + \frac{\partial U_1 V_1 h_1}{\partial x} + \frac{\partial}{\partial y} \left( V_1^2 h_1 + g \frac{h_1^2}{2} \right) + \frac{\rho_2}{\rho_1} g h_1 \frac{\partial h_2}{\partial y} = -\frac{h_1}{\rho_1} \frac{\partial P_s}{\partial y} - g h_1 \frac{\partial z_f}{\partial y} + \frac{\tau_{yb}}{\rho_1} \\
 \frac{\partial U_2 h_2}{\partial t} + \frac{\partial}{\partial x} \left( U_2^2 h_2 + g \frac{h_2^2}{2} \right) + \frac{\partial U_2 V_2 h_2}{\partial y} + g h_2 \frac{\partial h_1}{\partial x} = -\frac{h_2}{\rho_2} \frac{\partial P_s}{\partial x} - g h_2 \frac{\partial z_f}{\partial x} \\
 \frac{\partial V_2 h_2}{\partial t} + \frac{\partial U_2 V_2 h_2}{\partial x} + \frac{\partial}{\partial y} \left( V_2^2 h_2 + g \frac{h_2^2}{2} \right) + g h_2 \frac{\partial h_1}{\partial y} = -\frac{h_2}{\rho_2} \frac{\partial P_s}{\partial y} - g h_2 \frac{\partial z_f}{\partial y}
 \end{array} \right. \quad (9)$$

At last, also the velocities  $u_{s1}, v_{s1}, u_{s2}, v_{s2}$  are neglected. With these hypothesis equations (3) and (5) reduce to the equations (9). These equations, together with proper initial and boundary conditions, represent a very difficult problem for numerical integration. Even when the upper surface is a free surface and then the pressure  $P_s$  vanishes on it, the equations (9) form a partial differential system of six equations in non conservative form, fact which makes difficult the application of numerical methods with good shock-capturing and shock-fitting features (La Rocca et al., 2008). Moreover, performing the analysis of the eigenvalues of the partial differential system (9), it is found that wide ranges of the relevant physical parameters exist where these eigenvalues are complex, then revealing the non-hyperbolicity nature of the partial differential system (9). The loss of hyperbolicity causes instability during numerical integration (Garabedian, 1964; Bradford et al., 1997; Lyczkowski et al., 1978; Lee & Lyczkowski, 2000).

In order to overcome the abovementioned difficulties, assume the rigid-lid hypothesis, according to which the sum of the liquid layers thicknesses is constant with respect time and space:

$$h_1 + h_2 + z_f = H \quad (10)$$

being  $H$  the initial elevation of the upper surface. The consequences of the rigid-lid hypothesis are very interesting. Firstly, the mass balance equation for the upper layer is substituted by the algebraic relation (10) and the partial differential system (9) becomes:

$$\left\{ \begin{array}{l} \frac{\partial h_1}{\partial t} + \frac{\partial(U_1 h_1)}{\partial x} + \frac{\partial(V_1 h_1)}{\partial y} = 0 \\ \frac{\partial U_1 h_1}{\partial t} + \frac{\partial}{\partial x} \left( U_1^2 h_1 + g \left( 1 - \frac{\rho_2}{\rho_1} \right) \frac{h_1^2}{2} \right) + \frac{\partial U_1 V_1 h_1}{\partial y} = - \frac{h_1}{\rho_1} \frac{\partial P_s}{\partial x} - g \left( 1 - \frac{\rho_2}{\rho_1} \right) h_1 \frac{\partial z_f}{\partial x} + \frac{\tau_{xb}}{\rho_1} \\ \frac{\partial V_1 h_1}{\partial t} + \frac{\partial U_1 V_1 h_1}{\partial x} + \frac{\partial}{\partial y} \left( V_1^2 h_1 + g \left( 1 - \frac{\rho_2}{\rho_1} \right) \frac{h_1^2}{2} \right) = - \frac{h_1}{\rho_1} \frac{\partial P_s}{\partial y} - g \left( 1 - \frac{\rho_2}{\rho_1} \right) h_1 \frac{\partial z_f}{\partial y} + \frac{\tau_{yb}}{\rho_1} \\ \frac{\partial U_2 h_2}{\partial t} + \frac{\partial}{\partial x} (U_2^2 h_2) + \frac{\partial U_2 V_2 h_2}{\partial y} = - \frac{h_2}{\rho_2} \frac{\partial P_s}{\partial x} \\ \frac{\partial V_2 h_2}{\partial t} + \frac{\partial U_2 V_2 h_2}{\partial x} + \frac{\partial}{\partial y} (V_2^2 h_2) = - \frac{h_2}{\rho_2} \frac{\partial P_s}{\partial y} \end{array} \right. \quad (11)$$

Secondly, the pressure  $P_s$  does not vanish, as the upper surface is no more a free surface, being forced to remain flat. The pressure  $P_s$  represents the actual coupling term between the two liquid layers. Indeed, fourth and fifth equations (11) do not contain any forcing term, but the pressure terms. If these happen to vanish, the two liquid layers are uncoupled and the evolution of the lower layer cannot influence that of the upper layer.

Thirdly, the presence of the pressure  $P_s$  represents a non trivial problem in solving the equations (11). Indeed, while in the 2D and axisymmetric cases the pressure  $P_s$  can be easily eliminated from the motion equations (Rottmann & Simpson, 1983; Ungarish & Zemach, 2005), for the general case presented here this is not possible. The pressure  $P_s$  must be determined solving the motion equations together with a specific equation, which can be obtained starting from the following observation: the vector field  $\mathcal{V}$  ( $\mathcal{V} \equiv \{U_1 h_1 + U_2 h_2, V_1 h_1 + V_2 h_2\}$ ) is divergence free. Indeed, add the mass balance equations of the two liquid layers and account for (10):

$$\frac{\partial(h_1 + h_2)}{\partial t} + \frac{\partial(U_1 h_1 + U_2 h_2)}{\partial x} + \frac{\partial(V_1 h_1 + V_2 h_2)}{\partial y} = 0 \Rightarrow \frac{\partial(U_1 h_1 + U_2 h_2)}{\partial x} + \frac{\partial(V_1 h_1 + V_2 h_2)}{\partial y} = 0 \quad (12)$$

Then sum second and fourth equation (11) and third and fifth equation (11), differentiate these sums with respect to  $x$  and  $y$ , sum them again and account for the divergence free condition (12): as a consequence the following Poisson equation is obtained for the pressure  $P_s$ :

$$\begin{aligned} \frac{\partial}{\partial x} \left( \left( \frac{h_1}{\rho_1} + \frac{h_2}{\rho_2} \right) \frac{\partial P_s}{\partial x} \right) + \frac{\partial}{\partial y} \left( \left( \frac{h_1}{\rho_1} + \frac{h_2}{\rho_2} \right) \frac{\partial P_s}{\partial y} \right) - \frac{\partial^2}{\partial x^2} \left( U_1^2 h_1 + U_2^2 h_2 + g' \frac{h_1^2}{2} \right) - 2 \frac{\partial^2}{\partial y \partial x} (U_1 V_1 h_1 + U_2 V_2 h_2) \\ - \frac{\partial^2}{\partial y^2} \left( V_1^2 h_1 + V_2^2 h_2 + g' \frac{h_1^2}{2} \right) - \frac{\partial}{\partial x} \left( g' h_1 \frac{\partial z_f}{\partial x} - \frac{\tau_{xb}}{\rho_1} \right) - \frac{\partial}{\partial y} \left( g' h_1 \frac{\partial z_f}{\partial y} + \frac{\tau_{yb}}{\rho_1} \right) \end{aligned} \quad (13)$$

being the reduced gravity  $g'$  defined as:  $g' = g(1 - \rho_2/\rho_1)$ .

So, in the framework of the shallow water formulation, the dynamics of two layers of immiscible liquids, with a rigid lid, is governed by the equations (11), (13), given suitable initial and boundary conditions. Initial conditions refer generally to motions starting from a quiescent configuration with a given shape of the lower layer thickness:

$$U_1(x, y, 0) = 0, V_1(x, y, 0) = 0, U_2(x, y, 0) = 0, V_2(x, y, 0) = 0, h_1(x, y, 0) = f(x, y) \quad (14)$$

Boundary conditions are imposed in correspondence of rigid, impermeable surfaces. The normal velocity component and the normal derivative of the pressure vanish on these surfaces:

$$U_1 n_x + V_1 n_y = 0, U_2 n_x + V_2 n_y = 0, \frac{\partial P_s}{\partial x} n_x + \frac{\partial P_s}{\partial y} n_y = 0 \quad (15)$$

The first two boundary conditions (15) are physically consistent, while the third satisfies the solvability condition obtained integrating the Poisson equation (13) on the fluid domain.

The equations (11), (13), with the initial and boundary conditions (14), (15), set up the rigid-lid, two-layer formulation for 3D gravity currents with constant density.

### 3.3 The case of two liquid layers with variable density

In this case the density of the heavier layer can change mainly as a consequence of a sedimentation-resuspension dynamics. This case is representative for subaqueous turbidity currents, occurring e.g. when a heavy current of water and sediments flows under a lake or a sea. In this framework, variations of density due to temperature are considered of minor importance, although they can be accounted for by means of a suitable thermal energy balance (Pratson et al., 2001), which however will not be considered for the sake of simplicity. These turbidity currents form at the bottom of great water basins and represent an important mechanism of transport of sediments in deep water (Parker et al., 1986). Turbidity currents can attain high velocities (8-14 m/s) (Huang et al. 2005), they can be characterized by time scales varying from hours to weeks and flow inside of submarine canyons, which can attain depths of hundreds of meters, widths of thousands of meters and lengths of thousands of kilometers (Birman et al., 2009). These currents can damage the submarine structures (pipes, cables) they interact with and can change the morphology of the bottom, due to erosion and sedimentation (Kostic & Parker, 2007; Cantero et al., 2008). Moreover, turbidity currents can affect the quality of water, depending on the sediments they are made of. This is an environmental problem of increasing importance and it is worth examining briefly the case study of the artificial reservoir of Flix, situated near Tarragona, Spain (Costa et al. 2004). This artificial water reservoir, built on the river Ebro in 1948 for irrigation, water storage and production of energy, caused the accumulation of contaminated sediments, resulting from the chemical processes of a factory situated 700 meters upstream of the reservoir in the right margin of the Ebro. The contaminated

sediments, accumulated during over fifty years of industrial activity, contained very dangerous substances as DDT, Hexachlorineethylene, PCB, bicalcic phosphate, Mercury, Cyanide. On December 22<sup>nd</sup> 2001, after several days of very low temperatures, thousands of dead fish appeared in the river Ebro, close to the Flix reservoir, and the water analysis, carried out at the entrance of supply water plants of important cities as Tarragona, revealed levels of concentration of Mercury much higher than the normal. The most probable explanation of this fact was that the particular meteorological conditions could have caused a current of cold and dense water with enough strength to entrain the sediment from the bed and, therefore, to mix mercury with water. The resulting concentration of Mercury caused the murrain of fishes and made unusable the water for several months.

The mathematical modeling of this kind of gravity current, known as turbidity current, is very complicate. Here the approach of Pratson et al. (2001) will be followed and extended to the general 3D case. It is assumed that (Pratson et al., 2001; Kostic and Parker, 2007) the heavier liquid is a mixture made with a uniform sediment, characterized by a median diameter  $d_s$ , with depth averaged concentration  $C$ , flowing under an infinite layer of water. This latter assumption is very important, because it is possible to show that, as a consequence of it (Ungarish & Zemach, 2005; La Rocca & Bateman, 2010), the pressure  $P_s$  vanishes and the motion of the upper layer becomes negligible. Then the well known one layer formulation is obtained for the turbidity current and a considerable reduction of the equations number follows, because only the mass and momentum balance equations of the turbidity current have to be considered. Having introduced the depth averaged concentration  $C$ , the density of the heavy liquid layer is given by:

$$\rho_1 = \rho_2(1-C) + \rho_s C = \rho_2 + (\rho_s - \rho_2)C \tag{16}$$

being  $\rho_s$  the density of the sediments. In dealing with such gravity currents, it is usual to assume that the ratio:

$$\frac{\rho_1 - \rho_2}{\rho_2} = \frac{\rho_s - \rho_2}{\rho_2} C = RC \tag{17}$$

is small.  $R$  is defined as:  $R = (\rho_s - \rho_2) / \rho_2$ . The consequence is that the Boussinesq's approximation is valid (Kostic & Parker, 2007), according to which the changes in the density  $\rho_1$  are considered important only in the gravitational term. Substituting definition (16) in the partial differential system (5) and accounting for the Boussinesq's approximation, the mass and momentum balance equations assume the following form:

$$\begin{cases} \frac{\partial h_1}{\partial t} + \frac{\partial U_1 h_1}{\partial x} + \frac{\partial V_1 h_1}{\partial y} = \dot{q} \\ \frac{\partial U_1 h_1}{\partial t} + \frac{\partial U_1^2 h_1}{\partial x} + \frac{\partial U_1 V_1 h_1}{\partial y} + Rg \frac{\partial}{\partial x} (C h_1^2 / 2) = \dot{q} u_s + \tau_{xb} - gh_1 \frac{\partial z_f}{\partial x} \\ \frac{\partial V_1 h_1}{\partial t} + \frac{\partial U_1 V_1 h_1}{\partial x} + \frac{\partial V_1^2 h_1}{\partial y} + Rg \frac{\partial}{\partial y} (C h_1^2 / 2) = \dot{q} v_s + \tau_{yb} - gh_1 \frac{\partial z_f}{\partial y} \end{cases} \tag{18}$$

The mass exchange between the two layers is accounted for by means of the quantity  $\dot{q}$ : it represents the volume of water per unit surface and time, entrained by the heavier layer,

and is related to the mass per unit surface and time  $\dot{m}$  exchanged between the two layers by the approximate relations:  $\dot{q} \approx \dot{m}/\rho_1 \approx \dot{m}/\rho_2$ . The approximation is valid if  $RC \ll 1$ .

Due to the presence of the concentration  $C$  as a new variable, another equation is needed. Such an equation is obtained vertically averaging the sediment mass balance equation within the heavier layer. Omitting the details, the following equation is obtained:

$$\frac{\partial Ch_1}{\partial t} + \frac{\partial CU_1 h_1}{\partial x} + \frac{\partial CV_1 h_1}{\partial x} = c_{ss} \dot{q} + \frac{\partial}{\partial x} \left( K_x h_1 \frac{\partial C}{\partial x} \right) + \frac{\partial}{\partial y} \left( K_y h_1 \frac{\partial C}{\partial y} \right) + \dot{F} \quad (19)$$

where  $K_x, K_y$  are the dispersion coefficients along  $x$  and  $y$  directions (Fischer, 1979) and  $c_{ss}$  is the concentration of sediment at the separation surface. The term  $\dot{F}$  represents the flux of mass at the bottom and accounts for the sedimentation and re-suspension phenomena.

Initial and boundary conditions have to be imposed on the gravity current's thickness, on the velocity components and on the average concentration. Initial and boundary conditions on the gravity current's thickness and on the velocity components are identical to conditions (14) and (15). With regard to averaged concentration  $C$ , a given shape of the initial concentration is imposed as initial condition, while a vanishing mass flux is used as boundary condition, in correspondence of impermeable and fixed boundaries:

$$\begin{cases} U_1(x, y, 0) = 0, V_1(x, y, 0) = 0, h_1(x, y, 0) = f(x, y), & U_1 n_x + V_1 n_y = 0 \\ C(x, y, 0) = f_C(x, y), & K_x \frac{\partial C}{\partial x} n_x + K_y \frac{\partial C}{\partial y} n_y - C(U_1 n_x + V_1 n_y) = 0 \end{cases} \quad (20)$$

### 3.4 Closure relations

The proposed mathematical models (eqs. (11), (13) and eqs. (18), (19)) contain the unknown terms:  $\dot{q}, \tau_{xb}, \tau_{yb}, u_s, v_s, c_{ss}, \dot{F}, K_x, K_y$  whose meaning has been previously introduced. However, the simulation of realistic cases needs the definition of these unknown terms as functions of the resolved variables. In other words, it is necessary to introduce proper closure relations.

The volume flux of entrained liquid  $\dot{q}$  per unit surface has the physical dimensions of a velocity. For this reason is expressed as the product of the dimensionless entrainment coefficient  $e_w$  by the entrainment velocity  $U_e$ :

$$\dot{q} = e_w U_e \quad (21)$$

Following Kostic & Parker (2007), the entrainment coefficient  $e_w$  can be estimated by means of:

$$e_w = \frac{0.00153}{0.0204 + Ri} \quad (22)$$

Being  $Ri$  the Richardson number (7). The entrainment velocity can be estimated by the modulus of the velocity of the heavier layer:

$$U_e = \sqrt{U_1^2 + V_1^2} \quad (23)$$

The terms  $\tau_{xb}, \tau_{yb}$  are the tangential stresses exerted on the heavier layer by the bottom. In the case of constant densities they can be expressed by means of a friction coefficient  $\lambda$ :

$$\tau_{xb} = \rho_1 \lambda U_1 \sqrt{U_1^2 + V_1^2}, \quad \tau_{yb} = \rho_1 \lambda V_1 \sqrt{U_1^2 + V_1^2} \quad (24)$$

The friction coefficient can be in turn expressed by means of empirical formulas which make use of the gravity current Reynolds number (8) and the roughness of the bottom (see e.g. Cengel & Cimbala, 2006). In the case of variable density the terms  $\tau_{xb}, \tau_{yb}$  are usually expressed by means of the friction velocity, which in turn is assumed proportional to the vertically averaged turbulent kinetic energy  $K$  (Parker, 1986):

$$\begin{cases} \tau_{xb} = \rho_2 \frac{U_1}{\sqrt{U_1^2 + V_1^2}} u_*^2 & \tau_{yb} = \rho_2 \frac{V_1}{\sqrt{U_1^2 + V_1^2}} u_*^2 \\ u_*^2 = \alpha K \end{cases} \quad (25)$$

The proportionality constant  $\alpha$  is usually given the value 0.1 (Pratson et al., 2001), while the vertically averaged turbulent kinetic energy  $K$  is determined by the empirical equation:

$$\frac{\partial K}{\partial t} + U_1 \frac{\partial K}{\partial x} + V_1 \frac{\partial K}{\partial y} = \frac{u_*^2 \sqrt{U_1^2 + V_1^2}}{h_1} + \frac{(U_1^2 + V_1^2) \dot{h}}{2h_1} - \beta \frac{K^{3/2}}{h_1} - Rg \left[ C \left( W_s + \frac{\dot{q}}{2} \right) + W_s \dot{F} \right] - \dot{q} \frac{K}{h_1} \quad (26)$$

The various terms at RHS of (26) represent respectively: the production of kinetic energy due to turbulence, the production of kinetic energy due to the entrained liquid, the viscous dissipation of energy, the kinetic energy spent to hold the sediment in suspension (proportional to the sediment settling velocity  $W_s$ ), the kinetic energy spent to maintain in turbulent motion the entrained lighter liquid, the kinetic energy lost (if  $\dot{F} < 0$ ) or gained (if  $\dot{F} > 0$ ) due to the sedimentation-re-suspension dynamics, the kinetic energy spent to maintain the entrained lighter liquid in turbulent motion. The empirical coefficient  $\beta$  is calculated as in Launder & Spalding (1972).

The velocity components and the concentration on the separation surface ( $u_s, v_s, c_{ss}$ ) can be neglected. Indeed the velocity within the turbidity current increases from the bottom up to a maximum value and then decreases uniformly, until it attains a negligible value in correspondence of the separation surface, while the concentration on the separation surface decreases uniformly from the bottom, where it attains its maximum value (Fig. 1).

The diffusive flux of mass  $\dot{F}$  occurring in correspondence of the bottom is due to the settling and the re-suspension of sediment. It can be put in the form (Kostic & Parker, 2007):

$$\dot{F} = W_s (E_s - r_0 C) \quad (27)$$

where  $W_s$  is the sediment settling velocity. This latter can be calculated following Dietrich (1982), as a function of the non dimensional sediment diameter  $d^*$  ( $d^* = R \frac{g d_s^3}{\nu^2}$ ).

The non dimensional erosion coefficient  $E_s$  accounts for the entrainment of sediment and, according to Parker & Garcia (1993), is expressed as a function of the non dimensional parameter  $Z$  ( $Z = \frac{u_*}{W_s \nu} \sqrt{Rg d_s^3}$ ). Anyway, the non dimensional erosion coefficient  $E_s$  is often

assumed to be negligible with respect to the concentration of sediment at the bottom (Kostic & Parker, 2007), which is usually assumed proportional to the vertically averaged concentration  $C$ , by means of the dimensionless coefficient  $r_0$  ( $r_0 \geq 1$ ).

At last, the dispersion coefficients  $K_x, K_y$  can be defined in terms of the friction velocity and the gravity current's thickness, by means of empirical formulas, as e. g. those of Fischer et al. (1979). Such formulas are usually referred to the case of the dispersion of contaminant in a fluvial stream and, when used in a different context, the numerical values of the dispersion coefficients are affected by large uncertainty. Moreover, the turbidity current's dynamics is dominated by inertia and buoyancy forces, whose effects are more important than those due to the dispersion of sediment. Due to these reasons we will set the dispersion coefficients to zero.

#### 4. Numerical methods

A good numerical method, able to deal with the mathematical models developed in the previous section, should be able to reproduce correctly the key features of the considered phenomenon. These key features refer to the propagation of the front and to the sharp variations of the relevant physical quantities occurring in a narrow spatial interval between the gravity current and the lighter liquid. In other words, a good numerical method should possess good shock-fitting and shock-capturing characteristics.

The mathematical models formulated in the previous section refer to two particular cases: the constant density case and the variable density case. In the case of constant density, the mathematical model consists of the motion equations (11), of the Poisson equation (13) and the initial and boundary conditions (14), (15). In the case of variable density, the mathematical model consists of the motion equations (18), the concentration equation (19), the turbulent kinetic energy equation (26) and the initial and boundary conditions (20). Moreover, closure relations are integrant part of both the mathematical models.

The proposed mathematical models are rather complex. The strong coupling existing between the motion equations and the Poisson equation in the constant density case is particularly challenging. Anyway, by means of a suitable scaling and a formal perturbative expansion (La Rocca & Bateman, 2010), it is possible to eliminate this strong coupling and to adopt a solution procedure valid both for the constant and the variable density case. It is worth showing the essential points of the simplification of the motion equations, omitting the details of the scaling and the formal perturbative expansion. Consider equations (11) in the compact form:

$$\frac{\partial \mathbf{U}}{\partial t} + \frac{\partial \mathbf{F}}{\partial x} + \frac{\partial \mathbf{G}}{\partial y} = -\mathbf{P} + \mathbf{S} \quad (28)$$

being  $\mathbf{U}$  the vector whose components are the conserved variables:  $\mathbf{U} \equiv \{h_1, U_1 h_1, V_1 h_1, U_2 h_2, V_2 h_2\}$ . The vectors  $\mathbf{F}$ ,  $\mathbf{G}$ ,  $\mathbf{P}$ ,  $\mathbf{S}$  depend on the vector  $\mathbf{U}$  and can be defined comparing equations (11) with the compact form (28). Decompose  $\mathbf{U}$  as:  $\mathbf{U} = \mathbf{U}_0 + \mathbf{U}_c$ .  $\mathbf{U}_0$  satisfies the partial differential system:

$$\frac{\partial \mathbf{U}_0}{\partial t} + \left( \frac{\partial \mathbf{F}}{\partial x} + \frac{\partial \mathbf{G}}{\partial y} \right) \Big|_{\mathbf{U}=\mathbf{U}_0} = \mathbf{S} \Big|_{\mathbf{U}=\mathbf{U}_0} \quad (29)$$

and has the remarkable property that its components  $U_2 h_2|_0, V_2 h_2|_0$  are zero. Indeed, the evolution of  $U_2 h_2|_0, V_2 h_2|_0$  is described by the last two equations of the partial differential

system (11) without the pressure term. These two equations are homogeneous and so, if the initial values of  $U_2 h_2|_0, V_2 h_2|_0$  are zero, they remain zero. The partial differential system (29) is also known as the one-layer model, because it can be thought as a model which ignores completely the motion of the upper layer. It is possible to derive formally this one-layer model (La Rocca & Bateman, 2010) as the leading order approximation of a perturbative expansion of  $\mathbf{U}$  and the partial differential system (28) with respect to the small parameter  $h/H$ , being  $h$  the order of magnitude of the gravity current's thickness and  $H$  the sum of the thicknesses of the upper layer and the gravity current. The one-layer model is obtained in the limit  $h/H \rightarrow 0$  ( $H \rightarrow \infty$ ) (Ungarish & Zemach, 2005) and can be applied when the gravity current's thickness is expected to be negligible with respect to the thickness of the ambient liquid. Nevertheless, the one-layer model (29) is widely applied in the investigation of 2D, axisymmetric and 3D gravity currents also when the ratio  $h/H \rightarrow 0$  is not small and results are generally good (Ungarish, 2007a; Ungarish, 2007b; Ungarish, 2010; La Rocca et al., 2008). Once the one-layer solution  $\mathbf{U}_0$  is known, it is possible to determine a first approximation of the pressure  $P_s$ , solving the Poisson equation (13), with the RHS calculated in correspondence of the one-layer solution  $\mathbf{U}_0$ . Having determined the pressure  $P_s$ , it is possible to determine the correction  $\mathbf{U}_c$  by means of:

$$\left. \frac{\partial \mathbf{U}_c}{\partial t} + \frac{\partial}{\partial \mathbf{U}} \left( \frac{\partial \mathbf{F}}{\partial x} + \frac{\partial \mathbf{G}}{\partial y} \right) \right|_{\mathbf{U}=\mathbf{U}_0} \mathbf{U}_c = -\mathbf{P} \quad (30)$$

Solving again the Poisson equation with the RHS calculated in correspondence of  $\mathbf{U}_0 + \mathbf{U}_c$ , a better approximation of  $P_s$  is obtained. In turn, a new value of the correction can be determined from equations (30) and so on.

The core of the numerical model consists then in solving the one-layer partial differential system. This latter is fundamental not only in the constant but also in the variable density case, as the partial differential system (18) and the concentration equation (19) have the same structure of the one-layer partial differential system (29). The other steps of both the cases can be dealt with standard numerical methods: e.g. the Poisson equation can be solved with a SOR iterative method, while the partial differential system (30) can be solved with a Lax-Wendroff method.

The one layer partial differential system (29), being in conservative form, can be dealt with a finite volume numerical method, particularly suitable to deal with propagation of sharp discontinuities. The book of Toro (1999) is an excellent guide to these methods and shows that the Godunov formulation together with the use of an approximate Riemann solver is a common choice in dealing with hydraulic problems.

In this chapter the Godunov formulation with the approximate Riemann solver of Roe will be adopted for the solution of the one-layer partial differential system (29). The details of the numerical method and of its application to the present case are however omitted, for the sake of simplicity. The reader can find them in the book of Toro (1999) and in the papers of La Rocca et al. (2008), La Rocca et al. (2009).

## 5. Experimental setup for the realisation of 3D gravity currents

The setup, realized in the Hydraulics Lab of the University Roma TRE (Fig. 5), is a 3D, full-depth, lock exchange release experiment and it consists of a rectangular tank, divided into

two square parts (side  $L=1$  m) by a rigid wall, filled with tap water (density  $\rho_2$ ) and salty water (density  $\rho_1$ ,  $\rho_1 > \rho_2$ ) up to the same height  $H$ . At the centre of the wall there is a sliding gate AB which can be manually removed. The width of the gate is  $b=0.2$  m. The flat bottom of the tank ( $z_f=0$ ) can be smooth or be made rough by gluing on it uniform sediments, with diameter  $\varepsilon$ . A CCD video camera records the evolution of the gravity current with an acquisition frequency of 25 Hz. The images obtained from the records are digitized and analysed, so the instantaneous shape of the gravity current is obtained. In general, the top view of the gravity current is considered. Only in few cases the lateral view of the gravity current has been considered too (Fig. 3), but this latter can be used mainly for qualitative comparisons, being the image strongly distorted.

The preparation of the heavier liquid is very simple. It consists in adding a mass  $m_s$  of salt to the water, determined in order to obtain a given density  $\rho_1$  of the heavier liquid:

$$m_s = \frac{\rho_1 - \rho_2}{\rho_s - \rho_2} \rho_s V \quad (31)$$

$V$  is the total volume occupied by the heavier liquid and  $\rho_s$  is the density of the salt (NaCl).

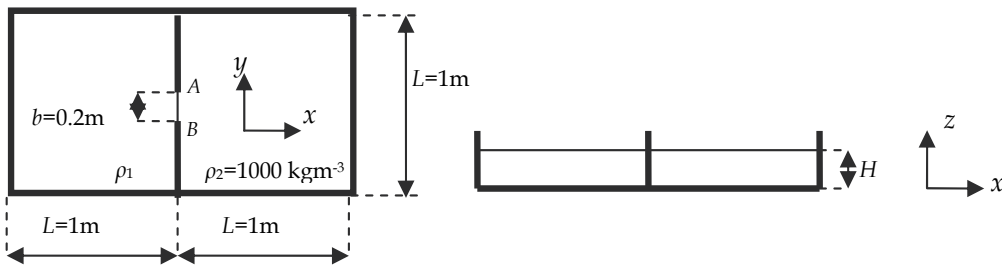


Fig. 5. Setup of the 3D lock exchange release experiment

The solution of water and salt is then coloured, in order to make easier the image analysis, and its actual density is measured by means of a picnometer. The runs considered are resumed in table 1.

## 6. Results

### 6.1 Validation of the mathematical models and the numerical methods

The mathematical models proposed in this chapter have to be validated reproducing results concerning with 2D gravity currents, because in literature there is a very wide choice of such results. Reference is made to 2D gravity currents generated by the full depth lock exchange release experiment. This latter is performed in a long and narrow channel (ratio width  $b$  over length  $L$ :  $b/L \ll 1$ ) so the prevailing longitudinal dimension  $L$  makes possible a reliable representation of the gravity current on the  $xz$  plane. In such a channel the lock is situated at a distance  $x_0$  from the wall. If the initial height of the heavier and the lighter liquid is the same, the lock exchange release is classified as full depth, otherwise as fractional depth. In this latter case, the ratio  $\phi$  of the initial height of the heavier liquid  $h$  on the total height  $H$  is an important parameter of the experiment, known as fractional depth.

The evolution of a 2D gravity current originated by a lock exchange release experiment is characterised by four phases: the very initial phase, the slumping phase, the self-similar or

inertial phase and the viscous phase. As soon as the lock is removed and after the very initial phase, the heavier liquid starts travelling forward, while the lighter liquid starts travelling backward. The slumping phase is characterised by a constant advancing velocity  $U_f$  and a constant height  $h_f$  of the heavier front and it ends as soon as the bore, caused by the reflection of the lighter front with the wall, reaches the gravity current's front (Ungarish & Zemach, 2005). In lock of finite length  $x_0$  the reflected wave reaches the forward advancing heavier front at a given instant of time, after which, the self-similar phase, characterised by time decreasing height and front velocity, starts. The viscous forces assume gradually increasing importance with respect to the inertial forces and eventually prevail on them. During the viscous phase the velocity of the front decreases more rapidly with time, with respect to the self-similar phase. Quite a long distance is required by the 2D gravity currents in order to develop the viscous phase (Huppert, 1982) and the evolution of experimental gravity currents is generally limited to the first three phases, i.e. until the self-similar phase.

Run	$\rho_1$ [kgm <sup>-3</sup> ]	$H$ [cm]	$V$ [m <sup>3</sup> ]	$m_s$ [kg]	$\varepsilon$ [mm]
1	1025	15	0.15	6.98	0.0
2	1015	15	0.15	4.19	0.0
3	1055	15	0.15	15.36	0.0
4	1015	15	0.15	4.19	0.7
5	1015	15	0.15	4.19	1.0
6	1015	15	0.15	4.19	1.6
7	1015	15	0.15	4.19	3.0
8	1025	15	0.15	6.98	0.7
9	1025	15	0.15	6.98	1.0
10	1025	15	0.15	6.98	1.6
11	1025	15	0.15	6.98	3.0
12	1017	10	0.10	3.17	3.0
13	1018	20	0.20	6.70	3.0
14	1028	10	0.10	5.21	3.0
15	1033	20	0.20	12.29	3.0
16	1019	15	0.15	5.31	3.0
17	1030	15	0.15	8.38	3.0
18	1017	10	0.10	3.17	0.0
19	1018	15	0.15	5.03	0.0
20	1019	20	0.20	7.08	0.0
21	1033	10	0.10	6.14	0.0
22	1033	15	0.15	9.22	0.0
23	1033	20	0.20	12.29	0.0

Table 1. Experimental runs

The behaviour of 2D gravity currents will be reproduced integrating numerically the "simplified" mathematical model, consisting of the one-layer partial differential system (29), the partial differential system for the correction term (30) and the Poisson equation (13), with the RHS calculated in correspondence of the one-layer solution  $U_0$ . This "simplified" mathematical model will be hereinafter denoted as the 3D partial differential system.

Moreover, setting the  $y$  velocity components to zero ( $V_i=0; i=1,2$ ) in the constant density equations (11) and omitting the derivatives with respect to  $y$ , it can be shown (Rottmann & Simpson, 1983; Ungarish & Zemach, 2005) that the pressure  $P_s$  can be eliminated from the motion equations and that the original five partial differential equations system (11) can be reduced to a partial differential system of two equations, hereinafter indicated as RL2D. This latter will be solved, by means of a Lax-Wendroff method, to obtain 2D numerical results. It is worth mentioning that all of numerical integrations were performed adopting the boundary conditions imposed on the velocities at the rigid walls of the tank. In literature (Ungarish, 2009b), a boundary condition imposed on the gravity current's front is usually adopted for 2D numerical gravity currents, except rare examples (D'Alessio et al., 1996). The choice of avoiding to impose a boundary condition on the gravity current's front is motivated by the fact that for 3D gravity currents it is very difficult or perhaps not possible to adopt a front condition. The validation process is also aimed to check the reliability of such a choice.

The slumping phase of gravity currents can be highlighted by experiments where the length of the lock is half of the total length of the channel (Shin et al., 2004; Lowe et al., 2005). In this case the velocity of the gravity current's front is quite well predicted by the Benjamin's formula for energy-conserving gravity currents (Shin et al., 2004). The experimental gravity currents considered in Lowe et al. (2005), with ratio  $r$  ( $r=\rho_2/\rho_1$ ) in the range  $0.607 < r < 0.993$ , were realized in a channel, covered with a rigid lid, length  $L$  ( $L \approx 2$  m), wide  $b$  ( $b=0.23$  m) and filled up to the height  $H$  ( $H=0.2$  m). In Fig. 6a, b the time history of the non dimensional position of the gravity current's front is plotted versus non dimensional time. The scaling is defined by:  $t^* = t\sqrt{g'h_0}/h_0$ ,  $x^* = x/h_0$ .

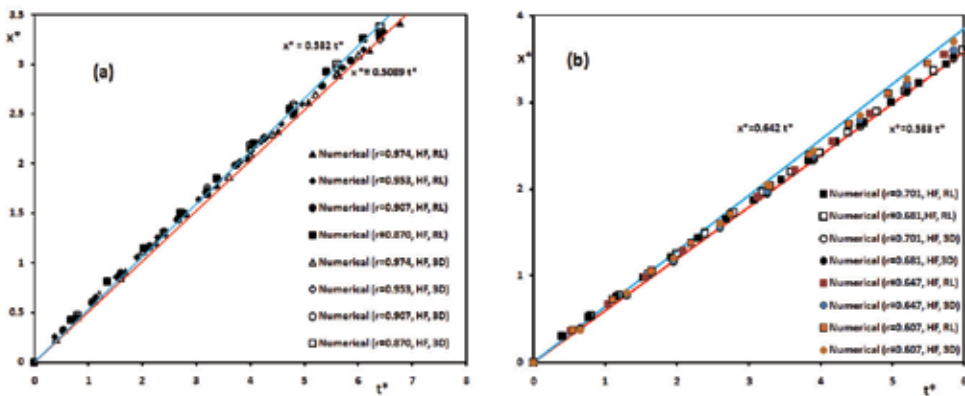


Fig. 6. a,b Slumping phase of Boussinesq ( $r > 0.8$ ) and non-Boussinesq ( $r < 0.8$ ) gravity currents. The results plotted in Fig. 6a,b are in good agreement. An interesting information can be obtained considering how the numerical data approximate the analytical value of the front velocity predicted by the energy conserving theory of Benjamin (Shin et al., 2004). This analytical value is equal, in dimensionless terms, to:  $u_f = \sqrt{1/2r}$ . The angular coefficients of the red and blue straight lines plotted in Fig. 6a,b, reported on the plot, are the non dimensional values of the analytical front velocity, obtained with the least (blue line) and the largest (red line) value of the ratio  $r$ . The agreement is quite good, showing that the 3D

partial differential system is able to reproduce 2D numerical results, when integrated in a 2D geometry, for quite a wide range of the density ratio.

The numerical and experimental space-time evolution of the thickness of the gravity current is shown in Fig. 7. Numerical results are obtained solving the RL2D partial differential system, the 3D partial differential system and the 2L2D partial differential system, obtained setting to zero the pressure  $P_s$ , the  $y$  velocity components and eliminating the derivatives with respect to  $y$  in the partial differential system (9). This 2L2D partial differential system, consisting of four partial differential equations, is able to describe the evolution of the gravity current thickness  $h_1$  and the upper surface  $h_1+h_2$ . The experimental results shown in Fig. 7 were obtained by means of a full depth lock exchange release experiment, conducted at the hydraulic lab of the DEHMA of the Politechnical University of Catalunya, in a transparent channel (length  $L=2$  m, width  $b=0.2$  m, height  $H=0.35$  m), with salty ( $\rho_1=1100$   $\text{kgm}^{-3}$ ) and fresh water ( $\rho_2=1000$   $\text{kgm}^{-3}$ ). The initial height of the lock was  $h_1=0.28$  m. The profiles are relative to 1 and 3 sec after the removal of the lock. The agreement between the experimental and the 2L2D numerical profiles is good. From Fig. 7, it is evident that the mathematical model is able to describe the evolution of the gravity current, which is in its slumping phase. The 2L2D numerical profile of the gravity current is in good agreement with the experimental profile not only concerning with the position of the front, but also with the position of the forward advancing bore, which gradually approaches the front.

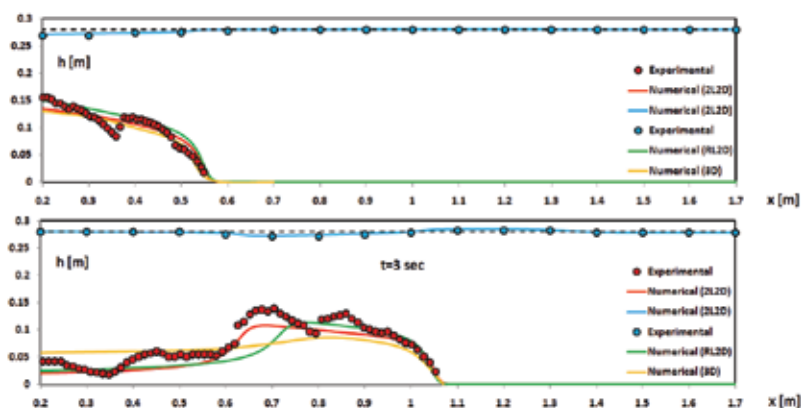


Fig. 7. Numerical and experimental profiles of a 2D gravity current

It is also surprising to see how the form of the gravity current is quite well reproduced by the 2L2D numerical results, despite of the fact that the entrainment of lighter liquid is neglected. The upper surface profile is well reproduced too. It is interesting to observe that the amplitude of the motion of the upper surface is small with respect to the gravity current's thickness. This fact justifies the rigid-lid hypothesis, whose validity depends on the value of the density ratio  $r$ : the smaller this ratio, the larger the amplitude of the free surface motion and the less reliable is the rigid-lid hypothesis (D'Alessio et al., 1996). The agreement between the experimental and the RL2D numerical profiles is fairly good. Indeed, it is evident from Fig. 7 that the RL2D simulations slightly overestimate the velocity of the forward advancing bore, with respect to the 2L2D numerical results, and then underestimate the position  $x_s$  where the bore reaches the front. This underestimation of  $x_s$  is typical for the RL2D simulations and it is also confirmed in the work of Ungarish and

Zemach (2005). At last, it is interesting to observe that the ratio of the height of the gravity current, just behind the front, on the initial height, is approximately equal to 1/3. This fact is in agreement with the theory of Benjamin (Shin et al., 2004), which predicts a value for such a ratio equal to 0.347 for the most dissipative gravity current. The experiments generally confirm that this kind of gravity current occurs during the slumping phase, after the bore is reflected from the left wall of the channel. The agreement between the experimental and the 3D numerical profiles is fairly good too.

The 2L2D and RL2D numerical simulations were obtained on a grid with approximately  $10^3$  computational points and a time step with an order of magnitude of  $10^{-4}$  sec. The 3D numerical simulations were obtained on a grid with approximately  $10^5$  spatial cells and a time step with an order of magnitude of  $10^{-5}$  sec.

## 6.2 Experimental and numerical results on 3D gravity currents

All of the experiments listed in Table 1 have been numerically reproduced, but for obvious reasons of space not all of the results will be presented.

In Fig. 8, the comparison between the experimental and numerical time histories of the position and the velocity of the front along  $x$  direction are shown. With reference to Table 1, curves plotted in Fig. 8 are relative to runs 1,2,4,5,6,8,9,10. Non dimensional time  $t^*$ , position

$x^*$  and velocity  $u^*$  are scaled as:  $t^* = \frac{t}{h_0/\sqrt{g'h_0}}$ ,  $x^* = \frac{x}{L}$ ,  $u^* = \frac{u}{\sqrt{g'h_0}}$ . The position of the

numerical front has been determined as in La Rocca et al. (2008). The agreement between the experimental and numerical results is fairly good for all of the cases. Indeed, the error, defined as in La Rocca et al. (2008), is no larger than 11%, which is a reasonable and consistent value with regard to the limits of the mathematical model and the experimental uncertainties. Numerical results plotted in Fig. 8 have been obtained by solving the one-layer partial differential system (29), i.e. without considering the correction due to the pressure  $P_s$ . This fact shows as the one-layer model is able to reproduce the dynamics of the 3D gravity current, while the correction gives information on the upper layer dynamics.

Both the experimental and numerical curves plotted in Fig. 8 show a two-phase dynamics during the evolution of the gravity current: an accelerating phase followed by a decelerating phase. The first phase is dominated by inertial-buoyancy forces, while during the second phase the effects of the friction force gradually become evident, through a reduction of the front's velocity. The fact that the reduction of the front velocity occurs during the second phase of motion is in qualitative agreement with the results of other works on 2D gravity currents flowing on a rough bottom (Hogg & Woods, 2001).

Discrepancies between numerical and experimental data occur mainly during the first phase of motion, i.e. the accelerating phase, and are due to a general overestimation of the numerical front velocity during this phase. This overestimation of the front velocity could be caused both by the difference between numerical and experimental initial conditions and by the intrinsic limitation of the mathematical model. The difference between numerical and experimental initial conditions is concerned with the removal of the lock: it is instantaneous in the numerical code, while it occurs during a finite interval of time in the laboratory experiments. Such a difference affects the motion of the gravity current during the first instants of motion. With regard to the intrinsic limitations of the mathematical model, it is worth mentioning that (Klemp et al., 1994) the shallow water and the one-layer approximations are questionable during the very initial phase of motion.

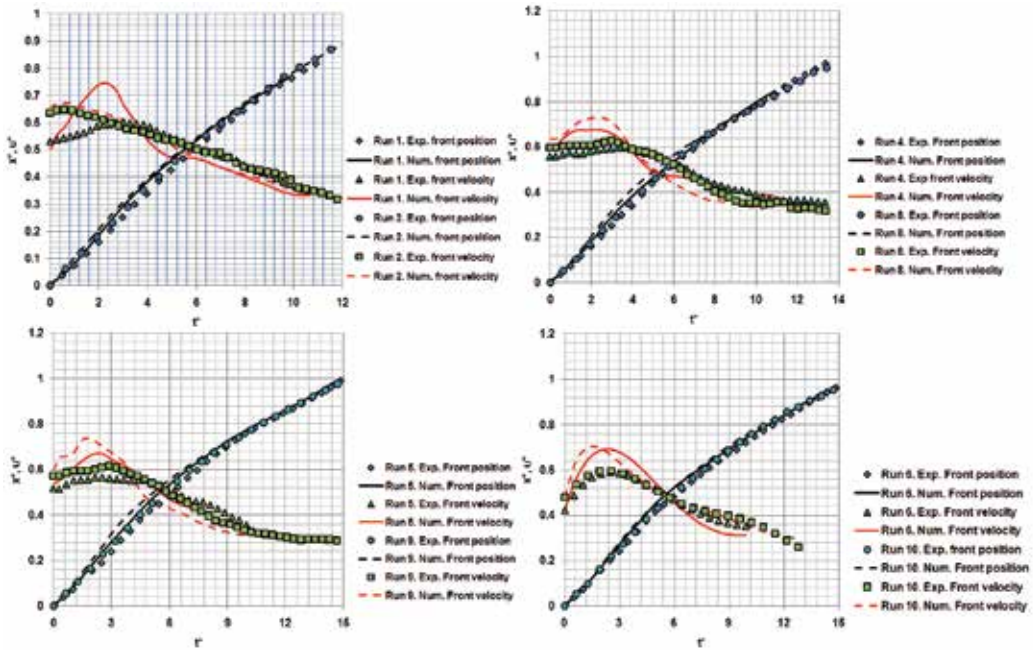


Fig. 8. 3D gravity current. Non dimensional front position  $x^*$  and velocity  $u^*$  versus non dimensional time  $t^*$ . Runs 1,2,4,5,6,8,9,10

In Fig. 9 the numerical and experimental top views of the gravity currents corresponding to the runs 2,4,5 at different instant of times are shown. These top views give an idea of the ability of the mathematical model and of the numerical method in reproducing the evolution of the gravity current not only along the  $x$  direction. The agreement between numerical and experimental results is quite good, except for the region near the gate, which is the most critical region of the flow, due to the high gradients of the hydrodynamic quantities in correspondence of the edges of the gate.

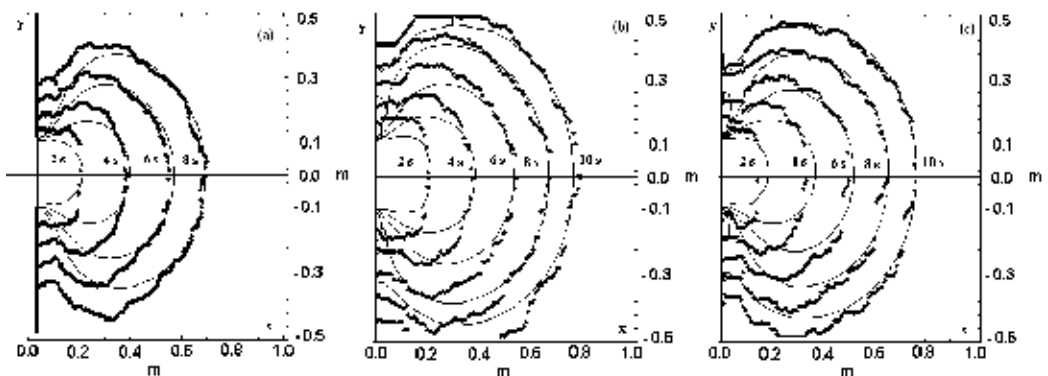


Fig. 9. Numerical and experimental top views of the gravity currents at different instants of time. The solution of the 3D partial differential system determines the motion of the upper layer. Presently no experimental results are at disposal to verify the correctness of the numerical

results. Nevertheless the numerical pressure and velocity fields are consistent with the experimental observations. Those plotted in Fig. 10a,b refer to the run 9, 5.6 sec after the removal of the gate. The structure of the velocity field of the gravity current and the lighter layer is shown in Fig.10a. Thanks to the symmetry of the flow field, Fig. 10a reproduces only half of the fluid domain. The top velocity field refers to the gravity current, while the bottom velocity field refers to the lighter liquid. The choking effect caused on the flow by the narrow opening of the gate is highlighted by the high values of the velocity attained in correspondence of the opening, which is the most critical region of the flow, due to the high value attained by the radius of curvature of the streamlines at the edges of the gate.

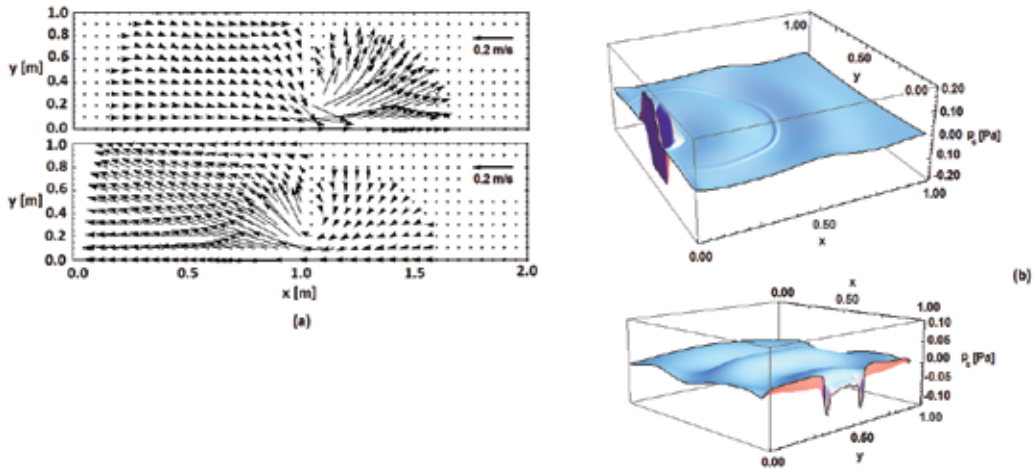


Fig. 10. a,b Velocity and pressure fields. Run 9, 5.6 seconds after the removal of the gate

The pressure field shown in Fig.10b shows that, apart from the region of the gate, the pressure  $P_s$  vanishes. This fact justifies the use of the one-layer model for modelling the dynamics of the 3D gravity currents. The plot is divided, for the sake of clarity of representation, into two parts, corresponding to the left and right parts of the tank shown in Fig. 5. In the region of the gate the pressure  $P_s$  shows large variations in small spatial intervals, corresponding to the strong deformation of the gravity current and to the sudden increase of velocity of this latter across the gate.

Another interesting feature reproduced by the pressure field, is the line of the gravity current's front, which is clearly apparent on the plot reproducing the right side of the tank (Fig. 10b). This pressure front corresponds to the gravity current's front velocity, shown in Fig. 10a, and separates the advancing front of heavier liquid from the quiescent lighter liquid.

Looking at the velocity field shown in Fig. 10a, it is possible to observe that along the streamline  $y=0$  (the symmetry streamline) the  $y$  velocity components  $V_1$ ,  $V_2$  vanish. Consequently, equation (14) becomes:

$$\frac{\partial(U_1 h_1 + U_2 h_2)}{\partial x} = 0 \Rightarrow U_1 h_1 + U_2 h_2 = \text{const} \quad (39)$$

The constant is set to zero, due to the fact that on the wall  $U_1=U_2=0$ . As a consequence of (39), the velocity of the lighter layer  $U_2$  along the streamline is related to that of the heavier layer  $U_1$  by the algebraic relation:

$$U_2 = -U_1 \frac{h_1}{H - h_1} \quad (40)$$

The simple relation (40) permits an interesting check on the validity of the numerical results, shown in Fig. 11.

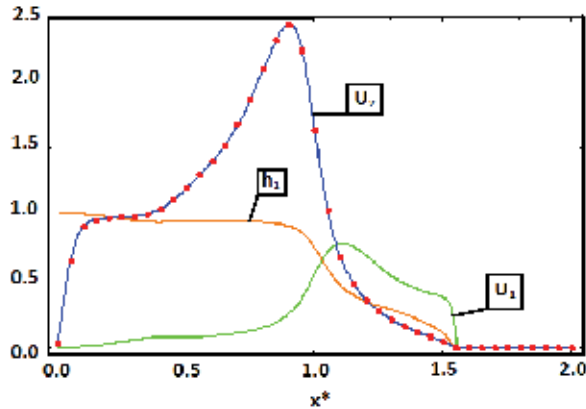


Fig. 11. Dimensionless profiles of the gravity current's thickness and the velocities. Run 9, 5.6 sec after the removal of the lock

In Fig.11 the dimensionless profile of the gravity current's thickness  $h_1/H$  (the orange line) and the dimensionless profile of the velocities  $\frac{U_1}{\sqrt{g'H}}, \frac{U_2}{\sqrt{g'H}}$  (respectively the green and the

blue line) along the symmetry streamline are plotted. The data refer to the run 9, 5.6 sec after the removal of the lock. The dotted line represents the velocity of the upper layer, calculated according to (40). The agreement between the dotted line and the continuous blue line is very good, showing that numerical data are consistent with the mathematical model. It is also worth noting the agreement on the position of the front, between the profile of the gravity current and the velocity profile  $U_1$ .

The numerical results considered until now were obtained assuming constant the densities of the two liquid layers. Nevertheless, in many circumstances of environmental importance, this assumption does not make sense. It is the case of the turbidity currents, which occur under a deep layer of fresh water (in lakes or seas) and consists of a mixture of water and heavy sediment. The most important feature in turbidity current's dynamics is that the sediment settles down and possibly can be put in re-suspension during the evolution of the current, then varying the concentration  $C$  and consequently reducing the excess density (17) and the driving buoyancy force (Hogg et al., 2000). In order to have an idea of the effect of settling of sediment on the turbidity current's dynamics, a numerical experiment inspired by the experimental work of Bonnecaze et al. (1993) has been performed. Bonnecaze et al. (1993) compared the behavior of 2D turbidity currents with the behavior of a 2D gravity current, all of them having the same initial excess density. The turbidity currents were realized making a suspension of water and silicon carbide particles with increasing diameter ( $9\mu\text{m} \leq d_s \leq 53\mu\text{m}$ ). The numerical experiment presented here refers to the comparison between the numerical results of run 2 ( $\rho_1=1015 \text{ kgm}^{-3}$ ) and the numerical results relative to turbidity currents with the same initial density, but realized with a mixture of water and silicon carbide particles, with increasing diameter ( $9\mu\text{m} \leq d_s \leq 53\mu\text{m}$ ). Numerical results were

obtained solving the equations (18), (19) and are shown in Fig. 12a,b. In Fig. 12a the numerical time histories of the current's front position are plotted.

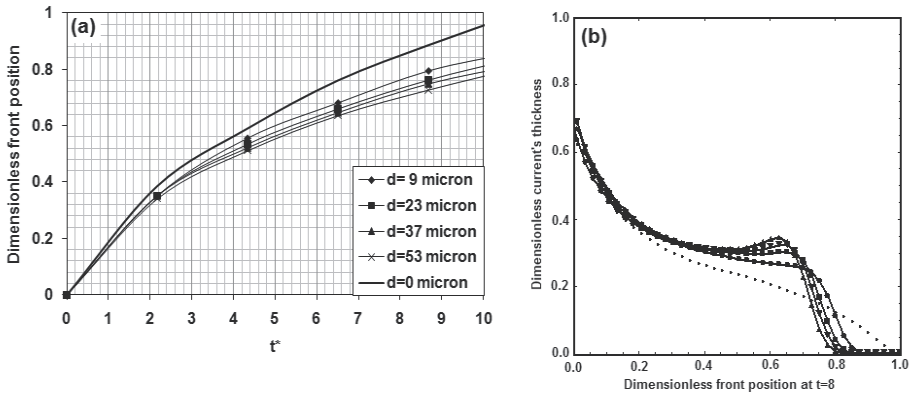


Fig. 12. Comparison between the constant density gravity current and the turbidity currents obtained with particles of increasing diameters

The front position is dimensionless and the scaling factor is represented by the front position attained by the gravity current 10 s after the start of the run. So the values on the vertical axis represent the percentage of the distance travelled at any instant of time by the turbidity current's front, with respect to that travelled by the gravity current's front. The time is

scaled as:  $t^* = \frac{t}{h_0 / \sqrt{g' h_0}}$ . The general behavior is in qualitative agreement with that

shown in Bonneau et al. (1993): as the diameter of the sediment increases, the front velocity decreases. Indeed, the settling of larger particles occurs more rapidly, thus making more effective the reduction of the excess density and then of the driving buoyancy force. The influence of the particles settling on the profile of the current's thickness is shown in Fig. 12b. In this figure, the thickness profiles, obtained at  $t^*=8$  and relative to the currents considered in Fig. 12a, are shown. The dotted line represents the gravity current; the circles, the squares, the overturned triangles and the upright triangles represent the turbidity currents made with diameters  $d_s$  respectively of 9  $\mu\text{m}$ , 23  $\mu\text{m}$ , 37  $\mu\text{m}$  and 53  $\mu\text{m}$ . The profiles are scaled with the initial height ( $H=0.15$  m), while the abscissa is scaled with the distance travelled by the gravity current at  $t^*=8$ .

Settling of particles causes a distortion of the gravity current profile. The distortion increases with the diameter of the particle. Nevertheless the volume of the gravity current remains practically constant. Indeed, the relative variation of volume is equal to 1.35% in the case of the turbidity current showing the maximum distortion, realized with particles of diameter  $d_s=53$   $\mu\text{m}$ .

### 6.3 Numerical simulation of entrainment at Flix reservoir

A qualitative study of the contamination event occurred in the Flix reservoir has been carried out by means of the software BANG 1DT (Herrero et al., 2009), firstly with a simple bathymetry consisting in a variable slope that ends in a horizontal section, secondly considering the actual bathymetry of the reservoir. BANG 1DT is essentially based on the one dimensional version of the equations (18), (19) and (26). The study was focused on the

influence of the slope, the initial velocity, the initial concentration of sediment and the temperature of water on the evolution of the density current, which could have caused the contamination of the Flix reservoir. In Figure 13 are plotted the profiles of the depth of the density current, of its velocity and density, at different instants of time, versus the distance travelled by the density current. These profiles have been obtained by BANG 1DT starting from the following initial conditions:

- slope: 1.0 %
- initial velocity: 1.0 m/s
- initial concentration: 0.05 mg/kg
- initial temperature: 7.0 °C
- external temperature: 15.0 °C
- sediment temperature: 15.0 °C

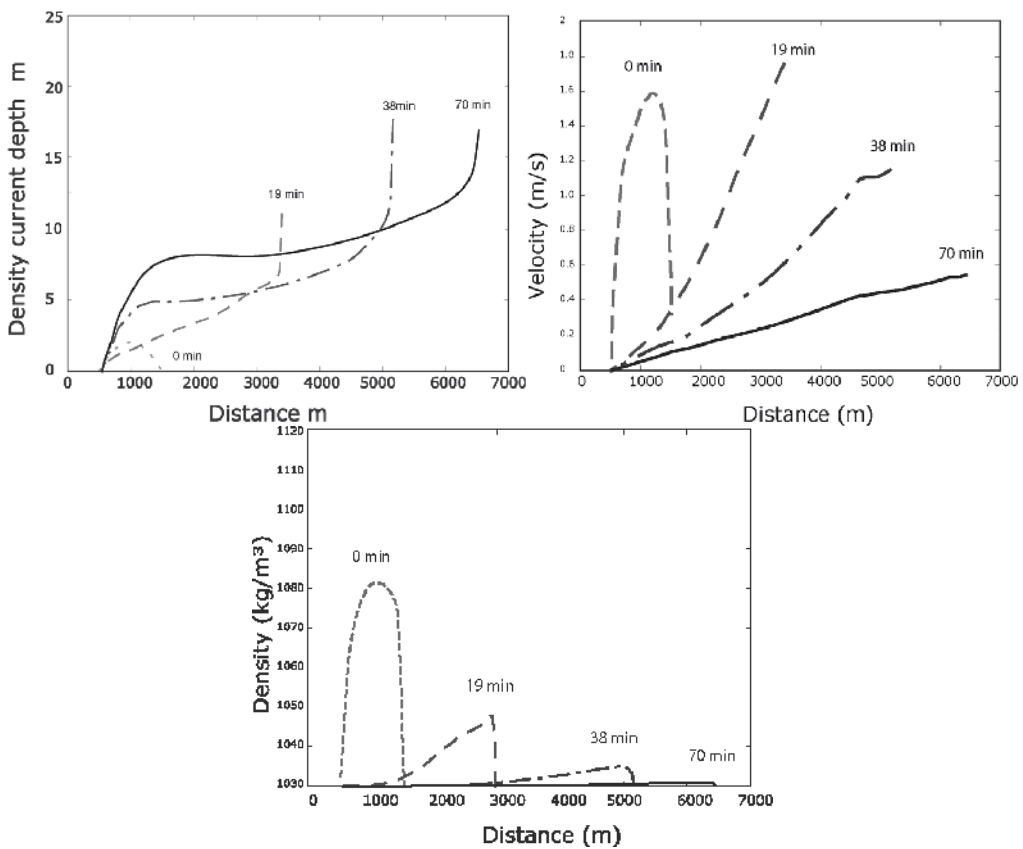


Fig. 13. Depth, velocity and density distribution of the density current along its path

The analysis of the case shown in Figure 13, as well as that of other cases (not reported here), showed that:

- a. the difference of temperature between two water bodies has a slight influence on the evolution of the density current, although this latter can be also caused by such a difference. The evolution of the density current is dominated by the gradients of sediment concentration.

- b. Sedimentation and erosion depend on the velocity of the density current.
- c. The qualitative behaviour of the density current is not affected by the slope of the bottom, while the erosion increases with the slope.

The influence of the initial length of the density current on the scour profile is also an interesting issue. Initial lengths of 500, 1000 and 1500 meters have been considered (Figure 14).

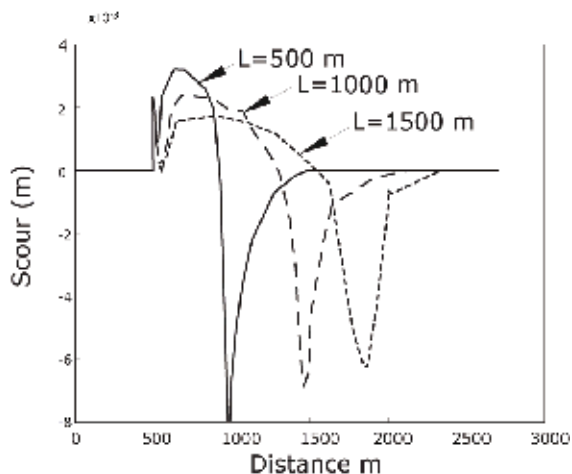


Fig. 14. Scour profile produced during the passage of the density current for three different initial lengths 500 m, 1000 m and 1500m

As the current length increases, the maximum depth of the scour decreases but the total volume of entrained sediment increases. This latter quantity is of primary importance and once it has been obtained, it is possible to compute the quantity of contaminant set into movement, starting from the concentration of this element at the bottom of the reservoir, obtained by means of suitable measurements procedures.

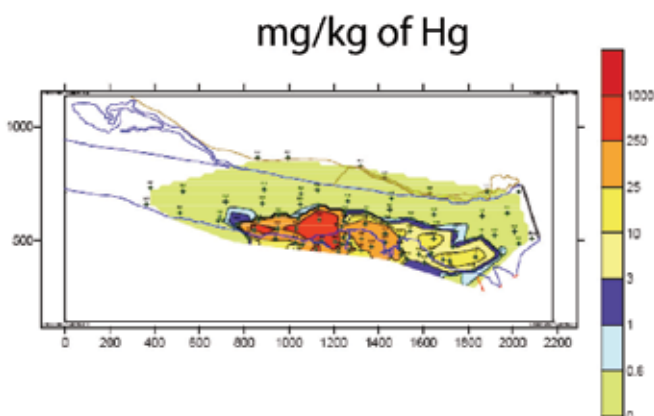


Fig. 15. Distribution of the concentration of Hg in the sediment fan in front of the chemical enterprise (Herrero et al. 2009)

As an example, in Figure 15 is shown the concentration of Hg at the bottom of the Flix reservoir after the contamination event (Herrero et al. 2009). In Table 2 are given the entrained volumes of sediment corresponding to the initial velocity of 1.0 m/s and 3.0 m/s and calculated by means of the scour profiles determined by BANG 1DT. Considering a density current 30 meters wide (a reasonable value for the considered case), these results would imply the mobilized volumes of mercury shown in the same Table. Assuming that the sediment entrained by the current has an average mercury concentration of 200 mg/kg and taking the value of 2650 kg/m<sup>3</sup> as characteristic for the density of sediment, the amount of mobilized mercury shown in Table 2 are obtained.

Initial velocity (m/s)	Eroded volume per width unit (m <sup>3</sup> /m)	Mobilized volume (m <sup>3</sup> )	Mass of mercury mobilized (kg)
1.0	1.5	45	23.85
3.0	18	540	286.2

Table 2. Eroded volume per unit width due to two different initial velocities current

These values have the same order of magnitude of those measured in water samples. The results obtained by the numerical model then give only a qualitative indication, which however confirms the potential dangerousness of the density current, as a cause for the mobilization of contaminated sediment in water bodies, and explains the contamination event of Flix as due to the formation of a density current. In this case study, the complexity of the geometry is one of the sources of uncertainty. The non-availability of the exact bathymetry of the upstream section of the river Ebro e.g. hindered a more realistic simulation of the density current and is then considered as a major weak point.

## 7. Conclusion

This chapter deals with mathematical, experimental and numerical modelling of 3D gravity currents. The motivation is that this kind of gravity currents has not been so frequently examined in scientific literature as 2D and axisymmetric gravity currents.

Two main cases have been examined: the constant density and the variable density case. Concerning with the constant density case, the attention has been focused on the problem of the double layer formulation and the determination of the pressure at the upper surface when the rigid lid hypothesis is assumed. A suitable simplified procedure has been proposed for solving the equations of motion and the Poisson's equation for the pressure. Concerning with the variable density case, the attention has been focused on the extension of known 2D mathematical models and on the effect of the resuspension and sedimentation dynamics in 3D turbidity current.

The comparison between numerical and experimental results, which refer to the simulation of 3D gravity currents, shows that the constant density, two-layer mathematical model reproduces correctly the key features of the dynamics of the considered physical phenomenon. Numerical results obtained in the variable density case make sense and are in qualitative agreement with the experimental observations found in literature.

Future work should go along two main directions: a systematic validation of the constant density, two-layer mathematical model and the realisation of an exhausting experimental campaign on 3D turbidity current.

At last a case study, concerning with the contamination event of the Flix reservoir has been considered. Results have to be carefully managed, due to the complexity of the phenomenon and to its intrinsic uncertainties. Nevertheless it is possible to claim that density and turbidity currents can be responsible for contamination of water bodies, as in this case study. This fact is a strong motivation for further studies on this subject.

## 8. References

- Benjamin, T. B. (1968). Gravity currents and related phenomena. *J Fluid Mech*, Vol. 31, n. 2, 209-248
- Bonnecaze, R. T.; Huppert, H. E.; Lister, J. (1993). Particle-driven gravity currents. *J Fluid Mech*, Vol. 250, 339
- Birman, V. K.; Martin J. E.; Meiburg E. (2005) The non-Boussinesq lock-exchange problem. Part 2. High-resolution simulations. *J Fluid Mech*, Vol. 537, 125-144
- Birman, V. K.; Meiburg E.; Kneller, B. (2009) The shape of submarine levees: exponential or power law? *J Fluid Mech*, Vol. 619, 367-376
- Bradford, F. S.; Katopodes, N. D.; Parker, G. (1997). Characteristic analysis of turbid underflows. *Journal of Hydraulic Engineering*, Vol. 123, no. 5, 420-432
- Cantero, M. I.; Balachandar, S.; Garcia, M. H. (2008) An Eulerian-Eulerian model for gravity currents driven by inertial particles, *International Journal of Multiphase Flow*, Vol. 34, 484-501
- Çengel, Y. A. & Cimbala, J. M. (2006) *Fluid Mechanics: Fundamentals and Applications*. Mc Graw-Hill, New York
- Costa, J.; Villarubia, M.; Bateman, A. 2004. Contribució i Evaluació del " Estudi de la Dinàmica dels Compostos Otganoclorats Persistents i Altres Contaminants en els Sistemes Aquàtics Continentals" Novembre 2003. Propuesta de Actuaciones en el Embalse de Flix. Universidad Politècnica de Catalunya-Universidad de Barcelona.
- D'Alessio, S. J. D.; Moodie, T. B.; Pascal, J. P.; Swaters, G. E. (1996). Gravity currents produced by sudden release of a fixed volume of heavy fluid. *Studies in Applied Mathematics*, Vol. 96, 359-385
- Dietrich, E. W. (1982). Settling velocity of natural particles. *Water Resour. Res.* Vol. 18, 1626
- Fischer, H.B.; List, J. E.; Koh, R. C. Y.; Imberger, J.; Brooks, N. H. (1979). *Mixing in inland and coastal waters*. Academic Press
- Garabedian, P. R. (1964). *Partial differential equations*. J. Wiley and Sons, New York
- García, M. H. & Parker, G (1993). Experiments on the Entrainment of Sediment into Suspension by a Dense Bottom Current. *AGU Journal of Geophysical Research (Oceans)*, Vol. 98, no. C3 (March), 4793-4807.
- Hallworth, M.; Huppert, H. E.; Ungarish, M. (2001). Axisymmetric gravity currents in a rotating system: experimental and numerical investigations. *J Fluid Mech*, Vol. 447, 1-29
- Hallworth, M.; Huppert, H. E.; Ungarish, M. (2003). On inwardly propagating high-Reynolds-number axisymmetric gravity currents. *J Fluid Mech*, Vol. 494, 255-274
- Härtel, C.; Meiburg, E., Necker, F. (2000a) Analysis and direct numerical simulation of the flow at a gravity-current head. Part 1. Flow topology and front speed for slip and no-slip boundaries. *J. Fluid Mech.*, Vol. 418, 189-212

- Härtel, C.; Carlsson, F., Thunblom, M. (2000b) Analysis and direct numerical simulation of the flow at a gravity-current head. Part 2. The lobe-and-cleft instability. *J. Fluid Mech.*, Vol. 418, 213-229
- Herrero, A.; Medina, V.; Bateman, A. (2009) Evaluation of resuspension due to density currents in Flix reservoir (Spain). *Proceedings of River Coastal and Estuarine Morphodynamics*, Santa Fé Argentina
- Hogg, A.J.; Ungarish, M.; Huppert, H.E. (2000) Particle-driven gravity currents: asymptotic solutions and box models. *European Journal of Mechanics B. Fluids* Vol. 19, 139-165
- Hogg, A. J. & Woods, A. W. (2001) The transition from inertia-to-bottom-drag-dominated motion of turbulent gravity current. *J. Fluid Mech.*, Vol. 449, 201-224
- Huang, H.; Imran, J.; Pirmez, C. (2005) Numerical Model of Turbidity Currents with a Deforming Bottom Boundary. *Journal of Hydraulics Research*, Vol. 131, no. 4, 283-293
- Huppert, H.E. (1982) The propagation of two-dimensional and axisymmetric viscous gravity currents over a rigid horizontal surface. *J. Fluid Mech.*, Vol. 121, 43-58
- Huppert, H. E. (2006) Gravity currents: a personal perspective. *J Fluid Mech*, Vol. 554, 299-322
- Huppert, H. E. & Simpson, J. E. 1980 The slumping of gravity currents. *J. Fluid Mech.*, Vol. 99, 785-799.
- Karman, T. Von (1940). The engineer grapples with nonlinear problems. *Bull. Am. Math. Soc.*, Vol. 46, 615.
- Keulegan, G. H. (1957). An experimental study of the motion of saline water from locks into fresh water channels. *Nat. Bur. Stand. Rept.* 5168
- Klemp, J. B.; Rotunno, R.; Skamarock, W. (1994) On the dynamics of gravity current in a channel. *J Fluid Mech*, Vol. 269, 169-198
- Kostic, S.; Parker, G. (2007) Conditions under which a supercritical turbidity current traverses an abrupt transition to vanishing bed slope without a hydraulic jump. *J. Fluid Mech.*, Vol. 586, 119-145
- La Rocca, M.; Adduce, C., Sciortino, G., Bateman Pinzon, A. (2008) Experimental and numerical simulation of three-dimensional gravity currents on smooth and rough bottom. *Physics of Fluids*, Vol. 20,1-15
- La Rocca, M.; Adduce, C.; Mele, P.; Sciortino, G. (2009) Numerical simulation of 3D submarine turbidity currents. *Proceedings of ISOPE 2009*, pp. 1-8, Osaka, June 2009
- La Rocca, M.; Bateman Pinzon, A. (2010) A perturbative method for double-layer shallow water equations. *Proceedings of CIMW 2010*, pp. 1-8, ISBN, Barcelona, June 2010
- Launder, B. E. & Spalding, D. B. (1972) *Mathematical Models of Turbulence*. Academic Press, London
- Lowe, R. J.; Rottman, J. W.; Linden, P. F. (2005) The non-Boussinesq lock-exchange problem. Part 1. Theory and experiments. *J Fluid Mech*, Vol. 537, 101-124
- Lee, W. H.; Lyczkowski, R. W. (2000). The basic character of five two-phase flow model equation sets. *International Journal for Numerical Methods in Fluids*, Vol. 33, 1075-1098
- Lyczkowski, R. W.; Gidaspow, D.; Solbrig, C. W.; Hughes, E. D. (1978). Characteristics and stability analysis of transients one-dimensional two-phase flow equations and their finite difference approximations. *Nucl. Sci. Eng.*, Vol. 66, 378-396
- Patterson, M. D.; Simpson, J. E.; Dalziel, S. B.; Van Heijst, G. J. F. (2006) Vortical motion in the head of an axisymmetric gravity current. *Physics of fluids*, Vol. 18, 1-7

- Parker, G.; Fukushima, Y.; Pantin, H. M. (1986) Self-accelerating turbidity currents. *J. Fluid Mech.* Vol. 171, 145–181.
- Pedloski, J. (1987). *Geophysical Fluid Dynamics*. Springer Verlag, Berlin/New York
- Prandtl, L. (1952) *Essentials of Fluid Dynamics*. Haffner, New York
- Pratson, L.; Imran, J.; Hutton, E.; Parker, G.; Syvitski, J. P. G. (2001). Bang 1-D: a one-dimensional Lagrangian model of turbidity currents mechanics. *Computers and Geosciences*, Vol. 26, no. 7, 705–720
- Ross, A. N.; Linden, P. F.; Dalziel, S. B. (2002). A study of three dimensional gravity current on a uniform slope. *J Fluid Mech*, Vol. 453, 239–261
- Rottman, J. W.; Simpson, J. E. (1983) Gravity currents produced by instantaneous releases of a heavy fluid in a rectangular channel. *J Fluid Mech*, Vol. 135, 95–110
- Shin, J. O.; Dalziel, S. B.; Linden, P. F. (2004) Gravity currents produced by lock exchange. *J Fluid Mech*, Vol. 521, 1–34
- Simpson, J. E. (1997). *Gravity Currents in the Environment and the Laboratory*. Cambridge University Press, Cambridge
- Simpson, J. E. & Britter, R. E. (1979). The dynamics of the head of a gravity current advancing over a horizontal surface. *J. Fluid Mech.*, Vol. 94, 477–495.
- Stoker, J. J. (1957). *Water waves*. Interscience Publishers Inc., New York
- Toro, E. F. (1999) *Riemann Solvers and Numerical Methods for Fluids Dynamics*. Springer, New York
- Ungarish, M. (2007a). A shallow-water model for high Reynolds number gravity currents for a wide range of density differences and fractional depths. *J Fluid Mech*, Vol. 579, 373–382
- Ungarish, M. (2007b). Axisymmetric gravity currents at high Reynolds number: On the quality of shallow-water modeling of experimental observations. *Physics of fluids*, Vol. 19, 1
- Ungarish, M. (2008). Energy balances and front speed conditions of two-layer models for gravity currents produced by lock release. *Acta Mech*, Vol. 201, 63–81
- Ungarish, M. (2009). Energy balances for gravity currents with a jump at the interface produced by lock release. *Acta Mech*, Vol. 211
- Ungarish, M. (2009b). *An introduction to gravity Currents and intrusions*. Chapman & Hall/CRC press, Boca Raton, London, New York
- Ungarish, M. (2010) The propagation of high-Reynolds-number non-Boussinesq gravity currents in axisymmetric geometry. *J Fluid Mech*, Vol. 643, 267
- Ungarish, M.; Zemach, T. (2005) On the slumping of high Reynolds number gravity currents in two-dimensional and axisymmetric configurations. *European Journal of Mechanics B/Fluids*, Vol. 24, 71–90
- Yih, C. S. (1947) *A study of the characteristics of gravity waves at a liquid interface*. M.S. Thesis, State Univ. of Iowa

# Numerical Simulation of Sediment Transport and Morphological Change of Upstream and Downstream Reach of Chi-Chi Weir

Keh-Chia Yeh<sup>1</sup>, Sam S.Y. Wang<sup>2</sup>, Hungkwai Chen<sup>3</sup>, Chung-Ta Liao<sup>1</sup>,  
Yafei Jia<sup>2</sup> and Yaoxin Zhang<sup>2</sup>  
<sup>1</sup>*National Chiao Tung University,*  
<sup>2</sup>*National Center for Computational Hydroscience and Engineering,*  
<sup>3</sup>*Water Resources Planning Institute*  
*China*

## 1. Introduction

Chi-Chi Weir was built across a mountain river, Choshui River, in Central Taiwan (Fig.1). Because of the steep bed slope, abundant upstream sediment supply and tropical typhoon climate, the morphological changes are rapid in typhoon seasons. Since its operation in 2002, the upstream and downstream reach of Chi-Chi Weir had serious sediment problems: the storage of Chi-Chi Weir could be filled up in just one significant typhoon event, and the downstream reach had serious channel incision problem (Fig.2). According to the measurements in 2003, the averaged total annual amount of sediment yield is about 14.77 million m<sup>3</sup> but only about 87% was transported to the downstream, and the capacity of the Weir loses about 1.92 million m<sup>3</sup> in a year. For the downstream channel, the main channel composed of weak bedrock is scoured seriously. Deposition only occurred over the point bars. Fig.3 shows the difference of the bed elevation between 2007 and 2004; it is seen that all the main channel has been eroded with the thalweg being eroded more than 6 m.

To evaluate and predict the trend of morphological changes in natural rivers, a user-friendly and advanced two-dimensional mobile-bed model was needed. In this chapter, a computational model, CCHE2D, was adopted to simulate and investigate the sediment transport and morphological changes of upstream and downstream reaches near the Chi-Chi Weir. The study reach is from the upstream Chilun Bridge to the downstream Minchu Bridge. Transport of both suspended load and bed load sediment with multiple grain-sizes and non-equilibrium transport conditions were simulated. In addition, the incision mechanism of soft bedrock in the downstream reach of Chi-Chi Weir was considered in the model. Simulation results were calibrated and validated with the measured data. The long-term simulation of the morphological change, other than calibration and validation cases, was also studied within the reservoir and downstream reaches, respectively. However, the long-term simulation results are not shown here.

This collaborative study was executed among National Center for Computational Hydroscience and Engineering, USA, Water Resources Planning Institute, Water Resources Agency, and National Chiao Tung University, Taiwan (Yeh et al., 2008; Zhang et al., 2009).

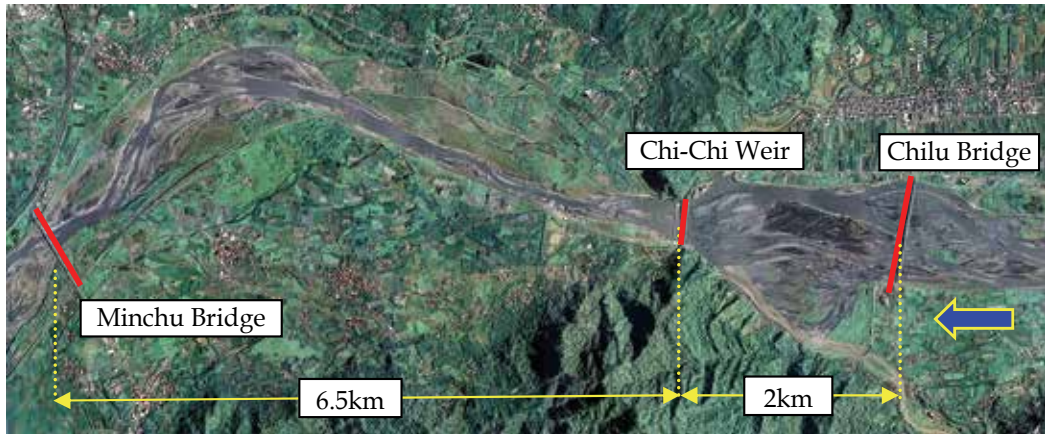


Fig. 1. Upstream and downstream reach of Chi-Chi Weir, Choshui River, Taiwan



Fig. 2. (a) Channel incision in downstream reach; (b) Sediment deposition in upstream reach

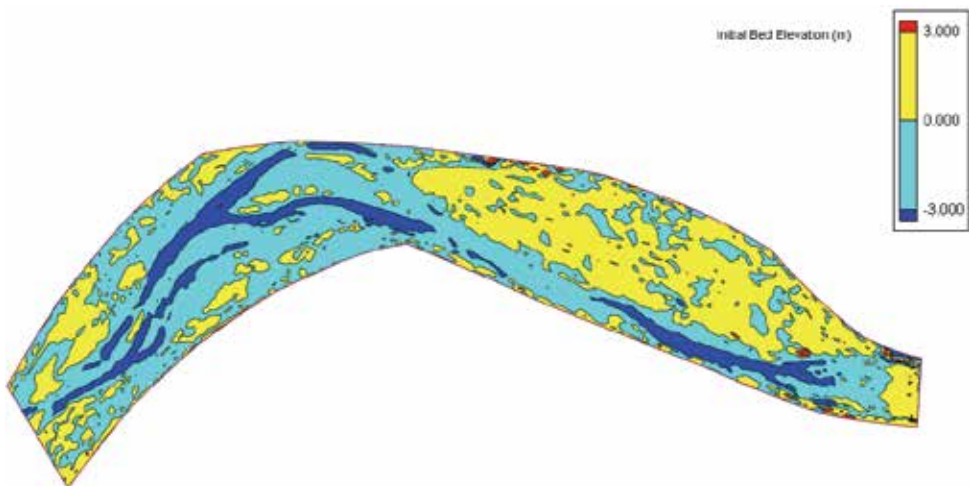


Fig. 3. Scouring and deposition pattern in the downstream channel of the Chi-Chi Weir (2004-2007)

## 2. Approaches

### 2.1 CCHE2D Hydrodynamic and sediment transport model

The CCHE2D model is a state-of-the-art numerical modeling system for two-dimensional, unsteady, turbulent river flow, sediment transport, and water quality prediction. The model is also designed for applications to multiple-process simulations in surface waters with complex geometry such as river bed and bank erosion with both uniform and non-uniform sediment and meander river migration. The model can be used for designing and evaluating the effects of the hydraulic structures, such as grade control structures, dikes, etc. The CCHE2D model uses a hybrid numerical method, the Efficient Element Method (EEM), which takes the advantages of both the Finite Element Method (FEM) and the Finite Volume Method (FVM). Depth-integrated two-dimensional equations (the continuity equation, the momentum equations, the  $k$ - $\epsilon$  turbulent equations, the sediment transport equations, etc.) are solved with multiple capabilities such as turbulent flow, wind-driven flow, tidal flow, and flow with vegetation effects (Jia and Wang, 1999, 2001a, and 2001b).

The CCHE2D model can simulate the transport of non-uniform sediment mixtures of multiple size classes with bed slope effects, secondary flow effect in curved channels, and avalanche effects. The capability of simulating the non-equilibrium sediment transport process is achieved by solving the following equations (Wu et al., 2000):

Suspended Load:

$$\frac{\partial (hC_k)}{\partial t} + \frac{\partial (UhC_k)}{\partial x} + \frac{\partial (VhC_k)}{\partial y} = \frac{\partial}{\partial x} \left( \epsilon_s h \frac{\partial C_k}{\partial x} \right) + \frac{\partial}{\partial y} \left( \epsilon_s h \frac{\partial C_k}{\partial y} \right) + \alpha \omega_{sk} (C_{*k} - C_k) \quad (1)$$

Bed Load:

$$\frac{\partial (\delta_b \bar{C}_{bk})}{\partial t} + \frac{\partial (\alpha_{bx} q_{bkx})}{\partial x} + \frac{\partial (\alpha_{by} q_{bky})}{\partial y} + \frac{1}{L_t} (q_{bk} - q_{b*}) = 0 \quad (2)$$

Bed Change:

$$(1 - p') \frac{\partial z_{bk}}{\partial t} = \alpha \omega_{sk} (C_k - C_{*k}) + (q_{bk} - q_{b*}) / L_t \quad (3)$$

where  $h$  is the local water depth,  $U$  and  $V$  are the depth-integrated velocity components in the  $x$  and  $y$  directions, respectively;  $\epsilon_s$  is the eddy diffusivity of sediment;  $C_k$  is the concentration of the  $k$ -th size class, and  $C_{*k}$  is the corresponding transport capacity;  $\alpha$  is the adaptation coefficient for suspended load;  $\omega_{sk}$  is the sediment settling velocity;  $q_{b*}$ ,  $q_{bk}$ ,  $q_{bkx}$  and  $q_{bky}$  are the bed load transport capacity, the bed load transport rate, and transport rate components in  $x$  and  $y$  directions, respectively;  $L_t$  is the adaptation length for bed load;  $p'$  is the porosity of bed material, and  $z_{bk}$  is the bed change.

The non-equilibrium adaptation length  $L_t$  characterizes the distance for a sediment process adjusting from a non-equilibrium state to an equilibrium state, which is related to the scales of sediment transport processes, bed forms and channel geometry.

## 2.2 CCHE2D bedrock model

The scouring of the bedrock is not a typical sediment transport problem because there are no sediment or bed materials on the rocky bed surface. A new capability has to be developed to handle this process. The research of Sklar and Dietrich (2001, 2004) is adopted, and a computer simulation module is developed to be integrated into the CCHE2D model.

Based on laboratory experiments, Sklar and Dietrich (2001) studied the process of bedrock abrasion by moving sediment particles. It was found that:

- The erosion rate decreases with the increase of the tensile strength of the bedrock.
- The erosion rate increases with the mass of the sediment particles; it will then decrease after a maximum value of the sediment mass rate has been reached. When sediment mass is low, its increase will add more particles to abrade the bed. After the maximum is reached, further increase of sediment will tend to cover the bed and thus reduce the erosion rate.
- The erosion rate will increase if the sediment particles are harder than the bed rock.

An empirical relation of the abrasion rate has been proposed later (Sklar and Dietrich, 2004), and it can be expressed as:

$$E = \frac{q_s w_{si}^2 Y}{L_s k_v \sigma_T^2} \left(1 - \frac{q_s}{q_t}\right) \quad (4)$$

where  $w_{si}$  = impact velocity of sediment particles (m/s),  $L_s$  = saltation length of sediment particles (m),  $q_s$  = sediment supply per unit width (kg/m/s),  $q_t$  = sediment transport capacity (kg/m/s),  $Y$  = Young's modulus of elasticity of bedrock (Pa),  $\sigma_T$  = tensile strength of the rock (Pa), and  $k_v$  = rock strength parameter (-).

The saltation length is expressed by an empirical equation:

$$\frac{L_s}{D_s} = 8 \left(\frac{\tau}{\tau_c} - 1\right)^{0.88} \quad (5)$$

And it is modified with a factor to account for the effect that the particle hop length grows rapidly as shear velocity  $u_*$  (m/s) approaches the particle fall velocity,  $w_f$  (m/s):

$$\frac{L_s}{D_s} = 8 \left(\frac{\tau}{\tau_c} - 1\right)^{0.88} \left[1 - \left(\frac{u_*}{w_f}\right)^2\right]^{-0.5} \quad \frac{u_*}{w_f} < 1 \quad (6)$$

The saltation length becomes infinite when  $u_* \rightarrow w_f$ .

where  $\tau$  = shear stress over the bed (Pa),  $\tau_c$  = sediment critical entrainment shear stress, and  $D_s$  = sediment particle size (m). The impact velocity of sediment particles on the bed is formulated as

$$w_{si} = 2w_{sd} = 0.8 \left[ \left(\frac{\rho_s}{\rho} - 1\right) g D_s \right]^{0.5} \left(\frac{\tau}{\tau_c} - 1\right)^{0.18} \left[1 - \left(\frac{u_*}{w_f}\right)^2\right]^{0.5} \quad (7)$$

where  $w_{sd}$  = sediment particle descendent velocity (m/s),  $\rho_s, \rho$  = sediment and water density (kg/m<sup>3</sup>), and  $g$  = gravitational acceleration (m/s<sup>2</sup>).

It assumes that there is no erosion of the bedrock by rolling bed load sediment particles, and the sediments are totally suspended. These two assumptions are not fully consistent with the experiment and field observation that even clear water could erode the soft bedrock. In sediment transport research, the criterion,  $u_* \rightarrow w_f$ , is generally considered as the initiation of sediment suspension rather than the complete suspension.

### 3. Simulation of sedimentation process upstream of the Chi-Chi Weir

#### 3.1 Mesh generation

A computational mesh (40 × 161) was generated using CCHE-MESH based on the measured cross sectional data in Oct. 2004. The measured cross sections are much finer in vertical resolution, which are more accurate and reliable than the DEM data, so the cross sections were used to interpolate the bed elevation for the computational meshes. Since the cross sections are not fine enough horizontally, special refinement treatment was performed for all the cross sections. The refinement is based on the interpolation between cross sections in the estimated flow direction. The mesh was extended about 140m upstream of Chilu Bridge (Fig. 4).

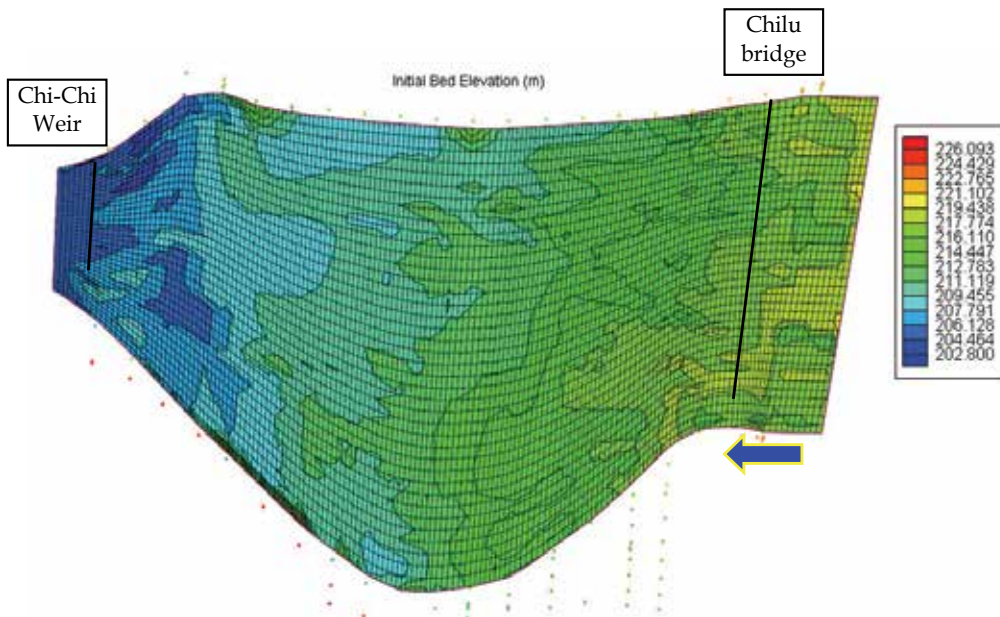


Fig. 4. Computational mesh with Oct. 2004's bed elevation as the initial condition

#### 3.2 Bed material and grain size

Bed samples obtained in July 2004 are used as initial bed composition within the reservoir. Table 1 and Table 2 list the representative grain sizes, in this study six size classes were selected to simulate the sediment transport upstream of Chi-Chi Weir. The location of the bed samples within the computational domain is shown in Fig.5.

Size Classes (mm)	Lower Limit (mm)	Upper Limit (mm)
0.0272	0.001	0.074
0.297	0.074	0.59
2.38	0.59	4.76
9.52	4.76	19.1
152	19.1	305
457	305	610

Table 1. Size classes in model

Sample	Class-1	Class-2	Class-3	Class-4	Class-5	Class-6
1	0.28	0.72	0.00	0.00	0.00	0.00
2	0.00	0.00	0.00	0.14	0.41	0.45
3	0.00	0.00	0.27	0.215	0.465	0.05
4	0.00	0.00	0.11	0.12	0.40	0.37
5	0.00	0.00	0.17	0.16	0.47	0.20
6	0.00	0.00	0.15	0.115	0.395	0.34

Table 2. Compositions of bed samples

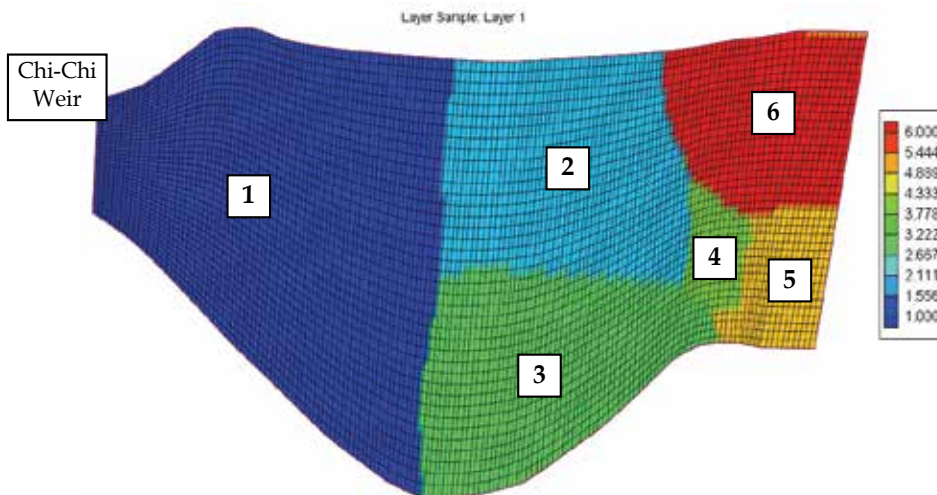


Fig. 5. Location of bed samples in July 2004

### 3.3 Boundary conditions

The typhoon events from August 2004 to June 2008 were selected to calibrate and validate the model (see Fig. 6). The sediment hydrograph data was obtained according to the relationship between the flow discharge and the sediment concentration. Since the Chi-Chi Weir is at the downstream boundary, the rating curve was used instead of stage hydrograph (see Fig. 7).

Although the suspended load transport is dominant within the reservoir, the bed load is also important. It is assumed that there is a small amount of the bed load coming from upstream of Chiluh Bridge. The bed composition data measured at CS 121 (Chiluh Bridge) is considered as the composition of the bed load. The composition of suspended sediment at Chiluh Bridge is shown in Fig. 8.

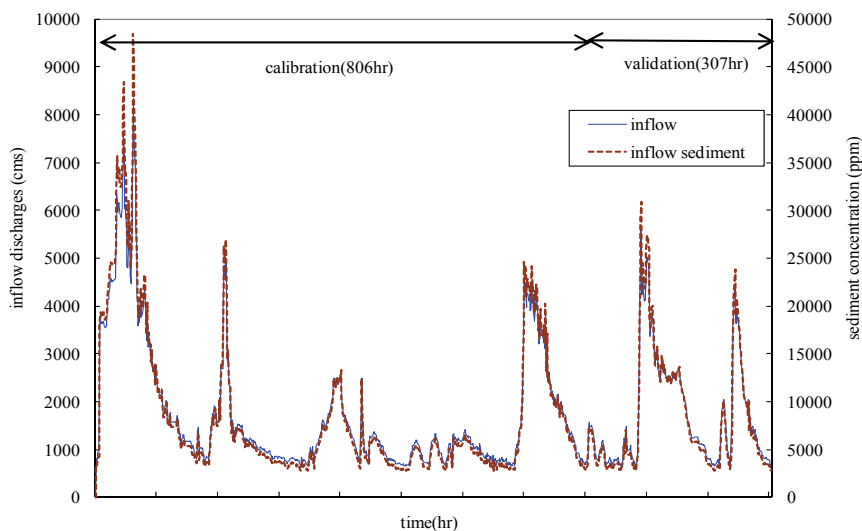


Fig. 6. Typhoon events from August 2004 to June 2008 (upstream boundary conditions)

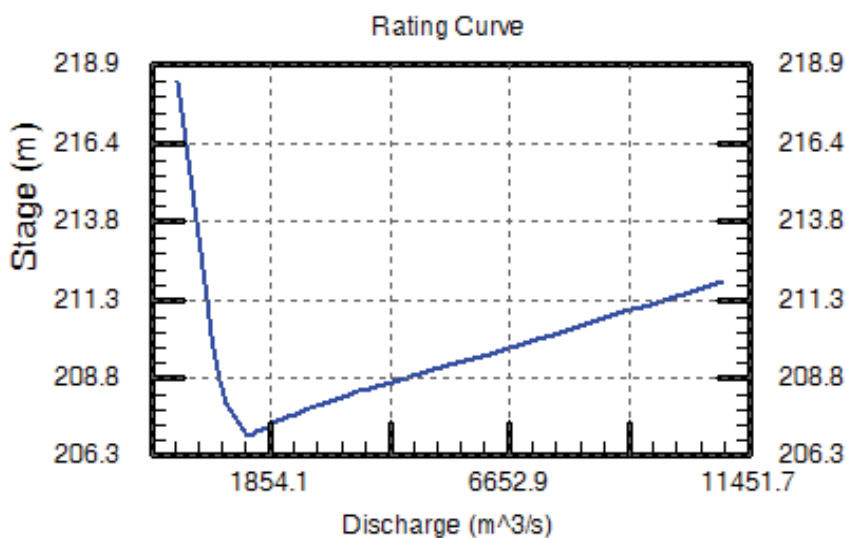


Fig. 7. Q-H rating curve at Chi-Chi Weir (downstream boundary condition)

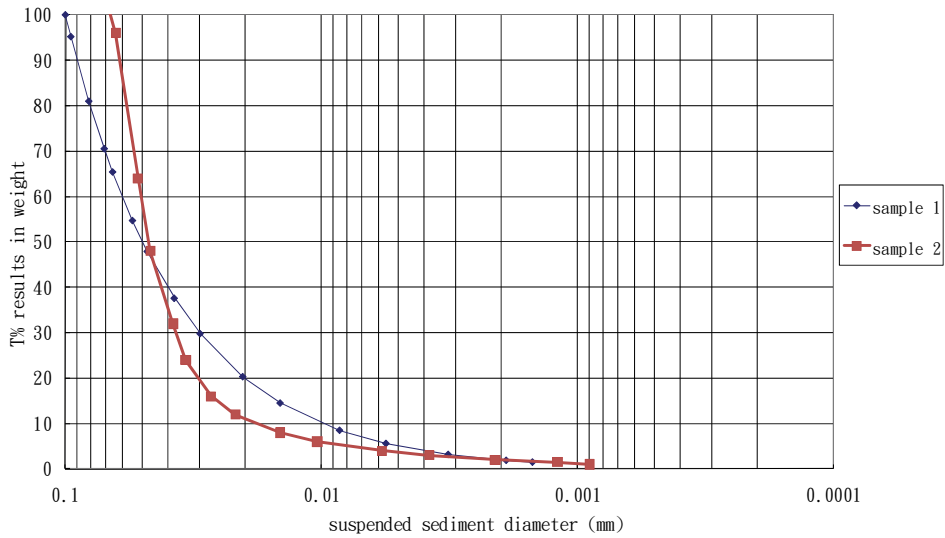


Fig. 8. Composition of suspended sediment at Chilú Bridge

### 3.4 Simulation results

The bed elevation was interpolated onto the computational mesh using the topographic data of Oct. 2004 and Jan. 2007, respectively. Fig. 9 shows the comparisons of the bed elevation change in this period (from 2004 to 2007). A large erosion area (A) was observed on the delta where deposition usually occurs, which was caused by extensive dredging in the simulation period. The delta with fine sediment extended further downstream toward the Weir site and formed two large depositions (B and C) which stopped a few hundred meters from the Weir. A scour hole (D) appeared immediately behind the Weir, which could be caused by three dimensionality of the flow and associated sediment transport.

The model was calibrated using the bed topography of Oct. 2004, the flow and sediment hydrograph from July 2004 to June 2006. Sensitivity studies were performed on the following main model parameters: (1) Ratio of bed load and suspended load (90% suspended sediment, 10% bed load; 95% suspended sediment, 5% bed load; and, 99% suspended sediment, 1% bed load); (2) Bed load adaptation length  $L_t$  (= 1000m, 1500m, 2000m, and 3000m); (3) Suspended load adaptation coefficient  $\alpha$  (= 0.01, 0.015, and 0.02); and, (4) Bed roughness  $n$  (= 0.04, 0.032, and 0.025). According to the simulation tests, 95% suspended load and 5% bed load produced more reasonable results, and the combination of bed roughness, bed load adaptation length and suspended load adaptation coefficient ( $L_t = 3000\text{m}$ ,  $\alpha=0.01$ , and  $n = 0.025$ ) produced the best results.

Fig. 10 shows the final flow field and the water surface level, and Fig. 11 shows the peak flow field and water surface level. When the flow discharge was low, large dry areas over the delta appeared. In the erosion zone A, the simulated results show slight depositions; in the deposition zones B and C, the model under-estimated the depositions; in the deposition zone E, under-estimated results were observed as well; the model predicted two scour holes instead of one in zone D; and, in deposition zone F, the simulation agrees well with the measurements.

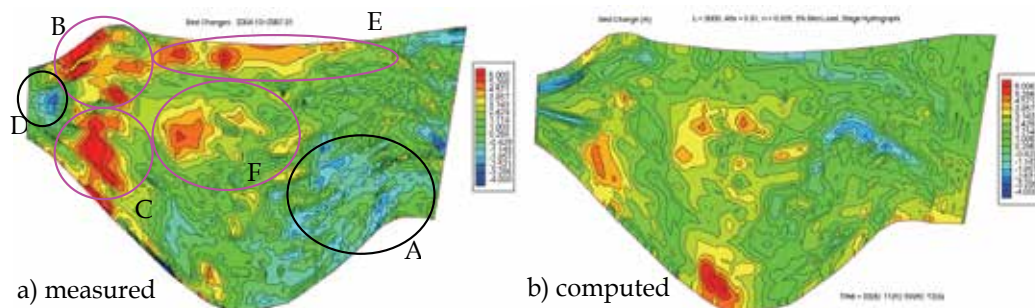


Fig. 9. Measured and computed bed changes

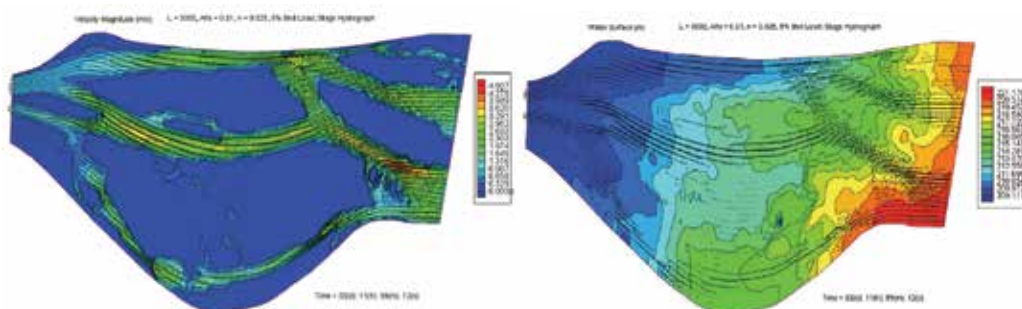


Fig. 10. Simulated flow field and water surface level

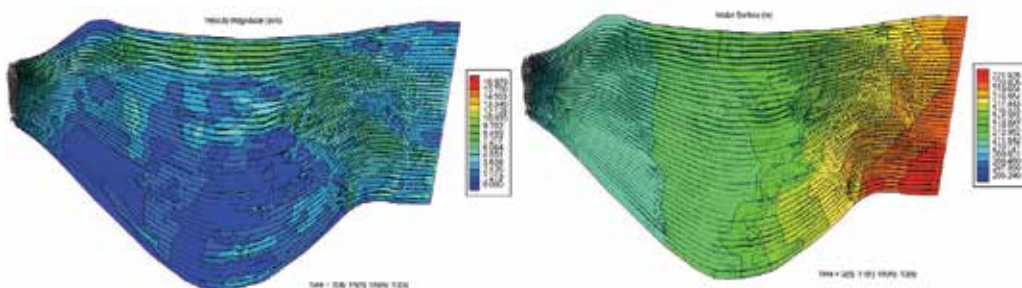


Fig. 11. Peak flow field and water surface level

Fig. 12 and Fig. 13 show the cross sections where the simulated bed elevations are compared with those measured in Oct. 2004 and Jan. 2007. For CS 1~4, the simulated results basically showed good agreements with the measurements except some small scour holes; for CS 5~10, the simulated results under-predicted the large erosions over the delta dredging area (zone A, Fig. 9); for CS 11~15, the simulation correctly predicted depositions, but underestimated near the right bank and over-estimated near the left bank; for CS 16~19, the simulated results under-estimated the depositions; and, for CS 20, the large scour hole in front of the Weir was not predicted well.

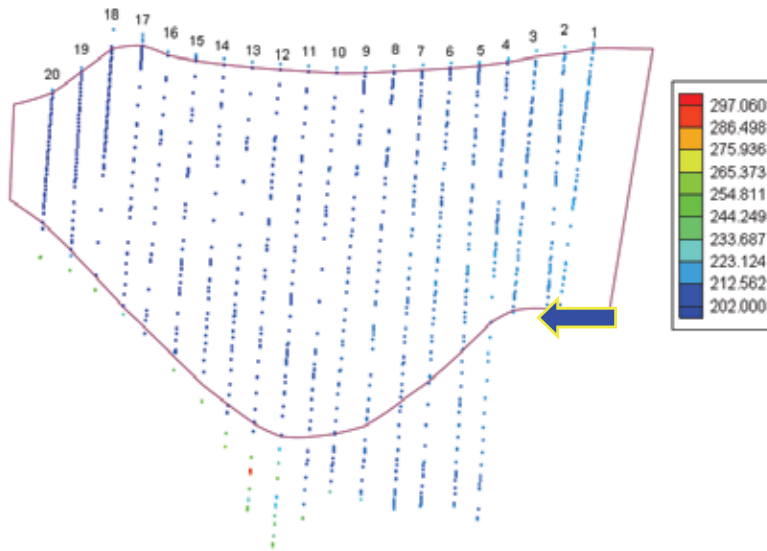
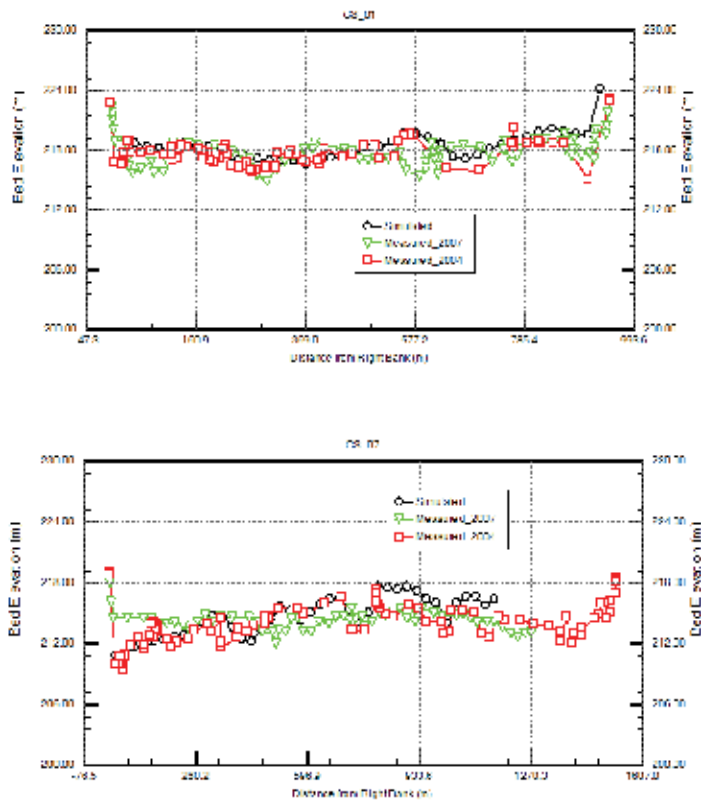


Fig. 12. Location of cross sections



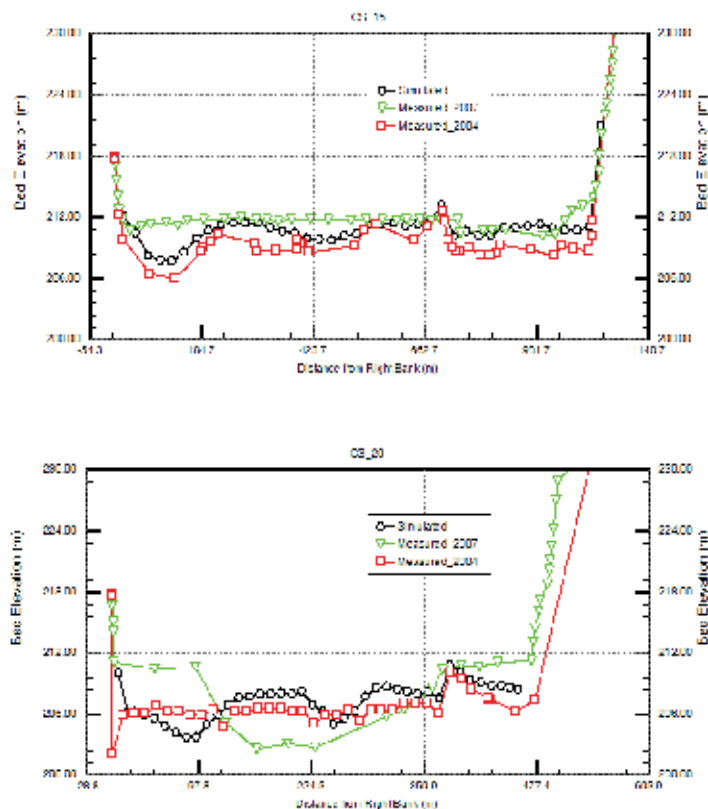


Fig. 13. Comparisons of cross sections

#### 4. Simulation of the bedrock scouring process downstream of the Chi-Chi Weir

In the channel downstream of the Chi-Chi Weir, the bedrock channel has been eroded significantly. The scour depth has reached as much as 10 m. A field inspection indicated that the bedrock was covered by a thin layer of coarse bed material before the Weir's operation; the bedrock scour started after this layer of bed material was washed away. Fig. 14 shows the scoured bed, floodplain with thin armor layer and the point bars. The erosion is mainly concentrated in the main channel, and the point bars nearby has slight deposition. From the field inspection and photos taken in the past, there is no deposition over the bare bedrock. The flow and the sediment just pass over the bedrock bed, and result in channel incision. The CCHE2D model was applied to simulate the bedrock scouring process. The same typhoon events from August 2004 to June 2008 as in the upstream study were selected to calibrate and validate the model. Since this is a site specific problem, new model capabilities have to be developed to handle the special need for rock scouring mechanism. A new computational module was developed and integrated into the CCHE2D model.



Fig. 14. Scoured channel bed downstream of the Chi-Chi Weir

#### 4.1 Mesh generation

The cross sectional data in 2004 was used to generate the computational mesh, which was then used to simulate the flow, sediment transport and bedrock incision. A computational mesh (29 x 131) was generated using CCHE-MESH (Fig.15). The study reach was from upstream Chi-Chi Weir to downstream Minchu Bridge.

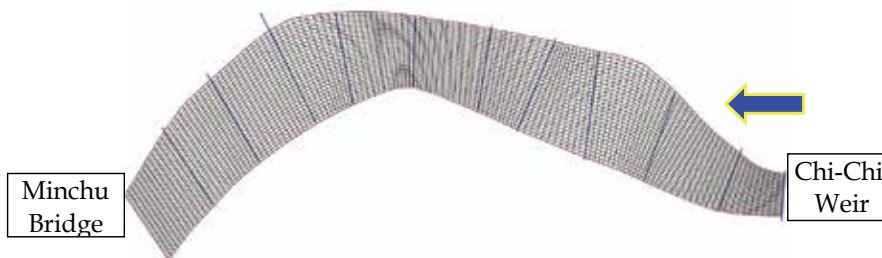


Fig. 15. Computational mesh in the channel downstream of the Chi-Chi Weir

#### 4.2 Simulation results

Fig. 16 indicates the computed water depth in the channel overlaid with the velocity vectors. Due to the complex topography and the unsteady flow, a special wetting and drying treatment technique was used, and the mass conservation of the solution is good. This can be checked easily with steady cases by integrating the flow mass flux along the channel. In the areas where dry elements exist among wet ones, the mass conservation could not be preserved as good as in the mean channel. The influence of the dry-wet elements on the momentum conservation is similar to that on the mass conservation.

In Fig. 17, the measured and the computed bed elevation changes were compared. The overall pattern of bed change is similar to what has been observed. The bedrock channel incision pattern agrees with the data better than that of the deposition over the point bars,

because only flows with high peak discharges were able to pass over the floodplains. Apparently, the erosion rate of the bedrock in the channel downstream of the Chi-Chi Weir is substantially larger than those used in the experiment (Sklar and Dietrich, 2001, 2004). The developed bedrock erosion model and the calibrated model parameters were validated using the observed flows and estimated sediment loads in the period from Jan. 2007 to June 2008. It was assumed that 90% of the sediment entering the downstream channel was in the form of suspended load, and 10% was bed load. This ratio is the same as that used in the case of calibration. The simulated erosion over the bedrock ranges from 1.0 to 2.2 meters with the larger erosion appearing near the Weir site (see Fig. 18). The largest erosion (about 3.2 m) is very close to the Weir, but the associated eroded area is small.

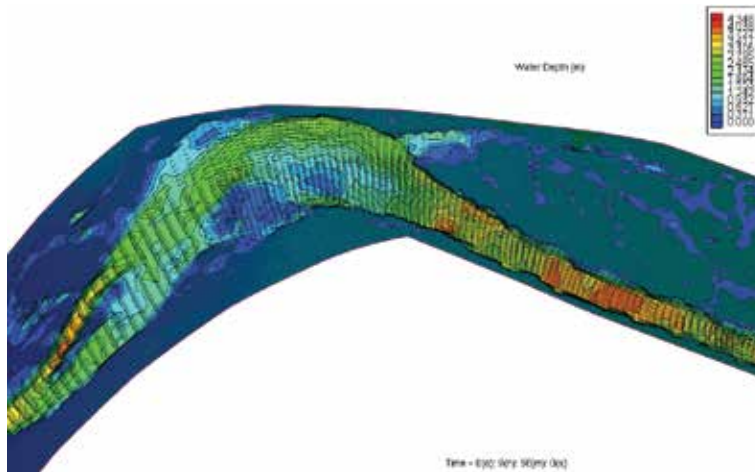


Fig. 16. Computed water depth and velocity field

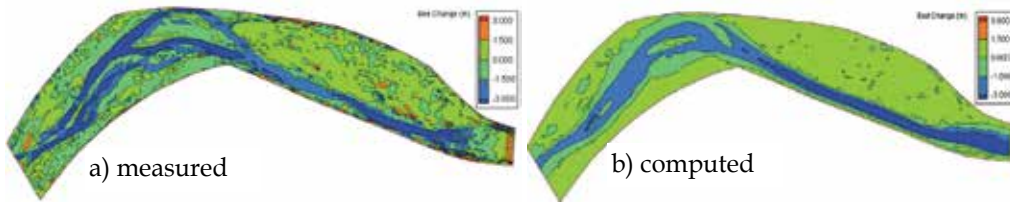


Fig. 17. Measured and computed bed changes (calibration case)

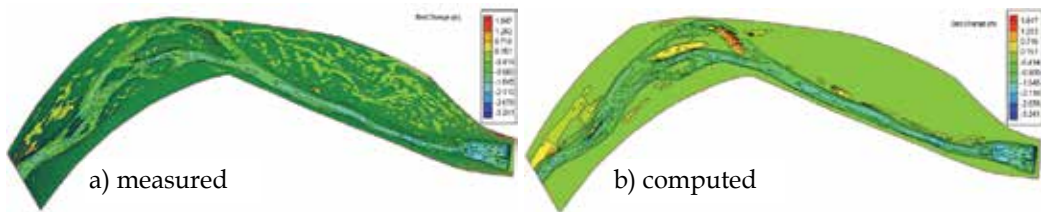


Fig. 18. Measured and computed bed changes (validation case)

Fig. 19 indicates the location of the measured cross sections. Fig. 20 compares the measured and computed cross sections. It can be seen that the simulation over-predicted erosion upstream of section 15, which might be due to the low horizontal resolution of the cross sectional data measured in 2008.

The agreement among sections 15 to 21 is better. Some cross sections agree well although the channel geometry and bed conditions are complicated. Downstream of the section 25, the calculation seems to over-predict the erosion somehow.

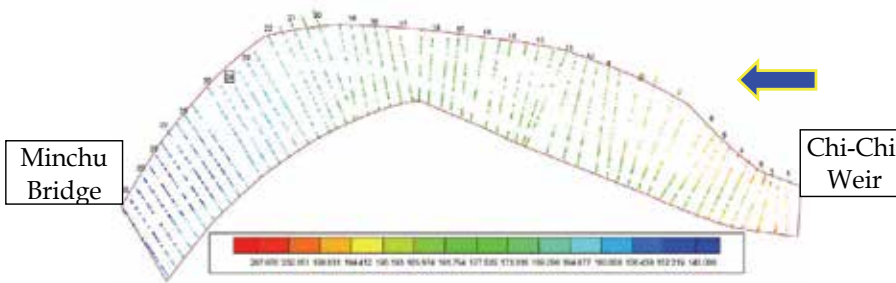
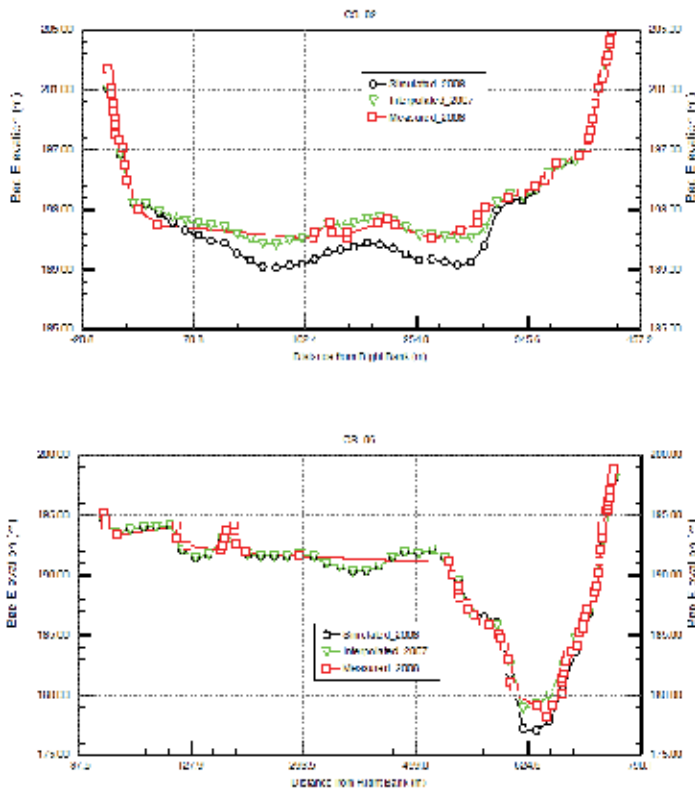


Fig. 19. Location of cross sections



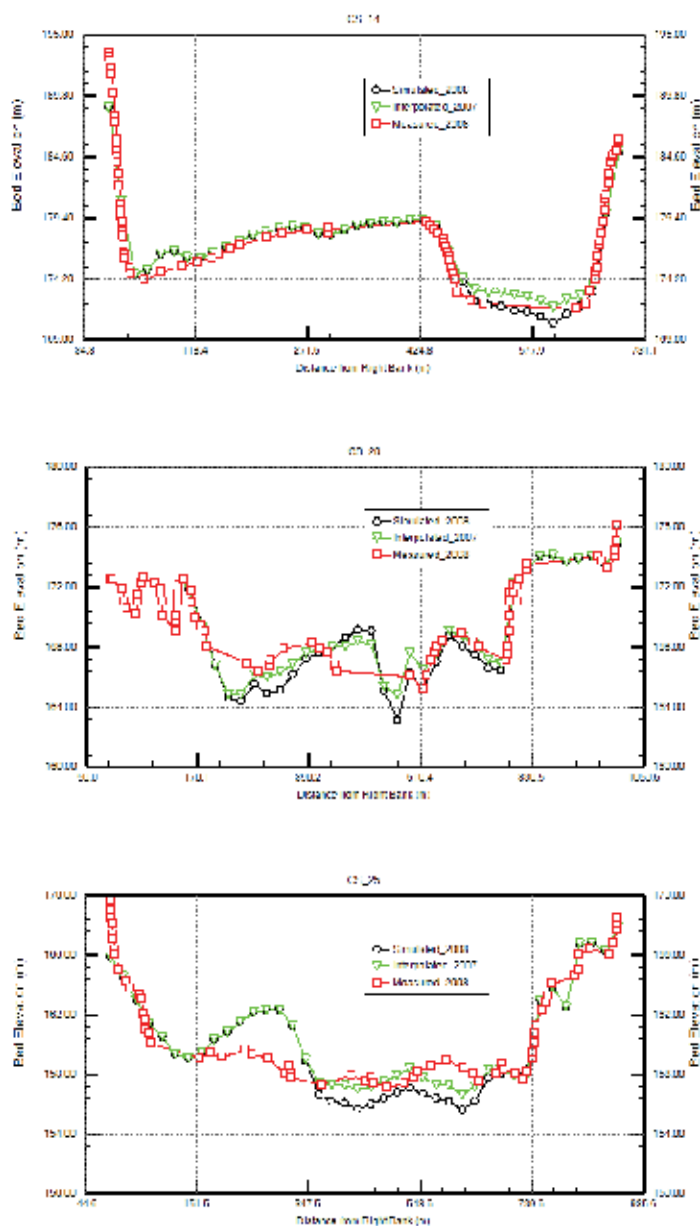


Fig. 20. Comparisons of the bed measured and computed cross-sections

### 5. Conclusions

The CCHE2D model was used to simulate the sediment transport and the bed morphological changes in the upstream and downstream reach of Chi-Chi Weir in Choshui River, Taiwan. The model has been modified to handle the bedrock erosion which was

feasible and applicable to the field engineering problem. Following conclusions are made according to the analysis of simulated results and measurements:

- Morphological changes occurred mainly during big flood events. Erosions are near the inlet and in front of the Weir. More depositions are distributed in the lower part of the reservoir, and near the right (north) bank.
- The model has been modified to handle the bedrock erosion and representing different erosion control structures. The bedrock erosion formula was modified to be feasible and applicable to the field engineering problem.
- Generally, the trend of the simulated bed change agreed with the observed pattern, but differences remain obviously. In the case of upstream Chi-Chi Weir, the model under-predicted a large scour hole close to the Weir and large erosions over the delta which are partially affected by the unknown amount of dredging. The scour hole in front of the Weir could be due to the three dimensionality of the flow and sediment transport, which could be solved better with a 3D model.
- The CCHE2D model is capable of simulating sediment transport and morphological changes within the study reach with unsteady boundary conditions for the flow and sediment. The wetting and drying treatment technique of the model makes simulations with complex morphology very efficient.
- The uncertainty of the data such as channel bed topography, sediment load, its composition and bed material composition may affect the prediction accuracy of the numerical model.

## 6. References

- Jia, Y. & Wang, S.S.Y. (1999). Numerical model for channel flow and morphological changes studies, *ASCE J. Hydraulic Engrg*, 125(9): 924-933.
- Jia, Y. & Wang, S.S.Y. (2001a). CCHE2D: Two-dimensional Hydrodynamic and Sediment Transport Model for Unsteady Open Channel Flows Over Loose Bed, *Technical Report*, NCCHE-TR-2001-1, Aug. 2001.
- Jia, Y. & Wang, S.S.Y. (2001b). CCHE2D Verification and Validation Tests Documentation, *Technical Report*, NCCHE-TR-2001-2, Aug. 2001.
- Sklar, L.S. & Dietrich, W.E. (2001). Sediment and rock strength controls on river incision into bed rock, *Geological Society of America, Geology*, 29(12): 1087-1090.
- Sklar, L.S. & Dietrich, W.E. (2004). A mechanistic model for river incision into bedrock by saltating bed load, *Water Resources Research*, Vol. 40, W06301, P:1-21.
- Wu, W., Wang, S. S. Y. & Jia, Y. (2000). Nonuniform sediment transport in alluvial rivers, *J. Hydraul. Res.*, Vol. 38, 2000, No. 6: 427-434.
- Yeh, K.C., Wang, S.S.Y., Jia, Y.F., Zhang, Y.X., Liao, C.T., & Lien, H.C. (2008). Implement and Application Study of NCCHE's River Migration Models (2/3), *Technical Report*, WRPI, 978-986-01-6377-3, Taiwan (in Chinese).
- Zhang, Y.X., Jia, Y.F., Yeh, K.C., Liao, C.T., & Wang, S.S.Y. (2009). Numerical simulation of sediment transport and morphological change of Jiji Weir Reservoir, *World Environmental & Water Resources Congress, ASCE-EWRI*, May 17-21, Kansas City, Missouri.

# Model for Predicting Topographic Changes on Coast Composed of Sand of Mixed Grain Size and Its Applications

Takaaki Uda<sup>1</sup> and Masumi Serizawa<sup>2</sup>

<sup>1</sup>*Dr. Eng., Executive Director, Public Works Research Center,  
1-6-4 Taito, Taito-ku, Tokyo 110-0016,*

<sup>2</sup>*Coastal Engineering Laboratory Co., Ltd., 301, 1-22 Wakaba, Shinjuku, Tokyo 160-0011  
Japan*

## 1. Introduction

In beach nourishment, predicting the changes in the longitudinal profile is important for estimating the effect of nourishment. When material composed of not only coarse sand but also fine sand is used in beach nourishment, a considerable amount of fine sand may be lost owing to offshore sand transport by waves, depending on the conditions of the beach slope. On the basis of the contour-line-change model proposed by Serizawa et al. (2003), which was derived using the concept of the equilibrium slope (Bakker, 1968), Uda et al. (2004) developed a model for predicting the change in the longitudinal profile as well as the change in the grain size distribution. Then, the model was applied to the results of the movable bed experiment using a large wave tank, in which the model beach was composed of sand of mixed grain size, to evaluate the model applicability (Fukuhama et al., 2007). The experimental results showed that sand of mixed grain size was sorted into fine and coarse sand, and that coarse sand was transported shoreward, forming a berm, whereas fine sand sunk to a zone deeper than the depth of closure. Although the experimental and predicted results were in good agreement in this application, the applicability of the model to the coasts was still inadequate. Therefore, the model was applied to the following two model cases: beach changes associated with the beach nourishment using fine and coarse materials on the Chigasaki coast in Kanagawa Prefecture, Japan (Yoshioka et al., 2008), and the formation of a 'conveyer belt' composed of gravel and fine sand observed on the Shimizu coast (Nishitani et al., 2008). In this paper, these applications of the model are summarized and the effectiveness of the model is shown.

## 2. Numerical model

A typical example of the grain size sorting is found at Pebble Beach in Cardiff, UK, where gravel accumulates and forms a gravel layer near the shoreline with the offshore bed being composed of only fine sand, as shown in Fig. 1 (Uda et al., 2004). The original concept of a model for predicting the changes in the longitudinal profile and grain size distribution was obtained from this observation.



Fig. 1. Sorting of grain size at Pebble Beach in Cardiff, UK, where gravel accumulates and forms gravel layer near shoreline

Consider a longitudinal profile and set the equilibrium slopes of gravel and fine sand as  $\tan \beta_1$  and  $\tan \beta_2$ , respectively, as shown in Fig. 2. When sand of mixed grain size is supplied to a beach with an initial slope of  $\tan \theta$ , cross-shore sand movement occurs; thus, the slopes of coarse and fine sand materials tend to approach  $\tan \beta_1$  and  $\tan \beta_2$ , respectively. In this case, the landward limit of beach changes is determined by the berm height,  $h_R$ , whereas in the offshore zone, sand is transported until the depth of closure,  $h_C$ , beyond which sand falls into a deeper zone while maintaining the repose angle of sand,  $\tan \gamma$ .

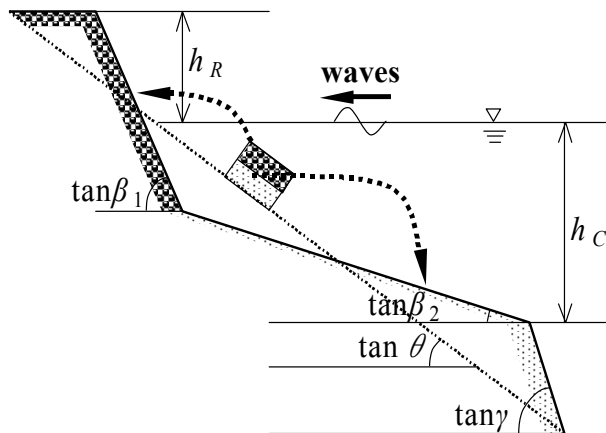


Fig. 2. Schematic diagram of concept of equilibrium slope corresponding to each grain size

Using the above concept, a numerical model was developed on the basis of the contour-line-change model proposed by Serizawa et al. (2003). Let the  $x$ - and  $z$ -axes be the longshore distance and depth, respectively, and  $Y$ , the offshore distance to a specific contour line. To consider the sorting of sand of different grain sizes by cross-shore sand transport, the depth distribution of cross-shore sand transport considering the grain size effect in mixing is required. We, therefore, expanded the cross-shore sand transport equation given by

Serizawa et al. (2003), which took into account the stabilization mechanism of the longitudinal profile, as reported by Bakker (1968).

Let  $\beta_c$  be the angle of the equilibrium beach slope at which the shoreward motion of the sand particle owing to wave action is balanced by the seaward motion due to gravity, and it is assumed that seaward sand transport occurs when angle  $\beta$  of the seabed slope exceeds  $\beta_c$ , and that shoreward sand transport occurs when angle  $\beta$  becomes smaller than  $\beta_c$ . The strength of cross-shore sand transport in restoring the equilibrium slope is assumed to be proportional to the wave energy dissipation rate per unit seabed length,  $\Phi$ , calculated as the shoreward component of energy flux at the breaking point,  $F_y$ , divided by the seabed length  $S \equiv (h_c + h_R) / \sin \bar{\beta}$ , between the depth of closure,  $h_c$ , and the berm height,  $h_R$ .  $\bar{\beta}$  is the average initial slope angle between  $h_c$  and  $h_R$ . In addition, by approximately assuming  $\beta_c$  for  $\bar{\beta}$ ,  $1/(h_c + h_R)$  is replaced by the intensity distribution function of cross-shore sand transport,  $\varepsilon_z(z)$ , which is assumed to be equivalent to the depth distribution of the longshore sand transport rate,  $\varepsilon_x(z)$ , given by Uda and Kawano (1996). Thus, this transport becomes

$$q_z = \varepsilon_z(z) \cdot K_z \cdot (EC_g)_b \cos^2 \alpha_{bs} \sin \beta_c \cdot \left( \frac{\cot \beta}{\cot \beta_c} - 1 \right), \quad (1)$$

$$\cot \beta = -\frac{\partial Y}{\partial z}. \quad (2)$$

The cross-shore transport of sand composed of mixed grain size can be modeled by expanding the concept of single grain size. The sorting of grain size populations, such as those of fine sand, medium and coarse sand, and gravel, can be modeled by introducing the equilibrium slope angle  $\beta_c^{(k)}$  which corresponds to each grain size population  $k$ . In this case, a grain size population is assumed to have a single equilibrium beach slope with a characteristic grain size  $d^{(k)}$ , for example, the median diameter of the grain size population.

By assuming that the mobility of sand of each grain size population by cross-shore movement under the same wave conditions is the same as that of longshore sand transport, the coefficient of the sediment transport rate according to the grain size  $d^{(k)}$ , which was given by Kamphuis et al. (1986) and Kumada et al. (2003), is introduced. Furthermore, assuming that the ratio of the exposed area of each grain size population to the entire sea bottom area is equal to the content of each size population in the exchange layer  $\mu^{(k)}$  (where  $k=1, 2, \dots, N$ ), the cross-shore sand transport rate of each grain size population  $q_z^{(k)}$  is derived by a method similar to that of Uda et al. (2004).

### Cross-shore sand transport

$$q_z^{(k)} = \mu^{(k)} \cdot \varepsilon_z(z) \cdot \gamma \cdot K_1^{(k)} \cdot (EC_g)_b \cos^2 \alpha_{bs} \sin \bar{\beta} \cdot (\cot \beta / \cot \beta_c^{(k)} - 1); k = 1, 2, \dots, N \quad (3)$$

$$K_1^{(k)} = \frac{A}{\sqrt{d^{(k)}}} \quad (4)$$

$$\cot \beta = -\partial Y / \partial z \quad (5)$$

$$\varepsilon_z(z) = \begin{cases} (2/h_c^3)(h_c/2 - z)(z + h_c)^2, & -h_c \leq z \leq h_R \\ 0, & z \leq -h_c, z \geq h_R \end{cases} \quad (6)$$

Here,  $q_z^{(k)}$  ( $k=1, \dots, N$ ) is the cross-shore sand transport per unit length in the longshore direction for each grain size population,  $\mu^{(k)}$  is the content of each grain size population ( $k$ ) in the exchange layer of sand,  $\varepsilon_z(z)$  is assumed to be equivalent to the depth distribution of the longshore sand transport  $\varepsilon_x(z)$  given by Uda and Kawano (1996), and  $d^{(k)}$  is a typical grain size of the grain size population.  $A$  is a coefficient that depends on the physical conditions of the beach,  $d^{(k)}$  in Eq. (4) has a unit of mm,  $\gamma$  is the ratio of the coefficient of cross-shore sand transport to the coefficient of longshore sand transport, and expresses the mobility of cross-shore sand transport relative to that of longshore sand transport,  $\alpha_{bs}$  is the angle between the wave crest line at the breaking point and each contour line, and  $\beta$  is the beach slope angle at each contour line.  $\bar{\beta}$  is the average beach slope angle between the berm height  $h_R$  and the depth of closure  $h_c$ , and  $\beta_c^{(k)}$  is the equilibrium beach slope angle. When the beach slope becomes steeper than the angle of repose of sand, sand is transported offshore by gravity. By this procedure, we can calculate the formation of a scarp in a zone larger than the berm height  $h_R$  and the sinking of sand in a zone larger than the depth of closure  $h_c$ .

### Longshore sand transport

$$q_x^{(k)} = \mu^{(k)} \cdot \varepsilon_x(z) \cdot K_1^{(k)} \cdot (EC_g)_b \cdot \left( \cos \alpha_{bs} \sin \alpha_{bs} - \xi \frac{1}{\tan \beta} \cdot \cos \alpha_{bs} \cdot \frac{\partial H_b}{\partial x} \right) \quad (7)$$

Here,  $q_x^{(k)}$  ( $k=1, \dots, N$ ) is the longshore sand transport per unit depth for each grain size population,  $\varepsilon_x(z)$  is the depth distribution of longshore sand transport, and  $\xi$  is the constant given by  $K_2^{(k)}/K_1^{(k)}$ , which depends on the physical conditions of the beach, where  $K_2^{(k)}$  is a function of  $K_1^{(k)}$  and is equivalent to the coefficient of Ozasa and Brampton (1980).  $\tan \beta$  is the beach slope in the surf zone and  $H_b$  is the breaker height.

### Mass conservation for each grain size

$$\frac{\partial y^{(k)}}{\partial t} = -\frac{\partial q_x^{(k)}}{\partial x} - \frac{\partial q_z^{(k)}}{\partial z} \quad (8)$$

$; k = 1, 2, \dots, N$

The total contour line change at a certain position is determined by the summation of the contour line changes of all grain size populations at that position.

$$\frac{\partial Y}{\partial t} = \sum_{k=1}^N \frac{\partial y^{(k)}}{\partial t} \quad (9)$$

### Change in content of each grain size population

$$\frac{\partial \mu^{(k)}}{\partial t} = \frac{1}{B} \left\{ \frac{\partial y^{(k)}}{\partial t} - \frac{\partial Y}{\partial t} \cdot \mu^{(k)} \right\} \quad (10)$$

$; k = 1, 2, \dots, N.$

The content of each grain size population in the new exchange layer formed during erosion is expressed as

$$\frac{\partial \mu^{(k)}}{\partial t} = \frac{1}{B} \left\{ \frac{\partial y^{(k)}}{\partial t} - \frac{\partial Y}{\partial t} \cdot \mu_B^{(k)} \right\}, \quad (11)$$

where  $\mu_B^{(k)}$  is the content of each grain size population on the sandy beach landward of the initial exchange layer. The width  $B$  of the exchange layer is determined with reference to the mixing depth reported by Kraus (1985). The above-mentioned equations were solved simultaneously.

### 3. Validation using experimental results

#### 3.1 Experiment using large wave tank and sand of mixed grain size

We first investigated the applicability of the present model to experiments using sand of mixed grain size, in which the changes in the longitudinal profile and cross-shore grain size distribution were investigated in a large wave tank. A movable bed experiment using sand of mixed grain size ranging widely from medium sand to silt was carried out using a 135-m-long, 2-m-wide and 5-m-deep wave tank to study the formative processes of an equilibrium beach and the grain size distribution (Meguro et al., 2005). The median diameter of grain size used was  $d_{50} = 0.62$  mm and the initial uniform slope was 1/20. Regular waves with a height of 0.6 m and a period of 3.5 s were generated for 78 h.

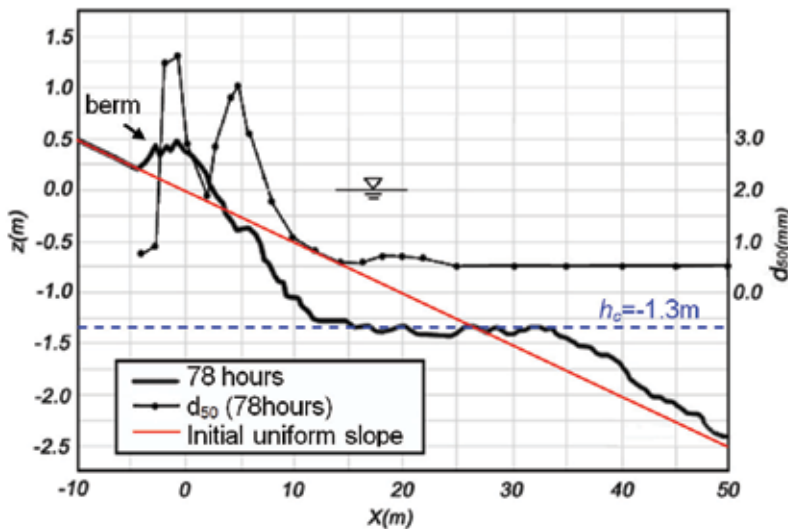


Fig. 3. Change in longitudinal profile and cross-shore distribution of  $d_{50}$  in experiment using large wave tank (Meguro et al., 2005)

Figure 3 shows the changes in the longitudinal profile and cross-shore distribution of  $d_{50}$  on the seabed. A flat seabed was formed by erosion at a depth of  $h_c = 1.3$  m on the initial uniform slope, and a steep foreshore with a slope of 1/6 was formed. The flat seabed near the depth  $h_c$  was covered with fine sand, whereas coarse sand selectively accumulated on the foreshore. From these findings, it is clear that sand of mixed grain size is sorted by wave action, with

coarse sand being deposited on the foreshore, forming a berm with a steep slope, and fine sand being transported offshore and deposited to form a gentle slope on the offshore bed.

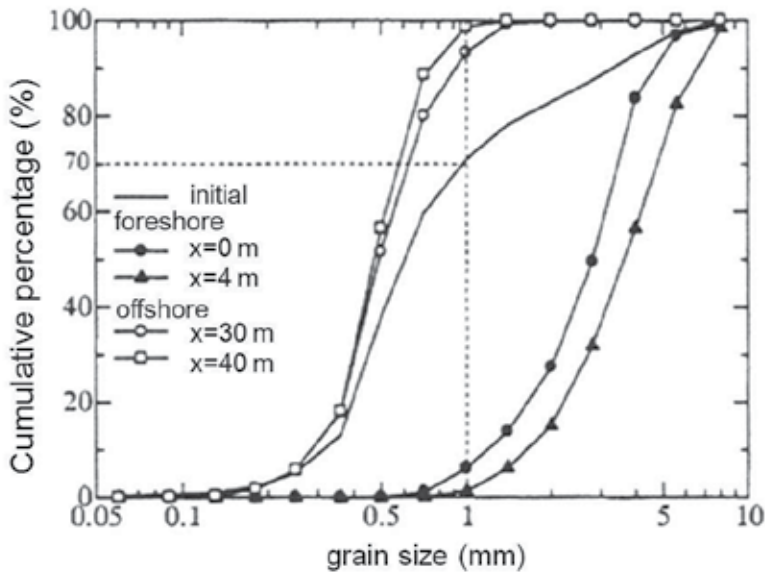


Fig. 4. Cumulative grain size distributions on foreshore and offshore beds in experiment

Figure 4 shows the cumulative grain size distributions on the foreshore and offshore beds. The grains in the foreshore and offshore zones are clearly separated into two grain size populations of grain sizes larger and smaller than 1 mm, respectively. On the basis of this result, hereafter, we simply refer to the grain size population with grain size smaller than 1 mm as fine sand and that with grain size larger than 1 mm as coarse sand. The experimental results are summarized as follows.

- Erosion occurred only in a zone shallower than the depth of closure  $h_c=1.3$  m.
- Coarse sand was transported shoreward, forming a 0.5-m-high berm and a foreshore with a slope of  $1/6$ .
- The volume of coarse sand contained in the erosion zone is limited, and the development of a berm depends on this volume of coarse sand. Although the berm height depends on the wave characteristics, a minimum volume of coarse sand is required for the development of a berm.
- Fine sand was transported to a zone deeper than  $h_c$ , and a slope of  $1/10$ , which was larger than the initial slope, was formed on the offshore bed.
- After a berm was sufficiently developed, the beach profile became stable, because the grain size on the foreshore matched the slope. The offshore flat bed near  $h_c$  also became stable because further erosion did not occur, resulting in the cessation of the offshore discharge of fine sand. Thus, the equilibrium condition is assumed to form only when a berm is sufficiently developed.

### 3.2 Calculation conditions for application to experimental results

As calculation conditions, two grain size populations with only grain sizes of  $d^{(1)}=0.45$  mm and  $d^{(2)}=3$  mm, which represent typical fine and coarse sands, respectively, and with no

overlap of the grain size distribution were assumed, because grain sorting occurred at a critical grain size of 1 mm in the experiment. These grain sizes were determined on the basis of the cumulative grain size distribution of the sand of mixed grain sizes used in the experiment; thus,  $d^{(1)}$  and  $d^{(2)}$  were approximately equal to  $d_{50}$  calculated from all the fine and coarse sand samples, respectively, and the mean grain size of all the samples  $d_m$  used in the experiment became equal to 1.21 mm.

Cases	Reproduction: $\mu^{(1)}=0.7$ and $\mu^{(2)}=0.3$ Prediction: Case 1: $\mu^{(1)}=0.1$ and $\mu^{(2)}=0.9$ Case 2: $\mu^{(1)}=0.3$ and $\mu^{(2)}=0.7$ Case 3: $\mu^{(1)}=0.5$ and $\mu^{(2)}=0.5$ Case 4: $\mu^{(1)}=0.9$ and $\mu^{(2)}=0.1$
Initial topography	Uniform slope of $\tan\beta=1/20$
Grain size	Number of grain sizes: $N=2$ Fine sand $d^{(1)}=0.45$ mm, Coarse sand $d^{(2)}=3$ mm Initial content $\mu^{(1)}=0.7$ and $\mu^{(2)}=0.3$
Width of exchange layer	$B=0.4$ m
Wave conditions	Breaker height: $H_b=0.75$ m ( $H_0=0.6$ m, $T=3.5$ s) Breaker angle: $\alpha_{bs}=0$ deg. Tide level: mean sea level
Depth of closure	$h_c=1.3$ m
Berm height	$h_R=0.5$ m
Coefficients of sand transport	$A=0.2$ and $\gamma=1.0$
Depth distribution of sand transport rate	Cubic equation given by Uda and Kawano (1996)
Equilibrium slope	$\tan\beta_c^{(1)}=1/100$ (fine sand) $\tan\beta_c^{(2)}=1/6$ (coarse sand)
Critical slope	Fine sand: $1/2$ on land and $1/10$ on seabed Coarse sand: $1/2$ on land and $1/3$ on seabed
Calculation domain	$z=+1.0$ m to $-3.0$ m
Mesh size	$\Delta z=0.1$ m
Time interval	$\Delta t=0.01$ h
Total time of calculation	$t=200$ h (20,000 steps)
Boundary conditions	$q_z=0$ at landward and offshore boundaries
Calculation method	Explicit finite difference method

Table 1. Calculation conditions

The initial content of sand was assumed to be  $\mu^{(1)}=0.7$  for fine sand and  $\mu^{(2)}=0.3$  for coarse sand, the same condition as that in the experiment. The initial beach profile is given a uniform slope of  $1/20$ , and  $h_R$  and  $h_c$  are set as  $h_R=0.5$  m and  $h_c=1.3$  m, on the basis of the experimental results. As equilibrium slopes, the gentle seabed slope composed of fine sand in the offshore zone and the steep seabed slope composed of coarse sand are given as  $\tan\beta_c^{(1)}=1/100$  and  $\tan\beta_c^{(2)}=1/6$ , respectively, with reference to the experimental results. The width  $B$  of the exchange layer is given by the thickness of the exchange layer divided by the slope. The thickness of the exchange layer is given as  $0.02$  m, which is 3% of the breaker height ( $H_b=0.75$  m), on the basis of the results obtained from the field observation by Kraus (1985), and  $B$  is set to be  $0.4$  m, obtained by dividing the exchange-layer thickness by the initial slope of  $1/20$ .

The critical slope of sinking for sand of each grain size is separately set on land and on the seabed, similarly to that in the work of Uda et al. (2004). In this study, the sinking of fine sand into the zone deeper than  $h_c$  is considered to be caused by gravity and the critical slope is given by a slope of  $1/10$ , which occurred in the experiment. In the other zone, the critical slopes are set to be  $1/2$  and  $1/3$  on land and on the seabed, respectively, as indicated by Uda et al. (2004).

The coefficient of sediment transport  $A$ , which defines the rate of beach change, was determined as  $A=0.2$  by a trial calculation, so that the numerical simulation can reproduce the development of a berm in 20 hours as in the case of the experiment. For the depth distribution of cross-shore sand transport, the same depth distribution of longshore sand transport as that in Eq. (6) given by Uda and Kawano (1996) was assumed. As the wave condition, the time-averaged breaker height taken from the observation results,  $H_b=0.75$  m, was used. Other calculation conditions, such as mesh size and time step, are shown in Table 1.

### 3.3 Results

#### 3.3.1 Comparison with experimental results

First, numerical simulation was carried out under the same conditions as those of the experiment. Figure 5 shows the change in the longitudinal profile with time for the contents of fine and coarse sand of  $\mu^{(1)}=0.7$  and  $\mu^{(2)}=0.3$ , respectively. Erosion starts from a shallow zone near the shoreline, and part of the sand is transported landward, forming a berm on the foreshore. Sand is also transported offshore, forming a small hump in the offshore zone. Figure 6 shows the measured and predicted longitudinal profiles after wave action. The results are in good agreement in terms of the formation of a berm and the flat offshore sea bottom and offshore depositions of sand. Figures 7(a) and 7(b) show the cross-shore distributions of the contents  $\mu^{(1)}$  and  $\mu^{(2)}$  corresponding to the profile changes shown in Fig. 5. The foreshore materials become only coarse sand ( $\mu^{(1)}=0$ ,  $\mu^{(2)}=1.0$ ), whereas the offshore seabed with a gentle slope becomes covered with only fine sand ( $\mu^{(1)}=1.0$ ,  $\mu^{(2)}=0$ ). As a result, the cross-shore distribution of the mean grain size shown in Fig. 8 is obtained. The grain size is large at  $3.0$  mm on the steep slope of the foreshore and on the berm, whereas on the offshore seabed, it becomes as small as  $0.5$  mm. These results correspond well to the cross-shore distribution of  $d_{50}$ , as shown in Fig. 3.

In conclusion, the changes in the longitudinal profile in the experiment were accurately reproduced in the numerical model. It was found that fine and coarse sands are sorted on model beaches composed of sand of mixed grain size, and that coarse and fine sands are transported shoreward and offshore, respectively, finally approaching the equilibrium slope corresponding to each grain size population.

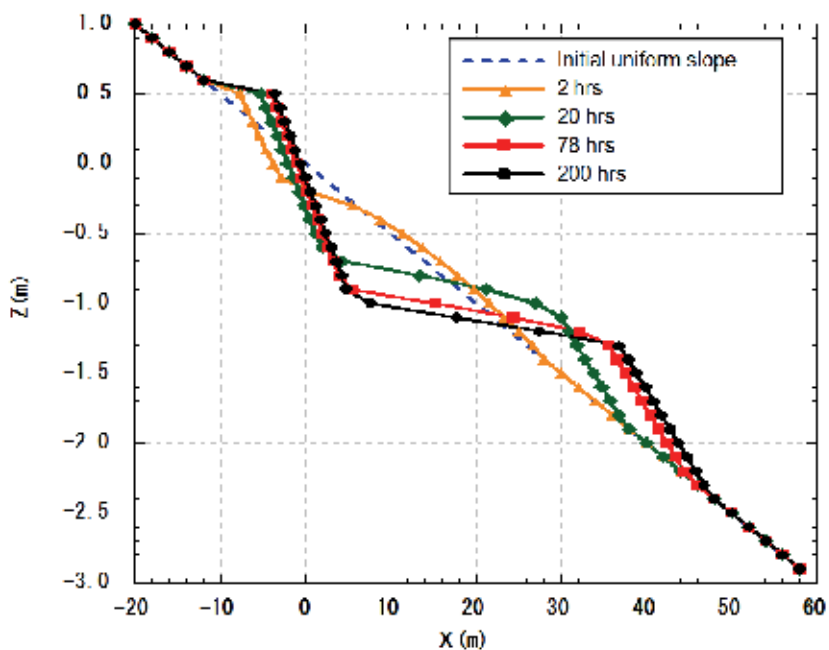


Fig. 5. Change in longitudinal profile with time for contents of fine and coarse sand of  $\mu^{(1)}=0.7$  and  $\mu^{(2)}=0.3$ , respectively

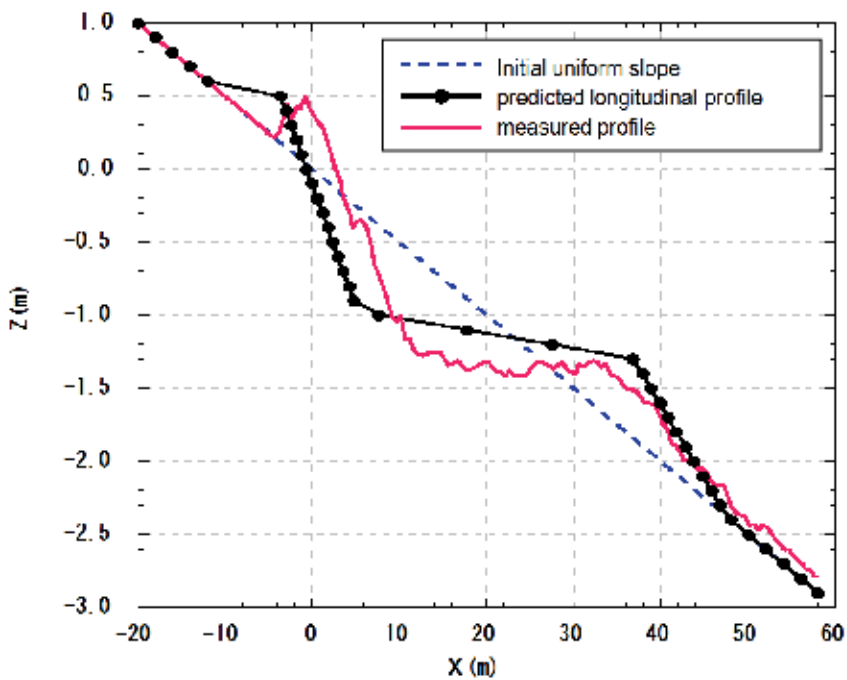


Fig. 6. Measured and predicted longitudinal profiles after wave action

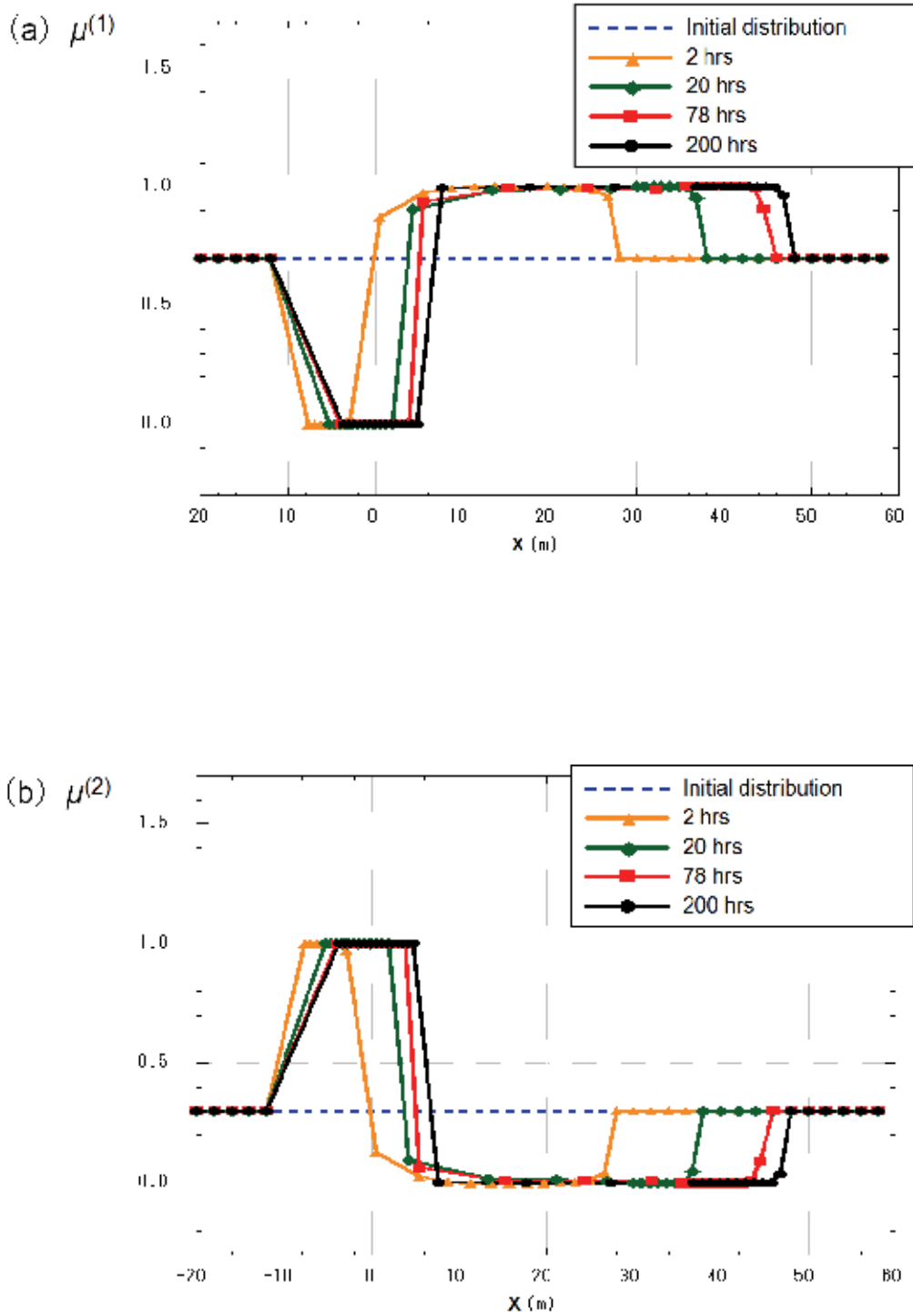


Fig. 7. Cross-shore distributions of contents  $\mu^{(1)}$  and  $\mu^{(2)}$  of fine and coarse sand, respectively

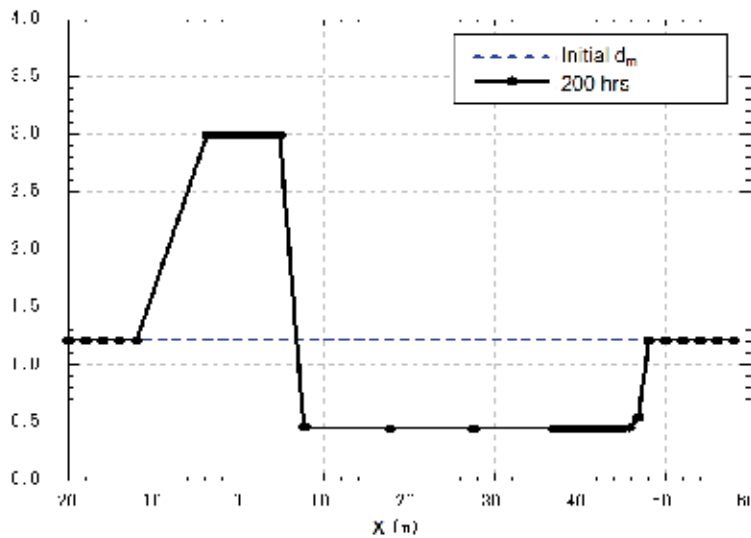


Fig. 8. Cross-shore distribution of mean grain size

### 3.3.2 Changes in initial content and equilibrium profile

The effect of the difference in the initial contents on the final, stable profile can be investigated, assuming the initial contents of fine and coarse sand are  $\mu^{(1)}=0.3$  and  $\mu^{(2)}=0.7$ , respectively. Figure 9 shows the results. As a result of the increase in the content of coarse sand, the volume of sand transported shoreward increased compared with that in the case shown in Fig. 5, and a berm predominantly developed. In contrast, a smaller volume of sand was transported offshore.

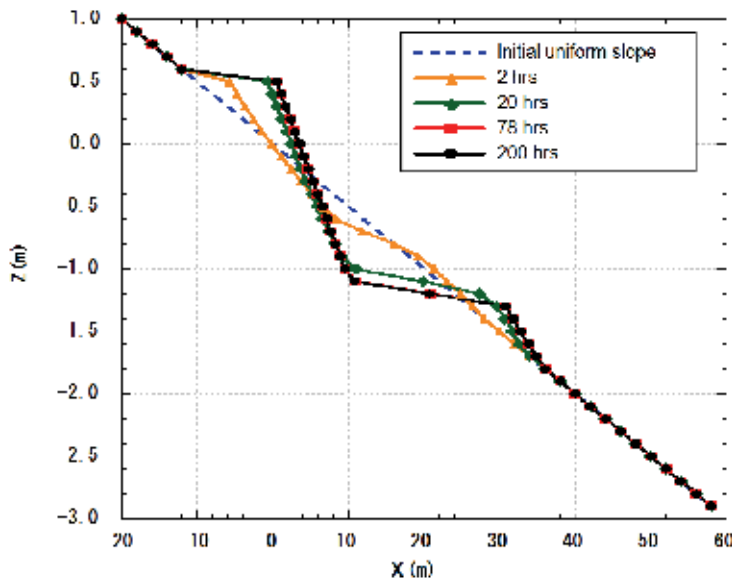


Fig. 9. Predicted changes in longitudinal profile when  $\mu^{(1)}$  and  $\mu^{(2)}$  are 0.3 and 0.7, respectively

Figure 10 shows the final, stable profiles in the cases where the initial contents ( $\mu^{(1)}, \mu^{(2)}$ ) were altered to (0.9, 0.1), (0.5, 0.5), (0.3, 0.7) and (0.1, 0.9), as well as the result of the reproduction case with (0.7, 0.3). A larger berm develops with the increase in the content of coarse sand,  $\mu^{(2)}$ . In contrast, a smaller berm develops with the increase in the content of fine sand,  $\mu^{(1)}$ , and offshore sand transport becomes dominant, accelerating the deposition of fine sand in the offshore zone. Thus, the grain size has a marked effect on the changes in the longitudinal profile. On a beach composed of only fine sand, offshore sand transport from the initial stage never converges and an equilibrium profile cannot be attained. The equilibrium profile is formed in the wave flume experiment only when a sufficient volume of coarse sand is available to cover the foreshore and to form a berm.

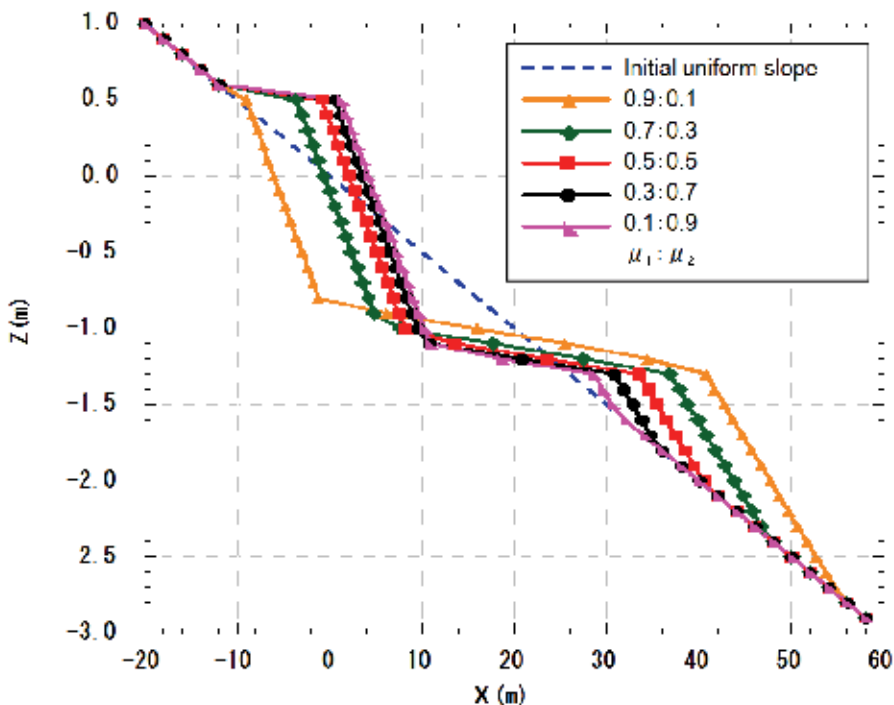


Fig. 10. Final, stable profiles in cases where initial contents ( $\mu^{(1)}, \mu^{(2)}$ ) are altered to (0.9, 0.1), (0.5, 0.5), (0.3, 0.7) and (0.1, 0.9), as well as result of reproduction case with (0.7, 0.3)

#### 4. Application of model to prediction of beach changes after nourishment at Chigasaki coast

##### 4.1 General conditions of Chigasaki coast

On the Chigasaki coast, which is located in Sagami Bay in Japan, beach erosion has been severe. The main causes of beach erosion are the decrease in fluvial sand supply from the Sagami River, triggered by the construction of several dams in the upstream basin, and the obstruction of longshore sand transport by the Chigasaki fishing port, located east of the river mouth (Fig. 11). As a measure against beach erosion, an artificial headland was built in 1991 and beach nourishment has been carried out since 1991. To significantly improve the coastal conditions, beach nourishment at a rate of  $3 \times 10^4 \text{ m}^3/\text{yr}$  has been planned with the

aim of recovering the foreshore to a width of 50 m downcoast of the fishing port. The numerical model was used for studying the difference in the response of nourishment sand of different grain sizes (Yoshioka et al., 2008).

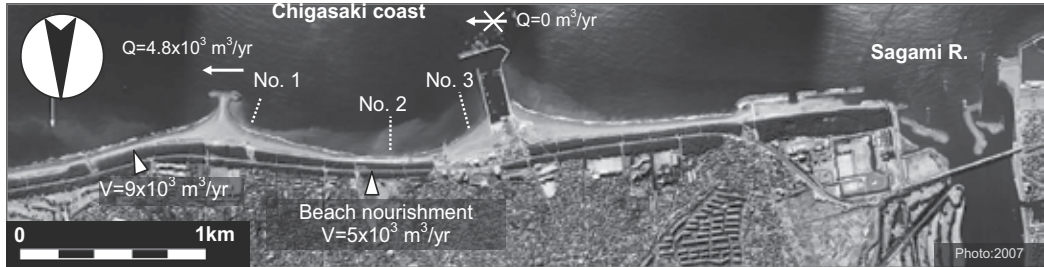


Fig. 11. Aerial photograph of Chigasaki coast and alignment of transects

#### 4.2 Calculation conditions

Figure 11 shows the calculation domain of the Chigasaki coast along with the alignment of transects. A Cartesian coordinate system is used. The bathymetric changes between 1991 and 2005 after the construction of the artificial headland were reproduced. Then, the topographic and grain size changes after 10 years were predicted for beach nourishment using sand of different grain sizes. Regarding beach nourishment, the same volume of sand as that used for annual nourishment was supplied at two locations, and the same amount of sand was extracted from the downcoast boundary of the calculation domain.

Figure 12 shows the depth distribution of  $d_{50}$  of all the seabed materials sampled, the grain size populations of which are separated into the following three categories: fine sand in a zone deeper than -5 m, medium and coarse sand between -5 m and the land, and gravel near the shoreline.

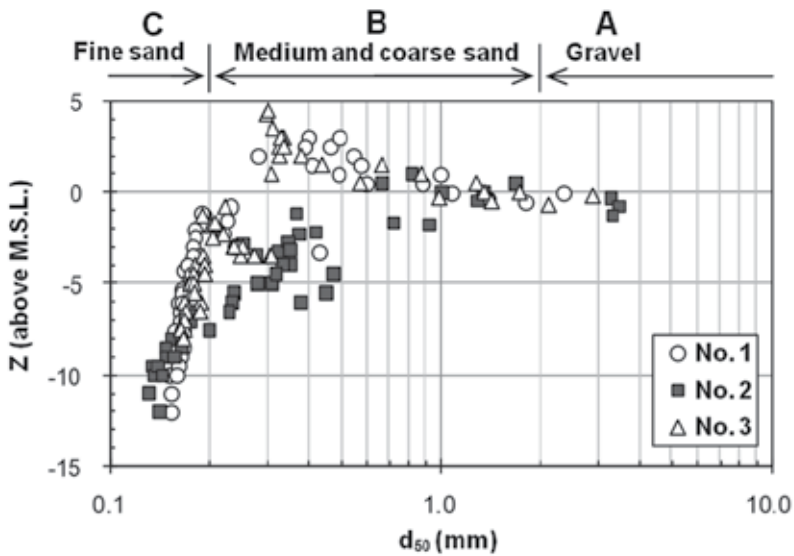
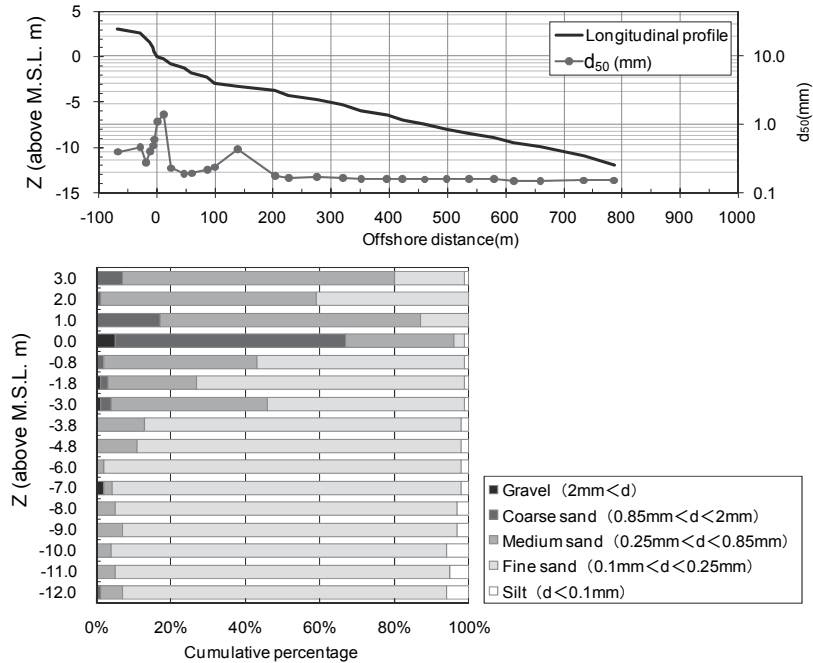


Fig. 12. Depth distribution of  $d_{50}$

(a) No. 1 (For location see Fig.1)



(b) No. 2 (For location see Fig.1)

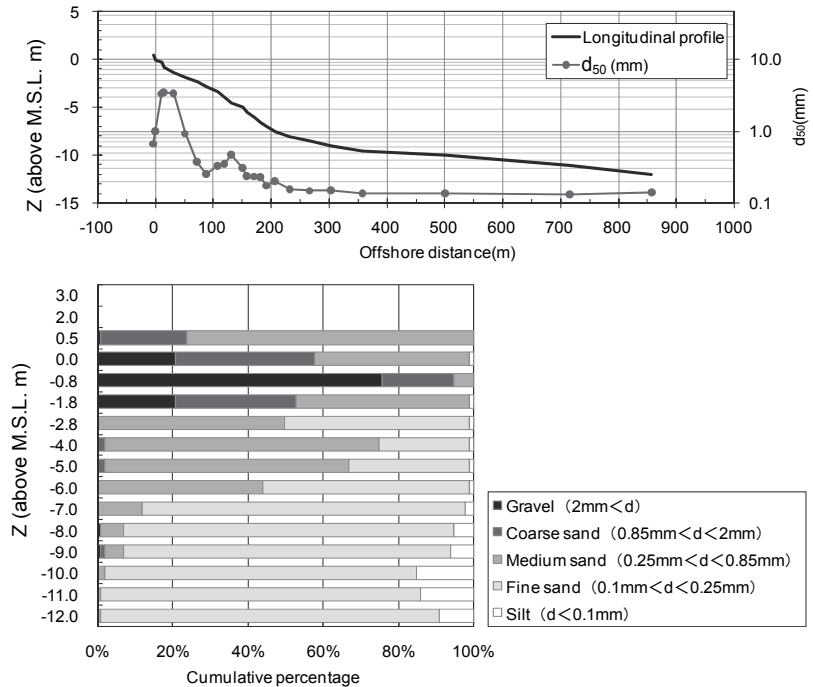


Fig. 13. Longitudinal profiles, cross-shore distributions of  $d_{50}$  and contents of grain sizes of bed materials along transect Nos. 1 and 2

Coordinate system	Cartesian coordinates considering actual seabed topography
Initial topography	Parallel, straight contour lines
Wave conditions	Energy-mean waves, $H_b=0.83$ m, $T=6.4$ s, and wave direction= $S6^{\circ}W$
Water level	Mean sea level
Depth of closure, $h_c$ and berm height, $h_R$	$h_c =9$ m and $h_R =3$ m
Grain size conditions	Grain size populations: Grain size 1: fine sand ( $d_{50}=0.15$ mm) Grain size 2: coarse and medium sand ( $d_{50}=0.20$ mm) Grain size 3: gravel ( $d_{50}=2.0$ mm)
	Equilibrium slope and thickness of exchange layer: Grain size 1: 1/80 and 0.625 m Grain size 2: 1/30 and 1.667 m Grain size 3: 1/10 and 5 m
	Contents for reproduction calculation: $\mu_1=0.48$ (grain size 1) $\mu_2=0.39$ (grain size 2) $\mu_3=0.13$ (grain size 3)
	Contents for prediction: $\mu_1=0.48, \mu_2=0.39, \mu_3=0.13$ (for present materials) $\mu_1=0.10, \mu_2=0.23, \mu_3=0.67$ (for coarse materials) $\mu_1=0.90, \mu_2=0.05, \mu_3=0.05$ (for fine materials)
Coefficients of sand transport	Coefficient of longshore sand transport: $K_x=0.387/\sqrt{d_{50}}$ Grain size 1: $K_x=0.1000$ Grain size 2: $K_x=0.0866$ Grain size 3: $K_x=0.0274$ Coefficient of cross-shore sand transport: $K_z=0.4K_x$ Ozasa and Brampton coefficient: $K_2=1.62K_z$
Depth distribution of sand transport rate	Cubic equation given by Uda and Kawano (1996)
Critical slopes for sinking of sand	1/2 on land and 1/3 on seabed
Calculation domain	$z=+3$ m to $-9$ m
Mesh size	$\Delta X=100$ m and $\Delta z=1$ m
Time interval	$\Delta t=50$ h, 180 steps /yr
Calculation period	From 1991 for reproduction and 10 years for prediction
Boundary conditions	Right boundary: reproduction $Q_{in}=0$ m <sup>3</sup> /yr Left boundary: $Q_{out}=1.4 \times 10^4$ m <sup>3</sup> /yr Landward and offshore boundaries: $q_z=0$
Calculation method	Explicit finite difference method

Table 2. Calculation conditions

Figure 13 shows the longitudinal profiles and cross-shore distributions of  $d_{50}$  along transect Nos. 1 and 2 located near the headland and in the eroded zone, respectively, as shown in Fig. 11, as well as the cumulative percentage of grain sizes at certain depths. It is clear that the beach material is mainly composed of fine sand ( $d=0.1-0.25$  mm) and medium and coarse sand ( $d=0.25-2$  mm). In addition, gravel appears in a depth zone between the shoreline and 1 m depth. Taking these characteristics into account, the following three grain size populations are required in the numerical simulation: population 1 sand with a grain size smaller than 0.2 mm; population 2 medium and coarse sand ( $d=0.2-2$  mm); and population 3 gravel ( $d>2$  mm). Furthermore, the equilibrium slopes corresponding to these grain size populations are  $1/80$ ,  $1/30$  and  $1/10$ , respectively, on the basis of the mean longitudinal slopes in the depth zone where each grain size population is dominant, as shown in Fig. 13.

In the reproduction calculation, the contents of the three grain size populations were determined from the observed data shown in Fig. 13, by taking the weighted average as a function of the seabed length. In the prediction, the contents of the three grain size populations (fine sand, medium and coarse sand, and gravel) were assumed to be 0.10:0.23:0.67 for coarse materials and 0.90:0.05:0.05 for fine materials on the basis of the materials to be used for nourishment, as well as the content of the present materials on the coast. The other calculation conditions are shown in Table 2. For incident waves, the energy-mean significant wave height of this coast ( $H_b=0.83$  m and  $T=6.4$  s) is used. The wave direction is determined by a trial-and-error method so as to obtain the best-fit result. The depth range in which beach changes occur is between the berm height  $h_R=3$  m and the depth of closure  $h_c=9$  m as revealed by the measured bathymetric changes. The wave diffraction due to the existence of the offshore reef and Chigasaki fishing port was calculated by the angular spreading method for irregular waves (Sakai et al., 2006).

### 4.3 Results of reproduction calculation

The beach changes between 1991, when the artificial headland was constructed, and 2005 were reproduced by numerical simulation. On the coast, beach nourishment to maintain the beach has been carried out since 1991, and a dynamically stable beach has now been formed without large changes in the shoreline position or beach topography. This dynamically stable beach topography was reproduced by the numerical calculation. Figure 14 shows the contours predicted under the dynamically stable condition, in which 5,000 and 9,000  $m^3$  of sand with the same contents of the three grain size populations as those measured on the present coast were supplied from two locations in the domain, and the same amount of sand was extracted from the left boundary. The measured shoreline configuration is also shown.

The predicted and measured shoreline configurations are in good agreement. This dynamically stable condition was reproduced by supplying sand at the rate of 5,000  $m^3/yr$  to the Chigasaki coast, which approximately agrees with the average rate of past beach nourishment of 4,800  $m^3/yr$ . Furthermore, the meandering of the contour lines deeper than 5 m off the artificial headland, and the concave profile, which changes from a steep slope near the shoreline to a gentle slope in the offshore zone, as shown in Fig. 13, were also reproduced in Fig. 14.

Figure 15 shows the predicted longitudinal profile and cross-shore mean grain size distribution. These results are in agreement with the measured values, as shown in Fig. 13(a), along the centerline of the pocket beach, by superimposing the shoreline position at  $Y=580$  m in Fig. 15 with that at  $Y=0$  m in Fig. 13(a). Gravel with a grain size larger than 2

mm is concentrated on the foreshore with an elevation higher than +1 m, the zone between the shoreline and 3 m depth is covered with fine sand with a grain size of 0.2 mm, and the seabed further offshore is covered with fine sand with a grain size of 0.15 mm. Thus, grain size sorting, from the coarse sand mainly composed of gravel on the foreshore to the offshore bed covered with fine sand, is well reproduced.

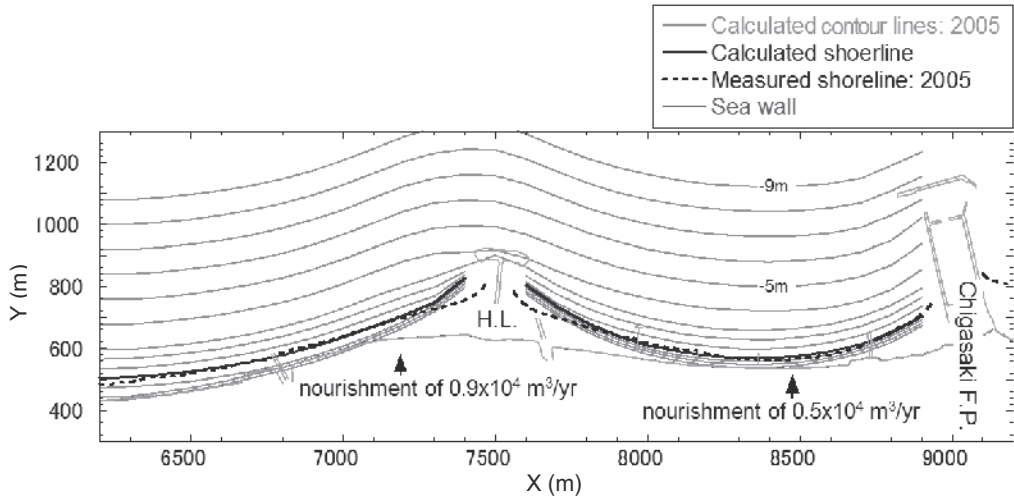


Fig. 14. Reproduced contour lines and comparison of measured and predicted shoreline configurations

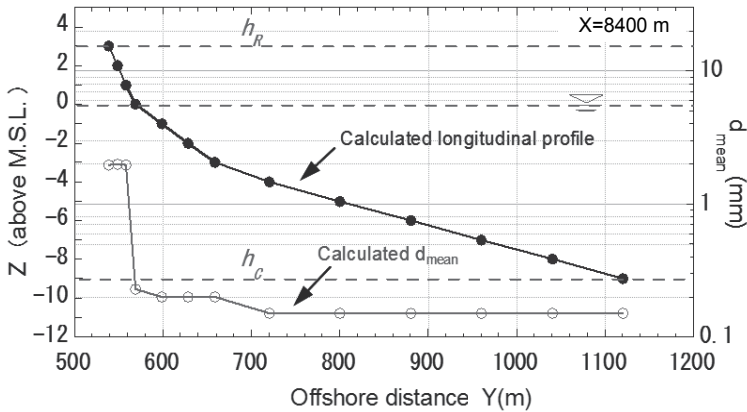


Fig. 15. Predicted longitudinal profile and cross-shore distribution of mean grain size

**4.4 Further applications**

By setting the minimum width of the beach to be nourished as 50 m, topographic and grain size changes after 10 years were predicted with several types of materials composed of grains with different sizes being used for beach nourishment. The nourishment site is located between  $X=8.4$  and  $X=8.6$  km, and the materials used for nourishment were supplied

from a berm on the shore face between the shoreline and 3 m height. The sand supply is assumed to be  $3.0 \times 10^4 \text{ m}^3/\text{yr}$  in accordance with the planned nourishment.

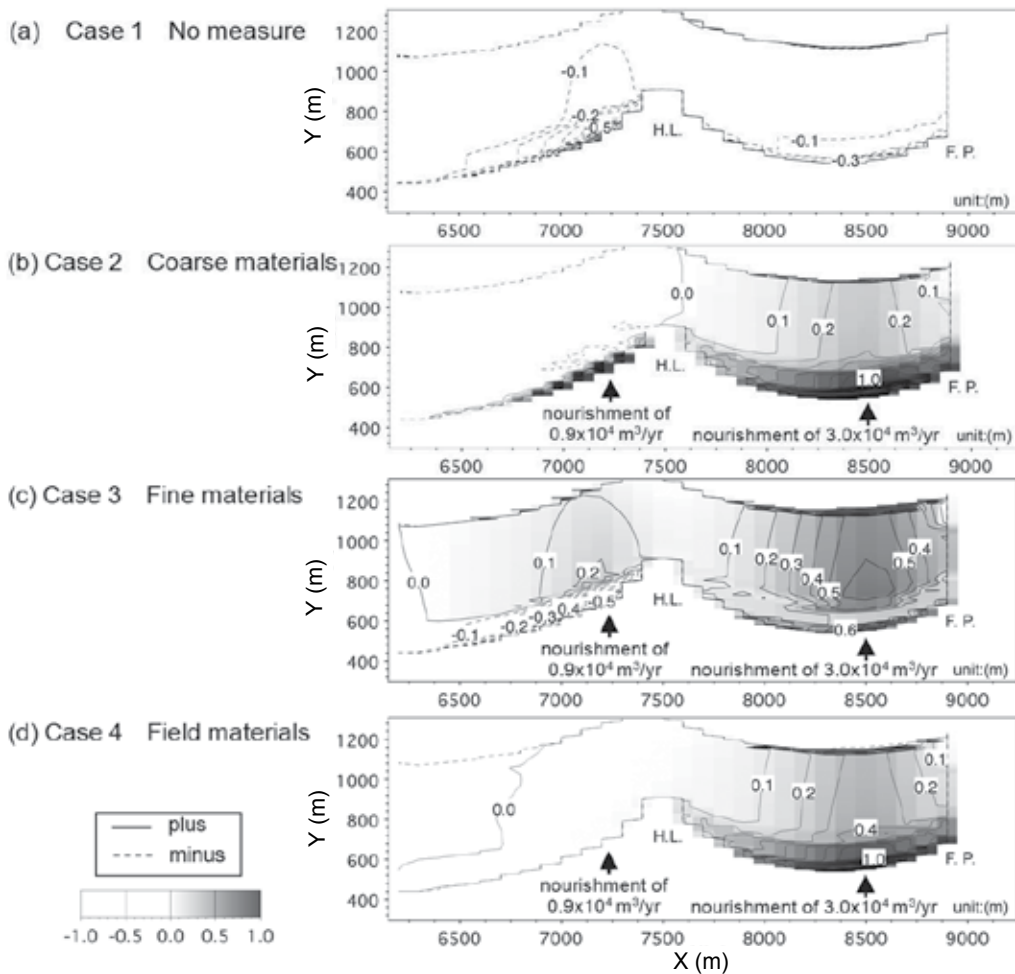


Fig. 16. Bathymetric changes relative to initial beach topography in four cases

Figures 16 and 17 show the planar distribution of the change in depth and the shoreline changes from the initial seabed topography in the following four cases: no nourishment (case 1), nourishment using coarse sand (case 2), nourishment using fine sand (case 3), and nourishment using sand with the same mean grain size as that of the current beach (case 4). When the beach receives no nourishment, further erosion occurs on the Chigasaki coast and east of the artificial headland, resulting in shoreline recession (Figs. 16(a) and 17(a)). For beach nourishment using coarse sand, the seabed level increases over an extensive area including the offshore zone, sand deposition is concentrated near the shoreline (Fig. 16(b)) and the shoreline markedly advances by up to 35 m, approaching the level of the shoreline in 1954 (Fig. 17(b)). Thus, beach nourishment using coarse sand is effective for protecting the shoreline.

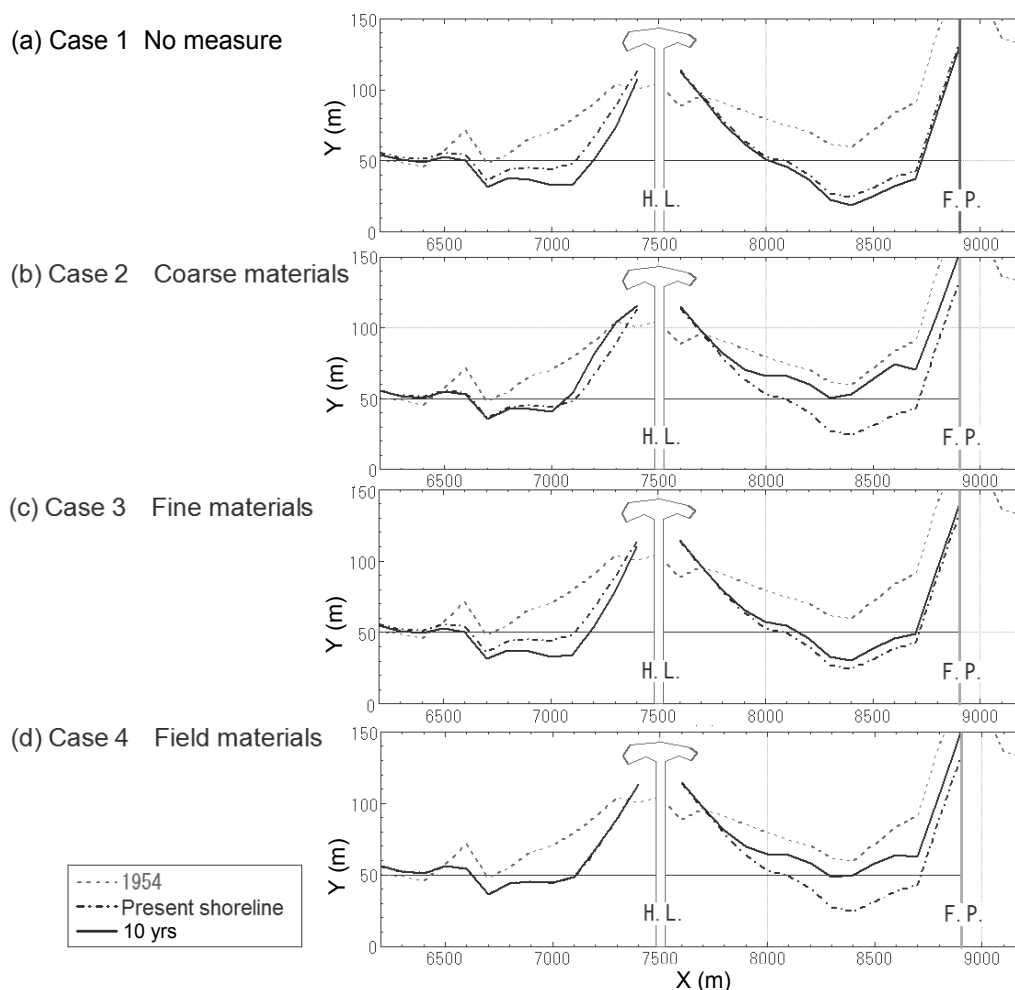
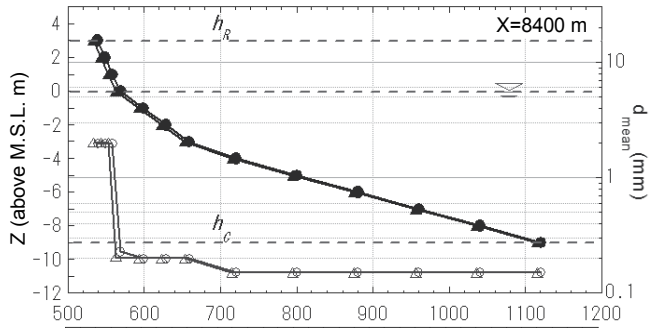


Fig. 17. Shoreline changes in four cases

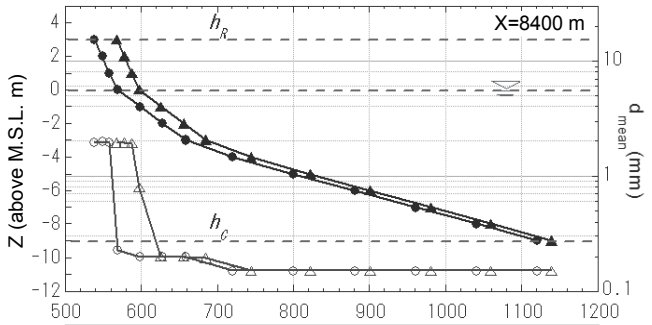
For beach nourishment using fine sand, the nourishment sand is mainly diffused offshore without being deposited near the shoreline, which is different from the case of nourishment using coarse sand (Fig. 16(c)). The increase in the seabed elevation over an extensive offshore zone is greater than that in the case of nourishment using coarse sand. In contrast, the shoreline advance is much less than that in the case of nourishment using coarse sand (Fig. 17(c)). Furthermore, the beach was further eroded east of the artificial headland, despite the beach nourishment west of the headland. For beach nourishment using sand with the same mean grain size as that of the beach, a significant nourishment effect was predicted, although this effect was less than that of beach nourishment using coarse sand (Fig. 16(d)), and a significant shoreline advance was predicted, as shown in Fig. 17(d).

Figure 18 shows the changes in the longitudinal profile and cross-shore mean grain size distribution along transect  $X=8.4$  km. When the beach receives no nourishment, a concave profile and the accumulation of coarse materials on the foreshore were predicted, as shown in Fig. 18(a), which are in good agreement with the measured results shown in Fig. 13. For

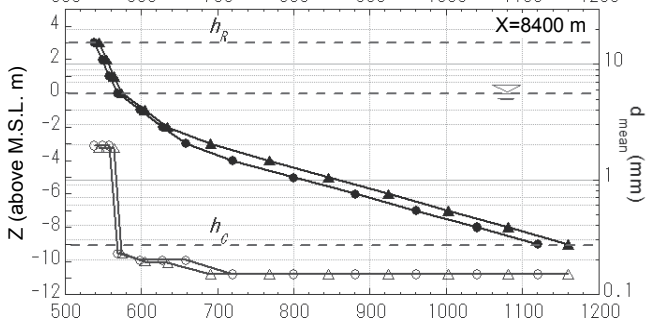
(a) Case 1 No measure



(b) Case 2 Coarse materials



(c) Case 3 Fine materials



(d) Case 4 Field materials

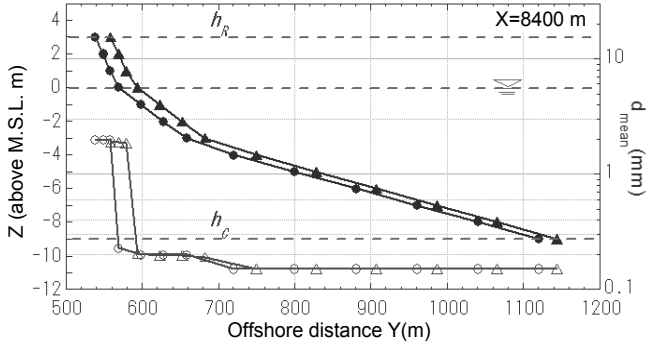
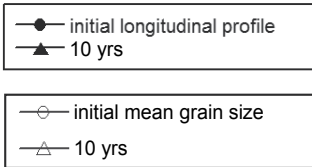


Fig. 18. Changes in longitudinal profile and mean grain size along centerline of pocket beach beach nourishment using coarse sand, the longitudinal profile generally moves offshore, and the bed materials in the zone where the longitudinal profile markedly moves offshore are mainly composed of sand with a grain size of 2 mm (Fig. 18(b)). In the case of beach

nourishment using fine sand, the change in the longitudinal profile shows that the shoreline advance is minimal, and the fine sand is transported offshore by its seaward movement and covers the offshore seabed (Fig. 18(c)). For beach nourishment using coarse sand and sand with the same mean grain size as that of the beach, coarse materials are selectively deposited near the shoreline. Finally, it is concluded that an excellent shore protection effect can be expected by beach nourishment using coarse sand or sand with the same mean grain size as that of the beach, whereas fine nourishment sand is widely diffused offshore, although beach nourishment using materials containing a large amount of fine sand is preferable for increasing the offshore seabed elevation.

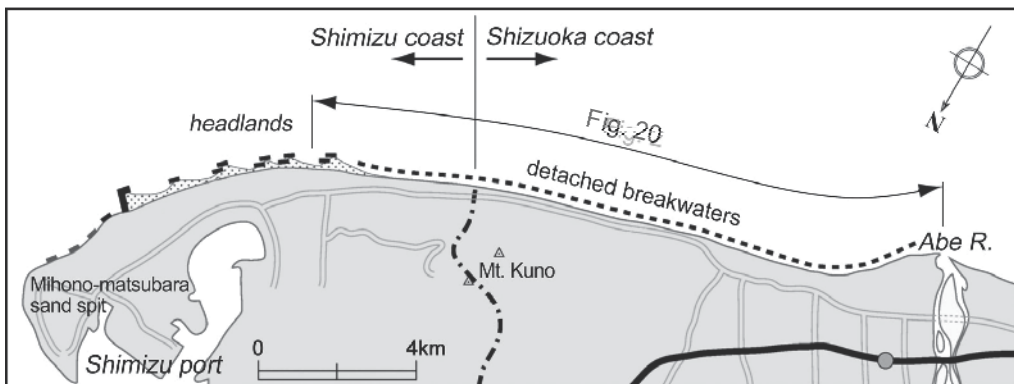
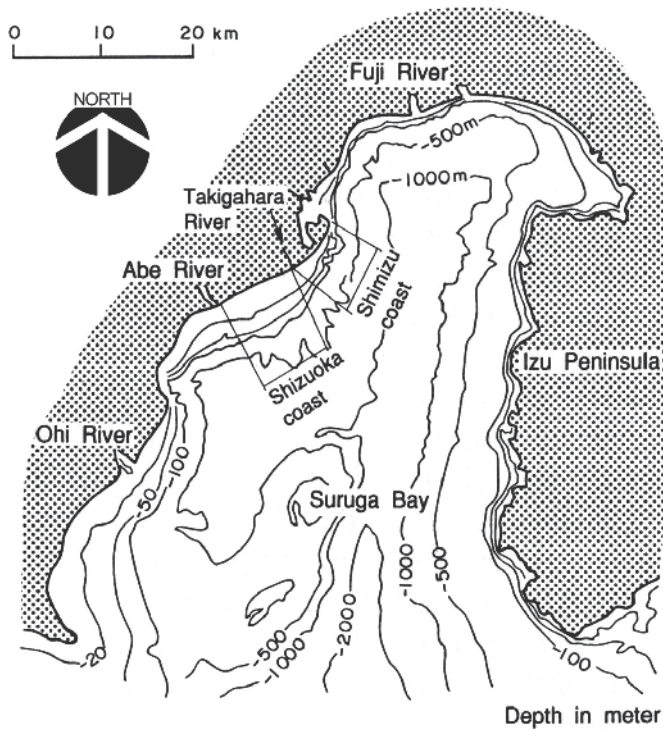


Fig. 19. Location of Shimizu coast

## 5. Application of model to prediction of beach changes on Shimizu coast

### 5.1 General conditions of Shimizu coast

Beach erosion has been severe on the Shimizu coast, which extends along the outer marginal coastline of the Mihono-Matsubara sand spit in Suruga Bay, as shown in Fig. 19, because of the decrease in longshore sand supply from the Abe River. As a measure against beach erosion, five sets of artificial headlands and an L-shaped groin were constructed between 1989 and 1999 (Uda et al., 2007). At present, the shoreline of this coast is barely maintained by these facilities and beach nourishment, and large topographic changes have been observed around these structures. Bathymetric surveys and bottom sampling have been carried out over an extensive area to investigate the mechanism of these beach changes. The analysis of the data sets suggests that there are two “conveyor belts” carrying gravel and fine sand along the coastline, and that these conveyor belts have been deformed as a result of the construction of the coastal structures. Here, the mechanism of the development and deformation of these conveyor belts is investigated using the present model (Nishitani et al., 2008).

### 5.2 Bathymetric changes, grain size distribution and shoreline changes

Figure 20 shows the bathymetry of the study area in March 2006. The transects of sea bottom sounding are arranged at 100 m intervals from the north end of the study area. Headland (HL) No. 1 is located at transect No. 65 at the south end of the study area, and the L-shaped groin (L-groin) is located at transect No. 32. In the study area, the contours in the zone deeper than 5 m smoothly extend alongshore, whereas those in the zone shallower than 5 m advance (retreat) south (north) of each headland because of their effect of blocking longshore sand transport. A submarine canyon with a very steep slope develops to the north of the L-groin.

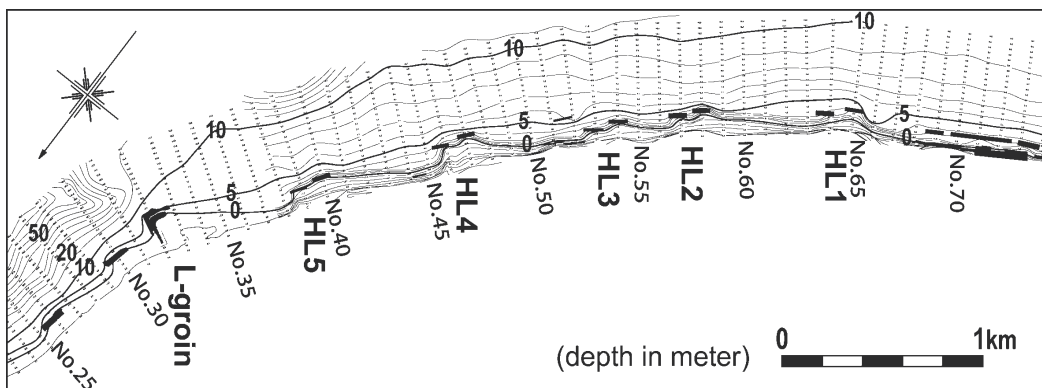


Fig. 20. Bathymetry of Shimizu coast and alignment of transects

Figure 21 shows the shoreline changes relative to the shoreline position in 1989 immediately before the construction of the artificial headlands. Since northward longshore sand transport prevails in the study area, the shoreline retreated downcoast of the headlands, which were successively constructed over time, resulting in a step-type coastline. The longitudinal profiles and depth changes in the median diameter  $d_{50}$  determined from the bottom sampling carried out in August 2006 were compared along several transects where typical shoreline changes were observed, as shown in Fig. 22.

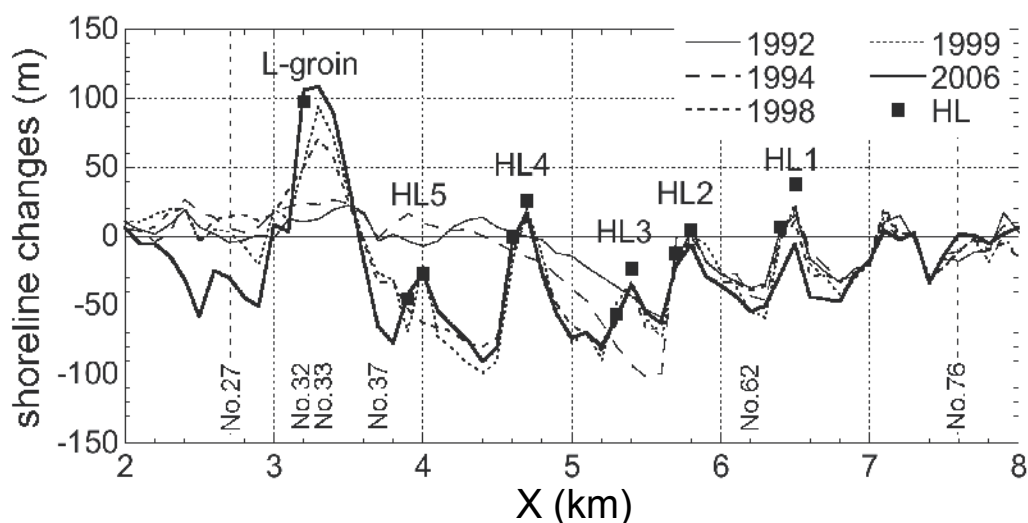


Fig. 21. Shoreline changes with reference to shoreline in 1989

Along transect No. 76, located at the south end of the study area, beach erosion occurred in the early years, but no large shoreline changes were observed, even in the comparison of the shoreline positions in 1989 and 2006 (Fig. 22(a)). A concave profile was formed with a steep slope of 1/10 from the foreshore to 4 m depth and a gentle offshore slope in the depth zone greater than 4 m. Corresponding to these slope changes, the foreshore is covered with gravel with median diameter  $d_{50}$  ranging between 10 and 30 mm, whereas  $d_{50}$  becomes as small as 0.18 mm in the depth zone between 4 and 7 m, and 0.16 mm in the zone deeper than 9 m. In particular, note that the offshore seabed with a slope of 1/50 at depths between 5 and 8 m is covered with fine sand.

Along transect No. 62, located downcoast of HL No. 1 where the shoreline significantly retreated between 1989 and 1992, we observed a steep slope mainly covered with gravel in the zone shallower than 2 m and with fine sand in the zone between 2 and 5 m. This slope was eroded, resulting in the parallel landward movement of the profile (Fig. 22(b)). In contrast, the seabed changes are negligible in the zone deeper than 5 m, where the seabed is covered with fine sand with  $d_{50}=0.16$  mm.

Along transect No. 37, located downcoast of HL No. 5, the shoreline receded after the construction of HL No. 5 (Fig. 22(c)). A convex profile had formed before the erosion, but a profile change from convex to concave occurred because of beach erosion, and the seabed shallower than 4 m depth was significantly eroded. In contrast, sand was deposited in the zone between 4 and 7 m deep, and  $d_{50}$  for the sand deposited in this zone is 0.16 mm. Thus, the selective deposition of fine sand in the offshore zone deeper than 4 m is in marked contrast to that of gravel near the shoreline.

Along transect No. 33 located 200 m south of the L-groin (Fig. 22(d)), the shoreline advanced by as much as 100 m between 1989 and 2006 with a parallel movement of the longitudinal profile. Major beach changes were observed up to a depth of 9 m, which is greater than the critical depth observed along the other transects. Note that gravel is deposited in the zone shallower than 3 m, whereas fine sand with  $d_{50}=0.16$  mm covers the seabed in the zone between 3 and 10 m deep;  $d_{50}$  increases with the depth of the seabed in the zone deeper than 10 m. This is a special characteristic only observed along this transect.

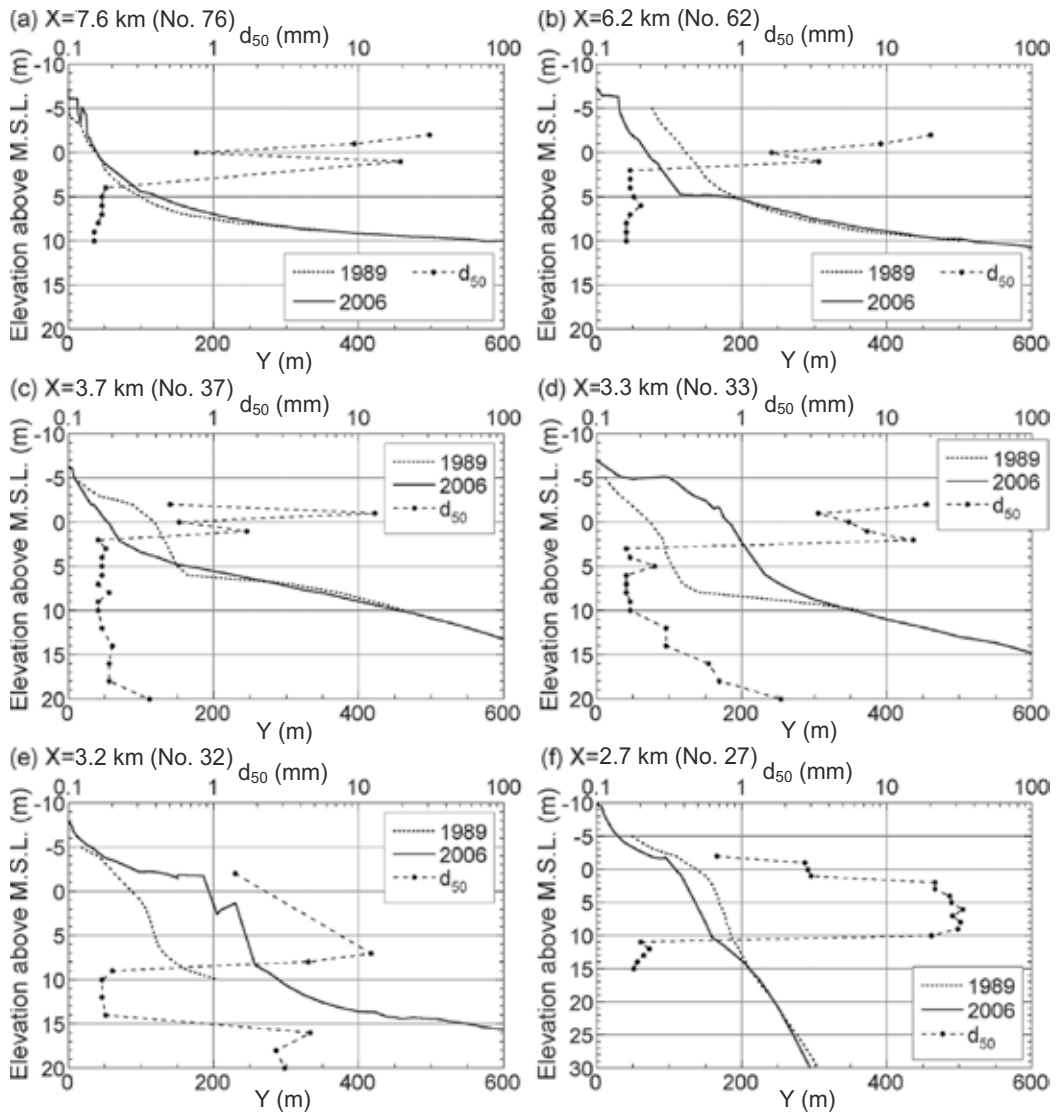


Fig. 22. Changes in longitudinal profile and depth distribution of  $d_{50}$

Along transect No. 32 located upcoast of the L-groin, the shoreline advanced by 110 m between 1989 and 2006, as shown in Fig. 22(e), because of the blockage of longshore sand transport by the L-groin, and the longitudinal profile between +2 and -8 m moved parallel with the shoreline advance. The profile in 1989 can be smoothly connected to the profile in 2006 by extrapolation, since a very gentle slope extends in the zone at a depth greater than 8 m. In contrast, the longitudinal profile in 2006 has a break at a depth of 8 m, and the seabed slope becomes gentle at this depth. Comparing the depth distribution of  $d_{50}$  and the profile in 2006, we found that  $d_{50}$  ranges between 1.4 and 12 mm, and gravel mainly accumulates in the zone shallower than 9 m, whereas the offshore seabed between 9 and 14 m is covered with fine sand with  $d_{50}=0.16$  mm, and then a gravel bed appears at depths greater than 14 m. Major beach changes can be observed up to a depth of 8 m, but the deposition of fine

sand with  $d_{50} = 0.16$  mm also takes place in the zone at depths between 8 and 10 m. However, a gravel bed appears again at a depth of about 15 m. This strongly indicates that the seabed in this area was covered with coarse sand and gravel in the past, but the zone at a depth near the depth of closure had been covered with fine sand as the shoreline advanced in recent years. Namely, it is assumed that there are two “conveyer belts”, each carrying mainly gravel and fine sand alongshore in zones shallower and deeper than approximately 3 m, respectively, and that the conveyer belt carrying gravel moved offshore because of the accretion of gravel near the shoreline, causing the offshore movement of the longitudinal profile, as schematically shown in Fig. 23; simultaneously, the other conveyer belt carrying fine sand was pushed offshore, resulting in the offshore gravel bed being covered with fine sand.

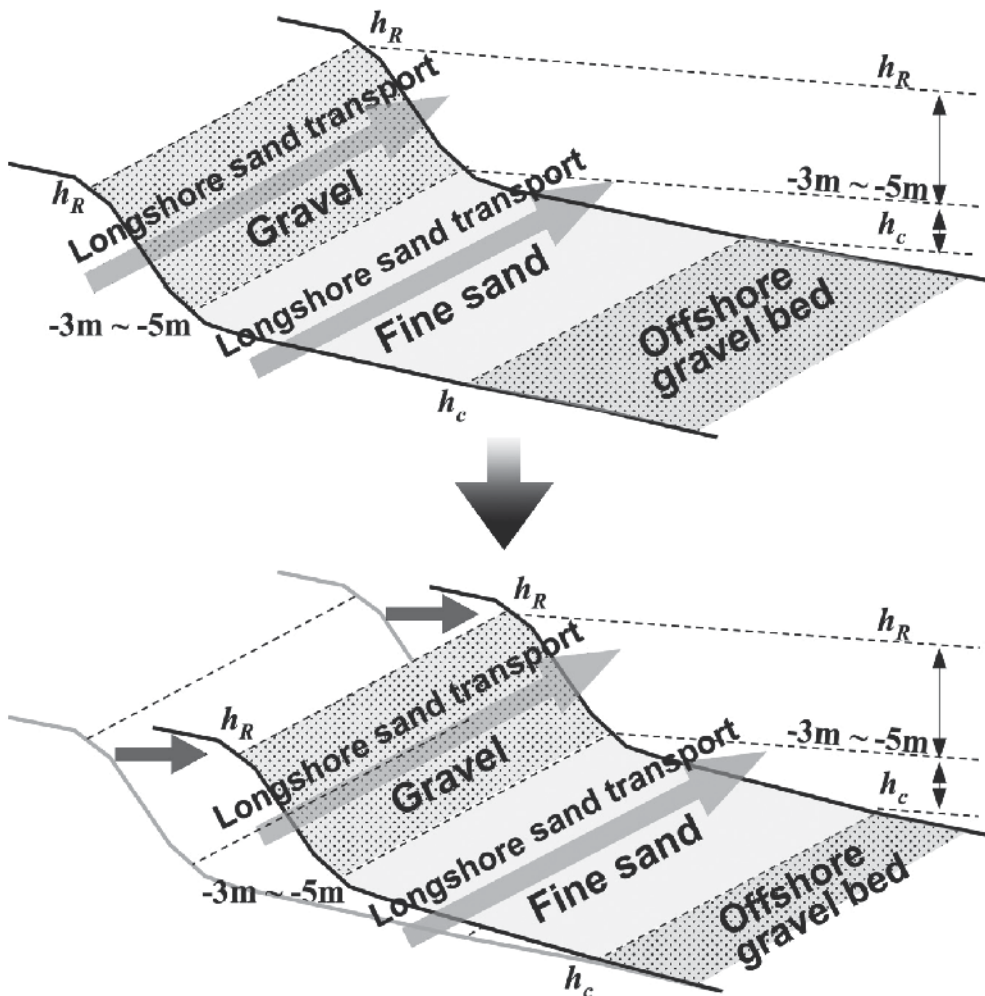


Fig. 23. Schematical explanation of conveyer belts, each carrying mainly gravel and fine sand Along transect No. 27 located north of the L-groin, where the shoreline significantly retreated after the construction of the groin (Fig. 22(f)), the beach slope between the shoreline and a depth of 30 m is as steep as 1/6. Major beach changes are observed up to a

depth of 10 m. The depth zone in which beach erosion occurred is covered with gravel, the median diameter of which ranges between 20 and 30 mm, but the seabed surface in the zone deeper than 10 m is covered with fine sand with  $d_{50}=0.2$  mm, which are the same features as those along transect No. 32, despite the steep slope in the offshore zone.

### 5.3 Calculation conditions

In the numerical prediction of beach changes, the difference in the equilibrium slope between the zones composed of gravel and fine sand must be taken into account. Before the construction of the artificial headlands, longshore sand was continuously transported alongshore at a constant rate, because no beach changes were observed in this area, i.e., the coast was under a dynamically stable condition; thus, a dynamically stable beach (Uda et al., 2007) was reproduced. In Fig. 24, the shoreline orientation gradually rotates counterclockwise and shifts by  $20^\circ$  between the south and north ends of the study area. The predominant wave direction of this coast is south, and under this oblique wave incidence, Snell's law gives a breaker angle of  $\alpha_b=17^\circ$  at the south end of the calculation domain (Uda et al., 2007). Taking this shift of the shoreline orientation into account, we change the incident angle of the waves linearly from south to north in the calculation domain. In this case, the wave height was decreased alongshore corresponding to the change in the wave direction, so that longshore sand transport flux remained constant before the construction of the headlands and that a dynamically stable beach could be simulated.

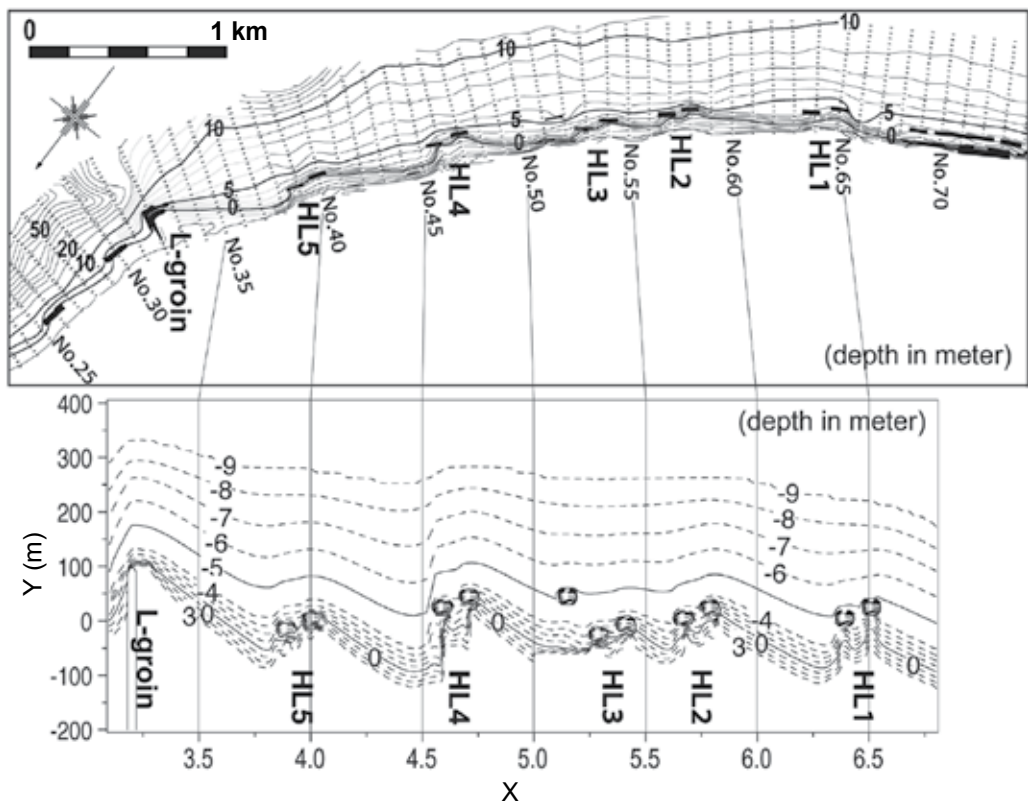


Fig. 24. Calculation domain

As the wave conditions, rough waves with a 5% probability of occurrence are selected on the basis of the results of wave observation off the Shimizu coast; beach changes are more significantly affected by rough waves than normal waves. The selected equivalent wave height  $H_0'$  and the wave period are 3 m and 9 s, respectively. The detached breakwaters were placed on this dynamically stable beach, and rough waves were generated for 15 years. Because the seabed is separated into a steep slope mainly composed of gravel in the zone shallower than 4 m and a gentle slope mainly composed of fine sand in the zone deeper than 4 m, as shown in Fig. 22, the changes in the grain size of the sand were implicitly modeled by the changes in the equilibrium slope, which depends on the grain size, by applying the contour-line-change model (Serizawa et al., 2003). In this study, the effect of the difference in grain size was implicitly included as the difference in the equilibrium slope in the ordinary contour-line-change model, assuming that the beach changes take place without the rapid mixing of sand between the beach near the shoreline and the offshore seabed, which are mainly composed of gravel and fine sand, respectively. Table 2 shows the calculation conditions.

Given the topography in 1983 before beach erosion as the initial condition, beach changes until 2006 were predicted while increasing the number of artificial headlands with time. The initial topography with straight parallel contours is set using an expanded coordinate system, to which curvilinear coordinates fixed along the shoreline in 1989 are assigned, in accordance with the method of Uda et al. (1998). The x-axis is taken to be alongshore and the y-axis is perpendicular to the x-axis. The beach slope was assumed to be 1/10 in the depth zone between +3 and -4 m, and 1/50 in the zone deeper than -4 m on the basis of the measured profiles. The depth of 4 m is a critical depth dividing the depth zones. The berm height  $h_R$  and depth of closure  $h_c$  were assumed to be 3 and -7 m, respectively, for the coarse sand forming a steep slope off the shoreline. To take into account the gradual beach changes observed in the zone deeper than 8 m, the movement of fine sand, mainly covering the seabed depth zone between 8 and 9 m, as typically shown in Fig. 22(d), must be considered. In this study, the depth distribution given by Uda and Kawano (1996) was used for the depth distribution of longshore sand transport in the depth zone between the berm height and 7 m depth, and a constant distribution of longshore sand transport accounting for 3% of all the total sand transport was assumed in the depth zone between 8 and 9 m. For the calculation in the vertical direction, the depth range between  $z=-7.5$  m and  $z=3.5$  m was divided into cells with  $\Delta z=1$  m. Since the seabed slope in the offshore zone is as gentle as 1/50, there is no sinking of sand to a deeper zone.

As a boundary condition, the longshore sand transport  $Q_{in}$  of  $1.3 \times 10^5$  m<sup>3</sup>/yr is introduced at the right boundary of the calculation domain between 1983 and 1990 as a natural condition; after 1990,  $3.5 \times 10^4$  m<sup>3</sup>/yr is assumed as the rate of natural sand supply from upcoast and from beach nourishment. At the left boundary, a free boundary permitting the transport of longshore sand is set; longshore sand transport along each contour line is invariant. Beach nourishment provides the source of sand at the shoreline. The coefficient of longshore sand transport is adjusted so that  $Q$  at any point along the initial shoreline is equal to  $Q_{inv}$ , satisfying the condition that the same amount of longshore sand transport as the inflow flows out through the left boundary. For this purpose, the coefficient of longshore sand transport  $K_x$  is selected to be 0.0059, which is two orders of magnitude smaller than the typical value. This is because the continuous action of rough waves that occur with a low probability throughout the year is assumed. The distances between the shoreline and the artificial headlands are given by the distances measured relative to the shoreline position in 1983. The wave sheltering effect of the artificial headlands is evaluated by the angular spreading method for irregular waves given by Sakai et al. (2006).

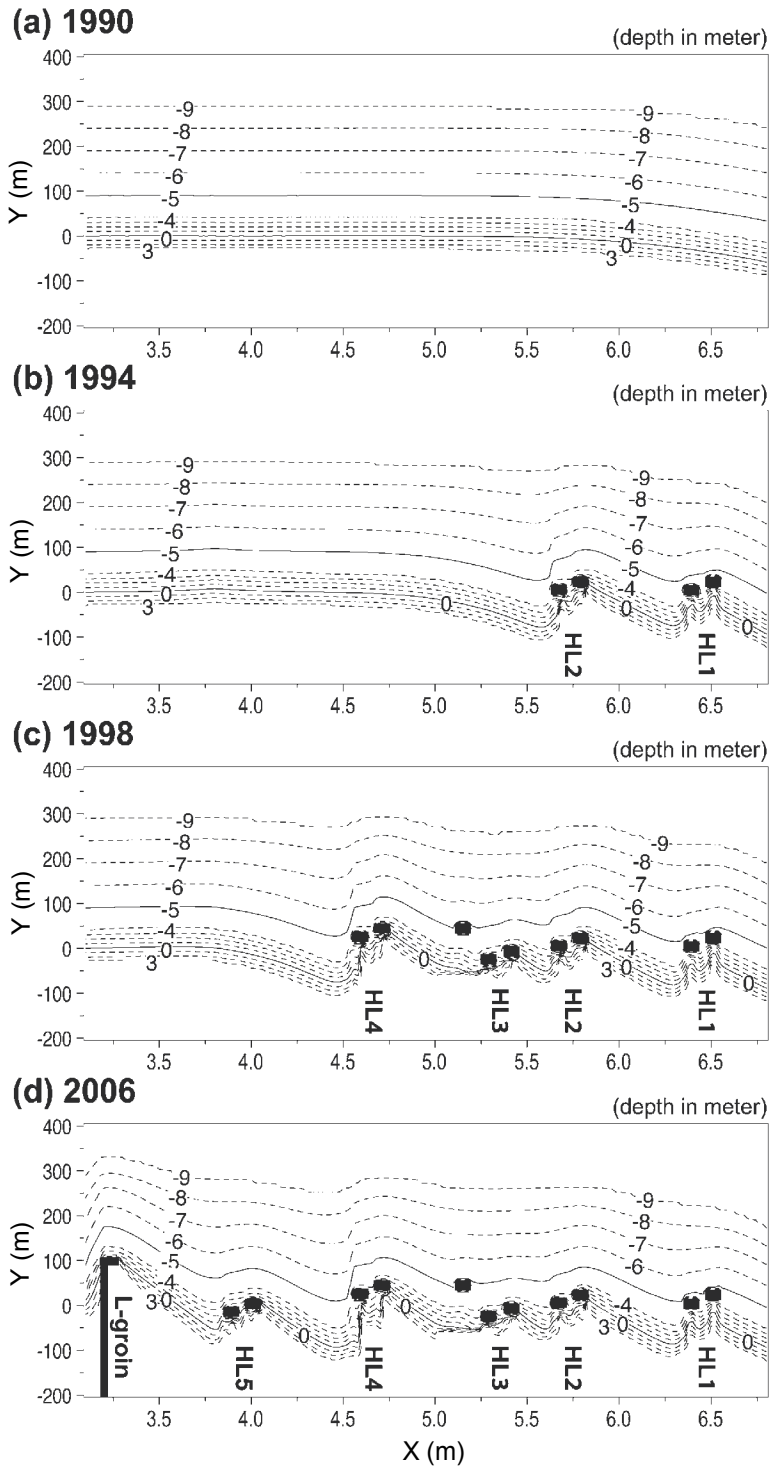


Fig. 25. Predicted bathymetries ((a) 1990, (b) 1994, (c) 1998, and (d) 2006)

Initial topography	Straight parallel contours (shoreline in 1983)
	Uniform slopes of $\tan\beta=1/10$ in depth zone shallower than -4 m and $\tan\beta=1/50$ in depth zone deeper than -4 m
Wave conditions	Breaker height: $H_0'=3$ m and $T=9$ s
	Breaker angle: $\alpha_b=17^\circ$ (wave direction: south) at south end with linear increase in breaker angle from $17^\circ$ to $37^\circ$
Tide level	Mean sea level
Depth of closure	$h_c = -7$ and $-9$ m for coarse and fine sand, respectively
Berm height	$h_R=3$ m
Coefficients of sand transport	$K_x=0.0059$ and $K_z=0.1K_x$
	$K_2=1.62K_x$ (Ozasa and Brampton, 1980)
Depth distribution of sand transport rate	Cubic equation given by Uda and Kawano (1996) between +3 and -7 m, and uniform distribution between -8 and -9 m
Equilibrium slope	$\tan\beta_c=1/10$ in depth zone shallower than -4 m
	$\tan\beta_c=1/50$ in depth zone deeper than -4 m
Critical slope	1/2 on land and 1/2 on seabed
Calculation domain	$z=+3.5$ to $-9.5$ m
Mesh size	$\Delta x=20$ m and $\Delta z=1$ m
Time interval	$\Delta t=10$ h
Total time of calculation	$t=10$ yr
Boundary conditions	Right boundary: $Q_{in}=1.3\times 10^5$ m <sup>3</sup> /yr between 1983 and 1990 (natural condition)
	$Q_{in}=3.5\times 10^4$ m <sup>3</sup> /yr after 1990 (natural sand supply +nourishment)
	Left boundary: free ( $dq_x/dx =0$ )
	Landward and offshore boundaries: $q_z=0$
Wave transmission coefficient	$K_t=0.5$ for artificial headland
Calculation method	Explicit finite difference method
Calculation of wave field	Angular spreading method (Sakai et al., 2006), $S_{max}=25$

Table 3. Calculation conditions

### 5.4 Results

Figure 25(a) shows the predicted bathymetry for 1990 immediately before the construction of HL Nos. 1 and 2. The sea bottom contours started to retreat from the upcoast boundary. Figure 25(b) shows the predicted bathymetry for 1994 after constructing HL Nos. 1 and 2. Since northward longshore sand transport was blocked by the construction of HL Nos. 1 and 2, the contours immediately downcoast of HL retreated, and simultaneously, the offshore contours meandered because of the changing direction of the movement of sand off the detached breakwaters. Figure 25(c) shows the predicted bathymetry for 1998 immediately before the construction of the L-groin. After the construction of the HLs, the eroded zone downcoast of the HLs also propagated northward. Finally, the predicted

bathymetry for 2006 is shown in Fig. 25(d). As a result of the construction of the L-groin, the shoreline advanced south of the L-groin. Upon examining the configuration of the seabed contours around the L-groin in detail in the predicted bathymetry for 2006, as shown in Fig. 25(d), it was found that the shoreline south of the groin advanced up to 100 m after the construction of the groin. This shoreline advance caused the offshore movement of the longitudinal profile in the zone shallower than 7 m, resulting in the further advance of the gentle slope covered with fine sand between the depths of 7 and 9 m. The predicted contours are in good agreement with the measured results shown in Fig. 20. Figure 26 shows the measured and predicted shoreline changes in 1983 and 2006. The predicted shoreline is in good agreement with the measured shoreline, although there are some variations at each headland.

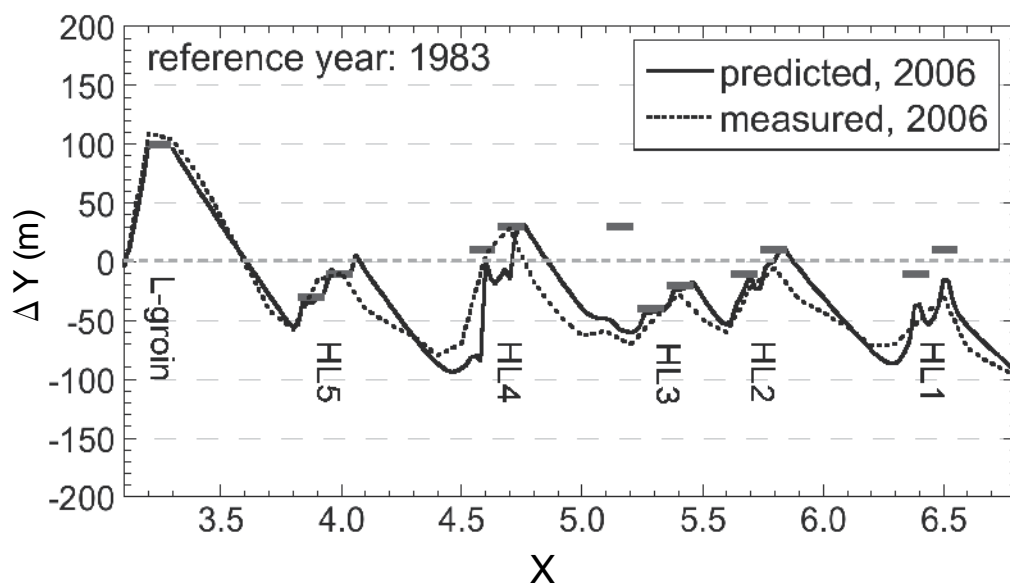


Fig. 26. Measured and predicted shoreline changes

## 6. Conclusions

A model for predicting the change in the longitudinal profile as well as the change in the grain size distribution was developed using the concept of an equilibrium slope corresponding to each grain size population. The model was applied to the analysis of the results of a large-scale movable bed experiment, and it accurately reproduced the characteristics indicating that sand of mixed grain size is sorted; coarse sand is transported shoreward to form a berm and fine sand is transported offshore to a zone deeper than  $h_c$ . It was confirmed that when the content of coarse sand increases, the foreshore becomes wide owing to the formation of a berm, and this contributes to the shoreline advance. In contrast, with an increase in the content of fine sand, the outflow of sand toward a zone deeper than  $h_c$  increases. The model was further applied to the Chigasaki coast where beach nourishment using materials of mixed grain sizes was carried out. It was concluded that the optimum method of nourishment was to use sand of mixed grain sizes containing coarse

and fine sand particles, although nourishment using gravel was effective for protecting the shoreline zone. In the third example, the model was applied to the Shimizu coast, where conveyer belts mainly carrying gravel and fine sand were found. The three-dimensional beach changes between 1983 and 2006 were predicted by this model, and the predicted shoreline changes were in good agreement with the measured values. Finally, it is concluded that the present model is highly applicable to predicting beach changes and grain size changes.

## 7. References

- Bakker, W. T. 1968. The dynamics of a coast with a groyne system, *Proc. 11<sup>th</sup> ICCE*, pp. 492-517.
- Fukuhama, M., T. Uda, M. Serizawa and T. Ishikawa. 2007. Change in longitudinal profile using sand of mixed grain size in large wave tank and its numerical simulation, *Coastal Sediments '07*, pp. 259-271.
- Kamphuis, J. W., M. H. Davies, R. B. Narim and O. J. Sayao. 1986. Calculation of littoral sand transport rate, *Coastal Engineering*, Vol. 10, pp. 1-12.
- Kraus, N. C. 1985. Field experiments on vertical mixing of sand in the surf zone, *J. Sedimentary Petrology*, Vol. 55, pp. 3-14.
- Kumada, T., A. Kobayashi, T. Uda and M. Serizawa. 2003. Development of predictive model of shoreline and grain size changes, *Coastal Sediments '03*, pp. 1-14.
- Meguro, S., K. Yamamoto and K. Fukuhama. 2005. Formation process of equilibrium beach responding to grain size of beach nourishment, *Annual J. Coastal Eng. JSCE*, Vol. 52, pp. 501-505. (in Japanese)
- Nishitani, M., T. Uda, M. Serizawa and T. Ishikawa. 2008. Measurement and prediction of deformation of conveyer belts carrying gravel and fine sand off Shimizu coast, *Proc. 31<sup>st</sup> ICCE*, pp. 2570-2582.
- Ozasa, H. and A. H. Brampton. 1980. Model for predicting the shoreline evolution of beaches backed by seawalls, *Coastal Eng.*, Vol. 4, pp. 47-64.
- Sakai, K., T. Uda, M. Serizawa, T. Kumada and Y. Kanda. 2006. Model for predicting three-dimensional sea bottom topography of statically stable beach, *Proc. 30<sup>th</sup> ICCE*, pp. 3184-3196.
- Serizawa, M., T. Uda, T. San-nami, K. Furuike and T. Kumada. 2003. Improvement of contour line change model in terms of stabilization mechanism of longitudinal profile, *Coastal Sediments '03*, pp. 1-15.
- Uda, T. and S. Kawano. 1996. Development of a predictive model of contour line change due to wave, *Proc. JSCE*, No. 539/II-35, pp. 121-139. (in Japanese)
- Uda, T., M. Sumiya, H. Yazawa, Y. Ohtani and Y. Atsusaka. 1998. Prediction of beach changes around Oyazawa-bana sand spit using expanded coordinate system, *Annual J. Coastal Eng.*, JSCE, Vol. 45, pp. 541-545. (in Japanese)
- Uda, T., T. Kumada and M. Serizawa. 2004. Predictive model of change in longitudinal profile in beach nourishment using sand of mixed grain size, *Proc. 29<sup>th</sup> ICCE*, pp. 3378-3390.

- Uda, T., M. Serizawa and T. Ishikawa. 2007. Evaluation of controlling effect of sand transport by detached breakwaters built on dynamically stable beach, *Coastal Sediments '07*, pp. 2460-2472.
- Yoshioka, A., T. Uda, G. Aoshima, K. Furuike and T. Ishikawa. 2008. Field experiment of beach nourishment considering changes in grain size and prediction of beach changes, *Proc. 31<sup>st</sup> ICCE*, pp. 2694-2706.

## **Part 3**

# **Reacting Flows and Combustion**



# Numerical Simulation of Spark Ignition Engines

Arash Mohammadi  
*KNToosi University of Technology*  
Iran

## 1. Introduction

Optimization processes for internal combustion engines requires application of advanced development tools. In addition to experimental method, numerical calculations are needed in order to obtain an insight into the complex phenomena in-cylinder processes. This chapter was organized for advances in computational fluid dynamic, heat transfer, and chemical reactions as applied to internal combustion engines. It provided an opportunity for specialists in the area of modeling flow and combustion in SI engines to provide powerful computational tools in the area of endeavor surrounding fluid dynamics. We examine computations for reactive flows in general with computational combustion in particular. In reactive flows, the conservation equations for chemical species are added to the Navier - Stokes system of equations. This addition also requires a modification of the energy equation. Furthermore, the sensible enthalpy is coupled with the chemical species, which contributes to the heat source and diffusion of species interacting with temperature. Thus, the chemically reactive flows and combustion require significant modifications of not only the governing equations, but also the existing computational methods discussed in this chapter. The aims of these computational developments have been: (1) to develop reliable engine tools for predicting the flow, temperature, etc fields; (2) to reduce the cost of current experiments that are used for most of the relevant engineering design; (3) to allow for a better understanding of physiochemical processes involved. Details of turbulent fluid motion in engines are required for determining combustion, thermal efficiencies, and level of emissions for development of cleaner, less noisy, and more efficient engines for a variety of designs and fuels.

## 2. Model building

The first step in numerical simulation consists in the construction of model describing and the technical processes. The prerequisite for this is that real process can be divided into single procession sections and hence broken down into partial problems. These partial problems must be physically describable and mathematically formulable. For the construction of parametrical models and for the simulation of temporally and spatially variable fluid, temperature and concentration fields with chemical reactions, the knowledge of thermodynamics, fluid dynamics, and combustion technology is an essential prerequisite.

Essentially, the modeling procedure can be subdivided into the following steps:

1. Define the system and boundaries from the environment, determine the relevant reservoirs as well as mass and energy flow between them.

2. Draw up balance sheets according to the unified scheme.
3. With the help of physical laws, describing the mass, momentum and energy flows.
4. Integrate the governing equations of model numerically, i.e. execute the simulation.
5. Validate the model, i.e. compare the calculated data with experimentally that existed or obtained.

### 3. Computational mesh

The discrete locations at which variables are to be calculated are defined by the numerical grid which is essentially a discrete representation of the geometric domain on which the problem should be solved. It divides the solution domain into a finite number of sub domains. Mesh generation is often the most decisive and most strongly limiting factor in CFD calculation today. A good computational mesh should consist of hexahedrons, be well adapted (i.e. also keep to the  $y^+$  rule that will discuss in 4.1.3) and sufficiently fine and adapted, so that the flow structure (free jet, flames,..) can be resolved. Another problem is mesh movement, which is solved by CFD code specifically, so that one has to rely closely in generating moving mesh.

#### 3.1 Grid generation

Regular or structured grid consists of families of grid lines with the property that members of single family do not cross each other and cross each member of the other family at once. The position of any grid point (or control volume) within the domain is uniquely identified by set of two or three indices for two or three dimensional problem, e.g. (i, j, k). An example of structured grid is shown in Fig .1. The disadvantage of structured grid is that they can be used for geometrically simple domain and for complex geometries like internal combustion engine with complex head and chamber geometry, intake and exhaust port and with valves that are needed to move in simulation, advanced grid generator like, ICEM-CFD should be used.

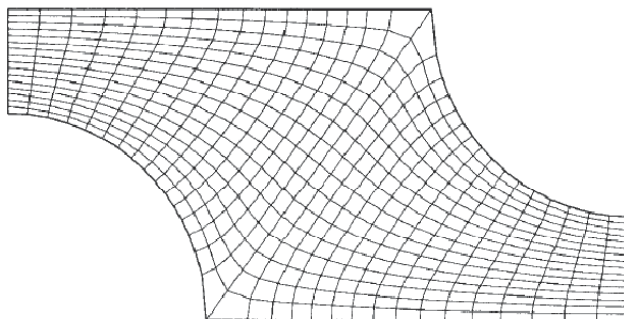


Fig. 1. Example of structured grid generation (Ferziger & Peric, 2002)

It has been shown through analysis and examples that the necessary of the numerical solution is strongly dependent on the grid or mesh used for the discretisation of the computational domain. Large mesh lengths lead to larger truncation error, whereas smaller mesh lengths increase the number of mathematical operations, resulting in larger CPU time and generate round of error. Also, larger gradients in a particular region demand finer grids that those needed coarse grid for regions where the gradients are smaller in order to resolve the changes in the variables. Complicated geometry and have smooth and finer mesh for the

regions with large gradients of variable that expected of the solution of the physical domain also passes challenge for discretisation, particularly near boundaries. Because of all these considerations, it is important to employ a grid which closely approximates a given geometry.

### 3.2 Multi zone grids

Multiple sub domains, each consisting of a specified mesh length, may be used to subdivide the given region in order to concentrate grid points near a thermal source or boundary, where large changes are expected to occur. In a block structured grid, there is two or more level subdivision of solution domain on the coarse level, there are blocks which are relatively large segments of the domain and they may or may not overlap. In Fig.2 a block structured grid with matching at interface is shown that is example of multi block structured grid.

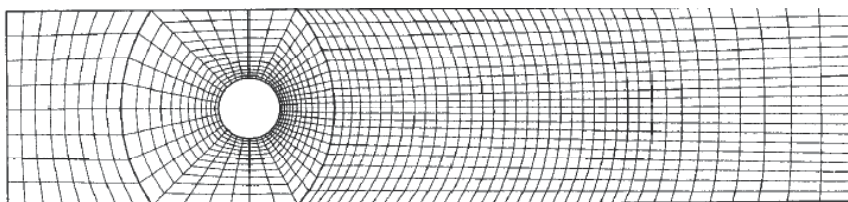


Fig. 2. Example of multi block structured grid (Ferziger & Peric, 2002)

### 3.3 Complex boundaries

In many practical problems, the boundaries are curved or have a shape that cannot be easily modeled by a regular mesh. Specialized discretisation equations may have to be developed for points near or on the boundaries. For more information, interested reader can refer to advanced books of grid generation like (Thompson, 1985).

## 4. Fluid mechanical simulations

CFD simulation is playing an increasingly important role in the simulation of engine processes, as it makes possible the most detailed physical description of the relevant processes. The most diverse processes in the engine field are considered, like charge changing, in cylinder flow, combustion, exhaust gas recirculation, and out flow process. A relatively costly process is still necessary: firstly, computational meshes must be generated, and after a definition of initial and boundary conditions, the actual calculation can be finally be started.

### 4.1 Governing equations

#### 4.1.1 The three dimensional flow fields

The basic equations that govern convective processes are obtained from conservation laws of mass, momentum, and energy. In the following, the basic equations of fluid mechanics will be briefly recapitulated. Considering a given location in the flow, the conservation of mass gives:

$$\frac{\partial \rho}{\partial t} + (\rho \vec{v}) = 0 \quad (1)$$

$\rho$  is the density of the fluid and  $\vec{v}$  the local vector velocity of fluid.

The principle of conservation of momentum, which equates the rate of change of momentum to the forces applied, (Navier - Stokes equation) gives:

$$\frac{\partial(\rho\vec{v})}{\partial t} + \nabla \cdot (\rho\vec{v}\vec{v}) = -\nabla p + \nabla \cdot \sigma + \vec{f} \quad (2)$$

$$\sigma = \mu[(\nabla\vec{v}) + (\nabla\vec{v})^T] + \lambda\nabla \cdot \vec{v} I \quad (3)$$

Where  $\nabla$  is operator of gradient,  $p$  the local pressure,  $\sigma$  viscous stress tensor for Newtonian fluid,  $\vec{f}$  is a body force per unit volume and may arise from gravitational,  $\mu$  is the first coefficient of viscosity, and  $\lambda$  is the second viscosity coefficient, related to the bulk viscosity  $\mu' = \lambda + 2/3 \mu$ . Therefore, bulk viscosity is taken as zero,  $\lambda = -2/3 \mu$ .

The energy equation is obtained from the principle of conservation of energy, as applied to a differential fluid element:

$$\frac{\partial(\rho I)}{\partial t} + \nabla \cdot (\rho\vec{v}I) = -p\nabla \cdot \vec{v} + \nabla \cdot [-k\nabla T - \rho D \sum_k h_k \nabla c_k] + \sigma : \nabla\vec{v} + S \quad (4)$$

Where  $I$  is the specific internal energy, exclusive chemical energy,  $k$  is thermal conductivity,  $T$  absolute temperature of fluid,  $D$  diffusion coefficient of mixture,  $h_k$  enthalpy diffusion of species  $k$ , and  $c_k$  concentration of species  $k$ .  $(-k\nabla T)$  is the contribution due to heat conduction.  $S$  the thermal source per unit volume and time,  $(-p\nabla \cdot \vec{v})$  the pressure work, and  $(\sigma : \nabla\vec{v})$  the viscous dissipation effects that representing the irreversible part of energy transfer due to viscous forces.

The equation set must still be completed. In compressible case however, the density must be determined. We obtain the density from the pressure by means of thermal equation of state.

$$p = \frac{\rho \bar{R}T}{M} \quad (5)$$

This equation now contain the temperature in addition, which by means of caloric equation of state:

$$I = \int_{T_0}^T c_{v(T)} dT + I_0 \quad (6)$$

That is linked with internal energy where  $I_0$  is the internal energy at reference state.

The transport equation for the concentration  $c_{(k)}$  of the particular species must be formulated,

$$\frac{\partial(\rho c_k)}{\partial t} + \nabla \cdot (\rho c_k \vec{v}) = \nabla \cdot (D_k \rho \nabla c_k) + s_k \quad (7)$$

With:

$$\sum c_k = 1 \quad (8)$$

Also, an additional diffusion term appears in the energy equation (4). If we have  $N$  species, only  $N-1$  equations of (7) should be solved. The last one obtains from equation (8).

#### 4.1.2 Turbulence models

Turbulent flows, which are of great practical importance, are three dimensional and time-dependent. Computer methods of solving the differential equations of fluid dynamics are well advanced even for three-dimensional time-dependent flows. For most engineering purposes it is unnecessary to resolve the detail of turbulent fluctuations. Only the effects of the turbulence on mean flow are usually sought. For turbulence model to be useful in general CFD code, it must have wide applicability, be accurate, simple and economical to

run. A turbulence model is a semi-empirical equation relating the fluctuating correlation to mean flow variables with various constants. When this equation is expressed as an algebraic equation, it is referred to as the zero equation models. When partial differential equations are used, they are referred to as one equation or two equation models depending on the number of PDE which utilized. These consist of sets of differential equations, and associated algebraic equations and constants, the solutions of which, in conjunction with those of the Navier-Stokes equations, closely simulate the behavior of real turbulent fluids. Two equation models of turbulence determine both the turbulence kinetic energy  $k$  and the characteristic length  $L$  from transport equations. Fortunately, the increased computational complexity is compensated by a dramatic increase in universality. The best known and most extensively tested two equation model is the so called  $\kappa$ - $\epsilon$  model, although several turbulence models have been developed for solving various turbulent flows. Among these,  $\kappa$ - $\epsilon$  model, where  $\kappa$  is the turbulent kinetic energy and  $\epsilon$  the rate of dissipation of turbulent energy, widely used. Both of these quantities are calculated from their governing differential equations. (Lander & Spalding, 1974) discussed this turbulence model. The equations for  $\kappa$  and  $\epsilon$  are solved simultaneously with the continuity, momentum, and energy equations to yield the flow and temperature distributions. For the further details see (Launder & Spalding ,1974). This model has been used by many investigator and compared with experimental data, and continues to be a popular choice for the study of turbulent flows of practical interest. At high Reynolds numbers, the transport equation for  $\kappa$  turbulent kinetic energy may be expressed:

$$\frac{\partial \rho k}{\partial t} + \nabla \cdot (\rho u k) = -\frac{2}{3} \rho k \nabla \cdot u + \sigma : \nabla u + \nabla \cdot \left[ \left( \frac{\mu}{Pr_k} \right) \nabla k \right] - \rho \epsilon \tag{9}$$

with a similar one for the dissipation rate,  $\epsilon$ :

$$\frac{\partial \rho \epsilon}{\partial t} + \nabla \cdot (\rho u \epsilon) = -\left( \frac{2}{3} c_{\epsilon 1} - c_{\epsilon 3} \right) \rho \epsilon \nabla \cdot u + \nabla \cdot \left[ \left( \frac{\mu}{Pr_\epsilon} \right) \nabla \epsilon \right] + \frac{\epsilon}{k} [c_{\epsilon 1} \sigma : \nabla u - c_{\epsilon 2} \rho \epsilon^s] \tag{10}$$

The standard values of  $\kappa$ - $\epsilon$  turbulence model constants  $c_{\epsilon 1}$ ,  $c_{\epsilon 2}$ ,  $c_{\epsilon 3}$ ,  $Pr_k$ , and  $Pr_\epsilon$  are constants whose values are determined from experimental and some theoretical considerations. The standard values of these constants are often used in engine calculation is given in below table:

$c_{\epsilon 1} = 1.44$	$c_{\epsilon 2} = 1.92$	$c_{\epsilon 3} = -1.0$	$Pr_k = 1.0$	$Pr_\epsilon = 1.3$
-------------------------	-------------------------	-------------------------	--------------	---------------------

So far we have considered convective process related to laminar flows, in which the flow is well ordered in which fluctuations and disturbances are small compared to the mean flow. Most of the convective processes that occur in industry especially, internal combustion engines, are not laminar and characterized by disturbances of large magnitude. Such flows are termed turbulent, and governing equations, may be obtained by taking the velocity, pressure, and temperature as fluctuating components superimposed on the mean values, e.g.,  $u = \bar{u} + u'$ , where  $u$  is the instantaneous value of velocity component,  $\bar{u}$  is time-averaged value, and  $u'$  fluctuating quantity. The total instantaneous quantities are substituted in the governing equations. Due to complexity with the determination of these turbulent fluctuations near solid boundaries, several simple models have been developed for the study of turbulent transport mechanism.

### 4.1.3 The turbulent law of the wall

However, there is still a problem concerning the boundary conditions. On the walls, a boundary layer is formed, in which the velocity decreasing because of friction to zero, i.e. the flow, becomes laminar. Thus in a turbulent flow the boundary layer consist of typically of laminar sub layer and a turbulent zone. The  $\kappa$ - $\epsilon$  model cannot be applied across the entire boundary layer. Moreover, the boundary layers are often so thin (especially in engines) that they are hardly numerically solvable anyway. Then usual way to overcome this problem is by deriving the so-called law of the wall. We now need a turbulent law of the wall i.e. an analytical boundary layer model, in order to calculate shear stress from the local velocities in the cell closest to the wall logarithmic law of the wall.

In engine calculations, ordinary uses turbulent law of the wall velocity condition with fixed temperature walls. For turbulent law of the wall conditions the tangential components are determined by matching to logarithmic profile:

$$\frac{v}{u^*} = \begin{cases} \frac{1}{\kappa} \ln(c_{tw} \zeta^{7/8}) + B & \zeta > R_c \\ \zeta^{1/2} & \zeta < R_c \end{cases} \quad (11)$$

Where  $\zeta = \frac{\rho y v}{\mu_{air}(T)}$  is the Reynolds number based on the gas velocity relative to the wall

which is evaluated at distance  $y$  from wall, and  $u^*$  is the shear speed, it is assumed that  $y$  is small enough to be in the laminar sub layer region of the turbulent boundary layer. The  $R_c$  defines the boundary between these two regions. The constant  $\kappa$ ,  $c_{tw}$ ,  $R_c$  and  $B$  are related to  $\kappa$ - $\epsilon$  model constant by :

$B=5.5$ ,  $c_{tw}=0.14$ ,  $\kappa=0.437$ ,  $R_c=114$  that commonly accepted values of the  $\kappa$ - $\epsilon$  constants.

For the numerical solution, the node nearest to the wall must remain within the boundary layer.

$$T - T_w = \frac{q_w Pr}{\kappa c_p \rho v_t} (\ln y^+ + const) \quad (12)$$

A law of the wall can be derived quite analogy for the temperature. For fixed temperature walls using the turbulent law of the wall condition,  $J_w$  is determined from the modified Reynolds analogy formula:

$$\frac{J_w}{\rho u^* c_p (T - T_w)} = \begin{cases} 1 / (Pr_t \frac{v}{u^*}) & \zeta \leq R_c \\ 1 / \{Pr_t [\frac{v}{u^*} + (\frac{Pr_t}{Pr} - 1) R_c^{1/2}]\} & \zeta > R_c \end{cases} \quad (13)$$

$T_w$  is the wall temperature and  $Pr_t$  is the Prandtl number of the laminar fluid.

## 5. Foundation of reaction

### 5.1 Chemical equilibrium

A general chemical equilibrium reaction with  $v'_{i,s}$  and  $v''_{i,s}$  representing the stoichiometric coefficients of reaction and products for the chemical species  $M_i$

$$\sum_{i=1}^N v'_{i,s} M_i \rightleftharpoons \sum_{i=1}^N v''_{i,s} M_i \quad (14)$$

Since every chemical reaction can be in principle run both forwards as well as backwards, the reaction arrow in (14) can be replaced with an equal sign. We hence obtain the general form of conservation of species:

$$\sum i (v''_{i,s} - v'_{i,s}) M_i = 0 \quad (15)$$

hence the stoichiometric coefficients are negative for all primitive and positive for all products. State of equilibrium can be interpreted as a situation, in which both the forward as well as reverse reactions progress with identical speed.

$$K_p(T) = \prod_i \left( \frac{p_i}{p_0} \right)^{(v''_{i,s} - v'_{i,s})} \quad (16)$$

The equilibrium constant  $K_p$  now contains the information about the equilibrium material composition in term of partial pressure  $p_i$  of the various species  $i$ .

## 5.2 Reaction kinetics

A one step chemical reaction of arbitrary complexity can be represented by the following stoichiometric equation:



Where  $v'_i$  are the stoichiometric coefficient of reactions and  $v''_i$  representing the stoichiometric coefficient of products,  $M_i$  molecular weight of  $i$ th chemical species, and  $N$  total number of component involved. For the chemical reaction species concentration, e.g. for the  $[M_i]$ , can be given with empirical formulation:

$$\frac{d[M_i]}{dt} = (k_f [A_a]^{v_a} [A_b]^{v_b} - k_r [A_c]^{v_c} [A_d]^{v_d}) \quad (18)$$

hence the first term on the right side describes the reaction rate of the forward direction and the second term the rate of the reverse reaction.  $k_f$  and  $k_r$  are thereby the so-called rate coefficient of the forward and reverse reactions. They must be determined experimentally for every particular chemical reaction. They are customarily represented with an Arrhenius formulation form:

$$K = AT^b \exp(-E_A / RT) \quad (19)$$

The constant  $A$  and the exponent  $b$  as well as the so-called activation energy  $E_A$  are summarized for many chemical reactions in extensive table.

## 6. Boundary conditions

Any numerical simulation can consider only a part of the real physical domain or system. The truncation of the domain leads to artificial boundaries, where we have to prescribe

values of certain physical quantities. Furthermore, walls which are exposed to the flow represent natural boundaries of the physical domain. The numerical treatment of the boundary conditions requires a particular care. An improper implementation can result in inaccurate simulation of the real system. Additionally, the stability and the convergence speed of the solution scheme can be negatively influenced. The following types of boundary conditions are in general encountered in the numerical solution of the Navier-Stokes equations:

1. Solid wall
2. Symmetry
3. Coordinate cut and periodic boundary
4. Boundary between blocks
5. Inflow or out flow
6. Pressure inlet or pressure outlet
7. Axes

## 7. Numeric

After selecting the mathematical model, suitable discretisation method should be chosen, i.e. a method for approximation differential equations by a system of algebraic equations, for the variables at some set of discrete locations in space and time. The most important approaches are finite difference (FD), finite volume (FV) and finite element (FE) methods.

In the following, some basic concepts of numerical fluid mechanics will be explained, in order to become acquainted with its most essential concepts, which are also of importance for practical work. The description that follows refers to a so called finite volume procedure, that is proven to be unconditionally stable, as accurate as the accuracy of current state of physical modeling permits, robust and efficient.

The starting point of the analysis is the set of three dimensional, partial differential equations that govern the phenomena of interest here. This set consists, in general, of following equations: the continuity equation; the three momentum equations that govern the conservation of momentum per unit mass (the velocity) in each three space directions (the Navier-Stokes equations); the equation for conservation of energy and species concentration, and the equations for a "turbulence model". We shall consider them in their most general form.

It is generally accepted that the turbulence model flow field in an IC engine strongly influenced its combustion process, thermal efficiency and emissions. Traditionally, knowledge of flow field has been extracted from experimental investigations which tend to be costly, lengthy and inflexible. The most widely used model of turbulence in IC engine research is the  $\kappa$ - $\epsilon$  model.

### 7.1 The finite volume method

Customarily, CFD codes work with the finite volume method. This approach guarantees the numerical preservation of conservative quantities for the incompressible flows. The FV method uses the integral form of the conservation of equations. The solution domain is subdivided into a finite number of control volumes, and the conservation equations are applied to each control volume. At centroid of each CV lie computational nodes at which the variable values are to be calculated. As a result, an algebraic equation for each CV is obtained. The FV method can accommodate any type of grid, so it is suitable for complex geometries.

However, the computational mesh ideally, be built hexahedratically. The conservation law for transport of a scalar in an unsteady flow has the general form:

$$\frac{\partial}{\partial t}(\rho \Phi) + \nabla \cdot (\rho u \Phi) = \nabla \cdot (\Gamma \nabla \Phi) + S_\Phi \tag{20}$$

$(\rho u \Phi)$  designates convection,  $(\Gamma \nabla \Phi)$  diffusion flows of and  $S_\Phi$  the corresponding local source. With the help of Gaussian law follows and by replacing the volume integrals of convective and diffusion term we obtain:

$$\begin{aligned} & \int_{CV} \left( \int_t^{t+\Delta t} \frac{\partial}{\partial t}(\rho \Phi) dt \right) dV + \int_t^{t+\Delta t} \left( \int_A n \cdot (\rho u \Phi) dA \right) dt \\ & = \int_t^{t+\Delta t} \left( \int_A n \cdot (\Gamma \nabla \Phi) dA \right) dt + \int_t^{t+\Delta t} \left( \int_{CV} S_\Phi dV \right) dt \end{aligned} \tag{21}$$

**7.2 The finite volume equations formulation**

Finite volume equations are derived by the integration of above differential equations over finite control volumes that taken together fully cover the entire domain of interest (Fig 3). These control volume are called "cells" Say P, for which the fluid-property value, are regarded as representative of the whole cell. It is surrounded by neighboring nodes which we shall denote by N, S, E, W, B and T. cells and nodes for velocity components are "staggered" relative to those for all other variables.

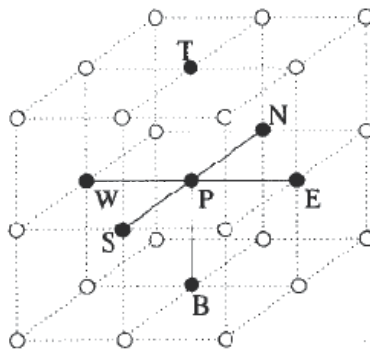


Fig. 3. Computational molecule in 3D domain(Patankar, 2002)

The integration involved is different to the usual Taylor-series expansion used in classical finite-difference technique, and results in different coefficients of algebraic equations that are finally obtained. The description that follows refers to a so called finite volume procedure, that is proven be unconditionally stable, as accurate as the accuracy of current state of physical modeling permits, robust and efficient.

**7.3 Discretisation and numerical solution of the momentum equation**

Finally, the momentum equation for the calculation of velocity and pressure by use of continuity equation should be considered. For numerical reasons, it is recommendable to resort to so called staggered grid, i.e. pressure and velocity are calculated on computational grids shifted to each other, the pressure for example in the cells and the velocity on the

nodes. The calculations of velocity commonly take place iteratively, for which several algorithms are known (e.g. SIMPLE, PISO, SIMPLER...). In final analysis, all have the fact in common that is first step the momentum equation is solved for the velocities of momentums kept constant. In the second step, pressure corrections are then calculated with the help of a poisson equation. For pressure with these pressure corrections, new velocities are then calculated again, and thud again, until a pre-given break off threshold for the convergence is reached.

**7.3.1 Discretisation of transient convection diffusion equation**

Transient three dimensional convection diffusion of a general property  $\Phi$  in a velocity field that  $\vec{v}$  govern by equation (20). The fully implicit discretisation equation is:

$$a_p \Phi_p = a_w \Phi_w + a_E \Phi_E + a_s \Phi_s + a_N \Phi_N + a_B \Phi_B + a_T \Phi_T + a^\circ_p \Phi_p + S_u \tag{22}$$

where:

$$a_p = a_w + a_E + a_s + a_N + a_B + a_T + a^\circ_p + \Delta F - S_p \tag{23}$$

with  $a^\circ_p = \frac{\rho_p \Delta V}{\Delta t}$  and  $\bar{S} \Delta V = S_u + S_p \Phi_p$

the neighbor coefficients of this equation for hybrid differencing scheme as follows:

$a_w$	$\max [F_w, (D_w + F_w/2), 0]$
$a_E$	$\max [-F_e, (D_e - F_e/2), 0]$
$a_s$	$\max [F_s, (D_s + F_s/2), 0]$
$a_N$	$\max [-F_n, (D_n - F_n/2), 0]$
$a_B$	$\max [F_b, (D_b + F_b/2), 0]$
$a_T$	$\max [-F_t, (D_t - F_t/2), 0]$
$\Delta F$	$F_e - F_w + F_n - F_s + F_t - F_b$

Table 1. The neighbor coefficients of this equation for hybrid differencing scheme (Patankar, 1980)

In the above expressions the values of F and D are calculated with the following formulae:

Face	W	E	S	N	B	t
F	$(\rho u)_w A_w$	$(\rho u)_e A_e$	$(\rho v)_s A_s$	$(\rho v)_n A_n$	$(\rho w)_b A_b$	$(\rho w)_t A_t$
D	$\frac{\Gamma_w}{\delta x_{WP}} A_w$	$\frac{\Gamma_e}{\delta x_{PE}} A_e$	$\frac{\Gamma_s}{\delta y_{SP}} A_s$	$\frac{\Gamma_n}{\delta y_{PN}} A_n$	$\frac{\Gamma_b}{\delta z_{BP}} A_b$	$\frac{\Gamma_t}{\delta z_{PT}} A_t$

**7.3.2 Different approach**

Employing the governing momentum equation and Poisson equation for the pressure, the numerical scheme may be based on the primitive variables. A stagger grid is employed, as shown in Fig.4 for two dimensional flows. The locations for the velocity components are placed at the faces of the control volume. If a uniform grid is used, the locations are exactly midway between the grid points. Therefore, the locations for the velocity components are agreed. Since the pressure difference between two adjacent grid points is the driving force for the velocity component. Located between these points, the finite difference

approximation is physically correct and will accept only reasonable velocity field. Also, the transport rates across the faces of control volumes can be computed without interpolation of velocity components. This approach has been adopted for several efficient schemes for flow computation, such as those discussed by (Patankar, 1980). If interest lies only in the steady state flow field and if a steady state is known to exist, the problem may be solved by iterative procedure, though time marching may also be employed to yield the steady state distribution at large time. The SIMPLER algorithm, discussed in detail by (Patankar, 1980), and outlined in the following section, for instance, employs a pressure-correction equation for correcting the velocities during iteration and a pressure equation for improving the pressure field.

### 7.3.3 The staggered grid

The finite volume method starts, as always, with discretization of the flow domain and of the relevant transport equations. First we need to decide where to store the velocities. It seems logical to define these at the same locations as the scalar variables such as pressure, Temperature, etc. However, if the velocity and pressure are both defined at the nodes of ordinary control volume, it is clear that, the influence of pressure is not properly represented in the discretization momentum equations, For more information (Blazek, 2001). A remedy for this problem is to use a staggered grid for velocity components (Harlow & Welch, 1965). The idea is to evaluate scalar variables, such as pressure, density, temperature etc., at ordinary nodal points but to calculate velocity components at staggered grids centered on the cell faces. The arrangement for a two dimensional flow calculation is shown in Fig. 4.

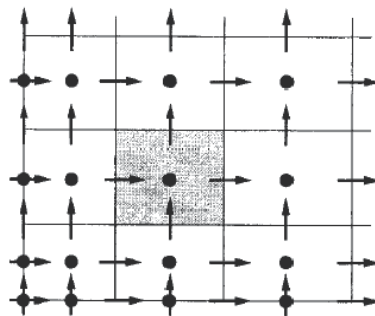


Fig. 4. Staggered grid (Patankar, 1980)

The scalar variables, including pressure, are stored at nodes marked ( $\bullet$ ). The velocities are defined at the cell faces in between the nodes and are indicated by arrows. Horizontal arrow ( $\rightarrow$ ) indicates the locations for  $u$ -velocities and vertical ( $\uparrow$ ) ones denote those for  $v$ -velocities. For the moment we continue to use the original E, W, N, S notation; the  $u$ -velocities are stored at scalar cell faces 'e' and 'w' and the  $v$ -velocities at faces 'n' and 's'. In a three dimensional flow the  $w$ -component is evaluated cell faces 't' and 'b'.

## 8. Simple algorithm

As discussed in the proceeding section, the governing equation for the flow may be solved in terms of derived variables, or in term of primitive variables consisting of the velocity components and the pressure.

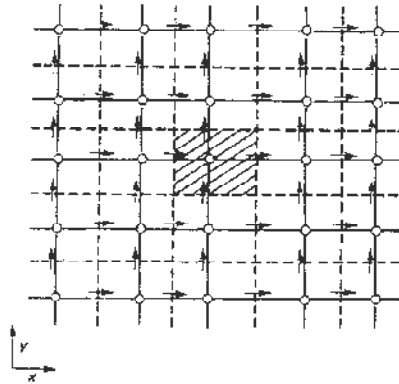


Fig. 5. Staggered location for the velocity components in a two dimensional flow(Patankar, 1980)

Still, pressure calculation has been major hurdle in, attracting researchers to the stream function-vorticity approach even for three dimensional flows. However, in the advent of Simple (Semi Implicit Method for Pressure Linked Equations) algorithm, along with its revised version Simpler and the enhancement such as Simplec (Van Doormaal & Raithby ,1984), the solution of the equations using primitive variable approach has become very attractive. In fact, Simple and Simple like algorithms are extremely popular for the solution of problems involving convective flow and transport. The basic approach involves the control volume formulation, with the staggered grid, as outlined in the proceeding section. This avoids the appearance of physically unrealistic wavy velocity fields in the solution to equations. The pressure difference between two adjacent points in the natural driving force for the velocity component located between these points and checkerboard pressure fields do not arise as possible solutions. The pressure at a chosen point is taken at arbitrary value and the pressures at other points are calculated as differences from the chosen pressure value.

Following (Patankar, 1980), if a guessed pressure field  $p^*$  is taken, the corresponding velocity field can be calculated from the discretised equations for the control volume shown in Fig. 6. These equations are of the form:

$$a_e u_e = \sum a_{nb} u_{nb}^* + b + (p_p^* - p_E^*) A_e \quad (24)$$

Where the asterisk on the velocity indicates the erroneous velocity field based on guessed pressure field. Here,  $a_{nb}$  is a coefficient that accounts for the combined convection-diffusion at the faces of the control volume, with  $nb$  referring to the neighbors  $e$  to the control volume,  $b$  includes the source terms except the pressure gradient, and  $A_e$  is the area on which pressure acts, being  $\Delta y^* \Delta z$  for 3D. The numbers of neighbor terms are 6 for three dimensional ones. Similar equations can be written for  $v_n^*$  and  $w_t^*$ , where  $t$  lies on the  $z$ -direction grid line between grid points P and T.  $p$  is the correct pressure and  $p'$  the pressure correction, we may write:

$$p = p^* + p', u = u^* + u', v = v^* + v', w = w^* + w' \quad (25)$$

Where the prime indicate corrections needed to reach the correct values that satisfy the continuity equation. Omitting the correction terms due to the neighbors, an iterative

solution may be developed to solve for the pressure and the velocity field. Then, the velocity correction formula becomes:

$$\begin{aligned}
 u_e &= u_e^* + \frac{A_e}{a_e} (p'_p - p'_E) \\
 v_n &= v_n^* + \frac{A_n}{a_e} (p'_p - p'_N)
 \end{aligned}
 \tag{26}$$

And similarly for  $w_t$ . From the time dependent continuity equation, the pressure correction equation is then developed as:

$$a_p p'_p = a_E p'_e + a_w p'_w + a_N p'_N + a_s p'_s + a_T p'_T + a_B p'_B + b
 \tag{27}$$

Where  $b$  is a mass source which must be eliminated through pressure correction so that continuity is satisfied. Here, T and B are neighboring grid points on the z direction grid line.

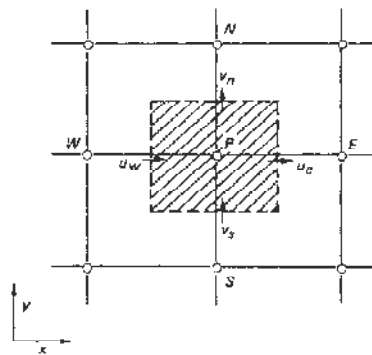


Fig. 6. Control volume for driving the pressure correction equation (Patankar, 1980)

The simple algorithm has the following main steps:

1. Guess the pressure field  $p^*$ .
2. Solve the momentum equation to obtain  $u^*, v^*$ , and  $w^*$ .
3. Solve the pressure correction equation to obtain  $p'$ .
4. Add  $p'$  to  $p^*$  to obtain the corrected pressure  $p$ .
5. Calculate  $u, v$  and  $w$  from  $u^*, v^*$  and  $w^*$  using velocity correction equations.
6. Treat the corrected pressure  $p$  as the new guess  $p^*$  and iterate the preceding procedure to convergence.

The revised version Simpler is quite similar to preceding algorithm and was developed mainly to improve the rate of convergence. In this case, the main steps are:

1. Guess the velocity field
2. Solve the pressure equation, which is similar to pressure correction equation, Eq. (26), to obtain the pressure distribution. In this equation  $p'$  is replaced by  $p$  and a different expression arise for  $b$ .
3. Treating the pressure field as  $p^*$ , solve the momentum equations to obtain  $u^*, v^*$  and  $w^*$ .
4. Solve the pressure correction equation to obtain  $p'$ .
5. Correct the velocity field but not the pressure.
6. Use the velocity field as the guessed distribution and iterate the preceding procedure to convergence.

The pressure at any arbitrary point in the computational domain is specified and pressure differentials from this value are computed. The boundary condition may be a given pressure, which makes  $p' = 0$ , or a given normal velocity which makes the velocity a known quantity at the boundary and not a quantity to be corrected so that  $p'$  at the boundary is not needed. For further details, (Ptankar, 1980) may be consulted.

## 10. Example

In the following simulation of SI internal combustion is discussed. We consider the intake, compression, combustion and exhaust process in an engine but only the results of mesh preparation and heat flux are discussed.

### 10.1 Grid generation

Prior to CFD simulation, computational mesh was generated for the engine using ICEM CFD scheme. The geometry of a mesh is composed of any arbitrary number of logical blocks that are patched together in a seamless fashion. Patching allows complex geometries to be created, block by block while minimizing the number of deactivated zones that surround the final mesh. The movement of piston/flow domain was resolved using the boundary motion feature of available code. During the solution process, as the piston moves, the internal mesh structure deforms automatically to optimize the mesh. The distortion of each individual cell occurs when the generated cell distortion reaches a certain level, and the solution is re-zoned onto new mesh. Mesh size ranged from about 90000 at BDC to about 46000 at TDC for computational studies.

### 10.2 Initial and boundary conditions

Computation starts at TDC. Initial charge densities were calculated based on ambient pressure of 0.85 bar and temperature of 300K at inlet valves opening. The standard  $\kappa - \varepsilon$  turbulence model in the code was used with an initial value of turbulent kinetic energy  $k$ , assumed 10 percent of the total kinetic energy based on the mean piston speed that supposed to be uniform. Radial velocity is initialized assuming a swirl ratio 0. Temperature was taken as 485K for liner, 600K for cylinder head and piston, 550K for intake valves, and 800K for exhaust valves.

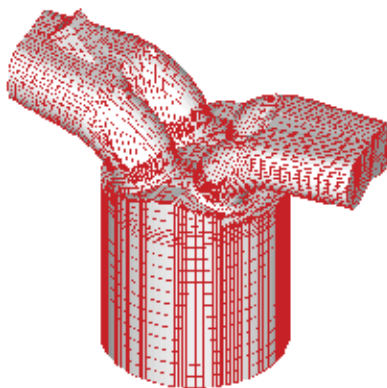


Fig. 7. Computational mesh at bottom dead center (Mohammadi et.al, 2009)

### 10.3 Discussion

In Figs. 8-a and b variations of heat flux and heat transfer coefficient on the cylinder head, liner, piston, intake and exhaust valves versus crank angle are illustrated. Heat flux has very low value in the intake and most part of compression process relative to the value of heat flux after combustion. Such quantities of heat transfer are usually negligible in experimental measurements. After combustion and release of chemical energy, heat flux rises rapidly when the flame arrives at each location, and it has maximum value at about 20 ATDC for all parts of the cylinder. Maximum heat flux and heat transfer coefficient are at intake valves that reach to  $5.4 \text{ MW/m}^2$  and  $3.82 \text{ kW/m}^2 \cdot \text{K}$  and the minimum value is on the cylinder wall with  $1.18 \text{ MW/m}^2$  and  $0.96 \text{ kW/m}^2 \cdot \text{K}$  respectively. Heat flux through combustion chamber walls is mainly due to gas-phase convection, fuel film conduction and chemical reactions.

From Fig. 8-a it can be seen that the peak heat flux take places on the intake valves because the gradient of temperature between gas and the valves surface are higher than other locations. Heat flux on the cylinder head is more than piston because flame initiate near head (spark plug is between inlet and exhaust valves) and arrives sooner to the surface of piston. Liner heat flux has lower value than other places because its location is further from flame than other locations and temperature of the wall is lower than other locations and flame is quenched near it.

Fig. 8-b shows that heat transfer coefficient on the intake and exhaust valves is almost equal and is the highest value, because the gas velocity (or Reynolds number) in this region is highest. Heat transfer coefficient on the cylinder head is more than piston and on the liner it has the lowest value where the temperature gradient and gas velocity are lowest.

After 60 degree, ATDC expansion cools the burned gases and heat flux decay to relatively low level.

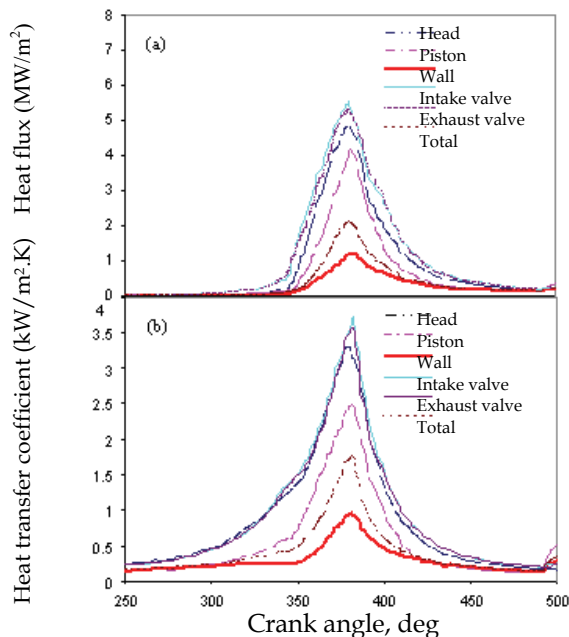


Fig. 8. Variation of: a) surface heat flux at various locations with crank angle, b) heat transfer coefficient at various locations with crank angle (Mohammadi et.al, 2009)

## 11. Conclusion

In this chapter CFD simulation of spark ignition engine was discussed. Fundamental of structured mesh generation, governing equation for Fluid mechanics, include, mass, momentum and energy equations, turbulence model and law of the wall, principle of equilibrium and kinetics reaction equation for combustion simulation were discussed. For numerical simulation of system of equations finite volume method for discretization of the equations was used, simple algorithm for solving the equations were discussed and in final one example of numerical simulation of heat flux and heat transfer coefficient in a spark ignition was discussed.

## 12. References

- Blazek, J. (2001). *Computational Fluid Dynamics : Principles and Applications*, Elsevier Science Publishing Co, ISBN 0080430090, UK.
- Chung, T. J. (2002). *Computational Fluid Dynamics*, Cambridge University Press, ISBN 0-521-59416-2, UK.
- Ferziger, J. H. & Peric, M. (2002). *Computational Method for Fluid Dynamics*, Springer, ISBN 3-540-42074-6, Germany.
- Heywood, J. B. (1988). *Internal Combustion Engine Fundamentals*, McGraw-Hill, ISBN 0-07-02863-X, USA.
- Hoffmann, A. (1989). *Computational Fluid Dynamics for Engineers*, John Wiley Engineering Educational system, ISBN 0-9623731-4-1, USA.
- Kuo, K. K. (2005). *Principle of Combustion*, John Wiley & Sons, ISBN 0-471-04689-2, USA.
- Launder, B. E. & Spalding, P. B. (1974). The numerical computation of turbulent flows, *Computer Method in Applied Mechanics and Engineering*, Vol 3 3, pp. 269-289.
- Mohammadi, A. & Yaghoubi, M. (2010). Estimation of instantaneous local heat transfer coefficient in spark ignition engines, *International Journal of thermal science*, Vol. 49, pp. 1309-1317.
- Mohammadi, A.; Jazayeri, A. & Ziabasharhagh. M. (2008). Numerical simulation of convective heat transfer in a spark ignition engine, *Proceeding of the ASME international combustion engine*, Illinois, USA, April 27-30, Chicago.
- Mohammadi, A.; Yaghoubi, M. & Rashidi, M. (2008). Analysis of local convective heat transfer in a spark ignition engine, *Journal of International Communication heat and mass transfer*, Vol 35, pp. 215-224.
- Patankar. S. V. (1980). *Numerical Heat Transfer and Fluid flow*, McGraw-Hill, ISBN 0-07-048740-5, USA.
- Thompson, J. F.; Warsi, Z. U. A, & Wayne Mastin, C. (1985). *Numerical Grid Generation*, Elsevier Science Publishing Co,.
- Versteeg, H. K. & Malalasekera, W. (1995). *An Intraduction to Computational Fluid Dynamics the Finite Volume Method*, Prentice Hall, Edinburg, ISBN 0-444-00985-X, England.

# Advanced Numerical Simulation of Gas Explosion for Assessing the Safety of Oil and Gas Plant

Kiminori Takahashi and Kazuya Watanabe  
*JGC Corporation*  
*Japan*

## 1. Introduction

The authors have deeply been interested in concerns about health, safety & environment (HSE) in recent years. HSE demands in engineering, particularly at the design and construction stages, are becoming stricter and stricter. In oil and gas plants, many pieces of equipment, and much of the piping, treat highly flammable gases, such as natural gas, methane, propane and hydrogen, which if released, can cause vapour cloud explosions. Therefore, gas explosions are major risks in oil and gas plants. In particular, safety evaluations in connection with gas leaks and explosions are becoming more important as a part of measures to reduce risks for plants at the design stage. A gas explosion simulation system had been developed in order to respond to the safety demands of society and for the purposes of efficient plant design within an appropriate level of investment.

This paper presents a mechanism of a gas explosion, methods for numerical simulations of gas explosions and case studies. To aid such simulations and calculations, advanced numerical simulations, integration of 3D Computer Aided Design (3D-CAD), Computational Fluid Dynamics (CFD) and Finite Element Analysis (FEA) are used. The integrated gas explosion simulation is utilized to predict gas dispersions, gas explosions, blast pressures and structural responses. Understanding the explosion phenomenon can help to avoid risks in oil and gas plants, and the integrated gas explosion simulation can be used to assess the safety of oil and gas plants.

## 2. Theory and numerical method

### 2.1 Mechanism of gas explosion

A gas explosion is the sudden generation and expansion of gases associated with increases in temperature and pressure which can cause structural damage. Blast pressures propagating away from the cloud center can cause extensive damage over a wide area. If combustion occurs in a medium of low initial turbulence without obstacles, the overpressure becomes very low. If obstacles are present, the flow will generate turbulence through the obstacles. The turbulence intensity will enhance combustion rates due to increase burning velocities, and then higher combustion rates will produce stronger expansion flows and the higher turbulence intensity. This cycle continues, generating higher burning velocities and increasing overpressures (Figure 1).

A deflagration is subsonic combustion. The burning velocity is subsonic and is much lower than the speed of sound in the unburnt gas. A detonation is a self-driven shock wave where the reaction zone and the shock zone are coincident. The burning velocity is supersonic and is much higher than the speed of sound in the unburnt gas. In a detonation, propagation velocities of the combustion waves can grow up to 2000 m/s with a pressure ratio across the detonation front up to 20.

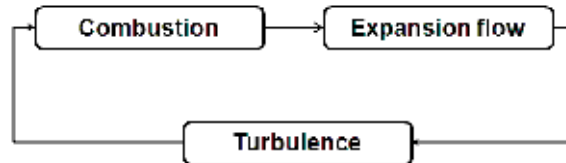


Fig. 1. Basic mechanism of gas explosion

## 2.2 Conventional method

Conventional methods for analysing a gas explosion are simple, are easy to use and give rough predictions of blast pressures in the field. In the conventional methods, such as the TNT equivalency model and the Multi-Energy model, the blast source strength is obtained after determining the obstacle density based solely on the total volume of the equipment, piping and structures. Therefore, the blast overpressure does not precisely reflect the complex geometries of actual plant equipment.

## 2.3 Computational Fluid Dynamics (CFD)

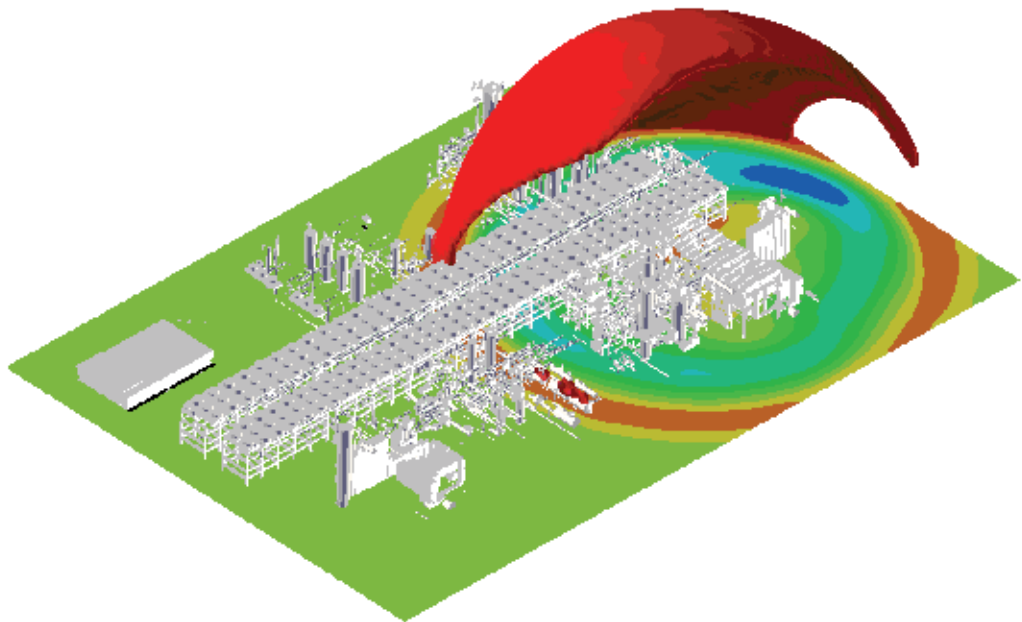


Fig. 2. Representation of gas explosion simulation

CFD is a computer-based tool for simulating the behavior of systems involving fluid flow, heat transfer, and other related physical processes. CFD models find numerical solutions to the partial differential equations, Navier-Stokes equations with turbulence models, gas diffusion models and combustion models governing the gas explosion process, and then can model complex geometries and provide a wealth of information about flow fields. Recently, CFD has been used for simulation of gas explosions because the strength of gas explosions depends on the geometry, such as size, confinement and turbulence-generating obstructions, and on the gas mixture, such as composition, location and quantity. CFD can provide information on maximum overpressure anywhere, overpressure at given points, average pressure on walls. Therefore CFD generates more realistic and more accurate information than conventional methods (Figure 2). However CFD generally includes numerical models of deflagrations, but does not include models of detonations.

### 2.4 Finite Element Analysis (FEA)

FEA is a numerical technique for finding approximate solutions of partial differential equations as well as of integral equations. By use of FEA, structural analysis comprises the set of physical laws and mathematics required to compute deformations, internal forces and stresses in mechanical, civil engineering, etc. This powerful design tool has significantly improved both the standard of engineering designs and the methodology of the design process in many industrial applications.

## 3. Integrated gas explosion simulation

Integrated explosion simulation comprises the series of four types of simulation (Figure 3), and can provide detailed information necessary for blast resistant design and risk assessment.

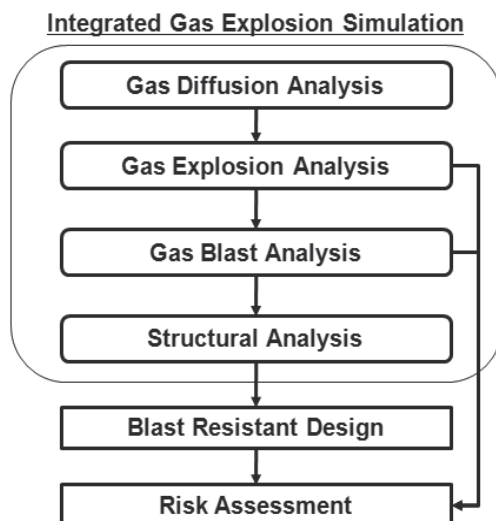


Fig. 3. Workflow of integrated gas explosion simulation

Blast resistant design is used to design buildings and civil engineering infrastructure to withstand explosions. Risk assessment is a step in a risk management, and is carried out by determining quantitative and qualitative values of risks. Quantitative risk assessment (QRA) represents the risks of accidents and suggests appropriate means of minimizing the risks. Frequency analysis in QRA estimates how likely accidents will occur, and frequency is usually obtained from analysis of the previous accident experience. For such cases, the frequency data are mostly derived from trusted statistical databases such as "UK HSE Offshore Hydrocarbon Release Statistics". The probability of a gas explosion is obtained by frequency analysis from gas leak scenarios. As a criterion for explosion risk, the probability of  $10^{-4}$  per year is generally considered reasonable as explosion design loads. Consequent analysis evaluates the resulting effects when accidents occur. These effects could be on the human body and plant facilities like equipment, piping and structures. The consequent data are usually overpressures obtained by gas explosion analysis or gas blast analysis, and are deformations and stresses obtained by structural analysis. Risk values can be obtained only by multiplying the magnitude of the consequences and their individual occurrence frequency. The phenomena of explosion can vary enormously depending upon conditions that contribute explosion. Therefore, determining the tendency of the phenomenon through simulations requires considerable numbers of runs with broad combination of each parameters.

### **3.1 Gas dispersion analysis**

Gas dispersion analysis is performed using CFX from ANSYS Inc., which is one of the most popular and advanced CFD tools. The gas dispersion analysis employs Navier-Stokes equations with turbulence models, gas diffusion models by the finite volume method. A gas leakage scenario in which such initial conditions as the kind of leaked gas, leak rate, leak direction, temperature, and wind direction and velocity, etc. are specified. Then, gas concentrations can be provided for a scenario.

### **3.2 Gas explosion analysis and gas blast analysis**

Gas explosion analysis and gas blast analysis are performed using AutoReaGas from TNO Prins Maurits Laboratory and Century Dynamic Inc., which is one of the special explosion CFD tools. The gas explosion analysis employs Navier-Stokes equations with turbulence models, gas diffusion models and combustion models by the finite volume method. In order to accurately represent steep gradients in shock waves, the gas blast analysis employs Euler equations without turbulence models, gas diffusion models and combustion models by Flux Corrected Transport (FCT) technique. FCT is widely used in the numerical simulation of gas dynamic phenomena. The reason is that FCT makes optimised use of numerical diffusion, then offers great accuracy and efficiency. The geometry of objects such as equipment, piping and structures can be translated from 3D-CAD data by use of the translator program developed by us. The initial conditions for the gas explosion analysis are used as the gas concentrations obtained from the gas dispersion prediction, and the initial conditions for the gas blast analysis are used as the overpressures obtained from the gas explosion prediction. These analyses can be used to simulate burning velocities and overpressures in deflagrations.

### 3.3 Structural response analysis

Structural response analysis is performed using Abaqus, which is one of the most advanced and powerful tools for this kind of analysis. The results of the gas blast analysis, such as time histories of the overpressures on the surfaces of the control building, are used as the loading conditions for the structural response analysis.

## 4. Case study

The geometry model for case studies is shown in Figure 4. This is a typical LNG plant, comprising a large number of objects, such as equipment, structures and piping, modeled in 3D-CAD, and the plot area is about 300 m x 200 m. The location of the gas leak is in the northeast area, and the control building is in the southwest area. This case study does not consider an internal explosion, like an explosion that takes place inside a reactor or a furnace. The leaked gas is assumed to be propane because methane and natural gas tend to cause a fire, rather than an explosion, because these gases are lighter than air and quickly rise and dissipate in the open air.

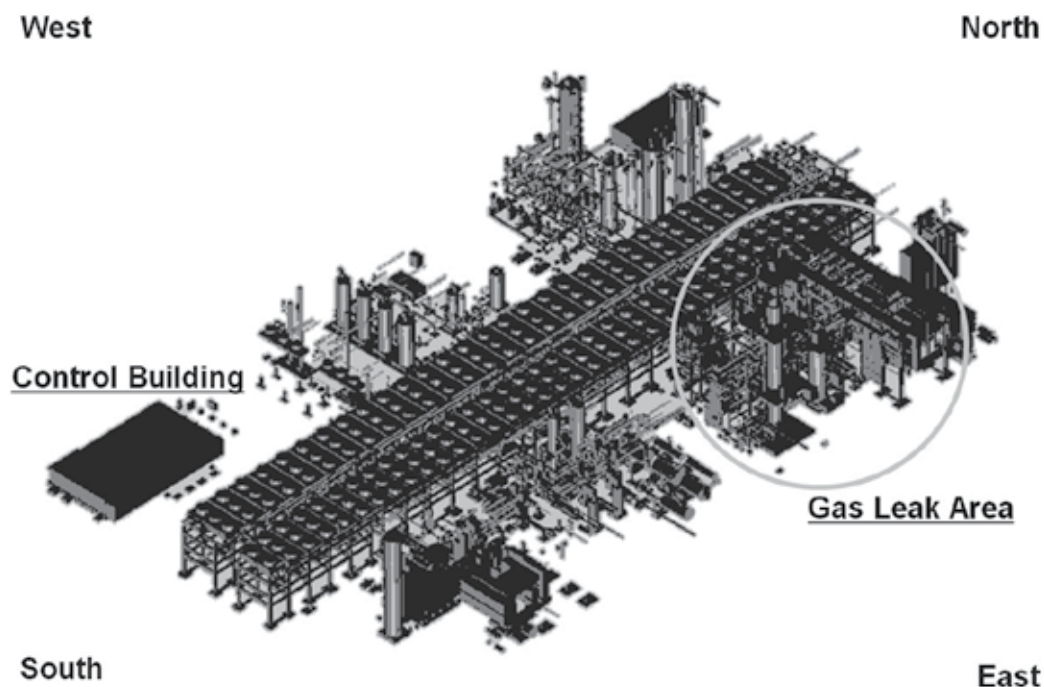


Fig. 4. Geometry model of typical LNG plant

### 4.1 Gas dispersion analysis

In this case study, it is assumed that a gas leak occurs in the northeast area (circled in Figure 4), and the conditions are those presented in Table 1. The gas dispersion prediction shows the gas cloud on the ground (Figure 5).

Ambient condition	Atmospheric temperature [K]	300
	Atmospheric pressure [atm]	1
	Wind velocity [m/s]	0
Gas leak condition	Service fluid	Propane gas
	Position of release	See Figure 5
	Height of release [m]	5
	Diameter of hole [m]	0.05
	Leak rate [kg/s]	50
	Leak direction	Horizontal in the northerly direction
Ignition condition	Ignition time after release [s]	30
	Position of ignition	See Figure 5
	Height of ignition [m]	2

Table 1. Gas leakage scenario

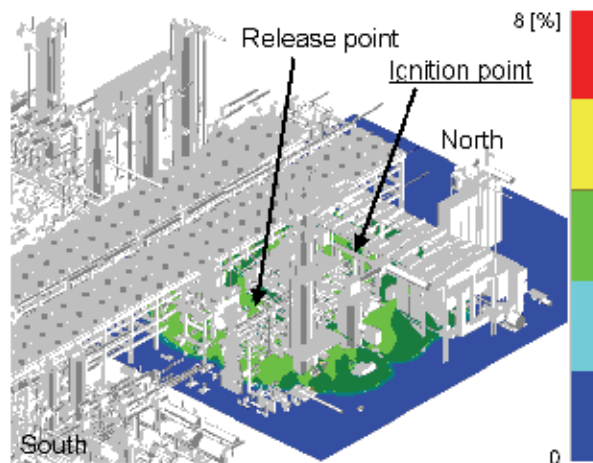


Fig. 5. Gas concentrations at 30 s after gas release

#### 4.2 Gas explosion analysis and gas blast analysis

The gas explosion prediction shows overpressures (Figure 6). The high overpressures indicate a strong explosion on the south side, while the low overpressures indicate a weak explosion on the north side. The overpressures are very important in determining the blast strengths.

The gas blast prediction shows overpressure time histories realistically (Figure 7). The blast waves of minimum overpressure appear after the blast waves of maximum overpressure, and the pressure gradient is very high in these areas, making it very dangerous in these areas. The maximum blast overpressure reached on the control building at 1 s after ignition. Figure 7 shows a characteristic of the gas blast phenomenon.

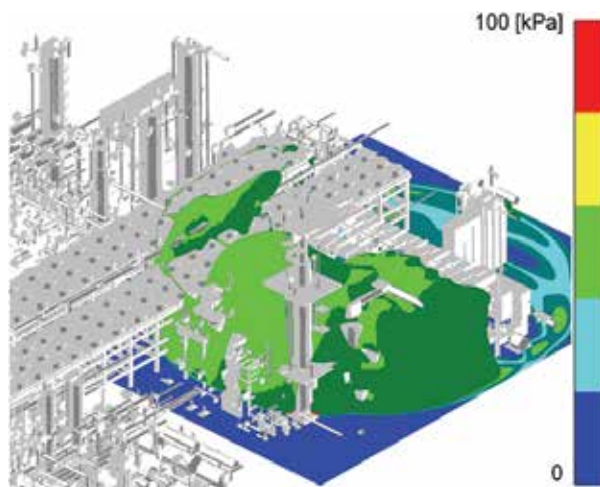


Fig. 6. Overpressures at 0.55 s after ignition

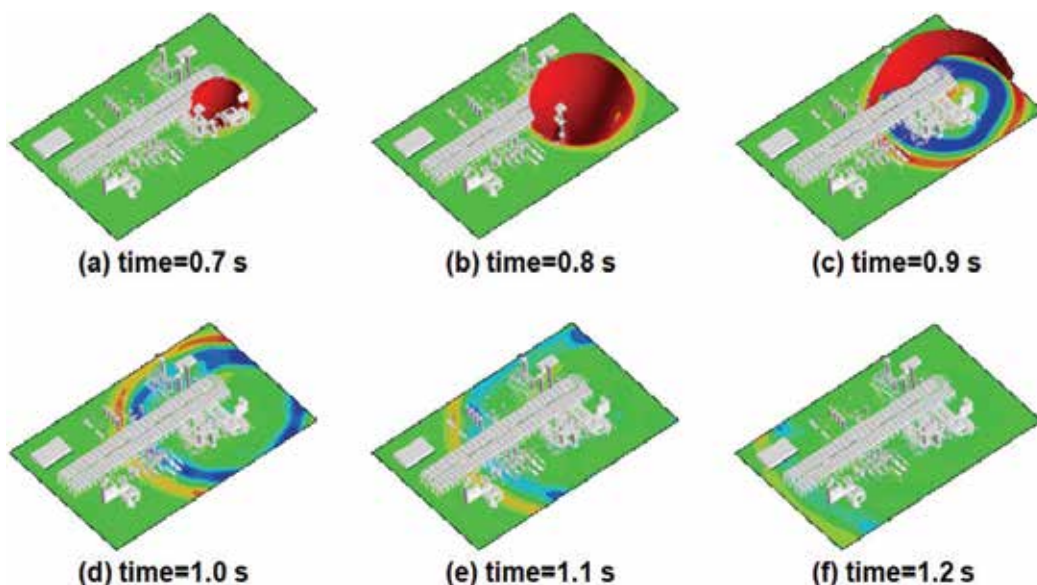


Fig. 7. Overpressure time histories after ignition (red shows positive overpressure and blue shows negative overpressure)

The shape of the blast waves is shown in Figure 8(a) and the time histories of the blast overpressures on the control building are shown in Figure 8(b). In this case study, the maximum blast overpressure on the control building is only 15 kPa, while the maximum explosion overpressure is over 100 kPa (Figure 6). Furthermore, it can be seen that the maximum overpressure on the side of the control building facing the explosion (gauge point X1) is two times higher than that on the roof (gauge point X2). Thus, this information is useful for the design of plant facilities.

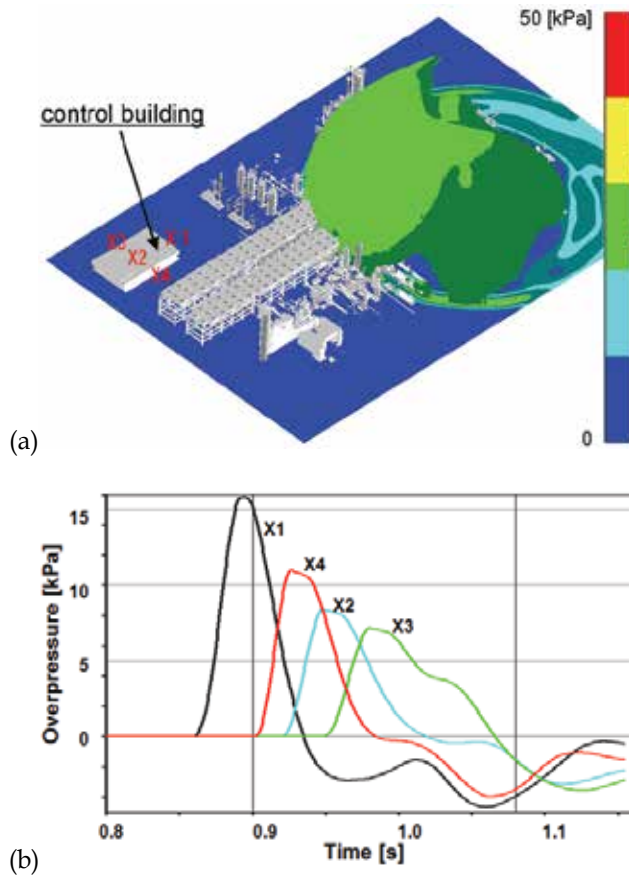


Fig. 8. Overpressures at 0.65 s after ignition (a) and overpressure time histories at gauge points X 1-4 on control building (b)

#### 4.3 Structural response analysis

The structural response prediction shows a deformation of the control building (Figure 9).

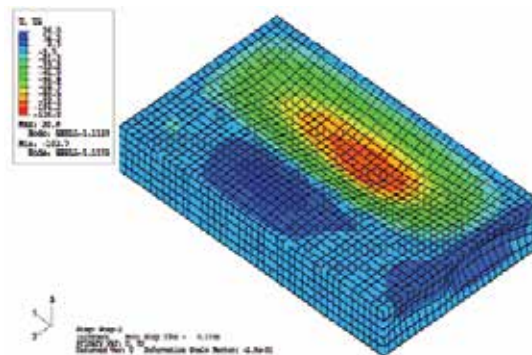


Fig. 9. Deformation of control building at 1.3 s after ignition

The control building is made of reinforced concrete and has two rooms, a floor area of 42 m x 25 m and a height of 5 m. In this case study, the maximum displacement on the roof is only about 100 mm, and is relatively small. Therefore, the structural integrity is sound.

## 5. Key conditions in gas explosion

The following case studies show the key conditions in gas explosions at a typical LNG plant. The geometry model is shown in Figure 4, and the ignition point is shown in Table 1 and Figure 5.

### 5.1 Gas cloud volume

In order to examine the relationship between gas cloud volumes and overpressures, the initial gas cloud of propane is distributed throughout a cylindrical volume at a theoretical fuel/air ratio of 1 (i.e., 4.0 vol.% propane in air) as shown in Figure 10.

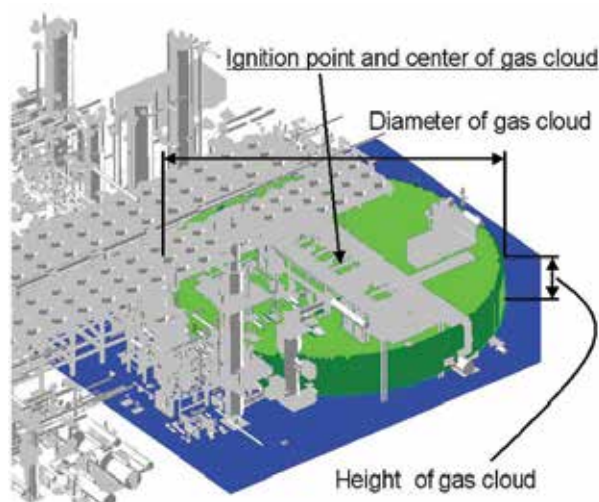


Fig. 10. Initial gas cloud of cylindrical shape (propane)

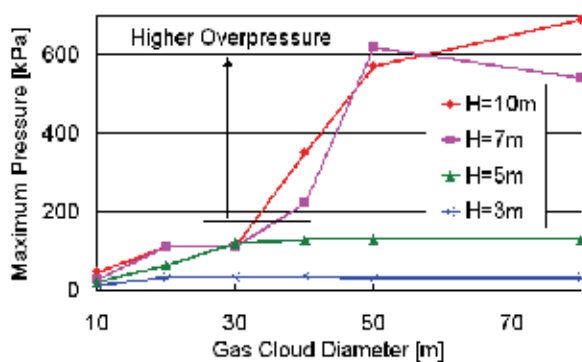


Fig. 11. Maximum overpressure vs. gas cloud diameter (propane)

Figure 11 shows that, at a height of 7 m or more, a diameter of 40 m or greater (volume  $>10,000 \text{ m}^3$ ) results in a high overpressure, while at a height of 5 m or below, a low overpressure results at any diameter (i.e., volume). Thus, a gas explosion requires a gas cloud with both a height of at least 7 m and a diameter of at least 40 m, to sustain the expansion flow. Therefore, the gas cloud volume alone is not sufficient information to accurately predict an explosion, and more information is required to predict an explosion.

## 5.2 Gas concentration

In order to examine the relationship between gas concentrations and overpressures, the gas cloud is initially distributed throughout the area at a uniform concentration. As shown in Figure 12, there is only narrow range to burn easily within the flammable limits, i.e., 3.5-5.0 % for propane and 9.0-9.5 % for methane, and results in high overpressure over 1500 kPa. On the other hand, it is unlikely that such a narrow gas concentration range exists in real plant situations. In a realistic situation involving leaked gas, sharp gradients of local concentrations exist.

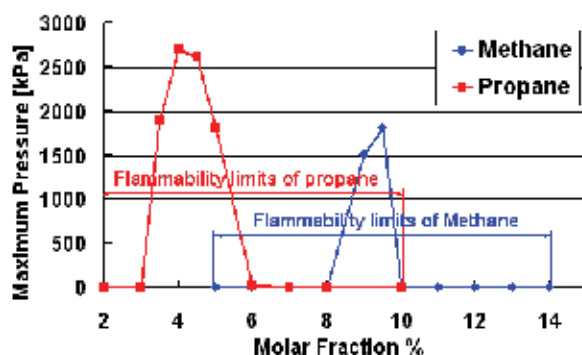


Fig. 12. Maximum overpressure vs. molar fraction (propane & methane)

## 5.3 Obstacle size

In order to examine the relationship between obstacle sizes and overpressures, obstacles are insufficiently imported from the 3D-CAD data.

Figure 13 shows that overpressures are much lower, under 1 kPa, when only large obstacles, i.e., objects greater than 1 m in any one dimension, are imported from the 3D-CAD data. But Figure 6 shows high overpressures over 100 kPa.

When gas is initially distributed throughout the area at the theoretical fuel/air ratio of 1 (i.e., 4.0 vol.% propane in air), Figure 14 shows the relationship between obstacle sizes and overpressures. Maximum overpressures generate over 1000 kPa when small objects, i.e., 0.2 m or less in all three dimensions are also imported from 3D-CAD data. Because the combination of both small and large obstacles creates strong turbulence, high flame velocities, high overpressures and finally explosions will occur, as explained above in Para. 2.1, Mechanism of gas explosion.

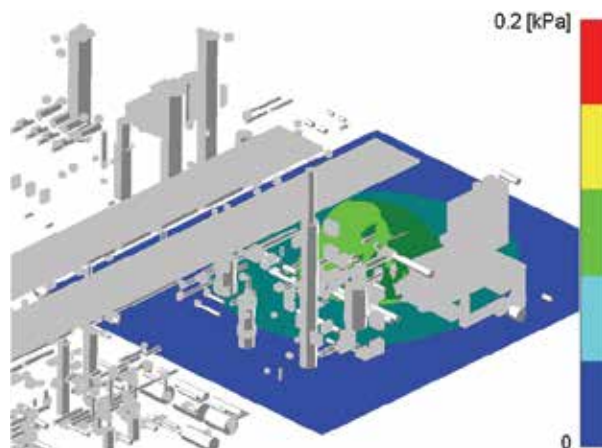


Fig. 13. Overpressures involving only large obstacles (obstacle size > 1m, propane)

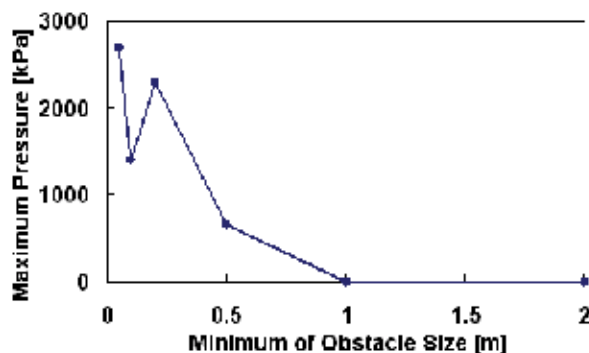


Fig. 14. Maximum overpressure vs. minimum of obstacle size (propane)

The case studies presented here demonstrate that the following conditions are necessary for gas explosions in typical oil and gas plants:

- Sufficient gas cloud diameter and height to sustain the gas expansion flow
- Gas concentrations close to the theoretical fuel/air ratio of 1 (i.e., 4.0 vol.% propane in air, or 9.5 vol.% methane in air)
- Both small and large obstacles to create strong turbulence

## 6. Conclusion

The gas explosion simulation system comprises high-level simulation technology using 3D-CAD, CFD and FEA. This system carries out computer simulations based on various conditions such as:

- Three-dimensional information including layouts for equipment, piping, and structures,
- Weather conditions such as wind direction, wind velocity, temperature, and atmospheric pressure,
- Gas conditions such as the type of gas leak and leak rate,

and predicts the behavior of gas leaks and their dispersions, fires, explosions, the spread of blast waves, and strength/deformation of structures. By designing blast resistance that reflects the simulation results and takes into account the impact on plant equipment and control building, and by conducting highly credible risk evaluation, the safety of the entire plant can be ensured.

This sort of simulation technology can be used in a wide range, such as gas processing plants, LNG plants, oil refining/petrochemical plants, as well as LPG Floating Production, Storage and Offloading (FPSO) plants. This system can provide detailed information that can be used to assess safety during the design stage. Understanding the explosion phenomenon can help to avoid risks in oil and gas plants. Therefore, this gas explosion simulation system can be used to assess the safety of oil and gas plants.

## 7. References

- Mercx, W.P.M. (1994). *Modelling and Experimental Research into Gas Explosions*, Overall Final report of the MERGE project CEC contract STEP-CT-0111
- C. J. H. van den Bosch. (1997). *Methods for the calculation of physical effects CPR 14E (Part 2)*, Committee for the Prevention of Disasters, ISBN:9012084870, Committee for the Prevention of Disasters
- Dorofeev S.B. et al. (1997). *Large scale combustion tests in the RUT facility: Experimental study, numerical simulations and analysis on turbulent deflagrations and DDT*, Transactions of the 14th International Conference on Structural Mechanics in Reactor Technology, Lyon, France, August 17-22
- CJ Hayhurst et al. (1998). *Gas Explosion and Blast Modelling of an Offshore Platform Complex*, 7th Annual Conference on Offshore Installations, London, December, 1998
- Natabelle Technology Ltd. (2000). *Explosion Pressures Evaluation in Early Project Phase*, Health & Safety Executive
- Jiang J. (2001). *Comparison of blast prediction models for vapor cloud explosion*, The Combustion Institute/Canada Section, 2001 Spring Technical Meeting, 13-16 may, 2001, pp. 23.1-23.6
- C. J. Lea. (2002). *A Review of the State-of-the-Art in Gas Explosion Modelling*, Health & Safety Laboratory
- M.A. Persund. (2003). *Safety Drivers in the Lay-out of Floating LNG Plants*, Third Topical Conference on Natural Gas Utilization, AIChE Pub. No. 176, ISBN 0-8169-0905-9, p359-372
- Firebrand International Ltd. (2004). *A critical review of post Piper-Alpha developments in explosion science for the Offshore Industry*, Health & Safety Executive
- P. Hoorelebeke. (2006). *Vapor Cloud Explosion Analysis of Onshore Petrochemical Facilities*, 7th Professional Development Conference & Exhibition, March 18-22, 2006
- Olav R. Hansen & Prankul Middha. (2008). *CFD-Based Risk Assessment for Hydrogen Applications*, pp. 29-34, AIChE Process Safety Progress (Vol.27, No.1), Wiley InterScience
- NORSOK Standard Z-013 Rev2 (2001). *Risk and emergency preparedness analysis*, Norwegian Technology Centre, 2001-09-01
- Fire and Explosion Guidance* ISSUE 1 (2007). ,ISBN: 1903003362 , OIL & GAS UK
- AutoReaGas User's Manual* Version3.1, Century Dynamic Inc. and TNO Prins Maurits Lab.

# Numerical Simulation of Radiolysis Gas Detonations in a BWR Exhaust Pipe and Mechanical Response of the Piping to the Detonation Pressure Loads

Mike Kuznetsov, Alexander Lelyakin and Wolfgang Breitung  
*Institute for Nuclear and Energy Technologies, Karlsruhe Institute of Technology  
Germany*

## 1. Introduction

Radiolysis gas ( $2\text{H}_2+\text{O}_2$ ) can accumulate in steam piping of Boiling Water Nuclear Reactor (BWR) in case of steam condensation. A detonation of radiolysis gas was the likeliest cause of the pipe ruptures in the Hamaoka-1 and Brunsbüttel accidents (Nakagami, 2002; Schulz et al., 2002). In both cases the failed pipes were initially under the operating pressure of 70 bar. During the detonation accident the pressure rose up to 1000 bar or more. In the current paper we consider a typical BWR exhaust pipe and first evaluate the maximum pressure load in case of a radiolysis gas detonation at an initial pressure of 1.6 bar and a temperature of 35 °C. Next, the mechanical response of the exhaust pipe and its possible damage will be numerically evaluated.

The typical exhaust pipe investigated in this study is shown in Fig. 1. It consists of two parts with an outer diameter of 510 and 419 mm fabricated from stainless steel DIN 1.4541. In reality, the exhaust pipe is filled with nitrogen initially. Radiolysis gas (RG) with steam can enter through an exhaust valve due to an opening procedure or due to a leak. In case of a slow long time steam condensation, the radiolysis gas can accumulate at the top of the exhaust pipe. Thus, without an additional ventilation, the “worst case” atmosphere in the exhaust pipe has an initial pressure of 1.6 bar (controlled by the 6 m height of the water level) and consists of radiolysis gas diluted with nitrogen.

According to the recommendations of the Reactor Safety Commission (Germany) for radiolysis gas control in BWR plants it is demanded to determine the reaction pressure for the highest radiolysis gas concentration which could arise. Our previous data analysis (Kuznetsov et al., 2007a) was based on the postulated detonation of pure radiolysis gas, consisting of a stoichiometric hydrogen-oxygen mixture, as the “worst case” scenario. In this study three levels of pressure loads for “worst case” conditions were evaluated in these works: (1) the stationary detonation pressure of about 29 bar; (2) the local deflagration-to-detonation transition (DDT) pressure of 62.5 bar; and (3) the reflected Chapman-Jouguet (CJ) pressure of 71 bar as the maximum detonation pressure that occurs at the tube end. The characteristic pressure loading time was estimated to be about 2 ms, which corresponds to the quasi-static loading regime for a tube of 510 mm outer diameter and 15 mm of wall

thickness (the weakest tube part). It was demonstrated that the reflected detonation wave at the end of the exhaust pipe causes a maximum circumferential strain of 0.11%. Normal detonation at the main part of the exhaust pipe causes a strain of about 0.045%. This means that "worst-case" scenario of radiolysis gas detonation would not lead to the structural damage of such pipe.

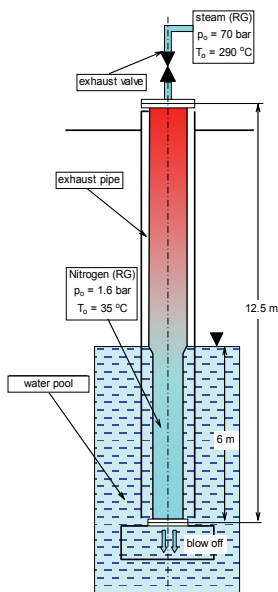


Fig. 1. Schematic of typical BWR exhaust pipe: radiolysis gas (RG) coloured in red

Detailed analysis of experiments (Kuznetsov et al., 2002; Schröder et al., 2006; Kuznetsov et al., 2007b) with radiolysis gas detonations in closed pipes showed that much higher maximum detonation pressures than the reflected pressure and the DDT pressure could occur in reality. The main purpose of this work is to find out the real "worst case" scenario in order to evaluate the integrity of a BWR exhaust pipe using a 1D numerical code for deflagration-to-detonation simulation (FA1D). These data are required for BWR safety analysis and future design guidelines for BWRs.

## 2. Experimental analysis of radiolysis gas detonations

In (Kuznetsov et al., 2007a) stoichiometric  $H_2-O_2$  mixtures were examined as a "worst case" scenario, because they have the highest energy density and thus the largest potential for pipe deformations. Radiolysis gas mixtures with arbitrary nitrogen dilutions have also been discussed in this work. According to the references (Schröder et al., 2006; Kuznetsov et al., 2007a) the principal sequence of a radiolysis gas combustion, schematically represented in Fig. 2, changes with growing nitrogen dilutions as follows:

- after weak ignition of the gas at  $x = 0$  a slower flame acceleration takes place compared to pure radiolysis gas;
- due to the longer foregoing deflagration process the DDT point shifts to the tube end;
- the precursor shock wave ahead of the flame has a smaller Mach number and thus a lower pressure amplitude;

- the DDT peak pressure increases on the one hand because of increasing pre-compression; on the other hand the theoretical CJ-pressure drops because of the nitrogen dilution;
- because of the longer run-up-distance to the DDT point the time gap between detonation onset and reflection decreases; this leads to the actual worst case situation when both processes overlap and the detonation is initiated at the pressure of the reflected precursor shock wave.

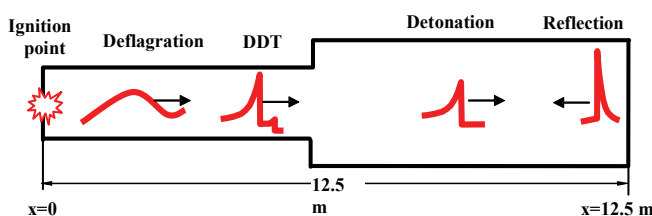


Fig. 2. Principal sequence of the combustion process in a BWR exhaust pipe with nitrogen diluted radiolysis gas

Thus, with increasing nitrogen dilution the DDT point shifts towards the tube end resulting in extremely high pressures as result of cumulative effects of pre-compression, reflection and local explosion during the DDT process itself. Because of smaller amount of remaining unburned material during the DDT process the resulting peak pressure from DDT and reflection will be shorten and the characteristic pressure load time will decrease. However reduced duration of a pressure load can cause a smaller dynamic load factor and less strain in a loaded tube (Kuznetsov et al., 2007b).

The total effect of nitrogen dilution on the maximum dynamic piping stress and strain cannot be evaluated without detailed numerical simulations, because of the co-existence of several gas dynamic effects. In this work therefore the influence of nitrogen dilution will be quantitatively determined by systematic numeric simulation of the radiolysis gas combustion sequence depicted in Fig. 2. The goal of the calculations is the evaluation of maximum pressures that can occur for the deflagration/detonation of  $2\text{H}_2+\text{O}_2+x\text{N}_2$  mixtures in an exhaust pipe. In a second step, the structural dynamic response of the exhaust pipe to the calculated dynamic pressure loads will be examined.

### 3. FA1D code description

#### 3.1 The model

For the numerical simulation of reacting flow problems a CFD “in house” code was developed. In order to simplify the program and to make it more quick and flexible, the program was based on the following assumptions:

- solution of the reactive Euler equations, i.e. neglect of molecular transportation processes such as diffusion, thermal conduction and viscosity;
- no turbulence;
- 1-dimensional geometry, i.e. neglect of real tube geometry (variable cross-section), radial gradients of concentrations, pressure, temperature and fluid velocity;
- one global dominant reaction for the  $\text{H}_2/\text{O}_2$ -combustion;
- prescribed flame acceleration law;
- temperature-dependent thermodynamic data for all components ( $\text{H}_2$ ,  $\text{O}_2$ ,  $\text{H}_2\text{O}$ ,  $\text{N}_2$ );

- 1<sup>st</sup> order solution procedure, numerical cell size in the present problem is 1-2 mm;
- adiabatic assumption (no heat losses of gas to tube wall);
- ideally reflecting boundary conditions at the tube ends.

In particular the last assumption leads to conservative results during the pressure computation. The model is based on the following 1D Euler equations:

$$\frac{\partial \rho}{\partial t} + \frac{\partial \rho u}{\partial x} = 0 \quad (1)$$

$$\frac{\partial \rho u}{\partial t} + \frac{\partial \rho u^2}{\partial x} + \frac{\partial p}{\partial x} = 0 \quad (2)$$

$$\frac{\partial E}{\partial t} + \frac{\partial u(E+p)}{\partial x} = -\sum r_i \cdot H_i^f \cdot Q \quad (3)$$

$$\frac{\partial \rho f_i}{\partial t} + \frac{\partial \rho u f_i}{\partial x} = \mu_i \cdot r_i \cdot Q \quad (4)$$

Here  $\rho$  - density,  $u$  - velocity,  $E$  - total energy per unit volume (kinetic+thermal),  $f_i$  - mass fraction of components,  $Q$  - reaction rate,  $r_i$  - stoichiometric coefficients (negative for reagents, positive for products),  $H_i^f$  - enthalpy of formation,  $\mu_i$  - molecular mass. Simulation of flame propagation is based on flame position tracking. Flame position is calculated as:

$$\frac{dX_{fp}}{dt} = u(X_{fp}(t), t) + FV(X_{fp}(t)) \quad (5)$$

Here  $FV(x)$  is a prescribed flame acceleration profile. To simulate a detonation,  $FV(x)$  can be set equal to the sound speed of burned gas. So, the reaction rate is calculated as follows:

$$Q = \begin{cases} Q_0 \cdot \frac{\rho f_l}{\mu_l} & x < X_{fp} \\ 0 & x > X_{fp} \end{cases} \quad (6)$$

Here  $l$  is the index of the limiting reagent (in our calculations -  $H_2$ ). The choice of  $Q_0$  is not very important. Its value determines only the width of the reaction zone. It should be sufficiently high, to make this zone narrow, but not very high to not disturb the numerical stability of the model. If we consider the computational cell where the flame front is, we will see that  $Q_0 = \frac{FV}{\Delta x}$  is a reasonable choice for the reaction rate.

However, such a simple model of combustion will result always in complete combustion of the reagents. The real equilibrium state after the combustion consists not only of products, but also of unreacted reagents and radicals representing intermediate stages of the combustion. The completeness of the combustion is determined mostly by the temperature but also by pressure and initial concentrations of species. To determine the completeness of the combustion it is necessary to consider reverse reactions together with the forward ones. The ratio of rates of forward and reverse reactions is determined by:

$$\frac{Q_f}{Q_r} = K = \left(\frac{P_{atm}}{RT}\right)^{\sum r_i} \cdot \exp\left(\sum r_i \cdot \left(\frac{S_i}{R} - \frac{H_i}{RT}\right)\right) \cdot \prod \left(\frac{\rho f_i}{\mu_i}\right)^{-r_i} \quad (7)$$

where  $S_i$  and  $H_i$  are molar entropy and enthalpy of species, respectively. The net reaction rate is then

$$Q = Q_f - Q_r = Q_f \cdot \left(1 - \frac{1}{K}\right) \quad (8)$$

So we can see that a correction factor has to be introduced to the reaction rate, which is determined by the thermodynamic properties of the mixture. It is not necessary to follow this formula exactly as long as we don't investigate detailed chemistry with exact reaction rates. The only important thing here is the sign of the net reaction rate and equilibrium point where  $K = 1$  and  $Q = 0$ . We found that the following approximate formula gives the same result as as the exact one, Eq. (8):

$$Q = Q_f \cdot \begin{cases} 1 & \ln K > 1 \\ \ln K & -1 < \ln K < 1 \\ -1 & \ln K < -1 \end{cases} \quad (9)$$

The advantage of this formula is the possibility to avoid an exponentiation at every cell in every time step. Another advantage is that the correction factor applied to the reaction rate is less than one by absolute value, so such a correction will not influence the numerical stability of calculations.

### 3.2 Flame acceleration model and code validation

An important part of the model is the simulation of the flame acceleration after the first weak ignition. This phase determines amplitude and length of the pre-compressed zone, which is formed ahead of the flame front in the unburned gas. The pressure amplitude depends particularly on the effective maximum burning velocity  $S_{max}$  of the turbulent flame developing in the pipe. Since the FA1D-code does not have any turbulence model, three radiolysis gas experiments in smooth pipes (Kuznetsov et al., 2002; Kuznetsov et al., 2005; Liberman et al., 2009) with different gas mixtures have been analyzed, to evaluate the effective burning speed  $S_{max}$  and the flame acceleration law.

Experimental data analysis showed that  $S_{max}$  normalized by the fundamental laminar flame speed  $S_L$  which lies in the range of  $S_L = 4 - 12$  m/s, practically doesn't change and has an average value of  $S_{max}/S_L = 17.5$ . This value is also consistent with general correlations for the turbulent burning speed  $S_T$  for different gases at high degree of turbulence which gives  $S_T/S_L$  values up to 17 (Bradley, 1992). Therefore the use of a maximum turbulent burning speed of  $S_{max} = 17.5 \cdot S_L$  for the examined radiolysis gas - nitrogen mixtures, seems to be a reasonable number for extrapolation to all diluted radiolysis gas mixtures in the present work. The laminar flame speed  $S_L$  for mixtures with unknown fundamental flame velocity was computed using the Cantera code with a verified planar flame model (Goodwin, 2001) and a detailed H/O/N reaction mechanism (Lutz, 1988).

A detailed sensitivity study showed that not only the maximum burning speed  $S_{max}$ , but also the flame acceleration from  $S_0$  up to  $S_{max}$  can affect the pressure in a pipe before and

after the DDT process. Figure 3 shows a simplified linear approximation of the flame speed evolution in a pipe used in Eq. (5) as the flame acceleration law along the tube. In good agreement with our experimental data (Lieberman et al., 2009) a linear flame acceleration law against distance in smooth channels corresponds to the case when the visible flame velocity is proportional to the flame area, which is for so called "finger" flames proportional to the distance along the tube,  $S(x) \sim k \cdot x$ . This leads to the exponential flame acceleration law against time as follows:

$$S(t) = S_0 \exp(k \cdot t) \quad (10)$$

where  $k = \sigma \cdot S_L / R$  is the exponential factor depending on the expansion ratio  $\sigma = \rho_u / \rho_b$  of unburned and burned components and tube radius  $R$ ;  $S_0 = S_L$  is the effective initial flame speed. So, with a smaller tube size and a higher mixture reactivity the flame accelerates faster.

For the general description of the deflagration, three main parameters are necessary: the initial flame speed  $S_0$ , the flame acceleration distance  $x_a$  which depends on the exponential factor  $k$  (Eq. (10)) and the maximum flame speed  $S_{max}$ . At the postulated DDT point  $x_D$  the flame speed is increased suddenly to the speed of sound in the burned gas  $C_p$ , which can be determined from thermodynamic calculations. This flame speed corresponds to the CJ-detonation.

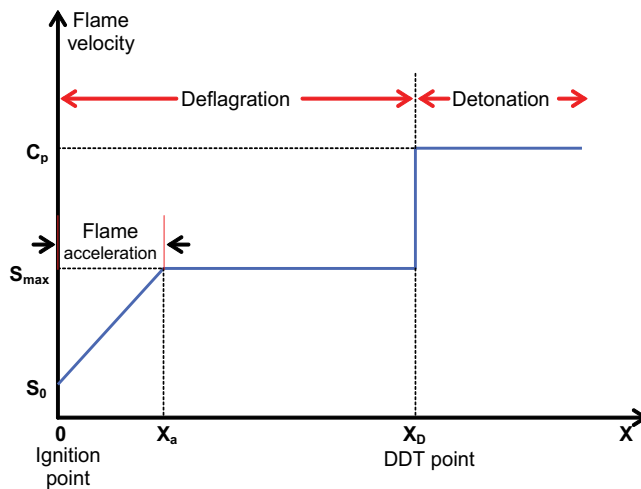


Fig. 3. Dynamics of the flame velocity in the 1D numerical model for DDT in radiolysis gas - nitrogen mixtures

The effects of the two free parameters  $S_0$  and  $x_a$  on the peak pressures were examined to be used in detailed model for the flame speed calculations. The flame model used here supplies conservative over-pressure before and after the DDT process.

The numerical model of FA1D was examined in a wide range of initial conditions for detonation experiments with radiolysis gas mixtures (Kuznetsov et al., 2002; Kuznetsov et al., 2005): tube lengths from 3 to 6 m; initial pressures from 0.7 to 10 bar; initial temperatures from 300K to 570K; without and with different inert gases as steam and nitrogen. The experimental validation of the code is required to adjust the three main parameters of the

flame acceleration: the initial burning speed  $S_0$ , the flame acceleration distance  $x_a$  and the maximum burning speed  $S_{max}$ , using experimentally determined trajectories for shock wave and flame front. The DDT point in the calculations was specified at the same distance as observed in the experiments.

Figure 4 shows one example for a comparison of experimental and calculated  $x-t$  diagrams for radiolysis gas detonation experiments with 40% H<sub>2</sub>O at 10 bar and 570K, with the DDT point  $x_D$  at 2 m. Such diagrams represent an array of pressure and light sensor records vs. time at the  $x$  position along the tube. According to the previous correlation a maximum burning speed  $S_{max} = 150$  m/s was assumed, an initial speed  $S_0 = 50$  m/s and an acceleration distance  $x_a = 0.5$  m were used in the calculations. The variable pressure scale is indicated by the tick at the right side for each pressure gauge position. In Fig. 4 measured and computed pressure and light signals are depicted. The experimental  $x-t$  diagram (Fig. 4, left) shows that behind the leading shock wave (SW) the radiolysis gas mixture is pre-compressed up to 15 bar compared to 10 bar of initial pressure. The calculations give a somewhat stronger leading shock wave with a pressure of 21 bar.

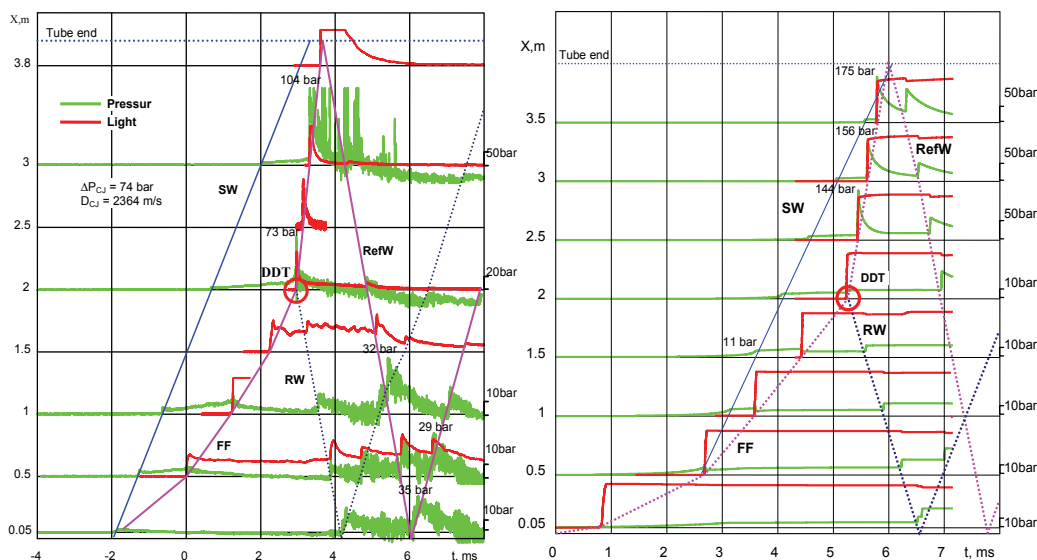


Fig. 4. Detonation experiment (left) and 1D numerical simulation (right) for a radiolysis gas mixture with 40% steam ( $p_0 = 10$  bar,  $T_0 = 300^\circ\text{C}$ ). Plotted lines: SW = shock wave; FF = flame front; RW = retonation wave; RefW = reflection wave

Generally, the measurements and calculations show good agreement of pressure and light signals and shock wave trajectories. The test calculations and further comparisons with experiments, will show that the developed 1D program is able to reproduce all necessary dynamic pressure effects and that it can be used for the prediction of real pressure loads.

#### 4. Structural dynamics response

For the computation of a pipe widening under a certain internal pressure the motion equation for a thin infinite expanded cylinder (Fig. 5) was solved. The tube with an outer

radius  $R$  and wall thickness  $h$  exposed to an isotropic internal overpressure  $p(t)$  experiences a deformation  $x(t)$ . To calculate the tube response at the different regimes of internal pressure loads the following assumptions are introduced: a) cylindrical symmetry; b) linear Hooke's law for deformations (linear elastic oscillator).

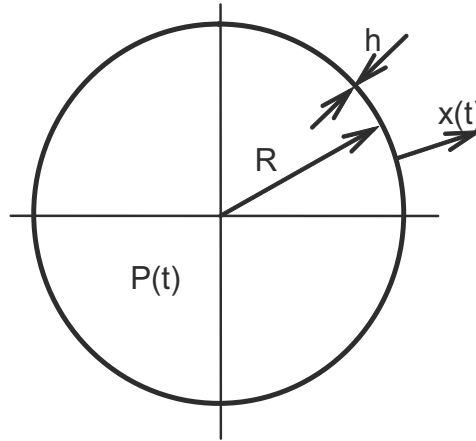


Fig. 5. Tube parameters

The following differential equation describes the structural response of a long pipe in the linear elastic approach:

$$\frac{\partial^2}{\partial t^2} x(t) + \mu \frac{\partial}{\partial t} x(t) + \Omega^2 x(t) = \frac{p(t)}{\rho \cdot h} \quad (11)$$

$$\Omega = \sqrt{\frac{E}{\rho \cdot (1 - \nu^2) \cdot R^2}} \quad (12)$$

where  $\Omega$  is the circular frequency of the tube;  $\nu$  is the Poisson's ratio;  $\mu$  is the damping factor;  $E$  is the Young's modulus of elasticity;  $\rho$  is the density;  $x(t)$  is the wall displacement. In terms of engineering strain  $\varepsilon = x/R$ , the following differential equation governs the structural response of a pipe:

$$\frac{\partial^2}{\partial t^2} \varepsilon(t) + \mu \frac{\partial}{\partial t} \varepsilon(t) + \Omega^2 \varepsilon(t) = \frac{p(t)}{\rho \cdot R \cdot h} \quad (13)$$

Of course, the model does not describe the behavior of a finite cylindrical shell like a tube with flanges. The time dependent pressure function  $p(t)$  might be described as an analytical function or as an output file of the pressure-time history from FA1D simulations. It also could be a measured pressure-time dependency obtained by pressure sensors. For simple pressure function  $p(t)$  equation (13) can be solved analytically. For complex pressure functions  $p(t)$  the differential equation (13) was solved numerically with a Runge-Kutta method.

**Static pressure load.** In the simplest case, the pressure does not depend on time  $p(t) = P_m = \text{const}$ . In this case the maximum tube response is

$$\varepsilon_m = \frac{P_m}{\rho \cdot R \cdot h \cdot \Omega^2} \quad (14)$$

Substitution of  $\Omega$  from Eq. (11) then gives for the maximum tube response

$$\varepsilon_m = \frac{R \cdot P_m}{E \cdot h} \quad (15)$$

which does not depend on the time (Fig. 6, left). The maximum displacement  $\varepsilon_m = 0.0025$  was calculated for stainless steel tube with the following properties as an example:

- |                   |                              |                        |                            |
|-------------------|------------------------------|------------------------|----------------------------|
| - Density         | $\rho = 8000 \text{ kg/m}^3$ | - Wall thickness       | $h = 2 \text{ mm}$         |
| - Young's modulus | $E = 200000 \text{ MPa}$     | - Circular frequency   | $\Omega = 200 \text{ kHz}$ |
| - Outer radius    | $R = 25 \text{ mm}$          | - Maximum overpressure | $P_m = 40 \text{ MPa}$     |

Formula (15) is often used to calculate the maximum design pressure of a tube under static pressure load. However, in the case of a detonation load, the pressure load is highly transient and propagates at high speed. In this case the static design pressure formula (15) gives a value for the maximum displacement that is too low. Let us consider why.

**Dynamic response.** The dynamic pressure response of the tube (Fig. 5) in simplified form with a damping factor of  $\mu = 0$  yields:

$$\frac{\partial^2}{\partial t^2} \varepsilon(t) + \Omega^2 \varepsilon(t) = \frac{p(t)}{\rho \cdot R \cdot h} \quad (16)$$

As an intermediate case from static to dynamic load a quasi-static pressure function can be considered, which is given by

$$p(t) = \begin{cases} 0 & t \leq 0 \\ P_m & t > 0 \end{cases} \quad (17)$$

The response of the tube can be calculated analytically as follows

$$\varepsilon(t) = \begin{cases} 0 & t \leq 0 \\ \varepsilon_m \cdot (1 - \cos(\Omega \cdot t)) & t > 0 \end{cases} \quad (18)$$

where  $\varepsilon_m$  is the static tube response given by Eq. (15). It follows from Eq. (18) that the maximum displacement under quasi-static loading is two times higher than in the static case:

$$\varepsilon(t)_{\max} = 2 \cdot \varepsilon_m = K \cdot \frac{R \cdot p_m}{E \cdot h} \quad (19)$$

So, an amplification factor of  $K = 2$  is determined for a displacement under quasi-static load compared to the static pressure loads. The analytical solution of equation (3) for the simplest step-wise pressure function  $p(t) = P_m = \text{const} (t > 0)$  is given in Fig. 6 (right). It really shows that the mechanical response of the tube (25 mm i.d., 2 mm wall thickness) to the dynamic

pressure load even in case of the same maximum pressure as for static load ( $p(t) = P_m$ ) can be two times higher.

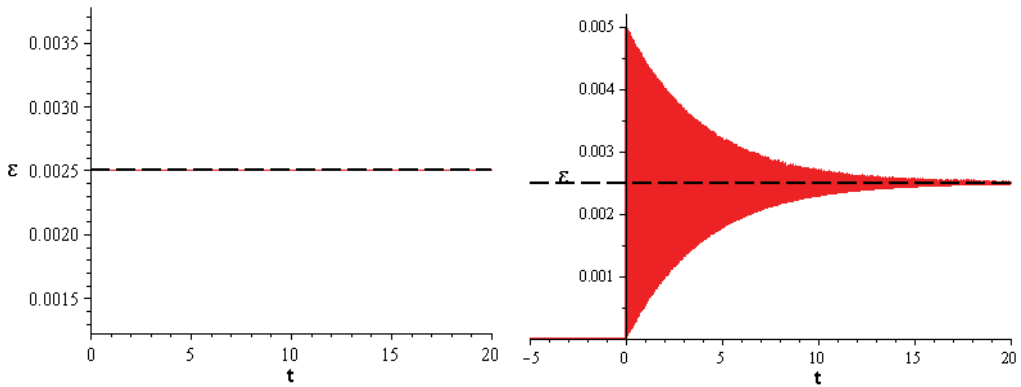


Fig. 6. Static (left) and quasi-static (right) tube responses

In accordance with Baker’s (1983) overview, the amplification factor  $K$  depends on the value of the product  $\Omega \cdot T$ , where  $T$  is the characteristic time of dynamic loading. For a detonation process, three different pressure profiles with characteristic time  $T$ , when  $\Omega \cdot T > 40$ , can be considered to be analytically derived for the appropriate piping deformation (see Fig. 7): rectangular (I), triangular (II) and exponential function (III), which is the most typical for detonation processes.

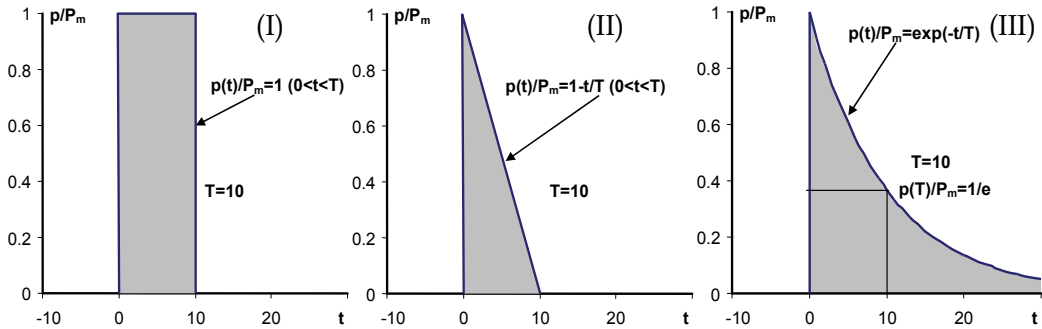


Fig. 7. Typical dynamic pressure functions  $p(t)$  used in eq. (16)

The same initial conditions as above for the stainless steel tube were used for the mechanical response calculations. The analytical solutions of equation (13) for these three cases with a damping factor of  $\mu = 0.5$  and characteristic time of the pressure load  $T = 10$  ms ( $\Omega \cdot T > 40$ ) are given in graphical form in Fig. 8. It was shown that the maximum displacement, which is equal to  $\epsilon_m = 0.005$ , for all cases is independent of the shape of the pressure impulse and only proportional to the maximum pressure  $P_m$ . In comparison with a static pressure load, where  $\epsilon_m = 0.0025$ , this means that the dynamic amplification factor is  $K = 2$  for maximum displacement, which is two times larger than for the static case, similar to that for quasi-static pressure loading regime when  $\Omega \cdot T > 40$ .

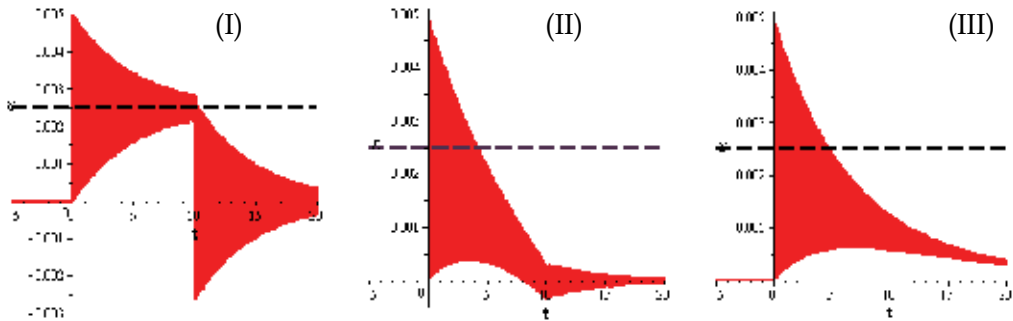


Fig. 8. Calculated tube response to the dynamic load in the quasi-static regime ( $\Omega \cdot T > 40$ )

In agreement with Baker (1983), it also was shown that in case of impulsive loads for  $T=0.1$  ms, when  $\Omega \cdot T < 0.4$ , the maximum displacement  $\epsilon_m$  of the tube under internal dynamic pressure load is proportional to the pressure impulse  $I = \int p(t)dt$ , independent of the shape of the pressure function  $p(t)$ . This explains why the smallest displacement was calculated for a triangular pressure impulse, which has the smallest pressure impulse of all three cases (Fig. 9). The corresponding ratio of the pressure impulses for three cases:  $I_I : I_{II} : I_{III} = P_m \cdot T : P_m \cdot T/2 : P_m \cdot T (1-1/e) = 2 : 1 : 1.3$  is the same as that for the calculated maximum displacements:  $\epsilon_I : \epsilon_{II} : \epsilon_{III} = 2 : 1 : 1.3$ . In the intermediate case of  $0.4 < \Omega \cdot T < 40$ , a transient regime will occur with an amplification factor in the range of  $0 < K < 2$ .

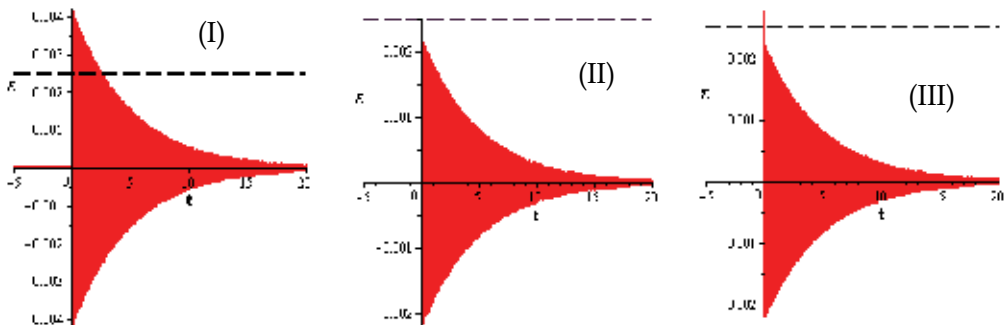


Fig. 9. Tube response to the pressure load in dynamic or impulsive regime ( $\Omega \cdot T < 0.4$ )

In the present work the time-dependent pressure load function  $p(t)$  in equation (13) was also taken from the gas dynamics code FA1D. For such a complex pressure function the differential equation (13) was solved numerically with a Runge-Kutta method. The numerically computed piping strain agreed with the analytical results for the above described simple cases.

Figure 10 shows an example for the calculated mechanical response to a pressure load with a highly resolved pressure function that includes the von Neumann spike, compared to that without von Neumann spike (low time resolution  $>10 \mu s$ ). This example demonstrates that the very narrow von Neumann spike has practically no effect on the resulting pipe strain. Under detonation pressure load the maximum displacement  $\epsilon_m$  is mainly determined by the Chapman-Jouguet pressure  $p_{CJ}$  which is the effective detonation pressure. Using equation

(13) with an amplification factor  $K = 2$  for  $p_m = 85$  bar, the maximum displacement  $\varepsilon_m = 0.14\%$  is very close to the calculated value of  $0.12\%$  obtained using the measured pressure  $p(t)$  and a Runge-Kutta method. The time of about 3 ms between two maxima of the strain oscillations (period of oscillations) according to equation (12) corresponds to the natural frequency of the real stainless steel exhaust pipe:  $\Omega = 20$  kHz. The maximum displacement always occurs in the first oscillation and it is twice as large (dynamic load factor  $K = 2$ ) in the quasi-static load regime, compared to the strain under static load of the same pipe. This can be regarded as an additional validation of the structural dynamics model used here.

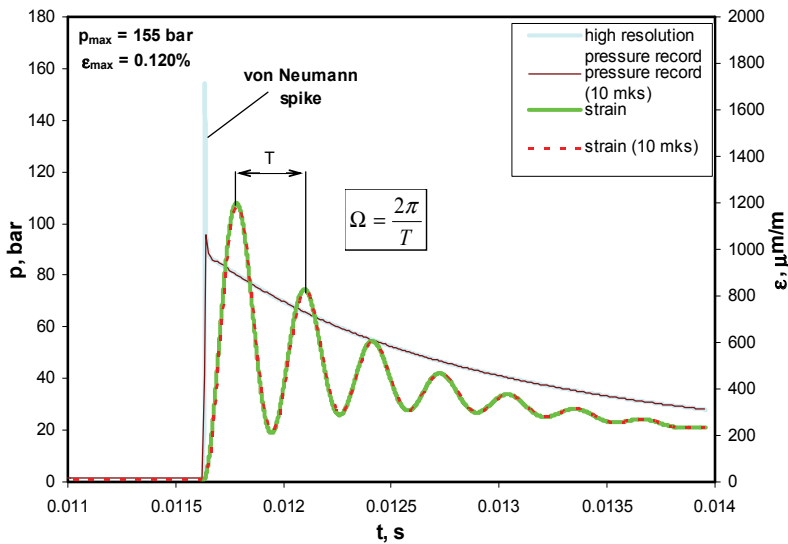


Fig. 10. Calculated mechanical response of exhaust pipe ( $D = 510$  mm,  $h = 15$  mm) under detonation pressure load of a radiolysis gas mixture with 40% nitrogen

## 5. Results of numerical simulations

With the described 1D computational program the detonation transitions in different radiolysis gas-nitrogen mixtures were simulated. Figure 11 summarizes all accomplished computations, whereby for each nitrogen dilution several values for run-up-distance to the DDT point ( $x_D$ ) were examined. The white band of realistic run-up-distances to the detonation onset shown in Fig. 11 was estimated using experimental data and our DDT model described previously (Kuznetsov et al., 2002; Kuznetsov et al., 2005). According to this model, the DDT can only occur if the thickness of the turbulent boundary layer in the unburned gas is 10 times higher than the detonation cell size. As Fig. 11 shows, this distance to the DDT point (open blue points) increases exponentially with increasing nitrogen dilution of the radiolysis gas and could reach approx. 8 m for 60%  $N_2$ . For 80%  $N_2$  in radiolysis gas the computed distance to the DDT is much larger than the pipe length ( $L = 12.5$  m).

Independent of the realistic range of run-up-distances for nitrogen diluted radiolysis gas mixtures, numerical calculations were performed outside the realistic range to examine the

influence of the run-up distance on the maximum pressure and pipe deformation. Main results of numerical calculations of maximum circumferential pipe strain under radiolysis gas detonation pressure loads are shown in Fig. 11 for all nitrogen dilutions and run-up-distances. Detonations of pure radiolysis gas (0%N<sub>2</sub>) and highly nitrogen diluted radiolysis gas (80%N<sub>2</sub>), giving low levels of deformations, will not be considered in details. Other calculations resulting in the highest strain will be analyzed in the next sections.

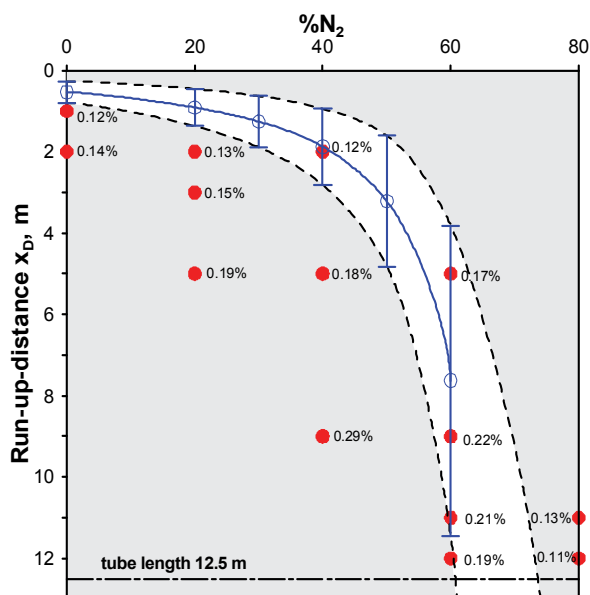


Fig. 11. Overview of the computations: dashed lines indicate upper and lower bounds of run-up-distances to DDT. For every computation the maximum calculated piping strain is indicated (as a label near red point)

### 5.1 Results for 20% nitrogen

For radiolysis gas - nitrogen mixtures with 20%N<sub>2</sub> three different distances from the ignition to the DDT point were simulated:  $x_D = 2, 3$  and  $5$  m (see red points in Fig. 11). The ignition of the radiolysis gas took place at  $x = 0$ . Figure 12 summarizes the computed pressure-time records (top), plotted at the sensors position (as an  $x-t$  - diagram), and peak pressure history (bottom) for the DDT point  $x_D = 2$  m.

Figure 12 (top) shows that DDT occurs 4 ms after the ignition. The blue dotted line corresponds to the position of the accelerating flame front (FF). The upper dotted black line shows the position of the precursor shock wave (SW) which leads to the formation of a pre-compressed and preheated zone ahead of the flame (of up to 1 m length). The strength of the precursor shock wave changes from 4.4 to 7 bar. It results in an overdriven detonation just after the DDT point with a maximum pressure of 110 bar compared to the 48 bar for a steady-state detonation (DW) beyond the pre-compressed zone. The maximum pressure (162 bar) occurs at the tube end due to the detonation reflection. The strength of the reflected wave (RW) decays rather fast from 162 bar to 46 bar over the length of 1.5m.

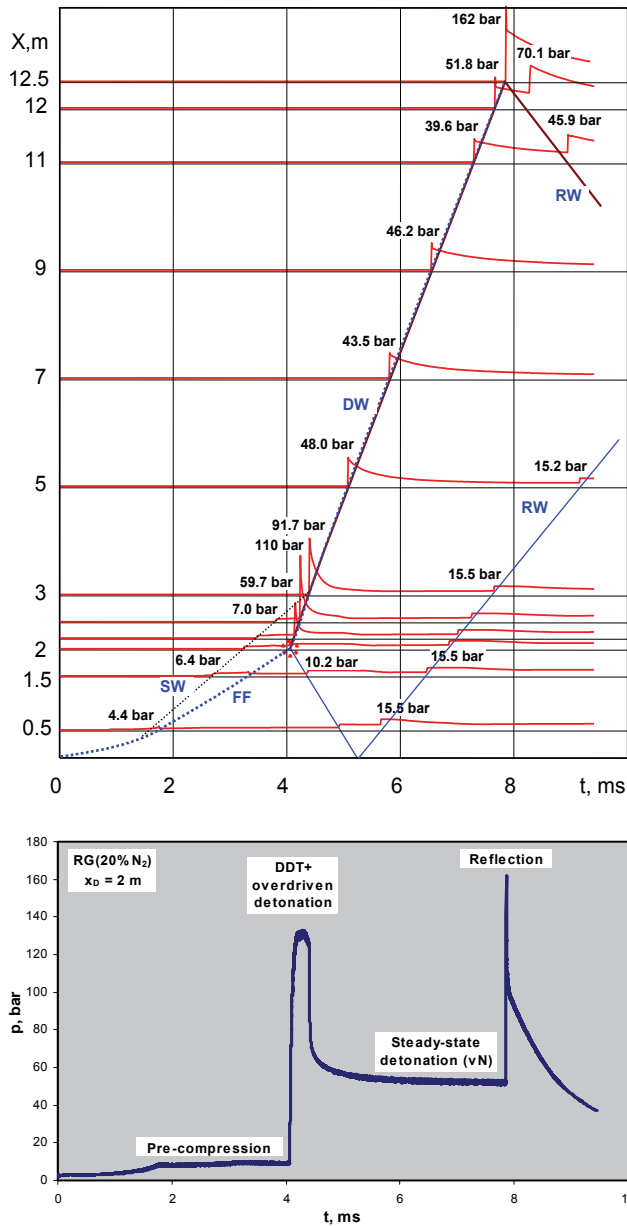


Fig. 12. Computed  $x-t$ -diagram (top) and computed peak pressure in the pipe (bottom) for radiolysis gas with 20% nitrogen and a DDT point at  $x_D = 2$  m

The maximum pressure history is shown in Fig. 12 (bottom). Four characteristic periods of pressure load can be distinguished from the peak pressure record: (I) pre-compression ( $P_m = 4.4-7$  bar); (II) DDT and overdriven detonation ( $P_m = 48-110$  bar); (III) steady-state detonation ( $P_m = P_{vN} = 43-48$  bar); (IV) detonation reflection ( $P_m = 162$  bar). Each time period can be spatially localized using the  $x-t$ -diagram. The first period takes place before the DDT

point  $x_D = 2$  m, the second one extends up to 1 m after the DDT point, period (III) is between  $x = 3$  m and end of the tube at  $x = 12.5$  m, and period (IV) is localized at the tube end  $x = 12.5$  m. The highest pressure corresponds to the DDT and to the reflection at the tube end.

For tube strain, the maximum pressure is not the only important pressure load characteristics. Another important property is the pressure impulse or characteristic pressure loading time. Figure 13 shows the dynamics of the pressure load function for several locations near the DDT point. The closer to the DDT point a pressure sensor is located, the higher is the measured maximum pressure, but the smaller becomes the pressure loading time or pressure impulse.

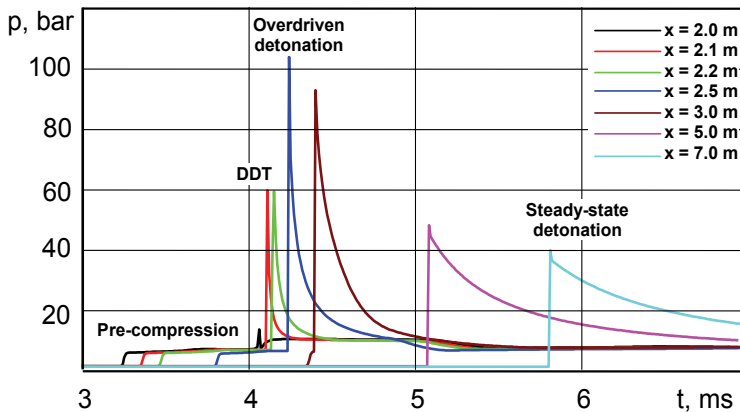


Fig. 13. Pressure load profiles for several locations near the DDT point ( $x_D = 2$  m)

The deformations of the modelled tube at different positions have been calculated using a 1D model for the mechanical response of an unconfined cylindrical shell to dynamic pressure loads. To be conservative, the tube dimensions of the weaker part (510x15 mm) were assumed for whole tube. Fig. 14 represents calculated strain signals in form of an  $x-t$ -diagram to demonstrate the mechanical piping response to the dynamic pressure load. As Fig. 14 shows, the maximum deformations occur close to the DDT point and at the tube end. However, the maximum pressure impulse was achieved at the distances more than 4 m. The calculated frequency of strain signal oscillations of about 20 kHz is consistent with exhaust pipe dimensions and stainless steel properties.

A comparison of the maximum pressure and maximum strain signal, shown in Fig. 15, demonstrates that the maximum pressure is indeed responsible for the maximum deformation of the pipe. This means that a quasi-static pressure loading regime takes place. Maximum pressure and maximum deformation are located at same positions. In fact, with a natural frequency of the pipe of 20 kHz the characteristic pressure load time has to be more than 2 ms to produce only pressure dependent strain. Generally, maximum deformation does not exceed the critical value for stainless steel  $\epsilon_m = 0.2\%$ . The computed strain reaches only 0.13% at the tube end.

As it follows from Fig. 15, the highly loaded zones with maximum deformation extend about 2 m after the DDT point and 1.5 m before the tube end. The mechanical response model gives the maximum strain directly at the tube end because the model does not take into account that in reality this part of the tube is much stronger due to the end flange.

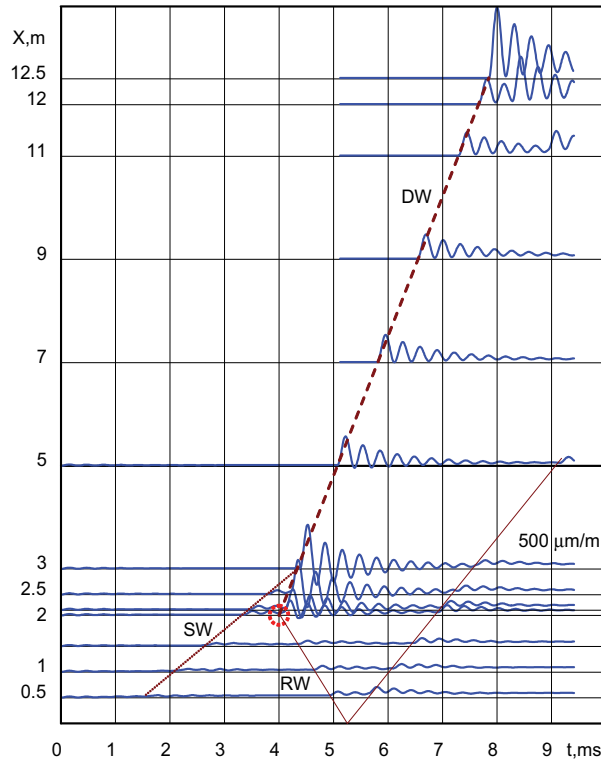


Fig. 14.  $X$ - $t$  diagram of strain wave propagation under radiolysis gas detonation: scale of a strain signal is shown on the right axis (1 division is  $500 \mu\text{m}/\text{m}$  or  $0.05\%$ ): SW = precursor shock wave; DW = detonation wave; RW = retonation wave

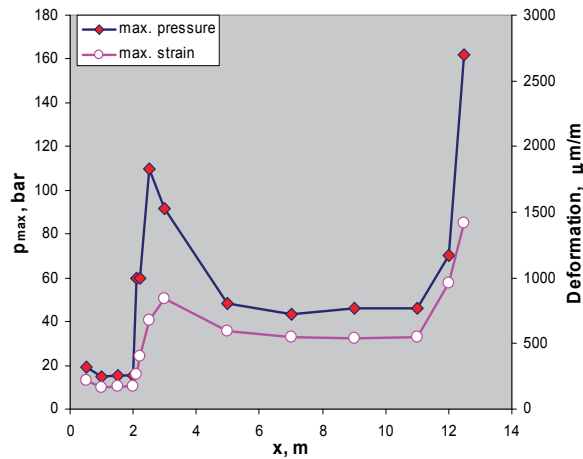


Fig. 15. Maximum pressure load and maximum deformation of the 12.5 m tube under radiolysis gas detonation loads

In the case of a later detonation transition ( $x_D = 3 \text{ m}$ ) qualitatively very similar results for calculated pressure load and mechanical response have been obtained. The maximum pipe

strain rises to 0.15% in this case. For a late detonation transition ( $x_D = 5$  m) the computed maximum piping strain is close to the plasticity limit  $\epsilon_m = 0.19\%$ . But these two cases with late DDT are already far outside of the realistic range of DDT point distances  $x_D$  that can be expected for the particular gas mixtures. It can be stated that for a late DDT-position longer pre-compressed zone and longer over-driven detonation zone with higher level of deformations can occur. For instance, the pre-compressed zone extends over 7.5 m for  $x_D = 5$  m, compared to 3 m for  $x_D = 2$  m.

### 5.2 Results for 40% nitrogen

For radiolysis gas - nitrogen mixtures with 40%N<sub>2</sub> three different distances from ignition to the DDT point were simulated:  $x_D = 2, 5$  and 9 m (see Fig. 11). The ignition of the radiolysis gas took place at  $x = 0$ . For the DDT point  $x_D = 2$  m the pre-compressed zone length extends over 4 m from the ignition point. A maximum pressure of about 88 bar for the over-driven detonation and 155 bar for the reflected pressure with a maximum strain of  $\epsilon_m = 0.12\%$  were obtained for this case. The maximum pressure was lower than in case of 20%N<sub>2</sub> because of less energetic radiolysis gas mixture.

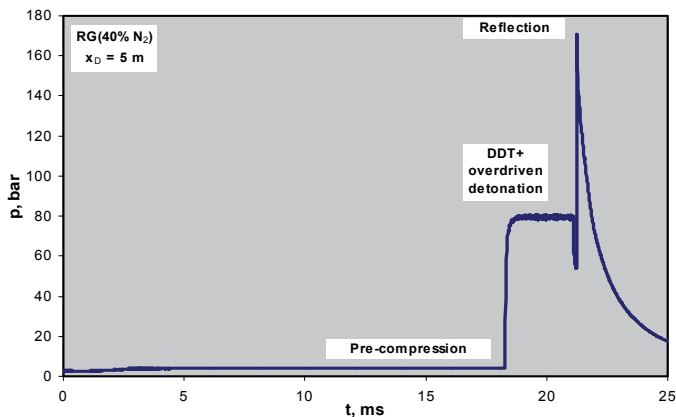


Fig. 16. Computed peak pressure record for radiolysis gas with 40% nitrogen and a DDT point at  $x_D = 5$  m

For the DDT point  $x_D = 5$  m the pre-compressed zone extends practically up to the tube end. A maximum pressure of about 80 bar for over-driven detonation and 170 bar for reflected pressure with a maximum strain of  $\epsilon_m = 0.19\%$  was observed in this calculation. The peak pressure record (Fig. 16) demonstrates that only an over-driven radiolysis gas detonation without steady-state CJ-detonation occurs in this case. The reflection of the over-driven detonation will be much stronger than the steady-state detonation.

The most dangerous scenario was observed for a late detonation initiation at  $x_D = 9$  m. In this case the precursor shock wave is reflected at the tube end before the detonation onset. Figure 17 shows an  $x-t$  diagram of the DDT process and simultaneously a peak pressure record for this scenario.

The peak pressure record (Fig. 17, bottom) demonstrates a significant difference of the maximum pressure level compared to all previous cases. First of all, due to the leading precursor shock wave reflection, the radiolysis gas mixture has two times higher initial

pressure prior the detonation (9.2 bar instead of 4.1 bar). This results in two times higher detonation pressure (165 bar instead of 87 bar for overdriven detonation without precursor shock wave reflection) which finally leads to a higher maximum hoop strain of  $\epsilon_m = 0.16\%$ . Both pressure effects of the reflection and over-driven detonation are superimposed in time with an extremely high resulting pressure of about 300 bar. It produces a very high tube deformation ( $\epsilon_m = 0.29\%$ ) which is higher than the yield limit ( $\epsilon_m = 0.2\%$ ) for stainless steel.

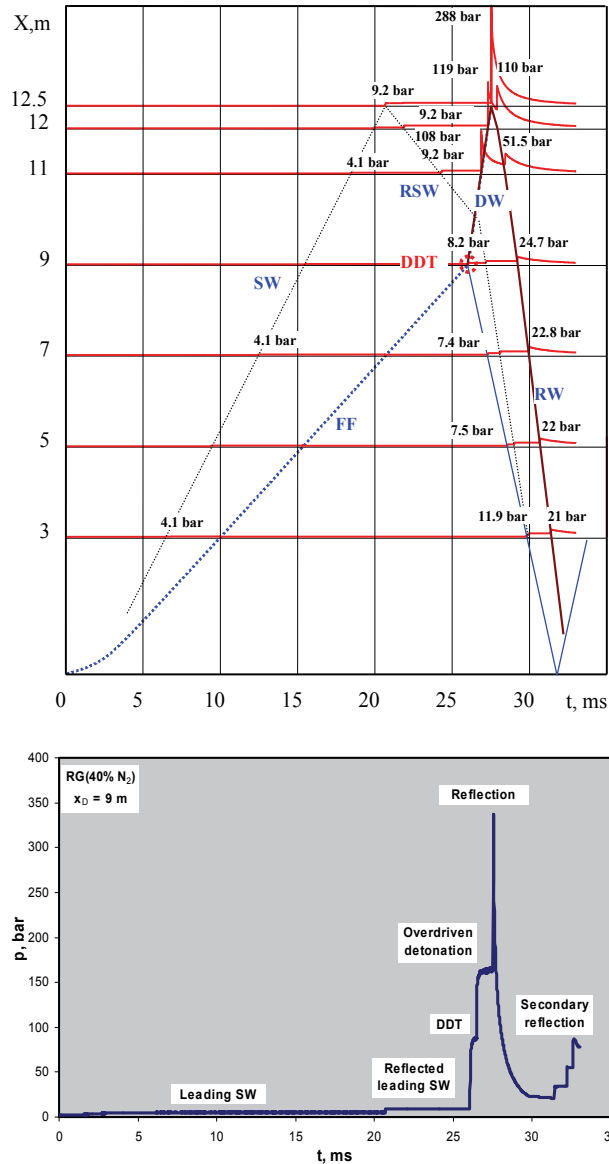


Fig. 17. Computed  $x-t$ -diagram (top) and computed peak pressure record (bottom) for radiolysis gas with 40 vol% nitrogen and a DDT point at  $x_D = 9$  m

### 5.3 Results for 60% nitrogen

For radiolysis gas - nitrogen mixtures with 60%N<sub>2</sub> four different distances from the ignition to the DDT point were simulated:  $x_D = 5, 9, 11$  and  $12$  m (Fig. 11). For the DDT point  $x_D = 5$  m the pre-compressed zone propagates practically up to the tube end with precursor shock reflection. This is practically the same behavior as for the 40%N<sub>2</sub> radiolysis gas mixture and a distance to the DDT point of  $x_D = 9$  m. The maximum reflected pressure was about 300 bar and the maximum strain was calculated to be  $\varepsilon_m = 0.17\%$ . In the simulations with later detonation onset at  $x_D = 9, 11$  and  $12$  m, the precursor shock wave was reflected several times at tube ends. In all these cases the maximum pressure achieved at the tube end was approx. 330 - 360 bar. A maximum deformation of  $\varepsilon_m = 0.22\%$  was calculated with a DDT point at  $x_D = 9$  m.

### 6. Evaluation of maximum deformations

For the computation of the stress and strain of the exhaust pipe a linear oscillator model was used in this work. Here a thin cylindrical piping segment will have a displacement by an elastic oscillation only, axial displacement was neglected. From the FA1D detonation calculations time-dependent internal pressures along the tube were determined for different radiolysis gas mixtures and different DDT points. The following properties were used in the calculations for the stainless steel No. 1.4541: Young modulus of elasticity  $E = 203000$  MPa and density  $\rho = 8000$  kg/m<sup>3</sup>.

In the present work we used Hooke's law (or the linear-elastic approach) for the calculations of stress-strain dependence. But in reality Hooke's law is only valid for the portion of the stress-strain curve before the yield limit when material becomes plastic. Another important issue for the computation of piping strain using real stress-strain curves is that material properties depend on the strain rate as well. Our previous experiments with radiolysis gas detonations in stainless steel pipes resulted in strain rates of  $\dot{\varepsilon} = 100-300$  1/s in the elastic and  $\dot{\varepsilon} = 1000-2000$  1/s in the plastic regime of deformation (Kuznetsov et al., 2007b). Appropriate stress-strain curves made by MPA Institute for same stainless steel No. 1.4541 are represented in Fig. 18 (Stadtmüller, 2006). Using zoomed initial part of this strain-strain curve for high strain rate  $\dot{\varepsilon} = 1000$  1/s we can see that even for the highest deformation  $\varepsilon_m = 0.22\%$  inside the realistic range of run-up-distances (see Fig. 11), obtained for 60%N<sub>2</sub> radiolysis gas detonation with a DDT point  $x_D = 9$  m, the tube expands practically in the linear elastic mode (Fig. 19). For the maximum calculated exhaust pipe deformation  $\varepsilon_m = 0.29\%$  outside the realistic range of DDT point we have to take into account plasticity of the material. With the assumption of the same value of the work of deformation  $W$  for elastic and plastic regime

$$W = R \cdot S \int_0^{\varepsilon_e} \sigma_{elastic} d\varepsilon = R \cdot S \int_0^{\varepsilon_p} \sigma_{plastic} d\varepsilon = const, \quad (20)$$

where  $R$  and  $S$  are piping radius and cross-section area, we can estimate the maximum plastic deformation corresponding to the calculated value  $\varepsilon_m = 0.29\%$  in an elastic approach. First estimation gives a value  $\varepsilon_m = 0.41\%$  for plastic deformation corresponding to the value  $\varepsilon_m = 0.29\%$  in an elastic approach. This means that even with nonrealistic DDT point taken as a "worst case" the maximum deformation does not exceed 1%.

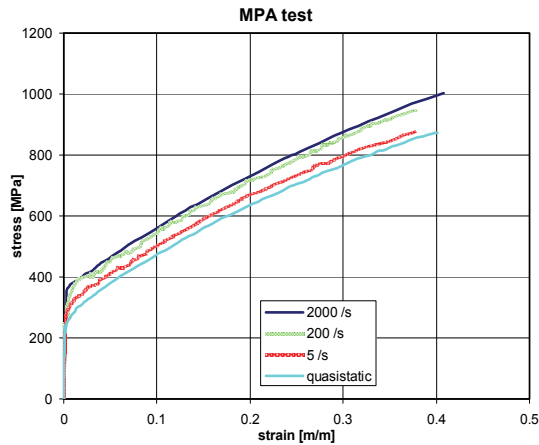


Fig. 18. Dynamic stress-strain characteristics for stainless steel No 1.4541 (Stadtmüller, 2006)

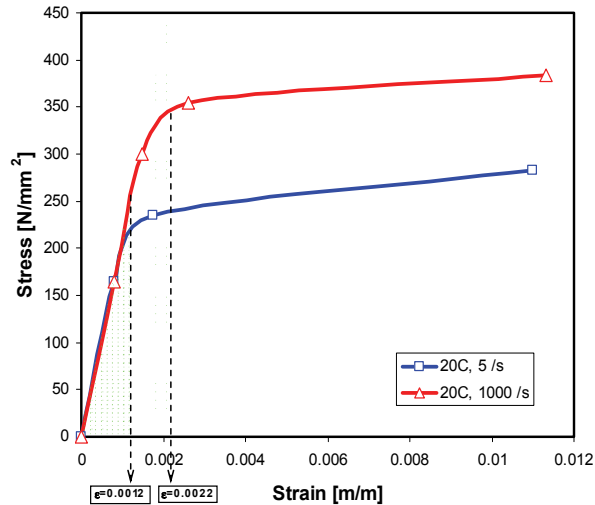


Fig. 19. Mechanical response of the exhaust pipe for dynamic detonation pressure load with a quasi-static ( $\dot{\epsilon} = 5/s$ ) and dynamic strain rate ( $\dot{\epsilon} = 1000/s$ )

## 7. Experimental verification of FA1D-code

Experiments on radiolysis gas detonation have been performed in a tube designed similar to a typical BWR exhaust tube. The tube was fabricated of austenitic stainless steel DIN 1.4541 with following material properties: Young modulus of elasticity  $E = 203000$  MPa and density  $\rho = 8000$  kg/m<sup>3</sup>. The tube was installed into a safety vessel with 80 mm wall thickness, certified for a static pressure of 100 bar. The tube with a length of 12.25 m consisted of two parts that were 4275 and 7501 mm long with different outer diameters and wall thicknesses: (I) 419x20 mm and (II) 510x15 mm. Both parts of the tube were connected via a conic part of 300 mm length and 20 mm wall thickness. Total weight of the piping structure with the flanges was approx. 3500 kg.

Stoichiometric hydrogen-oxygen mixtures diluted with 0 to 55% nitrogen at an initial pressure of 1.6 bar and a temperature of about 30 °C have been used in order to define initial conditions leading to the strongest detonation pressure and the maximum tube deformation. Several tests have been carried out at reduced initial pressures of 0.4 and 0.8 bar prior the main experimental series. Before each test the tube was evacuated up to a pressure of less than 0.1 mbar. After the evacuation the test mixture was injected into the test tube up to required initial pressure. The concentration of each mixture component was controlled via mass flow rates. The mixture quality was additionally checked by a gas analyzer connected via bypass line. The test mixture was ignited by a spark plug, mounted axially in the flange at the stronger part of the tube to reproduce the most conservative scenario where the maximum detonation pressure appears in the weakest part of the tube.

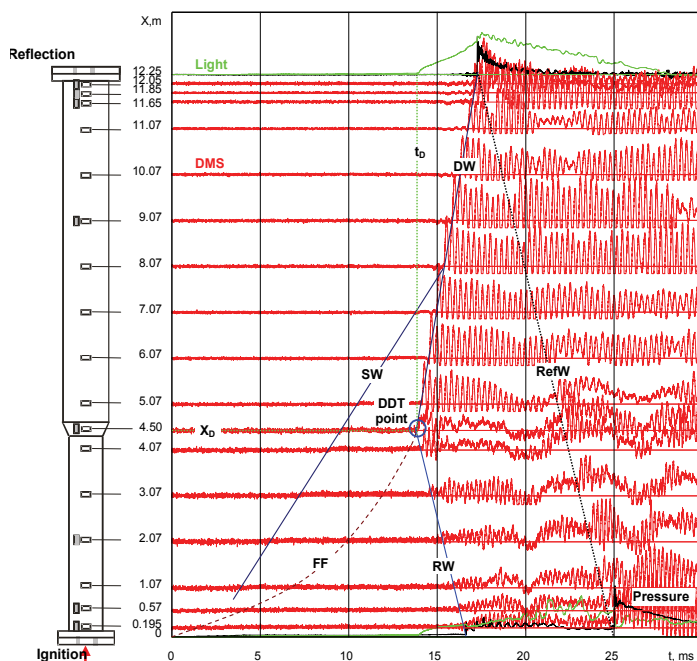


Fig. 20.  $X-t$  diagram of detonation process based on records of strain gauges (red lines), pressure sensors (black) and photodiodes (green): SW = precursor shock wave; FF = flame front; DW = detonation wave; RW = retonation wave; RefW = reflected detonation wave

A schematic of the tube and the gauges location is shown in Fig. 20. To record the radiolysis gas detonation pressure and dynamics of the flame propagation 4 pressure sensors and 2 photodiodes as light sensors were installed in both end flanges. The axial position of light sensors allows registering the DDT moment due to its very intensive light signal of the local explosion. 17 circumferential and 8 longitudinal DMS strain gauges with temperature compensation were fixed on the cylindrical surface of the tube to measure the tube deformations and the arrival time of the shock waves and the detonation wave.

Figure 20 demonstrates an example of  $x-t$  diagram of detonation process of radiolysis gas mixture with 40% nitrogen at 1.6 bar initial pressure. The diagram represents signal records in time for different sensors positions along the test tube. When shock wave or detonation wave arrives at a sensor position it causes a sharp increase of the signal. For instance, by

using the points with sharp pressure or strain increase as arrival time, the well pronounced trajectories of the precursor shock wave (SW), detonation wave (DW), reflected detonation wave (RefW), and retonation wave(RW) were identified on the  $x-t$  diagram (Fig. 20). Due to the precursor shock wave with a pressure of 3.5 bar and a velocity of 600 m/s, generated by an accelerating flame front (FF), an overdriven detonation takes place in the pre-compressed radiolysis gas mixture with an initial pressure of 3.5 bar. The subsequent detonation reflection from the end flange results in a significant increase of the detonation pressure with propagation of reflected detonation wave in opposite direction.

The experiments showed that with increasing nitrogen dilution, the DDT point shifts towards the tube end with production of extremely high pressure and piping deformation as result of the cumulative effects of pre-compression, reflection and local explosion during the DDT process.

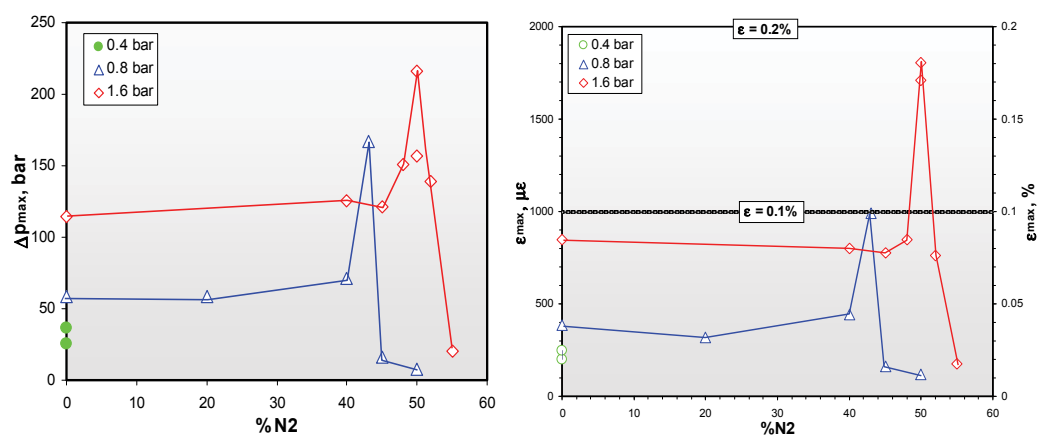


Fig. 21. Maximum experimental pressure load (left) and maximum measured hoop strain (right) along the tube vs. nitrogen dilution for different initial pressures (yield limits of 0.1% and 0.2% are shown)

Finally, all the experimental data on maximum pressure and maximum strain along the tube are summarized in Figs. 21 as a function of nitrogen dilution of radiolysis gas mixture. The experimental data for maximum hoop strain along the tested tube show that deformation of the pipe is consistent with level of pressure load. As it follows from these plots, the maximum pressure load and the maximum tube deformations occurred for nitrogen dilution of 50% at an initial pressure of 1.6 bar when a scenario with late detonation initiation was realized. This means that higher nitrogen dilution leads to the actually worst case scenario, in which the maximum tube deformation achieves a value of 0.17-0.18%, or practically two times higher than a scenario with detonation of pure radiolysis gas (0%N<sub>2</sub>) proposed in our previous work (Kuznetsov et al., 2007). Such level of experimental hoop strain is consistent with calculated deformations in the range of 0.19-0.22%, obtained for "late DDT" scenarios with run-up distances of 9-12 m from the ignition point (see Fig. 11). The lower experimental maximum strain can be explained due to the reinforcing effect of the end flange, which makes the cylindrical tube wall stronger, compared to the model of an unconfined cylindrical shell, assumed in the numerical calculations.

Generally, maximum tube deformations of 0.17-0.18% from radiolysis gas detonations are less than the yield limit of 0.2% for austenitic stainless steel. This means that the BWR

exhaust tube remains intact even in the worst case scenario of radiolysis gas detonation. Additionally, we have to point out that in case of combustion (no detonation initiation at nitrogen concentration more than 52 vol. %N<sub>2</sub>), as it follows from Fig. 21 (right), the maximum deformation is 10 times smaller than in case of the radiolysis gas detonation. This means that stoichiometric hydrogen-air mixture with 56%N<sub>2</sub> if it would be ignited from end flange in such a smooth and large (~0.5 m i.d.) tube without obstacles would not detonate. As it follows from the papers (Kuznetsov et al., 2005; Liberman et al., 2009), reduction of the tube diameter will shorten the run-up distance to detonation. This may be sufficient to initiate detonations in less reactive mixtures than in our tests. Decreasing of initial pressure reduces the mixture detonability and detonability limit shifts to lower nitrogen concentration as well.

## 8. Conclusions

To describe the deflagration-to-detonation transition (DDT) of radiolysis gas mixtures diluted with nitrogen and/or steam the new 1-dimensional computational code FA1D was developed and experimentally verified. The program allows performing a continuous mechanistic analysis of the complex processes with deflagration-to-detonation transition in closed pipes leading to the highest internal pressure loads.

For radiolysis gas mixtures with nitrogen dilution from 0 to 80% different DDT run-up-distances were postulated and resulting pressure loads and maximum deformations of an exhaust pipe with 510-mm o.d. and 15-mm wall thickness were calculated. The real "worst case" with a maximum pressure load and deformation always arose at the tube end as a result of a cumulative effect of precursor shock reflection, DDT and detonation reflection processes (so called "late detonation").

With a simplified linear-elastic model of piping response to dynamic pressure loads the results of the calculations were very close to the experimental data. The obtained calculated maximum strains are quite low and present no danger for the integrity of the exhaust pipe fabricated from the material DIN 1.4541. Nitrogen dilution of the radiolysis gas does not reduce the stress of the pipe. On the contrary, up to some critical nitrogen concentration it has a promoting effect on stress of the tube by producing "late detonation".

The real scale experiments with a BWR exhaust pipe showed that the detonation of nitrogen diluted radiolysis gas mixtures leads to significantly larger and safety-relevant piping deformation compared to pure radiolysis gas. Maximum pressure loads with maximum deformations occur just after the DDT point and near the reflection end. It was shown that even the real "worst-case" scenario of radiolysis gas detonation with the critical nitrogen dilution (50%N<sub>2</sub>) would not lead to a structural damage of the exhaust pipe.

## 9. Acknowledgments

We are very grateful to Mr. T. Franke and EnBW Kernkraft GmbH, Philippsburg, Germany for funding and technical support of this work.

## 10. References

Baker, W.E., Cox, P.A., Westine, P.S., Kulesz, J.J., Strehlow, R.A. (1983) *Explosion Hazards and Evaluation*, Elsevier Publ. Co., 277p.

- Bradley, D. (1992) How Fast Can We Burn? *24th Symposium (Int.) on Combustion*, pp. 247-262.
- Goodwin, D. G. (2001) *Cantera User's Guide*, California Institute of Technology, Pasadena, CA, USA
- Kuznetsov, M.; Alekseev, V.; Matsukov, I. & Dorofeev, S. (2002), Experiments on Flame Acceleration and DDT in Smooth Tubes with Radiolysis Gas for BWR Safety Applications, *Report Vargos Co. for FZK*, December 2002, Saint-Petersburg.
- Kuznetsov, M., Alekseev, V., Matsukov, I., Dorofeev, S. (2005) DDT in a Smooth Tube Filled with Hydrogen-Oxygen Mixtures, *Shock Waves*, 14(3), pp. 205 - 215.
- Kuznetsov, M.; Redlinger, R. & Breitung, W. (2007a) Evaluation of the Maximum Reaction Pressure from Radiolysis Gas Explosion in Pipes and the Corresponding Pipe Response, *Proc. Annual Meeting on Nuclear Technology*, pp. 211-216, German Nuclear Society, Karlsruhe, Germany.
- Kuznetsov, M.; Grune, J.; Redlinger, R.; Breitung, W.; Sato, K.; Inagaki, T. & Ichikawa, N. (2007b) Plastic Deformation and Tube Rupture under Radiolytic Gas Detonation Loads, *Proc. ICONE15*, ICONE15-10377, pp. 1-12, Nagoya, Japan.
- Lieberman, M.; Kuznetsov, M.; Ivanov, A. & Matsukov, I. (2009) Formation of the preheated zone ahead of a propagating flame and the mechanism underlying the deflagration-to-detonation transition, *Physics Letters A*, 373(5) pp. 501-510.
- Lutz, A. E. (1988) A Numerical Study of Thermal Ignition, *Sandia Report SAND88-8228*
- Nakagami, M. (2002) Pipe rupture incident of Hamaoka Nuclear power station Unit-1, *Report Chubu Electric Power Co., Inc.*, Japan.
- Schröder, V. & Hieronymus, H. (2006) Sicherheits-technisches Gutachten zu möglichen Explosionsdrücken im RA Druckentlastungssystem bei Radiolysegasreaktionen, *Bericht BAM*, März 2006, Berlin, Germany.
- Stadtmüller, W. (2006) MPA Stuttgart, Halbjahresbericht 2006-1, GRS-Förderkennzeichen 150, 1297, <http://grs-jsri.de>
- Schulz, H.; A. Voswinkel, & H. Reck (2002) Insights and Lessons Learned from the Brunsbuettel Piping Failure Event, *EUROSAFE Rep.*, GRS/IRSN, Forum for nuclear safety, Berlin

# Experimental Investigation and Numerical Simulation on Interaction Process of Plasma Jet and Working Medium

Yong-gang Yu, Na Zhao, Shan-heng Yan and Qi Zhang  
*Nanjing University of Science and Technology*  
China

## 1. Introduction

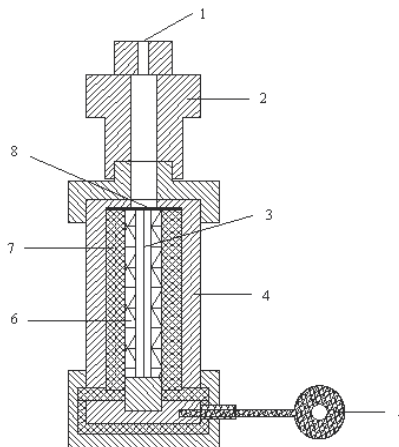
The interaction between the plasma jet and medium has been applied in the field as aerospace and armament. In order to meet the requirement of the spacecraft's orbital adjustment, gravitation compensate, position maintenance, orbital maneuver and the attitude control, many kinds of micro propulsion system, such as: micro electrical propulsion, micro cold air propulsion, micro laser propulsion, pulse plasma propulsion (Robert, 2003) and so on have been studied in many countries. The operation principle of the pulse plasma propulsion is as follows: the electric arc plasma forms by loading the electric energy at two ends of the capillary. The capillary plasmas with high temperature and pressure are then produced as the capillary wall can be burned by the electric arc. The plasma ejects out through the nozzle and pushes the chamber moving forward. In modern hypervelocity launching technique, the liquid propellant electrothermal-chemical technology (LPETC) is one of the effective one and develops well. The LPETC propulsion technology is a new propulsion technique to ignite the propellant by the high pressure and high temperature pulse plasma jet produced by capillary discharge. Accordingly, performance of the plasma jet and the interaction between the plasma jet and the medium (Nusca et al., 2001) is one of the key problems in plasma propulsion and the electrothermal-chemical launching technique. Lots of works have been done according the related field by many scholars. Taylor M J studied the free expansion processes of the plasma in the atmosphere as the discharge energy is 30KJ (Taylor, 2001). The distributions of parameters as the temperature and pressure have been got. The free expansion characteristics of the plasma jet have been studied by Kim J U et al. as the discharge energy is 3.1KJ(Kim & Suk, 2002). The temperature and density distribution of plasma and the shock wave structure of the incompleteness expansion jet have been got. The effects of discharge pulse length on the characteristics of plasma jet impacting the plate as the discharge energy is 3KJ has been studied by Lang-Mann Chang et al.(Chang, Harvard, 2007). Guo H B et al. studied the discharge characteristics in the capillary (Guo, Liu, et al., 2007). Zhang Q et al. studied the expansion characteristics of the plasma jet in atmosphere as the discharge energy is less than 100J (Zhang et al., 2009). Wilsion D E et al. proposed the plasma jet axisymmetry unstable model (Wilsion & Kim, 1999). The plasma jet is treated as over expansion supersonic speed instantaneous jet and the development of expansion wave and Mach disc have been

simulated. The interaction between the plasma jet and liquid has been studied by Kuo K K et al. by high speed camera and pulse X-ray imaging technology (Kuo et al., 1990). The expansion processes of Taylor cavity formed as the plasma jets into the liquid and the intensity distribution law of plasma have been got. Arensburg A studied the continuous expansion processes of the plasma jet in water by shadow imaging technology (Arensburg, 1993). The jet speeds, the mass flowrate entrainment by the liquid at two phase interface are studied quantitatively. The droplets' formation process due to the liquid entrainment was also studied. Zhou Y H studied the interaction characteristics between the plasma jet and the liquid medium in the cylinder inspection chamber (Zhou et al., 2003). Yu Y G et al. studied the interaction between the plasma jet and the liquid medium both in cylinder and the stepped-wall inspection chamber (Yu et al., 2009). The effects of the boundary shape on the expansion characteristics of plasma jet have been studied.

In this paper, the expansion characteristics of plasma jet in atmosphere and the interaction properties between the plasma jet and the liquid medium on the small discharge energy condition have been studied. The effects of the discharge voltage, nozzle diameter and the multilevel steps boundary shape of the stepped-wall chamber on the expansion characteristics of Taylor cavity caused by plasma jet have been mainly discussed. Two-dimensional axisymmetry mathematic model of the interaction between plasma jet and the liquid medium has been proposed based on the experiment. The expansion processes of plasma jet on the unsteady state condition have be simulated. The distribution performances of the pressure, velocity and temperature in flow field have been got.

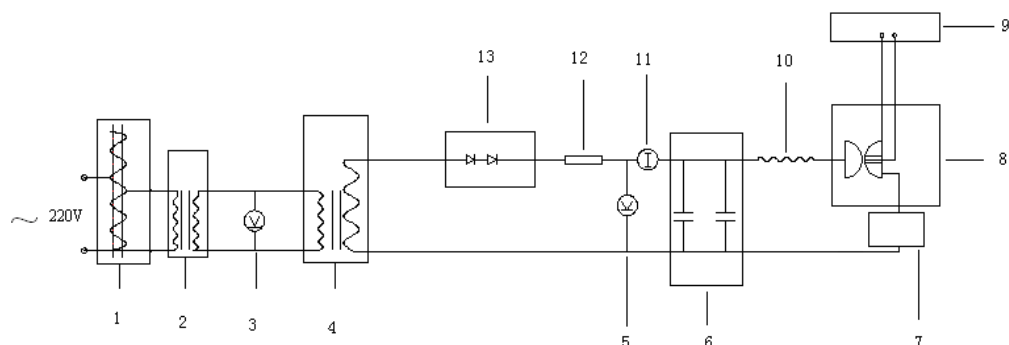
## 2. Experiment apparatus of plasma jet generator

The simulated experiment apparatus are composed of plasma generator, pulse power source and so on as shown in figure 1. The plasma generator is made up of polythene capillary, electrodes, metal detonating cord, the metal sealed film on the cathode, the insulator and the metal shell outside the capillary and so on. The pulse power supply is composed of the pulse forming network (PFN) whose energy is stored by capacitor as shown in figure 2.



1- nozzle; 2- joining; 3- exploding wire; 4- steel shell; 5- anode; 6- polyethylene capillary; 7- insulator; 8- copper film

Fig. 1. Schema of the experiment apparatus



1-autotransformer; 2-isolating transformer; 3-AC voltmeter; 4-step-up transformer; 5-DC voltmeter; 6-capacitor bank; 7-plasma generator; 8-discharge switch; 9-discharge trigger; 10-damping resistor; 11-charging ammeter; 12-current-limiting resistor; 13-rectifier stack

Fig. 2. Pulse-forming network setup

The capillary as the load of the discharge loop is connected to the pulse power supply. There is a hole in the cathode. The polythene pipe is ablated by the high power discharge. The plasma forms and flows into the nozzle through the hole in the cathode. The anode is connected to the high voltage output of the pulse power source and keeps sealed. The cathode connects earth by the body of the apparatus. The output intensity of the plasma is adjusted by changing the capacitors' discharge voltage and the discharge loop's parameters. The cathode of the plasma generator is sealed by the metal film before the experiment. The jet is started until the pressure in the capillary increasing to a threshold value in case of discharge is terminated as the electric arc is break-off too early. The diameter of the nozzle and the thickness of the film can be changed according the need of the experiment.

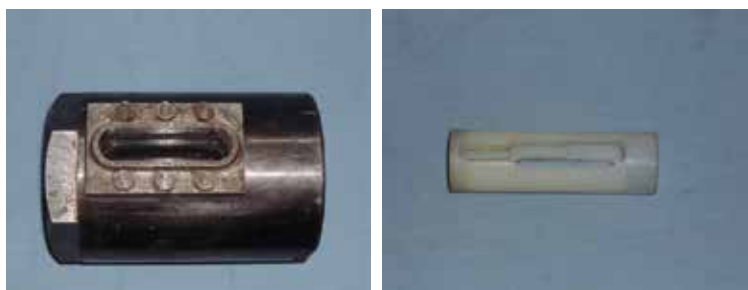


Fig. 3. Decomposition schema of the stepped-wall chamber

An inspection chamber is set up at the exit of the nozzle in order to study the interaction characteristics between the plasma jet and liquid medium visible. The inspection chamber is a cylinder liquid container and the 4 levels stepped-wall chamber is inserted into it, as shown in figure 3. There are inspection window at two opposite sides of the chamber near the nozzle and the window is sealed by chemical method. In order to eliminate the effects of the gravity, the experiment apparatus is placed upright and the plasma is injected upward. In addition, the top end of the chamber is open-end to the atmosphere in case of the window is broken by the over high pressure forming through the expansion of plasma jet. The high speed camera system is used to record the interaction processes between the plasma jet and the liquid medium. And the pressure in the capillary is measured by the pressure sensor.

### 3. Experiment results of the plasma jet expansion in atmosphere

Figure 4 shows the typical pictures of the sequence expansion processes of the plasma jet in the atmosphere as the discharge voltage is 2500V and the diameter of the nozzle is 4mm.

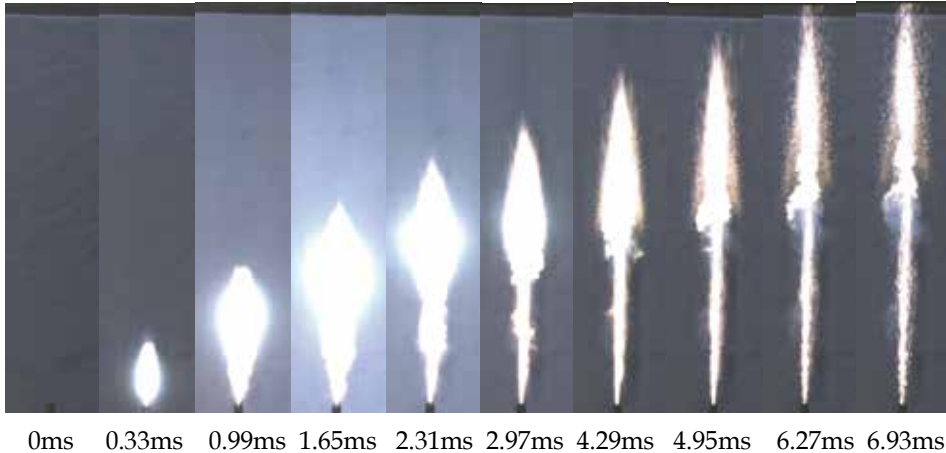


Fig. 4. Sequence processes of the plasma jet in the atmosphere

As shown in the figure, the plasma jet expands both along the axial and radial direction and the axial velocity is larger than the radial one. During the expansion of the plasma jet, the shape of the jet head changes from similar ellipsoid to taper and the jet shape is longer and thinner gradually. As shown in figure, as  $t=2.97-6.93\text{ms}$ , there is intensity turbulence dissipation phenomena as the plasma jet interacts with the atmosphere. At the beginning, the jet head is drupe and the turbulence is strengthened and the turbulent mixture region grows as the development of the jet. The brightness of the plasma jet reflects the temperature. During the plasma jet's expansion processes, the brightness of the plasma jet increases and then decay. The jet head is brighter. It indicates that at the initial of the jet, the temperature decreases after increases as the going of the time. And the jet head has a higher temperature.

#### 3.1 Effects of the discharge voltage on the expansion process of plasma jet

Figure 5 shows the sequence expansion processes of the plasma jet in the atmosphere as the discharge voltage is 2100V, 2500V and 3000V respectively and the nozzle diameter is 4mm. As shown in the figure, the expansion shape is similar at different voltages while the jet intensity is different. The larger is the discharge voltage, the larger is the jet intensity and the jet head's turbulence dissipation is greater. As the discharge voltage increases from 2100V to 2500V, the expansion is strengthened both in the axial and radial direction and the jet is brighter. But there is tiny effect of the voltage on the jet axial expansion as the discharge voltage changes from 2500V to 3000V, while the effect on the radial expansion is obvious. As the discharge voltage is 3000V, the radial expansion velocity is larger at initial and the turbulence dissipation is intensity in the later period. At the time after  $t=2.64\text{ms}$ , the mixture region of the plasma and the atmosphere is thick and the boundary is fade. The lightness of the plasma is brightest as the discharge voltage is 3000V as shown in the figure.

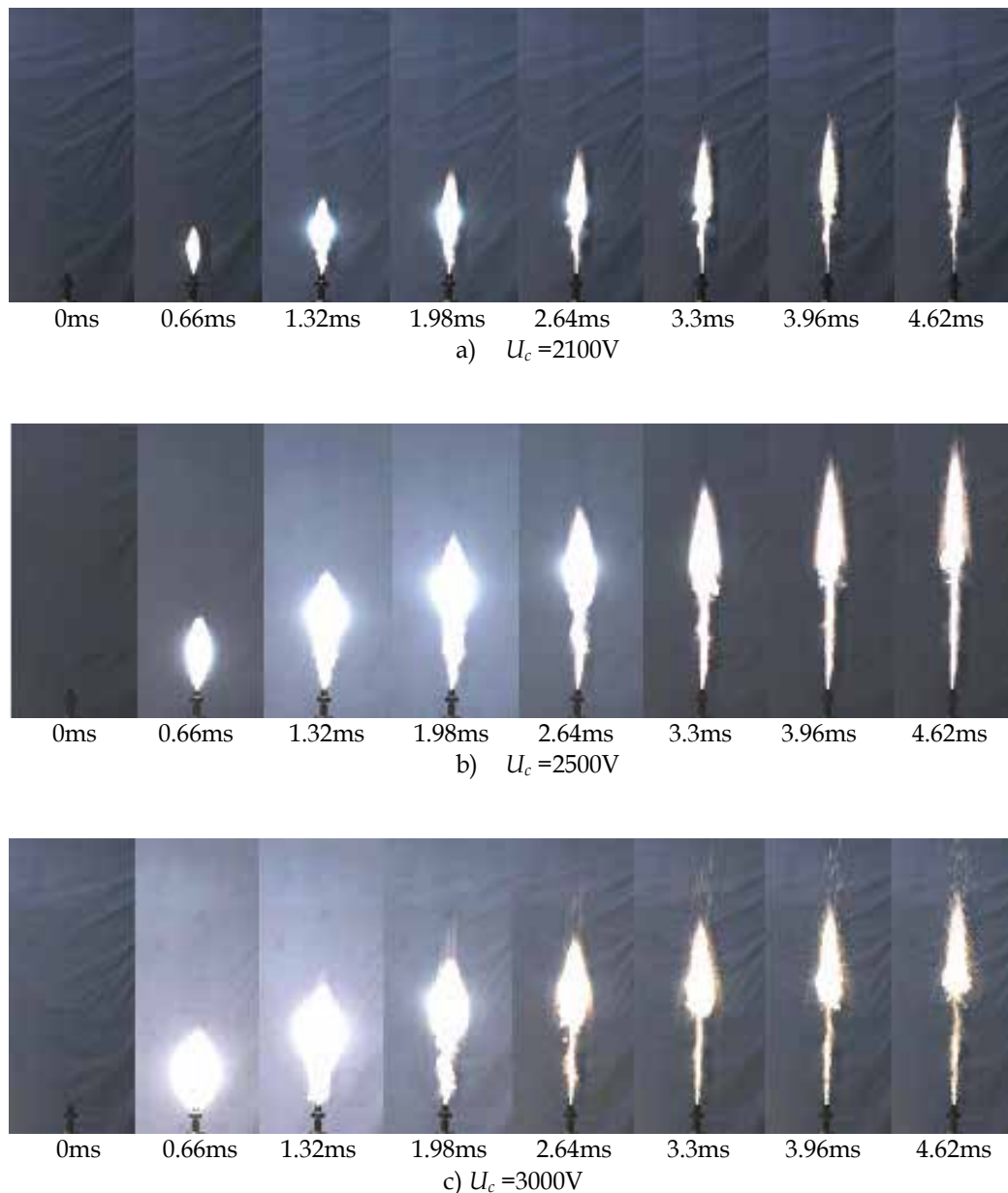


Fig. 5. Sequence expansion processes of the plasma jet in the atmosphere at different discharge voltages

The axial and radial expansion displacement of plasma jet can be got from the sequence expansion pictures. And according to the relationship between the expansion displacement and the time, the rules of the expansion velocity changing with time can be handled out. Figure 6 shows the axial ( $x$ ) and radial ( $r$ ) expansion displacement changing with the time at different discharge voltages. Figure 7 shows the axial ( $v_x$ ) and radial ( $v_r$ ) expansion velocity changing with time at different discharge voltages.

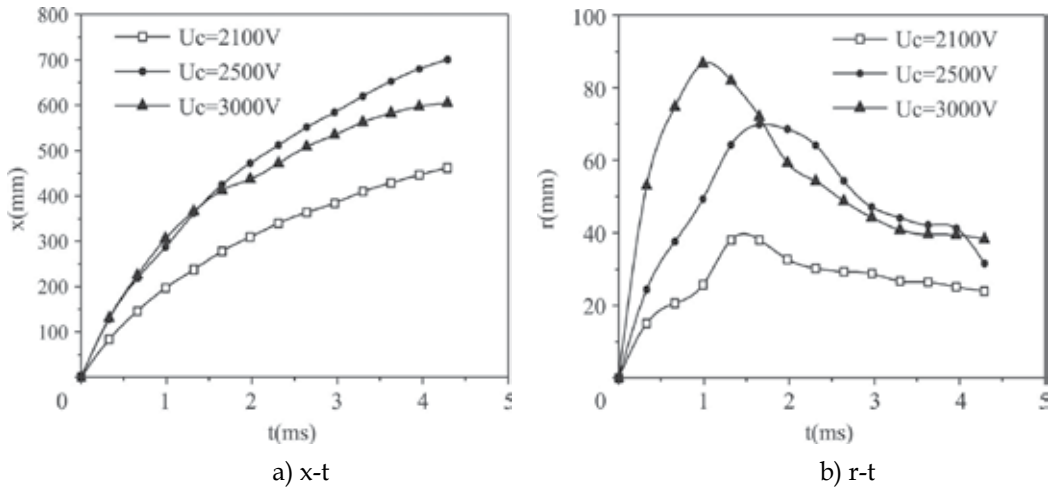


Fig. 6. The expansion displacement distribution of the plasma jet

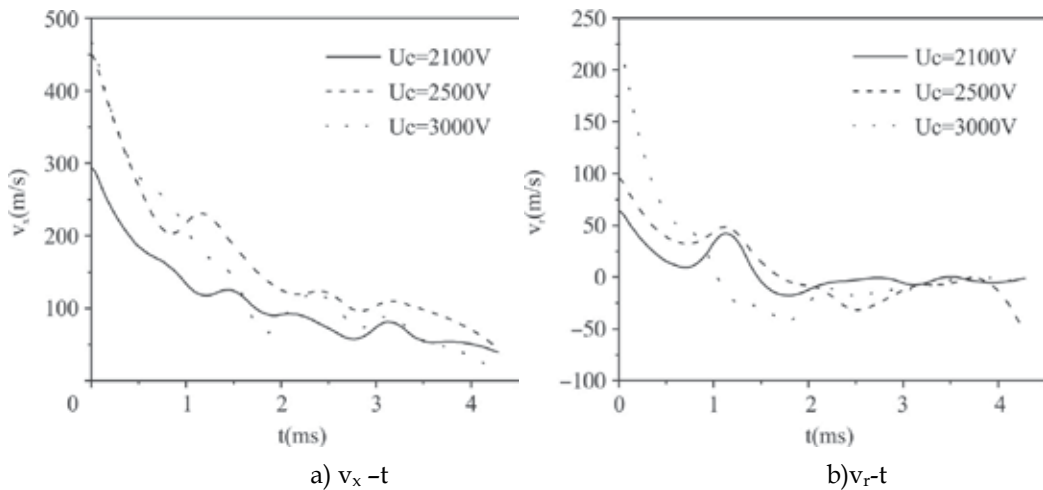


Fig. 7. The expansion velocity distribution of the plasma jet

As shown in figure 6(a), the axial displacement of the plasma increases obviously as the voltage changes from 2100V to 2500V. In the discharge voltage region of 2500V to 3000V, the axial displacement change is small but the radial displacement has a great change. As the discharge voltage is 3000V, the radial expansion velocity of the plasma jet is greater at the initial expansion, and the turbulence dissipation is higher, the decay of the axial and radial expansion velocity is greater too. The axial and radial expansion displacement as the voltage is 3000V may be less than that as the discharge voltage is 2500V in the last for the higher dissipation. The axial and radial velocity is decaying as the time goes on and the change curve is fluctuation. The relationships between the axial and radial expansion displacement with the discharge voltage are not monotonous. The velocity also does not change with the discharge voltage monotonously.

### 3.2 Effects of the nozzle diameter on the expansion process of plasma jet

The nozzles with diameter ( $d_0$ ) of 1.5mm and 2mm are adopted to study the effect of the nozzle diameter on the expansion characteristics of the plasma and the discharge voltage is 3000V. Figure 8 shows the axial displacement of the plasma jet changes with the time at different nozzle diameters.

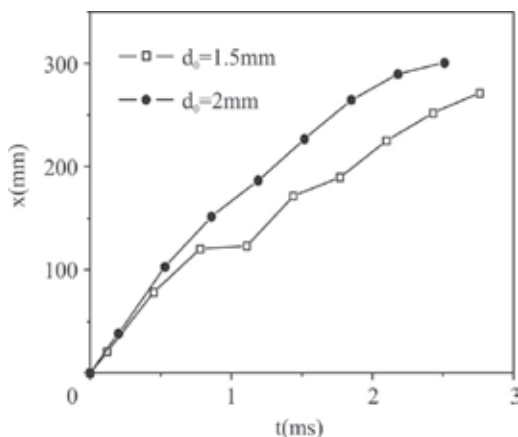


Fig. 8. Changing of the axial expansion displacement of the plasma jet with time at different nozzle diameters

As  $t=0\sim 0.5\text{ms}$ , the difference is small between the two curves as can be seen from the figure. And in the stage of  $t=0.5\sim 3\text{ms}$ , the bigger is the nozzle diameter, the greater is the axial displacement.

## 4. Experiment results of the plasma jet expansion in liquid

The multilevel stepped-wall simulated inspection chamber are adopted to study the interaction properties between the plasma jet and the simulated liquid medium at the cold experiment condition based on the work of Kuo K K(Kuo et al., 1990); Kim H J (Kim & Hong, 1995); Rott M (Rott & Artelt, 2005) and so on. The expansion characteristics of Taylor cavity formed by the plasma jet on different conditions can be observed. Some references about the combustion stability of the bulk-loaded liquid propellant controlled by the plasma ignition as can be given in the stepped-wall chamber.

### 4.1 Effects of the boundary shape on the expansion process of plasma jet

The first stage of the stepped-wall chamber is 14mm in diameter, and 30mm in length. The later three stages are all 30mm in length, and each stage's diameter is 6mm larger than its former one. Cylindrical chamber is 26mm in diameter, and 107mm in length. The chamber is full of water, and the plasma is ejected upward. The capacity of the capacitors is  $45\mu\text{f}$ , the charging voltage is 2500V, and the nozzle diameter is 2.5mm.

The sequential pictures of plasma jet expansion in water in stepped-wall chamber are illustrated in figure 9.

As can be seen in these pictures, a small, bulb like, bright bubble appears near the nozzle when plasma starts to jet out from nozzle, and the bubble expands downstream further with the plasma and forms the Taylor cavity. These pictures also show that in the expansion processes

of Taylor cavity, the plasma with high temperature and high luminance illuminates the liquid around Taylor cavity. At the time  $t=1\text{ms}$ , we can see some black dots obviously at the jet head, because the metal plasma produced by metal initiation wire is cooled down into opaque solid particles as the contact with the liquid. And after  $t=2\text{ms}$ , dark, smog like region appears at the frontal area of the jet. It can be explained as: when the plasma jets into the liquid, Kelvin-Helmholtz instabilities occur due to the dispatch of velocities at the gas-liquid interface, and the results of plasma jet entrainment to water leads to the liquid break-up, temperature reducing, finally the dark, smog like region forms. Starts from the time  $t=2\text{ms}$ , there have already been dark dots at the core of the bubble. This phenomenon demonstrates that the cavity can also entrain the surrounding liquid. The analytical results indicate that there is strong heat transfer and mass transfer at the gas-liquid interface.

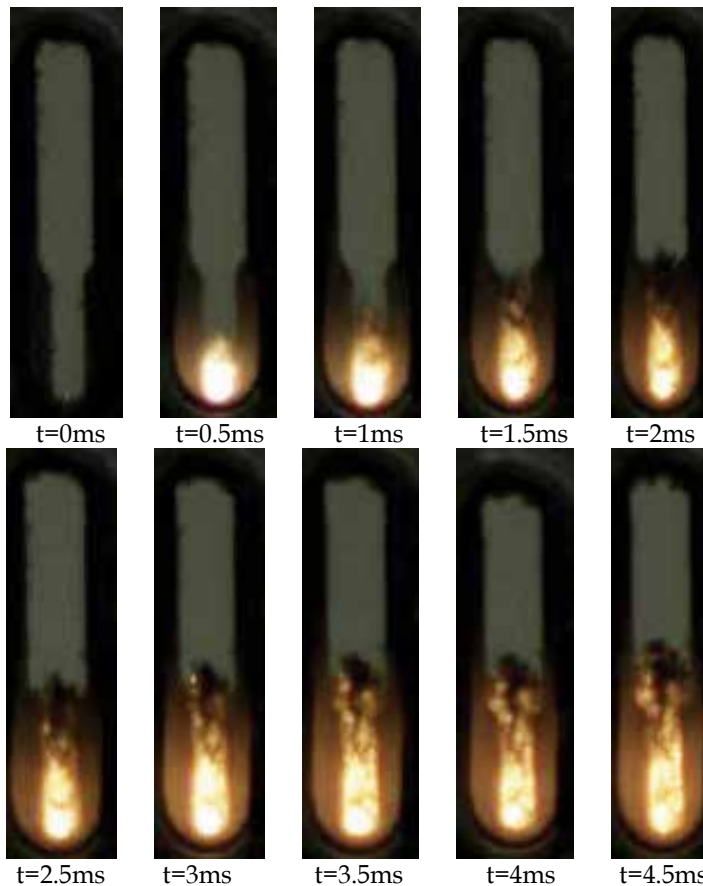


Fig. 9. Sequence pictures of plasma jet expansion in stepped-wall chamber

The chamber used in this experiment is stepped-wall chamber, so the radial expansion of Taylor cavity is restricted by the boundary, and the axial velocity is much greater than the radial velocity, as it is shown in figure 9. But in the traditional cylindrical chamber, the radial disturbance should be decreased obviously. So we carried out experiment in cylindrical chamber at the same conditions, i.e. the capacity of capacitors is  $45\ \mu\text{f}$ , the charging voltage is  $2500\text{V}$ , and the nozzle diameter is  $2.5\text{mm}$ . The expansion process of plasma jet is shown in figure 10.

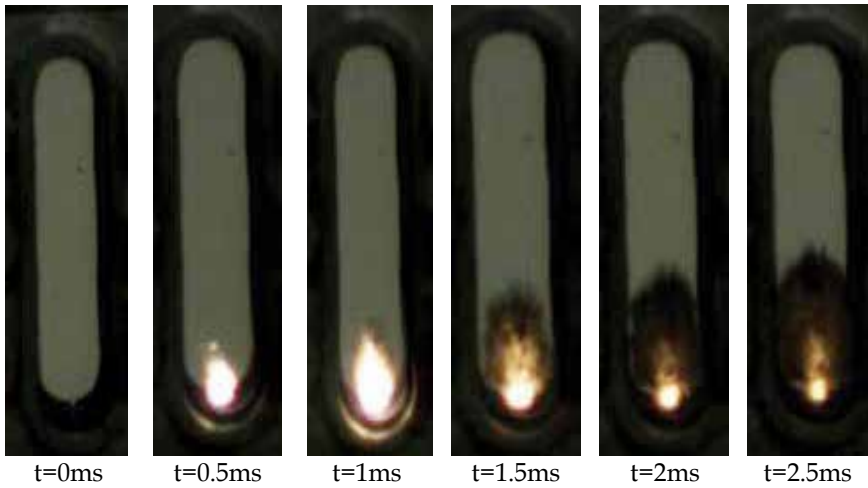


Fig. 10. Expansion process of plasma jet in cylindrical chamber

As it is shown in figure 9 and figure 10, the plasma jet is axisymmetric on the whole, somewhat similar to the expansion process of muzzle wave. The initial expansion velocity at the time when the Taylor cavity is formed is larger, and decreased gradually as the Taylor cavity expanding downward. At the same time, the size of Taylor cavity and the expansion velocity is varied with the difference of chamber structure. By comparing these two sets of pictures, we can see that most plasma energy has been exhausted before it reaches the first step (30mm in length). The water in stepped-wall chamber is less than that in cylindrical chamber, the momentum of plasma jet is small, so the axial velocity of plasma jet in stepped-wall chamber is greater than that in cylindrical chamber. The plasma jet is interrupted in stepped-wall chamber, but in cylindrical chamber it is not. It is because the boundary of stepped-wall chamber can enhance the radial disturbance to plasma jet. The axial expansion velocity of Taylor cavity can be deduced from the frontal locations of the cavity recorded in the pictures and the corresponding time. Axial velocities of Taylor cavity due to the consecutive expansion of plasma jet in different chambers are compared in figure 11.

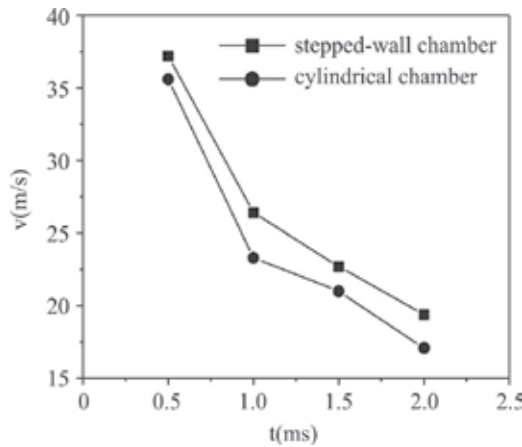
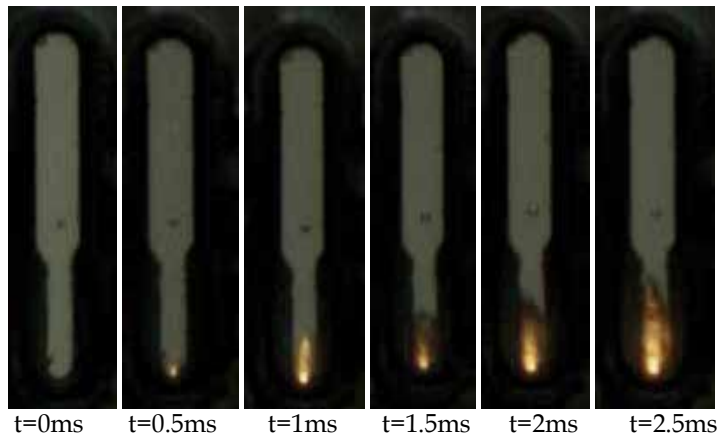
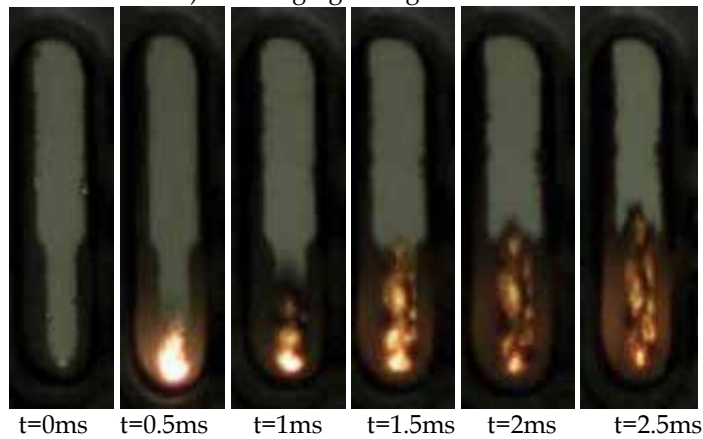


Fig. 11. Comparison of axial velocities of Taylor cavity in two different chambers

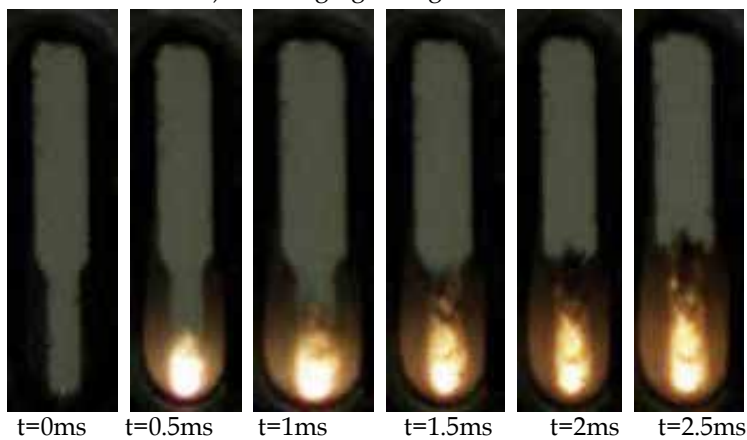
#### 4.2 Effects of discharge voltage on the expansion process of plasma jet



a) Discharging voltage = 2000V



b) Discharging voltage = 2300V



c) Discharging voltage = 2500V

Fig. 12. The sequential pictures of plasma jet expansion in water under different discharging voltages

In order to discuss the effect of discharging energy on the propagation of plasma jet in stepped-wall chamber, we adjust the discharging voltage to produce plasma jets with different discharging energy, while keeping the structure of stepped-wall chamber and capacity of capacitors unchanged (45 $\mu$ f). The discharging voltages in figure 6 are 2000V, 2300V and 2500V respectively. Because the conversion efficiency of the pulse power supply is 40%, the resulting discharging energy is 36J, 48J and 56J separately. The corresponding propagation processes of plasma jets are illustrated in figure 12(a), 12(b) and 12(c).

The pictures indicate that the larger the discharging energy is the brighter and the bigger the fireball is. The expansion velocity of Taylor cavity in axial direction is greater than that in radial direction as the plasma jet moving upward. When plasma jet develops to a certain degree, a shadow region appears at the jet head, i.e. the luminance is reduced, as the result of liquid vaporization and temperature reducing. The plasma jet is interrupted earlier, and its attenuation is faster while the discharging energy is smaller.

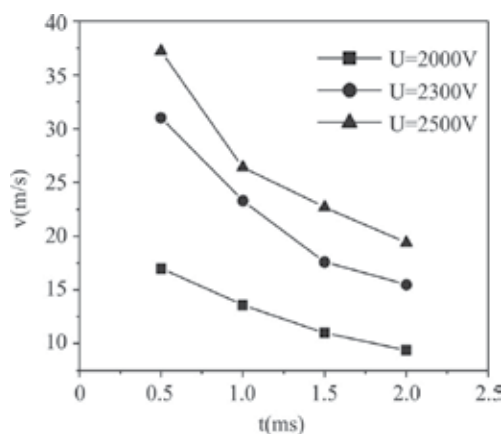


Fig. 13. Changing of the expansion velocity of Taylor cavity with time under different discharging voltages

By measuring the frontal location of Taylor cavity away from the nozzle and its corresponding time, the axial expansion velocity of Taylor cavity can be calculated. As shown in figure 13, the plasma jet velocity has a descending tendency on the whole, and the velocity increases with the increasing of discharging energy at the same time.

## 5. Mathematical and physical models of the Interaction process of plasma jet and working medium

### 5.1 Physical model

According to the constrained expansion character of the plasma jet in stepped-wall chamber, combination with the experimental conditions, the following hypotheses are needed for the physical processes of the jet expansion:

1. The expanding processes of the plasma jet in atmosphere and liquid are the unsteady processes of two-dimensional axial symmetry.
2. Treat the plasma mixture as the ideal gas and without consideration of the chemical reaction between plasma and liquid.
3. Neglect the influence of the secondary factor like electromagnetic force, mass force and the volume force.

4. The  $k-\varepsilon$  model is used to describe the turbulent mixing effect between plasma and liquid in the processes of the plasma jet expansion.
5. The radiation is neglected and the plasma is in partial heat balance condition.

## 5.2 Mathematical model

1. Equation of mass conservation:

The mass conservation equation is as follow:

$$\frac{\partial \rho}{\partial t} + \frac{\partial(\rho u)}{\partial x} + \frac{\partial(\rho v)}{\partial r} + \frac{\rho v}{r} = 0 \quad (1)$$

In which  $x$  is the axial coordinate,  $r$  is the radial coordinate,  $u$  is the axial velocity and  $v$  is the radial velocity.

2. Equation of momentum conservation

Equation of axial momentum conservation:

$$\frac{\partial}{\partial t}(\rho u) + \frac{\partial}{\partial x}(\rho u u) + \frac{\partial}{\partial r}(\rho u v) + \frac{\rho u v}{r} = \frac{1}{r} \frac{\partial(r P_{xr})}{\partial r} + \frac{\partial P_{xx}}{\partial x} \quad (2)$$

Equation of radial momentum conservation:

$$\frac{\partial}{\partial t}(\rho v) + \frac{\partial}{\partial r}(\rho v v) + \frac{\partial}{\partial x}(\rho v u) + \frac{\rho v v}{r} = \frac{1}{r} \frac{\partial(r P_{rr})}{\partial r} + \frac{\partial P_{rx}}{\partial x} \quad (3)$$

For Newtonian fluid, the stress tensor and the strain rate tensor are listed as follows respectively ( $\mu$  is the dynamic viscosity):

$$p_{xx} = -p + 2\mu \left( \varepsilon_{xx} - \frac{1}{3} \text{div} \vec{V} \right), \quad \varepsilon_{xx} = \frac{\partial u}{\partial x}$$

$$p_{rr} = -p + 2\mu \left( \varepsilon_{rr} - \frac{1}{3} \text{div} \vec{V} \right), \quad \varepsilon_{rr} = \frac{\partial v}{\partial r}$$

$$p_{xr} = p_{rx} = 2\mu \varepsilon_{xer}, \quad \varepsilon_{rx} = \varepsilon_{xr} = \frac{1}{2} \left( \frac{\partial u}{\partial x} + \frac{\partial v}{\partial r} \right)$$

3. Equation of energy conservation:

$$\begin{aligned} \frac{\partial(\rho E)}{\partial t} + \frac{1}{r} \frac{\partial(r \rho v E)}{\partial r} + \frac{\partial(\rho u E)}{\partial x} = \frac{1}{r} \frac{\partial}{\partial r} \left[ r \left( v P_{rr} + u P_{rx} + \kappa \frac{\partial T}{\partial r} \right) \right] \\ + \frac{\partial}{\partial x} \left( v P_{xr} + u P_{xx} + \kappa \frac{\partial T}{\partial x} \right) \end{aligned} \quad (4)$$

in which,  $T$  is the temperature and  $\kappa$  is the heat transfer coefficient of the fluid.

4. Equation of state:

$$p = \rho R T \quad (5)$$

5. The basic equations of turbulent flow is as follows:

$$\left\{ \begin{array}{l} \frac{\partial}{\partial t}(\rho u) + \frac{1}{r} \frac{\partial}{\partial r}(\rho r u v) + \frac{\partial}{\partial x}(\rho u) = -\frac{\partial p}{\partial x} + \\ \quad v \left[ \frac{1}{r} \frac{\partial}{\partial r^2}(\rho r u) + \frac{\partial^2}{\partial r^2}(\rho u) + \frac{\partial^2}{\partial x^2}(\rho u) \right] \\ \frac{\partial}{\partial t}(\rho v) + \frac{1}{r} \frac{\partial}{\partial r}(\rho r v v) + \frac{\partial}{\partial r}(\rho v) = -\frac{\partial p}{\partial r} + \\ \quad v \left[ \frac{1}{r} \frac{\partial}{\partial r^2}(\rho r v) + \frac{\partial^2}{\partial r^2}(\rho v) + \frac{\partial^2}{\partial x^2}(\rho v) \right] \end{array} \right. \quad (6)$$

### 5.3 Initial and boundary conditions

The parameters of the computational domain is equal to the ambient at the initial. To the inlet of the computational domain, i.e, the outlet of the nozzle, the parameters are due to the experiment:  $p = p(t)$ ,  $T = T(t)$

In the stepped-wall or the cylinder computational domain, there is reverse flow as the jet compacts to the wall for the effects of chamber structure on the gas expansion. The wall boundary is the fixed wall. The face of the chamber opposite to the nozzle is the outlet face. The outlet pressure is set equal with the atmosphere pressure before the plasma expands to the outlet face.

## 6. Numerical simulation on expansion performance of plasma jet in atmosphere

The simulated conditions is the same with the experiment condition as the discharge voltage is 2500V and the nozzle diameter is 4mm. The expansion processes of plasma jet in atmosphere are simulated by Fluent software. The distribution characteristics of pressure, density, temperature and velocity have been got.

Figure 14 shows the distribution contours of pressure(Pa), density(kg/m<sup>3</sup>), temperature(K) and velocity(m/s) at the initial of the plasma jet as t=25μs. As shown in the figure, there is a Mach disc like pressure peak at the plasma jet head. The pressure, density and temperature in this region are all larger. While, upward the Mach disc, the pressure, density and temperature are lower but the velocity is higher.

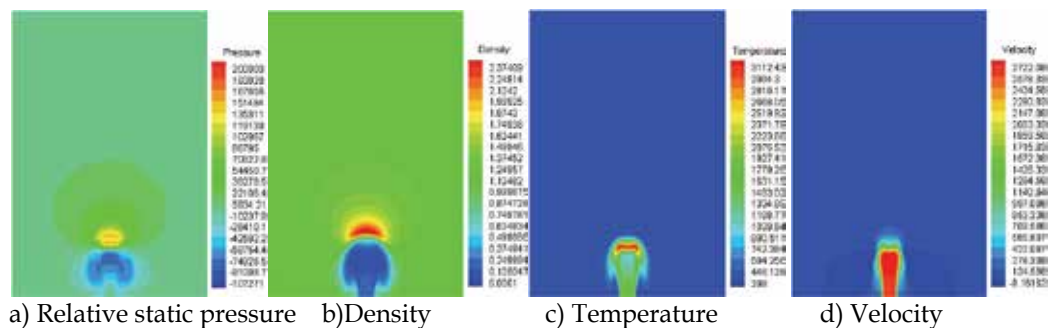


Fig. 14. Contours of pressure, density, temperature and velocity at the initial of plasma jet

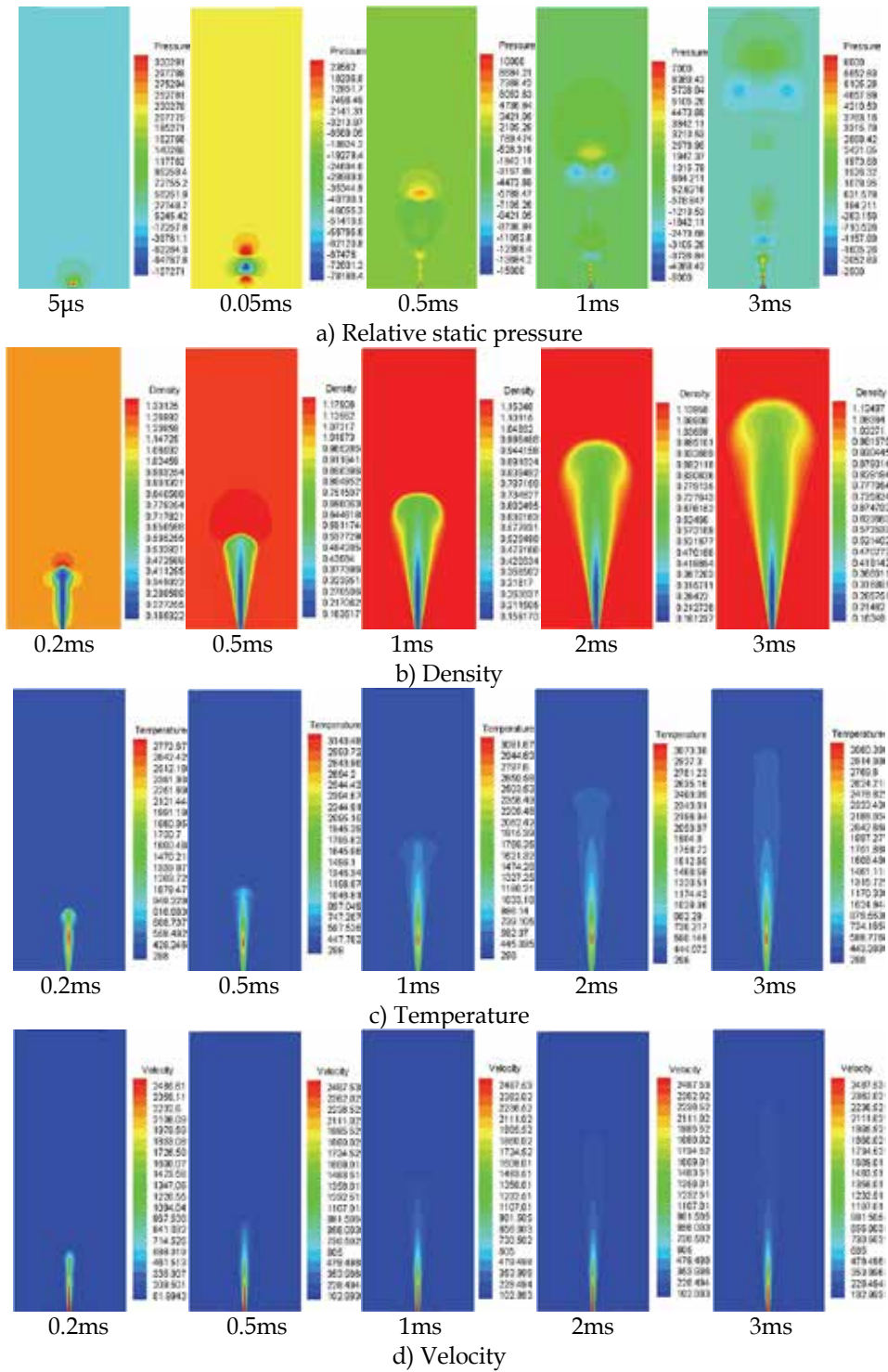


Fig. 15. Contours of pressure, density, temperature and velocity of the plasma jet

Figure 15 shows the sequence contours of relative static pressure(Pa), density(kg/m<sup>3</sup>), temperature(K) and velocity(m/s) as the plasma jet expands in the atmosphere. The pressure wave moves forward in a sphere shape as the plasma jet out the nozzle as show in figure 15(a). The pressure is alternated from high to low in the flow field during the develop processes and the pressure is fluctuated in space. The pressure fluctuation close to the nozzle is intense. The pressure of the jet head is high all along. As the time goes on, the pressure of the flow field is close to the ambient pressure.

As shown in figure 15(b), at t=0.2ms, the plasma is compressed strongly for the great high pressure at the plasma jet head, and the gas density is relatively high. As the time goes on, the pressure at the plasma jet head decreases fast and the gas density is close to the ambient density gradually. As shown in figure 15 (c) the temperature increases at first and decreases then with the increases of the axial displacement away from the nozzle. The temperature along the radial direction. As shown in figure 15 (d), the velocity both decreases along the axial and radial direction.

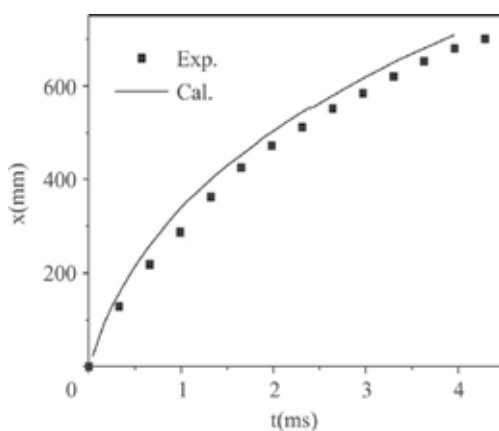


Fig. 16. Changing of the axial expansion displacement of plasma jet with time

The axial expansion displacement of plasma jet can be handled out through the sequence pictures of density. Figure 16 shows the simulated and experiment results of the axial displacement of plasma jet. They match well with each other as can be seen in the figure.

## 7. Numerical simulation on expansion performance of plasma jet in liquid

According to the experiment condition, the processes that the plasma jet into the liquid medium are simulated both in the cylinder and the cylindrical stepped-wall structures to study the parameters distribution characteristics in the flow field.

### 7.1 Numerical results of the stepped-wall boundary shape

The simulated conditions are: The capacity of the capacitors is 45µf, the charging voltage is 2300V, and the nozzle diameter is 2.5mm. The first stage of the stepped-wall chamber is 14mm in diameter, and 30mm in length. The later three stages are all 30mm in length, and every diameter is 6mm larger than its former one. The liquid medium is water.

#### 1. The pressure distribution

Figure 17 shows the isobars of the plasma jet flow field in stepped-wall chamber, the vertical ordinate is pressure and the unit is Pa.

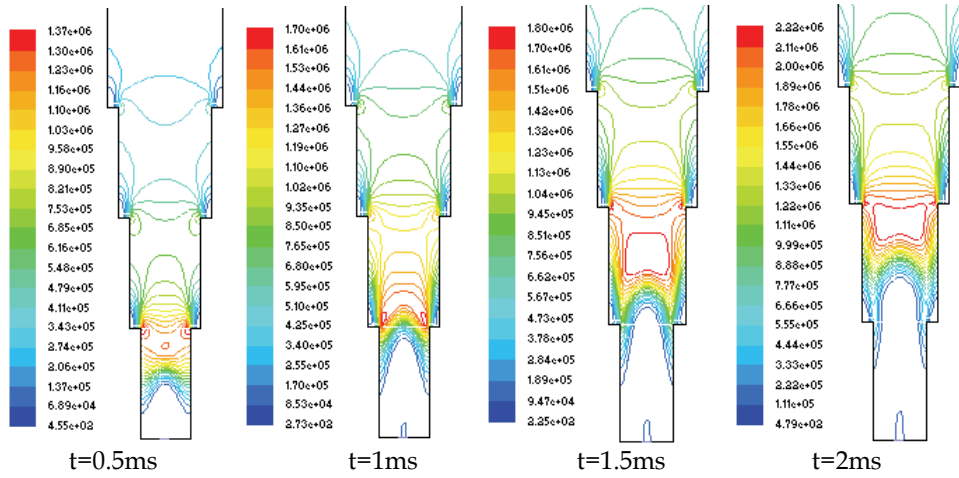


Fig. 17. Isobars of the plasma jet in stepped-wall chamber

As shown in the figure, the isobars are dense and pressure gradient is higher in the front of the plasma jet. In the initial expansion of the plasma jet, there is round pressure centre in the front of the plasma jet head. The high pressure zone grows as time goes on. At  $t=1.5\text{ms}$ , the shape of the high pressure zone centre becomes cone frustum. At  $t=2\text{ms}$ , the edge of the high pressure zone similar to an inverted cone frustum has a radial expansion at the 2nd step attributed to the radial induced. There is an obviously pressure fluctuation during the processes of the plasma jet expansion. When jet impinges against the wall at the steps, the reverse flow occurs, so the low pressure zones can be observed from the figure.

In order to quantitative describe the pressure distribution of the jet flow field, take the pressure at the centre axis and the section at the position 45mm away from the nozzle into account. Figure 18 indicates the changes of the pressure through time at different points on the axis (the direction of jet centre axis is  $y$  longitudinal axis, perpendicular to the nozzle is  $x$  transverse axis).

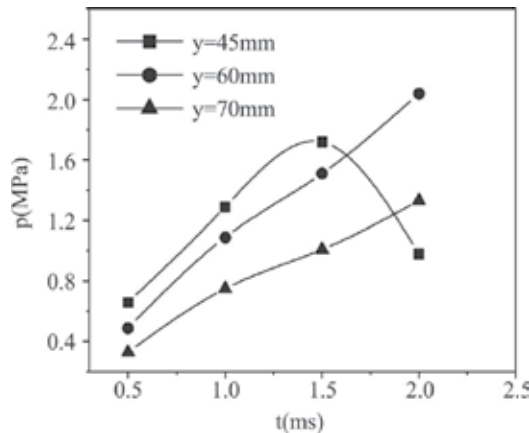


Fig. 18. Changing of the axial pressure with time

Figure 19 shows the pressure-time curves at the section which is 45mm distance from the nozzle. Overall, the pressure on axis is increasing as time goes on. At the distance of 70mm

from the nozzle, the pressure has a stable increase for the further distance from the nozzle. At  $y = 45\text{mm}$ , the pressure has a rapid increase as time goes on. When  $t = 0.5\text{ms}$ ,  $p = 0.66\text{MPa}$ . While  $t = 1\text{ms}$ ,  $p = 1.29\text{MPa}$ . The pressure gets to the biggest  $1.72\text{MPa}$  at  $t = 1.5\text{ms}$ , the high pressure zone propagates to  $y = 45\text{mm}$  at the same time, then it goes ahead. The pressure at the surface which is  $45\text{mm}$  from the nozzle is decreasing. On the radial direction, at the section  $y = 45\text{mm}$ , the pressure is increasing before  $t = 1.5\text{ms}$  because of the high pressure zone propagation. But the closer to the boundary, the smaller the pressure is. After  $t = 1.5\text{ms}$ , the high pressure zone passes across the section at  $y = 45\text{mm}$  and the boundary pressure has a rapid decrease. The low pressure zone forms on the boundary.

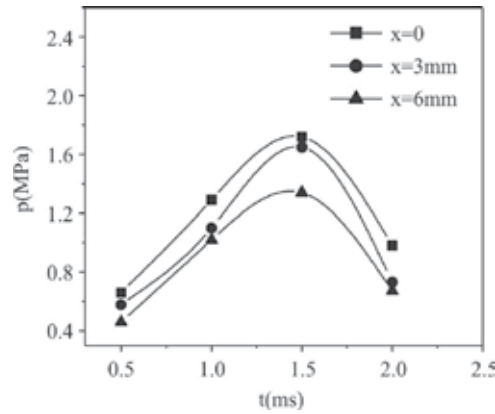


Fig. 19. Radial pressure-time curves

2. The velocity distribution

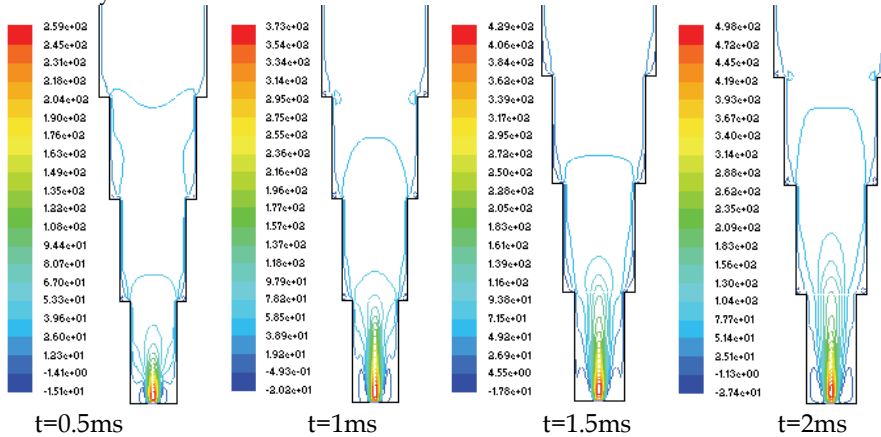


Fig. 20. Isovels of the plasma jet in stepped-wall chamber

The isovels distributions of the plasma jet expansion in the liquid are shown in figure 20 (vertical ordinate is velocity, unit: m/s). It can be observed from the figure that the biggest jet velocity is near the nozzle. The velocity gradient at the interface of gas and liquid is larger, in addition, the velocity is easy to decrease when the plasma jet expands in the liquid for its light quality. As shown in the figure that the velocity is very high in the jet centre but it has a sharp fall near the wall. As the time goes on, the Taylor cavity is expanding along the axial direction. At  $t = 1.5\text{ms}$ , the head of plasma jet has crossed the first step.

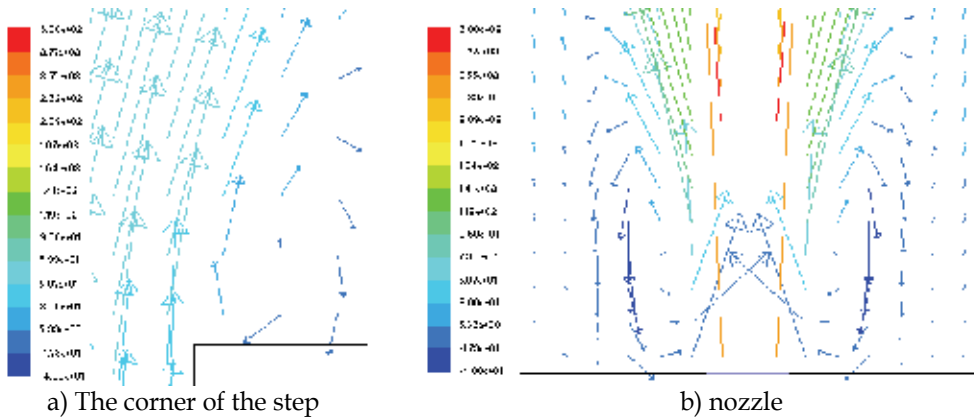


Fig. 21. Partial velocity vector diagrams at the corner of the step and the nozzle

Figure 21(a) shows the velocity vector at the steps. The ring isovels and the negative velocity can be observed from the figure due to the radial turbulence and the reverse flow attributed to the impinging of the jet against the wall at steps. At  $t=2\text{ms}$ , the jet head has propagated to the 1.5th step. Figure 21(b) shows the partial velocity vector at the nozzle. During the processes of the plasma jet propagation, ring isovels can be observed near the nozzle because of the strong turbulence mixture of the gas and liquid, that is the reverse flow phenomenon, and there are negative velocity can be seen in the isovels.

### 3. The temperature distribution

Fig.22 shows the isotherm of the plasma jet during the expansion in the stepped-wall chamber, the vertical ordinate is temperature and the unit is K. As shown in the figure, the temperature in axial direction is higher than that in the radial direction. The temperature close to the nozzle is highest, and it reduces to the ordinary temperature in very short distance along the axis. In radial direction, the temperature also decreases readily near the nozzle due to the completely mixture of the plasma jet and the liquid. After all, plasma jet in the liquid attenuates quickly and the heat is easy to diffuse. As the expansion of the jet, the temperature reduces quickly.

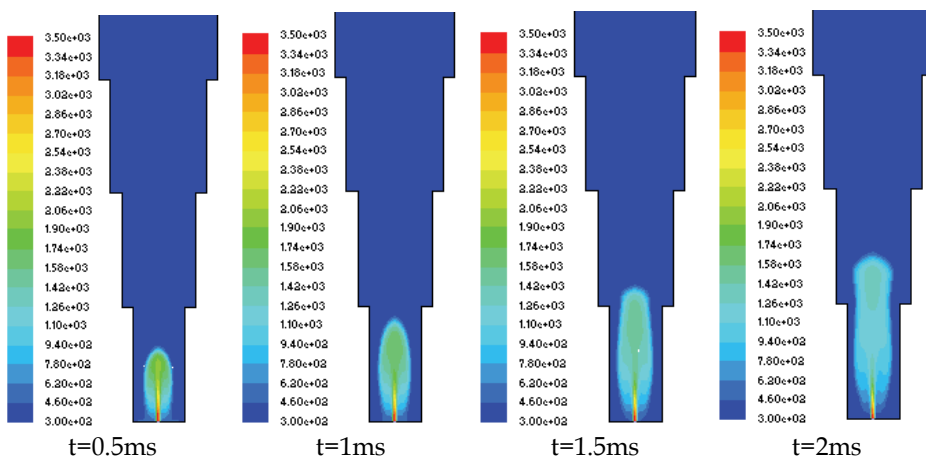


Fig. 22. Isotherms of plasma jet in the liquid

In order to describe the temperature distribution of the jet flow field quantitative, take the value at the centre axis and the section 15mm away from the nozzle into account. Figure 23 indicates the changes of the temperature through time at different points 10mm, 15mm and 25mm away from the nozzle on jet centre axis. Figure 24 shows the temperature-time curve at the section which is 15mm distance from the nozzle.

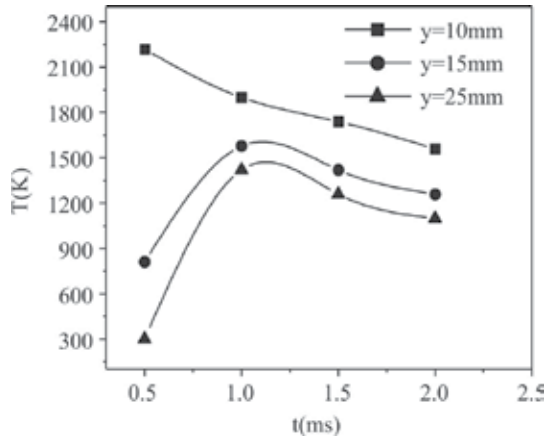


Fig. 23. Changing of axial temperature with time

As shown in the figure, the axial temperature is higher at the position nearer to the nozzle. At  $t=0.5\text{ms}$ , the temperature is 2300K at the position 10mm away from the nozzle, 812K at 15mm away from the nozzle and 300K at 25mm away from the nozzle; as time goes on, the temperature increases gradually at 15mm and 25mm away from the nozzle. At  $t\approx 1\text{ms}$ , the temperature gets the largest value and then decreases. And the temperature are 1600K, 1260K and 1100K respectively at the three point (10mm, 15mm and 25mm away from the nozzle); at the section of 15mm away from the nozzle, the radial temperature decreases faster, the temperature is lower at the position nearer the boundary, at  $t=2\text{ms}$  the temperature is 1260K, 900K and 760K at the radial position of 0mm, 3mm and 6mm of the section 15mm away from the nozzle respectively.

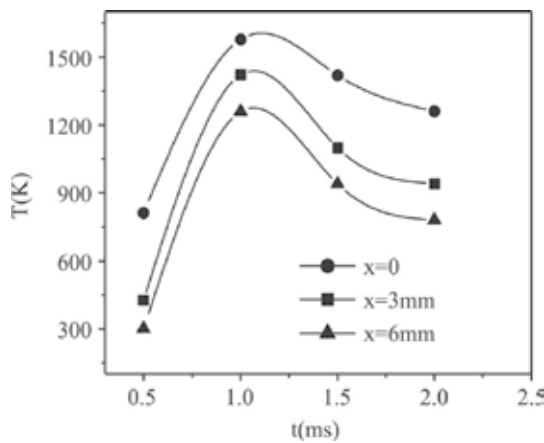


Fig. 24. Changing of radial temperature with time

Through the isothermal, the Taylor cavity expansion displacement of plasma jet at different time can be got. Figure 25 shows the compare of the simulated value with the experimental results shown in figure 12(b). As shown in the figure, they mach well with each other.

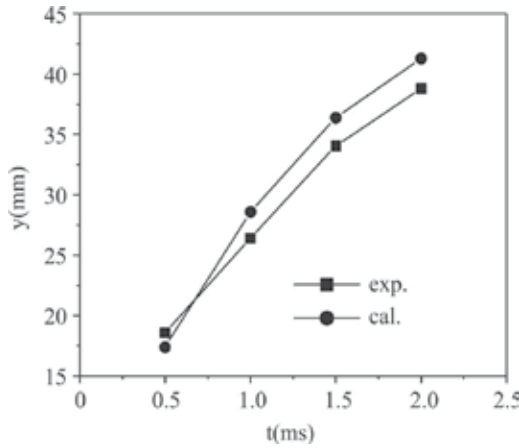


Fig. 25. Compare of the experiment and the calculated value of the Taylor cavity

**7.2 Numerical results of the cylindrical boundary shape**

The simulated conditions are as follows: The capacity of the capacitors is  $45 \mu f$ , the charging voltage is 2300V, and the nozzle diameter is 2.5mm. The diameter of the cylindrical chamber is 26mm and its total length is 107mm. The liquid medium is water.

1. The pressure distribution

Figure 26 shows the isobars of the plasma jet in cylinder chamber, the vertical ordinate is pressure and the unit is Pa. The pressure gradient is higher and the isobars are dense on the interface of the plasma jet and the liquid. There is a larger high pressure region in a tapered shape in front of the jet head. It grows and moves forward gradually. The expansion velocity in axial direction is larger than that in radial direction and the low pressure region forms at the boundary of the chamber which can be seen in the figure.

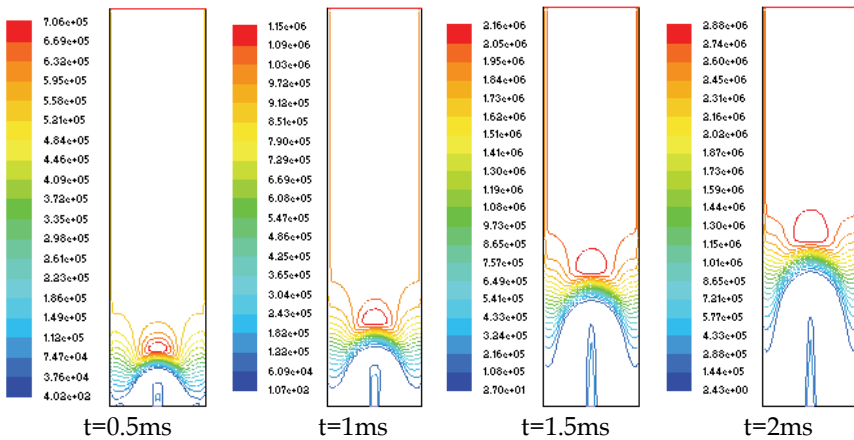


Fig. 26. Isobars of the plasma jet in liquid in cylinder chamber

Compared with the stepped-wall structure, the isobars distribution are different, especially the high pressure region's shape. The high pressure region moves keeping a tapered shape in the cylindrical chamber. While in the stepped-wall chamber, the high pressure region is in a cone frustum shape, the high pressure region expands along the radial direction and there is low pressure region both at the boundary and the steps due to the entrainment of the stepped-wall shape.

2. The velocity distribution

The isovels distributions of the plasma jet expansion in the liquid in the cylindrical chamber are shown in figure 27 (vertical ordinate is velocity, unit: m/s).

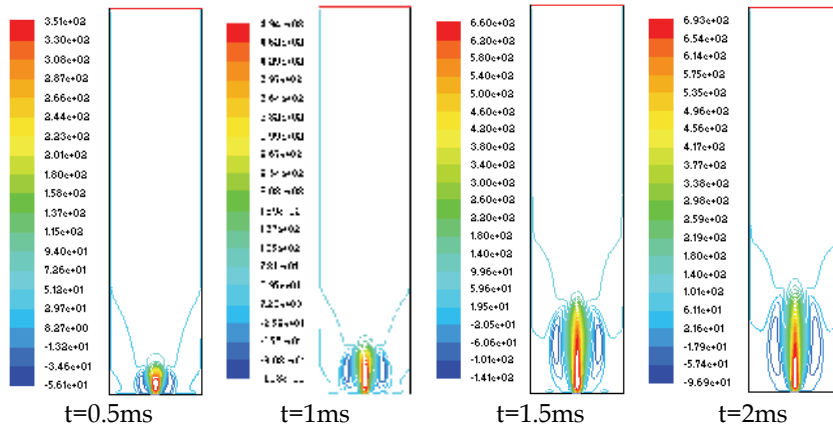


Fig. 27. Isovels of the plasma in the liquid in cylinder chamber

In the cylindrical chamber, the isovels are dense near the nozzle and the largest velocity is on the axis. The reverse flow forms around the largest velocity region. The reverse flow region grows during the expansion. And there is great disturbance on the gas-liquid interface.

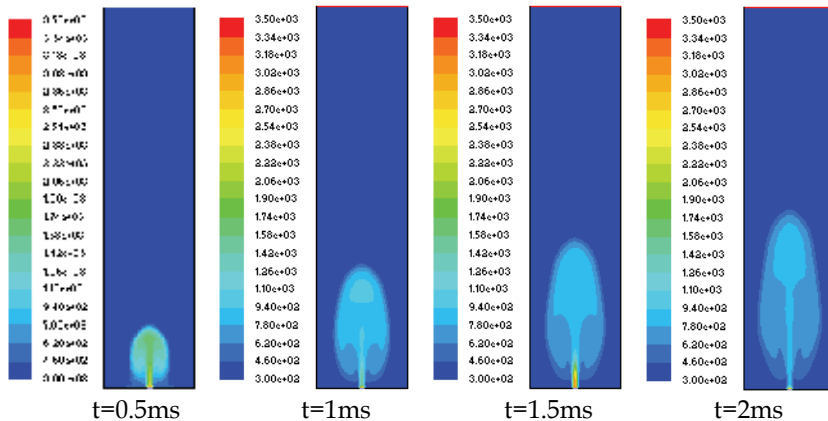


Fig. 28. Isotherms of the plasma jet in the liquid in cylinder chamber

Compared with the stepped-wall chamber, the isovels are denser near the axis and the velocity gradient is bigger on the gas-liquid interface. Due to the radial induction of the

steps in the stepped-wall chamber, the jet momentum diffuses along the radial direction of steps. The isovels' gradient of the jet head is lower at the steps.

### 3. The temperature distribution

Figure 28 shows the isotherms of the plasma jet during the expansion in the stepped-wall chamber, the vertical ordinate is temperature and the unit is K. As can be seen in the figure, in the cylindrical chamber, the axial expansion of the jet is obvious and the radial expansion is slower relatively. There is a tapered isothermal region at the head of the jet and it moves forward. The temperature at the nozzle is highest and it reduces quickly along the axial direction. Compared with the stepped-wall chamber, the temperature decreases more easily along the axial direction in the cylinder chamber.

According to the isotherm, the expansion displacement of the Taylor cavity can be acquired. Figure 29 shows the comparisons between the numerical simulation results and the experimental results. They coincide well with each other.

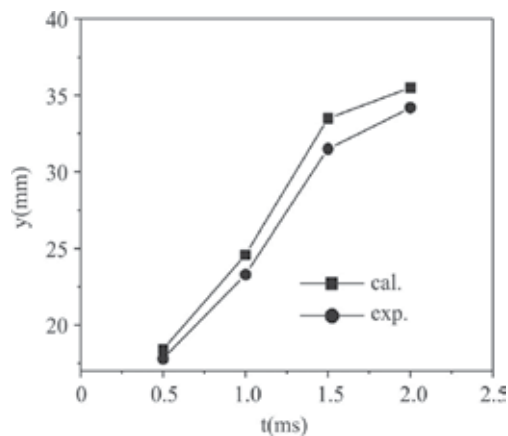


Fig. 29. Compare of the experiment and the calculated value of the Taylor cavity's displacement

## 7.3 Numerical results of different discharge voltages

According the experimental condition as show in figure 12, the stepped-wall structure is: the nozzle diameter is 2.5mm, the capacity of the capacitor group is  $45\mu F$ , and the discharge voltage is 2000V, 2300V and 2500V respectively. And the discharge jet energy is 36J, 48J and 56J respectively taking the conversion efficiency of the pulse electrical source is about 40% into account. At these conditions, the effects of different discharge voltage on the plasma jet are simulated.

### 1. The pressure distribution

Figure 30 shows the isobars of the plasma jet on different discharge voltage, the vertical ordinate is pressure and the unit is Pa. As shown in the figure, the larger is the discharge voltage, the earlier the pressure centre of the jet head forms in a cone frustum shape, and the pressure value at the centre is larger. The discharge voltage in figure 30 (a) is the least and there is no obvious pressure centre in 2ms. In figure 30 (b), there is a cone frustum pressure centre at  $t=1.5ms$  and the high pressure value is 1.80MPa. While in figure 30 (c), the cone frustum pressure centre forms as  $t=1ms$  and the high pressure value is 2.05MPa. Otherwise, in figure 30 (c), due to the radial expansion, the cone frustum pressure centre is stretched, there are two small pressure centres at the 2<sup>nd</sup> step and move according the boundary of step.

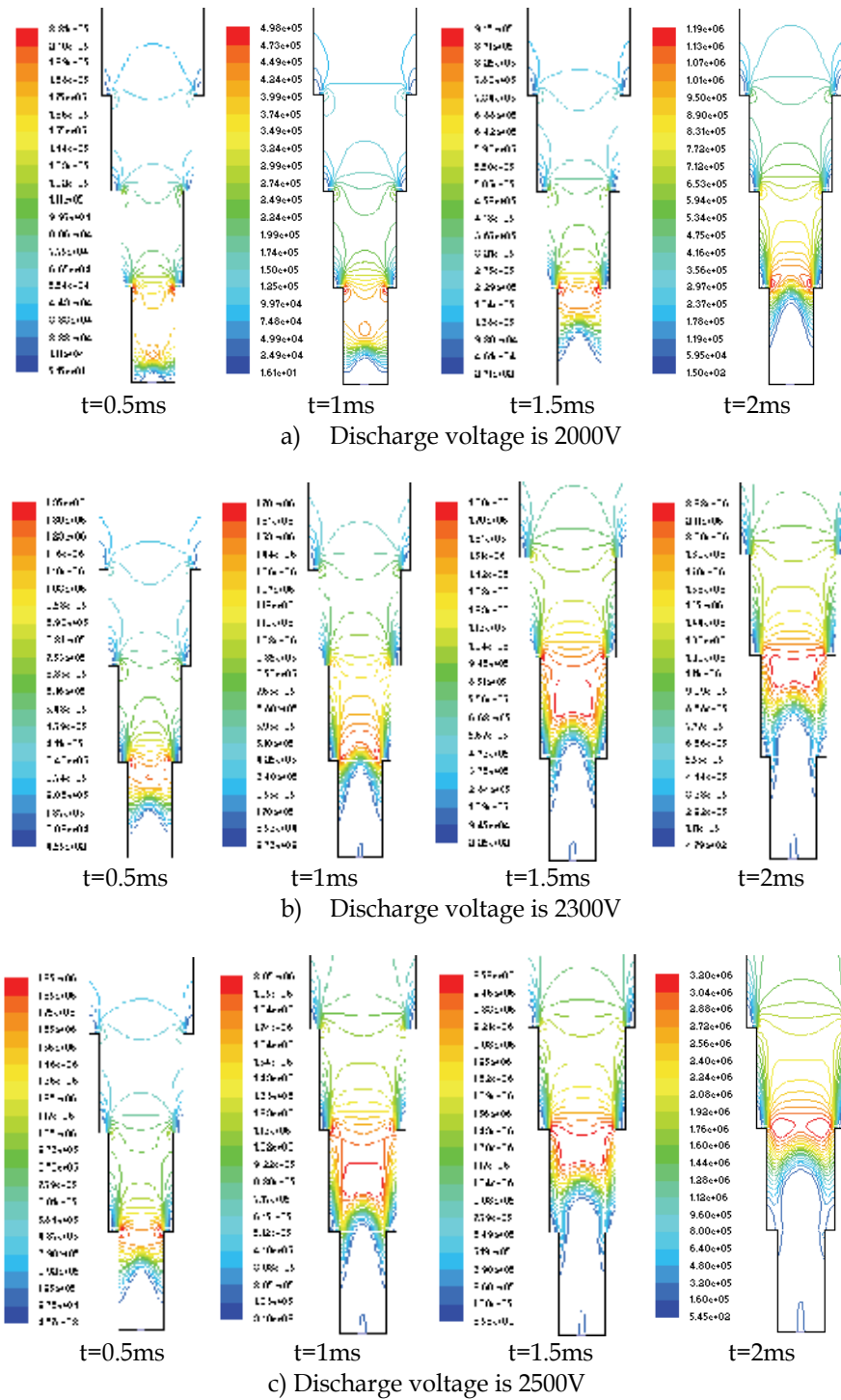
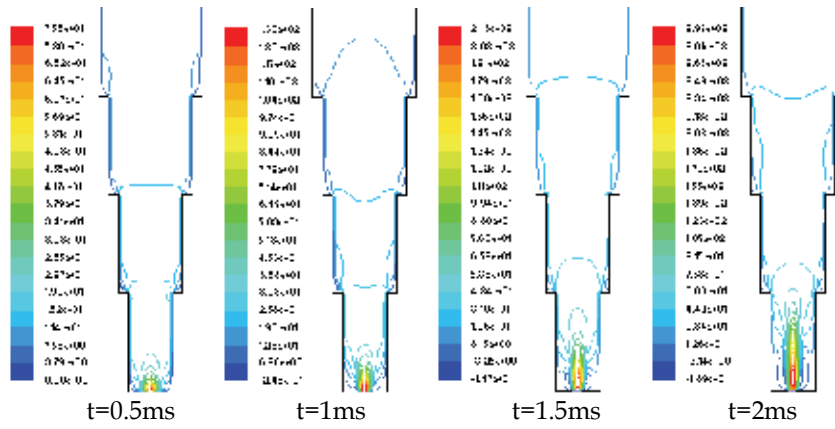
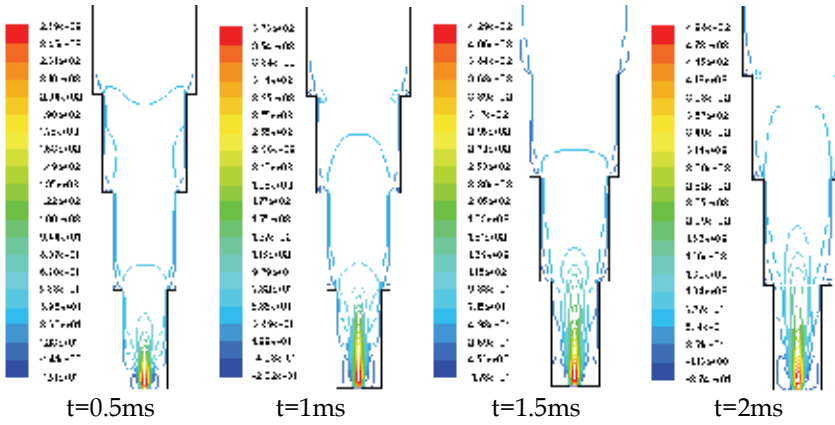


Fig. 30. Isobars of the plasma jet at different discharge voltages

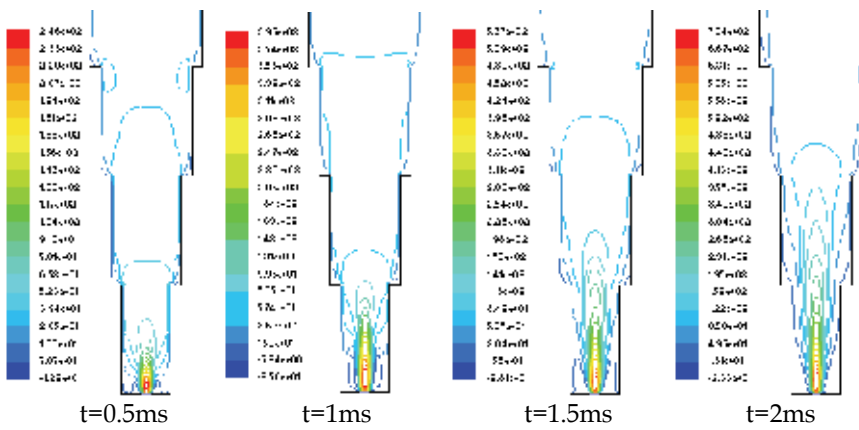
2. The velocity distribution



a) Discharge voltage is 2000V

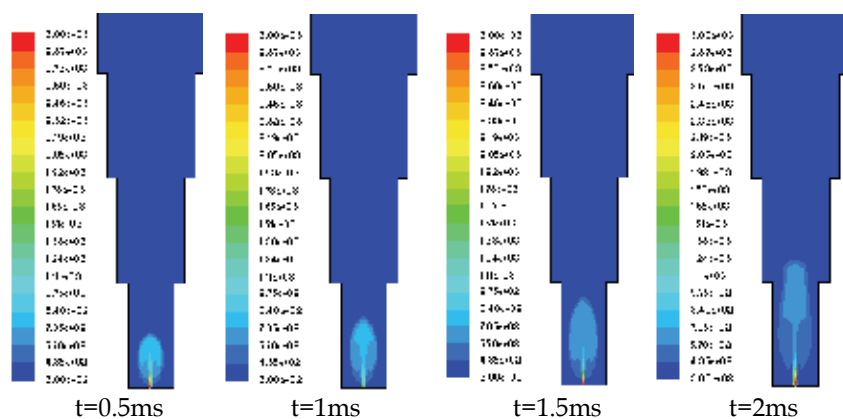


b) Discharge voltage is 2300V

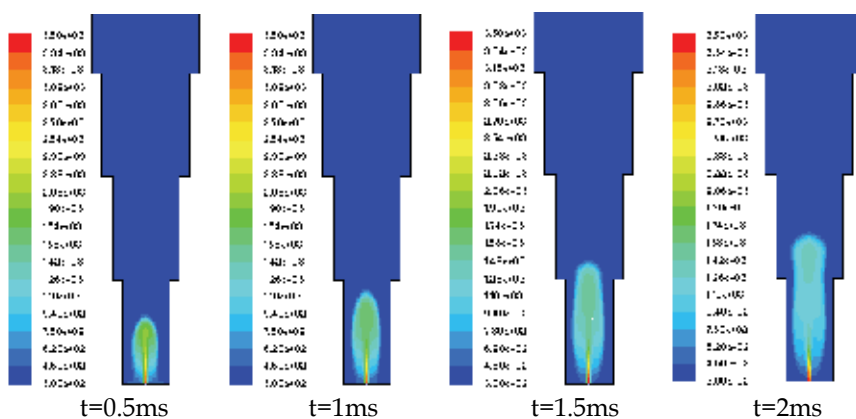


c) Discharge voltage is 2500V

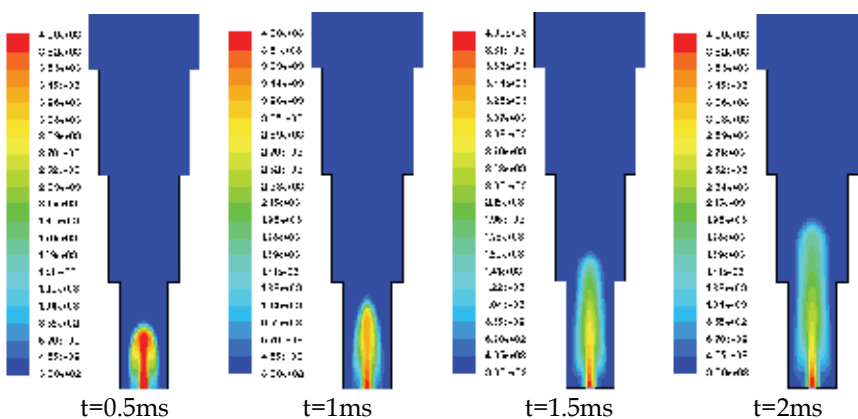
Fig. 31. Isovels of the plasma jet at different discharge voltages



a) Discharge voltage is 2000V



b) Discharge voltage is 2300V



c) Discharge voltage is 2500V

Fig. 32. Isotherms of the plasma jet at different discharge voltages

Figure 31 shows the isovels of the plasma jet, the vertical ordinate is velocity and the unit is m/s. As shown in the figure, the larger is the discharge voltage, the expansion of the region which has the biggest jet velocity is faster. At  $t=1.5\text{ms}$ , the biggest velocity region expand to 15mm away from the nozzle in figure 31(a), 30mm away from the nozzle in figure 31 (b) and about 35mm away from the nozzle in figure 31 (c). The larger is the discharge voltage, the isovels are denser near the jet core, the velocity gradient is larger on the gas-liquid interface, the bottom reverse flow region forms earlier and attenuation is also faster. In figure 31(c), there are no obvious reverse flow isovels at  $t=2\text{ms}$ .

### 3. The temperature distribution

Figure 32 shows the isotherms of the plasma jet at different discharge voltages, the vertical voltage is temperature and the unit is K. As shows in the figure, the larger is the discharge voltage, the higher is the temperature at the nozzle and the temperature increases faster, the high temperature region in figure 32(c) is more obvious; the larger is the discharge voltage, the slower is the heat dissipation of the jet.

Take the temperature change at the position 20mm away from the nozzle for example to illustrate the effect of the discharge on the temperature. At  $t=1.5\text{ms}$ , in figure 32(a), the temperature is 970K, the temperature is 1530K in figure 32 (b) at the same time which is 1.6 times to the value in figure 32 (a), and the temperature is 3320K in figure 32(c) at  $t=1.5\text{ms}$  which is 3.3 times to the value in figure 32 (a).

## 8. Conclusions

The experiment and the theoretical study of the expansion characteristics of the plasma jet both in atmosphere and the bulk-loaded liquid medium are mainly discussed in this chapter. The expansion processes of the plasma jet are recorded by the high speed camera system, and the effects of the discharge energy and the chamber structures on the plasma jet expansion processes are analysed. Two-dimensional axial symmetry model of the interaction between the plasma jet and the liquid medium are proposed based on the experiment and the simulations are conducted. The change characteristics of pressure, temperature and velocity in the jet flowfield are got. According to the experiment and the simulation results, the following conclusions can be got:

1. During the expansion of the plasma jet in atmosphere, the shape of jet head changes from ellipsoid to taper as the going of the expansion. The brightness of the jet enhances at first then decays. The jet head is brightest. The axial and the radial expansion velocity both have a fluctuation and the axial velocity is larger than the radial one. The later peak is lower than the former one which can be seen from the distribution of the axial velocity changing with time.
2. As soon as the plasma eject into the atmosphere, there is a sphericity pressure wave at the nozzle exit. As the going of the expansion, the pressure wave moves and attenuates quickly. The pressure alternates from high to low at the initial expansion stage.
3. There is intense turbulence dissipation during the expansion of the plasma jet in atmosphere. The jet head is in drape shape at first and the turbulence is strengthened as the gonging of the expansion, the turbulence mixture region grows. The larger is the discharge voltage, the greater is the plasma jet initial expansion velocity, and the reverse flow entrainment and dissipation are more intense. While the relationship between the axial displacement of the plasma jet and the discharge voltage is not monotony and there is a critical discharge voltage.

4. As the plasma jet into the liquid, the initial expansion velocity of the Taylor cavity is higher. As the Taylor cavity moves downwards, the velocity decreases and the axial velocity is larger than the radial one. The lightness of the jet head decays as the jet develops to some stage which is caused by the water vapor and the temperature decreases. There is intense heat and mass transfer between the plasma and liquid on the Taylor cavity surface.
5. The structure of the inspection chamber affects the shape and expansion velocity of Taylor cavity. The radial disturbance of the boundary structure to the plasma jet in stepped-wall chamber is higher than that in the cylinder chamber. There is subsection phenomenon during the plasma expansion and the lower is the plasma jet energy, the earlier is the subsection shows which cannot be seen in the cylinder structure.
6. The high pressure region of plasma jet head moves keeping the taper shape in the cylinder chamber; while in stepped-wall chamber, the high pressure is in cone frustum shape at initial, and the high pressure expands along the radial due to the radial entrainment of the steps, there are two small pressure center and moves towards the steps. The larger is the discharge voltage, the higher is the kinetic pressure at the jet axis and the pressure gradient is bigger.
7. The isovels are dense near the nozzle and the jet core, the velocity gradient is larger on the interface. The further away from the nozzle, the smaller is the velocity. The velocity at the axis is highest. There is reverse flow near the jet core which has the biggest velocity and the reverse flow region grows as time goes on. There is also reverse flow at the step corner in the stepped-wall structure, and the minus velocity occurs.
8. In cylinder chamber, the isotherms of plasma jet head moves keeping in taper shape while in blunt body shape in the stepped-wall chamber. The axial temperature is higher than the radial one. The temperature decreases rapidly as the going of the jet. The larger is the discharge voltage, the higher is the temperature near the nozzle and the temperature at the axis increases faster.

## 9. Acknowledgement

This work is supported by National Nature Science Foundation of China (No.50776048).

## 10. References

- Arensburg, A. (1993). X-ray diagnostics of a plasma-jet-liquid interaction in electrothermal guns. *Journal of Applied Physics*, Vol. 5, No. 73, (1993), pp. 2145-2154, ISSN 0021-8979
- Chang, L M. & Howard, S L. (2007). Influence of Pulse Length on Electrothermal Plasma Jet Impingement Flow. ARL-TR-4348
- Guo, H B.; Liu, D Y. & Zhou, Y H. (2007). Experimental Study of Pulsed Discharge Property of Plasma Generator. *Journal of Nanjing University of Science and Technology(Natural Science)*, Vol. 4, No. 31, (2007), pp. 466-469, ISSN 1005-9830
- Hsiao, C.; Phillips, G. & Su, F. (1993). A Numerical Model for ETC Gun Interior Ballistics Applications. *IEEE Transaction on Magnetics*, Vol. 1, No. 29, (1993), pp. 567-572, ISSN 0018-9464
- Kim, H J. & Hong, S H. (1995). Comparative Measurements on Thermal Plasma Jet Characteristics in Atmospheric and Low Pressure Plasma Sprayings. *IEEE Transactions on Plasma Science*, Vol. 5, No. 23, (1995), pp. 852-858, ISSN 0018-9464

- Kim, J U. & Suk, H. (2002). Characterization of High-density Plasma Produced by Electro-thermal Capillary Discharge. *Applied Physics Letters*, Vol. 3, No. 80, (2002), pp. 368-370, ISSN 0003-6951
- Kuo K.K., Cheung, F B., & Hsieh, W H. (1990). Experiments study of plasma/fluid interaction in a simulated CAP gun, *27th JANNAF combustion subcommittee meeting*, pp.365-375, Maryland, USA, 1990(1)
- Li, X Q. ; Hong, Y J. & He, G Q. (2010). Reviews of the Propulsive Characteristics Study on Liquid Propellants for Laser Propulsion. *Journal of Propulsion Technology*, Vol. 1, No. 31, (2010), pp. 105-110, ISSN 1001-4055
- Robert, H F.(2003). Advanced Space Propulsion for the 21st Century. *Journal of Propulsion and Power*, Vol. 6, No. 9, (2003) , pp.1129-1154, ISSN 0748-4568
- Rott M. , Artelt C. & Höschel T. (2005). Experimental Investigation of Hypervelocity Plasma Jets Generated with a Coaxial Arc Device. *IEEE Transactions on Magnetics*, Vol. 1, No. 41, (2005), pp. 220-225, ISSN 0018-9464
- Taylor, M J. (2001). Measurement of the Properties of Plasma from ETC Capillary Plasma Generators. *IEEE Transactions on Magnetics*, Vol. 1, No. 37, (2001), pp. 194-198, ISSN 0018-9464
- Weidong, S. (2004). Active Electrospray Ionization for Efficient Electric Thrusters. AIAA 2004-3942, 2004
- Wilson, D E. & Kim, K J. (1999). Theoretical Analysis of an External Pulsed Plasma Jet. *IEEE Transaction on Magnetics*, Vol. 1, No. 35, (1999), pp. 228-233, ISSN 0018-9464
- Yu, Y G. , Yan S H. & Zhao N. (2009) Influence of Boundary Shape on Interaction Process of Plasma Jet and Liquid Media, *Proceedings of the 14th International Symposium on Applied Electromagnetics and Mechanics*, pp. 197-198, Xian, China, 2009.9, ISBN 978-4-931455-14-6
- Yu, Y G. ; Yan, S H. ; Zhao, N. et al. (2009). Experimental Study and Numerical Simulation on Interaction of Plasma Jet and Liquid media, *2009 Asia-Pacific Power and Energy Engineering Conference*, pp. 3750-3754, Wuhan, China, 2009.3, ISBN 978-1-4244-2487-0
- Zhang, Q. ; Yu, Y G. ; Lu, X. et al. (2009). Study on Propagation Properties of Plasma Jet in Atmosphere, *Proceedings of the 2009 International Autumn Seminar on Propellants, Explosives and Pyrotechnics*, pp. 463~468, Kunming, China, 2009.9, ISBN 978-7-03-025394-1
- Zhou, Y H. ; Liu D Y. & Yu Y G. (2003). Expansion characteristics of transient plasma jet in liquid. *Journal of Nanjing University of Science and Technology (Natural Science)*, Vol. 5, No. 27, (2003), pp. 525-529, ISSN 1005-9830



*Edited by Lutz Angermann*

This book will interest researchers, scientists, engineers and graduate students in many disciplines, who make use of mathematical modeling and computer simulation. Although it represents only a small sample of the research activity on numerical simulations, the book will certainly serve as a valuable tool for researchers interested in getting involved in this multidisciplinary field. It will be useful to encourage further experimental and theoretical researches in the above mentioned areas of numerical simulation.

Photo by Mike\_Kiev / iStock

**IntechOpen**

